JOHANNES GUTENBERG UNIVERSITÄT MAINZ

JG|U

CATALIGHT

Embedding Molecular Light-Driven Catalysts in Soft Matter

Kumulative Dissertation zur Erlangung des Grades
"Doktor der Naturwissenschaften"
Dr. rer. nat.
im Promotionsfach Chemie

am Fachbereich Chemie, Pharmazie,
Geographie, und Geowissenschaften
der Johannes Gutenberg-Universität Mainz

Vorgelegt von
M.Sc. Marcel Langer
geboren in Aalen

Mainz, 2025

CC BY 4.0

Amtierende Dekanin von dem Department Chemie:

[redacted]

Betreuer/Erstgutachter:

[redacted]

Zweitgutachterin:

[redacted]

Tag der mündlichen Prüfung:

*~ Nothing in life is worthwhile unless you take risks. **Fall forward.** Every failed experiment is one step closer to success. ~*

Denzel Washington

Abstract

Sustainable energy conversion of solar radiation into productive chemical reactivity can be implemented by heterogeneous light-driven catalysis. Here we report progress in the development of two separate hierarchically structured soft matter composites consisting of porous polymeric supports, electrostatically embedded with molecular thiomolybdate or polyoxometalate (POMs) catalysts and model molecular photosensitizers. We demonstrate the use of these composites for the light-driven hydrogen evolution reaction (HER) and water oxidation catalysis (WOC), respectively.

First, we discuss recent advances in thiomolybdate chemistry, emphasizing that any newly developed multifunctional material must be critically assessed, as the identification of active sites and HER mechanisms is highly dependent on heterogenization and precise reaction conditions. Deposition strategies for thiomolybdates and their pioneering and emergent applications, particularly in electro- and photocatalysis, are further outlined.

We then highlight the challenges and benefits of complementary and valuable analytical tools in evaluating the structural integrity, stability and reactivity of POMs embedded in soft matter matrices. In addition, we provide a synopsis of the key principles of soft matter chemistry, their hybridization strategies with POMs and their potential applications.

Next, we present the visible light-driven water oxidation activity of novel nanoporous block copolymer membranes. Multimodal *in situ*, *operando* and *ex situ* analyses of the so-called “WOCbranes” showed a uniform and stable distribution of photosensitizer and catalyst on the micro- and macroscale. However, variations in the O_2 evolution rates were also observed, indicating inhomogeneities in the pore size distribution within the matrix.

We also recite the preparation, optimization and functionalization of stimuli-responsive polyampholytic hydrogels for light-driven HER and WOC. Despite the difficulties in maintaining the mechanical integrity of the hydrogel scaffold under oxidative conditions, we unveil a positive effect of the polymer environment on photoactivity and stability of the molecular building blocks under optimized catalytic conditions and infer an attractive approach for self-repair of the dye mediated by reversible electrostatic interactions.

Finally, a comprehensive outlook delineates prospective research directions, focusing on the challenges that arise when ruthenium polypyridyl-based chromophores are used in organic and aqueous solvent mixtures to drive photocatalysis.

Zusammenfassung

In der vorliegenden Arbeit wird die nachhaltige Energieumwandlung von Sonnenstrahlung in produktive chemische Reaktivität durch heterogene lichtgetriebene Katalyse untersucht. Zu diesem Zweck entwickelten wir zwei unterschiedliche hierarchisch strukturierte Weichstoffkomposite auf der Basis von porösen Polymeren, die elektrostatisch mit molekularen Thiomolybdat- oder Polyoxometallat-Katalysatoren (POMs) sowie molekularen Modell-Photosensibilisatoren funktionalisiert wurden, und demonstrieren ihre Verwendung für die lichtgetriebene Wasserstoffentwicklungsreaktion (HER) bzw. Wasseroxidationskatalyse (WOC).

Zunächst werden die jüngsten Fortschritte in der Thiomolybdat-Chemie untersucht. Dabei wird die Notwendigkeit einer kritischen Bewertung neu entwickelter multifunktioneller Materialien betont, da die Identifizierung aktiver Stellen und HER-Mechanismen stark von der Heterogenisierung und den präzisen Reaktionsbedingungen abhängt. Außerdem werden Abscheidungsstrategien für Thiomolybdate und ihre bahnbrechenden und vielversprechenden Anwendungen erörtert. Der Fokus liegt hierbei auf den Bereichen der Elektro- und Photokatalyse.

Die Herausforderungen und Vorteile wertvoller, sich ergänzender Analyseinstrumente zur Bewertung der strukturellen Integrität, Stabilität und Reaktivität von POMs, die in Weichstoffmatrizen eingebettet wurden, werden danach erläutert. Darüber hinaus geben wir einen Überblick über die wichtigsten Prinzipien der Chemie weicher Materie, ihre Hybridisierungsstrategien mit POMs und deren potenzieller Anwendungen.

Im Anschluss stellen wir die durch sichtbares Licht angetriebene Wasseroxidationsaktivität neuartiger nanoporöser Blockcopolymer-Membranen vor. Multimodale *in situ*, *operando* und *ex situ* Analysen der sogenannten „WOCbranes“ zeigten auf der Mikro- und Makro-Skala eine homogene und stabile Verteilung von Photosensibilisator und Katalysator. Jedoch wurden auch Variationen in den O_2-Entwicklungsraten beobachtet, was auf Inhomogenitäten in der Porengrößenverteilung innerhalb der Matrix hindeutet.

Darüber hinaus beschreiben wir die Herstellung, Optimierung und Funktionalisierung von stimulierungs-responsiven Polyampholyt-Hydrogelen für die lichtgesteuerte HER und WOC. Trotz bestehender Schwierigkeiten die mechanische Integrität des Hydrogel-Gerüsts unter oxidativen Bedingungen aufrechtzuerhalten, konnte ein positiver Effekt der Polymerumgebung auf die Photoaktivität und Stabilität der molekularen Bausteine unter optimierten katalytischen Bedingungen festgestellt werden. Außerdem konnte anhand unserer Beobachtungen ein attraktiver Ansatz für die Selbstreparatur des Farbstoffes durch reversible elektrostatische Wechselwirkungen abgeleitet werden.

Abschließend werden in einem umfassenden Ausblick künftige Forschungsrichtungen aufgezeigt, wobei der Schwerpunkt auf den Herausforderungen liegt, die sich ergeben, wenn Chromophore auf Ruthenium-Polypyridyl-Basis in organischen und wässrigen Lösungsmittelgemischen zum Antrieb der Photokatalyse verwendet werden.

Table of Contents

Abstract ..... **V**

Zusammenfassung ..... **VII**

Table of Contents ..... **IX**

List of Figures ..... **XI**

List of Tables ..... **XIII**

List of Abbreviations ..... **XV**

List of Compounds ..... **XIX**

Notation ..... **XIX**

Scientific Contributions ..... **XXI**

List of Publications in Peer-Reviewed Journals XXI

Conferences and Conference Contributions XXIII

Research Visit XXIII

1. Introduction **1**

1.1 Status Quo of the Global Energy Budget 1

1.2 Biomimicry – Nature-Inspired Design 5

1.3 Nature as an Inspiring Role Model 9

1.3.1 Biological Photosynthesis 9

1.3.2 Hydrogen-Evolving Enzymes 17

1.4 Artificial Photosynthesis 20

1.4.1 General Overview 20

1.4.2 Detailed Insights into an Artificial Photosystem 23

1.5 Photochemistry of the Molecular Chromophore $[Ru(bpy)_3]^{2+}$ 30

1.6 Polyoxometalate Chemistry 37

1.6.1 Structural Diversity 38

1.6.2 Self-Assembly in Aqueous Solution 44

1.6.3 Applications of POMs – WOC Activity 47

1.7 Thiomolybdate Chemistry 50

1.7.1 Applications of Thiomolybdates – HER Activity 52

1.8 From Homogeneous to Heterogeneous Photocatalysis 56

1.8.1 Soft Matter Composites 59

2. Objective 63

3. Results and Discussion 67

3.1 Active Sites of Thiomolybdates – {MLa-4} 71

3.2 Characterization of POM-Soft Matter Composites – {MLa-1} 76

3.3 POM-functionalized Membranes for WOC – {MLa-2} 80

3.4 Photoactive Hydrogels – {MLa-5} 86

4. Summary and Perspectives 93

4.1 Photodegradation of $[Ru(bpy_3)]^{2+}$ in Organic Solvents – {MLa-6} 110

5. References 115

6. Publications 137

6.1 {MLa-1}: Polyoxometalate-Soft Matter Composite Materials: Design Strategies, Applications, and Future Directions 137

6.2 {MLa-2}: Multimodal Analysis of Light-Driven Water Oxidation in Nanoporous Block Copolymer Membranes 157

6.3 {MLa-4}: Thiomolybdate Clusters: From Homogeneous Catalysis to Heterogenization and Active Sites 181

6.4 {MLa-5}: Poly(dehydroalanine)-Based Hydrogels as Efficient Soft Matter Matrices for Light-Driven Catalysis 205

6.5 {MLa-6}: *In situ* Formation of an Active Oxygen Evolution Catalyst *via* Photodegradation of $[Ru(bpy)_3]^{2+}$ 235

Acknowledgement 265

Declaration of Honesty in Academic Work 267

Curriculum Vitae 269

List of Figures

1.1 Fuel type-specific primary energy consumption in the year 2023 1
1.2 Representation of renewable energy sources 2
1.3 A perspective green footprint towards a sustainable hydrogen economy 4
1.4 Design thinking strategies 7
1.5 A proactive, modified design thinking scheme as a guide for this work 8
1.6 *Z*-scheme of electron transport in natural photosynthesis 10
1.7 Förster resonance energy transfer (FRET) and oxidative electron transfer 11
1.8 The natural oxygen-evolving complex (OEC) 12
1.9 Simplified scheme of the classic Kok cycle for the OER mechanism in nature .. 14
1.10 I2M and WNA mechanisms 15
1.11 The enzymatic HER active site cofactors 19
1.12 Redox reaction and thermodynamics of water splitting 21
1.13 A homogeneous, molecular approach to artificial photosystems 22
1.14 HER mechanisms: Volmer-Heyrovsky and Volmer-Tafel pathways 24
1.15 Simplified Jablonski diagram 31
1.16 Reactivity of the photoexcited state 32
1.17 $[Ru(bpy)_3]^{2+}$: UV-Vis absorption spectrum and simplified MO diagram 33
1.18 Photophysical properties and photochemical redox processes of $[Ru(bpy)_3]^{2+}$ ... 35
1.19 Possible decomposition pathway of oxidized $[Ru(bpy)_3)]^{3+}$ 36
1.20 Different connection modes between polyhedral units in POMs 38
1.21 Common POM clusters 40
1.22 The five rotational isomeric structures of the Keggin anion 41
1.23 Structural diversity of POMs 43
1.24 Proposed mechanism for the self-assembly of POMs 45
1.25 Synthesis of an Iso-POM and formation of the Keggin anion 46
1.26 POM-OECs and comparison of their light-driven WOC activity 49
1.27 The two prototype thiomolybdate clusters $\{Mo_3\}$ and $\{Mo_2\}$ 50
1.28 Oxothiomolybdate clusters: $[Mo_2O_2(\mu\text{-}S)_2(S_2)_2]^{2-}$ and $[Mo_2O_2(\mu\text{-}S)_2(S_2)(S_4)]^{2-}$.. 52
1.29 Homogeneous light-driven HER of $\{Mo_3\}$ 54
1.30 Homogeneous, heterogeneous and heterogenized molecular photosystems 58
1.31 POM-polymer hybrids with divergent chain configurations 61

1.32 Overview of 1D-3D POM-polymer hybrid architectures 62

2.1 Approaches used in this work: literature-based and experimental studies.....65

3.1 Possible active sites of {Mo_3} and proposed HER mechanisms.....72
3.2 Illustration of the functionalized nanoporous block copolymer membrane.....80
3.3 Membrane functionalization under batch conditions to form WOCbranes 81
3.4 Characterization of the WOCbranes by STEM/EDX 82
3.5 Light-driven *operando* OER studies of the WOCbranes 83
3.6 Stability studies on the WOCbranes using μXRF and ATR-IR.....84
3.7 Synthesis route to obtain PDha-based hydrogels 86
3.8 Characterization of PDha-based hydrogels by ^{13}C CP-MAS NMR and FTIR 87
3.9 Swelling properties of PDha-based hydrogels 88
3.10 Attachment of $[Ru(bpy)_3]^{2+}$ to PDha-based hydrogels.....89
3.11 PDha-based hydrogel performance as PS in light-driven HER and WOC 91

4.1 Summary of this work.....93
4.2 Soft matter composite membrane of the 2nd generation.....97
4.3 Soft matter composite membrane of the 3rd generation 98
4.4 Proposed chemical structure of the synthesized PS-catalyst dyad.....100
4.5 (Post-)organofunctionalization of {Mo_3} by 3,4-dimercaptobenzaldehyde 101
4.6 The notion of solid-state frameworks composed of molybdenum sulfides 103
4.7 General chemical structures of the PSs perylene monoimide and BODIPY 104
4.8 Advanced analytical tools for the study of molecular light-driven catalysis 106
4.9 Light-driven OER studies in the project {MLa-6}.....111
4.10 UV-Vis spectrum of the isolated green oily deposit obtained after OER.....112
4.11 Postulated reaction scheme for the formation of the WOC-active blue dimer ...113
4.12 Structurally related Ru polypyridyl PSs and their OER photoreactivity 114

List of Tables

i Overview of abbreviations used in this work ..... XV–XVII

ii Overview of POMs and thiometalates and their respective abbreviations XIX

3.1 Key (*in situ*/*operando*) techniques to study POMs in soft matter matrices 78

List of Abbreviations

Table i – Part 1 Overview of abbreviations used in this work.

Abbreviation	Description
μXRF	micro-X-ray fluorescence spectroscopy
AFM	atomic force microscopy
a-MoS_x	amorphous molybdenum sulfides
AscOH	ascorbic acid
ATP	adenosine triphosphate
ATR-IR	attenuated total reflection infrared spectroscopy
BODIPY	4,4-difluoro-4-bora-3a,4a-diaza-*s*-indacene
bpy	2,2'-bipyridine
CHN-EA	elemental analysis of carbon, hydrogen and nitrogen
CP-MAS	cross-polarization magic angle spinning
DFT	density functional theory
DMF	*N*,*N'*-dimethylformamide
DOE	design of experiments
DS	degree of swelling
DSC	dynamic scanning calorimetry
EDTA	ethylenediaminetetraacetic acid
EDX	energy-dispersive X-ray spectroscopy
EPR	electron paramagnetic resonance spectroscopy
FRET	Förster resonance energy transfer
FTIR	Fourier transform infrared spectroscopy
GHG	greenhouse gas
HDS	hydrodesulfurization
HEC	hydrogen-evolving catalyst
HER	hydrogen evolution reaction
HOMO	highest occupied molecular orbital
HR-CS-GFAAS	high resolution-continuum source-graphite furnace atomic absorption spectroscopy
HR-TEM	high-resolution transmission electron microscopy
I2M	interaction of two metal-oxo units

Table i – Part 2 Overview of abbreviations used in this work.

Abbreviation	Description
ICP-OES/AES	inductively coupled plasma optical/atomic emission spectroscopy
IEP	isoelectronic point
IR	infrared
ISC	intersystem crossing
LC	ligand-centered
LED	light-emitting diode
LMCT	ligand-to-metal charge transfer
LOD	limit of detection
LUMO	lowest unoccupied molecular orbital
MC	metal-centered
MD	molecular dynamics
MeCN	acetonitrile
MeOH	methanol
MLCT	metal-to-ligand charge transfer
MM	molecular mechanics
MO	molecular orbital
MOF	metal-organic framework
NADPH	nicotinamide adenine dinucleotide phosphate
NHE	normal hydrogen electrode
NMP	nitroxide-mediated polymerization
NMR	nuclear magnetic resonance spectroscopy
OAc^-	acetoxy group
OEC	oxygen-evolving complex
OER	oxygen evolution reaction
PCET	proton-coupled electron transfer
PCR	PDha-to-crosslinker ratio
PDha	poly(dehydroalanine)
PEGDGE	poly(ethylene glycol) diglycidyl ether
POM	polyoxometalate
PS	photosensitizer

Table i – Part 3 Overview of abbreviations used in this work.

Abbreviation	Description
PS*	excited state of the photosensitizer
PS-*b*-PDMAEMA	polystyrene-*block*-poly(2-(dimethylamino)ethyl methacrylate
(P)XRD	(powder) X-ray diffraction
QM	quantum mechanics
r.t.	room temperature
ROS	reactive oxygen species
Ru-PS	$[Ru(bpy)_3]^{2+}$
SECM	scanning electrochemical microscopy
SEM	scanning electron microscopy
SOA	sacrificial oxidizing agent
SOMO	singly occupied molecular orbital
SRA	sacrificial reducing agent
STEM	scanning transmission electron microscopy
TBA^+	tetra-*n*-butylammonium
*t*BAMA	*tert*-butoxycarbonylaminomethacrylate
TEA	triethylamine
TEOA	triethanolamine
TGA	thermogravimetric analysis
TOF	turnover frequency
TON	turnover number
TXRF	total reflection X-ray fluorescence analysis
UV-Vis	ultraviolet-visible spectroscopy
WNA	water nucleophilic attack
WOC	water oxidation catalysis
XPS	X-ray photoelectron spectroscopy

List of Compounds

Table ii Overview of the polyoxometalate and thiometalate compounds mentioned in this work and their respective abbreviations.

Formula	Abbreviation
$[V_4O_{12}]^{4-}$	$\{V_4\}$
$[V_{10}O_{28}]^{6-}$	$\{V_{10}\}$
$[\{Ru_4(\mu\text{-}O)_4\text{-}(\mu\text{-}OH)_2(H_2O)_4\}(\gamma\text{-}SiW_{10}O_{36})_2]^{10-}$	$\{Ru_4\}$
$[Mn_4V_4O_{17}(OAc)_3]^{3-}$	$\{Mn_4V_4\}$
$[Co_4(H_2O)_2(\alpha\text{-}PW_9O_{34})_2]^{10-}$	$\{Co_4\}$
$[Mo_3S_{13}]^{2-}$	$\{Mo_3\}$
$[Mo_2S_{12}]^{2-}$	$\{Mo_2\}$

Notation

In the context of this work, the molecular clusters are designated according to the square bracket notation that is customary in thiometalate and polyoxometalate chemistry, *e.g.* $[Mo_3S_{13}]^{2-}$ or $[Co_4(H_2O)_2(\alpha\text{-}PW_9O_{34})_2]^{10-}$. To simplify nomenclature, enhance readability and to avoid extensive cluster formulas, an abbreviation with curly brackets has been introduced. The information displayed is limited to the number and type of metal centers in the cluster, *e.g.* $\{Mo_3\}$. This notation remains consistent in representing the complete formula of the cluster unit, inclusive of its charge. Polyoxometalates of the "sandwich type" are an exception to this rule. In this case, only the number of transition metal heteroatoms present in the cluster is denoted, as exemplified for $\{Co_4\}$.

Geometric coordination motifs are indicated by the notation in square brackets, *e.g.* $[MO_y]$ (M = *addenda* atom, y = 4-7). The specification of the corresponding charge is neglected, since only the provision of structural information on the polyhedral geometry is intended. For example, an octahedral subunit with six coordinating oxygen atoms to a metal center is referred to as $[MO_6]$. Furthermore, single and double bonds between metal and oxygen atoms are represented by M–O and M=O, respectively, and ligands bridging x metal centers are labeled by μ_x (*e.g.* the μ_2-oxo ligand represents an M–O–M bond).

Scientific Contributions

Research articles are of great importance for disseminating scientific advances to the public, including reports of new findings on past, present and future challenges and problems. Review articles offer a valuable opportunity to provide an overview of the state-of-the-art in a scientific field, communicate current research insights and highlight future research directions, taking into account the reconciliation and extension of previous research. In addition, summarizing a broad selection of scientific studies can uncover the significance and ramifications of interdisciplinary correlations, clarify definitional ambiguities or expose inconsistencies in previous publications. This critical assessment of key developments over an extensive time period facilitates easier access to this knowledge for other scientists and the development and shaping of new research ideas.[1,2]

Scientific conferences serve as a further platform for the discussion of advanced results with experts, the exchange of current research-based issues, the conceptualization of new frameworks and solutions, and the promotion of "thinking outside the box".

List of Publications in Peer-Reviewed Journals

The following reviews and research articles were published as a result of work undertaken during my years of study and in the course of this dissertation:

{MLa-1} "*Polyoxometalate-Soft Matter Composite Materials: Design Strategies, Applications, and Future Directions*", J.-H. Kruse,‡ M. Langer,‡ I. Romanenko, I. Trentin, D. Hernández-Castillo, L. González, F. H. Schacher,* C. Streb,* *Adv. Funct. Mater.* **2022**, *32*, 2208428.

DOI: 10.1002/adfm.202208428

{MLa-2} "*Multimodal Analysis of Light-Driven Water Oxidation in Nanoporous Block Copolymer Membranes*", J. Kund,‡ J.-H. Kruse,‡ A. Gruber, I. Trentin, M. Langer, C. Read, G. Neusser, D. Blaimer, U. Rupp, C. Streb,* K. Leopold, F. H. Schacher,* C. Kranz,* *Angew. Chem. Int. Ed.* **2023**, *62*, e202217196.

DOI: 10.1002/anie.202217196

{MLa-3} "*$PM_{2.5}$ at a semi-rural site near Beijing, China*", J. Boman,* M. Langer, X. Pei, S. Guo, R. K. Pathak, S. M. Gaita, M. Hu, M. Hallquist, *X-Ray Spectrom.* **2023**, *52*, 447-456.

DOI: 10.1002/xrs.3383

{MLa-4} "*Thiomolybdate Clusters: From Homogeneous Catalysis to Heterogenization and Active Sites*", S. Batool,‡ M. Langer,‡ S. N. Myakala, M. Heiland, D. Eder, C. Streb,* A. Cherevan,* *Adv. Mater.* **2024**, *36*, 2305730.

DOI: 10.1002/adma.202305730

{MLa-5} "*Poly(dehydroalanine)-Based Hydrogels as Efficient Soft Matter Matrices for Light-Driven Catalysis*", T. Çeper,‡ M. Langer,‡ N. Vashistha, B. Dietzek-Ivanšić, C. Streb, S. Rau, F. H. Schacher,* *Macromol. Rapid. Commun.* **2024**, *45*, 2300448.

DOI: 10.1002/marc.202300448

{MLa-6} "*In situ formation of an active oxygen evolution catalyst via photodegradation of $[Ru(bpy)_3]^{2+}$*", M. Langer, A. K. Mengele, R. Müller, J. C. Wetzel, J. Mayer, S. Rau,* C. Streb,* *Dalton Trans.* **2025**, *54*, 4861–4865.

DOI: 10.1039/d5dt00233h

Notes: All publications listed are discussed within this work (see chapter 3 and 4) and reprinted with the permission of the respective publisher (see chapter 6), with the exception of {MLa-3}, which is not part of this dissertation.

Authors who contributed equally to the respective publications and are therefore joint first authors of these works have been marked with the symbol "‡". The corresponding authors are indicated with an asterisk "*".

Conferences and Conference Contributions

The following conferences were attended during my doctoral studies and the corresponding scientific contributions were made:

19/07/2021 – 22/07/2021 **INPOMS EPSRC-JSPS C2C Conference (*Participation*)**
International Network on Polyoxometalate Science
digital

21/09/2022 – 23/09/2022 **INPOMS Electrochemistry Workshop (*Participation*)**
International Network on Polyoxometalate Science
Newcastle (United Kingdom)

11/04/2023 – 14/04/2023 **FMOCS VII Conference (*Research Flash Talk*)**
Frontiers in Metal Oxide Cluster Science
Title: "*Polyoxometalate-functionalized Membranes for Water Oxidation Catalysis*"
Tarragona (Spain)

25/07/2023 – 29/07/2023 **25th ISPPCC Conference (*Poster*)**
International Symposium on the Photochemistry and Photophysics of Coordination Compounds
Title: "*$[Mo_3S_{13}]^{2-}$: Reactivity Aspects, Active Sites and Heterogenization*"
Ulm (Germany)

Research Visit

During my doctoral studies, a three-month research stay in the group of [redacted] in the Department of Chemistry and Biochemistry at the University of California, San Diego (UCSD) in the USA was completed between October and December 2023 holding a German Academic Exchange Service (DAAD) scholarship. The focus was on the development of new energy storage materials.

1. Introduction

In what manner might a continuous energy supply be ensured without recourse to environmentally harmful technologies? Chapter 1.1 provides an analysis of the current global energy landscape, emphasizing the associated economic and social concerns, and proposes a possible solution to this problem. A corresponding biomimetic guideline is elaborated in chapter 1.2. Subsequently, the chapters 1.3 and 1.4 present the most salient principles observed in nature and an inspired design idea. The theoretical background of this approach is described in chapters 1.5–1.8 and complemented by selected examples from the state-of-the-art research.

1.1 Status Quo of the Global Energy Budget

In the 21st century, human society is confronted with pervasive trends of steady population growth and technological progress, concomitant with economic expansion and advancing industrialization. In this context, global energy consumption, which stood at *ca.* 77 GJ per capita in 2023, is projected to undergo an annual increase of approx. 1.3% over the next two decades. In the modern global energy economy, carbon or hydrocarbon-based energy sources, such as coal, natural gas and oil, persist to dominate with a share of over 80% (see Figure 1.1).[3–7] However, the extraction, processing and combustion of fossil fuels are associated with detrimental consequences for our ecosystem, including the

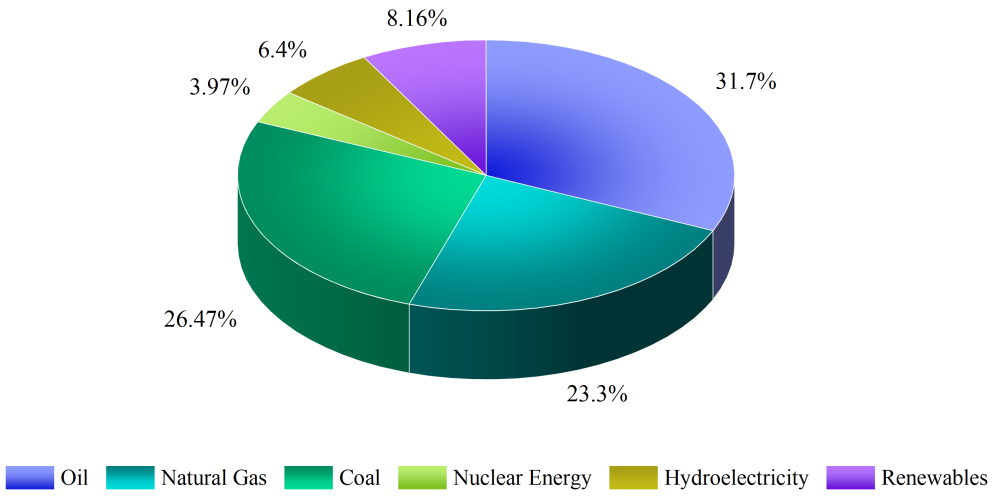


Figure 1.1 Fuel type-specific primary energy consumption in the year 2023. The data was adopted from the Energy Institute Statistical Review of World Energy 2024.[5]

emission of greenhouse gases (GHGs), which contribute to global warming, extreme weather events, uncontrollable sea level rise, air pollution and increased health risks.[8–11] In addition, given the finite nature of fossil feedstock reserves, a considerable depletion of accessible resources, *e.g.* mineral raw materials, is to be anticipated.[12,13]

As a result, a substantial societal awareness of a more environmentally sustainable future has emerged in recent years, coupled with a pronounced impetus for the development of renewable energy supply systems. In response to this current state of affairs, national and international governments, as well as numerous energy policy organizations, have set ambitious global climate targets.[14,15] For instance, the European Union is pursuing a strategy of net-zero CO_2 emissions by 2050, with the objective of limiting global warming to below 2 °C, as outlined in the Paris Agreement of 2015.[16] This commitment entails several policy implications, including the reduced reliance on fossil fuels and an increased financial support for the development of clean energy alternatives that have a minimal ecological impact and embody a sustainable, green anima.[17] Furthermore, the strategic investment in well-established large-scale renewable energy sources, such as wind farms, solar energy plants (*e.g.* photovoltaic modules), biomass technologies, hydropower systems and geothermal power plants is imperative (see Figure 1.2).[18,19]

However, the complete transition from fossil fuels to exclusively renewable energy systems is impeded by several factors, such as limited storage capacity, high costs of implementation, the need to preserve geopolitically mandated ecosystem services, and dependence on seasonality or weather conditions that prevent a continuous energy supply.[20,21] Therefore, the quest for effective and sustainable solutions must be expedited to circumvent the intermittent nature of renewable energy and draw up a balanced system

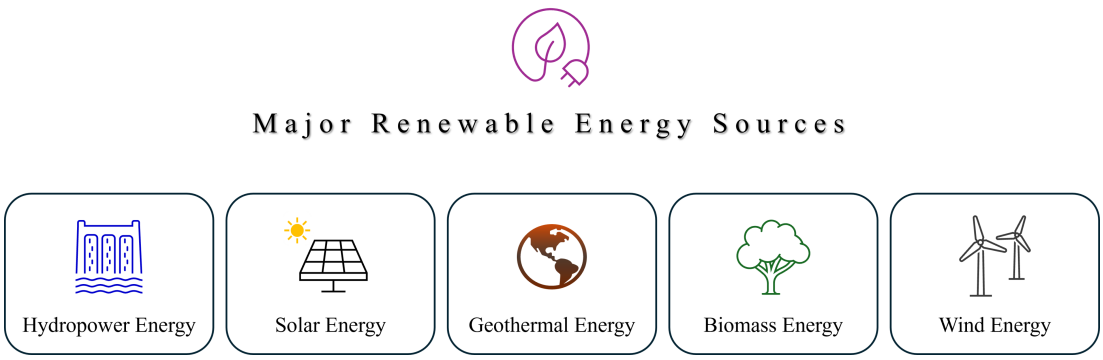


Figure 1.2 Schematic representation of various renewable energy sources, including hydropower, solar, geothermal, biomass and wind energy.[18,19]

for the management of energy generation, transportation, storage and consumption.[22] To this end, there is an ongoing pursuit of a suitable energy carrier that possesses a high intermediate storage capacity and enables the on-demand delivery of excess energy from an external source through an efficient transportation network.[23,24]

Hydrogen, for example, is an auspicious carbon-free fuel and at the same time a viable energy carrier. This molecule is defined by a low molecular weight and a high molar heat of combustion, leading to an exceptional gravimetric energy density of 120-142 MJ kg^{-1}. Due to its notorious reactivity and the greater thermodynamic stability of hydrogen-containing compounds, this relatively simple element is found on Earth in combination with other elements rather than as a pure hydrogen molecule (H_2). Therefore, H_2 must first be produced from various hydrogen resources like water (*e.g.* fresh water, ocean), alcohols (*e.g.* methanol (MeOH)) or biological molecules (*e.g.* biomass feedstocks).[25,26] To this end, outdated, harmful hydrogen production technologies such as steam reforming or hydrocarbon pyrolysis can nowadays be replaced by contemporary, sustainable alternatives, namely photolysis, electrolysis, biophotolysis and thermolysis, provided that the energy required and consumed for these processes is also obtained from the above-mentioned renewable energy sources (see Figure 1.2).[27–29]

The photocatalytic splitting of water (H_2O) into molecular oxygen (O_2) and H_2 is regarded as a pivotal vector for the production of carbon-neutral, sustainable fuels. This process is advantageous due to its simplicity and cost-effectiveness in converting solar energy.[30] Moreover, in addition to suitable photocatalysts, the redox reaction requires merely two other resources that are abundant on Earth: Water, a raw material that appears to be "infinitely" available for H_2 synthesis, and energy-rich photons of the solar spectrum, which can meet all of humanity's energy needs. Furthermore, sustainable H_2 production and the subsequent release of hydrogen-bound energy results in no GHG emissions; on the contrary, solely O_2 and recombined H_2O are liberated as clean by-products. This process therefore enables a complete energy-fuel cycle with a green footprint.[31,32]

However, current photocatalytic systems suffer from inefficient conversion rates of solar energy to H_2 of less than 3%. This deficiency can be attributed to the high energetic activation barrier of the water splitting reaction, the recombination of photogenerated electrons and holes, the narrow visible light response range of photoactive compounds, and the unfavorable recombination of the generated H_2 and O_2 back to H_2O. Further

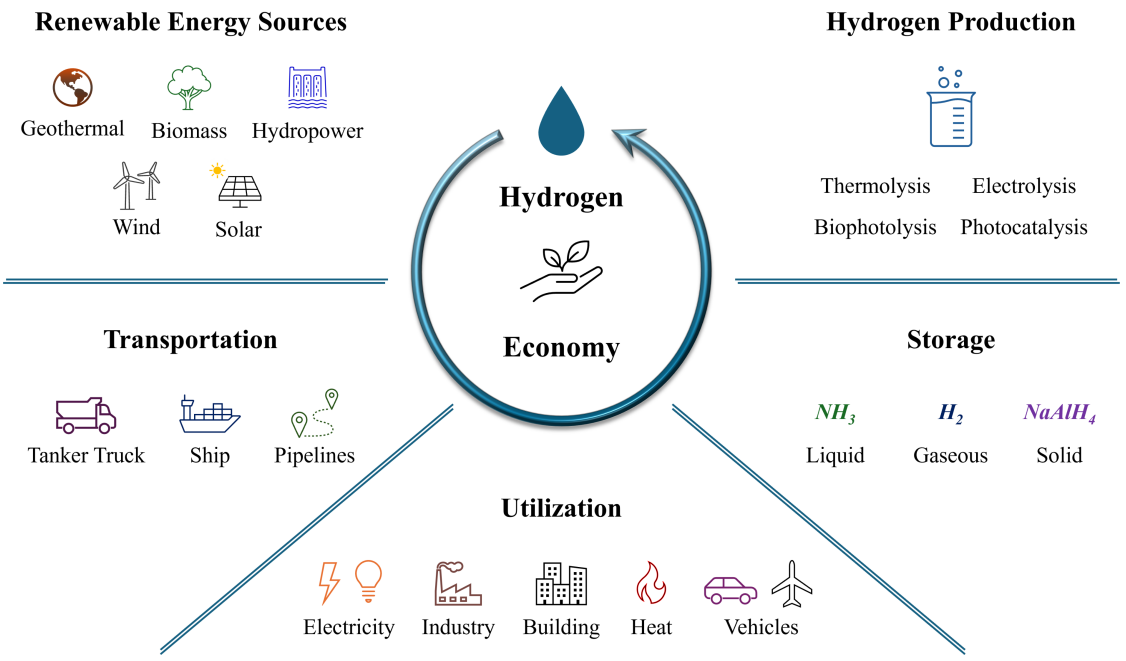


Figure 1.3 A perspective green footprint towards a sustainable hydrogen economy: Hydrogen is produced through sustainable conversion methods such as thermolysis, electrolysis, biophotolysis and photocatalysis using only renewable energy sources based on geothermal, biomass, hydropower, wind and solar energy. Hydrogen is transported *via* tanker trucks, ships and recycled pipelines that are currently used to transport fossil fuels. Hydrogen is safely stored using different technologies, *e.g.* as liquid ammonia, compressed gaseous H_2 or solid hydrides, until the energy carrier is used in various consumption sectors.[40]

challenges concern the activity, selectivity, stability and robustness of the catalysts for the oxygen evolution reaction (OER) and the hydrogen evolution reaction (HER), as well as the high cost, scarcity and lack of scalability of suitable materials for large-scale applications.[33–35] Intensified research is therefore essential to overcome these obstacles and improve the overall efficiency of catalytic systems with respect to unlocking the significant commercial potential of the photocatalytic water splitting reaction. In this context, it is also worth investigating how nature deals with its own energy supply to gather inspiration for innovative design ideas. A widely used strategic approach for this purpose is presented in chapter 1.2.

Nonetheless, the prospect of "green" H_2 production has become a key area to address the twin problems posed by the accelerating progression of climate change and the dwindling energy supply, while the global energy demand continues to grow exponentially.[36] Hydrogen is anticipated to emerge as a preeminent energy carrier in the future, with a projected share of around 22% of the total energy consumption by the year 2050.[37] The feasibility of a future global hydrogen economy with a secure production, distribution, storage and end-utilization is therefore conceivable (see Figure 1.3).[38–40]

1.2 Biomimicry – Nature-Inspired Design

Nature offers a vast array of fascinating biological systems with inspiring functional processes and activities that are characterized by exceptional precision and efficiency in tackling various problems. For instance, nature is able to form resilient materials with optimized morphologies and topologies that possess antibacterial properties,[41] self-healing capabilities,[42] robustness,[43,44] sensory auxiliary mechanisms,[45] thermal insulation[46] or other beneficial traits depending on the external influences.[47,48] The capacity to develop unique, advantageous structures is augmented by a series of complex yet vital processes, including dynamic self-assembly,[49] biomineralization,[50] the global water cycle,[51] soil formation[52] and O_2 production.[53] Consequently, nature engages in sophisticated strategic management by continuously discovering, developing and assembling essential resources to address the immense global challenges that similarly affect human society.

Intriguingly, nature provides straightforward, efficient and sustainable solutions that are inspiring and offer numerous benefits when it comes to creating an empathetic, human-centered approach to innovation. Since their characteristics and mechanisms can be extensively explored, understanding the underlying processes, principles and patterns in the bio-based systems and the pertinent structure-function relationships is essential to attain solution-oriented guidance for critical and complex humanoid problems in the environmental, economic and social domains. The subsequent mimicking of biological concepts and their creative translation into artificial products opens up new opportunities, such as the technological development of advanced materials to exploit specific chemical, biological, mechanical, electrical, sustainable and multiple synergy effects. Beyond that, the properties of existing systems can be optimized to near-perfection.[54,55]

The term "*Biomimicry*" (Greek: *bios* = life, *mimesis* = imitation) refers to a design thinking approach that draws inspiration from nature and focuses on adapting and imitating the principles associated with it. In particular, this methodology connects biology with the practical, everyday challenges of human design. The transition from biomimicry thinking to the creation of artificial products is referred to as "*biomimetics*" and involves the analysis of biological functions and systems, the abstraction of relevant knowledge and the transfer and application of this knowledge to human contexts. The aim of this process is to develop innovative design ideas and artificial models that address

real-world issues. Thus, according to Janine Benyus, nature is perceived as a model, mentor and measure capable of generating intricate systems with great efficiency.[56–58] It is important to underscore that the objective of biomimetics is not to replicate or test the biological system itself. To illustrate, the utilization of fireflies to produce light is not deemed an imitation of nature. Instead, the transfer of knowledge regarding the complex bioluminescence chemistry and the emulation of this functional strategy from nature to cast light on the dark is considered biomimetics.[59,60]

The design, development and applications of biomimicry are generally diverse. Two historical prime examples are Leonardo da Vinci's first aircraft proposals, which were based on his observations and findings on the aerodynamics of bird and bat wings,[61,62] and the commercial hook and loop fasteners of the Swiss company Velcro, which were invented by George de Mestral and inspired by the natural attachment mode of the burdock plant.[63] The success of biomimetic products extends to various fields, including architecture,[64] automotive and mechanical engineering,[65,66] structural coloring,[67] sensors,[68] information technology,[69] biomedicine,[70,71] coatings,[72] environmental protection,[73] catalysis[74] and sustainable energy storage.[75] A recent review by Goel and colleagues provides further examples of bio-inspired materials.[55]

The fundamental concepts of biomimicry thinking can be delineated within a conceptual framework known as the "Design Spiral", which was developed by Carl Hastrich in collaboration with the Biomimicry Guild. This framework builds on the foundational developments outlined above. The strategic path commences with the identification of a problem and the definition of the associated functions, including the criteria and constraints required for the design (*Define*), followed by their transcription into biological terms (*Biologize*). In this regard, two questions must be posed: What is the intended purpose of the desired design and how does nature fulfill this function? In addressing the second question, analogies in nature that perform the same or similar functions and incorporate essential characteristics must be examined in detail (*Discover*, *e.g.* animals, plants, bio-based micro- and macro-structural patterns, ecosystems, *etc*.). The knowledge acquired from this analysis is then transformed into a sustainable, inventive biomimetic design idea through abstract translations of the biological paradigm. In a subsequent brainstorming session, several solutions are considered (*Abstract*). Finally, prototypes are developed based on the key lessons learned from nature (*Emulate*), which are further

tested and assessed for their feasibility (*Evaluate*). Depending on the result, the design can be gradually refined through scientifically sound and structural iterations of diverging and converging phases until the desired artificial product is achieved (*Repeat*). A correspondingly modified "Design Spiral" is shown in Figure 1.4a.[76–78]

The term "biomimicry" is widely interpreted in the extant literature due to its use in various areas of education and application. Different design thinking strategies have been developed,[78–82] with the "Problem-Driven" approach to biomimetics being the most common in real-world settings. In this instance, the initial impetus for seeking a remedy to a human need stems from an identified problem. The preliminary investigation of the biological system with the problem-related functions, modes or mechanisms serves as a source of inspiration for the exploration of relevant design principles. This stage is similar to the initial step of the previously described "Design Spiral", which is followed by the development of replicable, innovative technological ideas in a non-linear or dynamic progression characterized by feedback and refinement in the loops to solve the problem at hand. Accordingly, the six phases of the "Problem-Driven" approach are as follows: 1) Problem definition, 2) Problem reframing, 3) Biological solution search, 4) Biological solution definition, 5) Principle extraction and 6) Principle application. Figure 1.4b schematically summarizes this conceptual framework, which is often referred to as the "Top-Down" or "Challenge-to-Biology" method.[79–82]

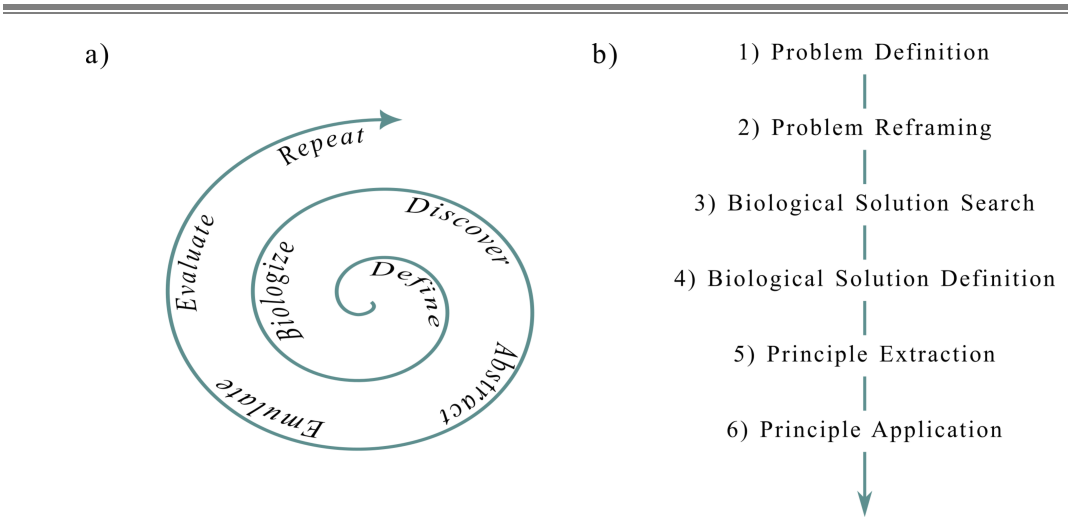


Figure 1.4 Design thinking strategies employ a combination of key concepts to solve an identified problem by abstracting and detaching from an appropriate biological model and the principles applied to it. This process involves the assessment of feasibility, performance and opportunities for continuous improvement. **a)** Biomimicry Design Spiral: The design thinking concepts are illustrated in the form of a spiral as adopted from the Biomimicry Research Institute and originally drafted by Carl Hastrich.[76] **b)** Problem-Driven, Top-Down or Challenge-to-Biology approach to biomimicry, respectively.[80–82]

Figure 1.5 presents a proactive and highly simplified blend of the two design thinking strategies presented above in order to increase clarity. This scheme serves as a basis for answering the research question defined in chapter 1.1. The current problem of energy scarcity and the sustainability conundrum, along with the fundamental dimensions and characteristics of this challenge have already been outlined and thoroughly examined according to the step titled *Identify* in chapter 1.1. The subsequent phase reframes the problem through the *Discovery* of criteria and constraints, thereby fostering a symbiotic relationship with the environment, which seeks to address the question: How does nature deal with this challenge? A potential model can be found in the biological photosynthesis that occurs in the leaves of plants and trees. This process is responsible for harvesting solar energy, its conversion into a sustainable fuel and its natural preservation in the form of energy-rich chemicals.[83] Beyond this, the enzymes hydrogenase and nitrogenase, which catalyze the synthesis of H_2 and its subsequent utilization, represent remarkable systems that merit heightened scrutiny.[84] The theoretical background of their salient strategies and pivotal mechanisms are described in the ensuing chapter 1.3. Subsequently, the bio-based knowledge is transferred to artificial systems by specifying the physico-chemical prerequisites, thereby emulating natural principles, as outlined in the step of *Explore*. In the subsequent step, *Create*, a design idea is formulated. The concept is then subjected to a thorough review to ascertain its feasibility and efficiency, with any rectifications being proposed or implemented in accordance with the step *Evaluate*.

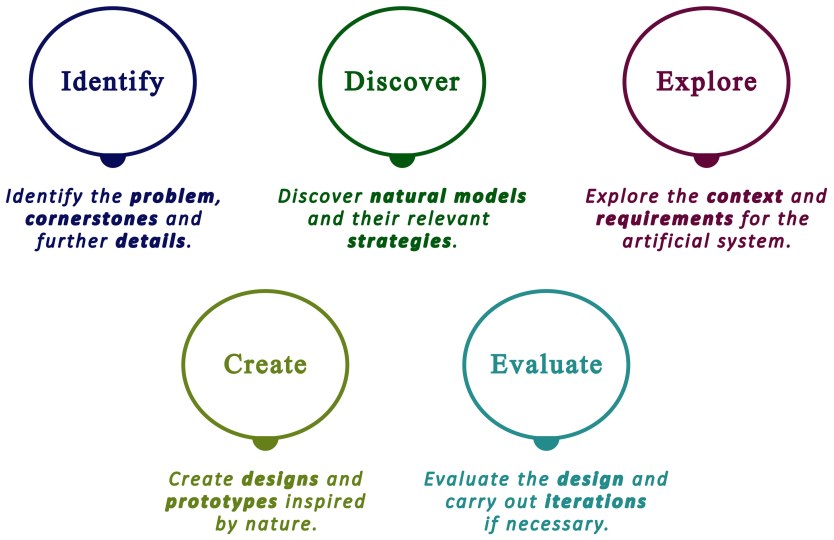


Figure 1.5 A proactive, modified design thinking scheme grounded in general biomimicry concepts is posited as a guide for the subsequent discussion. The methodology is applied in the sequence "Identify – Discover – Explore – Create – Evaluate" and the steps are discussed in chapters 1.1, 1.3, 1.4–1.8, 2 and 3.

1.3 Nature as an Inspiring Role Model

This chapter provides a comprehensive overview of the essential natural processes and structural characteristics that are important for biological photosynthesis and H_2-evolving enzymes. The theoretical background corresponds to the "*Discovery*" phase of the design thinking model depicted in Figure 1.5 and thus forms the foundation for the subsequent step "*Explore*". In this phase, the requirements for an inventive, artificial design that enables green, sustainable energy conversion are defined.

1.3.1 Biological Photosynthesis

Plants, trees, green algae or cyanobacteria, as well as certain unique microorganisms such as the leaf sheep sea slug, are capable of oxygenic photosynthesis.[85,86] Solar energy serves as an infinite energy reservoir that is converted into chemical energy through a complex series of redox processes and subsequently stored in the form of chemical bonds within the biomass. The most significant reactions in photosynthesizing chloroplasts are the oxidation of H_2O to O_2 and protons (H^+) with the concurrent reductive synthesis of nicotinamide adenine dinucleotide phosphate (NADPH) and the formation of adenosine triphosphate (ATP) using the energy of a proton gradient.[85,87]

The individual redox processes that occur during aerobic photosynthesis can be described by the so-called "*Z*-scheme" (see Figure 1.6).[87,88] The enzymatic photosystems I and II contain light-harvesting complexes (LHC), which are typically pigments with extended π-systems, such as carotenoid, phycobilin or chlorophyll in green plants. These molecular complexes absorb photons with sufficient energy from sunlight according to the Franck-Condon principle (for more details, see chapter 1.5). Wavelengths in the visible spectrum up to 700 nm and 680 nm are deemed suitable for photosystem I and II, respectively. The energetic electrons are transferred directly to a unique chlorophyll dimer, which is located in the reaction center of the respective photosystem. This dimer is also referred to as their "special pair" and is abbreviated as P680 or P700 according to its absorption wavelength. The electron transfer process up to this point unfolds through consecutive Förster resonance energy transfer (FRET) steps driven by long-range Coulombic dipole-dipole interactions (Δμ, see Figure 1.7a), culminating in the initial photoinduced charge separation of electrons and holes by the primary oxidation of the excited P680* and

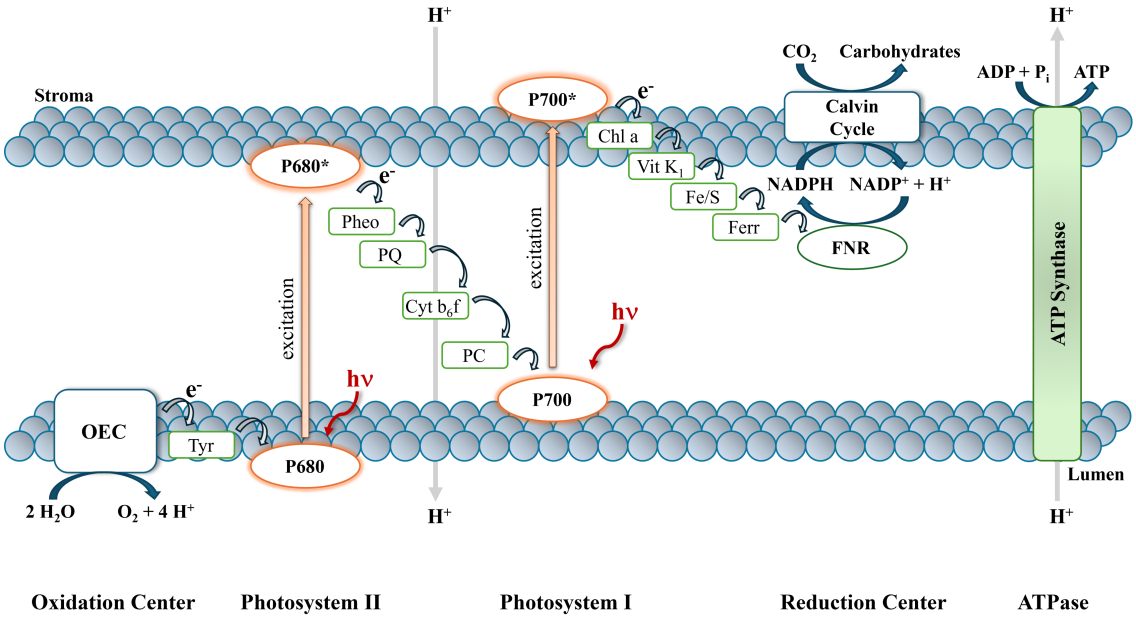


Figure 1.6 *Z*-scheme of natural photosynthesis showing the most important electron transfer steps and the essential reactions that occur within the thylakoid membrane. Note that the relative positions of the individual components to each other imply divergent energy levels, but do not represent absolute values or valid energetic distances. The oxidation center is located on the low pH side of the thylakoid membrane, which is designated as the lumen. The dark Calvin cycle and ATP synthase occur on the high pH side, which is called the stroma. The directed proton gradient is indicated by light gray arrows. Successive single electron steps are shown by dark gray directional arrows, with the first downhill energetic electron transfer indicated by e^-. In brief, the H_2O-derived electrons are transferred *via* a complex cascade of various proton-coupled redox reactions to generate high-energy carbohydrates involving two dissimilar photocenters excited by photons (hν) of sufficient energy. The abbreviations used for the compounds involved are as follows: OEC: oxygen-evolving complex; Tyr: tyrosine; P680: photoactive special pair of photosystem II; Pheo: pheophytin; PQ: plastoquinone; Cyt b_6f: cytochrome b_6f; PC: plastocyanin; P700: photoactive special pair of photosystem I; Chl a: chlorophyll a; Vit K_1: vitamin K_1; Fe/S: iron-sulfur-based clusters; Ferr: ferredoxin; FNR: ferredoxin-NADP reductase; NADP: nicotinamide adenine dinucleotide phosphate; ADP: adenosine diphosphate; P_i: inorganic phosphate; ATP: adenosine triphosphate.[87,88]

P700*. The effective separation of the charges is further promoted by their transportation to the reductive and oxidative catalytic centers *via* successive charge transfer steps involving several suitable and highly organized electron mediators (*e.g.* electron transfer, see Figure 1.7b).

Accordingly, pheophytin (Pheo) oxidizes the photoexcited special pair P680* to the radical cation $P680^{+\bullet}$, while the excited state of P700* is oxidized by chlorophyll a (Chl a) to $P700^{+\bullet}$. The corresponding electrons are transferred from P680 to P700 in an optimized electron transfer chain between the two photosystem centers *via* individual mobile redox carriers, including two lipophilic plastoquinones (PQ), the solubilized metal protein cytochrome b_6f (Cyt b_6f) and plastocyanin (PC), to finally reduce the radical cationic state of $P700^{+\bullet}$. Conversely, vitamin K_1 (Vit K_1), iron-sulfur-based protein clusters (Fe/S) and

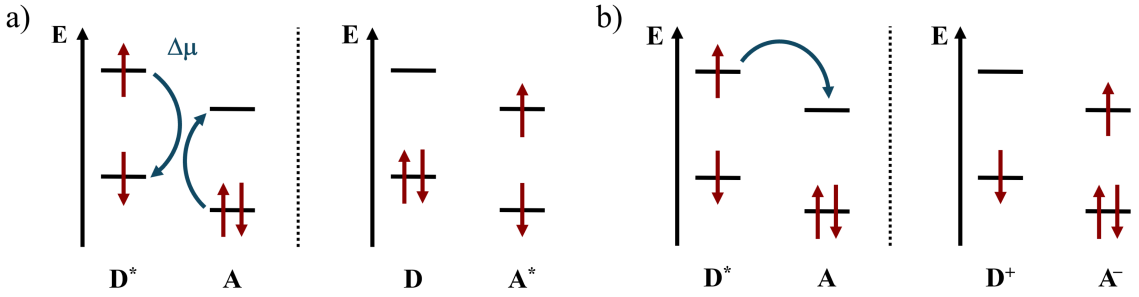


Figure 1.7 Simplified schemes illustrating the fate of energetic electrons in natural photosynthesis: **a)** Förster resonance energy transfer (FRET) from an excited molecule D* to an acceptor molecule A *via* dipole-dipole interactions (Δμ) that regenerate the donor molecule D and form the electronically excited acceptor molecule A*. **b)** Oxidative electron transfer from an excited molecule D* to an acceptor molecule A, forming the donor cation D^+ and the acceptor anion A^-.[87]

ferredoxin (Ferr) play a pivotal role in the effective electron transport from Chl a to the reduction center ferredoxin nicotinamide adenine dinucleotide phosphate reductase (FNR). The NADPH formed is then used to reduce fixed CO_2 from the atmosphere to energy-rich carbohydrates in the so-called Calvin cycle. This process is independent of light and is therefore often referred to as the "dark" reaction. Concurrently, the strong oxidant $P680^{+\bullet}$, with an estimated redox potential of 1.2-1.3 V *vs.* NHE (normal hydrogen electrode), is recovered from tyrosine (Tyr). This amino acid previously received the corresponding electrons from the natural oxygen-evolving complex (OEC), which in turn extracted the electrons from the substrate H_2O *via* accessible aquo-binding sites.[87–96]

Consequently, a unidirectional, energetically downhill path of energized electrons *via* several redox reactions is required to promote the essential sequences of charge separation and transfer. The kinetic disparities among the vital building blocks with respect to the directional photosynthetic electron transfer are assimilated in various organelles by their physical separation and integration with precise spatial and temporal orientation in a continuous three-dimensional (3D) network of a stacked lipid bilayer. This elaborate energy-transducing membrane system, known as the thylakoid membrane, also facilitates contact with the reactant H_2O.[87,96–98]

Following a series of four photon absorptions and subsequent passage through the energy transfer cascade, the resultant products are two fully reduced hydroquinone molecules and the fourfold oxidized OEC. In this state, the OEC is able to oxidize coordinated water ligands, resulting in the formation of O_2 and H^+. The concomitant electrochemical proton gradient between the two sides of the thylakoid membrane (stroma and lumen) is then

used to form ATP from inorganic phosphate (P_i) and adenosine diphosphate (ADP) *via* ATPase or ATP synthase, a molecule that covers the requisite energy demands in biological cells.[87,93,96]

Hence, the entire process can be summarized as the transfer of four electrons from the weak reducing agent H_2O to the reduction center FNR *via* an intricate non-cyclic light-induced electron and energy transport chain to ultimately store solar energy in chemical bonds of high-energy carbohydrates formed in the "dark" reaction.[87,89] In relation to the present work, the theory described in the current chapter focuses exclusively on the light-driven water oxidation that occurs in photosystem II and the inherent OEC.

The OEC is encapsulated on the low pH side of the thylakoid membrane (see Figure 1.6) and is sustained during catalysis by primary and secondary interactions with carboxylate and imidazole residues of amino acids from the protein matrix (see Figure 1.8a). Together with the abundant water molecules present in photosystem II, an extensive network of H-bonds is established, which is discussed to ensure the effective mobility of molecules and thus the transport of H_2O, O_2 and H^+ through the cellular reaction channels.[93,94,99]

The structure of the natural OEC was elucidated crystallographically by Umena, Kawakami and colleagues at a resolution of 1.9 Å. The cluster core consists of three redox-active manganese centers (Mn) and a divalent, redox-inert calcium ion (Ca^{2+}). The metal ions are bridged by four μ-oxo ligands with divergent bond lengths, resulting in a

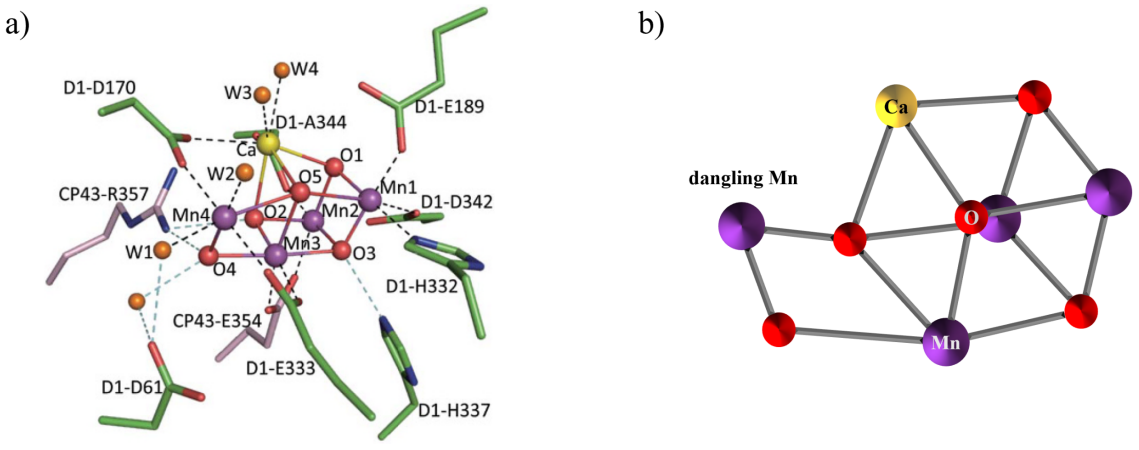


Figure 1.8 The natural oxygen-evolving complex (OEC): **a)** Stereo view of the [Mn_4CaO_5] cluster and its ligand environment. Cropped from original and reproduced with permission.[99] Copyright 2011, Springer Nature Limited. **b)** Simplified ball-and-stick model of the distorted [Mn_4CaO_5] cluster and the asymmetric chair-like configuration. **Color scheme:** purple: Mn; yellow: Ca; red: O; orange: H_2O ligands (abbreviated here as W); mainly green: amino acid ligands from the protein pocket.[99]

distorted heterocubane structure of the complex. The shape is extended to an asymmetric chair-like configuration by the fourth so-called “dangling Mn” ion, which is located outside the cube (see Figure 1.8b). Therefore, the pentanuclear inorganic cluster of the OEC is usually abbreviated with the formula [Mn_4CaO_5]. The coordination sphere of the dangling Mn (six ligands in total) and the Ca^{2+} (seven ligands in total) is completed by two water ligands each, which are considered as potential substrates for the oxygen bond formation. The subsequent evolution of O_2 is facilitated by two chloride ions (Cl^-) located in close proximity to the OEC periphery. These anions are theorized to contribute to the maintenance of the coordinative cluster environment of the OEC or facilitate the transfer of H^+ as part of the H-bonding network.[94,99] However, the molecular [Mn_4CaO_5] cluster is extremely sensitive to ionic strength, pH fluctuations and irradiation (*e.g.* light and high-intensity X-rays). These influences lead to structural instability, undesired redox reactions of the Mn centers and altered cluster structures. Therefore, the actual 3D structure of the cluster remains to be thoroughly analyzed, and there is still a debate about its true OER mechanism.[93,94]

For instance, the research group of Sun has proposed and described possible intermediate OEC structures that occur during the light-driven water oxidation catalysis (WOC) in the so-called Kok cycle (see Figure 1.9). The initial ground state S_0 is characterized by {Mn_3^{III}, Mn^{IV}}, *i.e.* three Mn centers are in oxidation state III and one Mn ion exhibits the higher oxidation state IV. Since four electrons are required for the oxidation of H_2O, the OEC must be oxidized four times before one O_2 molecule can be liberated, which occurs through four distinct, successive single electron transfer steps mediated by a redox-active $Tyr^{+\bullet}$. Each oxidation of the cluster is accompanied by a decrease in the electron density at the coordinated water ligands, a polarization of the corresponding O–H bond, an increased acidification of the aquo-related protons and their subsequent deprotonation. This process leads to charge compensation and emphasizes the importance of a concerted proton-coupled electron transfer (PCET) mechanism. Furthermore, the hydroxo ligand formed in the intermediate S_3 state increases the electron density at the high-valent Mn^{IV} center due to a stronger electron-donating effect according to the spectrochemical series, resulting in a decreased oxidation potential of $Mn^{IV/V}$. Therefore, a subsequent oxidation to Mn^V along with deprotonation is feasible. Consequently, a total of four intermediate structures ($S_0 \rightarrow S_4$) are implicated in the Kok cycle, which are characterized by different

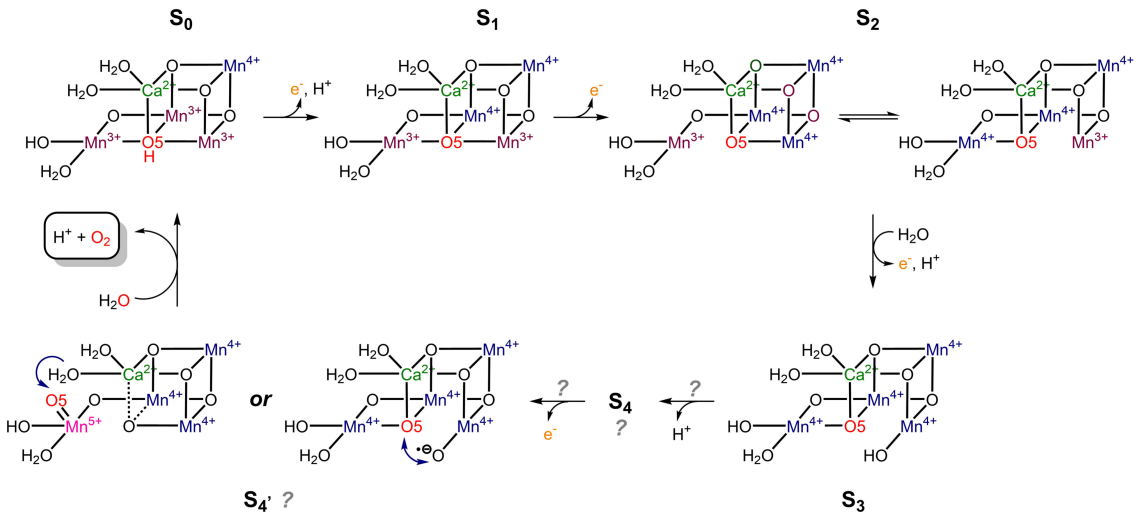


Figure 1.9 Simplified scheme of the classic Kok cycle for the OER mechanism by the natural OEC in photosystem II including the generally proposed structures of the intermediate states "S" and proton-coupled electron transfer (PCET) processes. It is important to point out that the oxidation state of the Mn centers and the mechanism itself have not been definitively confirmed and persist as subjects of controversy. For instance, the S_4 state has not yet been identified by spectroscopic methods. In addition, the realistic representation of the distorted cluster structure has been omitted for reasons of clarity. The metastable S_2 state is believed to transition from the S_1 state through the exchange of a μ_3-oxo to a μ_2-oxo bridge involving the oxygen atom O5. The S_2 state is comprised of two interconvertible, isoenergetic structures that differ structurally by the position of O5 and its bond with the dangling Mn atom and electronically by their valence distribution and spin multiplicity. It is anticipated that these characteristics play a crucial role in facilitating the binding of a water molecule as a second substrate during the transition to the S_3 state. The structural flexibility of O5 supports the assignment of a water exchangeable μ-oxo bridge at the transition to the S_4' state. Thus, this ligand is regarded as one of the water-substrate sites. The other water-substrate binding site is attributed to Ca^{2+} in the S_0 state. In the final step, the formation of O_2 can proceed *via* either a radical coupling mechanism or a nucleophilic attack of another water ligand.[101,102]

stored charge equivalents, *e.g.* {Mn_2^{III}, Mn_2^{IV}} in the dark stable S_1 state. In the final step of the Kok cycle, the active S_4' intermediate state is capable of forming an O–O bond through interactions with the oxygen atom labeled "O5", whereupon O_2 is released. Mechanistic insights into the bond formation between the two oxygen atoms remain enigmatic, as the $S_4 \rightarrow S_0$ transition occurs spontaneously, independently of light and thus on a very fast timescale.[94,100–102]

However, two different mechanisms are conceivable for this step, which is also regarded to be rate-limiting: The intramolecular interaction of two metal-oxo units (I2M, see Figure 1.10a) involves the coupling of two adjacent metal-oxo radical units. The radical character, the spin density and the increased intermolecular affinity of the oxo group are crucial for the formation of the dinuclear species [M–O–O–M]. Further oxidation of the metal center occurs prior to the liberation of O_2. In contrast, the alternatively proposed WNA mechanism (see Figure 1.10b) includes the nucleophilic attack of a free water

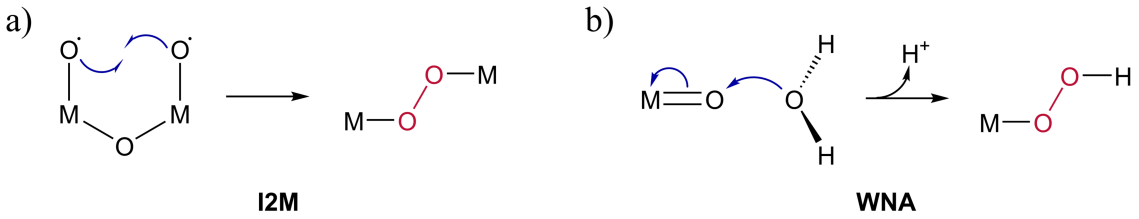


Figure 1.10 Two major mechanistic pathways for the formation of O–O bonds by OECs in WOC: **a)** Interaction of two metal-oxo units (I2M). **b)** Water nucleophilic attack (WNA).[103,104]

ligand in the immediate vicinity or bound to the neighboring Ca^{2+} on the electrophilic oxygen atom of a high-valent metal-oxo group (*i.e.* Mn^{V}=O). This electrophile was previously formed by successive oxidation of the OEC. Accordingly, the formation of a metal hydroperoxide intermediate with the formula [M–OOH] occurs when the highest occupied molecular orbital (HOMO) of the water molecule and the lowest unoccupied molecular orbital (LUMO) of the metal-oxo complex successfully interact. Subsequent to this initial interaction, the metal center within the [M–OOH] bond undergoes further oxidation, resulting in the instability of the metal-bound peroxo intermediate and the release of O_2 concomitant with the re-reduction of the Mn center. The obligatory abstraction of a hydrogen atom is presumably supported by the amino acid residues of the protein matrix. PCET is therefore indispensable in this process.[94,102–104]

As a result of harmful by-products (*e.g.* reactive oxygen species (ROS)), excess excitation energy and the harsh oxidizing conditions during water splitting, electron transport in the organelles is deactivated and the OEC is oxidatively damaged after less than 30 min of operation under illuminated catalytic conditions. However, continuous water oxidation is ensured by natural self-healing mechanisms involving selective biodegradation and dissociation of damaged subunits, their replacement by *de novo* protein synthesis and incorporation of these proteins into the partially disassembled photosystem II complex, relegation of cofactors, and reassembly of the OEC by its photoactivation. This self-repair is primarily based on synergies, such as dynamic and reversible changes, that are achieved by the integration of all structural units in the thylakoid membrane.[93,95]

In conclusion, the thylakoid membrane plays a critical role as a structural and functional platform that enables the spatial organization and temporal regulation of photosynthetic processes, including light harvesting and redox reactions that are essential for energy conversion, transfer and storage. The light-driven reactions are precisely coordinated by

the embedding and compartmentalization of all functional components, such as proteins, pigments and photosynthetic cofactors, within the architecture of a lipid bilayer. The spatial proximity, orientation and energetic alignment of these components facilitate optimal light absorption, efficient energy transfer within the two photosystems and fast, directional and effective electron transport between them. In addition, the regulated exchange, diffusion and movement of electron carriers, water molecules and ions across the membrane are enabled, while the coupled, coordinated transport of electrons and protons establishes an electrochemical proton gradient that serves as a driving force for ATP synthesis. Energetically wasteful processes, such as charge recombination, electron leakage and reverse reactions, are minimized simultaneously. Furthermore, lipid-protein interactions contribute to the stability and activity of the cofactors by forming a protective barrier against oxidative stress and other harmful influences. The thylakoid membrane also exhibits a high degree of structural and functional flexibility, enabling dynamic responses to changing environmental conditions (*e.g.* fluctuations in light quality or intensity) through repair mechanisms and structural adaptations. These adjustments ensure the maintenance of an optimal electron transport rate, thereby sustaining productive photosynthesis. In summary, the embedding of photosynthetic cofactors in the thylakoid membrane generates structural and energetic synergies that are fundamental for the execution of light-dependent reactions of natural photosynthesis.[96–98]

1.3.2 Hydrogen-Evolving Enzymes

Nature uses two metalloenzymes, namely nitrogenase and hydrogenase, in various microorganisms like anaerobic bacteria and green algae for the (photo)synthetic reduction of H^+ to H_2. Nitrogenase irreversibly forms H_2 as a by-product of nitrogen fixation under predominantly anaerobic and nitrogen-deficient conditions. In contrast, hydrogenase is responsible for the reversible generation and consumption of H_2 at neutral pH and ambient conditions in an aqueous environment, exhibiting low energetic barriers and high turnover numbers and turnover frequencies (TONs and TOFs, see chapter 1.4). In photosynthetic algae, these enzymes accept electrons from the photosystem I *via* an electron bifurcation mechanism, using reduced ferredoxin and NAD(H) as redox partners to drive the HER. The structural and mechanistic properties of these enzymes have been elucidated by numerous spectroscopic, structural, functional and theoretical techniques.[105–109]

Hydrogenases are generally divided into three main classes: [FeFe]-, [NiFe]- and [Fe]-hydrogenase. These enzyme subclasses diverge in terms of the metal content in their active sites, molecular weight, electron carrier specificity, cellular localization and stability to heat and oxygen. Despite these distinctions, the enzymes demonstrate commonalities in their catalytic HER activity, which is based on the structure of an iron-containing (Fe) protein with acid-labile sulfur atoms (S).[110–112]

The most active [FeFe]-hydrogenase is composed of a $[Fe_4S_4]^{2+}$ subcluster linked to a [FeFe]-complex *via* the thiolate of a bridging cysteine unit. It has been postulated that the cubane-shaped domain functions as a capacitor during catalysis and donates electrons to the covalently bound dinuclear moiety, which serves as the catalytic center. The redox-active distal Fe^d center contains a vacant coordination site that is accessible for hydrogen binding to form an Fe-hydride intermediate. In contrast, the proximal Fe^p center exhibits a saturated coordination sphere and limited redox activity, ensuring the stability of the cluster during the two-electron HER process (see Figure 1.11a). The enzyme's stability is further enhanced by the second coordination sphere, which comprises hydrophobic interactions and H-bonding contacts with amino acid moieties of the protein pocket. Ionic interactions, which are also present within the second coordination sphere, result in allosteric effects, a variable H-bonding network and the distribution of electron density across the cofactor. Therefore, it is hypothesized that the protein environment further modulates the properties of the cofactor and serves as highly conserved channels for the

shuttling of electrons and protons along the second and outer coordination sphere to the catalytically active sites. These findings underscore the importance of synergistic effects and a hierarchical microenvironment surrounding the catalytic sites.[109,113–117]

The other two active site structures of hydrogenase are based either on a heterodinuclear metal pair consisting of redox-active nickel (Ni) linked to a redox-inert Fe^{II} ion *via* two thiolate-bridged cysteine residues (see Figure 1.11b),[118,119] or on a phylogenetically unrelated mononuclear iron complex, which additionally differs from the other two cofactors by the absence of an electron-transferring Fe-S cluster (see Figure 1.11c).[120,121] The importance of redox-active transition metals and sulfur-based ligands for the HER mechanism of hydrogenase is evident from these structural features.

However, the other H_2-evolving enzyme nitrogenase is of greater interest for the present work. Three homologous isoforms have been identified that differ primarily in the composition of the active site of their catalytic subunit by containing either the heterometal center molybdenum (Mo), vanadium (V) or iron (Fe). The most prevalent and best-studied cofactor is the [MoFe]-based cluster, also known as [FeMoco]. This cluster provides substrate reduction sites that are essential for the reductive conversion of nitrogen to ammonia and the obligatory H_2 evolution side reaction. The catalytic site is based on a metal-sulfur framework with the general net stoichiometry $[MoFe_7S_9C]$. Three bridging sulfide ligands and an interstitial μ_6-carbide ligand connect $[MoFe_3S_3]$ and $[Fe_4S_3]$ cluster fragments. The coordination sphere of the active Mo^{IV} center is completed by an organic homocitrate molecule (see Figure 1.11d). In addition, two phosphorus-containing clusters are present in the immediate vicinity, functioning as an initial electron relay.[122–126] Notably, the presence of a Mo center and the binding of protons to sulfide ligands appear to be a crucial factor for the HER activity of nitrogenase. This finding is of significant interest for the design of artificial hydrogen-evolving catalysts (HECs).[127]

It should also be mentioned that the mechanisms of enzymatic proton reduction at the atomic level are not yet fully understood due to the complexity arising from the diversity of reaction sequences involved. Therefore, there is an emphasis on the use of modern characterization methods to achieve a more profound comprehension of these processes. Notwithstanding this, a prevailing consensus exists within the scientific community concerning the involvement of PCET processes, which also plays a pivotal role in biological photosynthesis.[128,129]

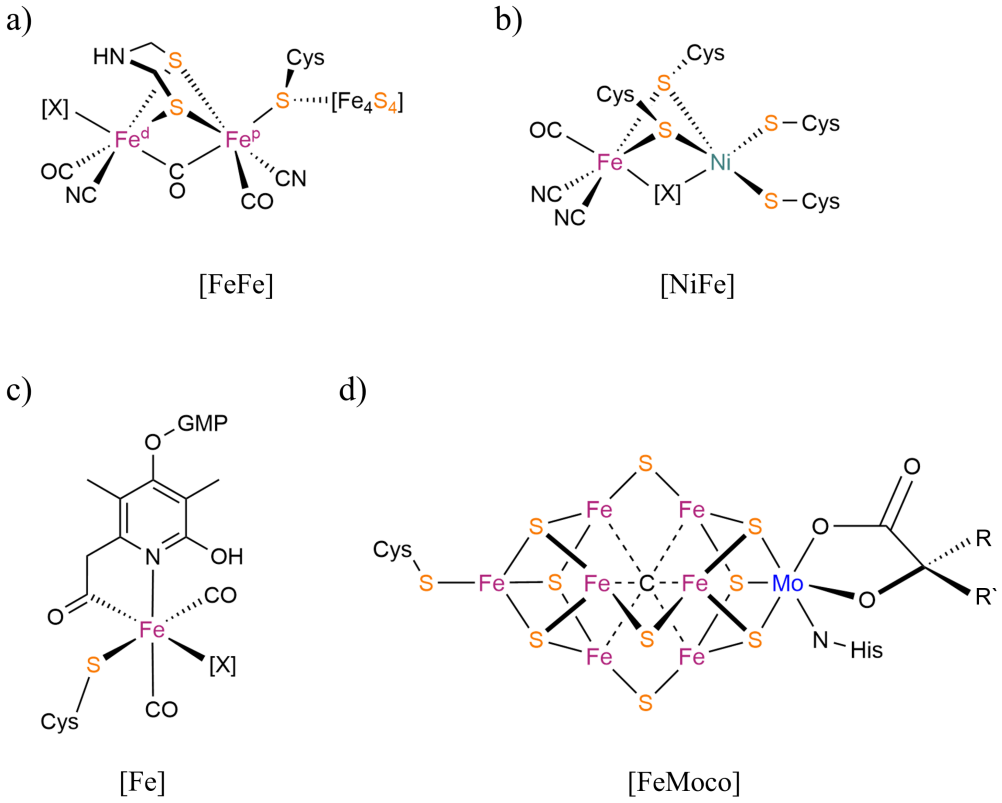


Figure 1.11 Schematic representation of the enzymatic HER active site cofactors discussed in this chapter: **a)** [FeFe]-hydrogenase, **b)** [NiFe]-hydrogenase, **c)** [Fe]-hydrogenase, **d)** [FeMoco]-nitrogenase.[118,126] The amino acids cysteine and histidine are designated "Cys" and "His", respectively. The abbreviation "GMP" is used for the nucleotide guanidine monophosphate. [X] indicates the potential catalytic binding site in the cofactors of the hydrogenases. The residues in [FeMoco] are R = $CH_2CH_2COO^-$ and R` = CH_2COO^-.

1.4 Artificial Photosynthesis

According to the biomimicry concepts shown in Figure 1.5, the next step is to ask and answer two questions: How can the vital functions, processes and mechanisms observed in biological photosynthesis (see chapter 1.3.1) and H_2-evolving enzymes (see chapter 1.3.2) inspire and promote the development of innovative artificial model systems for "green" energy production? In a broader context, this question is extended to how the pertinent principles can be mimicked in order to arrive at sustainable methods that also circumvent the second central issue of impending energy depletion (see chapter 1.1). The following sections of this introductory chapter 1 are dedicated to a more thorough exposition of the promising approach of artificial photosynthesis. The theoretical aspects of this approach are presented, with a particular emphasis on the design of inter- and intramolecular photosystems that operate predominantly under homogeneous conditions. Additionally, the underlying principles for the potential heterogenization of molecular components on suitable support materials are delineated.

1.4.1 General Overview

The development of artificial photosystems for the light-driven oxidative OER and the reductive HER aims to systematically utilize solar energy for the splitting of H_2O into O_2 and H_2, analogous to aerobic photosynthesis.[88,130] However, the subsequent reduction of CO_2 to energy-rich carbohydrates (*e.g.* glucose) is not considered in this scheme, as the storage of solar energy by means of H_2 is generally more realistic (see chapter 1.1).[131]

The complexity of the *Z*-scheme (see Figure 1.6) already indicates that a holistic approach is required for artificial photosynthesis to efficiently produce the clean energy carrier H_2, since the direct conversion of water by a catalytic species and the balancing of the rates of the two half-reactions are immensely difficult. The necessity for disparate redox environments, different solubilities and the spatial separation of the evolved O_2 and H_2, given their potential to interfere with mutual photoreactions, poses significant obstacles. To address these challenges, a complex multidisciplinary, multifunctional and multiscale mimetic is required for artificial photosynthesis. This approach often involves the initial segmentation of the overall water splitting process into the two independent half-reactions: the oxidative OER and the reductive HER (see Figure 1.12). The spatial

Oxidation	$2\ H_2O$	⟶	$O_2 + 4\ H^+ + 4\ e^-$	$E^0 = -1.23$ V
Reduction	$2\ H^+ + 2\ e^-$	⟶	H_2	$E^0 = 0.00$ V
Reaction	$2\ H_2O$	⟶	$O_2 + 2\ H_2$	$\Delta G^0 = 4.92$ eV

Figure 1.12 Redox reaction and thermodynamics of water splitting: The electrochemical potentials E^0 are given *vs.* NHE under standard conditions.[139]

separation of these processes enables the systematic investigation and optimization of the individual experimental conditions, as well as other specific requirements. Moreover, the undesired recombination of opposite charges, such as oxidized and reduced species, can be prevented, ensuring the integrity and efficacy of the two photoreactions.[55,132–134]

The molecular approach to artificial photosynthesis generally necessitates at least three functional components to execute one of the two redox reactions: a photosensitizer (PS), a sacrificial oxidizing or reducing agent (SOA/SRA) and a catalytic redox center (OEC or HEC, see Figure 1.13). The PS is responsible for harvesting visible light by absorbing photons with sufficient energy and for the primary directional energy propagation. The corresponding half-reaction of water splitting is mimicked by sacrificial redox agents, which ensure irreversible and effective spatial separation of the charges (*i.e.* electrons and holes) by quenching the excited PS state (PS*). The provision of reductive or oxidative equivalents facilitates the subsequent efficient directed electron transfer between the PS and the two distinct reactive catalytic centers. This process can be further enhanced by the use of suitable charge relay species, extending the described photosystems to four components. Finally, robust OECs and HECs are used to accumulate the charges. These species are characterized by vacant substrate binding sites for H_2O or H^+ and are capable of directing the charges to the subsequent OER or HER. The key to the successful development of artificial photosystems on a molecular basis therefore lies in the efficient thermodynamic and kinetic interplay of the compounds involved, which requires redox compartmentalization through the alignment of energy levels between PS, catalyst and SOA/SRA, as well as the prevention of charge recombination.[88,134–137]

The thermodynamically and kinetically demanding half-reaction of WOC is regarded as the bottleneck of artificial photosynthesis. According to the redox reaction for water splitting shown in Figure 1.12, the minimum electrochemical potential of water oxidation is designated as 1.23 V *vs.* NHE, which corresponds to a thermodynamic Gibbs free

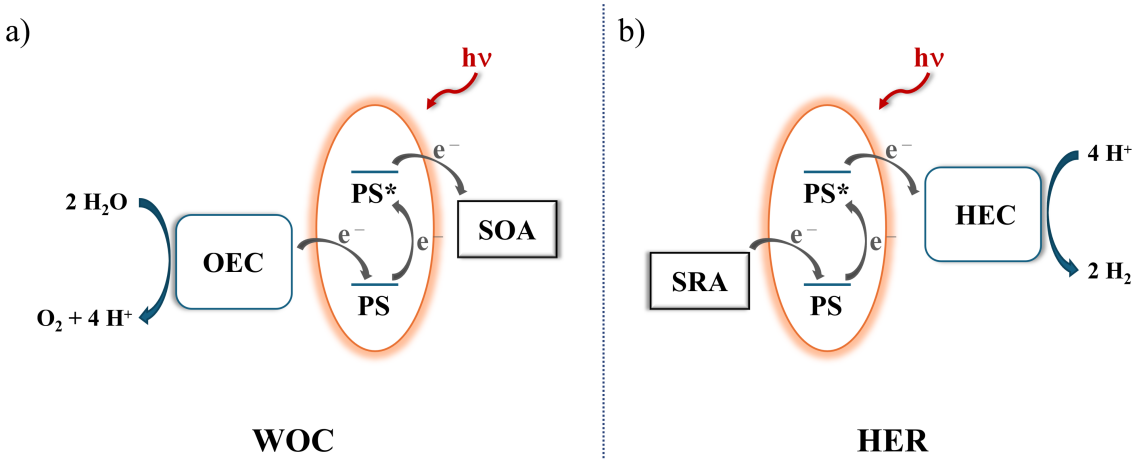


Figure 1.13 A homogeneous, molecular approach to artificial photosystems for the respective separate redox half-reactions of light-driven water splitting: **a)** WOC and **b)** HER. The PS is the light-harvesting component that mimics chlorophyll and the pertinent processes in the photosystems I and II. The electron relay and the complementary half-reaction, as depicted in the *Z*-Scheme of biological photosynthesis, are replaced and mimicked by the SOA and SRA, which act as electron acceptors and electron donors, respectively. OECs and HECs mimic the functions of the active centers of the [Mn_4CaO_5] cluster and the H_2-evolving enzymes, respectively. In summary, the substrate H_2O is oxidized to O_2, while H^+ are reduced to H_2. The relative arrangement of the individual compounds to each other indicates their energetic correlations.[88,103]

energy of *ca.* 237 kJ mol^{-1} under standard conditions. In addition, OER involves the transfer of four electrons and four protons from two molecules of water, whereas HER requires two PCET processes. Thus, the artificial OEC must be oxidized fourfold in the final stage of the light-driven reaction and allow bond rearrangements to liberate one molecule of O_2 (*cf.* Figure 1.9). Consequently, research and development of efficient photocatalysts for artificial photosynthesis are critical to reduce and overcome the high kinetic activation barriers of the reaction, accelerate the underlying dynamics and achieve an overall optimal catalytic rate for the splitting of water into its elements.[102,136,138,139]

1.4.2 Detailed Insights into an Artificial Photosystem

This chapter provides a comprehensive overview of criteria for catalyst species, PS and sacrificial agents, along with related considerations such as heterogenization of the molecular components and the application of appropriate performance indicators.

Catalysts for WOC and HER

According to chapter 1.4.1, the focus of current research is on the individual development of WOC- or HER-active photosystems. This strategy implies a reverse catalyst design to generate diverse properties, as the OEC and HEC usually operate under different catalytic conditions. However, common prerequisites for economically viable catalysts are their earth abundance as well as high intrinsic activity, selectivity and stability under turnover conditions, which translates into accelerated reaction rates.[102,140] Furthermore, the integration of several functional sites into their catalytic structures is imperative.

Firstly, accessible coordination sites are indispensable for the binding of the substrates H_2O in OER and H^+ in HER. These sites allow sufficient spatial proximity for the efficient formation of a bond between two oxygen or two hydrogen atoms. Secondly, a proton-transfer site with local proton management is necessary to avoid the formation of high-energy intermediates and thus level the redox potentials of the intermediates accordingly. This charge compensation facilitates the accumulation of multiple charge equivalents and thus promotes the overall redox reaction. In the case of the OER, the presence of suitable redox-active sites capable of forming high-valent intermediates is also essential to support the accumulation and utilization of multiple charge equivalents at high redox potentials. These species play a crucial role in reducing the thermodynamic and kinetic activation barrier, thereby accelerating the reaction rates for the WOC.[102,140,141]

The activity and stability of the catalysts is therefore determined, *inter alia*, by their ability to perform PCET reactions and their superior control of the local pH.[141] The proton-coupled transfer of four electrons in the oxidation of H_2O to O_2 by the OEC can occur *via* either an inter- or intramolecular I2M or WNA mechanism, which were previously described in exemplary fashion for the natural OEC (see Figure 1.10).[104] In contrast, the HEC must meet the reductive twofold electron transfer process.[138]

In electrocatalysis and under acidic conditions, the underlying HER mechanism can be described by either the Volmer-Heyrovsky pathway or the Volmer-Tafel pathway (see Figure 1.14). Irrespective of the reaction type, the adsorption of H^+ on the catalyst surface and the subsequent formation of H* as a result of electron transfer from the catalyst to the hydrogen atom constitutes the first mechanistic step, which is referred to as the Volmer reaction. According to the Sabatier postulate, the strength of the hydrogen-catalyst bond should be neither too strong nor too weak. Hence, an optimal Gibbs free energy of hydrogen adsorption ($\Delta G_{H^*} = 0$) is a prerequisite for an efficient HEC. At low H* surface coverage, the subsequent H_2 formation proceeds *via* the Heyrovsky reaction, in which PCET is involved in the electrochemical desorption of H* (see Figure 1.14a). Conversely, high surface coverage of H* favors the Tafel reaction, which describes the recombination of two adjacent surface-bound H* to form and liberate H_2 (see Figure 1.14b).[142–147] The rate-limiting step in these electrocatalytic HERs can be determined by Tafel slope analysis, which distinguishes the corresponding reactions based on the following values: approx. 30 mV dec^{-1} (Tafel reaction), approx. 40 mV dec^{-1} (Heyrovsky reaction) and approx. 120 mV dec^{-1} (Volmer reaction).[147–150]

The required features are typically met by catalysts based on (transition) metals. In this context, the intrinsic reactivity and product selectivity can be enhanced by adjusting the steric configuration and electronic properties of the active metal centers. This can be accomplished, for example, by incorporating suitable ligands into the molecular catalyst structure.[102,103] This nanostructuring also enables the exposure of more accessible active sites, which further emphasizes the importance of the tunability of the catalyst.[102,138]

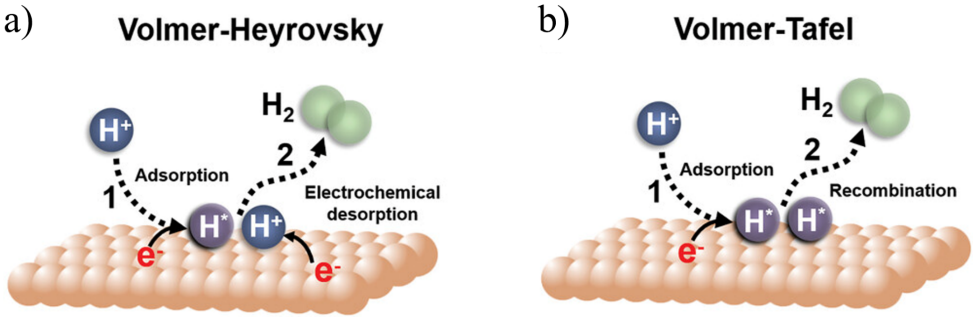


Figure 1.14 Simplified HER pathways under acidic and electrocatalytic conditions: **a)** Volmer-Heyrovsky mechanism, in which H_2 formation proceeds *via* PCET and electrochemical desorption steps. **b)** Volmer-Tafel mechanism, in which two hydrogen atoms adsorbed on the catalyst surface (H*) recombine to form H_2. Reproduced under the terms of the CC BY 4.0 license.[147] Copyright 2023, The Authors, Advanced Materials published by Wiley-VCH GmbH.

However, colossal stability and robustness of the OEC and HEC under harsh oxidative or reductive conditions is paramount to ensure their long-term durability in catalysis, as molecular repair or self-healing is quite difficult.[103,104,151] In addition, the catalysts must demonstrate a high degree of resistance to thermal, irradiative and hydrolytic degradation processes, including undesired WNA, attack by ROS and poisoning reactions.[133,138] Moreover, the cost-effectiveness of the catalyst is a crucial consideration for industrial applications and its compatibility with the PS and sacrificial agent species is essential for promoting the light-driven approach, *e.g.* by establishing well-matched redox potentials.[103,138]

Consequently, a number of factors must be considered in the development of efficient and robust molecular catalysts for WOC and HER. Inspiration can be found in the structural features of the natural OEC (see chapter 1.3.1) and the HER-active enzymes (see chapter 1.3.2), which emphasize the need for suitable (transition) metal centers and the presence of appropriate supporting ligands.[102,104]

The list of molecular catalysts investigated for WOC includes, for example, the dinuclear "blue dimer" complex based on ruthenium (Ru) (see chapter 4.1),[141] various iridium (Ir)-containing coordination compounds,[152] and molecular mimics of the natural photosynthetic OEC based on Mn,[153] to name but a few. In addition, numerous examples of heterogeneous OECs have been investigated within the photoelectrochemical and photochemical approach of WOC (*e.g.* Co_3O_4).[154] Polyoxometalates (POMs) have also garnered considerable attention as OEC due to their remarkable stability under harsh oxidative conditions and their ability to reversibly store a large number of electrons within their structures.[138,140] A comprehensive overview of this class of compounds is provided in chapter 1.6, with specific OEC examples discussed in the subchapter 1.6.3.

With respect to HER, noble metals,[155] metal oxides,[156] metal sulfides,[157] metal-organic frameworks (MOFs),[158] transition metal nanoparticles deposited on graphene oxide supports,[159] polymeric graphitic carbon nitride[160] and porous 3D networks[161] have shown efficient HEC properties. Notably, nanostructured molybdenum sulfides (MoS_2) exhibited comparable HER activity to platinum (Pt)-based electrocatalysts.[85,147] These compounds remain the ultimate benchmark HECs due to their exceptional activity, efficiency and durability, despite their low earth abundance and high costs.[24,138] In the molecular HER approach, for instance, various cobaloxime catalysts are outstanding HEC

representatives.[162] The mimicking of the active site of hydrogenase is also an active area of research.[133] Furthermore, biomimetic approaches related to the HER activity of the sulfide-bridged molybdenum atom in the active site cofactor of nitrogenase are of interest for the design of sustainable light-driven HECs. In this regard, the chemistry of thiomolybdates as molecular mimics of MoS_2 has received profound attention due to their ease of study under catalytic conditions, including the identification of active sites at the molecular level.[147,163] The characteristics of this class of compounds are described in chapter 1.7 and their HER activity is discussed in more detail in the subchapter 1.7.1.

Photosensitizers

The second essential unit in a molecular photosystem is a PS species that mimics the functions of chlorophyll in biological photosynthesis. As indicated in chapter 1.4.1 and explained theoretically in chapter 1.5, strong absorption in the visible light spectrum (*i.e.* high molar extinction coefficients) and excellent reactivity for charge separation in the excited PS* state are desirable. Thus, all kinetic relaxation processes of the PS must be slower than the outer-sphere electron transfer reactions to the catalyst to avoid charge recombination. Directed electron transfer by intermolecular collisions is generally promoted by a highly efficient population of an excited state with sufficient energy, exceptional photostability and reasonable longevity. Appropriate redox potentials and high luminescence quantum yields are corresponding characteristics. In this regard, dyes with easily tunable redox and excited state properties are preferable. Further prerequisites are a reversible redox behavior and suitable thermodynamic potentials of the native, oxidized or reduced PS species to enable the progression of a photocatalytic cycle. Additionally, the emission properties must be readily discernible to facilitate quenching studies, which is beneficial for obtaining detailed mechanistic information to improve the interactions between the individual compounds in the photosystems.[91,164–171]

Contemporary molecular PSs include chromophores based on non-precious metals, which are characterized by an extended π-system, as well as metal-containing coordination compounds with pronounced metal-to-ligand charge transfer (MLCT) properties. A high tunability of the aromatic systems and organic ligands is preferred to allow facile modulation of the photophysical dye properties, such as the generation of

low-lying unoccupied π*-orbitals. However, steric pressure or hindrance of the ligand periphery is generally unfavorable, as these effects typically result in reduced electron transfer rates.[169–171] Well-known PS representatives include dendrimers,[172] metalated porphyrins,[173] metallophthalocyanines,[174] organic rylene derivatives,[171] and Eosin Y,[175] among others. The most prominent and most commonly used PS is tris(2,2'-bipyridine)ruthenium(II) ($[Ru(bpy)_3]^{2+}$). This inorganic dye finds application in the photosensitization of both WOC and HER.[170] The corresponding photophysicochemical properties are described in detail in chapter 1.5. Conversely, semiconducting materials such as titanium dioxide (TiO_2),[176] quantum dots (*e.g.* CdSe)[177] or conjugated polymers[178] are often used for heterogeneous approaches to artificial light-driven HER.

Sacrificial Agents

In the domain of biological photosynthesis, the WOC and the HER are interconnected *via* an intricate electron transport chain.[88] In order to develop separated artificial photosystems, each half-reaction must be replaced by a sacrificial agent. This substitution enables the successful and rapid recovery of the original PS state and supports an efficient charge separation. Hence, these compounds must possess the ability to oxidatively or reductively quench the PS* by supplying the required charge equivalents. Furthermore, their fast and irreversible sacrificial degradation into inert molecules is crucial to avoid the above-mentioned recombination processes. However, this consumption also imposes limitations on the durability of the photocatalytic systems. In addition, these species are known to form radicals during catalysis, which underscores the need to avoid any interference with the catalytic reactions.[133–136,179]

SOAs are used for the subsequent oxidation of the PS in light-driven WOC. Therefore, these species must have energetically lower LUMOs than the energetically higher singly occupied molecular orbital (SOMO) of PS* (see Figure 1.7b). In contrast, a singly reduced PS in the light-driven HER is obtained by transferring an electron from an energetically higher HOMO of an SRA to an energetically lower SOMO of PS*. The compartmentalization of the energetic states is therefore a prerequisite for electron transfer processes to be thermodynamically feasible.[179,180] These mechanistic aspects are discussed in more detail in chapter 1.5 and illustrated schematically in Figure 1.18.

Peroxodisulfate ($S_2O_8^{2-}$) is commonly employed as a one-electron SOA for light-driven WOC, producing sulfate and anionic sulfate radicals that can oxidize another PS molecule (see Figure 4.11). Alternatively, $[Co(NH_3)_5Cl]^{2+}$ can also be used as an SOA, as its singly reduced complex irreversibly decomposes into hydrolyzed Co^{2+}(aq), ammonium (NH_4^+) and Cl^- ions under acidic conditions.[135,181,182]

Triethanolamine (TEOA), triethylamine (TEA), ethylenediaminetetraacetic acid (EDTA) and ascorbic acid (AscOH) are often used as SRAs in light-driven HER, as they can be oxidized more readily than water. The selection of an optimal compound is contingent upon the pH of the reaction medium. For instance, excessive protonation of TEOA or TEA can impair their efficacy as SRA, while AscOH experiences a weaker reducibility than its deprotonated form ascorbate. Therefore, AscOH is most effective at a pH > 4, while EDTA operates at a neutral pH between 5 and 7. The optimum pH range for TEA and TEOA is close to their pK_a values of 7.9 and 10.7, respectively.[133,136,179]

Additional Remarks

In addition to the thermal and photochemical stability under oxidative or reductive conditions of all compounds involved in the independent photosystems, the establishment of a chemical potential gradient between these units for intermolecular electron transfer and the regeneration of the original PS and catalyst structures, their solubility in H_2O or in an appropriate solvent mixture (*e.g.* in combination with acetonitrile (MeCN), MeOH, or *N*,*N'*-dimethylformamide (DMF)) is also required to ensure an effective photocatalytic cycle in WOC or HER.[83,133,166]

In 1977, the research group of Lehn and Sauvage presented one of the first molecular model systems for the light-driven HER. In this approach, $[Ru(bpy)_3]^{2+}$ served as PS, $[Rh(bpy)_3]^{3+}$ functioned as electron relay, TEOA acted as SRA and colloidal Pt particles were used as HEC.[135] Since that period, several homogeneous molecular photosystems have been documented in the scientific literature.[102,104,134,183]

However, despite the advantages of the separated homogeneous molecular approach for light-driven WOC and HER, the primary goal of artificial photosynthesis is still to combine the oxidation and reduction steps under spatiotemporal and energetic control

(*i.e.* control over the relative location of the components, the rates of competing processes, the energy of the excited state and the redox potentials), as demonstrated in nature by the thylakoid membrane.[132,172] Following the optimization of the individual half-reactions under homogeneous conditions, the subsequent step in the development of a sustainable, high-performance artificial photosystem involves compartmentalization by incorporating the described molecular catalyst and PS species into a proficient supramolecular, nanostructured matrix, such as a polymer membrane scaffold. This heterogenization ensures close spatial proximity between the individual building blocks in order to improve the electron transfer rates, stability and catalytic durability.[103,139,184] In this regard, a comprehensive understanding of the intricate intermolecular interactions between all components and the support material is imperative to leverage synergistic effects and optimize the catalytic performance (see chapter 1.8).[24,172]

In summary, the challenges concerning the inherent parasitic energy losses, *e.g.* in charge separation and charge transfer, need to be overcome.[136] In addition, diffusion-controlled reactions must be enabled and the formation of PS-catalyst aggregates prevented to optimize the intricate interactions between PS, sacrificial agent and catalyst.[167,185,186] The comparative evaluation of the complex interplay of light absorption, charge separation, charge transfer (*i.e.* PCET) and catalytic turnover by redox reactions also requires the application of suitable performance indicators. For instance, TONs and TOFs provide evidence on the stability of the catalyst under turnover conditions and assess its intrinsic activity by measuring the catalytic rate per active site (see eq. (1) and (2)). It is important to note that the variation in the amount of product formed ($\Delta n(\text{product})_{\text{formed}}$) does not equal to the total amount of product formed, as this figure can be influenced by factors, such as the delayed release of the gaseous products H_2 or O_2 and their slow diffusion to the detection device.[147,187]

$$\text{TON} = \frac{\Delta n(\text{product})_{\text{formed}}}{n(\text{catalytically active species})} \tag{1}$$

$$\text{TOF} = \frac{\text{d TON}}{\text{d } t_{\text{reaction}}} \tag{2}$$

1.5 Photochemistry of the Molecular Chromophore $[Ru(bpy)_3]^{2+}$

$[Ru(bpy)_3]^{2+}$ is a molecular chromophore that exhibits unique redox, photophysical and photochemical characteristics. Since the seminal reports by Lehn, Sauvage and colleagues from 1977 to 1979, this coordination compound and its numerous derivatives have been extensively studied as a PS in photocatalytic experiments, with a particular emphasis on intermolecular electron and energy transfer processes in artificial photosynthesis.[188–190]

The structure of $[Ru(bpy)_3]^{2+}$ was first synthesized and resolved by F. H. Burstall in 1936.[191] The Ru^{II} center with a molecular d^6-configuration is octahedrally coordinated by three bidentate 2,2'-bipyridine (bpy) ligands.[192] The bpy nitrogen atoms bear σ-donor orbitals, while the aromatic rings contribute delocalized π-donor and π*-acceptor orbitals. In the electronic ground state, the HOMOs are localized at the Ru metal center, while the LUMOs are assigned to the bpy ligands.

In general, an electronically excited configuration is obtained by irradiating the molecular ground state (S_0) with photons (hν) of sufficient energy that triggers the promotion of an electron from occupied to vacant molecular orbitals (MOs) of higher energy states (*i.e.* S_1, S_2, *etc.*). Each state is subdivided into several vibrational states, whose population is determined by the energy of the absorbing photon, as specified in the Franck-Condon principle. The subsequent interconversions between different excited states and/or the ground state are illustrated in Figure 1.15 based on a simplified Jablonski diagram.

The absorption of photons (A) generates an initial, non-equilibrated, higher excited state (*e.g.* S_2). When the ambient temperature is increased, thermal deactivation (not shown) or non-radiative processes, including vibrational relaxation (VR), 100%-efficient spin-allowed internal conversion (IC) between two excited states sharing the same spin (*e.g.* $S_2 \rightarrow S_1$ with S = singlet) or spin-forbidden electron transfer to non-emissive excited states *via* intersystem crossing (ISC) between two states with divergent multiplicity (*e.g.* $S_1 \rightarrow T_1$ with T = triplet) become feasible, which occur within a very short time range. Luminescence events such as the fluorescence (F) from S_1 and the phosphorescence (P) from T_1 emit light with dissipative energy content (hν'). The energy difference to the absorption is referred to as the Stokes shift. These 1^{st}-order physical intramolecular deactivation pathways determine the lifetime of the excited species, which are usually relatively transient due to their high energy content. They compete with static quenching

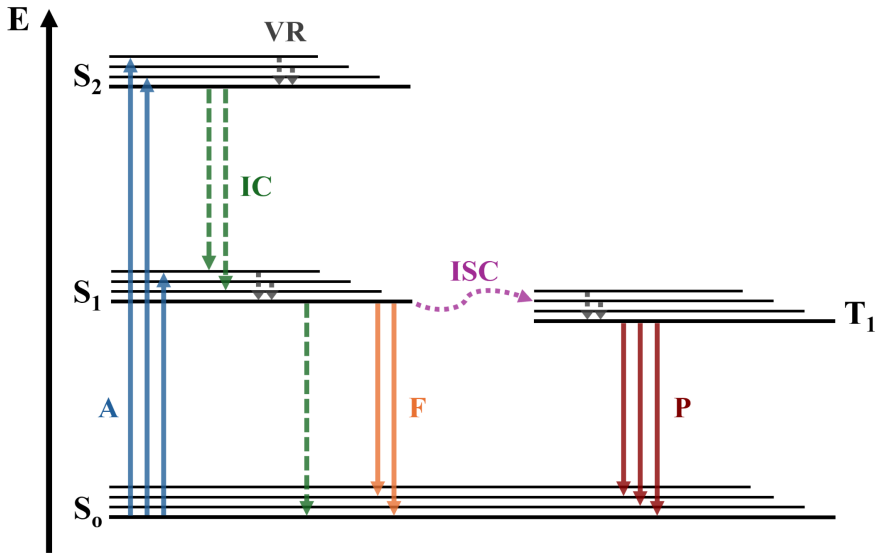


Figure 1.15 Simplified Jablonski diagram to describe photophysical processes: The ground state is denoted S_0, the first and second excited singlet states are abbreviated S_1 and S_2, respectively, and the first excited triplet state is represented by T_1. Higher singlet and triplet states are omitted from this scheme for the sake of clarity. The individual states consist of several energetically closely spaced vibrational states that are in thermal equilibrium (non-bold lines). The absorption of photons (A) and the excitation of an electron into electronic states of higher energy is shown by blue bold lines. Fluorescence (F, orange bold lines) and phosphorescence (P, red bold lines) are emitting deactivation pathways. Non-radiative processes include thermal deactivation (not shown), vibrational relaxation (VR, gray dashed lines), internal conversion (IC, green dashed lines) and intersystem crossing (ISC, purple dashed line). VR takes place within the vibrational states of an excited state, while IC and F involve states with the same multiplicity (*e.g.* $S_2 \rightarrow S_1$ or $S_1 \rightarrow S_0$), and ISC and P with alternating multiplicity (*e.g.* $S_1 \rightarrow T_1$ or $T_1 \rightarrow S_0$). Note that static and dynamic chemical quenching processes that terminate on S_0 are not shown in this scheme.[193]

mechanisms through irreversible chemical interactions between the excited state and the environment, yielding distinct products such as isomers. However, for photocatalytic applications, a prolonged lifetime of the excited state is favorable. One method to achieve this is through phosphorescence, where the promoted electron is trapped in a triplet state, leading to a slow return to the ground state due to the spin-forbidden process. This extended lifetime paves the way for additional 2nd-order bimolecular dynamic quenching mechanisms through encounters with other molecules in solution (*vide infra*).[193–196]

The high reactivity of the excited state is defined by an altered electronic conformation consisting of two half-occupied MOs, with one electron present in the LUMO and one missing in the HOMO. The low-energy SOMO has an increased electron affinity (E_A), *i.e.* the unoccupied orbital can more easily accept another electron. The higher-energy SOMO has a reduced ionization energy (E_I), which enables unburdened electron removal. Therefore, the photoexcited state functions as both a more potent oxidant and a more effective reductant compared to the corresponding ground state (see Figure 1.16a). Redox

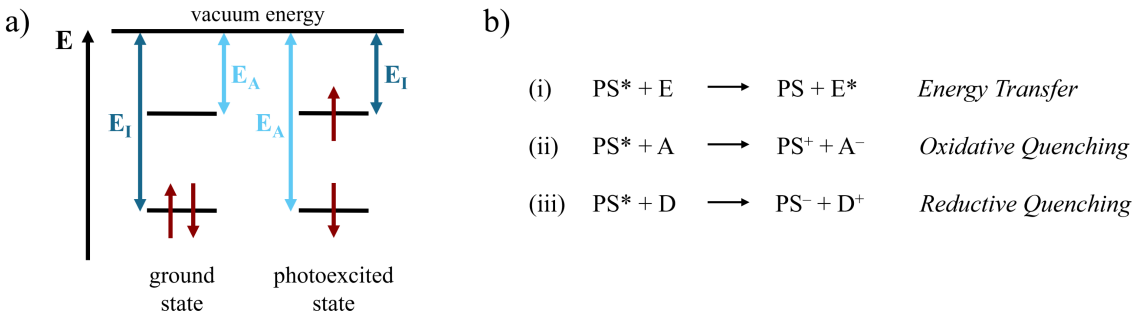


Figure 1.16 Reactivity of the photoexcited state: **a)** Simplified MO diagram illustrating the orbital occupation of a molecular chromophore in its electronic ground state and in its photoexcited state. The electron affinity (E_A) is defined by the energy difference between the vacuum energy and the lowest vacant MO (*i.e.* the LUMO in S_0 and the lowest-energy SOMO in the photoexcited state). The ionization energy (E_I) describes the energy gap between the vacuum energy and the highest occupied MO (*i.e.* the HOMO in S_0 and the highest-energy SOMO in the photoexcited state).[197] **b)** The excited PS* state can undergo three possible bimolecular reactions if the emission lifetime of the PS is adequate: (i) energy transfer with a molecule E (*e.g.* FRET or Dexter energy transfer), (ii) oxidative quenching by an acceptor molecule A or (iii) reductive quenching in the presence of a donor molecule D.[167]

transformations that take place on comparable timescales to the ground state relaxation, such as efficacious charge separation *via* intermolecular energy or electron transfer reactions (*e.g.* FRET, oxidative or reductive quenching; see Figure 1.16b), are thus possible. The corresponding energy diagrams for reactions (i) and (ii) have already been discussed in Figure 1.7 in relation to natural processes (see chapter 1.3.1).[167,195–197]

Ultraviolet-visible spectroscopy (UV-Vis) is a method by which various electronic transitions can be visualized and quantified. As depicted in Figure 1.17a, the UV-Vis spectrum of $[Ru(bpy)_3]^{2+}$ in MeCN at room temperature (r.t.) exhibits three distinct types of electronic transitions, which can be reasonably predicted and deduced from the simplified MO diagram shown in Figure 1.17b. The extended π-system of the aromatic bpy ligands is known to trigger intense ligand-centered (LC) ππ*-transitions at 185 nm (not shown in the spectral range) and 285 nm. A metal-centered (MC) dd-transition is partially forbidden by the rule of Laporte, leading to the very weak shoulder at 322 nm. Another weak shoulder in close proximity at 344 nm can be associated with π_M- and antibonding σ_M*-orbitals. MLCT involving d-orbitals of the metal that are easily oxidizable and π*-orbitals of the ligand that are easily reducible absorb energetic photons at 240 nm and 450 nm, respectively. These transitions lead to the formation of the lowest excited singlet and triplet states. It is also noteworthy that at r.t. three energetically similar ^{3}MLCT states are in thermal equilibrium, resulting in their behavior being practically equivalent to that of a single ^{3}MLCT state.[170,198,199]

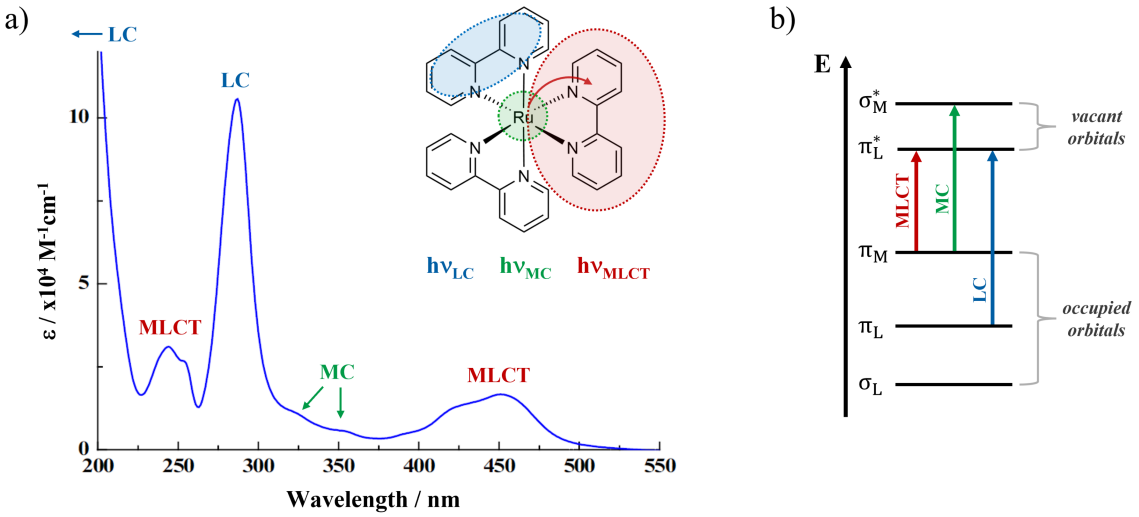


Figure 1.17 Excitation-induced electronic transitions in $[Ru(bpy)_3]^{2+}$: **a)** UV-Vis absorption spectrum of $[Ru(bpy)_3](PF_6)_2$ in MeCN at 298 K. Adapted and reproduced with permission.[198] Copyright 2017, Elsevier B.V. The specification of the different electronic transitions (blue: LC, green: MC, red: MLCT) has been modified for stylistic purposes without altering the original meaning. They have been assigned to the UV-Vis bands according to reference[170] and are indicated by colored ellipses in the additional structural conformation of the octahedral complex shown in the UV-Vis spectrum. **b)** Schematic representation of a simplified MO diagram applicable to $[Ru(bpy)_3]^{2+}$ showing three distinct types of low-energy electronic transitions in approximate octahedral symmetry. Notes: The ground state of the complex is characterized by a distorted D_3 symmetry. Theoretically, MLCT can also occur from the HOMO π_M. Another possible electronic transition, namely ligand-to-metal charge transfer (LMCT) from π_L to σ_M^*, is omitted as it is not discernible in the UV-Vis spectrum of $[Ru(bpy)_3]^{2+}$. The LUMO is represented by the π_L^*-orbital.[170]

Nielsen and colleagues observed a red shift of the ^{1}MLCT band from 452 nm to 430 nm in comparison to the UV-Vis spectrum measured in the gas phase. This observation suggests the presence of a permanent dipole moment in the excited state, accompanied by a distortion in the π-system with a change in local symmetry and a transition from the point group D_3 to C_2. This finding further indicates that the excited electron is localized and involves only one of the three bpy ligands. In contrast, no band shift upon solvation was observed for other electronic transitions, implicating that the chemical environment has no impact on these excited states and consequently that their promoted electrons are delocalized.[200,201] These results are corroborated by resonance-enhanced Raman and transient infrared (IR) spectroscopic studies.[202,203]

The ^{3}MLCT intensity, lifetime and quantum yield are dependent on the pH, the ambient temperature and the type of solvation sphere.[204] In addition, the lifetime of the excited state can be specifically quenched or extended by precise modulation of the intrinsic ligand properties.[170] For instance, the introduction of electron-withdrawing or electron-donating ligands can reduce or increase the HOMO-LUMO band gap, thereby exerting a

stabilizing or destabilizing effect on the affected orbitals. The versatile functionalization options allow for precise fine-tuning of the congruent structure-property correlations, as demonstrated by Hernández-Castillo, González and colleagues in a comprehensive compilation from a theoretical perspective.[205] The redox and absorption properties can be adjusted in a similar manner, with reduced energy gaps for LC, MC and MLCT leading to bathochromic shifts in the absorption and emission bands.[206] Thus, judicious design of ligands is a potent strategy to achieve desired properties of Ru-based PSs.[170]

In summary, the high molar extinction coefficients (ε, see Figure 1.17a) and the relatively long excited state lifetime of $[Ru(bpy)_3]^{2+}$ ($\tau \sim 600$ ns in aqueous media[207] and ~ 870 ns in MeCN at r.t.[208]) initially lead to an excited ^{1}MLCT state. This state rapidly transitions to the lowest excited ^{3}MLCT state *via* ISC due to vibrational and solvent relaxation.[209,210] The fast and efficient population of this state is facilitated by the heavy Ru atom due to its strong spin-orbit coupling, which enables the mixing of ^{1}MLCT and ^{3}MLCT states.[211] The lowest excited ^{3}MLCT state determines the exceptional photochemical and photophysical properties of the molecular chromophore, as described in the Kasha's rule, which takes into account the population principles defined by the Boltzmann equilibrium distribution.[195] For example, the large energy gap to the ground state confers the complex a red luminescence emission of moderate yet pronounced intensity at approx. 620 nm.[212] Furthermore, the high chemical stability of $[Ru(bpy)_3]^{2+}$ in the ground state, in the lowest excited state and in the one-electron oxidized and one-electron reduced forms was demonstrated, as no ligand dissociation was observed.[213] These properties are valuable for sundry photocatalytic applications, especially for photo-assisted organic synthesis,[214] photodynamic therapy,[215] and renewable energy conversion.[216]

This molecular chromophore is of particular interest for the role of the PS in artificial photosynthesis due to its strong absorption capacity, its longevity and the associated reactivity of the excited ^{3}MLCT state with regard to bimolecular interactions with suitable reaction partners (see chapter 1.4). Additionally, a comprehensive understanding of the kinetics of photoinduced charge transfer and the timescales of the product recombination reactions has already been acquired.[217]

In the context of visible light-driven OER, the excited PS* state can undergo oxidative quenching by suitable SOAs that possess sufficient electrochemical potentials, reaching as low as -0.86 V *vs*. NHE (*e.g.* persulfate). The *in situ* formed, one-electron oxidized

$[Ru(bpy)_3]^{3+}$ complex is a strong chemical oxidant with a redox potential of +1.26 V *vs*. NHE and is reduced again by fast secondary interactions with auspicious OECs under the liberation of O_2. Conversely, in the presence of electron-donating SRAs and compatible HECs, H^+ can undergo photochemical reduction *via* either an oxidative or a reductive pathway. The mechanism in operation depends primarily on the thermodynamics, kinetics and electronic properties of the reactants. The catalytic cycles differ more specifically in the quenching mechanism of PS^*. In the reductive pathway, the singly reduced strong reducing agent $[Ru(bpy)_3]^+$ with a redox potential of -1.28 V *vs*. NHE is photogenerated by SRAs with a sufficient electrochemical potential up to +0.84 V *vs*. NHE (*e.g.* TEA).

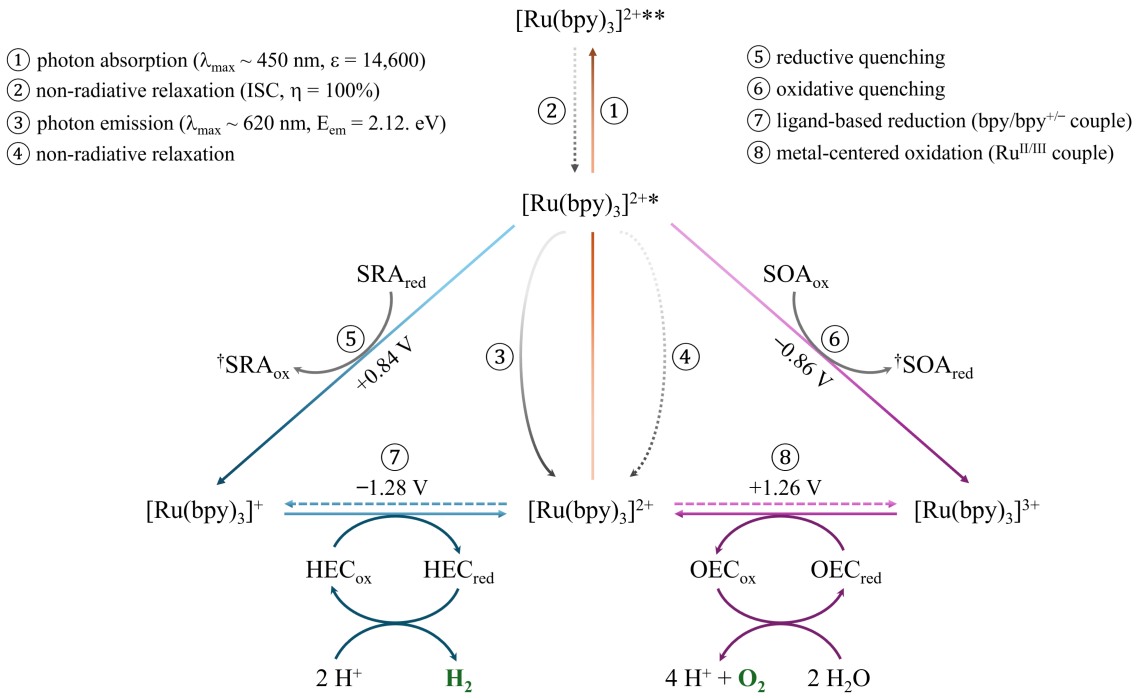


Figure 1.18 Photophysical properties (①-④) and photochemical redox processes (⑤-⑧) of $[Ru(bpy)_3]^{2+}$ as PS for light-driven WOC and HER: ① The absorption of photons (orange arrow) leads to the formation of $[Ru(bpy)_3]^{2+**}$, which represents the initial, higher-energy, spin-allowed ^{1}MLCT state. ② Efficient non-radiative relaxation by ISC yields the thermally equilibrated, lowest spin-forbidden excited ^{3}MLCT state represented by $[Ru(bpy)_3]^{2+*}$. ③/④ The excited state can be deactivated by either non-radiative processes (dashed gray arrows) or by the emission of a photon with an energy content of 620 nm (bold gray arrow). Note that theoretically 2.12 eV are available for energy transfer processes. ⑤ The blue bold arrows show the photocatalytic HER cycle, which comprises reductive quenching of PS* with suitable SRAs to form $[Ru(bpy)_3]^+$, subsequent re-oxidation of the PS in the presence of HECs and proton reduction to H_2. ⑥ The purple bold arrows depict the light-driven WOC cycle, which involves oxidative quenching of PS* with appropriate SOAs to form $[Ru(bpy)_3]^{3+}$, subsequent re-reduction of the PS in the presence of OECs, and liberation of O_2 upon water oxidation. When SOA is replaced by HEC and OEC by SRA, this pathway is also representative of the oxidative HER mechanism. † describes the sacrificial nature of these species due to their consumption during the photocatalytic cycle. ⑦ The ligand-centered chemical reduction of $[Ru(bpy)_3]^{2+}$ is shown by the blue dashed line. ⑧ The metal-centered chemical oxidation of $[Ru(bpy)_3]^{2+}$ is described by the purple dashed line. The respective electrochemical potentials for each redox process are given *vs.* NHE in aqueous solution at r.t. Note that no stoichiometric information is provided.[135,218,219]

This mechanism involves ligand-centered reduction processes that are best described by $[Ru^{II}(bpy)_2(bpy^{-})]^{+}$. Subsequent electron transfer to molecular HECs restores the original PS conformation. Once another electron has been preserved, the HEC can produce H_2. On the other hand, the PS* can also be initially oxidatively quenched through primary collisions with HECs species. Immediate reactions with SRAs enable the subsequent reductive regeneration of $[Ru(bpy)_3]^{2+}$. After completion of a further cycle, H_2 is released. Figure 1.18 provides a synopsis of the diverse reversible photophysical and photochemical redox properties of $[Ru(bpy)_3]^{2+}$ discussed in this chapter.[135,218–220]

However, $[Ru(bpy)_3]^{2+}$ is not ultimately stable under photocatalytic conditions. Photo-decomposition was observed in low-polarity solvents due to the loss of one of the bpy ligands. This is because the Ru–N bonds are labile and can be cleaved as a result of a stronger population of thermally activated excited ^{3}MC states. Water, hydroxo, chlorido, MeCN or other suitable coordinating groups can bind to vacant Ru metal sites to form $[Ru(bpy)_2X_2]^{2+n}$ (X = substituent containing the charge "n", *e.g.* $[Ru(bpy)_2Cl_2]$).[221–224] Van Houten and Watts therefore claimed that the observed photoactivity is due to ligand substitution rather than photoredox reactions.[225] In a related study, Bonnet and co-workers outlined another oxidative degradation pathway, which pertains to the instability of the oxidized PS in neutral and alkaline solutions (see Figure 1.19). Here, the α-carbon atoms of the bpy ligands exhibit susceptibility to attack by hydroxide (OH^-). A cascade of oxidation reactions, initiated by persulfate or a second $[Ru(bpy)_3]^{3+}$ molecule, leads to the decomposition of PS during progressive light-driven WOC.[226] It should be noted that ruthenium oxide, a potential oxidation product, exhibits catalytic activity towards OER. Therefore, the formation of solid particles must be excluded (*e.g.* by dynamic light scattering) in the evaluation of photocatalytic systems that use Ru-based PSs.[227]

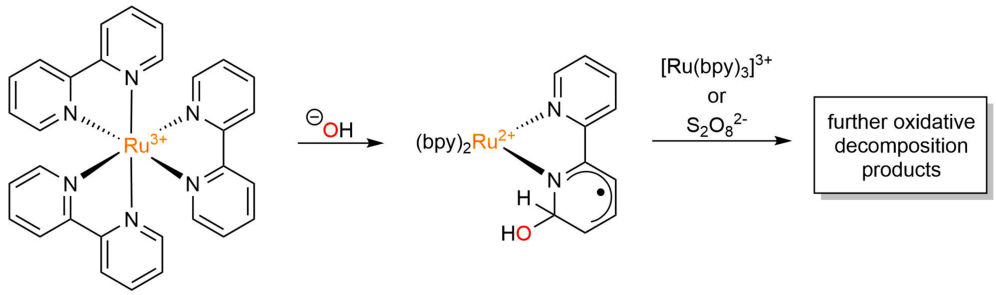


Figure 1.19 Possible decomposition pathway of oxidized $[Ru(bpy)_3)]^{3+}$ by the attack of hydroxide ions on the α-carbon atoms of the bpy ligands during visible light-driven WOC in neutral or alkaline media in the presence of persulfate as SOA.[226]

1.6 Polyoxometalate Chemistry

POMs are molecular clusters of high-valent early transition metals and oxygen that typically exhibit exceptional redox activity. This universal class of inorganic compounds generally (though not exclusively) encompasses polyanionic species with the general formula $[M_xO_y]^{n-}$, where M is designated as the *addenda* atom. The molecular structures can be rationalized by highly symmetrical Platonic or Archimedean $[MO_y]$ subunits (y = 4-7), which are connected by their corners, edges or more rarely by their faces sharing one, two or three μ-oxo bridging M–O–M bonds (see Figure 1.20). High metal oxidation states are a requisite to almost completely compensate for the immense negative charge of the cluster that originates from the oxo anions. In contrast, oxo ligands have been shown to stabilize multiple oxidation states of the *addenda* atoms. This results in flexible metal distances with both strong and weak M–M-interactions, which provide favorable binding sites in close spatial proximity for a variety of substrates. For instance, effective bond formation between two oxygen atoms in WOC can be greatly facilitated (*cf.* mechanistic details for the natural OEC described in chapter 1.3.1). Hence, POMs are regarded as excellent reactive catalysts for a range of different oxidation reactions.[228–232]

The raw spectrochemical effect of the hard Lewis oxo base is also responsible for reduced d-orbital energies of the respective *addenda* atoms. This, in turn, provides for progressively decreasing surface nucleophilicity due to the formation of strong multiple metal-ligand bonds in the unique self-assembly process of small polyhedral building blocks, such as $[MO_4]$ tetrahedra, to larger 2D or 3D architectures. Consequently, POMs are constructed by both primary σ-bonds occurring in bridging oxo units and terminating M–O(H) groups as well as strong, stabilizing π-bonds with short terminal M=O character. In this way, various discrete, quasi-spherical cluster structures with versatile topologies are generally accessible.[231–233]

POM motifs also exhibit a striking structural diversity associated with eminent properties of outstanding tunability as almost every element of the periodic table can be incorporated into their scaffolds *via* an extensive library of connection modes between various linkable units, including different *addenda* atoms, several heteroatomic templates and diverse organic or organometallic functionalities.[234] The following chapters 1.6.1–1.6.3 will address the most salient aspects of POM chemistry in relation to this work.

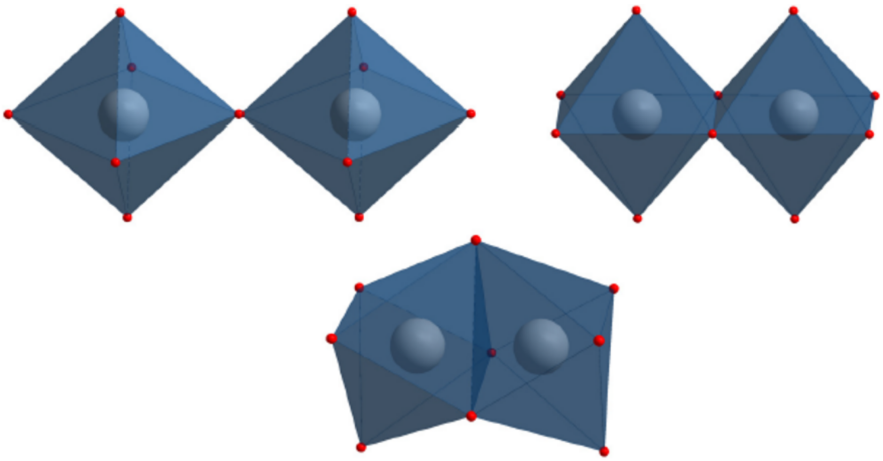


Figure 1.20 Mixed polyhedral and ball-and-stick representations of different connection modes between polyhedral units in POMs. **Top left:** Corner-sharing [MO_6] octahedra *via* a μ_2-oxo ligand. **Top right:** Edge-sharing [MO_6] octahedra *via* two μ_2-oxo ligands. **Bottom:** Face-sharing [MO_6] octahedra *via* three μ_2-oxo ligands. **Color scheme:** dark blue: [MO_6] octahedra; gray: *addenda* atom M; red: oxygen atoms O of the respective oxo ligands. Reproduced under the terms of the CC BY-NC 4.0 license.[229] Copyright 2024, Ulm University.

1.6.1 Structural Diversity

Tungsten, molybdenum and vanadium in electronic d^0- or d^1-configuration, *i.e.* W^{VI}, Mo^{VI} and V^V, are traditionally used as *addenda* atoms to form POMs.[231,232] In recent decades, increasingly advanced developments in polyoxoniobate (Nb^V) and -tantalate (Ta^V) chemistry have also been reported.[235] These transition metals are characterized by a favorable charge-to-ionic radius ratio and the availability of unoccupied d-orbitals that allow effective bonding to oxygen atoms.[231] Depending on their chemical composition, POMs can be divided into two primary subclasses: isopolyoxometalates (Iso-POMs) and heteropolyoxometalates (Hetero-POMs).

Iso-POMs are described by the general formula $[H_zM_xO_y]^{n-}$. These structures exclusively contain *addenda* atoms of a single type and a variety of (protonated) oxo ligands, which considerably impedes cluster formation in terms of structural and spatial flexibility and stability.[232,236] In addition, they characteristically possess high negative charges and strong basic oxygen surfaces, endowing them promising building block capabilities for post-modifications and further structural rearrangements, leading to the formation of more extensive cluster systems. The final motif is thereby strongly dependent on the solvent and counterion used, which is described in more detail in chapter 1.6.2.[237]

A prevalent Iso-POM is the Lindqvist anion $[M_6O_{19}]^{n-}$ (M = Mo, W, Nb, Ta), which consists of a hexametalate scaffold (see Figure 1.21a). Each *addenda* atom is peripherally bridged by four μ_2-oxo ligands and binds an additional oxo anion in a terminal fashion. The six $[MO_6]$ octahedra are connected by a common vertex and are condensed over the edges around a central μ_6-oxygen atom, arranging themselves in an idealized O_h point group symmetry.[238–240]

Although vanadium is more focused on the formation of Iso-POMs, the classic Lindqvist anion cannot be attained. Instead, the systematic replacement of μ-oxo ligands with stabilizing organic ligands is imperative.[240] Remarkably, polyoxovanadates demonstrate a greater synthetic complexity than polyoxomolybdates or -tungstates, which arises from the incorporation of octahedral $[VO_6]$, square pyramidal $[VO_5]$ or tetrahedral $[VO_4]$ moieties into their frameworks.[241] Two prime examples of the polyoxovanadate family are the tetravandate $[V_4O_{12}]^{4-}$ ($\{V_4\}$) and decavanadate $[V_{10}O_{28}]^{6-}$ ($\{V_{10}\}$) clusters.[242,243]

Hetero-POMs are preferably formed by Mo and W and represent the second generic class of POMs with the general formula $[X_zM_xO_y]^{n-}$ ($z \leq x$). These compounds contain at least one additional heteroatom X, which is typically an element from the p- or d-block of the periodic table (*e.g.* Si, P, Co, *etc.*).[232,233] The impact of both the *addenda* and the heteroatoms on the final structural, chemical and electronic properties of the cluster is significant. This impact is evident in the redox potential of the cluster shell, the light absorption characteristics and the acidity of the protonation sites.[244] In addition, the heteroatoms can serve as synthetic structure-directing template ions (*e.g.* phosphate, chloride, *etc.*). In such instances, their coordination spheres are often reflected in the final cluster motif and thereby enforce an additional stabilizing effect. Hence, Hetero-POMs show a higher degree of structural variability compared to Iso-POMs and both compound classes exhibit decisive disparities in their properties.[231,237]

The Keggin anion $[XM_{12}O_{40}]^{n-}$ ($M = W^{VI}, Mo^{VI}$; $X = Si^{IV}, P^{V}$, *etc.*) is the most prominent Hetero-POM archetype and was first prepared unconsciously by J. J. Berzelius in 1826. However, the molecular structure could not be identified until J. F. Keggin documented the structure of a related heteropolyacid in 1933, which he resolved by X-ray powder diffraction analysis (see Figure 1.21b).[245,246] The framework consists of a central $[XO_4]$ tetrahedron surrounded by twelve distorted edge- and corner-sharing $[MO_6]$ octahedra. Three of these octahedra self-organize into an edge-shared $[M_3O_{13}]$ subunit around a

trigonal C_3 axis. The four so-called triads are aligned tetrahedrally in a corner-sharing mode with respect to the central template tetrahedron. Twelve additional oxo ligands are terminally bound to the *addenda* atoms, resulting in an overall point group symmetry T_d for the α-Keggin anion.[232,247,248] The β-isomer of the Keggin anion in deviating C_{3v} symmetry is obtained by rotating the triad at the tip of the polyanion by 60°, as illustrated by dark blue octahedra in Figure 1.22. The rotation of a second, third and fourth triad by 60° yields the γ-, δ- and ε-isomers, respectively, as once proposed by Baker and Figgis. These isomers are severely destabilized, attributable to the rotation of the triads and the augmented number of close M–M contacts, which gives rise to an increase in repulsive coulombic interactions.[232,244] However, the α-Keggin anion shows notable stability and has the highest acid strength and availability among the Hetero-POMs.[248]

Two further selective representatives of Hetero-POMs are namely the Wells-Dawson $[X_2M_{18}O_{62}]^{n-}$ and the Anderson-Evans cluster $[XM_6O_{24}]^{n-}$. The first heteropoly anion consists of two identical "half units", each containing a central tetrahedral template heteroanion (see Figure 1.21c). In contrast, the Anderson-Evans scaffold adopts an octahedral geometry of the heteroatom (see Figure 1.21d).[249–251]

Selective transition metal substitution is frequently employed to markedly modify the electronic cluster properties of a parent POM compound while preserving its structural integrity. The integration of electron-rich and redox-active metal centers (*e.g.* Co^{II}, Mn^{III},

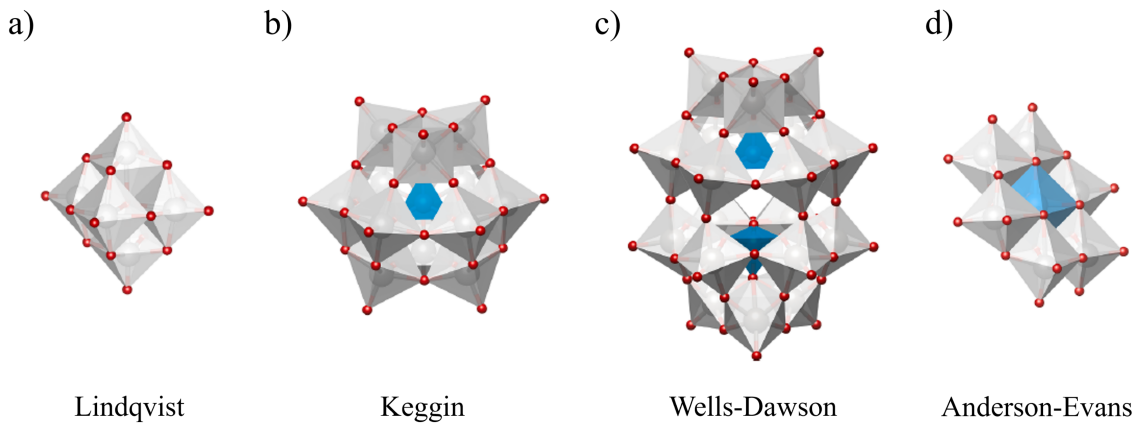


Figure 1.21 Mixed polyhedral and ball-and-stick representations of common POM clusters, highlighting their structural diversity: **a)** Lindqvist anion $[M_6O_{19}]^{n-}$. **b)** Keggin anion $[XM_{12}O_{40}]^{n-}$. **c)** Wells-Dawson anion $[X_2M_{18}O_{62}]^{n-}$. **d)** Anderson-Evans anion $[XM_6O_{24}]^{n-}$. **Color scheme:** gray: *addenda* atoms M and their octahedral $[MO_6]$ units; blue: heteroatom X and its polyhedral $[XO_y]$ unit; red: oxygen atoms O of the respective oxo ligands. Adapted and reproduced under the terms of the CC BY-NC-ND 4.0 license.[251] Copyright 2023, The Authors, American Chemical Society.

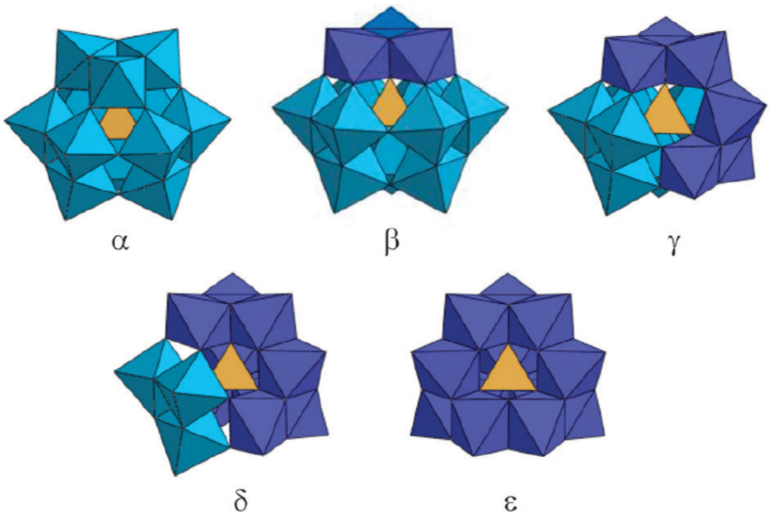


Figure 1.22 Schematic representations of the five rotational isomeric structures of the Keggin anion. The rotation of a triad consisting of three octahedral [MO_6] units is shown in dark blue. The β-, γ-, δ- and ε-isomers of the α-Keggin anion are obtained by rotating one, two, three or all four triads by 60°. The template tetrahedron [XO_4] is shown in orange. Non-rotated triads are represented by teal [MO_6] octahedral units. Reproduced with permission.[244] Copyright 2012, The Royal Society of Chemistry.

Ru^{II}, *etc.*) is particularly favored for (photo)catalytic purposes. In this regard, Streb and colleagues have demonstrated enhanced photoactivity in the visible light range for isostructural vanadium-substituted molybdate and tungstate Lindqvist clusters. They have also deciphered various reaction mechanisms that depend on the *addenda* atom and the presence of oxygen.[252] Transition metals can also be encapsulated between individual POM fragments to yield so-called sandwich-type structures, which are usually stabilized by linking heteroatoms and exchangeable water molecules. These metal centers are available for post-functionalization or provide access to catalytically active sites.[253] An example compound is presented in chapter 1.6.3.

Organic or organometallic functionalities can be incorporated into POM frameworks by covalent or non-covalent means. The linkage of these functionalities by electrostatic interactions, such as H-bonds, ionic contacts or van der Waals forces, is referred to as "Class I" materials and can be obtained, for example, through ion exchange reactions. Class II materials are hybrids with strongly covalently bonded organic and inorganic units. Metal oxide surfaces can be directly functionalized through various methods, including grafting, self-aggregation *via* condensation reactions, displacement of labile oxo ligands, encapsulation and post-functionalization using classical organic reactions such as cycloaddition, cross-coupling or esterification.[253,254] The symmetrical or asymmetrical attachment of different functional units to POM frameworks can be

achieved, for example, by the linkage strategy as outlined by Streb and co-workers. A bifunctional organic tether with a phosphonate as POM anchor and an organic azide group as linkable "Click" moiety was introduced as the basis for various post-functionalization reactions (note: "Click chemistry" refers to the Huisgen copper(I)-catalyzed alkyne-azide 1,3-dipolar cycloaddition).[255] Further examples of organic and organometallic POM compounds, including organosilyl, -phosphonyl, -stannyl, -arsonyl, -tin, -nitrogen (*i.e.* nitrido, imido, imine, diazenido and hydrazido) and alkoxo (*e.g.* carboxylato) derivatives, to name but a few, have been extensively discussed elsewhere.[253,254]

These organic-inorganic hybrids are of particular interest for the development of various functional devices (see chapter 1.6.3), as redox potentials, solubility, acid-base behavior and optical properties can be tuned with a high degree of precision. Enhanced stability, increased catalytic efficiency with reliable selectivity and improved biological activity with reduced toxicity represent the most significant developments in this field.[254] The overarching objective of functionalization can thus be described as the exploitation of the intrinsic physicochemical properties of POMs and the various synergistic effects of the functionalities. For instance, the integration of alkyl groups with variable chain lengths leads to enhanced flexibility and hydrophobicity, thereby enabling the potential formation of POM micelles.[253]

Lacunary POM clusters are preferably utilized in the aforementioned functionalization processes. These defect species are obtained by the controlled addition of a base and suitable reactants that allow the selective and formal removal of one or more metal oxo sites, *i.e.* [M=O] vertices, by hydrolysis.[232,253] Their terminal oxygen atoms at the periphery of the lacunar clusters have higher charges, stronger basicity and thus increased nucleophilicity, which facilitates subsequent reactions with a variety of electrophiles bearing organic or organometallic groups.[253,254] In particular, lacunary tungsten-based Keggin clusters show high robustness and can be systematically linked to form larger 3D and supramolecular assemblies.[256] Alternatively, various transition metals or diverse heteroanions can occupy the vacant metal binding sites (*vide supra*).[254]

Terminal or bridging oxo ligands can also be substituted with nitrosyl (NO^{-}), (di-)sulfide (S_2^{2-}, S^{2-}), isolobal or isoelectronic groups, such as nitrido (N^{3-}). These structural modifications can lead to the emergence of synergistic or even novel properties, which could be valuable for a plethora of applications (see chapters 1.6.3 and 1.7).[233,254]

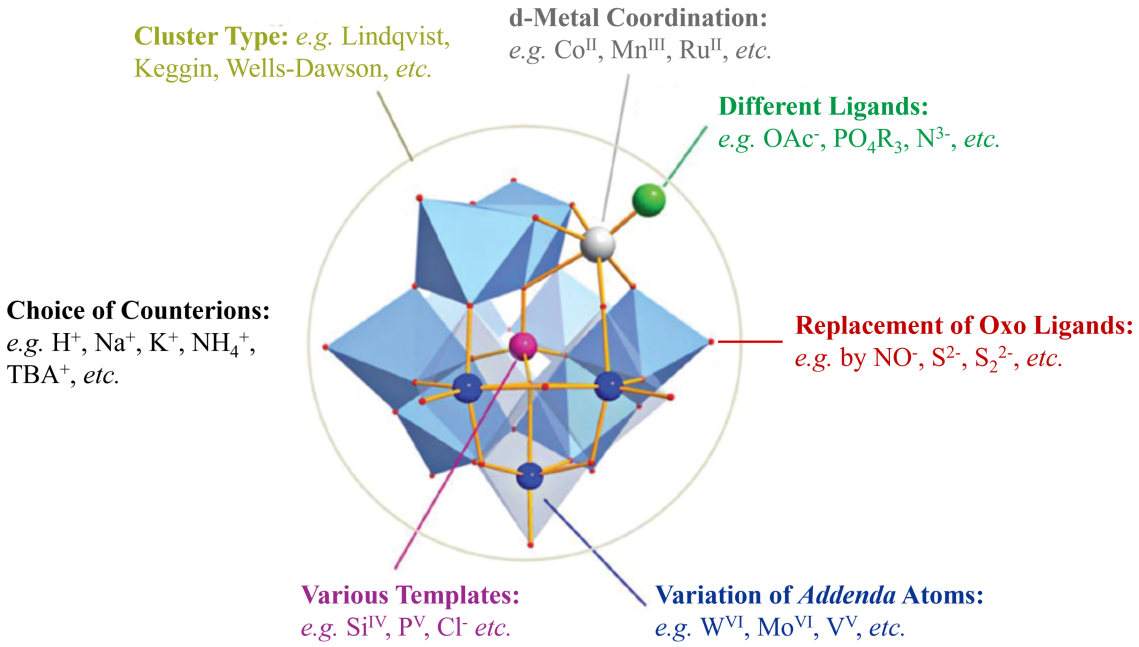


Figure 1.23 Structural diversity of POMs by variation of the cluster type (yellow) using distinct *addenda* atoms (dark blue) and/or template molecules (purple; note: Cl^- is a spherical template ion). Further chemical modifications concern the use of different cations (black), the replacement of oxo ligands (red) and the functionalization of the (lacunary) cluster by organic or organometallic ligands (green) as well as heteroatoms, in particular p- or d-type elements (gray). Adapted and reproduced under the terms of the CC BY 3.0 license.[257] Copyright 2015, The Royal Society of Chemistry. Modifications have been made to the examples, including the addition of the choice of counterions and the replacement of oxo ligands for the sake of contextual clarity, without altering the original meaning of the figure.

Figure 1.23 provides a synopsis of the structural diversity of POMs, particularly with regard to shape, size, charge and composition, which are accessible through numerous chemical modifications:

(i) Various arrangements of cluster types, *e.g.* Lindqvist, Keggin, Wells-Dawson, *etc.*

(ii) Variation of the *addenda* transition metal atoms, *e.g.* W^{VI}, Mo^{VI}, V^{V}, *etc.*

(iii) Multiple (spherical) template-forming ions, *e.g.* Si^{IV}, P^{V}, Cl^-, *etc.*

(iv) Cluster functionalization by p- or d-type heteroatoms, including transition metals, lanthanoids and certain non-metals, *e.g.* Co^{II}, Mn^{III}, Ru^{II}, *etc.*

(v) Functionalization by various organic or organometallic ligands, *e.g.* acetoxy groups (OAc^-), organophosphonyl (PO_4R_3; R = organic residue), N^{3-}, *etc.*

(vi) Replacement of oxo ligands, *e.g.* by NO^-, thio (S^{2-}, S_2^{2-}), *etc.*

(vii) Different inorganic or organic counterions, *e.g.* H^+, sodium (Na^+), potassium (K^+), NH_4^+, tetra-*n*-butylammonium (TBA^+), *etc.*[257]

1.6.2 Self-Assembly in Aqueous Solution

POMs are typically prepared by one-pot synthesis in aqueous or organic solutions at r.t. or elevated temperatures. Conventional methods are complemented by alternative techniques, including hydrothermal, continuous flow, microwave and ionic liquid methods.[237,258] The rational and systematic design of desired POM molecules is a synthetic challenge because certain parameters have a decisive influence on the surface reactivity of the oxometalate building blocks, their successive structural rearrangements in solution and their final aggregation into molecular structures.[233] Parameters must be carefully adjusted to enable controlled and predictable synthesis of POM structures with predefined properties tailored to specific applications. Primary cluster formation is determined by the identity, concentration and order of addition of precursors and reactants, such as metal oxide anions, acids and heteroanions. Secondary reaction parameters that affect, for example, the topology include solution pH, temperature, pressure, reaction time, irradiation, ionic strength of the reaction mixture, type of solvent and type of counterions, and the presence of redox agents and additional ligands.[258–260]

As previously indicated, the elements W, Mo and V are preferred for the synthesis of POMs. Their small and reactive metal oxide anions (*i.e.* WO_4^{2-}, MoO_4^{2-} and VO_4^{3-}) serve as fundamental building blocks that can be linked into larger POM frameworks through condensation reactions. Despite the elusive nature of the precise reaction mechanism, it is widely acknowledged that the self-assembly of oxometalate precursors is initiated by acidification (see Figure 1.24). The initial protonation of the terminal oxo ligands results in slight elongations of the M–O bond and less electron-deficient metal centers. Subsequently, a nucleophilic attack by H_2O is facilitated, resulting in the expansion of the metal coordination sphere from a tetrahedron (y = 4) to an octahedron (y = 6). The reactive $H_x[MO_6]^{(6-x)-}$ fragments are stabilized by internal proton-transfer between two adjacent hydroxo ligands and M=O double bond reformation. This is confirmed, *inter alia*, by simulations of molecular dynamics (MD). The extended building blocks then undergo a condensation reaction driven by entropy *via* olation or oxolation with the cleavage of labile aquo ligands. This reaction yields solvated, dinuclear *cis*-di-oxometalate species. Consecutive steps of protonation of terminal oxo ligands, accompanied by M–O bond polarization and oligo-water-condensation reactions with further reactive fragments, promote linkage to larger building blocks until strong π-back-

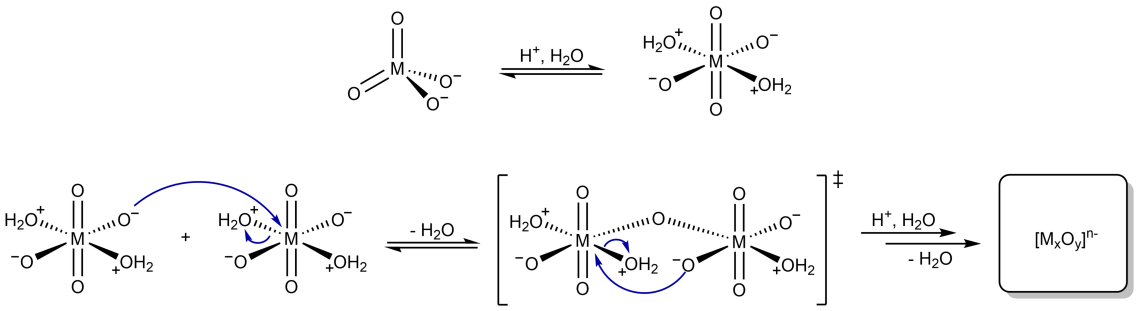


Figure 1.24 Schematic representation of the proposed mechanism for the acid-induced oligocondensation of an oxometalate precursor into discrete $[M_xO_y]^{n-}$ clusters. Note that the mechanism of self-assembly remains to be fully elucidated. Decrease in pH initiates the protonation of the small tetrahedral precursor molecules and the formation of octahedral $H_x[MO_6]^{(6-x)-}$ fragments. The ensuing rise in bond polarization facilitates the subsequent formation of μ-oxo bridges, concomitant with the elimination of H_2O. The propagation of olation and/or oxolation reactions (olation: M–OH + M–OH_2 → M–(OH)–M + H_2O; oxolation: M–OH + M–OH → M–O–M + H_2O) promotes further aggregation into discrete structures.[258]

bonding to terminal oxo ligands significantly increases the positive partial charge on the *addenda* atoms, which in turn reduces the basicity and nucleophilicity of the terminal oxygen atoms. The μ-oxo ligands become kinetically inert, thereby preventing further uncontrolled and infinite growth into solid-state metal oxide particles. Instead, an effective growth termination mechanism is established, leading to the formation of discrete molecular structures with defined sizes and topologies.[258,260–262]

The final cluster motif of the respective polyoxotungstates, -vanadates or -molybdates correlates strongly with the metal concentration and the pH-dependent equilibrium distribution of metal oxide fragments in solution. For instance, the nuclearity of the dissolved molybdenum oxide fragments increases with decreasing pH.[263–266] A general equation for the formation of an Iso-POM is shown in Figure 1.25a.[232]

The depicted scheme does not indicate the necessity of an appropriate match between charge-balancing cations and anionic POM clusters. Intrinsic electrostatic interactions have been shown to regulate the effective and selective crystallization and isolation of pure-phase POMs at the molecular level. Furthermore, the cations modulate solubility in both aqueous and polar organic solvents and play a pivotal role as structure-directing templates in the self-assembly of oxometalate precursors. The size, charge and symmetry of the cations dictate the reactivity of the various POM building blocks in solution, which affects the properties of the final cluster architecture.[236,267] For instance, heteropolyacids with H^+ as the counterion exhibit remarkable stability and display pronounced Brønsted

a) $p\,[MO_4]^{n-} + q\,H^+ \rightleftharpoons H_x[M_pO_y]^{m-} + (4p\text{-}y)\,H_2O$

b) $12\,MoO_4^{2-} + PO_4^{3-} + 24\,H^+ \rightleftharpoons [PMo_{12}O_{40}]^{3-} + 12\,H_2O$

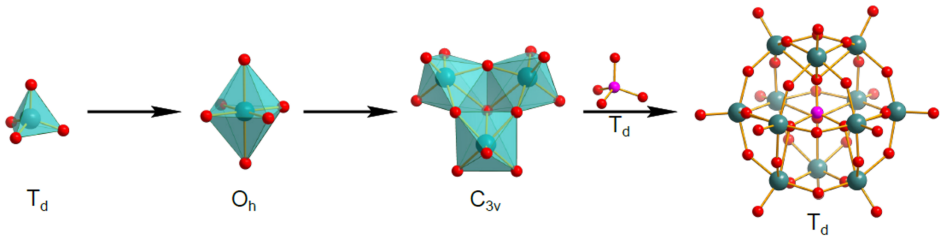


Figure 1.25 POM synthesis: **a)** General equilibrium equation for the formation of an Iso-POM. The number of protons q required for the formation of an iso-polyanion $H_x[M_pO_y]^{m-}$ can be calculated by $q = 8p–2y+x$. Note: q and p are to be regarded as formal definitions, as many Iso-POMs are not prepared by direct acidification of the precursor.[232] **b)** Exemplary illustration of the formal self-assembly process to the heteropoly Keggin anion $[PMo_{12}O_{40}]^{3-}$ by oligocondensation of the molybdate ion MoO_4^{2-} in acidic aqueous medium using the tetrahedral template heteroanion phosphate (PO_4^{3-}). The T_d symmetry of the precursor $[MoO_4]^{2-}$ is first extended to an octahedral $H_x[MoO_6]^{n-}$ fragment by accepting two additional oxo ligands. These intermediates are reactive and form trinuclear subunits (triads) with C_{3v} symmetry, which subsequently assemble with the aid of the template to form the α-Keggin cluster. The structural arrangement reflects the tetrahedral environment of the template molecule. Note: The triad shown is merely a postulated intermediate, as the compound has not yet been isolated. Nevertheless, several *in situ* studies provide evidence of their linkage. **Color scheme:** teal: *addenda* atom Mo and their polyhedral $[MoO_x]$ units; red: oxygen atoms O of the respective oxo ligands; pink: phosphorus P of the template heteroanion PO_4^{3-}. The mixed polyhedral ball-and-stick representation of the Keggin cluster formation was reproduced under the terms of the CC BY-NC 4.0 license.[229] Copyright 2024, Ulm University.

acidity.[233] Other commonly employed counterions include simple, small-sized NH_4^+, bulky organic cations like TBA^+ and alkali metals like Na^+, K^+, *etc.*[260]

Oxometalate precursors can also undergo template-promoted condensation reactions in the presence of heteroanions such as phosphate (PO_4^{3-}) or silicate (SiO_4^{4-}), yielding the corresponding Hetero-POMs.[237] The formal self-assembly to the α-Keggin structure of the molybdophosphoric acid anion $[PMo_{12}O_{40}]^{3-}$ is exemplified in Figure 1.25b, which additionally indicates the geometrical transformations for each step.[229,258]

In addition to the traditional synthesis in aqueous chemistry, POMs can also be obtained from non-aqueous solutions. For example, labile, organically soluble vanadate precursors (*e.g.* $\{V_4\}$) can be deliberately fragmented by reaction with coordinating organic solvents (*e.g.* MeCN). The reactive intermediates that are formed *in situ* self-assemble into distinct cluster frameworks through a condensation crosslinking strategy. These frameworks are then stabilized by coordinative interactions with templating organic aprotic solvent molecules.[268] The molecular recognition resulting from the type of solvent leads to a vast cluster topology and supramolecular cluster architectures.[237,258]

1.6.3 Applications of POMs – WOC Activity

The chemical and physical properties of POMs, *e.g.* redox activity, solubility in various aqueous and polar organic solvents, ability to promote electron transfer reactions, and thermal, chemical and mechanical stability, can be readily tailored to various applications. The structural diversity at the molecular scale also facilitates the selective modulation of magnetic, optical and electrical features as well as the imparting of antibacterial, antiviral or anticancer properties. In addition, ion pairing effects, particularly with molecular PSs, and the implementation of heterogenized approaches are possible as a result of the high negative charge and nucleophilic oxygen surfaces within the molecular structure.[269,270]

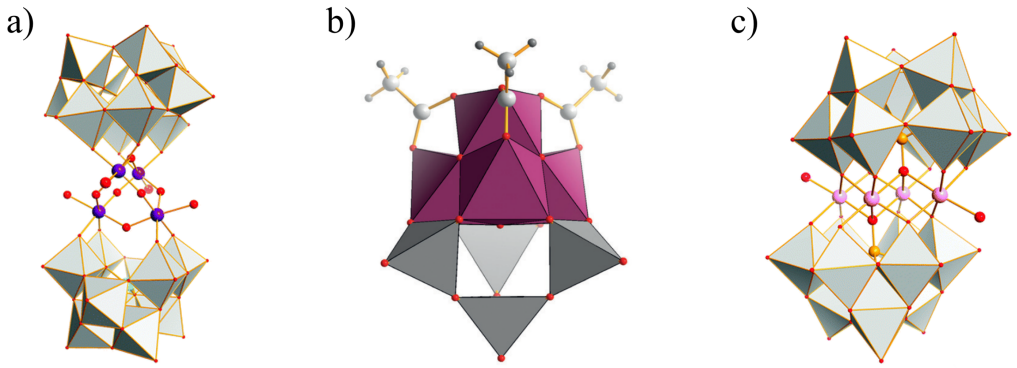
Consequently, POMs have garnered attention for their potential use in a wide range of multidisciplinary fields, including nano- to supramolecular material science,[271–273] (bio)analytical chemistry,[274] sensor technology,[275] medicine,[276–278] mineralization and purification,[279–281] molecular magnetism and spintronics,[282–284] photochromism,[285,286] homogeneous and heterogeneous (photo)catalysis,[287–290] energy conversion and storage,[291–293] and model systems for solid-state metal oxides.[294]

Furthermore, the use of functionalized POMs as OECs in electro- and light-driven WOC holds great promise. Transition metal substitution provides redox-active sites capable of abstracting an electron from water or oxo ligands, while lacunary POM fragments can stabilize the physical cluster architecture under harsh hydrolytic and oxidizing conditions. The reversible uptake and release of a specific number of electrons in PCET processes is assisted by the terminal and bridging oxo ligands in close proximity to redox-active sites. In contrast, exchangeable organic ligands can be utilized to introduce accessible water binding sites, which can also exert an additional stabilizing effect.[140]

Intriguingly, POMs are known to undergo photo-induced redox reactions as a result of light-dependent LMCT processes, generating reactive SOMOs with oxocentric diradical character ($W^{V\bullet}$–$O^{\bullet}$). However, their photoactivity is often severely hindered by their poor visible light absorption capacity. Thus, POM-OECs are usually combined with light-collecting PSs and terminal electron-accepting SOAs to engineer sustainable systems for the conversion of light into storable energy equivalents (see chapters 1.4 and 1.5).[295] The subsequent section will delineate three prominent POM-OECs, with a particular emphasis on a POM that will be further explored in the ensuing experimental part of this work.

One of the first POM-mediated WOC activities under chemical and photochemical conditions was reported for the sandwich-type tetranuclear Ru-based polyoxotungstate $[\{Ru_4(\mu\text{-}O)_4\text{-}(\mu\text{-}OH)_2(H_2O)_4\}(\gamma\text{-}SiW_{10}O_{36})_2]^{10-}$ ($\{Ru_4\}$; see Figure 1.26a). A remarkable TON of 180 was observed for the light-driven reaction in aqueous buffered media at ambient temperature.[296,297] However, the WOC performance of this system is surpassed by that of the manganese-based molecular polyoxovanadate cluster $[Mn_4V_4O_{17}(OAc)_3]^{3-}$ ($\{Mn_4V_4\}$), which serves as a synthetic model of the natural OEC in its reduced S_1 state. The active site is constituted by a mixed-valent $[Mn_4O_4]$ cubane core, which is stabilized by a hybrid organic-inorganic coordination sphere (see Figure 1.26b). The organo-soluble POM cluster operates in combination with $[Ru(bpy)_3]^{2+}$ (hereafter: Ru-PS) and $Na_2S_2O_8$ in a MeCN:H_2O mixture (9:1, v/v) with a TON of 1,150.[298] However, $\{Mn_4V_4\}$ readily decomposes in H_2O into chemically WOC-active colloidal Mn-V-oxide particles, which limits the homogeneous light-driven OER to predominant organic systems.[299]

In most cases, the utilization of the inaugural cobalt-based POM-OEC model $[Co^{II}_4(H_2O)_2(\alpha\text{-}PW_9O_{34})_2]^{10-}$ ($\{Co_4\}$) is favored for novel inquiries in aqueous systems with respect to formulating cost-effective large-scale applications. The economic viability of $\{Co_4\}$ over $\{Ru_4\}$ stems from the fact that the framework is based only on earth-abundant metals, thereby eliminating the use of precious metal centers. The molecular sandwich-type structure was first synthesized in 1973 by Weakley, Evans and colleagues and consists of a flat $[Co_4O_4]$ core of edge-linked $[CoO_6]$ octahedra. Two stabilizing oxidation-resistant lacunar Keggin-type polyoxotungstate ligands provide proton-transfer sites in close vicinity to the redox-active cobalt sites (see Figure 1.26c). In a subsequent study, Hill, Lian and colleagues reported a strong pH dependence for the visible light-driven WOC performance and a crucial role of the type and concentrations of reactants used. The combination of the catalyst with Ru-PS and $S_2O_8^{2-}$ as SOA in an 80 mM sodium borate buffer at pH 8.0 yielded TONs reaching up to 220.[300–303] In contrast to $\{Mn_4V_4\}$, a higher stability to oxidative and hydrolytic degradation under turnover conditions was observed, which can be attributed to the absence of organic ligands. In this regard, the authors excluded the *in situ* formation of heterogeneous WOC-active cobalt species, as structural features of hydroxide ($Co(OH)_2$), oxide (CoO_x) or hydrated ions ($Co^{2+}(aq)$) could not be detected. Thus, $\{Co_4\}$ is robust against coordinative lability and fast ligand exchange mechanisms within the prevailing chemical oxidation parameters.[303–305]



{Ru_4}	**{Mn_4V_4}**	**{Co_4}**
TON = 180	TON = 1150	TON = 224
TOF = 0.08 s^{-1}	TOF = 1.75 s^{-1}	TOF = 0.83 s^{-1}

Figure 1.26 Mixed polyhedral and ball-and-stick representations of POM-OECs and comparison of their light-driven WOC activity in the presence of the molecular Ru-PS and the SOA $S_2O_8^{2-}$ by reporting TONs and TOFs. **a)** $[\{Ru_4(\mu\text{-}O)_4\text{-}(\mu\text{-}OH)_2(H_2O)_4\}(\gamma\text{-}SiW_{10}O_{36})_2]^{10-}$ ($\{Ru_4\}$). Reproduced with permission.[305] Copyright 2012, The Royal Society of Chemistry. **b)** $[Mn_4V_4O_{17}(OAc)_3]^{3-}$ ($\{Mn_4V_4\}$). Cropped from original and reproduced with permission.[298] Copyright 2016, Wiley-VCH Verlag GmbH & Co. KGaA, Weinheim. **c)** $[Co_4(H_2O)_2(\alpha\text{-}PW_9O_{34})_2]^{10-}$ ($\{Co_4\}$). Reproduced with permission.[305] Copyright 2012, The Royal Society of Chemistry. TONs and TOFs are assigned according to the references.[297,298,300] **Color scheme:** purple: Ru^{IV}; plum: $Mn^{III/IV}$; pink: Co^{II}; teal: template heteroatom Si; orange: template heteroatom P; dark gray: *addenda* atom V and their octahedral [VO_6] units; light gray: *addenda* atom W and their octahedral [WO_6] units; red: oxygen atoms O of the respective oxo ligands; the organic ligands in b) are denoted by light gray large spheres of C and gray small spheres of H.

However, a significantly reduced WOC activity and stability under electrocatalytic conditions was observed for a structural analog of $\{Co_4\}$ incorporating manganese instead of cobalt ions. These findings underscore the challenges inherent in the design of bio-inspired POM-OECs for water oxidation. The results also emphasize the necessity for more systematic research into structure-property relationships, the identification and validation of detailed mechanistic events and the development of potential self-repair mechanisms in molecular-based WOC systems.[306]

1.7 Thiomolybdate Chemistry

This chapter is mainly based on the investigations reported in the review article **{MLa-4}**[147] and is supplemented by pertinent examples from the literature.

Molecular molybdenum sulfide clusters, also known as thiomolybdates, were initially investigated as biomimetic models for the cofactors of the active sites of nitrogenase and hydrogenase, which are pivotal for the HER in biological systems (see chapter 1.3.2). The general structure is based on redox-active molybdenum centers coordinated by S^{2-} or S_2^{2-} ligands.[307,308] The most common thiomolybdate prototypes are the $[Mo^{IV}_3S_{13}]^{2-}$ ({Mo_3}) and $[Mo^{V}_2S_{12}]^{2-}$ ({Mo_2}) clusters. These two compounds were first synthesized in 1978 by Müller and colleagues *via* ligand exchange and reduction of an oxomolybdate precursor (*e.g.* $(NH_4)_6[Mo^{VI}_7O_{24}]$) in an aqueous solution using an excess of polysulfide ions. Their respective structures were unambiguously elucidated by single-crystal X-ray analysis, which revealed three different ligand types: apical S^{2-}, bridging S_2^{2-} and terminal S_2^{2-} (see Figure 1.27).[309,310] The apical μ_3-S^{2-} ligand, which is only present in the triangular {Mo_3} and connects all three Mo^{IV} centers, plays a crucial role in the thermal transformation of {Mo_3} into the hexagonal MoS_2 lattice, since the initial dimerization and stacking of individual cluster molecules originate from this ligand.[311]

In contrast to high-valent POMs, the sulfur-based ligands stabilize the molybdenum centers in reduced oxidation states, as evidenced by the above formulas of {Mo_3}, {Mo_2}

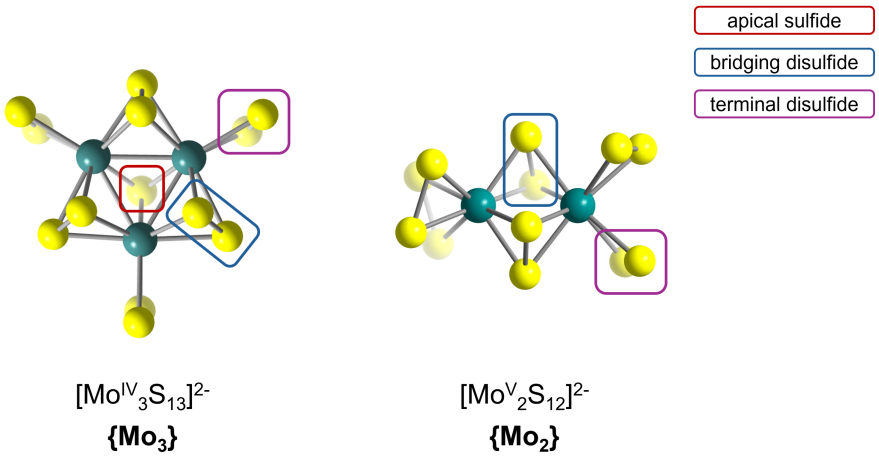


Figure 1.27 Ball-and-stick representations of the two prototype thiomolybdate clusters {Mo_3} (left) and {Mo_2} (right), highlighting the different ligand types: terminal S_2^{2-} (purple), bridging S_2^{2-} (blue) and apical S^{2-} (red). **Color scheme:** teal: Mo; yellow: sulfur atoms S of the respective S^{2-}/S_2^{2-} ligands. Cropped, adapted and reproduced under the terms of the CC BY 4.0 license.[147] Copyright 2023, The Authors, Advanced Materials published by Wiley-VCH GmbH.

and the heptamolybdate precursor. This disparity can be attributed in part to the larger ionic radius of S^{2-}, which bears an equivalent charge to O^{2-}, resulting in weaker Lewis-base properties with lower electronegativity, increased polarizability and reduced π-donor capabilities. On the other hand, the bulky diatomic S_2^{2-} ligand favors a high coordination number and formally occupies two coordination sites of the metal centers, leading to excellent steric shielding of the Mo atoms by forming small MoS_2-angles.[309] In addition, this group introduces the same electrical charge of -2 as the monoatomic S^{2-} ligand, which limits the structural and electronic stabilization of high-valent molybdenum centers as well as the formation of high cluster charges. Therefore, thiomolybdate species generally tend to form low-nuclearity aggregates.[231]

These discrepancies are also reflected in their different applications (see chapter 1.7.1). Polyoxomolybdates exhibit diminished thermodynamic stability in reductive media due to the "over-reduction" of molybdenum. High negative charges cannot be stabilized, which leads to the degradation of the clusters. However, the electronic structure cannot be further oxidized, which allows their use as stable oxidation catalysts. Conversely, thiomolybdates are robust under reducing conditions but decompose in oxidative reaction environments. Their redox reactivity is therefore often associated with electronic transitions of the sulfide/disulfide redox couple (*i.e.* S^{2-}/S^{-}), while the 4d-electrons of molybdenum are stabilized in covalent Mo–Mo bonds. Intramolecular redox reactions, in which the sulfide is oxidized and the Mo center is reduced, can thus readily occur. Such reactions are triggered, for example, by heating or hydrogen adsorption *via* initial protonation at the affine sulfide ligands.[163]

Combinations of POM and thiomolybdate moieties in a common framework by linking oxo- and sulfide ligands are also known. Prominent examples of these oxothiomolybdate clusters are $[Mo_2O_2(\mu\text{-}S)_2(S_2)_2]^{2-}$ and $[Mo_2O_2(\mu\text{-}S)_2(S_2)(S_4)]^{2-}$, which differ solely in the replacement of a terminal disulfide ligand by a tetrasulfide group (see Figure 1.28).[312] The terminal S_2^{2-} ligands of the former cluster can further be selectively oxidized by iodine to $[Mo_2S_2O_2]^{2+}$ building blocks, which can be linked in alkaline solution in a reversible self-condensation reaction *via* alternating hydroxo double-bridges to form the neutral, cyclically arranged molecular dodecameric "wheel" $[Mo_{12}S_{12}O_{12}(OH)_{12}(H_2O)_6]$. This cluster structure is characterized by a central cavity of *ca.* 11 Å and shows good host-guest properties.[313,314]

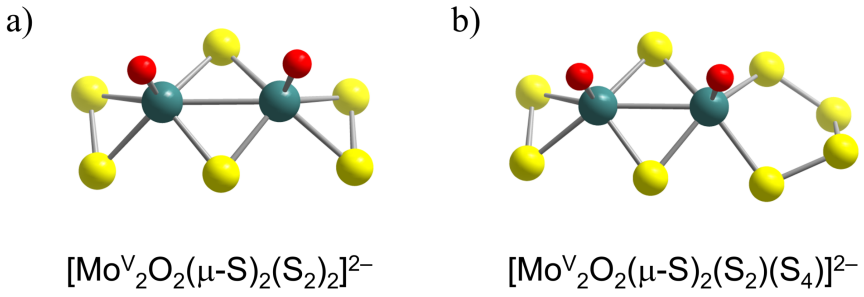


Figure 1.28 Ball-and-stick representations of the oxothiomolybdate clusters **a)** $[Mo^{V}_2O_2(\mu\text{-}S)_2(S_2)_2]^{2-}$ and **b)** $[Mo^{V}_2O_2(\mu\text{-}S)_2(S_2)(S_4)]^{2-}$. **Color scheme:** teal: Mo; red: oxygen atoms O of the respective oxo ligands; yellow: sulfur atoms S of the respective S^{2-}/S_2^{2-} ligands. Cropped, adapted and reproduced under the terms of the CC BY 4.0 license.[147] Copyright 2023, The Authors, Advanced Materials published by Wiley-VCH GmbH.

Examples of structurally related thiotungstates (*e.g.* $[W_3S_9]^{2-}$),[315] or oxothiotungstates (*e.g.* $[W_2O_2(\mu\text{-}S)_2(S_2)(S_4)]^{2-}$)[312] as well as the modification of (oxo)thiomolybdates by organofunctionalization have also been reported,[316,317] demonstrating the great structural diversity of this inorganic compound class, which can be leveraged to enhance the understanding of structure-property-reactivity relationships.

1.7.1 Applications of Thiomolybdates – HER Activity

Heterogeneous MoS_2-based catalysts are traditionally employed as efficient and robust co-catalysts for the removal of sulfur, oxygen or other metals from petroleum feedstocks during the conversion of crude oil into valuable products such as gasoline or kerosene. The corresponding industrial hydrotreating processes of hydrodesulfurization (HDS), hydrodeoxygenation (HDO) and hydrodemetallization (HDM) involve hydrogenation or hydrogenolysis reactions, each requiring the prior activation of hydrogen with molybdenum sulfide sites by hydrogen adsorption on the catalyst surface.[318] This step resembles the Volmer reaction in the electrochemical HER (see chapter 1.4), indicating a potential reactivity of molybdenum sulfides for H_2 production. Therefore, cost-effective and long-term stable crystalline, amorphous and nonstoichiometric molybdenum sulfides with S-to-Mo ratios higher than two (*i.e.* MoS_2, a-MoS_x and MoS_{2+x}, respectively) have garnered attention as promising alternatives to expensive and scarce noble metal-based high-performance electro- and photocatalysts for the HER. Specifically, a-MoS_x shows comparable HER activity rates to established Pt-based HECs.[319–322]

The breakthrough in this field of research is based on two crucial studies. First, it was discovered that the edge-sites of crystalline MoS_2 sheets play a decisive role in the HER mechanism, while the basal planes are catalytically inert.[323] Second, it was found that the composition of HER-active a-MoS_x consists of coordination polymer chains formed by highly ordered discrete {Mo_3} clusters, which share each two terminal S_2^{2-} ligands.[324] Thiomolybdates can thus be considered as homogeneous mimics of heterogeneous, nanostructured molybdenum sulfides, providing atomic insights and a more profound understanding of their HER performance. The molecularly well-defined scaffolds and the structural versatility can be used to decipher active sites, rationalize mechanistic pathways of catalyst activation and deactivation, and tune HER reactivity (see chapter 3.1) in a similar manner as previously described for WOC-active POMs (see chapter 1.6.3), using a wide range of modern (*in situ*/*operando*) analytical techniques.[325] The first report of electrochemical HER activity was published in 2008 by Chorkendorff and co-workers for the cubane-type $[Mo_3S_4(H_2O)_9]^{4+}$.[326] A decade later, the first visible light-driven HER reactivity studies with {Mo_3} and Ru-PS under homogeneous conditions were independently performed by Min and co-workers[327] and Streb and colleagues.[328]

Min and co-workers investigated the effect of primary catalysis parameters on the HER performance of {Mo_3}. They examined a range of catalyst and PS concentrations, their molar ratios and several SRAs of organic identity, including amines and carboxylic acids. Their findings indicate that AscOH can donate both protons and electrons, which supports PCET processes and thus promotes the light-driven HER. Furthermore, the use of the organic dye Eosin Y has been shown to be not conducive to drive photocatalysis by {Mo_3} due to insufficient excited state interactions between PS and SRA, which hinders the efficient operation of a reductive quenching mechanism. The authors have further shown that {Mo_3} acts as an oxidative quencher for Ru-PS in this particular photosystem (*cf.* the mechanistic details shown in Figure 1.18).[327]

In contrast, Streb and colleagues conducted mechanistic studies of {Mo_3} in MeOH/H_2O mixtures in the presence of Ru-PS and the SRA AscOH using Raman spectroscopy and density functional theory (DFT) calculations. The authors discovered variations in the HER activity depending on the number of terminal S_2^{2-} ligands dynamically exchanged with aquo ligands (see chapter 3.1) and used these insights to optimize the solvent ratio to 10:1 (MeOH:H_2O, v/v, pH 6.0) to stabilize the most reactive {Mo_3} derivative, which

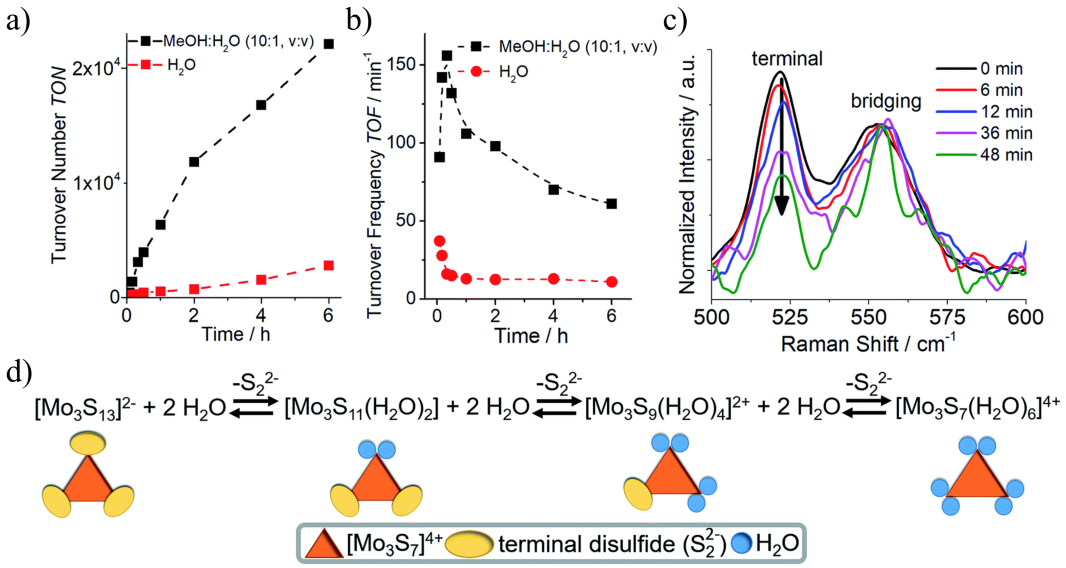


Figure 1.29 Catalytic performance of {Mo3} in visible light-driven HER under homogeneous conditions: **a)** Effect of solvent mixtures on the TONs in HER catalysis. **b)** Effect of solvent mixtures on the TOFs in HER catalysis. Both performance metrics indicate faster deactivation of {Mo3} under aqueous conditions. Conditions: 0.3 µM {Mo3}, 20 µM Ru-PS, 0.1 M AscOH. **c)** *In situ* Raman analysis confirms a possible exchange of the terminal S_2^{2-} ligands under catalytic conditions, followed by the *in situ* formation of catalytically more active species. Conditions: 0.3 mM {Mo3}, MeOH:H2O (1:1, v/v). **d)** Schematic illustration of the proposed exchange of terminal S_2^{2-} ligands with aquo ligands. Reproduced with permission.[328] Copyright 2018, Royal Society of Chemistry.

shows outstanding TONs of *ca.* 23,000 within 6 h and *ca.* 41,000 under continuous irradiation for 24 h with a maximum TOF of approx. 156 min^{-1} (see Figure 1.29). Moreover, deactivation by ion pairing and colloid formation by aggregation of the anionic catalyst and the cationic PS were observed at higher concentrations of {Mo3}.[328] Remarkably, the HER performance can be further enhanced by the addition of non-innocent NH_4^+ ions, which can potentially extend the lifetime of PS* or support the intermolecular collision-induced PCET processes by providing proton management *via* additional H-bonds.[329]

{Mo3} can also be combined with UV light-sensitive PSs, such as the POM cluster $[H_4SiW_{12}O_{40}]$, using ethanol as SRA. This molecular photosystem showed sustained HER reactivity over a period of 40 h and exhibited a maximum TON of 6,876.[330]

When investigating the light-driven homogeneous HER reactivity of dimeric {Mo2} coupled with Ru-PS and AscOH, significantly lower TONs of *ca.* 1,630 within 6 h and an initial TOF of *ca.* 720 h^{-1} were observed. The formation of H_2 strongly depends on the solvent mixture, with the highest HER efficiency being achieved in pure MeOH. In contrast to the deactivation pathway of {Mo3}, no complete exchange of terminal S_2^{2-}

ligands was observed for {Mo_2} under turnover conditions, indicating a higher stability in the presence of coordinating ligands. Instead, the degradation of the PS was found to be responsible for the loss of reactivity during long-term catalysis, emphasizing the need for more redox-stable PSs.[331]

Intrinsic light-driven HER reactivity has also been probed and demonstrated for organofunctionalized thiomolybdates.[316] However, the stability and durability of HECs under turnover conditions can be significantly improved if photocatalysis is shifted from the solution-phase to heterogenized thiomolybdates on functional supports.[332] The respective deposition strategies are scrutinized in more detail in chapters 1.8 and 3.1.

The theoretical aspects of thiomolybdate chemistry were published in "*Thiomolybdate Clusters: From Homogeneous Catalysis to Heterogenization and Active Sites*", Samar Batool,‡ Marcel Langer,‡ Stephen N. Myakala, Magdalena Heiland, Dominik Eder, Carsten Streb,* and Alexey Cherevan,* *Adv. Mater.* **2024**, *36*, 2305730.

For more detailed information, see chapter 6.3.

1.8 From Homogeneous to Heterogeneous Photocatalysis

Hitherto, a molecular approach of a three-component system consisting of a POM, SOA and PS for the light-driven WOC and a thiomolybdate, SRA and PS for the photocatalytic HER has been described. These redox-reactive photosystems are often operated in solution, as the individual compounds can be utilized "as-prepared". Under homogeneous conditions, the well-defined molecular components are particularly amenable to various viable experimental and theoretical studies that allow for a detailed investigation of their functions and stability in the photocatalytic processes.[163,303,333]

For instance, the occupation of distinct energy states of the PS during light absorption and subsequent electron or energy transfer steps to the catalyst can be explored and rationalized in interface chemistry using *operando* and time-resolved spectroscopic methods, while DFT calculations can be employed to predict the active sites of a catalyst, the impact of solvent molecules or potential deactivation pathways with respect to possible transformations of the catalyst or degradation of the PS.[328,334,335] Therefore, profound mechanistic insights can be obtained at the atomic scale, which can be used to refine structural, molecular and correlating physicochemical properties and to optimize key reaction parameters, *e.g.* by implementing "Quality by Design" concepts. Access to this in-depth information is also valuable for the controlled development of highly active, selective and robust compounds and their efficient intermolecular interactions under homogeneous conditions, ensuring easy tailoring of the entire catalytic photosystem to the biomimicry of biological photosynthetic processes.[332,336–338]

Although homogeneous catalysts generally exhibit higher substrate conversion rates per active site and enhanced selectivity compared to conventional heterogeneous catalysts, these values can deteriorate considerably due to critical stability drawbacks inherent to the molecular species, which are often susceptible to the harsh photocatalytic redox conditions.[336,337] This manifests itself, for example, in a rapid ligand exchange of $\{Mo_3\}$ or the degradation of POMs during catalytic redox cycles.[328,339] Moreover, the catalytic concentration is often constrained to a specific range due to undesirable side reactions, such as ion pairing between charged species and their aggregation. These reactions impede the controlled diffusion and collision of dissolved molecules, resulting in reduced overall reaction rates.[163,186,339]

The aforementioned concerns can be addressed by heterogenizing the molecular units on functional solid supports,[333,336] which typically results in robust materials with sustained catalytic activity. This approach offers several other advantages, including the possibility of integration into photoreactors, easy separation of the catalyst, its recovery after operation and thus improved recyclability and longer reuse in combination with a more convenient and sustainable processing of the material.[332,340–342] In most cases, heterogeneous catalysts are also considered "green" and are more economical than their homogeneous counterparts. This aligns with the criteria for compatibility with large-scale and industrial applications.[333]

However, the heterogenization of molecular compounds is concomitant with a number of challenges. Firstly, the physicochemical properties of the molecular entities, such as the intrinsic catalytic activity and the selectivity of the homogeneous catalyst, must be preserved post-integration into the support materials to guarantee their functionality in the light-driven WOC or HER. Secondly, limitations in mass transfer must be avoided. Ensuring sufficient diffusion capacity of substrates and products can be achieved, for example, by optimizing the porosity of the matrix by tuning the hydrophobic and hydrophilic properties. Thirdly, a well-defined morphology of the substrate with a high specific surface area is required to ensure the accessibility of highly compacted active sites. Conversely, surface poisoning, aggregation or leaching of heterogenized species during use and recycling, leading to deactivation, must be prevented.[102,303,343,344] These optimizations pose a particular challenge due to the intricacy of the systems, which hinders their straightforward analytical investigation, especially the application of *in situ* methods, and thus the comprehension of multiphase processes at their surface.[338]

Nevertheless, the integration of nanostructured catalysts and chromophores into advanced heterogeneous support materials has been shown to yield tailored material designs and synergistic effects that offer new opportunities to combine the exceptional stability, durability, high surface area viability, efficient catalyst recovery and reusability of a heterogeneous photocatalytic system with the high catalytic activity, selectivity, tunability, accessibility of active sites and mass transfer efficiency of a homogeneous photocatalytic system.[303,341] This desired bridge is shown schematically in Figure 1.30.

It is noteworthy that electrostatic or covalent deposition of molecular building blocks such as POMs, thiomolybdates and Ru polypyridyl complexes on a variety of inorganic and

organic substrates is generally feasible due to their structural versatility, which allows for facile processing in different solvents.[267,325] The list of hard matter composites based on metal oxides and semiconductors, which are widely used because of their high thermal and photochemical stability, decent performance in catalysis and simple recycling,[345] comprise rutile TiO_2 surfaces,[176] (mesoporous) organosilica hosts,[346] carbon nanotubes (CNTs),[347] carbon nitrides (CN_x),[348] quantum dots (*e.g.* CdX with X = S, Se, Te),[349] porous silica nanoparticles,[350] MOFs,[351] and various (metal oxide) electrodes,[352] to name but a few. Some of these materials exhibit photosensitization capabilities and can therefore replace noble metal-based PSs by providing electrons or holes for the water splitting reaction. However, the intrinsic activity is often remarkably enhanced when additional co-catalysts are immobilized on their surface.[147,353]

An alternative blueprint of interest is the use of soft matter composites, such as hierarchically well-defined nanostructured polymer networks (*e.g.* porous block copolymer[332] or Nafion membranes[354]) and supramolecular architectures (*e.g.* hydrogels[355]), which can be considered as biomimetics of the thylakoid membrane as they provide spatial control of molecular PS and catalyst. The defined microenvironment regulates reactivity, such as the management of PCET processes, by exploiting the synergistic effects of short-range interactions between molecules and support.[332,356] Despite a generally lower stability compared to inorganic substrates, which explains their less widespread technological use, these matrices offer greater adaptability and flexibility.[357] Given their relevance for this work, more attention is paid to this class of materials in the following chapter 1.8.1.

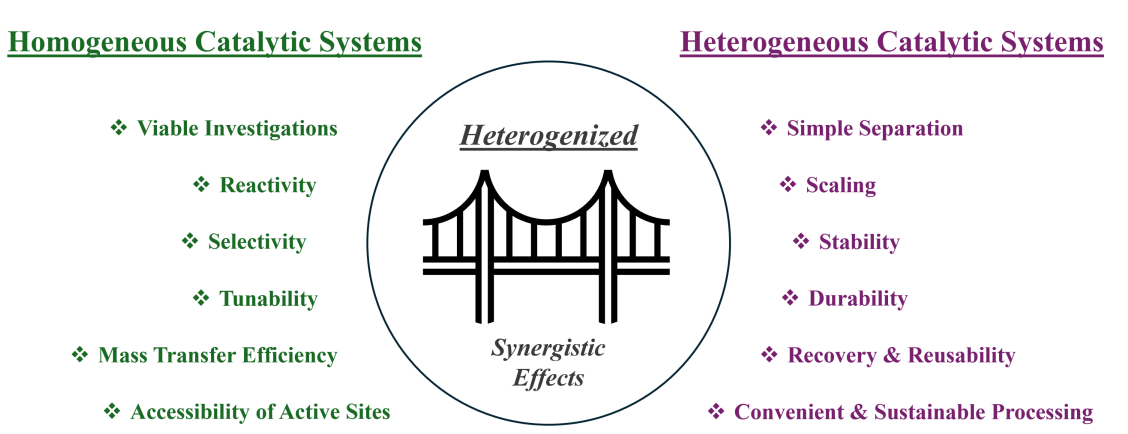


Figure 1.30 Heterogenized molecular photosystems with the attempt to combine the advantages of homogeneous and heterogeneous catalysis *via* synergistic effects of the supporting material and the molecular building blocks.[303,341]

1.8.1 Soft Matter Composites

This chapter is mainly based on the investigations reported in the review article **{MLa-1}**[358] and on the theoretical background described in the research article **{MLa-5}**.[359] The concepts are supplemented by pertinent examples from the literature.

Polymers, vesicles and surfactants represent a few examples of soft matter that can be preserved by various polymerization strategies at different length scales, ranging from nano- to micrometers.[360] Advancements in 3D printing techniques have also facilitated the fabrication of hierarchically more complex structures.[361] Soft matter matrices are characterized by weak, intermolecular interactions (*e.g.* H-bonding or dipolar forces) that prevail at the molecular level and contribute to unique and tunable properties of the material at the macroscopic scale. Their flexibility is exemplified by the regulation of domain functionalities within polymer units that can reversibly respond to external forces (*e.g.* pH, light, temperature, *etc.*), resulting in stimuli-responsive materials with adjustable reactivity behavior.[362,363] In contrast, hard matter structures are typically rigid, as they are built up by strong covalent or ionic interactions.[360]

The combination of two or more polymer chains, which differ chemically from each other, at one or more junction points leads to the formation of block copolymers.[364] The composition and properties of these materials can be easily modified through chemical alterations of the monomers to tailor the desired functions.[365,366] Block copolymers also possess the ability to self-assemble into versatile and unconventional structures, such as porous membranes (see chapter 3.3)[367] or hydrogels (see chapter 3.4).[359]

Hydrogels are molecular 3D networks consisting of crosslinked polymers that interact intermolecularly through flexible covalent or non-covalent interactions, such as physical entanglements. The inclusion of positively or negatively charged subunits, accompanied by a weakly acidic or basic character, leads to polyampholytic hydrogels, which exhibit a high capacity for water absorption.[368,369] When oppositely charged units or ionizable groups are present within the same repeating unit, they are classified as zwitterionic. The structural and mechanical properties of hydrogels, such as the degree of swelling (DS), can be tuned by the net charge and charge density as a function of the pH.[370] The mesh size and volume of the hydrogel are enlarged in the charged state (*i.e.* when it is present as a polycation or -anion) due to dominant repulsive interactions, while attractive

electrostatic forces between balanced, oppositely charged functional groups lead to the shrinkage of hydrogels. Consequently, the most stable and compact conformation is attained at charge neutrality, which occurs near the isoelectronic points (IEPs). Furthermore, an augmented salinity has been observed to suppress swelling by compensating charges through the so-called "anti-polyelectrolyte effect".[371–373] Hence, the morphology and pore size of hydrogels can be meticulously adjusted to obtain high surface areas compatible with the immobilization of molecular hard matter species such as POMs or thiomolybdates.[133]

The development of soft matter composites was originally inspired by biomineralization, where the combination of organic and inorganic components results in unique structures with specific functions (*e.g.* bones in vertebrates).[50] This principle of heterogenization can be applied to all nanostructured soft matter systems that integrate vacant binding sites on suitable polymer building blocks to obtain soft matter composites. The merging of soft and hard matter gives rise to synergistic or even novel physicochemical properties that are otherwise inaccessible, which can be used to precisely tune reactivity, selectivity and stability patterns at the molecular level. For instance, this can be achieved by altering the local polarity in the microenvironment of catalytic sites.[345,374] This approach also enables the fabrication of macroscopic, multifunctional materials like membranes or gels that can be integrated into technologically meaningful devices for various applications (see chapter 3.2).[359,367] Thus, soft matter composites can also be considered as promising artificial models of the thylakoid membrane, enabling the enhanced spatial control of surface-ornamented or matrix-arranged "hard" molecular photoactive species such as catalysts, chromophores and quenchers within a "soft" block copolymer matrix, in which their 3D accessibility can boost the overall catalytic activity.[375]

Soft matter composites can further be categorized according to the type of interactions. In this interpretation, the classification of organofunctionalized POMs defined in chapter 1.6.1, is reversed. Class I hybrids are predicated on covalent interactions, while Class II hybrids comprise non-covalently bonded POMs on soft matter matrices.[376] The subsequent sections provide a concise overview of the general embedding strategies used in the synthesis of the both types of POM-soft matter composites.

The use of modified POMs with organic anchoring groups is often a prerequisite for accessing Class I hybrids.[376] The structural diversity of polymers and the ensuing

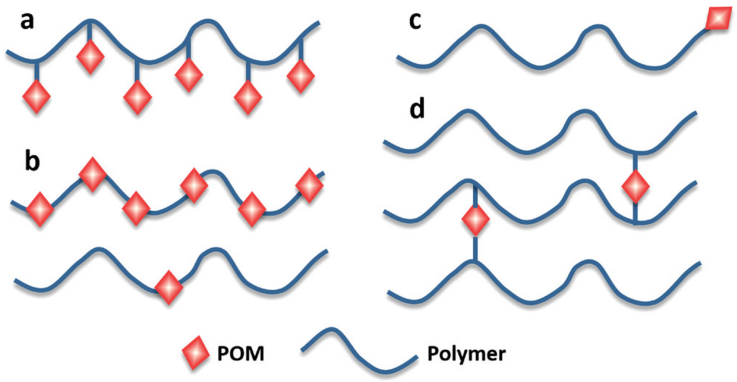


Figure 1.31 Illustration of different POM-polymer hybrids with divergent chain configurations: **a)** side chain, **b)** backbone, **c)** head-tail and **d)** crosslinked. Note that dendrimer structures, which are not shown, are also possible. Reproduced under the terms of the CC BY 4.0 license.[358] Copyright 2022, Battelle Memorial Institute, Advanced Functional Materials published by Wiley-VCH GmbH.

challenges in the processability of POM-soft matter composites, *e.g.* due to potential solubility issues, generally necessitate a customized immobilization strategy for each system.[377,378] Conventional methods for embedding POMs in soft matter include direct polymerization grafting processes of POM-modified monomers, such as free radical polymerization,[379] step-growth polymerization (*e.g.* polycondensation or polyaddition *via* cycloaddition or Click reactions),[380,381] ring-opening (metathesis) polymerization (RO(M)P),[382] atom transfer radical polymerization (ATRP),[383] and reversible-addition-fragmentation chain-transfer polymerization (RAFT)[384] as well as post-polymerization modifications like transesterification.[385] In this way, POMs can be precisely integrated into polymer side chains or polymer backbones *via* different configurations to form linear, branched or head-tail POM-polymer hybrids. Furthermore, the formation of crosslinked networks and dendrimeric structures is also possible (see Figure 1.31).[377]

The preparation of Class I hybrids is synthetically more demanding than the electrostatic bonding of anionic POMs to cationic polymer sequences in Class II hybrids.[345] The use of block copolymers allows the construction of hierarchical 1D-3D structures by direct mixing of soluble POMs and polymers or by post-functionalization of the preformed polymer (see Figure 1.32).[386] However, non-covalent interactions are more susceptible to the operating conditions, *e.g.* changes in pH. This sensitivity can be an advantage for the recovery and recycling of POMs due to the reversibility of the bonding mode, but it can also present an obstacle when unstable bonds are cleaved, leading to the leakage of POM clusters or other molecularly charged species. Both effects were observed in the two experimental studies in this work, which are discussed in more detail in chapter 3.

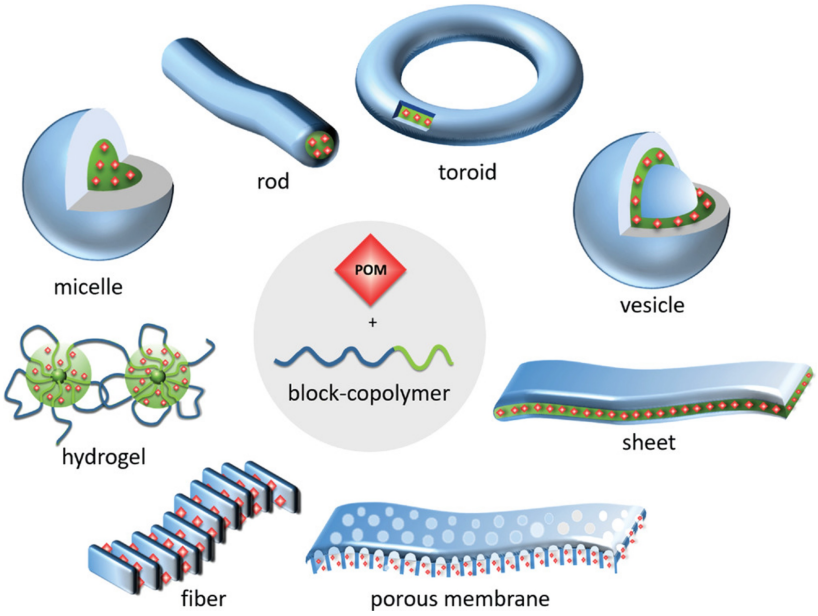


Figure 1.32 Overview of 1D-3D POM-polymer hybrid architectures resulting from the self-assembly of block copolymers. Reproduced under the terms of the CC BY 4.0 license.[358] Copyright 2022, Battelle Memorial Institute, Advanced Functional Materials published by Wiley-VCH GmbH.

The theoretical background to soft matter and soft matter composites was published in "*Polyoxometalate-Soft Matter Composite Materials: Design Strategies, Applications, and Future Directions*", Jan-Hendrik Kruse,‡ Marcel Langer,‡ Iuliia Romanenko, Ivan Trentin, David Hernández-Castillo, Leticia González, Felix H. Schacher,* and Carsten Streb,* *Adv. Funct. Mater.* **2022**, *32*, 2208428.

The theoretical background to hydrogels was published in "*Poly(dehydroalanine)-Based Hydrogels as Efficient Soft Matter Matrices for Light-Driven Catalysis*", Tolga Çeper,‡ Marcel Langer,‡ Nikita Vashistha, Benjamin Dietzek-Ivanšić, Carsten Streb, Sven Rau, and Felix H. Schacher,* *Macromol. Rapid. Commun.* **2024**, *45*, 2300448.

For more detailed information, see chapter 6.1.

2. Objective

The twin problems of climate change and the imminent energy shortage are inextricably linked to the need for a unified global energy transition strategy. To address this critical bottleneck in green energy conversion and storage, new solutions with high performance, durability and sustainability are required. Inspiration can be drawn from structural and mechanistic concepts found in nature, namely biological photosynthesis.

In brief, catalysts, chromophores and sacrificial agents interact at the molecular level in an artificial light-driven three-component photosystem to split H_2O. In this context, POM and thiomolybdate catalysts have been shown to be key compounds for the oxidative OER and reductive HER, respectively. Both inorganic clusters mimic crucial structural and physicochemical functions of their natural counterparts. They are highly redox-active, proficient in storing a specific number of electrons, perform multi-PCET reactions and demonstrate exceptional stability under photocatalytic conditions. In addition, they show chemical processibility in solutions and exhibit a great structural diversity. Mechanistic studies on compounds with slightly modified structural features allow the optimization of the associated properties and thus the adaptation to desired functions (*cf.* chapter 1).

In recent decades, significant progress has been made in the field of solar-to-energy conversion with the development of several prototypes of homogeneous POM- and thiomolybdate-based photosystems. However, these systems encounter challenges related to the stability, selectivity and processability of earth-abundant and high-performance photocatalysts, as well as the accessibility of active sites, which is critical for an efficient catalysis. To realize the full potential of artificial leaves, a holistic approach is necessary that mimics the complex interplay of all essential building blocks for light-driven catalysis across multiple scales. As a result, efforts in current chemistry are shifting towards the heterogenization of molecular entities with a particular focus on the development of photoactive hybrid soft matter composites.

Consequently, the objective of this work can be divided into two approaches that aim to establish fundamental principles for the effective conversion of solar light into chemical energy equivalents under heterogenized conditions (see Figure 2.1).

(i) Literature-based Studies

Two independent literature-based review studies are targeted to shed light on the conceptual framework of heterogenized thiomolybdates and POMs on different substrates. The compilation of several state-of-the-art scientific results on these specific research topics should facilitate the recognition of multidisciplinary correlations as well as relevant, partly undiscovered inconsistencies. The theoretical insights acquired from these studies can be used to continuously drive research development and encourage the rational design of next-generation materials for WOC and HER.

The first project, designated as **{MLa-4}**, delves into the theoretical background of thiomolybdates and their role as molecular models for a-MoS_x in HER studies, a subject that has been previously described in chapter 1.7. The primary objective is to identify active sites within prominent thiomolybdate scaffolds and to elucidate HER reactivity mechanisms under both homogeneous and heterogeneous electro- and photocatalytic conditions. This endeavor will facilitate the establishment of valuable structure-property relationships that may prove instrumental in the development of new and more efficient thiomolybdate-based HECs and their deposition on a variety of functional substrates.

The second project **{MLa-1}** investigates the chemistry of soft matter composites, which have already been briefly introduced in chapter 1.8.1. These composites are of particular interest due to their structural resemblance to the thylakoid membrane, exhibiting remarkable structural flexibility and offering multiple attachment modes for the incorporation of molecular units, such as POMs. However, their combination is often accompanied by an increase in the complexity of the entire system. Consequently, the characterization of POMs embedded in these networks poses significant challenges, especially for soft matter composites containing multiple functional groups, which can severely impair the evaluation of the molecular units in terms of structural integrity, stability and thus (photo)catalytic activity. For this reason, a comprehensive list of suitable analytical methods is being compiled to assist researchers in acquiring profound information on such POM-soft matter materials in the future.

Apart from that, both projects share the motivation to provide a progressive review of current developments and emerging applications based on selected reports from the extant literature.

(ii) Experimental Studies

According to the step *Create* shown in Figure 1.5, the superordinate purpose of the experimental part of this work is to conceptualize, execute and advance the embedding of light-driven molecular moieties into functional, hierarchical nanostructured soft matter materials. Therefore, two distinct soft matter matrices were developed: a nanoporous block copolymer membrane in project **{MLa-2}** and a polyampholyte hydrogel in project **{MLa-5}**. Both soft matter composites were subsequently functionalized with molecular species, including a chromophore and additionally either a POM-OEC or a thiomolybdate HEC. The photocatalytic performance in OER and HER and the stability of the molecular components under comparable conditions to the homogeneous systems were evaluated using various *in situ*, *operando* and *ex situ* analytical techniques.

It should be noted that all the projects presented were carried out as part of the Deutsche Forschungsgemeinschaft (DFG) Transregional Collaborative Research Center TRR 234 "*CataLight*". Therefore, the implementation and modalities of these results further aim to emphasize the importance and breadth of inter- and multidisciplinary collaborative research involving the expertise of a large number of differently trained chemists for this and other prospective work.

Finally, chapter 4 provides a broad outlook on future research directions and current perspectives, focusing on the effects of a solvent change to predominantly organic systems by investigating the photodegradation of the well-known Ru-PS in combination with the SOA $S_2O_8^{2-}$ in MeCN:H_2O at a volume ratio of 9:1. The corresponding results of the project with the designation **{MLa-6}** are discussed in detail in chapter 6.5.

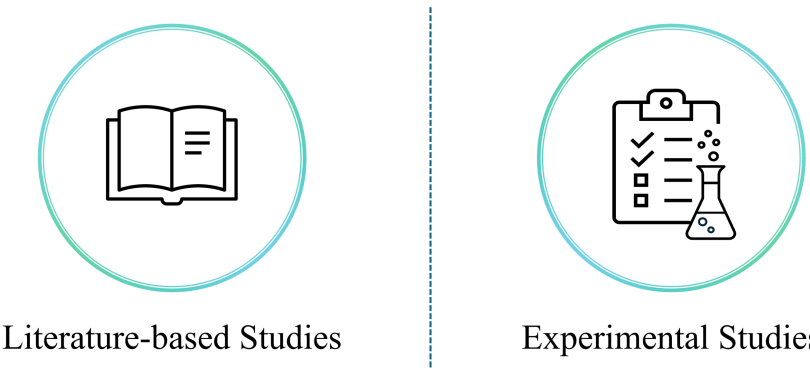


Figure 2.1 Overview of the two research approaches employed in this work: (i) literature-based studies and (ii) experimental studies.

3. Results and Discussion

In this chapter, the integration of molecular components into soft matter for light-driven chemistry is discussed in more detail. In addition, a comprehensive and critical evaluation of both our experimental results and the results of other relevant systems in the literature is presented, which corresponds to the final step of the design thinking scheme shown in Figure 1.5.

Molecular POMs and thiomolybdates are highly active catalysts for the WOC and HER under homogeneous conditions.[300,328] However, POMs tend to degrade into colloidal or nanostructured metal oxides, metal hydroxides or solvated metal ions, while thiomolybdate clusters can transform into solid molybdenum sulfide species under harsh electro- and photocatalytic conditions. The decomposition products may also possess the targeted properties, such as redox- or catalytic activity, which significantly impedes the determination of their true catalytic performance.[387] In addition, the compatibility of homogeneous catalysis with large-scale technological deployments is often compromised by the difficulty of separating and recovering the catalysts.[388] Therefore, the spatially controlled embedding of all essential molecular building blocks for light-driven catalysis on high surface area matrices is desirable and necessary in order to develop heterogeneous models for sustainable artificial photosynthesis.[389]

Modifiable soft matter materials, such as microporous block copolymers, are particularly well-suited for the compartmentalization of molecular PS and catalyst units within a 3D network, as charge separation and migration as well as surface reaction processes can be effectively promoted.[375,390] However, the immobilization process can result in a loss of mechanical integrity of both the molecular building blocks and the chemical supports or drastically alter their original photocatalytic properties, posing new challenges in material characterization and the identification of the true active sites within a given photosystem. Nonetheless, this information is of utmost importance for the evaluation and validation of the catalytic performance of the material, and this knowledge is crucial for the design of prospective catalytic photosystems.[140]

In the project **{MLa-4}** (see chapter 3.1), mechanistic insights into active sites and HER mechanisms of thiomolybdates were scrutinized considering reactivity and stability studies under homogeneous and heterogenized conditions. We critically evaluate the

differences reported in prominent examples from the literature in terms of material preparation and exact reaction conditions, as well as the type of support and the type of thiomolybdate cluster used. In addition, we provide a concise overview of the underlying principles of thiomolybdate heterogenization and assess recent advancements in surface-supported thiomolybdate applications using appropriate performance indicators, with a particular focus on electro- and photocatalysis. Furthermore, we present other current and emerging trends of thiomolybdate research and emphasize the need for in-depth studies through a combination of experimental and theoretical techniques, preferably applied *in situ* or *operando*.[147]

In particular, complementary analytical methods are required to unravel the structural integrity and effects on long-term stability of molecular catalysts embedded in soft matter materials and to assess changes in reactivity or selectivity upon heterogenization. As part of the project **{MLa-1}** (see chapter 3.2), we have developed a comprehensive list of state-of-the-art and more sophisticated analytical tools for the characterization of POM-soft matter composites, including microscopic, spectroscopic and computational technologies. The challenges and advantages of each method are briefly discussed. In this way, we have developed a guideline for the evaluation of inorganic molecular POMs incorporated into soft matter matrices. It is noteworthy that the study of soft matter systems containing heterogenized thiomolybdates or Ru-based PS complexes can also benefit from these characterization approaches. Furthermore, the key principles of soft matter chemistry were covered, general deposition strategies for accessing POM-soft matter hybrids were delineated and pioneering applications in this interdisciplinary field of research were presented.[358]

The POM cluster {Co_4}, which was introduced and described in chapter 1.6.3, plays a pivotal role in the experimental part of this work. This POM cluster was selected as the OEC model for visible light-driven WOC studies. As mentioned in the introduction, the incorporation of reactive metal sites, in this case cobalt, into a POM framework allows for the fine tuning of cluster properties, such as electronics, which mediate the reactivity and stability in redox processes. {Co_4} has already been thoroughly characterized and demonstrates hydrolytic and oxidative stability under photocatalytic conditions. Its OER activity in WOC has been the subject of extensive research, including optimization under a range of photochemical and electrochemical conditions (see chapter 1.6.3 for further

details), ensuring the comparability of our work with other systems documented in the literature. In addition, the high negative charge of -10 can be utilized for the electrostatic attachment of the cluster to various soft matter matrices bearing cationic groups.[300,391]

The anionic thiomolybdate HEC model {Mo_3} (see chapter 1.7) can be embedded in soft matter matrices in a similar manner by using attractive electrostatic interactions between cationic polymer chains and the anionic cluster. It is assumed that the incorporation of these anionic units reverses the overall surface charge, which can then be utilized to electrostatically co-immobilize the cationic chromophore Ru-PS (see chapter 1.5), or *vice versa* if anionic polymer chains were initially present.[332]

The molecular components must be spatially arranged in a flexible soft matter scaffold that can be easily chemically derivatized, as their proximity is a prerequisite for efficient intermolecular electron transport between PS, catalyst and SOA or SRA, thus facilitating an effective photocatalytic cycle.[390] In this regard, we have developed and demonstrated the preparation of two distinct functional, hierarchical, nanostructured soft matter supports and established the incorporation of OER-active {Co_4} and HER-active {Mo_3} together with the Ru-PS complex *via* non-covalent interactions.

In project **{MLa-2}** (see chapter 3.3), {Co_4} and Ru-PS were embedded in a nanoporous block copolymer membrane. We focused in particular on the multimodal analysis of these soft matter composites. The so-called WOCbranes were thoroughly characterized before and after light-driven WOC by adequate reactivity and stability studies. We employed scanning transmission electron microscopy combined with energy-dispersive X-ray spectroscopy (STEM/EDX), thermogravimetric analysis (TGA), total reflection X-ray fluorescence analysis (TXRF), high resolution-continuum source-graphite furnace atomic absorption spectroscopy (HR-CS-GFAAS) and micro-X-ray fluorescence spectroscopy (μXRF) for quantitative analysis of the functionalized membranes and for investigating the distribution of the molecular units within the membrane pores on a microscopic and macroscopic scale. In addition, fundamental results on the homogeneity and morphology of the membranes were obtained. Attenuated total reflection infrared spectroscopy (ATR-IR) studies were performed to assess and demonstrate the stability of {Co_4} under photocatalytic conditions. The evolution of O_2 at the WOCbranes was quantified by spatially and temporally resolved *operando* scanning electrochemical microscopy (SECM) in close proximity to the membrane surface. This method was adopted to avoid

a potential underestimation of O_2 values resulting from gas entrapment in the pores of the membranes. Hence, sub-millimeter sized regions of the membrane could be examined, providing critical data on WOC reactivity, insights into the heterogeneity of the membrane, spatial distribution and loading of the POM-OEC and Ru-PS, and molecule-in-matrix stability of the catalyst under reaction and long-term storage conditions.[367]

In project **{MLa-5}** (see chapter 3.4), we developed pH-responsive and polyampholytic polymer hydrogels based on crosslinked poly(dehydroalanine) (PDha) as an artificial model of the thylakoid membrane by enabling the attachment of molecular photosynthetic units under spatial control. A comprehensive investigation was conducted into various polymer compositions and gelation parameters to ascertain suitable swelling properties, contingent upon pH, salinity and solvent factors, which are pertinent for optimal mass transport in the ensuing photoredox reactions. The pH-dependent reversible electrostatic adsorption capacity of Ru-PS was also studied in detail. In this context, we investigated the PS-functionalized hydrogels as heterogeneous light-harvesters in visible light-driven HER and WOC using $\{Mo_3\}$ and $\{Co_4\}$, respectively. Furthermore, we demonstrated a possible approach for self-repair of degraded molecules in these 3D soft matter matrices. In contrast to the work in project {MLa-2}, the quantification of O_2 and H_2 was performed *via* state-of-the-art bulk analysis methods, focusing on the proof-of-principles. Subsequently, the irradiation-dependent catalytic activity and selectivity of these photosystems were compared with corresponding studies in homogeneous solutions. The performance of these systems was optimized with respect to molecular and external influencing parameters, such as the DS of the hydrogel or the concentrations of catalyst and PS. In the case of OER, the influence of the hydrogel matrix on the Ru-PS stability and its decomposition pathways was investigated using UV-Vis spectroscopy. Besides, the mechanical integrity of the organic hydrogel scaffold under WOC conditions and the rate-limiting diffusion limitations of catalysts and products were explored.[359]

The results of the individual projects are discussed in more detail in the following chapters 3.1–3.4, with a particular focus on the experimental work.

3.1 Active Sites of Thiomolybdates – {MLa-4}

The active sites of a catalytic species play a crucial role in terms of its energetics, kinetics and stability under reaction conditions. Thus, studies on structure-property relationships are indispensable to facilitate advancements in the design of effective, reliable and robust catalysts. However, mechanistic investigations on crystalline or amorphous materials are considerably hindered by the presence of multiple reactive sites and ambiguities in their atomistic structure. To overcome these obstacles, the use of molecular catalyst models is recommended to improve the understanding of active sites, rationalize the actual reaction mechanism and discern potential deactivation pathways. Nevertheless, it is imperative to consider possible changes in structure and composition that may occur throughout the lifecycle of the catalyst, from deposition to post-catalysis stages.[163]

This project focuses on thiomolybdate prototype clusters, their analogs and derivatives as molecular models for a-MoS_x catalysts previously introduced in chapter 1.7. The present literature-based study encompasses the identification of active sites and HER reactivity mechanisms under both homogeneous and heterogeneous conditions. To this end, we have correlated various state-of-the-art results from pioneering mechanistic studies based on experimental (*e.g.* spectroscopic data), theoretical (*e.g.* DFT calculations) or a combination of both methods. The findings were summarized in a comprehensive table giving details on the catalyst, the experimental conditions and whether the catalysis was homogeneous or heterogeneous. Where appropriate, additional information on the type of support, material preparation and references to electrochemical or photochemical processes were included. Moreover, immobilization strategies for thiomolybdates were outlined and their applications discussed, with a focus on electro- and photocatalysis.[147]

The three distinct possible active sites of $\{Mo_3\}$ and the four divergent HER mechanisms proposed at these sites are summarized schematically in Figure 3.1.

The exchange of terminal S_2^{2-} ligands is widely accepted as the pivotal mechanism for the HER of $\{Mo_3\}$ under typical homogenous turnover conditions. The reactivity towards the production of H_2 is observed to increase when the solvent and reactant H_2O partially replaces these ligands. However, complete substitution of all terminal S_2^{2-} ligands results in a substantial decrease in HER rates. These observations indicate the formation of different structural derivatives of the type $[Mo_3S_{13-x}(H_2O)_x]^{(2-x)-}$ on various timescales and

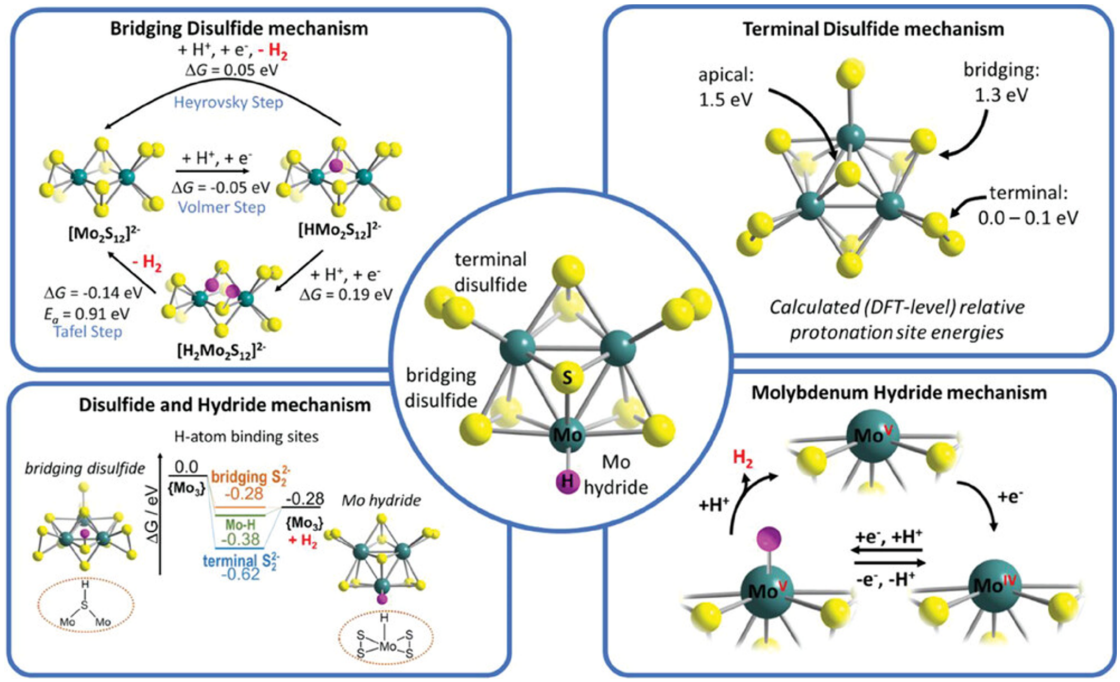


Figure 3.1 Illustration of possible active sites within the prototype {Mo3} (center) and proposed HER mechanisms at these active sites discussed in the literature, including the bridging disulfide mechanism (top left), the terminal disulfide mechanism (top right), the disulfide and hydride mechanism (bottom left) and the molybdenum hydride mechanism (bottom right). Reproduced under the terms of the CC BY 4.0 license.[147] Copyright 2023, The Authors, Advanced Materials published by Wiley-VCH GmbH.

their coexistence in solution (see Figure 1.29d). Consequently, this study provides evidence for the hypothesis that the terminal S_2^{2-} ligands play an important mechanistic role and that molecular thiomolybdates exhibit a highly dynamic behavior under reaction conditions.[328] Gas-phase fragmentation studies and thermochemical stability DFT calculations, which show remarkable differences in the energetics of different protonated sulfide ligands, further support the preferential adsorption of hydrogen *via* the Volmer step at these active sites and the mechanistic relevance of their exchange during HER catalysis (see Figure 3.1, top right).[392]

The substitution of terminal S_2^{2-} ligands in thiomolybdate compounds can also be used for their covalent attachment to heterogeneous supports. In this regard, the remaining bridging S_2^{2-} ligands of structurally intact deposited clusters are often considered a critical factor for electro- and photochemical HER at the molecular level.[176,393] However, some studies remark the possibility of different or perhaps multiple active sites (see Figure 3.1, bottom left)[176,328] and discuss additional effects that contribute to the HER activity, such as the presence of Mo^V or vacant coordination sites on the Mo center that form Mo-oxo intermediates, both of which contribute to the mediation of PCETs at reactive

molybdenum sulfide sites and stabilization of corresponding hydrogen sulfide bonds.[394] It is noteworthy that the majority of the studies have identified the Volmer-Heyrovsky type HER mechanism as the predominant pathway for H_2 formation, which appears to be favored irrespective of the type of catalyst or reaction conditions used (*cf.* chapter 1.4, see Figure 3.1, top left).[312,395]

However, a deviation from these trends is often observed when molecularly well-defined thiomolybdate clusters serve primarily as precursors or precatalysts to generate more complex nanostructures, such as surface-supported a-MoS_x as catalytically active species for electrocatalytic HER. In such instances, the molybdenum hydride mechanism is most commonly identified, which operates *via* redox-active Mo^{IV}[324] or Mo^{III}[396] centers as active sites and the formation of intermediate Mo^{V}–H moieties (see Figure 3.1, bottom right).[397] In addition, the formation of oxidized Mo-oxo species is discussed as a central deactivation pathway, as proton diffusion to the Mo sites may be severely restricted.[398]

These discussions have already revealed massive contradictions in identifying the active sites of thiomolybdate-HECs, their stability under turnover conditions and understanding the underlying mechanistic processes. The complexity is further compounded when organofunctionalized thiomolybdate clusters or mixed oxothiomolybdate derivatives are studied with the aim of controlling reactivity. In this context, numerous potential active sites have been discussed and yet no consensus or tendency towards a single dominant mechanism has emerged.[399] For instance, in the case of oxothiomolybdates, the hypothesis is that HER activity stems from the combined action of several mechanisms that benefit from the flexible execution of PCET at disparate active sites.[400]

These studies also indicate that the type of catalyst and substrate are decisive for the HER reactivity and stability of supported thiomolybdates. Therefore, we further investigated the effects of structural fine-tuning in terms of the origin and composition of the clusters, the relevant design principles for their heterogenization and the use of the composites in catalytic electro- and photochemical HER using prominent examples from the literature.

Molecular thiomolybdates can either be incorporated into (micro)porous matrices or anchored to the surface of solid-state supports *via* electrostatic, covalent or weaker non-covalent interactions using the strategies of dip-coating, solvothermal deposition, layer-by-layer assembly or electrodeposition.[325] Moreover, the fate of the cluster during the

deposition process may be intentionally or unintentionally chemically transformed into nanostructured amorphous or crystalline particles, which need to be critically evaluated prior to and after mechanistic studies to ensure the validity of the results (*vide supra*). For example, adverse effects related to cluster aggregation could be avoided by lowering the loading of the catalyst,[356] which also improves the dynamics of charge separation and electron transfer at the interface,[348,401] light-penetration in the case of photoactive substrates[349] and thus the efficiency of the overall HER performance.[332]

We have used overpotentials, TOFs, the main experimental conditions employed and Tafel slope analysis (see chapter 1.4) as key metrics for evaluating the intrinsic HER activity, stability and durability of supported thiomolybdates in electrocatalytic applications. However, these figures of merit are determined by the electrochemical surface area, which is not comparable for different supports with identical geometric surface areas. Therefore, a thorough examination is essential.[402] In terms of photocatalysis, we have used TONs and TOFs to investigate the stability and light-driven HER performance of various thiomolybdates employed as molecular co-catalysts. This benchmarking of heterogeneous photocatalytic HER should also be critically assessed, as most studies assume that each deposited cluster participates in the reaction, which can distort the true performance of the material.[187,403,404] To sum up, the results of this study show that surface-anchoring of thiomolybdates on functional substrates *via* strong interactions is a viable strategy to improve the stability and long-term reactivity of various thiomolybdates under catalytic conditions.

In addition to HER, thiomolybdates have applications in purification procedures such as selective ion capturing (*e.g.* Ag^+),[405] photocatalytic oxidative dye degradation,[406] remediation of sulfur-containing wastewater,[407] indoor air purification by acetone mineralization[408] and thermal catalysis (*e.g.* HDS).[409] A comparative analysis of the fundamental mechanistic concepts underlying these diverse applications may offer novel insights into the functions of thiomolybdates, thereby facilitating advancements in future thiomolybdate research endeavors, as demonstrated by our broad outlook in this review.

In summary, we have shown that gaining mechanistic insights into thiomolybdates is not straightforward. It is evident that a variety of active sites and molybdenum- or disulfide-mediated HER mechanisms are conceivable, which are contingent upon the precise reaction conditions (*e.g.* pH, type of solvent, light or electrical current, *etc.*), the type of

substrate and the structural characteristics of the cluster at the molecular level. This complexity is further reflected in the varying HER performances observed in heterogeneous electro- and photocatalytic applications. Notwithstanding the challenges posed by the intricate HER mechanisms of thiomolybdates, the individual studies contribute to a deeper understanding of these processes. The emerging use of combined advanced experimental and theoretical methods, applied *in situ* or *operando*, holds great promise to further elucidate the observed reactivity trends, explore the principles of catalyst deposition and investigate the effects of interactions with the substrate. These methods can also shed light on the temporal changes in the physical and electronic cluster structure as the reaction progresses (*e.g.* ligand loss, ligand exchange, oligo- or polymerization of individual cluster units, formation of MoS_x fragments, chemical interaction with the substrate surface, *etc.*), and thus facilitate the development of superior thiomolybdate model systems for the electro- and photocatalytic HER.

These investigations were published in "*Thiomolybdate Clusters: From Homogeneous Catalysis to Heterogenization and Active Sites*", Samar Batool,‡ Marcel Langer,‡ Stephen N. Myakala, Magdalena Heiland, Dominik Eder, Carsten Streb,* and Alexey Cherevan,* *Adv. Mater.* **2024**, *36*, 2305730.

For more detailed information, see chapter 6.3.

3.2 Characterization of POM-Soft Matter Composites – {MLa-1}

Soft matter materials are suitable supports for the heterogenization of molecular POMs. The synergies between organic and inorganic compounds can be harnessed for advances in green, sustainable solar and electrochemical energy conversion.[345] The embedding of POMs in soft matter matrices can be synthetically accessed using the design strategies described in chapter 1.8.1. However, the subsequent characterization of these materials poses a major challenge, as the presence of different organic functionalities and inorganic transition metals with variable redox states can strongly affect the spectroscopic data or microscopic patterns, which complicates the direct and reliable analysis of POMs with only a single measurement method. In addition to validating the structural integrity and stability of clusters immobilized in heterogeneous matrices, the investigation of mechanistic pathways related to POM-mediated reactivity and selectivity is also a great challenge, particularly when degradation products with similar activities are formed, which interfere with the appraisal of the true material performance.[140,387] Thus, a comprehensive array of complementary characterization techniques is necessary to obtain a thorough understanding of POM-soft matter materials from the molecular to the macroscopic scale.

In this work, we highlight some of the current challenges in the evaluation of molecular species embedded in heterogeneous matrices and frame a comprehensive guide for their characterization with valuable analytical technologies aimed at shedding light on structural and compositional aspects of POMs and their miscellaneous properties, as well as establishing structure-property relationships with respect to different applications.[358]

The key characterization techniques described in this work comprise various state-of-the-art and more sophisticated surface spectroscopic, microscopic and other powerful analytical methods, including Fourier transform infrared spectroscopy (FTIR), ATR-IR, Raman spectroscopy, X-ray photoelectron spectroscopy (XPS), nuclear magnetic resonance spectroscopy (NMR), UV-Vis absorption and emission spectroscopies, elemental analysis (CHN-EA), inductively coupled plasma optical/atomic emission spectroscopy (ICP-OES/AES), scanning electron microscopy (SEM) in combination with EDX, high-resolution transmission electron microscopy (HR-TEM), atomic force microscopy (AFM), TGA, dynamic scanning calorimetry (DSC), electron paramagnetic resonance spectroscopy (EPR) and various electrochemical analysis methods, such as

voltametric- or bulk electrolysis. Table 3.1 contains additional remarks on each set of characterization technique. It should also be noted that the combination of advanced analytical methods operated *in situ* or *operando* is especially suited to enable the accurate characterization of POM-soft matter composites.

An experimental example of the extension of *ex situ* bulk methods to multimodal *in situ* and *operando* analysis techniques for the characterization of POM-soft matter materials is presented in the project {MLa-2} (see chapter 3.3). This work includes critical insights into the catalytic performance of reactive sites and other fundamental limitations, such as inhomogeneous distribution of active compounds, inaccessibility of catalytic sites, mass transport limitations or poor light penetration into the bulk material.[367]

The present review report also emphasizes the importance of combining experiment and theory to acquire profound knowledge about a particular system, even if the calculation of multi-configurational scenarios of POMs is not straightforward. Contemporary computational studies, such as atomistic quantum mechanics (QM) grounded in DFT or *ab initio* wave function methods,[410] classical theoretical approximations, including all-atom and coarse-grained MD using molecular mechanics (MM) based on parameterized force fields,[411] and hybrid QM/MM simulations,[412] which combine both approaches to derive high-precision results, can be used to investigate POM integration and interaction modes in soft matter matrices. These studies can also assist in the general interpretation of experimental data by modeling geometries, spectroscopic spectra and various properties of POMs (*e.g.* optical, molecular, electronic and magnetic properties).[413] The synthetic step of embedding POMs in polymers or other soft matter environments and the reaction mechanisms that the hybrid material performs can also be simulated, while molecular docking can be used for the identification of binding targets and the positioning of POMs within soft matter matrices.[414] The merits, drawbacks and constraints of the computational methods have been discussed in terms of their accuracy, time-scales and system variables (*e.g.* size) that can be analyzed.

Therefore, a concise overview of these experimental and theoretical approaches has been furnished, accompanied by the substantiation of their applicability through the presentation of pertinent examples from the literature.

Table 3.1 Key (*in situ*/*operando*) techniques for the analysis of POMs embedded in soft matter matrices.

Technique	Features & Characterization
ATR-IR/FTIR	• probes surface/bulk of the solid sample • presence, integrity, stability & leaching of the POM • investigation of the interactions between POM and polymer • tracking progress in reactivity studies
Raman	• higher signal resolution than with conventional IR • note: a high excitation laser power can damage the sample • presence, integrity, substrate binding & distribution of the POM • POM stability: structural changes & degradation
XPS	• surface sensitive (top few nm) & use in ultra-high vacuum • typical binding energies & assignment of metal oxidation states • elemental composition of solids • surface-processes: conversion, degradation, diffusion & leaching • structural & chemical changes before/after reactions
NMR	• POM presence & integrity • POM-polymer interactions in solution or in the solid state • reactivity profile of the embedded POM
UV-Vis	• luminescence properties & photochromism • studies on the presence & the reactivity of the POM
CHN-EA & ICP-OES/AES	• elemental composition & POM/organic-contents • POM stability & leaching
SEM/EDX	• nanometer resolution for structural & elemental information • morphology of the matrix, micro- & nanostructures • presence & distribution of the POM • matrix changes during reactions
HR-TEM	• atomic resolution of thin samples with large differences in the electron density of the POM and the soft matter matrix • POM distribution
AFM	• ambient conditions & non-pretreated samples • surface topology & roughness of the matrix • POM distribution
TGA	• thermal stability & decomposition temperature of the sample • POM content
DSC	• melting/solidification behavior & glass transitions of the sample
EPR	• electronic states of the POM & their changes during reactions • assessment of the POM reactivity
Electrochemical Analysis	• redox activity of the POM • accessibility of the oxidation states of the POM • electron storage/transfer capability of the sample • changes in the reversibility of the material

We have also undertaken a prospective analysis of the future directions of this interdisciplinary research domain, which derives significant benefit from the combination of POMs and soft matter. Specifically, stimuli-responsive matrices have the ability to trigger and augment the physicochemical properties of accessible POM clusters (*e.g.* redox states, luminescence, *etc.*) through the regulated alteration of certain parameters (*e.g.* pH, light, heat, electricity, humidity, *etc.*). This adaptability can be used to engineer smart and selective materials in the fields of theranostics,[415] sensorics,[257] catalysis[416] or electrochemistry.[417] In this vein, we have developed a pH-stimuli-responsive hydrogel in the project {MLa-5}, which is presented in chapter 3.4.[359] Another synergistic effect is employed in biomedical applications. The toxicity, selectivity, stability and mode of action of POMs can be decisively mediated by biologically-inspired soft matter matrices, whereby the antiviral, anticancer, antitumoral and antimicrobial activity of POMs can be exploited more effectively in *in vivo/vitro* applications.[276,418] Conversely, the fabrication of functional nanodevices for molecular electronics, encompassing quantum computers, spintronics, molecular junctions and non-volatile rewritable multilevel memories, is predicated on the precise deposition of electronically and magnetically active POMs with controllable redox- and spin-states on flexible, processable and scalable soft matter polymer matrices.[419–421] These hybrid materials are also increasingly utilized in solar and electrochemical energy conversion and storage (*e.g.* in batteries, supercapacitors, fuel cells, *etc.*), as well as in photocatalysis and electrocatalysis.[257,422,423]

In summary, this literature-based study introduced the research field of POM-soft matter composites and conducted an in-depth study of valuable characterization methods and their limitations for understanding the relationships between structure and reactivity. Prospectively, the development of advanced and complementary analytical techniques will further facilitate the application-driven design of soft matter composites.

These investigations were published in "*Polyoxometalate-Soft Matter Composite Materials: Design Strategies, Applications, and Future Directions*", Jan-Hendrik Kruse,‡ Marcel Langer,‡ Iuliia Romanenko, Ivan Trentin, David Hernández-Castillo, Leticia González, Felix H. Schacher,* and Carsten Streb,* *Adv. Funct. Mater.* **2022**, *32*, 2208428.

For more detailed information, see chapter 6.1.

3.3 POM-functionalized Membranes for WOC – {MLa-2}

Nanoporous block copolymer membranes are attractive supporting materials with unique morphologies and controllable chemical functionalities.[364] Various photoactive and reactive molecular compounds required for sustainable energy conversion can be encapsulated in the matrix either *via* electrostatic[424] or covalent interactions.[425] The concept of heterogenization has already been demonstrated for a hybridized POM-based catalyst with respect to the oxidation of organic substrates like tetrahydrothiophene or anthracene on so-called POMbranes.[391] Another example is the heterogenization of the {Mo_3}-HEC together with a molecular dye to form so-called soft matter HERbranes.[332]

In this study, we have built upon these findings and developed nanoporous polystyrene-*block*-poly(2-(dimethylamino)ethyl methacrylate (PS-*b*-PDMAEMA) block copolymer membranes for the light-driven WOC. The soft matter matrices were co-functionalized with the {Co_4}-OEC and the light-harvester Ru-PS through non-covalent interactions to yield so-called WOCbranes (see Figure 3.2). The photocatalytic activity and the stability of the molecular components under operating conditions were investigated using several complementary analytical techniques.[367]

The fabrication of the polymer membranes was executed in three distinct steps. First, the macroinitiators polystyrene and DMAEMA were gradually polymerized by nitroxide-mediated polymerization (NMP). The synthesized block copolymer structures then self-assemble into nanoporous membranes *via* a process known as non-solvent induced phase

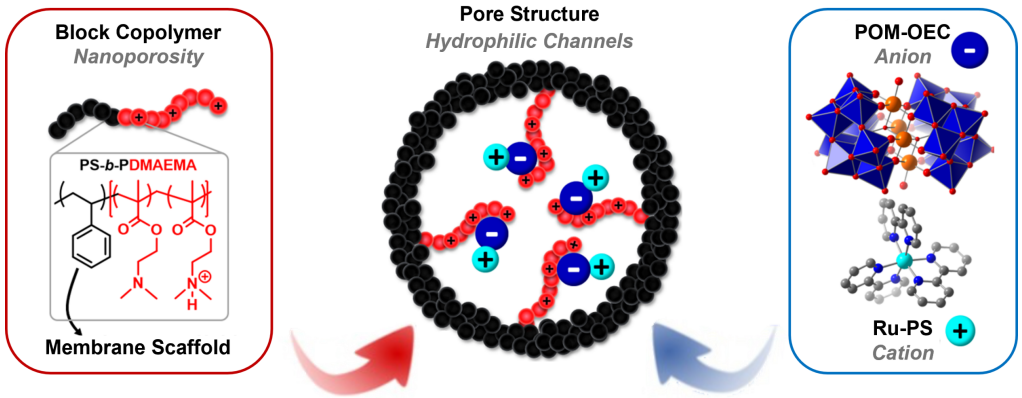


Figure 3.2 Illustration of the nanoporous block copolymer membrane consisting of polystyrene-*block*-poly(2-(dimethylamino)ethyl methacrylate (PS-*b*-PDMAEMA), co-immobilized anionic {Co_4} (POM-OEC) and cationic Ru-PS through electrostatic interactions. Adapted and reproduced under the terms of the CC BY-NC 4.0 license.[367] Copyright 2023, The Authors, Angewandte Chemie International Edition published by Wiley-VCH GmbH.

separation (NIPS).[426] SEM and TEM studies have shown that the resulting soft matter materials have a sponge-like morphology, adjustable thickness and pores of varying shapes, densities and sizes (20-30 µm). Polystyrene was selected as the hydrophobic backbone of the membrane to provide mechanical rigidity, while hydrophilic and protonatable DMAEMA serves as an anchor for POM immobilization.[427] The positive partial charge of the protonated amino side chain groups facilitates the electrostatic binding of anionic {Co_4} when the pristine membrane patches are immersed in a concentrated aqueous solution of the POM-OEC for several hours (see Figure 3.3a). Note that {Co_4} was previously synthesized according to a literature known procedure.[303] It is hypothesized that the high negative POM charge of –10 induces a charge inversion at the membrane surface, which subsequently and similarly enables the embedding of the cationic Ru-PS through electrostatic interactions. In the further course of this work, three different immobilization batches were prepared from two independently manufactured membranes with varying thicknesses and studied for their activity and stability in WOC.

The successful embedding of the molecular units was primarily indicated by the optical color change from colorless (typical for the pristine membrane) to light purple (typical for {Co_4}) to orange (typical for Ru-PS, see Figure 3.3b) depending on the individual functionalization steps. Microscopic confirmation of the attachment of Keggin-type POM and Ru-PS to the polymer membrane was provided by high-resolution STEM/EDX analyses, which showed a uniform distribution of Co, W, O and Ru in the inner pores of the membrane (see Figure 3.4). The EDX maps revealed high oxygen contents stemming from {Co_4} and yielded an excellent concurrence between the calculated Co:W ratio of

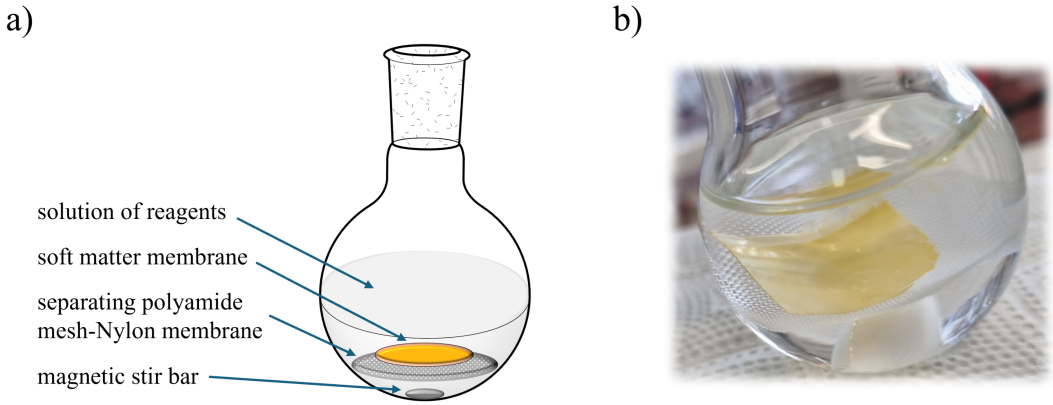


Figure 3.3 Formation of WOCbranes: **a)** Schematic representation of membrane functionalization under batch conditions.[391] **b)** Photograph of a fabricated WOCbrane patch stored in ultrapure water, which shows the characteristic orange color of Ru-PS embedded in the last functionalization step.

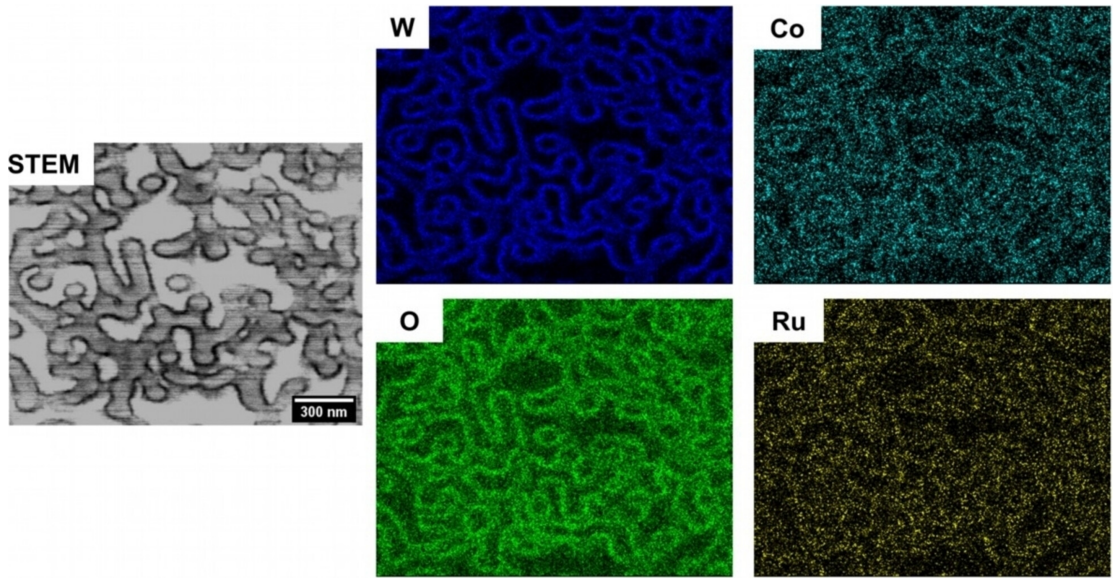


Figure 3.4 STEM/EDX maps of the elemental distribution of W, Co, O and Ru. Reproduced under the terms of the CC BY-NC 4.0 license.[367] Copyright 2023, The Authors, Angewandte Chemie International Edition published by Wiley-VCH GmbH.

0.26 and the element ratio within the POM molecule itself (Co:W = 0.22). Due to the overlap of the Ru and Cl signals in the EDX, the Ru content of the PS was quantified by HR-CS-GFAAS and the data were correlated with the TGA and μXRF results. A low loading of approx. 3.7 wt% was found for the Ru-PS, while the {Co_4} loading gave around 38.8 wt%. The determined Co:Ru ratio thus indicates that on average only every 50th POM molecule interacts with a PS molecule *via* electrostatic forces. The observed low PS loading can be attributed to repulsive electrostatic interactions with unoccupied, positively charged PDMAEMA units, which outweigh the attractive interactions with the anionic POM.

Liquid-phase visible light-driven WOC studies were performed with this novel POM- and Ru-PS-functionalized PS-*b*-PDMAEMA membrane in the presence of the SOA $Na_2S_2O_8$ in an oxygen-free buffered aqueous solution using a fiber-coupled light-emitting diode (LED; λ = 470 nm). The photocatalytic conditions employed in this study were adopted from the literature.[300] O_2 was quantified *in operando* using a customized static SECM cell equipped with Pt microelectrodes, which allowed the acquisition of spatially and temporally resolved data in local proximity to the WOCbranes. During the measurement, the membrane was gently purged with a moderate continuous argon flow of 1 mL min^{-1} to release O_2 that might have been trapped in the membrane pores. The configuration of the setup is depicted schematically in Figure 3.5a.

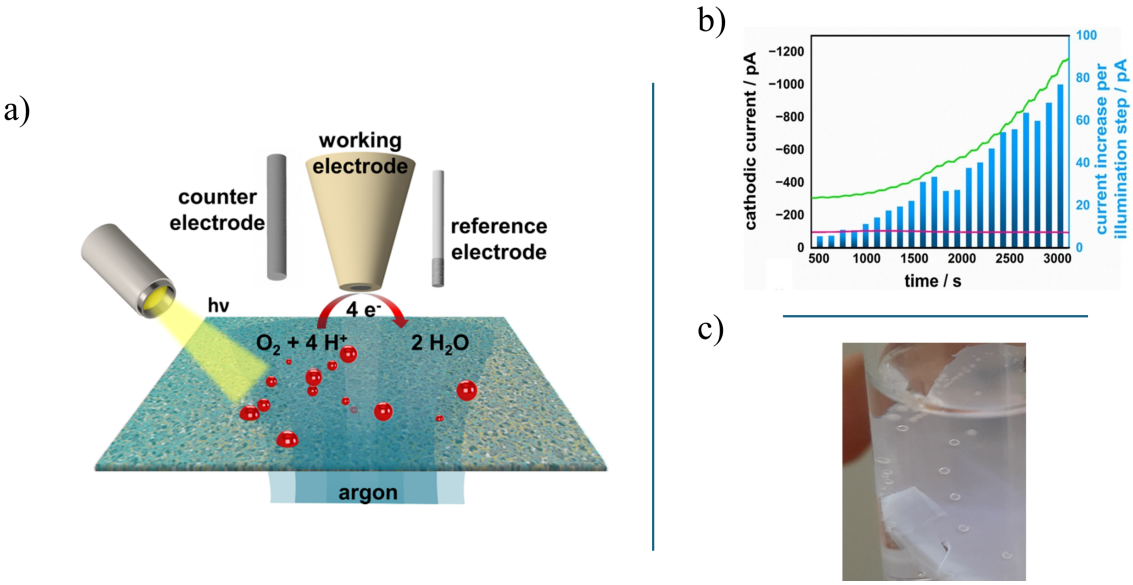


Figure 3.5 Light-driven *operando* OER studies of the WOCbranes: **a)** Schematic illustration of local *operando* O_2 measurements on a WOCbrane (SEM in false colors) using SECM. **b)** Exemplary current response at the Pt microelectrode under illumination (green) and under dark conditions (magenta) in the presence of 5 mM $Na_2S_2O_8$ in a 100 mM borate buffer solution. Note that the irradiation was started after 500 s. The blue bars show the increase in cathodic current per illumination step. **c)** Photograph of O_2 bubbles on the surface of a WOCbrane patch after light-driven WOC in 100 mM borate buffer solution with 5 mM $Na_2S_2O_8$. Adapted and reproduced under the terms of the CC BY-NC 4.0 license.[367] Copyright 2023, The Authors, Angewandte Chemie International Edition published by Wiley-VCH GmbH.

The light-dependent O_2 evolution was observed by an exponential increase of the cathodic current at the SECM tip upon illumination (see Figure 3.5b, green curve) and verified by a constant background current in the dark (see Figure 3.5b, magenta curve). The observed variations in O_2 evolution rates ranged from 0.18-1.10 fmol s^{-1} with delayed onsets of approx. 60-180 s to 9 min, which depends on the WOCbrane area and membrane thickness studied. This variability is an indication of the heterogeneity of the membrane in terms of pore size and pore space distribution. The thickness of the membrane and the lower degree of functionalization also seem to prolong the catalytic activity from a few minutes up to 66 min, suggesting a stabilizing effect due to the embedding of the molecular components in the soft matter matrix. However, the higher the polymer densities and the smaller the pore sizes, the greater the delay. These observations indicate severe limitations of mass transport and diffusion within the membrane, which is corroborated by the emergence of O_2 bubbles on the surface of an illuminated WOCbrane patch after it has been stored in ultrapure water for several hours (see Figure 3.5c).

Furthermore, we conducted a series of *ex situ* leaching and stability studies of the POM-OEC before and after photocatalysis, given the established knowledge of the degradation

of {Co_4} under electrochemical WOC conditions.[428] TXRF and EDX analyses revealed minor instabilities due to the leaching of POM-related elements. However, both methods only examine small WOCbrane patches. To obtain more comprehensive information at the macroscopic scale, we additionally used the non-destructive 2D elemental mapping technique μXRF. While minor inhomogeneities were observed between the element distributions of Co and W before and after illumination, the corresponding data showed no appreciable losses of active sites (see Figure 3.6a). Consequently, the observed variations and limitations in O_2 evolution cannot be attributed solely to POM degradation or uneven POM and PS loadings. It is imperative to consider mass transport and diffusion effects as well as potential matrix heterogeneities, such as inhomogeneous pore connectivity within the WOCbranes, as plausible explanations for the observed limited performance in heterogeneous WOC.

This assumption is supported by ATR-IR analysis (see Figure 3.6b), which confirms the stability of the POM under the given conditions. The IR spectrum of {Co_4} remained

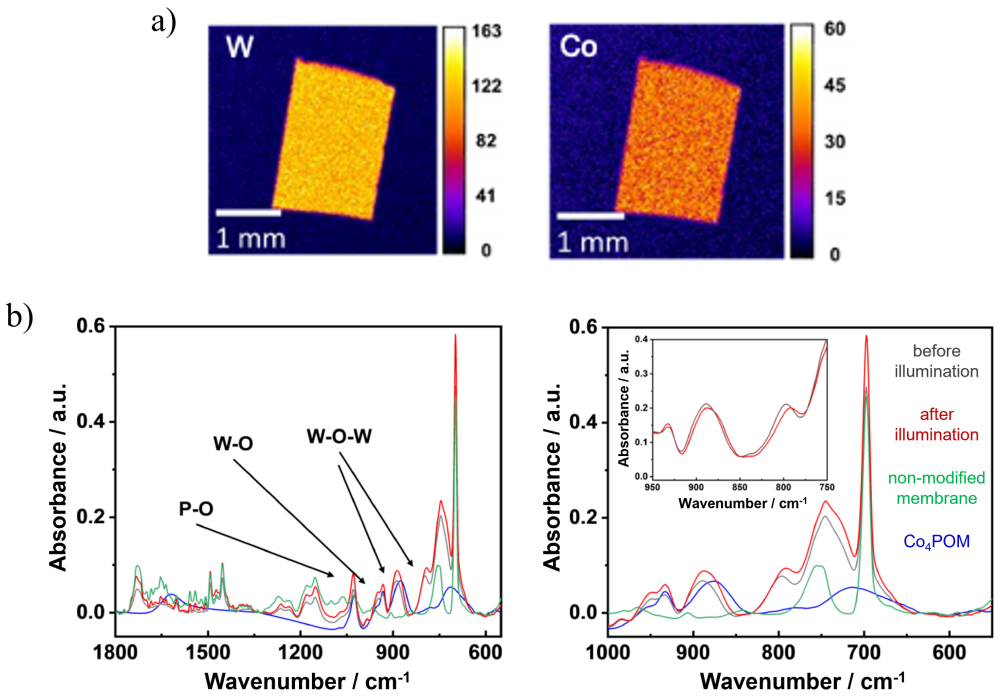


Figure 3.6 Stability studies on the WOCbranes: **a)** Exemplary μXRF maps showing the homogeneous distribution of W and Co on a WOCbrane piece after preparation and storage in ultrapure water. **b)** ATR-IR spectra of {Co_4} (blue), the pristine polymer membrane (green) and the POM-modified membranes before (gray) and after 30 min illumination (red) in 100 mM borate buffer solution with 5 mM $Na_2S_2O_8$. The inset on the right displays the respective normalized IR spectra of the POM-modified membrane before (gray) and after illumination (red). Both IR spectra show the molecular integrity of {Co_4}. Adapted and reproduced under the terms of the CC BY-NC 4.0 license.[367] Copyright 2023, The Authors, Angewandte Chemie International Edition published by Wiley-VCH GmbH.

unchanged after immobilization or photocatalysis, with minimal shifts in the W–O–W signal that were assigned to electrostatic interactions with the membrane. In addition, the absence of IR-active vibrational modes of various cobalt oxide species within the limit of detection (LOD) of the instrument suggests that {Co_4} remains intact.[429,430] However, a modest leaching of Co, W and Ru from the supernatant of WOCbranes was observed upon prolonged storage in ultrapure water, as evidenced by TXRF and HR-CS-GFAAS analysis over a period of up to six days.

In summary, this project offers a valuable approach to obtain spatially and temporally resolved *in situ* and *operando* WOC reactivity data as well as *ex situ* information on the spatial distribution for molecular PS and molecular POM-OEC systems heterogenized in nanoporous block copolymer membranes. We have demonstrated a synergistic effect of heterogenization through a prolonged catalytic activity compared to corresponding homogeneous conditions.[300] However, the observed unfavorable OEC:PS ratio and the reduced light penetration necessitate further optimization of these 1st generation WOCbranes, for example by integrating covalent attachment strategies (see chapter 4).

These results were published in "*Multimodal Analysis of Light-Driven Water Oxidation in Nanoporous Block Copolymer Membranes*", Julian Kund,‡ Jan-Hendrik Kruse,‡ Andreas Gruber, Ivan Trentin, Marcel Langer, Clarissa Read, Gregor Neusser, Dominik Blaimer, Ulrich Rupp, Carsten Streb,* Kerstin Leopold, Felix H. Schacher,* and Christine Kranz,* *Angew. Chem. Int. Ed.* **2023**, *62*, e202217196.

For more detailed information, see chapter 6.2.

3.4 Photoactive Hydrogels – {MLa-5}

Polyampholyte hydrogels represent a promising class of soft matter materials, which are characterized by a high surface area and potential applications in fields like drug delivery and purification processes.[368,431] Of particular interest are stimuli-responsive hydrogels that bear both weakly functional anionic and cationic Lewis acid and base groups (*e.g.* carboxylic acid and amine). These hydrogels offer distinct advantages, including the ability to fine-tune structural and mechanical properties through precise pH adjustment, allowing the formation of stable internal networks with potential recyclability of immobilized molecularly charged species.[133,370] The integration of these subunits into polyampholytic scaffolds with spatial control enables 3D access to more active sites, which is beneficial for heterogeneous catalysis to promote artificial photosynthesis.[375]

In this work, we synthesized and examined a series of pH-responsive hydrogels based on crosslinked PDha with dynamic net charges and charge densities. We investigated their swelling behavior upon changes in pH, salinity and solvent, as well as the reversible adsorption of an organometallic PS model with the aim of understanding the potential for self-repair. The light-harvesting hybrid hydrogels were further studied in heterogeneous light-driven HER and OER and the effects of the soft matter matrix on catalyst and PS performance were assessed *via* several reactivity and stability studies.[359]

The preparation of the PDha-based polyampholyte hydrogels was carried out in three consecutive steps (see Figure 3.7). First, the hydrolyzed PDha, which bears amine base and carboxylic acid groups in each repeating unit, was synthesized by controlled radical

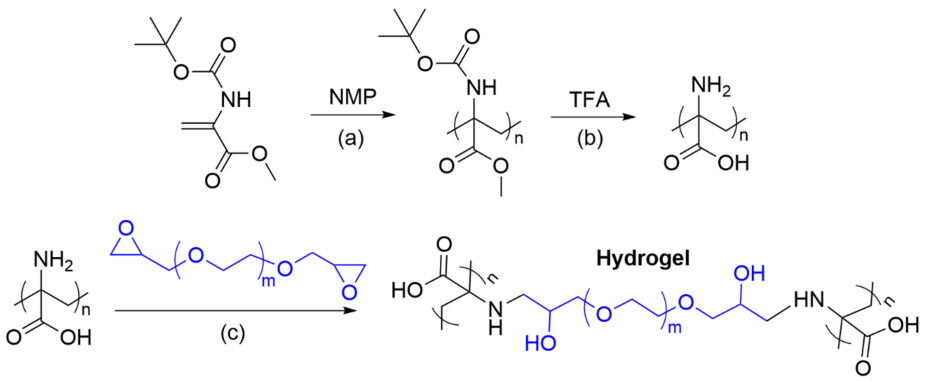


Figure 3.7 Synthesis route to obtain PDha-based hydrogels: (a) radical NMP of *t*BAMA, (b) deprotection of P*t*BAMA by TFA to yield PDha and (c) crosslinking of PEG, which bears epoxide groups, to obtain the polyampholytic hydrogel. Reproduced under the terms of the CC BY 4.0 license.[359] Copyright 2024, The Authors, Macromolecular Rapid Communications published by Wiley-VCH GmbH.

NMP of *tert*-butoxycarbonylaminomethacrylate (*t*BAMA) and cleavage of the protecting methoxy and *tert*-butyloxycarbonyl (Boc) groups from polymerized P*t*BAMA by trifluoroacetic acid (TFA).[432] Subsequently, poly(ethylene glycol) diglycidyl ether (PEGDGE) was subjected to a chemical crosslinking reaction with the amine moieties of PDha *via* a ring-opening reaction of epoxides under alkaline conditions, resulting in the formation of the final transparent hydrogel. This step in conjunction with the gelation process enabled the efficient removal of the remaining methoxy groups.[433] The structural formation of PDha and the hydrogel was confirmed by ^{13}C cross-polarization magic angle spinning (CP-MAS) NMR and FTIR (see Figure 3.8).

The composition of the hydrogel and the gelation parameters, such as reaction time and viscosity of the solution, were optimized by kinetic studies according to the molecular weight (M_n) of PDha and the crosslinker PEGDGE, the polymer concentrations and the PDha-to-crosslinker ratio (PCR, w/w). It was found that a higher average polymerization degree of 180 of P*t*BAMA promoted the crosslinking reaction, which we attributed to a greater extent of chain entanglements. The optimal composition for the hydrogels was determined to be a preferred PCR of w/w 1:1 and PEGDGE with a M_n of 2,000 g mol^{-1}, as these conditions yielded self-supporting scaffolds that exhibited the best mechanical, durability, diffusion and swelling properties.

A high DS is of particular importance to enable the free movement of additives and gas molecules through the pores of the hydrogel. PDha is present as a polycation at pH ≤ 5 and as a polyanion at pH ≥ 10 and it is zwitterionic in the pH range 5 to 10, being almost

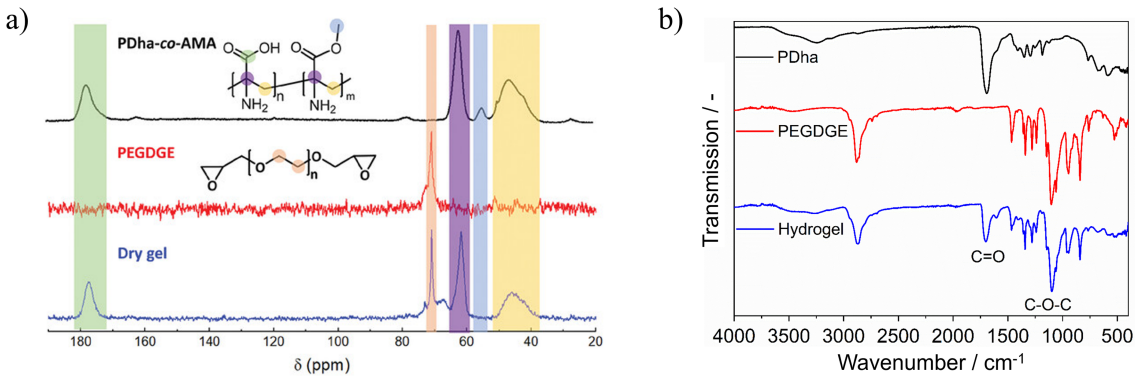


Figure 3.8 Characterization of PDha-based hydrogels: **a)** ^{13}C CP-MAS NMR spectra of PDha, PEGDGE and the dry hydrogel. **b)** FTIR spectra of PDha, PEGDGE and the corresponding hydrogel. Adapted and reproduced under the terms of the CC BY 4.0 license.[359] Copyright 2024, The Authors, Macromolecular Rapid Communications published by Wiley-VCH GmbH.

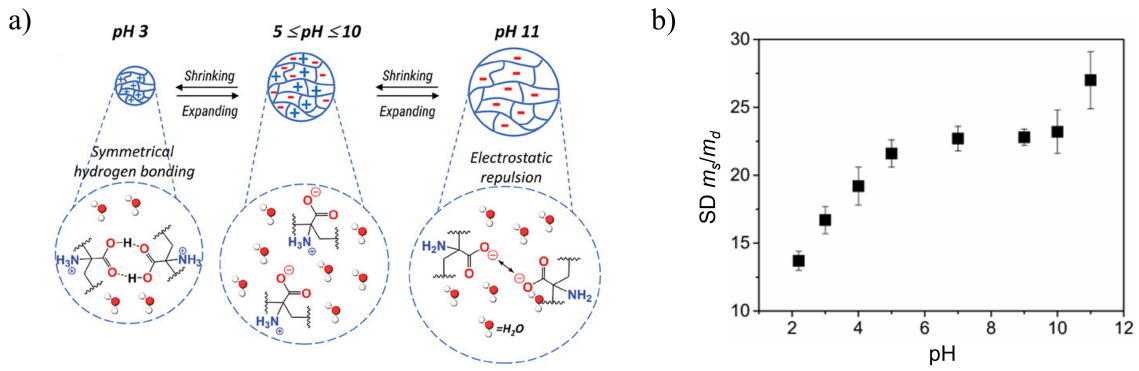


Figure 3.9 Swelling properties of PDha-based hydrogels: **a)** Schematic illustration of the pH-dependent swelling behavior showing possible dominant interactions, especially attractive H-bonds at low pH *vs.* repulsive electrostatic interactions at high pH. **b)** Swelling degree (SD) as a function of the pH for the hydrogel based on PEG with M_n = 2,000 g mol^{-1}. Reproduced under the terms of the CC BY 4.0 license.[359] Copyright 2024, The Authors, Macromolecular Rapid Communications published by Wiley-VCH GmbH.

charge-neutral near the IEP of PDha.[432] Thus, the pH-dependent net charge and charge density of PDha significantly impact the DS, as shown in Figure 3.9.[434–436] At low pH, the presence of attractive symmetrical H-bonds between carboxylic acid groups transcends the repulsive electrostatic forces between positive charges, resulting in reduced DS values of 13.7 ± 1 at pH 2.2 in deionized H_2O. However, as the pH increases, the electrostatic repulsion prevails due to the progressive deprotonation of the carboxylic acid groups, leading to gradually increased DS values of 22.7 ± 0.8 at pH 7 in the zwitterionic state and 27 ± 2 at pH 11.[437] This transition is further evidenced by FTIR. The ionic strength was maintained throughout these studies to ensure comparability, as different salinities can affect the volume and mesh size of the hydrogels (see chapter 1.8.1). This behavior was reflected in a reduced DS at increased ionic strength, which is due to ion screening of the positive and negative charges on the polyampholytic PDha. Furthermore, a remarkable swelling capacity was observed in highly polar organic solvents (*e.g.* MeOH, DMF, MeCN and acetone), albeit the highest DS of PDha-based hydrogels was obtained in deionized H_2O.

We further examined the adsorption capacity of hydrogels composed of PDha crosslinked with PEGDGE (M_n = 6,000 g mol^{-1}) in response to alterations in pH using the molecular cationic Ru-PS model. Dye adsorption at neutral pH was monitored by the optical color change of the hydrogel (see Figure 3.10a) and quantified as a function of the initial dye concentration and contact time with the hydrogel based on changes in the UV-Vis spectra of the supernatant using the characteristic absorption properties of Ru-PS. In correlation

with adsorption isotherms, diffusion kinetics and leaching studies of the chromophore, we observed stable dye attachment due to ligand stacking and electrostatic interactions between the PS complex and the hydrogel. The adsorption capacity of *ca.* 18 mg g^{-1} within 4 h decreased drastically with increasing pH, which could be attributed to the occupation of vacant binding sites by the cation of the base. Conversely, the acidification of the medium to pH 2 resulted in the controlled desorption of Ru-PS due to the emergence of repulsive electrostatic interactions directed towards the polycationic state of the hydrogel.[434] These observations collectively demonstrate the reversible adsorption and inherent stability of charged Ru-PS as a function of pH, signifying a great potential for the recycling, repair or exchange of degraded molecular units within the hydrogel.

The UV-Vis and emission spectra recorded for the swollen functionalized hydrogels also showed that the photophysical properties of the organometallic dye were preserved within the soft matter matrix (see Figure 3.10b). This feature was optimal for studying the role of the hydrogels as heterogeneous light-harvesters in independent photocatalytic HER and OER with {Mo_3}-HEC and {Co_4}-OEC, respectively. The synthesis methods used for both molecular catalysts have been previously documented in the literature.[303,328] The subsequent incorporation strategy of the molecular compounds into the hydrogel followed a similar approach to the preparation of the previously described WOCbranes using attractive electrostatic interactions between cationic Ru-PS, anionic catalysts and the zwitterionic hydrogel, which exhibited a high charge density (see chapter 3.3).[367]

First, we verified an efficient electron transfer between the hybrid hydrogels with a fixed Ru-PS content of 95 µM and different concentrations of the respective quencher catalysts

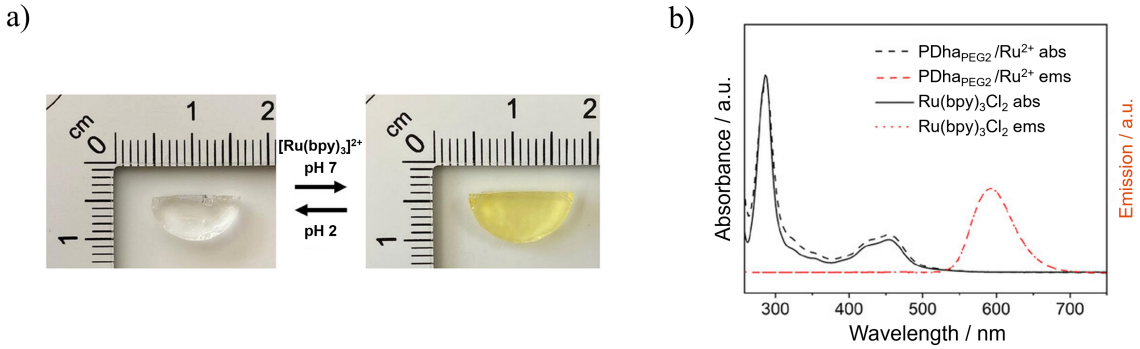


Figure 3.10 Attachment of Ru-PS: **a)** Photographs of the reversible adsorption of Ru-PS by PDha-based hydrogels upon changes in pH. **b)** Absorption and emission spectra of Ru-PS in H_2O and embedded in a PDha-based hydrogel. Adapted and reproduced under the terms of the CC BY 4.0 license.[359] Copyright 2024, The Authors, Macromolecular Rapid Communications published by Wiley-VCH GmbH.

{Mo_3} and {Co_4} by independent nanosecond transient emission quenching studies at different time delays under excitation at 500 nm and additional Stern-Volmer analysis. We then conducted light-driven HER and OER experiments in a customized photoreactor, which was equipped with a blue LED (λ = 453 nm). Contrary to the project {MLa-2}, we investigated the reactivity of the PDha-PS-based hydrogels *via* bulk analysis techniques. Head-space gas chromatography was used to quantify H_2, and the amount of O_2 in the solution and gas phase was determined by fluorescence-based oxygen sensors.[438]

The HER studies were performed with the SRA TEA in a solvent mixture of H_2O and MeOH. The organic solvent increases the solubility of TEA, the stability of {Mo_3} and thus the HER performance, but also reduces the DS of the hydrogel.[328] An equal volume ratio was defined as a favorable compromise between these individual factors. Initial observations indicated a reduction in HER activity in freeze-dried hydrogels compared to homogeneous conditions, which could be explained by diffusion limitations for gaseous H_2 from the hydrogel. For this reason, we optimized the concentrations of dye and catalyst according to their diffusivity into the hydrogel. The highest yield of 3,590 μmol g^{-1} H_2 with a corresponding TON of 2,983, assuming that all catalyst molecules participated in the HER, was achieved with 0.9 M TEA, 100 μM Ru-PS and 0.534 μM {Mo_3}. The use of elevated concentrations of {Mo_3} led to a decline in the HER performance, which was attributed to the accumulation of {Mo_3} at the hydrogel surface, thereby impeding its diffusion into the 3D hydrogel architecture. Furthermore, a change of the SRA to 0.9 M TEOA resulted in reduced H_2, while 0.1 M AscOH at a pH of 5.5 led to a substantial increase in the HER, reaching 7,360 μmol g^{-1} H_2 (see Figure 3.11a). However, this refinement was concomitant with the destabilization of the electrostatically bound PS.

Light-driven WOC trials of the functionalized hydrogels with 5 μM {Co_4}, 100 μM Ru-PS and 5 mM $Na_2S_2O_8$ as SOA in 80 mM borate buffer at pH 8 yielded 0.7 μmol O_2 after 40 min, which corresponds to a TON of 70, assuming that all catalyst clusters present were involved in the OER. However, an excess of {Co_4} led to a decrease in the dye loading, which in turn resulted in diminishing OER rates. In contrast to HER, electrostatic binding of Ru-PS and {Co_4} to the swollen hydrogels prior to WOC was imperative to circumvent ion-pairing effects between the two solutes and the ensuing diffusion limitations into the hydrogel network, as evidenced by substantial changes in the UV-Vis spectrum.[339] The homogeneous distribution of the molecular units in the cross-section

of the hydrogel was qualitatively verified by SEM/EDX maps of POM- and PS-related elements. In addition, we performed control experiments in homogeneous solutions to ensure a comparative analysis under identical photocatalytic conditions. However, significant deviations from literature reports were ascertained, possibly due to major experimental discrepancies in sample preparation, O_2 quantification or light intensity.[300] Nevertheless, experiments with reduced Ru-PS concentrations suggested a more effective OER with sustained catalytic activity and improved charge transfers within the hydrogel, as some of the O_2 evolved might be trapped in the matrix.

Finally, we investigated the effect of the hydrogel environment on the photostability of immobilized Ru-PS. The O_2 evolution under illumination was monitored for 27 d and the results were evaluated with reference to comparable WOC studies performed under homogeneous conditions (see Figure 3.11b). Remarkably, the decomposition of Ru-PS

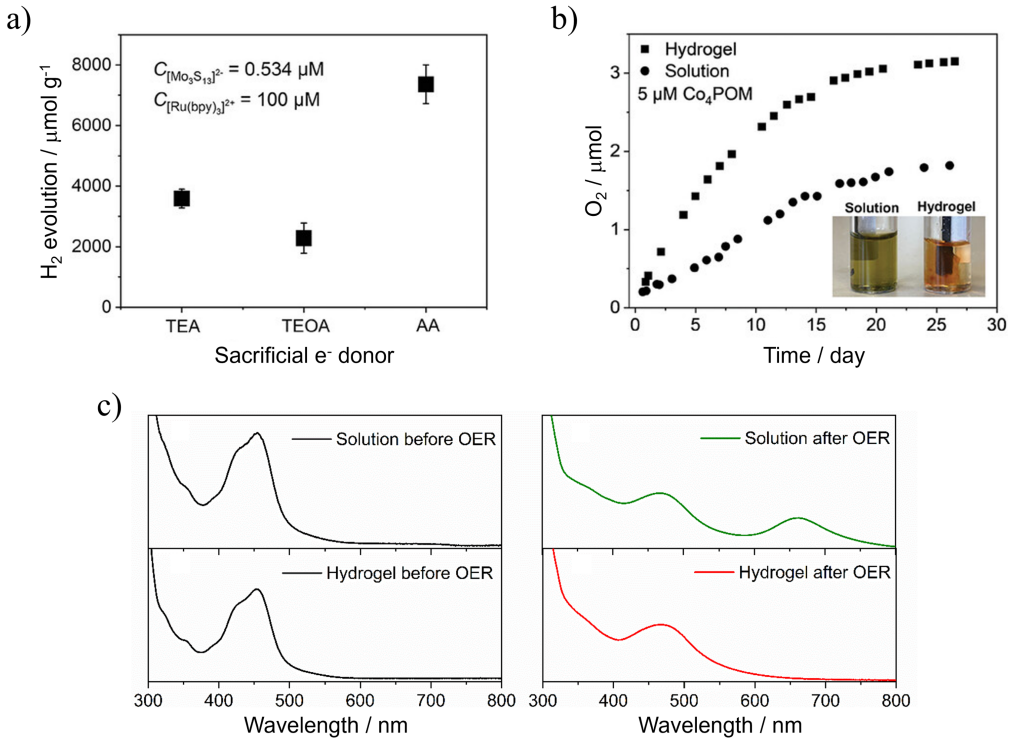


Figure 3.11 Evaluation of the light-driven catalytic performance of functionalized PDha-based hydrogels: **a)** Amounts of H_2 evolved per gram dry gel to compare the effect of SRA on the H_2 evolution performance. Conditions: 0.9 M TEA, 0.9 M TEOA, 0.1 M AscOH (here abbreviated as AA), 0.534 µM {Mo_3}, 100 µM Ru-PS, MeOH:H_2O (1:1, v/v), LED with λ = 453 nm. **b)** Comparison of the amounts of O_2 evolved in long-term O_2 evolution studies between light-driven OER in the hydrogel and light-driven OER in solution under homogeneous conditions. Inset photographs show the corresponding samples after the photocatalytic OER. Conditions: 5 mM $Na_2S_2O_8$, 5 µM {Co_4}, 100 µM Ru-PS, 80 mM sodium borate buffer, LED with λ = 453 nm. **c)** UV-Vis spectra of the corresponding solution and hydrogel samples obtained before and after long-term light-driven OER. Adapted and reproduced under the terms of the CC BY 4.0 license.[359] Copyright 2024, The Authors, Macromolecular Rapid Communications published by Wiley-VCH GmbH.

could be detected after only one day by an optical color change to a dark orange, which remained stable for the hydrogel. In contrast, the homogeneous solution showed a green coloration over time. Subsequent post-catalytic UV-Vis studies revealed significant differences to the spectra recorded before OER (see Figure 3.11c). Comparative reports of Ru-PS degradation in the presence of $S_2O_8^{2-}$ by Yoon and colleagues[439] suggested the formation of WOC-active Ru-dimers as possible decomposition products with limited diffusion capacity in the hydrogel, while catalytically inactive Ru-oligomers could be formed as degradation products during homogeneous OER catalysis. These stability differences of Ru-PS could provide a rationale for the higher O_2 evolution rates, chemical yields related to the SOA, and TONs observed for the hydrogels.

Further rheological analyses and ^{13}C CP-MAS NMR studies showed an increased DS and a loss of the characteristic crosslinker signals. These results indicate that the harsh WOC conditions exert a detrimental effect on the mechanical stability and structural integrity of the hydrogel scaffold over an extended period of exposure.

In summary, in this project we have developed pH-responsive polyampholyte hydrogels based on crosslinked PDha and demonstrated facilitated charge transfer in light-driven HER and OER by providing close spatial proximity of the functional molecular units for artificial photosynthesis. The hydrogel network has a significant impact on the activity and stability of PS and catalyst and enables repair approaches through pH-mediated reversible adsorption. *Operando* spectroscopic studies can be used in the future to obtain more detailed information on the exact decomposition pathway of Ru-PS within the hydrogel, while mass transfer limitations during catalysis can be addressed by covalent PS immobilization and the operation of WOC under flow conditions. The utilization of alternative crosslinkers should also be considered to maintain the mechanical, optical and chemical integrity of the hydrogel matrix under catalytic conditions.

These results were published in "*Poly(dehydroalanine)-Based Hydrogels as Efficient Soft Matter Matrices for Light-Driven Catalysis*", Tolga Çeper,‡ Marcel Langer,‡ Nikita Vashistha, Benjamin Dietzek-Ivanšić, Carsten Streb, Sven Rau, and Felix H. Schacher,* *Macromol. Rapid. Commun.* **2024**, *45*, 2300448.

For more detailed information, see chapter 6.4.

4. Summary and Perspectives

A design thinking strategy based on biomimetic concepts was implemented according to the steps shown in Figure 4.1. First, a number of challenges were compiled, including elevated energy consumption and the necessity for more sustainable energy conversion technologies. Artificial photosynthesis is regarded as a fundamental cornerstone for realizing a "green" future in the energy sector, which can be addressed, for example, by integrating molecular building blocks, such as catalysts and PSs, into multifunctional soft matter matrices in close spatial proximity to each other. The structural prerequisites for these compounds can be found in nature, *e.g.* in HER-active enzymes. In the presence of sacrificial agents, such as SOA or SRA, the functional composites can then perform productive light-driven HER or WOC. Similar to biological photosynthesis, an array of efficient electron and energy transfer processes are required (*e.g.* PCETs). Hence, to ultimately advance the rational, knowledge-based design of high-performance heterogeneous light-driven WOC and HER model systems using molecular POMs and thiomolybdates as key catalytically active materials, two distinct approaches were pursued in this work.

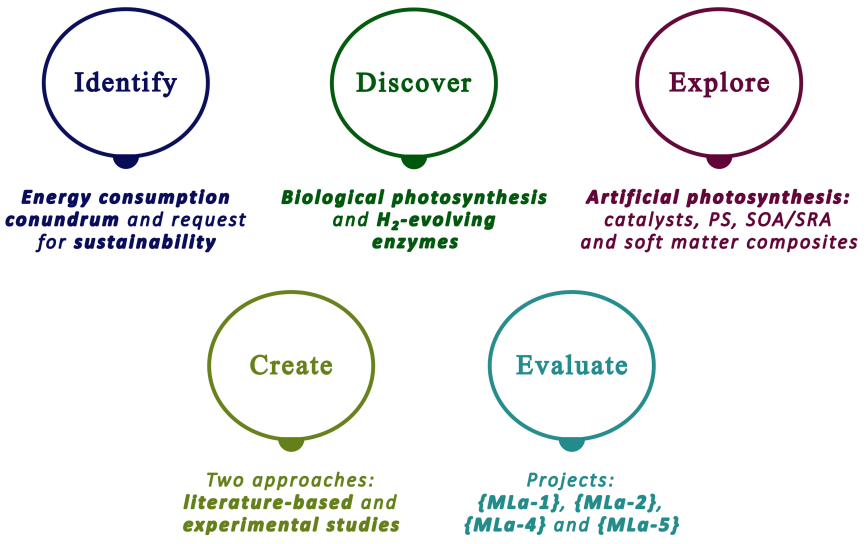


Figure 4.1 Illustrative summary of this work *via* the scheme for biomimetic design thinking presented in chapter 1.2: First, critical energy consumption and the demand for greater sustainability were identified as fundamental problems and pertinent cornerstones in chapter 1.1. The structural and functional concepts of biological photosynthesis and H_2-evolving enzymes were described in chapter 1.3 as promising natural models. The prerequisites for the development of an artificial photosystem based on a molecular three-component system consisting of a catalyst and a PS heterogenized on soft matter supports in the presence of sacrificial agents were elaborated in chapters 1.4–1.8. Finally, suitable approaches for creating biomimetic designs and prototypes were presented and critically evaluated in detail in chapters 2 and 3.

The two literature-based studies summarize the current understanding of thiomolybdate and POM chemistry, as well as recent developments in their heterogenization on various supports, such as soft matter substrates. Experimental and theoretical advances were highlighted by pioneering and emerging applications reported in the literature. Challenges and opportunities in the characterization of POM-soft matter composites were elucidated and reactivity changes in HER were discussed based on various detected active sites in electro- and photocatalytically active thiomolybdates. The influence of varying reaction conditions, encompassing both homogeneous and heterogeneous operation, underscores the necessity for careful evaluation of newly designed photocatalytic systems from a mechanistic perspective. The two reviews also offer systematic, comprehensive and valuable insights into the structure-property-performance relationships of molecular inorganic catalysts and immobilization strategies on functional supports. These insights are expected to facilitate the exploration and refinement of functional material fabrication methods for the wider scientific community and pave the way for their future widespread technological application. The projects further recommend in-depth investigations, such as several complementary pre- and post-catalytic analyses, to assess the stability and fate of molecular building blocks after heterogenization and facilitate the understanding of complex reactivity patterns and mechanistic processes under catalytic conditions.

In the two experimental works, synthetic heterogenization routes were developed for the incorporation of molecular catalysts (*i.e.* {Co_4}-POM and {Mo_3}-thiomolybdate) and inversely charged PS (*i.e.* Ru-PS) into suitable soft matter matrices (*i.e.* nanoporous block copolymer membranes and polyampholyte hydrogels) by electrostatic anchoring. A series of *in situ*, *operando* and *ex situ* studies were conducted to explore the structural integrity, stability, reactivity and selectivity for light-driven WOC and HER of the heterogenized photosystems at the micro- and/or macroscale. The distribution of catalyst and PS on the surface of the matrix was found to be stable and uniform for both soft matter composites. Furthermore, the reactivity studies indicated enhanced accessibility of catalytically active sites and an increased charge transfer between spatially separated reactive subunits in the soft matter environment. In the case of the hydrogel, it was shown that the high density of dynamic charges in the scaffold can be utilized for the controlled, stepwise and pH-mediated reversible adsorption of the molecular entities. This finding suggests the potential for self-repair of degraded subunits and the avoidance of prior PS and catalyst

aggregation in highly concentrated solutions. Leaching and stability studies were also performed, showing increased Ru-PS stability in the hydrogel environment and only minor degradation of {Co_4} in the WOCbrane. However, the structural integrity of the OEC could only be validated in the LOD range of the ATR-IR measurement device.

In this way, conceptual proof-of-principle studies were performed, providing essential insights into the exemplary design of multifunctional materials, the characterization of heterogenized molecular building blocks and the application of these soft matter hybrid systems in light-driven WOC and HER. It was demonstrated that both hierarchically nanostructured soft matter matrices are suitable hosts for the conversion of a given homogeneous photosystem into a heterogenized assembly. The close spatial proximity of the molecular building blocks for light-driven catalysis ensured their structural integrity, catalytic reactivity in OER and HER, and enhanced electron transfer. In comparison to homogeneous systems, the composite materials exhibited increased (long-term) stability, simplified handling and potential recyclability.

However, fundamental material limitations were also identified in terms of the stability of the composite materials under the harsh catalytic conditions, the minor leaching of the molecular units, the severe heterogeneities in the pore size distribution in the membranes, the restricted mass transport of additives and products through the pores in both soft matter materials (as evidenced, for instance, by the delayed release of O_2 bubbles after irradiation of the WOCbranes), and the diffusion limitations of the catalysts in the hydrogels, all of which affect the overall catalytic performance of the photosystems. Therefore, the assertion by Ziegenbalg and colleagues that "*a complex interplay between the molecular properties of the involved chemical species, the environment around the active components, and the presence of light of suitable intensity and wavelength*" determines the "*overall performance of photocatalytic reactions*" is also sufficiently accurate as a finding for this work.[187,440]

In essence, each research project underscores the significance of cultivating interdisciplinary collaborative frameworks between molecular design, soft matter chemistry, materials integration, light-driven catalysis, photoreactor engineering, and functional and mechanistic characterization to acquire a deeper understanding and judicious optimization of structure-property relationships. This, in turn, fosters the

rational development of advanced high-performance HER and WOC photocatalytic soft matter composite systems characterized by high efficiency, selectivity and stability.

Despite the difficulties in predicting the optimal configuration of the critical parameters, subsequent modifications and additional studies are essential for enhancing these soft matter composite photosystems. For example, the prevention of gas accumulation can be addressed by varying the ratio between hydrophilic and hydrophobic blocks and precisely and rationally tuning the membrane thickness, pore connectivity and pore size distribution *via* "design of experiments" (DOE, *vide infra*) studies. A similar strategy can be employed to improve the 3D accessibility of the molecular units in both soft matter matrices, thereby boosting the catalytic activity and facilitating the detection of actual substrate conversion rates, allowing a better comparability with related homogeneous systems. In addition, the chemical modification of the block copolymers and crosslinkers could improve the long-term stability of the materials under harsh oxidizing conditions, and the optimization of the surface areas could prevent reduced light penetration into the bulk material.

The subsequent sections delve into the intricacies of promising approaches for further optimization of these photosystems.

Next Generation Membranes

The electrostatic embedding of molecular catalysts and PSs in nanoporous block copolymer membranes, as outlined in the project {MLa-2}, represents the 1st generation of membranes. In light-driven WOC studies, an unfavorable catalyst-to-PS ratio and minor leaching of the POM-OEC were observed. To address these limitations, the controlled covalent immobilization of the molecular building blocks on the soft matter scaffold is imperative. However, this process requires the precise introduction of suitable binding sites in the catalysts, PS and the block copolymer architecture. Thus, a diverse array of monomers must be used in the preparation of the membrane, while the ligand periphery of the Ru-based PS complex and the POM and thiomolybdate cluster structures of the catalysts necessitate modification with accessible, reactive functional groups. The subsequent functionalization process to produce the corresponding Class I hybrids is also not entirely straightforward, as explained in chapter 1.8.1. Consequently, a gradual transition from purely electrostatic to covalent functionalization is aimed for.

Photocatalytically active 2nd generation membranes have already been successfully developed by our cooperating groups.[357] An analog of the Ru-based light-absorbing unit bearing an amine group was used for the nucleophilic substitution of a chloride leaving group of a vinyl benzyl chloride (VBCl) copolymer block. The authors observed larger amounts of immobilized PS compared to the electrostatic embedding strategy. However, they also noted the formation of aggregates and different protonation states of the PS complexes within the membrane, resulting in the heterogeneity of the sample and different intermolecular interactions between PS and the membrane architecture.

Nevertheless, these conceptual foundations serve as an optimal starting point for further adaptations. To this end, we have applied an alternative method in which a bpy-containing acrylate monomer is used for the covalent bonding of a $[Ru(bpy)_2]^{2+}$ unit (*e.g.* $Ru(bpy)_2(SbF_6)_2$).[441–443] The subsequent electrostatic attachment of anionic catalysts, such as $\{Co_4\}$ or $\{Mo_3\}$, is in turn enabled by the integration of hydrophilic DMAEMA blocks into the nanoporous block copolymer membrane. This step has previously been demonstrated for the functionalization process described in chapter 3.3 (see Figure 4.2). Initial tests verified the successful loading of PS and $\{Co_4\}$ as well as a homogeneous distribution of the catalyst on the membrane surface, as determined by TGA and μXRF analysis. The OER reactivity of these WOCbranes was confirmed by *operando* SECM measurements, which showed comparable reaction rates of *ca.* 0.38 fmol s^{-1} to the 1st generation membranes. This finding indicates a limited interaction between the

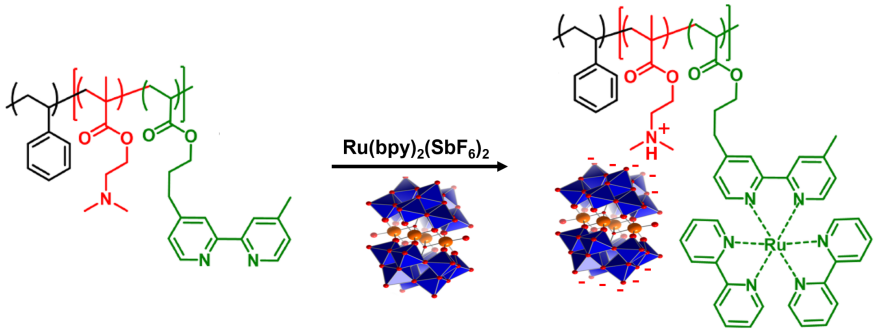


Figure 4.2 Soft matter composite membrane of the 2nd generation: The formation of this WOCbrane is attempted by the covalent bonding of $Ru(bpy)_2(SbF_6)_2$ to 2-(4-(4'-methyl-2,2'-bipyridyl))propyl-acrylate units (bpyPA, green) and the electrostatic bonding of anionic $\{Co_4\}$ to protonated DMAEMA units (red) of the terpolymer PS-*b*-P(DMAEMA-*co*-bpyPA). Polystyrene is again used as the hydrophobic backbone to ensure mechanical rigidity. The schematic representation of the membrane components has been cropped, adapted and reproduced under the terms of the CC BY 4.0 license.[444] Copyright 2023, Friedrich Schiller University Jena. The illustration of $\{Co_4\}$ was cropped, adapted and reproduced under the terms of the CC BY-NC 4.0 license.[367] Copyright 2023, The Authors, Angewandte Chemie International Edition published by Wiley-VCH GmbH.

covalently immobilized PS and the electrostatically bound POM-OEC. In addition, a prolonged activity of approx. 48 min to 114 min was observed, which could be attributed to an increased stability of the PS. However, TXRF studies also revealed considerable leaching of tungsten and, thus, of the entire POM cluster after irradiation.[444]

Therefore, the focus is directed towards the development of 3rd generation membranes, in which the membrane scaffold is covalently co-functionalized with both molecular units to effectively mitigate cluster instabilities. Furthermore, it is anticipated that a certain proximity between the catalyst and the PS molecules deposited on the membrane with high loadings will ensure efficient energy transfer, which is required for effective light-driven catalysis. In preliminary experiments, we attempted to covalently bind the POM-OEC $\{Mn_4V_4\}$ to the membrane surface by exchanging the acetate ligands with competing acrylic acid moieties of the hydrophilic block copolymer (see Figure 4.3). However, the design is still in its infancy, as there are synthetic challenges associated with the solubility of the POM molecule, while the membrane must not be dissolved, and in the retention of the POM structure after functionalization, as the cluster tends to decompose in H_2O or MeOH (see chapter 1.6.3). This solubility problem also affects the subsequent integration of the PS $[Ru(bpy)_2(ipPhNH_2)]^{2+}$ ($ipPhNH_2$ = 2-[4-phenylamino]-1*H*-imidazo[4,5-*f*][1,10]phenanthroline), which is to be incorporated analogously to the 2nd generation membranes. The use of a different POM species or the introduction of alternative anchoring groups within the membrane could provide decisive progress in the fabrication of 3rd generation membranes.[444]

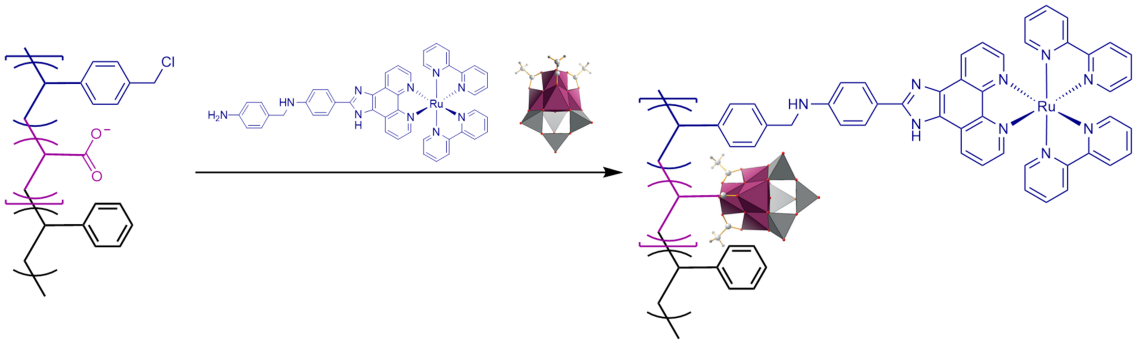


Figure 4.3 Soft matter composite membrane of the 3rd generation: The formation of this WOCbrane is attempted by the covalent bonding of $[Ru(bpy)_2(ipPhNH_2)]^{2+}$ to VBCl units (blue) and the covalent bonding of $\{Mn_4V_4\}$ to acrylic acid units (AA, purple) of the terpolymer PS-*b*-P(VBCl-*co*-AA). Polystyrene is again used as the hydrophobic backbone to ensure mechanical rigidity. The illustration of $\{Mn_4V_4\}$ was cropped, adapted and reproduced with permission.[298] Copyright 2016, Wiley-VCH Verlag GmbH & Co. KGaA, Weinheim.

The ion pairing effects observed in the catalytic studies of the photoactive polyampholyte hydrogels can also be reduced by the covalent integration of PS and catalyst. The establishment of dynamic covalent bonds, for instance, *via* Schiff-base chemistry for pH-reversible covalent anchoring of molecular components, is an intriguing concept to obtain the possibility of self-repair mechanisms.[445]

Functionalization of Thiomolybdates

With regard to the development of 3rd generation HERbranes, the covalent bonding of thiomolybdates to soft matter supports can be achieved by the formation of Mo–O–X bonds (X = residue of the substrate), accompanied by the loss of the terminal S_2^{2-} ligands, as previously reported for hard matter composite materials.[176] The incorporation of organic or organometallic functionalities could expand the range of feasible synthetic methodologies for the covalent deposition of intact and active HEC thiomolybdate cores, such as $[Mo_3S_7]^{4+}$.

In this approach, the objective is to functionalize $\{Mo_3\}$ with a bpy ligand by exchanging a terminal S_2^{2-} ligand. The bpy could also be equipped with an amine group that can be nucleophilically substituted with chloride groups, using the same synthetic principles as for the 2nd generation membranes (*vide supra*). Alternatively, the thiomolybdate cluster could be directly attached to the bpy moiety of the other 2nd generation membrane (see Figure 4.3). However, it is necessary to establish a synthesis concept that addresses the anticipated challenges related to solubility, purification and crystallization, while steering the equilibrium towards the desired product.

Therefore, we first tested the structural modification of thiomolybdates with different bidentate ligands and reproduced the linkage of bpy ligands to the $[Mo_3S_7]^{4+}$ framework following the procedure of Kim, Tripathi and colleagues.[446] The $[Mo_3S_7Br_6]^{2-}$ scaffold was identified as a suitable precursor for the synthesis of the neutral monofunctionalized cluster $[Mo_3S_7Br_4(bpy)]$. The structural features were confirmed by NMR, ATR-FTIR, UV-Vis and single crystal X-ray diffraction (XRD) analyses. A threefold substitution of the cuboidal $[Mo_3S_7]^{4+}$ core with the ligand 1,10-phenanthroline (phen) was also achieved, indicating the successful establishment of a universal functionalization route to obtain covalently functionalized thiomolybdates. It should be noted that the coordination

of bpy to a related $[Mo_3S_4]^{4+}$ core *via* a different, more complicated two-step approach has also been documented in the literature.[447]

The covalent bonds between thiomolybdate clusters and organic functionalities, as established by the previously developed synthetic routes, can also be considered as suitable linkers for the design of PS-catalyst dyads with tunable photophysical properties for the catalytic HER. These dyads could subsequently be attached to soft matter matrices *via* covalent interactions. This approach offers not only additive synergy effects but also the advantage of ultimate control over the spatial proximity and geometric orientation of PS and catalyst. The design of these multicomponent complexes could promote rapid, non-diffusion-limited intramolecular electron transfer, effective charge separation and the prevention of their recombination between different redox states that contribute to the photocatalytic cycle.[133] A preliminary study suggests the successful formation of such a dyad using $[Ru(tbbpy)_2(tpphz)]^{2+}$ (tbbpy: 4,4'-di-*tert*-butyl-2,2'-bipyridine; tpphz: tetrapyrido[3,2-a:2'3'-c:3'',2''-h:2''',3'''-j]-phenazine) as the chromophore unit and $(TEA)_2[Mo_3S_7Br_6]$ as the catalyst precursor, which was supported by a series of spectroscopic and electrochemical analyses (see Figure 4.4). However, further in-depth characterizations are necessary to unambiguously verify this assumption.

In addition, the enhanced structural diversity of the two organically functionalized thiomolybdates and the formed dyads can be further exploited in homogeneous HER studies to obtain an improved understanding of manipulating excited state lifetimes as

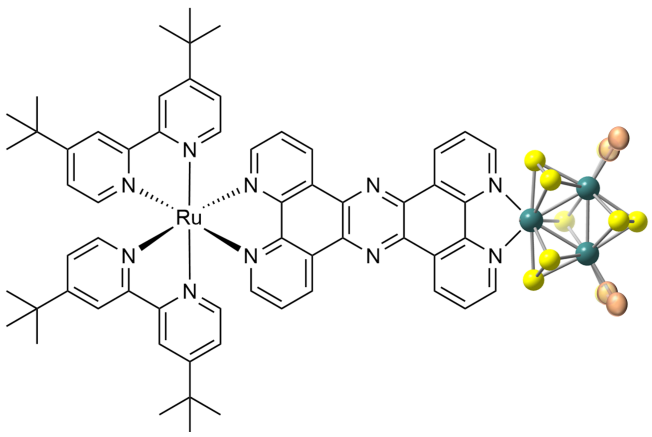


Figure 4.4 Proposed chemical structure of the PS-catalyst dyad obtained by the microwave-assisted reaction of $[Ru(tbbpy)_2(tpphz)]^{2+}$ with the $(TEA)_2[Mo_3S_7Br_6]$ cluster in MeCN. **Color scheme:** teal: Mo; yellow: sulfur atoms S of the respective S^{2-}/S_2^{2-} ligands, peach: Br atoms of the bromide ligands. The illustration of the $\{Mo_3\}$ part was cropped, adapted and reproduced under the terms of the CC BY 4.0 license.[147] Copyright 2023, The Authors, Advanced Materials published by Wiley-VCH GmbH.

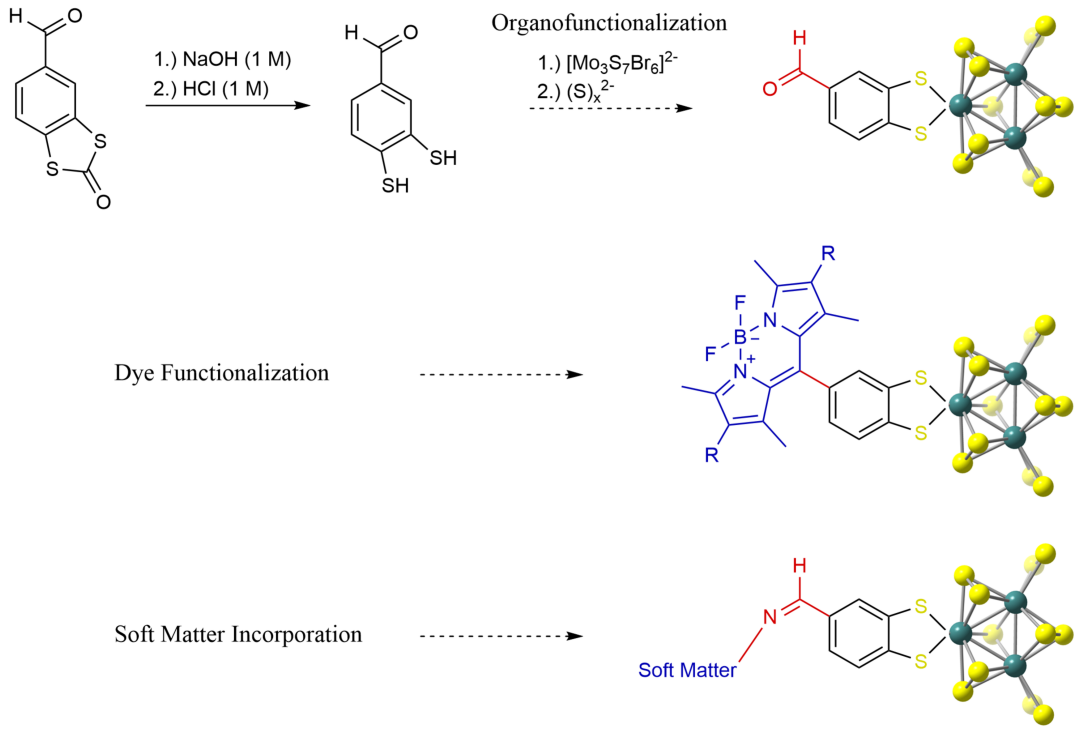


Figure 4.5 Schematic synthetic pathway for the organofunctionalization of the thiomolybdate cluster {Mo_3} using the proligand 3,4-dimercaptobenzaldehyde. The formyl group is accessible for various chemical post-modifications, such as the design of dyads (*e.g.* using BODIPY derivatives) or the incorporation of {Mo_3} into soft matter matrices through covalent interactions, *e.g.* using functional imine groups. **Color scheme:** teal: Mo; yellow: sulfur atoms S of the respective S^{2-}/S_2^{2-} ligands; blue: functional unit obtained by post-modification; red: formyl group or the structural bridge. The illustration of the {Mo_3} part was cropped, adapted and reproduced under the terms of the CC BY 4.0 license.[147] Copyright 2023, The Authors, Advanced Materials published by Wiley-VCH GmbH.

well as active sites in conjunction with their mechanistic processes, including the PCET mechanism and activation and deactivation pathways, as outlined in chapter 3.1.

Another promising proligand for the organofunctionalization of thiomolybdates is 3,4-dimercaptobenzaldehyde. The formyl group can undergo further modification to yield unimolecular photocatalytic dyads (*e.g.* using 4,4-difluoro-4-bora-3a,4a-diaza-*s*-indacene (BODIPY) dyes, *vide infra*) or to enable the covalent incorporation into soft matter matrices (see Figure 4.5).[448] Initial studies indicated a possible organofunctionalization of the thiomolybdate cluster, as evidenced by NMR and ATR-FTIR studies.

These results were published in part by [redacted] in his Master thesis in 2024. The thesis entitled "*Organic Functionalization of Thiomolybdate Clusters for HER-Catalysis*" was supervised by Marcel Langer.

Broadening the Scope of Photosystems

Apart from the HER activity of thiomolybdates and organofunctionalized derivatives, to the best of my knowledge, there are no reports in the literature on homogeneous light-driven H_2 production by oxothiomolybdates. However, electrocatalytic and theoretical studies have already suggested potential HER reactivity pathways.[312,400,449] Therefore, this auspicious class of compounds merits thorough exploration under photocatalytic conditions, accompanied by a performance comparison with $\{Mo_3\}$ and $\{Mo_2\}$ or other thiomolybdate analogs. This methodological approach will facilitate the determination of structural effects on the active sites and the underlying mechanisms, thus improving the understanding for the design of advanced HECs. The two prototype clusters depicted in Figure 1.28 serve as a good starting point for this investigation. Furthermore, it is known that the functionalization of oxothiomolybdates with bpy ligands leads to the formation of $[Mo_2O_2S_2I_2(bpy)_2]$, which could further broaden the scope of HER research to their possible covalent heterogenization on soft matter supports (*cf.* Figure 4.2).[450]

Molecular molybdenum sulfides could also be transformed into 1D-3D coordinative solid-state frameworks by bridging individual clusters with transition metal cations, such as Co^{II} or $Fe^{II/III}$, through the exchange of labile terminal S_2^{2-} ligands. The objective of this process is to develop well-defined heterogeneous materials with porous networks and high surface areas for light-driven HER. This approach holds great promise in broadening the understanding of MoS_x-based structure-reactivity relationships, enhancing the HER activity by providing a larger number of accessible active sites with tunable properties, impeding undesired side reactions or the formation of degradation products, promoting repair mechanisms, and establishing design principles that can be universally applied to the development of a novel class of “green” sustainable energy storage materials. This idea draws inspiration from the conversion of POMs into analog coordination networks as reported by the research group of A. M. Schimpf[451,452] (see Figure 4.6a) and from proof-of-principles studies on the linkage of thiomolybdate clusters *via* organic linkers leading to metal-organic sulfides (MOS) as developed by O. M. Yaghi and colleagues.[453] Initial attempts under similar synthesis conditions to POM linkage proved unsuccessful, as various thiomolybdate clusters and their derivatives underwent decomposition to MoS_2 particles, which was evidenced by PXRD analysis (see Figure 4.6b). Thus, further efforts are needed to thoroughly explore the potential of this new and interesting field of research.

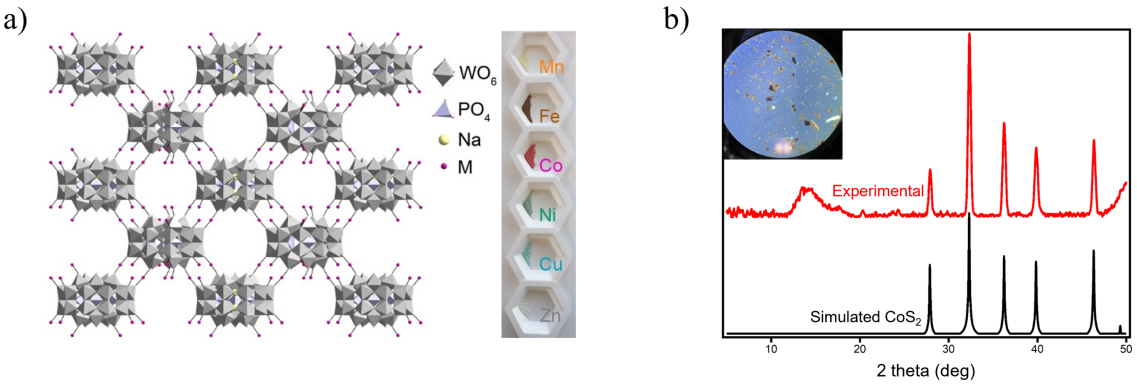


Figure 4.6 The notion of solid-state frameworks composed of molybdenum sulfides: **a)** Inspiring work by the Schimpf group, who prepared coordination networks of POMs bridged by a broad selection of metal cations. Reproduced with permission.[451] Copyright 2019, American Chemical Society. **b)** PXRD patterns of the crystals obtained by the aqueous hydrothermal reaction of {Mo_3} with Co^{2+} salt and simulated CoS_2. The inset photograph shows fine needles of the product resolved under the microscope.

In addition to the development of advanced WOC-active composites, the reactivity scope of heterogenized POMs on the presented soft matter matrices (see chapters 3.3 and 3.4) can also be extended to the catalytic photooxidation of alcohols to support studies on substrate and product selectivity. Depending on the intrinsic photoactivity of the POM, it can be used either as a catalyst and PS simultaneously or in combination with an external dye. The latter approach is based on the same principles of heterogenization and analogous reactivity mechanisms as shown for the visible light-driven WOC.[454] Initial studies were performed with the nanoporous block copolymer membranes described in the project {MLa-2} (see chapter 3.3), which were electrostatically functionalized with either the anionic vanadomolybdate oxidation catalyst $[PV_2Mo_{10}O_{40}]^{5-}$[455] or the aerobic oxidation catalyst $[Ba_4(dmso)_{14}V_{14}O_{38}(NO_3)]$[456] together with Ru-PS. However, no meaningful conversion rates were determined for 2-propanol, hydroxymethylfurfural and benzyl alcohol by ^{1}H-NMR, although the development of a distinct almond-like odor from benzaldehyde indicated catalytic reactivity. This discrepancy could therefore be attributed to the low sensitivity of the benchtop instrument. Interestingly, an intrinsic alcohol oxidation activity of Ru-PS was also detected, underscoring the necessity for further intensive studies to fully comprehend these initial findings.

The results of the heterogeneous alcohol oxidation were published in part by [redacted] in his Master thesis in 2022. The thesis entitled "*Polyoxometalate based copolymers visible light-driven alcohol oxidation: quality screening of reactivity for different substrates*" was supervised by Marcel Langer.

Explore "Green" Photosensitizers

In this work, the only PS used was the transition metal-based complex Ru-PS. The factors of low earth abundance, high costs and the tendency for photodissociation of the ligands under operating conditions (see chapter 6.5) call for increased research into suitable and sustainable PS alternatives for WOC or HER. Organic dyes with electron-poor or electron-rich structures are particularly promising photoactive materials that are generally regarded as "green".

A representative class of molecular organic PSs are rylene-based dyes, such as perylene monoimide (see Figure 4.7a). Their structures are readily accessible synthetically and can be easily modified to further adjust their electrochemical and photophysical properties. Specifically, the adjustment of the energy density to absorb visible light and the lifetime of the excited triplet states to increase the photostability enables their subsequent use as PS in light-driven reactions. Furthermore, the functionalization of these dyes with suitable anchors enables their processing into dyads or their integration into soft matter matrices using a range of intermolecular interactions. The ability to sensitize $\{Mo_3\}$ in light-driven HER has already been described in two independent studies. In the first report, the reagents were utilized under quasi-homogeneous conditions with the aid of a solubilizer. In contrast, the second work reports on the electrostatic deposition of the compounds on a hydrogel network. This approach circumvents the issue of limited solubility of the

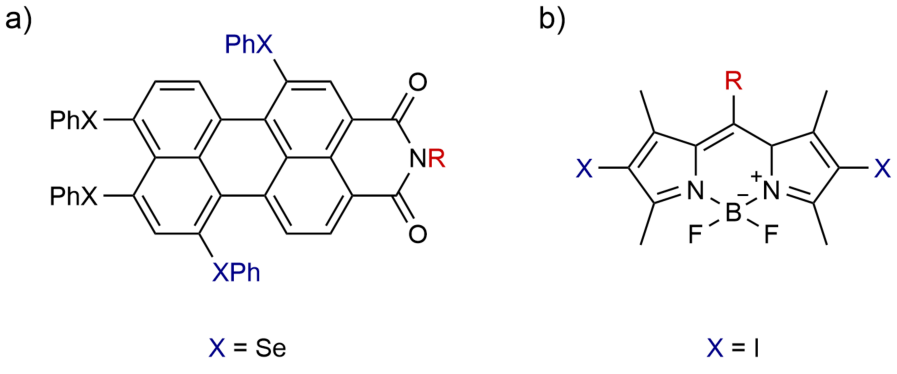


Figure 4.7 General chemical structures of various chromophores that are considered "green": **a)** Perylene monoimide. The π-system can be readily modified in the *bay* region (blue) to tailor its function as a PS in photocatalytic water splitting. Specifically, selenophenoxy substituents possess suitable absorption properties and have been shown to be advantageous in the generation of long-lived triplet states. The electrostatic bonding to soft matter matrices can be established by integrating suitable charged residues at the amide group, *e.g.* with R = carboxylate (red).[458] **b)** BODIPY, *e.g.* 2,6-diiodo-1,3,5,7-tetramethyl-BODIPY (blue). In this case, the electrostatic bonding to soft matter matrices is possible by altering the *meso* position of BODIPY with appropriate charged entities, *e.g.* R = aniline to introduce a positive charge or R = benzoic acid to accept an overall negative charge (red).[459]

catalyst and PS, ensures their optimal spatial proximity and facilitates the subsequent reuse of the photocatalytically active material. Both catalytic systems also demonstrate improved durability through a prolonged activity in HER studies.[457,458]

BODIPY derivatives (see Figure 4.7b) represent another class of earth-abundant PSs capable of driving photocatalytic reactions. A vast library of structural modifications enables precise regulation of relevant properties, resulting in long-lived, easily accessible triplet states and the ability to yield efficient electron transfer rates. These dyes can function as active PS in light-driven HER when deposited on soft matter matrices, thereby overcoming the challenges of hydrophobicity and rapid charge recombination.[459] A third green and sustainable dye that meets the criteria for participation in light-driven reactions, is Eosin Y.[175]

In contrast to the aforementioned studies, there is a paucity of literature regarding the use of these compounds in combination with {Co_4} for photocatalytic WOC. Therefore, a selection of electron-rich perylene-based dyes was examined under homogeneous conditions. However, the initial investigations did not reveal significant OER rates, suggesting that further efforts are needed in the development of these PS species and the tailoring of their physicochemical properties to enable efficient charge transfer in WOC.

The results of the studies on perylene-based PSs were published in part by [redacted] in her Bachelor thesis in 2022. The thesis entitled "*Metal-containing vs. metal-free photosensitizer (PS) and their application as molecular chromophores in homogeneous light-driven water oxidation catalysis (WOC)*" was supervised by Marcel Langer.

Advanced *in situ* and *operando* Analyses

As cautiously elaborated in the two literature-based studies {MLa-1} and {MLa-4}, a comprehensive understanding of the catalytic mechanisms and a thorough grasp of the interactions between PS, catalyst and sacrificial agent can only be obtained by combining a wide range of complementary investigative methods to study photochemical systems. In particular, vibrational spectroscopy (*i.e.* IR and Raman) could be increasingly used, as these methods are sensitive to characteristic spectral features of the molecular compounds. In addition to the *ex situ* application of techniques, their extensive use *in situ*

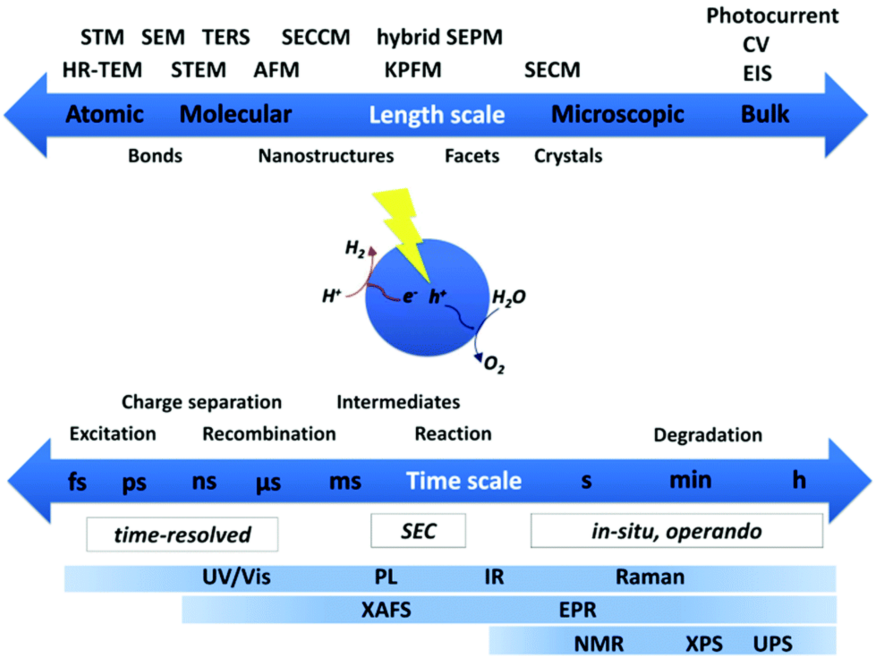


Figure 4.8 Advanced analytical techniques commonly used to characterize molecular species: Insights into material properties at various length scales ranging from the bulk to the atomic level can be obtained and correlated with data recorded for processes with timescales ranging from hours to the femtosecond regime to assess the overall light-driven catalytic activity. Reproduced under the terms of the CC BY 3.0 license.[335] Copyright 2021, The Royal Society of Chemistry.

or *operando* is proposed to unravel deactivation pathways in light-driven WOC, HER or alcohol oxidation and to more easily identify active sites of the respective molecular catalysts. Furthermore, structural information can be derived from these real-life data sets, including the molecular integrity, stability and activity of PS and catalyst upon heterogenization on multifunctional supports, as well as before, during and after light-driven catalysis. The employment of spatially and time-resolved spectroscopic, spectro-electrochemical and electrochemical methods is advantageous in the acquisition of fundamental knowledge regarding the intricate interplay occurring on multiple length- and timescales. This encompasses light absorption, charge separation, electron and energy transfer processes to the catalytic centers and their reactivity mechanisms (see Figure 4.8).[335] The use of an array of analytical tools was exemplarily demonstrated in our multimodal analysis of WOCbranes in the project {MLa-2} to ascertain a homogeneous distribution of active compounds. The interpretative results obtained were unequivocally validated and verified. Moreover, fundamental limitations, such as inaccessibility of active sites, poor light penetration and limited mass transport, could be concluded from these results (see chapter 3.3).

Experimental Design

A more profound comprehension of structure-function relationships can also be attained through theoretical simulations that assist the interpretation of experimental observations, as well as through the systematic approach of statistical DOE studies, which reduces the experimental effort and increases the quality of information. Therefore, DOE emerges as a valuable instrument for optimizing a multitude of critical performance parameters, including reactant type and concentration, pH ranges, pressure, ionic strength, solvent type, light frequencies and intensities, temperature, stirring speed, and flow rate, among others.[460,461] It should be noted that achieving quantitative comparability and reliable, reproducible and unbiased results is contingent upon the implementation of discrete performance indicators under defined conditions. The integration of chemical engineering principles in the execution of *in situ* and *operando* studies can essentially support this process.[187]

Smart Reactor Design

The polyampholyte hydrogels in {MLa-5} and the nanoporous block copolymers in {MLa-2} exhibited gas entrapment within their pores, which was attributed to the "delayed" release of bubbles subsequent to light-driven catalysis. Additionally, diffusion limitations for the reactive molecular species were observed due to ion pairing between PS and catalyst. This hinders the full potential of the catalytic activity from being examined. The optimization of these micro- and macroscopic mass transport effects can be achieved through the intuitive, customized design of suitable photoreactors using flow conditions. This approach can also enhance the loading of the components within the internal pores of the soft matter matrices, exceeding the loading capabilities of conventional immobilization strategies.

The interplay between mass transport and reaction rate is also influenced by the flow rate and light intensity. However, an excess of photons and the presence of overly concentrated species can have a detrimental effect on the overall catalytic performance by promoting competing side reactions, such as the oxidative degradation of Ru-PS (see Figure 1.19). This effect was recently confirmed by Ziegenbalg, Rau and colleagues,[440] who demonstrated a significant influence of dynamic *vs.* pulsed irradiation by correlating

reduced external energy with lower concentrations of excited PS* species in solutions. This observation led to a notable improvement in the TONs of a known three-component WOC system, as evidenced by a substantial reduction in oxidized PS accumulations. In addition, our initial studies in collaboration with the [redacted] group at Ulm University on the response of the benchmark system for WOC consisting of {Co_4} and Ru-PS under homogeneous conditions to dynamic irradiation confirmed the design of an energy-saving system with pulsed irradiation, as only 25% photons are needed after 12 h to achieve comparable TONs to static irradiation. These results imply that precise control over the spatiotemporal photon availability and the overall radiation field is essential for the lifetime of a photocatalytic system. Moreover, synchronization of mass transport with the timescales of the photoreaction is crucial to enhance photon delivery to the bulk, to avert the initiation of PS degradation and to improve the photocatalytic efficiency.

Furthermore, we observed strong variations in temperature and pressure during *operando* O_2 quantification depending on the time of day, indicating a strong influence of ambient conditions on the photocatalytic performance. These results imply that the integration of a tempered system and the development of advanced photoreactors are inevitable compared to the original relatively simple, customized reactors used for activity studies of hydrogel-incorporated HECs and OECs in project {MLa-5} (see chapter 6.4) and the light-driven OER studies of Ru-PS in organic media in project {MLa-6} (see chapter 6.5). The corresponding design must take into account a number of physical and chemical requirements, such as solvent resistance, a closed system with a limited number of reflections prior to reaching the reaction vessel to ensure efficient monochromatic irradiation and avoid any light scattering, enhanced heat transfer to maintain a constant reaction temperature, precise adjustment of light intensity, frequency and wavelength by switchable LEDs with variable radiant power, the possibility to study a variety of experimental parameters, *etc.* Hence, the use of 3D-printed photoreactors, which are both modular and customizable, as well as expandable, as published by our colleagues, is projected to guarantee reproducible and comparable data sets in the future. This assertion is substantiated by the experiments with the {Mo_3} HER photosystem.[462]

Another field of study that has been previously underestimated but is experiencing rapid growth in chemistry is artificial intelligence. For instance, the multidisciplinary efforts to design functional materials outlined in this work can be adapted to the proliferation of

machine learning to leverage the profound system-based knowledge generated for straightforward and expeditious advancements.[463]

Summary of the Perspectives

In summary, a series of catalytically applicable prototype systems can be developed to investigate how the physicochemical properties and reactivity of the selected molecular catalysts and PSs change when they are integrated into soft matter matrices. In addition, comprehending the role of the matrix in the stability and the degradation of the molecular components can be used to develop advanced materials for HER and WOC. The study of metal-free compounds is particularly desirable. Nonetheless, careful examination of various reaction parameters (*e.g.* pH, solvent composition, light, *etc.*) is always required to determine the critical effects on matrix and component stability, to understand molecule-in-matrix reactivity and to optimize the individual catalytic systems. In particular, complementary *in situ* and *operando* methods are favored to evaluate the intrinsic kinetics and thermodynamics of the composites under operating conditions and to elucidate the mechanisms of HER and WOC at the molecular level. The employment of smart reactor designs is instrumental in circumventing additional limitations in mass transport, a pivotal aspect in attaining efficiency and productivity benchmarks, which are indispensable for the commercialization of these materials. As discussed in the following chapter 4.1, meticulous analysis and blank studies are always required for each set of reaction conditions, especially when Ru-PS is used as the PS to drive photocatalysis.

4.1 Photodegradation of $[Ru(bpy_3)]^{2+}$ in Organic Solvents – {MLa-6}

The photophysical properties of Ru-PS and its ability to undergo both oxidative and reductive photoredox reactions were described in detail in chapter 1.5. The molecular metal complex is therefore often used as a PS in light-driven reactions, such as HER and OER, in both aqueous[300,464] and non-aqueous media,[219,298] as the solubility is regulated by the counter anion.[465,466] However, the PS is not innocent and shows intrinsic WOC activity in the presence of the SOA $S_2O_8^{2-}$ under aqueous conditions. In this context, Yoon and colleagues described two divergent fast, photoinduced decomposition pathways depending on the initial PS concentration. At low PS concentration, the well-known "blue dimer" is formed (see the chemical structure shown in Figure 4.10), which is active for WOC in its fully oxidized state. Conversely, at high PS concentration, the formation of catalytically inactive Ru μ-oxo oligomers is observed.[439]

In this project, we applied the research approach of Yoon and co-workers to a solvent mixture with a predominant organic composition and performed catalytic and mechanistic studies using *operando* O_2 quantification and *operando* UV-Vis to investigate the photostability of $[Ru(bpy)_3](PF_6)_2$ in the presence of $S_2O_8^{2-}$.[467]

Figure 4.9a illustrates the experimental setup for the light-driven OER, which consists of a reaction vessel equipped with O_2-sensitive sensors for the solution and the gas phase. The vessel is placed in a customized air-cooled photoreactor and is illuminated with a blue LED. The necessity of PS, SOA and photons as well as the integrity of an inert-atmosphere setup was verified by adequate reference measurements. Figure 4.9b shows a representative OER profile of the prototype system, wherein the use of a known water oxidation catalyst was deliberately omitted, along with the applied reaction conditions.

The total O_2 evolution of 24.1 ± 1.9 μmol with a durability of about 3-4 h provides a clear evidence for the OER activity of this specific photosystem. The stoichiometric equivalence between the two-electron acceptor $S_2O_8^{2-}$ and the four-electron donor H_2O was confirmed, indicating that the sustained OER activity is limited by the complete consumption of the SOA. In addition, the rapid degradation of PS and the formation of various intermediates are indicated by the optical color changes over time (see inset photographs in Figure 4.9b), which are not observed in the absence of $S_2O_8^{2-}$. In consideration of these observations, which imply an unequivocal link between SOA and

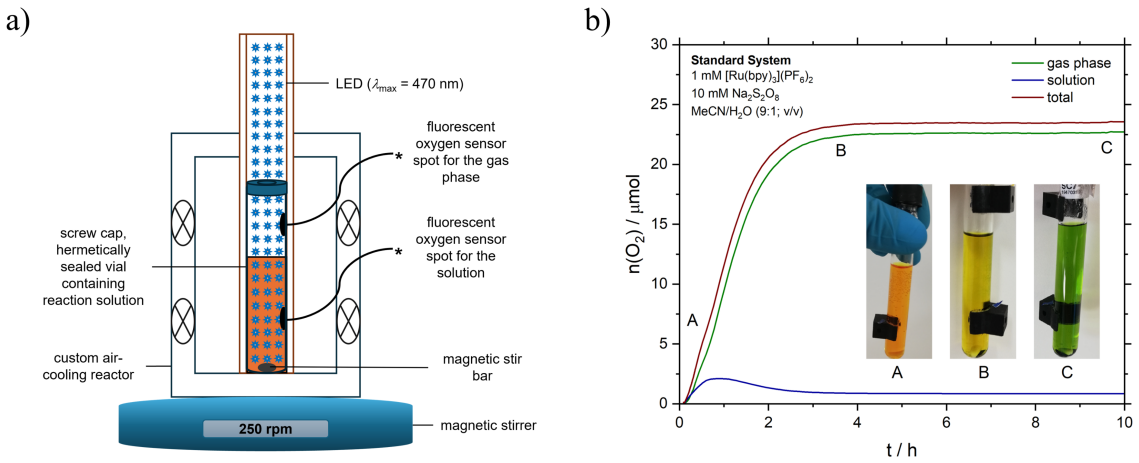


Figure 4.9 Light-driven OER studies: **a)** Schematic representation of the experimental setup employed, illustrating the simultaneous *in operando* O_2 quantification in solution and in the gas phase *via* fiber-optic fluorescent O_2 sensor spots detached in the inner wall of the reaction vessel, which is placed in a custom-built air-cooled photoreactor. **b)** Light-driven O_2 evolution profile in the gas phase (green curve), in solution (blue curve) and in total (red curve) of the investigated OER system. Conditions: 1 mM $[Ru(bpy)_3](PF_6)_2$, 10 mM $Na_2S_2O_8$, MeCN:H_2O (9:1; v/v), LED with $\lambda = 470$ nm and power density of *ca.* 50 mW cm^{-2}. The inset photographs show the pre- and post-catalytic reaction solutions as a function of reaction time: (A) intense orange ($t = 0$ h), (B) yellow ($t \approx$ 3-10 h) and (C) green, often accompanied by an oily deposit ($t \geq 10$ h). Adapted and reproduced under the terms of the CC BY 3.0 license.[467] Copyright 2025, The Royal Society of Chemistry.

the photochemical process, we propose two possible mechanisms: either a persulfate-dependent oxidation of the PS to a Ru^{3+} species[468] or an (oxidative) PS degradation promoted by $S_2O_8^{2-}$ and sulfate radical anions.[226] In both cases, the active OER species are formed from the precursor Ru-PS in organic media.

We monitored the fate of Ru-PS under catalytic and diluted conditions upon irradiation by tracking the changes in the relevant absorption characteristics *via operando* UV-Vis studies. The expected immediate oxidation of $[Ru(bpy)_3]^{2+}$ to $[Ru(bpy)_3]^{3+}$ was witnessed directly at the beginning. The subsequent formation of two additional species can be postulated, as the absorption spectrum underwent changes within a timescale of *ca.* 30-45 min and again after approx. 3 h, which can be attributed to the formation of blue dimer-type species with different oxidation states of the Ru centers. In correlation with other experimental results, these spectroscopic changes can alternatively be assigned to the rapid accumulation of oxidized PS, its slow consumption by the formation of the catalytically active species and, at a certain point in catalysis, its reduction back to a Ru^{II} species by the present catalyst, provided that sufficient catalyst has formed and no further accumulation of Ru^{III} occurs.

The UV-Vis spectrum of the separated green oily deposit obtained after long-term OER supports the formation of two related Ru μ-oxo dimer structures that differ only in the oxidation states of the metal centers, namely the orange Ru_2(III,IV) dimer and the blue Ru_2(III,III) dimer (see Figure 4.10). For this reason, a similar photodegradation pathway of Ru-PS in the presence of $S_2O_8^{2-}$ can be postulated under both aqueous and non-aqueous conditions. The OER reactivity correlates in the initial catalytic phase with the formation of WOC-active Ru μ-oxo dimers at low concentrations. However, inactive Ru μ-oxo species, such as the oligomers described by Yoon and colleagues, might become dominant with the preceding reaction, leading to a decrease in O_2 evolution. Therefore, a complex interplay between Ru-based active and inactive species is likely.

We also found that the solvent MeCN plays a crucial role, as its replacement by DMF or acetone led to the loss of OER activity. Even a lower proportion of MeCN in the mixture with H_2O significantly reduced O_2 production. Thus, PS degradation and its conversion to the catalytically active species are critically affected by the polar, protic solvent MeCN, which is underpinned by ligand exchange mechanisms from bpy to MeCN induced by light or the oxidation of the Ru center, as reported in the literature for Ru bipyridyl-based PSs.[223,224,469] Further catalytic and mechanistic studies in the presence of an excess of

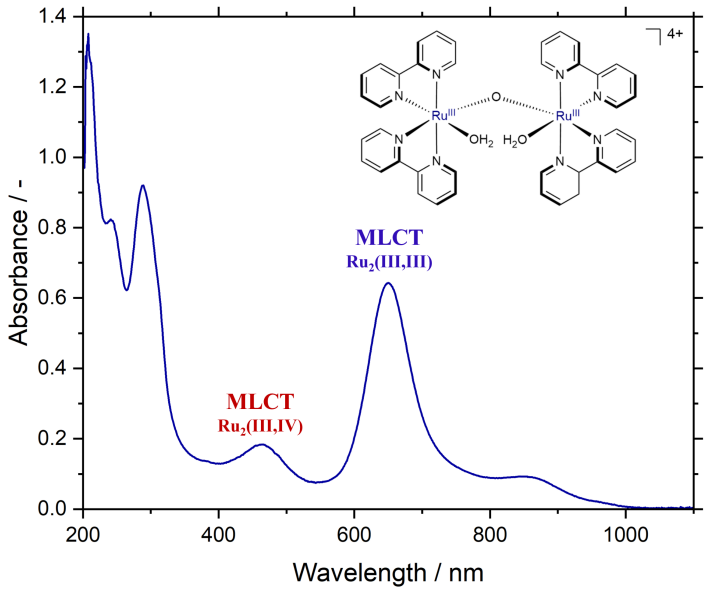


Figure 4.10 UV-Vis spectrum of the isolated green oily deposit obtained after a typical light-driven OER under prototype conditions. The electronic transitions at 464 nm and 650 nm indicate the simultaneous formation of orange Ru_2(III,IV) and blue Ru_2(III,III) dimers.[439] The inset chemical structure represents the blue dimer. Further electronic transitions can be observed at 208 nm and 288 nm (LC, $\pi\pi^*_{bpy}$), 242 nm (MLCT) and two shoulders at 383 nm and 854 nm (dπdπ). Adapted and reproduced under the terms of the CC BY 3.0 license.[467] Copyright 2025, The Royal Society of Chemistry.

free bpy ligand support the necessity to lose a bpy ligand for PS degradation and its ensuing conversion to the active species, as diminished OER activity was observed. In light of these observations and in consideration of literature reports, we postulated a plausible reaction scheme, as shown in Figure 4.11.

The study was concluded with the question of whether the type of ligand has an impact on the photodegradation of the PS and whether the findings can also be transferred to other structurally related Ru polypyridyl-based PSs. Therefore, we investigated the five Ru-based PSs shown in Figure 4.12. Despite the presence of comparable reactivity patterns, the significant disparities in the maximum light-driven OER rates suggest that the use of heteroleptic PSs can effectively hinder the *in situ* formation of an active OEC, such as a Ru-dimer. This is likely attributable to the suppression or prevention of polypyridyl ligand exchange.

In summary, the present project yielded critical information and mechanistic insights into the most widely used PS in photochemistry. An effective strategy was presented to

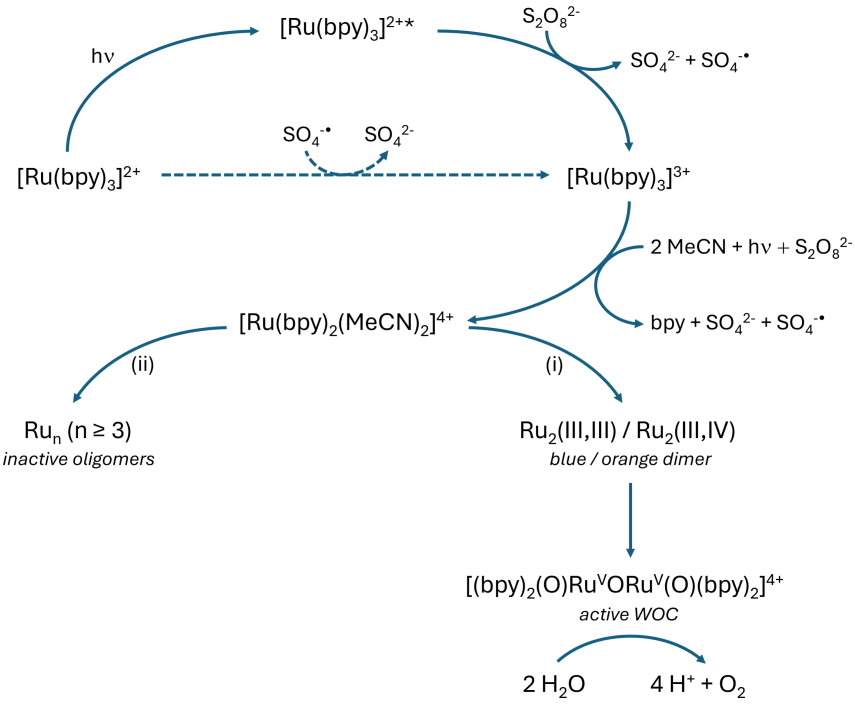


Figure 4.11 Postulated reaction scheme for the formation of the active OEC of the blue dimer type using Ru-PS in non-aqueous MeCN solution and in the presence of $S_2O_8^{2-}$. (i) Further oxidation to OER-active dimers by $[Ru(bpy)_3]^{3+}$ or $S_2O_8^{2-}$ in the presence of a minor PS^{3+} concentration. (ii) Formation of OER-inactive Ru μ-oxo oligomers when the PS^{3+} concentration is increased. The stoichiometry has been omitted for the sake of clarity and the water ligand could also be substituted by other ions in the solution, *e.g.* sulfate, to form dimer derivatives. Adapted and modified from references.[224,439] Reproduced under the terms of the CC BY 3.0 license.[467] Copyright 2025, The Royal Society of Chemistry.

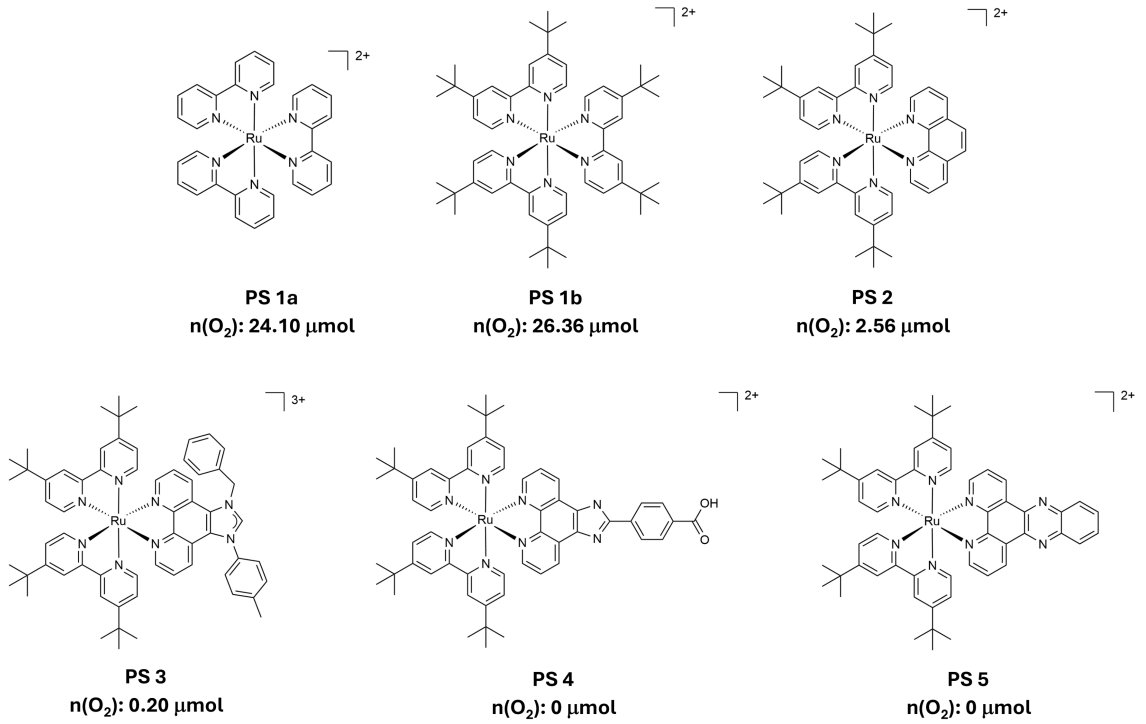


Figure 4.12 Various structurally related Ru polypyridyl PSs and their maximum OER photoreactivity: PS1a: $[Ru(bpy)_3](PF_6)_2$; PS1b: $[Ru(tbbpy)_3](PF_6)_2$; PS2: $[Ru(tbbpy)_2(phen)](PF_6)_2$; PS3: $[Ru(tbbpy)_2(p\text{-tolbip})](PF_6)_3$; PS4: $[Ru(tbbpy)_2(ipphCOOH)](PF_6)_2$ and PS5: $[Ru(tbbpy)_2(dppz)](PF_6)_2$. Abbreviations: tbbpy = 4,4'-di-*tert*-butyl-2,2'-bipyridine; phen = 1,10-phenanthroline; *p*-tolbip = 1-(4-methylphenyl)-3-benzyl-1*H*-imdazo[4,5-*f*][1,10]-phenanthroline; ipphCOOH = 4-(1*H*-imidazo[4,5-*f*][1,10]-phenanthroline -2-yl)benzoic acid; dppz = dipyrido[3,2-*a*:2',3'-*c*] phenazine. Reproduced under the terms of the CC BY 3.0 license.[467] Copyright 2025, The Royal Society of Chemistry.

prevent the light-induced oxidative conversion of Ru-PS in the presence of $S_2O_8^{2-}$ and MeCN to OER-active blue dimer analogs, which occurs notably faster in the organic solvent than under purely aqueous conditions. These results clearly emphasize that careful analysis and blank studies are always essential for the evaluation of new photosystems.

These results were published in "*In situ formation of an active oxygen evolution catalyst via photodegradation of* $[Ru(bpy)_3]^{2+}$", Marcel Langer, Alexander K. Mengele, Riccarda Müller, Julius C. Wetzel, Judith Mayer, Sven Rau,* and Carsten Streb,* *Dalton Trans.* **2025**, *54*, 4861–4865.

For more detailed information, see chapter 6.5.

5. References

[1] A. Sturma, V. Ritschl, S. Dennhardt, T. Stamm, in *Wissenschaftliches Arbeiten und Schreiben* (Eds.: V. Ritschl, R. Weigl, T. Stamm), Springer-Verlag, Berlin, Heidelberg, **2023**, pp. 207–222.

[2] R. W. Palmatier, M. B. Houston, J. Hulland, *J. Acad. Mark. Sci.* **2018**, *46*, 1–5.

[3] P. J. Megía, A. J. Vizcaíno, J. A. Calles, A. Carrero, *Energy Fuels* **2021**, *35*, 16403–16415.

[4] J. L. Holechek, H. M. E. Geli, M. N. Sawalhah, R. Valdez, *Sustainability* **2022**, *14*, 4792.

[5] Energy Institute, *Statistical Review of World Energy*, **2024**.

[6] G. Mutezo, J. Mulopo, *Renew. Sustain. Energy Rev.* **2021**, *137*, 110609.

[7] S. H. Mohr, J. Wang, G. Ellem, J. Ward, D. Giurco, *Fuel* **2015**, *141*, 120–135.

[8] D. Pivetta, G. Volpato, G. Carraro, C. Dall'Armi, L. Da Lio, A. Lazzaretto, R. Taccani, *Int. J. Hydrogen Energy* **2024**, *52*, 1084–1103.

[9] H. Hou, W. Lu, B. Liu, Z. Hassanein, H. Mahmood, S. Khalid, *Sustainability* **2023**, *15*, 2048.

[10] A. G. Olabi, M. A. Abdelkareem, *Renew. Sustain. Energy Rev.* **2022**, *158*, 112111.

[11] K. Franke, J. F. Garcia, C. Kleinschmitt, F. Sensfuß, *Renew. Energy* **2024**, *226*, 120376.

[12] M. Höök, X. Tang, *Energy Policy* **2013**, *52*, 797–809.

[13] N. Chayaamor-Heil, N. Hannachi-Belkadi, *Buildings* **2017**, *7*, 19.

[14] J. Cifuentes-Faura, *Air Qual. Atmos. Health* **2022**, *15*, 1333–1340.

[15] H. Heubaum, F. Biermann, *Energy Policy* **2015**, *87*, 229–239.

[16] F. Johnsson, J. Kjärstad, J. Rootzén, *Clim. Policy* **2019**, *19*, 258–274.

[17] I. Dincer, C. Acar, *Int. J. Energy Res.* **2015**, *39*, 585–606.

[18] A. K. Worku, D. W. Ayele, D. B. Deepak, A. Y. Gebreyohannes, S. D. Agegnehu, M. L. Kolhe, *Adv. Energy Sustainability Res.* **2024**, *5*, 2300273.

[19] Saul Griffith, in *Speciesism in Biology and Culture: How Human Exceptionalism is Pushing Planetary Boundaries* (Eds.: B. Swartz, B. D. Mishler), Springer, Cham, **2022**, pp. 181–203.

[20] Q. Hassan, P. Viktor, T. J. Al-Musawi, B. Mahmood Ali, S. Algburi, H. M. Alzoubi, A. Khudhair Al-Jiboory, A. Zuhair Sameen, H. M. Salman, M. Jaszczur, *Renew. Energy Focus* **2024**, *48*, 100545.

[21] P. Moriarty, D. Honnery, *Energy Policy* **2016**, *93*, 3–7.

[22] E. T. Sayed, A. G. Olabi, A. H. Alami, A. Radwan, A. Mdallal, A. Rezk, M. A.

Abdelkareem, *Energies* **2023**, *16*, 1415.

[23] A. S. Sánchez, E. P. Junior, B. M. Gontijo, P. de Jong, I. B. dos Reis Nogueira, *Renew. Sustain. Energy Rev.* **2023**, *183*, 113527.

[24] F. Alasali, M. I. Abuashour, W. Hammad, D. Almomani, A. M. Obeidat, W. Holderbaum, *Energy Sci. Eng.* **2024**, *12*, 1934–1968.

[25] I. Rolo, V. A. F. Costa, F. P. Brito, *Energies* **2024**, *17*, 180.

[26] H. Ellison, in *Energy for a Sustainable World: From the Oil Age to a Sun-Powered Future* (Eds.: N. Armaroli, V. Balzani), Wiley-VCH Verlag, Weinheim, **2011**, pp. 279–299.

[27] S.-Y. Ahn, K.-J. Kim, B.-J. Kim, G.-R. Hong, W.-J. Jang, J. W. Bae, Y.-K. Park, B.-H. Jeon, H.-S. Roh, *Renew. Sustain. Energy Rev.* **2023**, *186*, 113635.

[28] M. Gopinath, R. Marimuthu, *Int. J. Hydrogen Energy* **2022**, *47*, 37742–37759.

[29] H. Balat, E. Kirtay, *Int. J. Hydrogen Energy* **2010**, *35*, 7416–7426.

[30] S. Imran, M. Hussain, *Int. J. Hydrogen Energy* **2024**, *77*, 975–996.

[31] J. T. Tran, K. J. Warren, S. A. Wilson, C. L. Muhich, C. B. Musgrave, A. W. Weimer, *WIREs Energy Environ.* **2024**, *13*, e528.

[32] F. Qureshi, M. Tahir, *Int. J. Hydrogen Energy* **2024**, *69*, 760–776.

[33] P. Zhou, I. A. Navid, Y. Ma, Y. Xiao, P. Wang, Z. Ye, B. Zhou, K. Sun, Z. Mi, *Nature* **2023**, *613*, 66–70.

[34] K. Villa, J. R. Galán-Mascarós, N. López, E. Palomares, *Sustain. Energy Fuels* **2021**, *5*, 4560–4569.

[35] Z.-Y. Yu, Y. Duan, X.-Y. Feng, X. Yu, M.-R. Gao, S.-H. Yu, *Adv. Mater.* **2021**, *33*, 2007100.

[36] N. Abas, A. Kalair, N. Khan, *Futures* **2015**, *69*, 31–49.

[37] R. Vezzoni, *Environ. Innov. Soc. Transit.* **2024**, *50*, 100817.

[38] R. Singh, M. Singh, S. Gautam, *Mater. Today Proc.* **2021**, *46*, 5420–5427.

[39] M. M. Aba, I. L. Sauer, N. B. Amado, *Int. J. Hydrogen Energy* **2024**, *57*, 660–678.

[40] L. Zhang, C. Jia, F. Bai, W. Wang, S. An, K. Zhao, Z. Li, J. Li, H. Sun, *Fuel* **2024**, *355*, 129455.

[41] K. Glinel, P. Thebault, V. Humblot, C. M. Pradier, T. Jouenne, *Acta Biomater.* **2012**, *8*, 1670–1684.

[42] C. Dooley, D. Taylor, *Fatigue Fract. Eng. Mater. Struct.* **2017**, *40*, 655–669.

[43] M. C. Fernandes, J. Aizenberg, J. C. Weaver, K. Bertoldi, *Nat. Mater.* **2021**, *20*, 237–241.

[44] B. Wijerathne, T. Liao, K. K. Ostrikov, Z. Sun, *Small Struct.* **2022**, *3*, 2100228.

[45] A. Tripathy, Md. J. Nine, D. Losic, F. S. Silva, *Mater. Sci. Eng. R* **2021**, *146*,

100647.

[46] S. Metwally, S. M. Comesaña, M. Zarzyka, P. K. Szewczyk, J. E. Karbowniczek, U. Stachewicz, *Acta Biomater.* **2019**, *91*, 270–283.

[47] M. K. Ahamed, H. Wang, P. J. Hazell, *Constr. Build. Mater.* **2022**, *320*, 126195.

[48] B. Bhushan, *Philos. Trans. R. Soc. A* **2009**, *367*, 1445–1486.

[49] H.-T. Feng, J. W. Y. Lam, B. Z. Tang, *Coord. Chem. Rev.* **2020**, *406*, 213142.

[50] L. A. Estroff, *Chem. Rev.* **2008**, *108*, 4329–4331.

[51] R. P. Allan, M. Barlow, M. P. Byrne, A. Cherchi, H. Douville, H. J. Fowler, T. Y. Gan, A. G. Pendergrass, D. Rosenfeld, A. L. S. Swann, L. J. Wilcox, O. Zolina, *Ann. N. Y. Acad. Sci.* **2020**, *1472*, 49–75.

[52] H. Lin, *Soil Sci. Soc. Am. J.* **2011**, *75*, 2049–2070.

[53] J. Barber, *Nat. Plants* **2017**, *3*, 17041.

[54] K.-Z. Ivanić, Z. Tadić, M. A. Omazić, *Holist. Approach Environ.* **2015**, *5*, 19–36.

[55] N. K. Katiyar, G. Goel, S. Hawi, S. Goel, *NPG Asia Mater.* **2021**, *13*, 1–16.

[56] S. L. T. McGregor, *Transdiscipl. J. Eng. Sci.* **2013**, *4*, 57–65.

[57] P. E. Fayemi, K. Wanieck, C. Zollfrank, N. Maranzana, A. Aoussat, *Bioinspir. Biomim.* **2017**, *12*, 011002.

[58] H. Dicks, *Philos. Technol.* **2016**, *29*, 223–243.

[59] M. Chaurasia, S. Srivastava, *Int. J. Eng. Appl. Sci. Technol.* **2020**, *4*, 545–549.

[60] A. Lebdioui, *Ecol. Econ.* **2022**, *202*, 107585.

[61] S. P. Sane, *J. Appl. Sci. Eng.* **2016**, *19*, 1–6.

[62] R. Ren, *J. Educ. Humanit. Soc. Sci.* **2023**, *21*, 18–25.

[63] D. Vokoun, P. Sedlák, M. Frost, J. Pilch, D. Majtás, P. Šittner, *Smart Mater. Struct.* **2011**, *20*, 085027.

[64] E. Jamei, Z. Vrcelj, *Appl. Sci.* **2021**, *11*, 7514.

[65] C.-M. Yang, J.-Y. Hung, Y.-L. Wang, Y.-H. Lien, *Int. J. Innov. Manag.* **2019**, *7*, 49–56.

[66] E. Islas-García, M. Ceccarelli, R. Tapia-Herrera, C. R. Torres-SanMiguel, *Biomimetics* **2021**, *6*, 17.

[67] L. Feng, F. Wang, H. Luo, B. Qiu, *Dyes Pigment.* **2023**, *210*, 111019.

[68] S. Tomita, S. Ishihara, R. Kurita, *ACS Appl. Mater. Interfaces* **2019**, *11*, 6751–6758.

[69] T.-J. Huang, *Int. J. Autom. Comput.* **2017**, *14*, 520–531.

[70] T. G. Kim, H. Shin, D. W. Lim, *Adv. Funct. Mater.* **2012**, *22*, 2446–2468.

[71] V. Perricone, T. B. Grun, F. Marmo, C. Langella, M. D. Candia Carnevali, *Bioinspir. Biomim.* **2021**, *16*, 011001.

[72] Y. Gu, W. Zhang, J. Mou, S. Zheng, L. Jiang, Z. Sun, E. Wang, *Adv. Mech. Eng.* **2017**, *9*, 1–13.

[73] I. Y. Miranda-Valdez, T. Mäkinen, X. Hu, J. Lejon, M. Elamir, L. Viitanen, L. Jannuzzi, J. Koivisto, M. J. Alava, *Adv. Eng. Mater.* **2024**, 2400233.

[74] J. Navarro-Alapont, C. Negro, S. Navalón, A. Dhakshinamoorthy, D. Armentano, J. Ferrando-Soria, E. Pardo, *Inorg. Chem.* **2024**, *63*, 13681–13688.

[75] H. Wang, Y. Yang, L. Guo, *Adv. Energy Mater.* **2017**, *7*, 1601709.

[76] M. K. Islam, P. J. Hazell, J. P. Escobedo, H. Wang, *Mater. Des.* **2021**, *205*, 109730.

[77] N. Shedroff, in *Design Is the Problem: The Future of Design Must Be Sustainable* (Ed.: M. Justak), Rosenfeld Media, Brooklyn, New York, **2009**, pp. 109–120.

[78] L. Stevens, H. Kopnina, K. Mulder, M. De Vries, *Int. J. Technol. Des. Educ.* **2021**, *31*, 797–814.

[79] N. Verbrugghe, E. Rubinacci, A. Z. Khan, *Biomimetics* **2023**, *8*, 107.

[80] M. C. Austin, D. Garzola, N. Delgado, J. U. Jiménez, D. Mora, *Biomimetics* **2020**, *5*, 40.

[81] M. Helms, S. S. Vattam, A. K. Goel, *Des. Stud.* **2009**, *30*, 606–622.

[82] R. M. A. El-Zeiny, *Procedia - Soc. Behav. Sci.* **2012**, *50*, 502–512.

[83] T. J. Meyer, *Acc. Chem. Res.* **1989**, *22*, 163–170.

[84] O. Bičáková, P. Straka, *Int. J. Hydrogen Energy* **2012**, *37*, 11563–11578.

[85] J. Barber, P. D. Tran, *J. R. Soc. Interface* **2013**, *10*, 20120984.

[86] H. Wägele, O. Deusch, K. Händeler, R. Martin, V. Schmitt, G. Christa, B. Pinzger, S. B. Gould, T. Dagan, A. Klussmann-Kolb, W. Martin, *Mol. Biol. Evol.* **2011**, *28*, 699–706.

[87] J. M. Berg, J. L. Tymoczko, Gregory J. Gatto jr., L. Stryer, *Stryer Biochemie*, Springer Spektrum, Berlin, Heidelberg, **2013**.

[88] B. König, *Chemical Photocatalysis*, De Gruyter, Berlin, Boston, **2020**.

[89] M. Hervás, J. A. Navarro, M. A. De La Rosa, *Acc. Chem. Res.* **2003**, *36*, 798–805.

[90] M. P. Johnson, *Essays Biochem.* **2016**, *60*, 255–273.

[91] D. M. Arias-Rotondo, J. K. McCusker, *Chem. Soc. Rev.* **2016**, *45*, 5803–5820.

[92] M. E. El-Khouly, E. El-Mohsnawy, S. Fukuzumi, *J. Photochem. Photobiol. C: Photochem. Rev.* **2017**, *31*, 36–83.

[93] W. Lubitz, E. J. Reijerse, J. Messinger, *Energy Environ. Sci.* **2008**, *1*, 15–31.

[94] J. P. McEvoy, G. W. Brudvig, *Chem. Rev.* **2006**, *106*, 4455–4483.

[95] E.-M. Aro, I. Virgin, B. Andersson, *Biochim. Biophys. Acta* **1993**, *1143*, 113–134.

[96] J. Barber, *Chem. Soc. Rev.* **2009**, *38*, 185–196.

[97] J. P. Dekker, E. J. Boekema, *Biochim. Biophys. Acta* **2005**, *1706*, 12–39.

[98] A. Rast, S. Heinz, J. Nickelsen, *Biochim. Biophys. Acta* **2015**, *1847*, 821–830.

[99] Y. Umena, K. Kawakami, J.-R. Shen, N. Kamiya, *Nature* **2011**, *473*, 55–60.

[100] B. Kok, B. Forbush, M. McGloin, *Photochem. Photobiol.* **1970**, *11*, 457–475.

[101] N. Cox, D. A. Pantazis, F. Neese, W. Lubitz, *Acc. Chem. Res.* **2013**, *46*, 1588–1596.

[102] B. Zhang, L. Sun, *Chem. Soc. Rev.* **2019**, *48*, 2216–2264.

[103] X. Liu, S. Inagaki, J. Gong, *Angew. Chem. Int. Ed.* **2016**, *55*, 14924–14950.

[104] X. Wu, F. Li, B. Zhang, L. Sun, *J. Photochem. Photobiol. C: Photochem. Rev.* **2015**, *25*, 71–89.

[105] R. R. Eady, J. R. Postgate, *Nature* **1974**, *249*, 805–810.

[106] D.-H. Kim, M.-S. Kim, *Bioresour. Technol.* **2011**, *102*, 8423–8431.

[107] J. Xuan, L. He, W. Wen, Y. Feng, *Molecules* **2023**, *28*, 1392.

[108] H. Land, M. Senger, G. Berggren, S. T. Stripp, *ACS Catal.* **2020**, *10*, 7069–7086.

[109] J. A. Birrell, P. Rodríguez-Maciá, E. J. Reijerse, M. A. Martini, W. Lubitz, *Coord. Chem. Rev.* **2021**, *449*, 214191.

[110] C. Wang, Z. Lai, G. Huang, H.-J. Pan, *Chem. Eur. J.* **2022**, *28*, e202201499.

[111] A. I. Krasna, *Enzyme Microb. Technol.* **1979**, *1*, 165–172.

[112] M. W. W. Adams, L. E. Mortenson, J.-S. Chen, *Biochim. Biophys. Acta* **1981**, *594*, 105–176.

[113] S. T. Stripp, B. R. Duffus, V. Fourmond, C. Léger, S. Leimkühler, S. Hirota, Y. Hu, A. Jasniewski, H. Ogata, M. W. Ribbe, *Chem. Rev.* **2022**, *122*, 11900–11973.

[114] R. Cammack, *Nature* **1999**, *397*, 214–215.

[115] D. W. Mulder, E. M. Shepard, J. E. Meuser, N. Joshi, P. W. King, M. C. Posewitz, J. B. Broderick, J. W. Peters, *Structure* **2011**, *19*, 1038–1052.

[116] R. Rohac, L. Martin, L. Liu, D. Basu, L. Tao, R. D. Britt, T. B. Rauchfuss, Y. Nicolet, *J. Am. Chem. Soc.* **2021**, *143*, 8499–8508.

[117] M. Winkler, J. Duan, A. Rutz, C. Felbek, L. Scholtysek, O. Lampret, J. Jaenecke, U.-P. Apfel, G. Gilardi, F. Valetti, V. Fourmond, E. Hofmann, C. Léger, T. Happe, *Nat. Commun.* **2021**, *12*, 1–10.

[118] S. Qiu, Q. Li, Y. Xu, S. Shen, C. Sun, *Wiley Interdiscip. Rev. Comput. Mol. Sci.* **2020**, *10*, e1422.

[119] H. Ogata, W. Lubitz, Y. Higuchi, *J. Biochem.* **2016**, *160*, 251–258.

[120] S. Shima, O. Pilak, S. Vogt, M. Schick, M. S. Stagni, W. Meyer-Klaucke, E. Warkentin, R. K. Thauer, U. Ermler, *Science* **2008**, *321*, 572–575.

[121] S. Shima, U. Ermler, *Eur. J. Inorg. Chem.* **2011**, 963–972.

[122] F. V. Schmidt, L. Schulz, J. Zarzycki, S. Prinz, N. N. Oehlmann, T. J. Erb, J. G. Rebelein, *Nat. Struct. Mol. Biol.* **2024**, *31*, 150–158.

[123] J. W. Peters, R. K. Szilagyi, *Curr. Opin. Chem. Biol.* **2006**, *10*, 101–108.

[124] O. Einsle, D. C. Rees, *Chem. Rev.* **2020**, *120*, 4969–5004.

[125] D. R. Dean, J. T. Bolin, L. Zheng, *J. Bacteriol.* **1993**, *175*, 6737–6744.

[126] L. Deng, H. Wang, C. H. Dapper, W. E. Newton, S. Shilov, S. Wang, S. P. Cramer, Z.-H. Zhou, *Commun. Chem.* **2020**, *3*, 145.

[127] W.-J. Wei, P. E. M. Siegbahn, *Chem. Eur. J.* **2022**, *28*, e202103745.

[128] J. W. Peters, G. J. Schut, E. S. Boyd, D. W. Mulder, E. M. Shepard, J. B. Broderick, P. W. King, M. W. W. Adams, *Biochim. Biophys. Acta - Mol. Cell Res.* **2015**, *1853*, 1350–1369.

[129] I. Dance, *Dalton Trans.* **2024**, *53*, 7996–8004.

[130] G. Ciamician, *Science* **1912**, *36*, 385–394.

[131] H. Dau, C. Limberg, T. Reier, M. Risch, S. Roggan, P. Strasser, *ChemCatChem* **2010**, *2*, 724–761.

[132] M. Hansen, S. Troppmann, B. König, *Chem. Eur. J.* **2016**, *22*, 58–72.

[133] J. Amaro-Gahete, M. V. Pavliuk, H. Tian, D. Esquivel, F. J. Romero-Salguero, S. Ott, *Coord. Chem. Rev.* **2021**, *448*, 214172.

[134] S. Berardi, S. Drouet, L. Francàs, C. Gimbert-Suriñach, M. Guttentag, C. Richmond, T. Stoll, A. Llobet, *Chem. Soc. Rev.* **2014**, *43*, 7501–7519.

[135] E. Amouyal, *Sol. Energy Mater. Sol. Cells* **1995**, *38*, 249–276.

[136] A. J. Bard, M. A. Fox, *Acc. Chem. Res.* **1995**, *28*, 141–145.

[137] J. Turner, G. Sverdrup, M. K. Mann, P.-C. Maness, B. Kroposki, M. Ghirardi, R. J. Evans, D. Blake, *Int. J. Energy Res.* **2008**, *32*, 379–407.

[138] N. Li, J. Liu, B.-X. Dong, Y.-Q. Lan, *Angew. Chem. Int. Ed.* **2020**, *59*, 20779–20793.

[139] M. H. V. Huynh, D. M. Dattelbaum, T. J. Meyer, *Coord. Chem. Rev.* **2005**, *249*, 457–483.

[140] D. Gao, I. Trentin, L. Schwiedrzik, L. González, C. Streb, *Molecules* **2020**, *25*, 157.

[141] F. Liu, J. J. Concepcion, J. W. Jurss, T. Cardolaccia, J. L. Templeton, T. J. Meyer, *Inorg. Chem.* **2008**, *47*, 1727–1752.

[142] F. Liu, C. Shi, X. Guo, Z. He, L. Pan, Z.-F. Huang, X. Zhang, J.-J. Zou, *Adv. Sci.*

2022, *9*, 2200307.

[143] H. Ooka, J. Huang, K. S. Exner, *Front. Energy Res.* **2021**, *9*, 654460.

[144] J. K. Nørskov, T. Bligaard, A. Logadottir, J. R. Kitchin, J. G. Chen, S. Pandelov, U. Stimming, *J. Electrochem. Soc.* **2005**, *152*, J23–J126.

[145] Z. W. Seh, J. Kibsgaard, C. F. Dickens, I. Chorkendorff, J. K. Nørskov, T. F. Jaramillo, *Science* **2017**, *355*, 146.

[146] T. B. Ferriday, P. H. Middleton, M. L. Kolhe, *Energies* **2021**, *14*, 8535.

[147] S. Batool, M. Langer, S. N. Myakala, M. Heiland, D. Eder, C. Streb, A. Cherevan, *Adv. Mater.* **2024**, *36*, 2305730.

[148] S. Anantharaj, S. Noda, *Mater. Today Energy* **2022**, *29*, 101123.

[149] S. Gupta, N. Patel, A. Miotello, D. C. Kothari, *J. Power Sources* **2015**, *279*, 620–625.

[150] A. Saraby-Reintjes, *Electrochim. Acta* **1986**, *31*, 251–254.

[151] A. K. Mengele, S. Rau, *JACS Au* **2023**, *3*, 36–46.

[152] J. Gao, Y. Liu, B. Liu, K.-W. Huang, *ACS Nano* **2022**, *16*, 17761–17777.

[153] W. Ruettinger, M. Yagi, K. Wolf, S. Bernasek, G. C. Dismukes, *J. Am. Chem. Soc.* **2000**, *122*, 10353–10357.

[154] X. Deng, Harun Tüysüz, *ACS Catal.* **2014**, *4*, 3701–3714.

[155] C. Li, J.-B. Baek, *ACS Omega* **2020**, *5*, 31–40.

[156] Y. Zhu, Q. Lin, Y. Zhong, H. A. Tahini, Z. Shao, H. Wang, *Energy Environ. Sci.* **2020**, *13*, 3361–3392.

[157] Q. Zhu, Q. Xu, M. Du, X. Zeng, G. Zhong, B. Qiu, J. Zhang, *Adv. Mater.* **2022**, *34*, 2202929.

[158] B. Zhu, R. Zou, Q. Xu, *Adv. Energy Mater.* **2018**, *8*, 1801193.

[159] S. Xue, W. Zhang, Q. Zhang, J. Du, H.-M. Cheng, W. Ren, *Carbon* **2020**, *165*, 122–128.

[160] G. Liao, Y. Gong, L. Zhang, H. Gao, G.-J. Yang, B. Fang, *Energy Environ. Sci.* **2019**, *12*, 2080–2147.

[161] C. Wang, W. Li, X. Lu, S. Xie, F. Xiao, P. Liu, Y. Tong, *Int. J. Hydrogen Energy* **2012**, *37*, 18688–18693.

[162] K. C. Cartwright, A. M. Davies, J. A. Tunge, *Eur. J. Org. Chem.* **2020**, 1245–1258.

[163] M.-L. Grutza, A. Rajagopal, C. Streb, P. Kurz, *Sustain. Energy Fuels* **2018**, *2*, 1893–1904.

[164] J. Van Houten, R. J. Watts, *Inorg. Chem.* **1978**, *17*, 3381–3385.

[165] V. Balzani, G. Bergamini, F. Marchioni, P. Ceroni, *Coord. Chem. Rev.* **2006**, *250*, 1254–1266.

[166] L. Wang, *Catalysts* **2022**, *12*, 919.

[167] K. Kalyanasundaram, *Coord. Chem. Rev.* **1982**, *46*, 159–244.

[168] N. Kandoth, J. Pérez Hernández, E. Palomares, J. Lloret-Fillol, *Sustain. Energy Fuels* **2021**, *5*, 638–665.

[169] J.-H. Shon, T. S. Teets, *ACS Energy Lett.* **2019**, *4*, 558–566.

[170] A. Juris, V. Balzani, F. Barigeletti, S. Campagna, A. Belser, A. von Zelewsky, *Coord. Chem. Rev.* **1988**, *84*, 85–277.

[171] E. Kozma, M. Catellani, *Dyes Pigment.* **2013**, *98*, 160–179.

[172] V. Balzani, A. Credi, M. Venturi, *ChemSusChem* **2008**, *1*, 26–58.

[173] M. Natali, E. Deponti, D. Vilona, A. Sartorel, M. Bonchio, F. Scandola, *Eur. J. Inorg. Chem.* **2015**, 3467–3477.

[174] J. R. Darwent, P. Douglas, A. Harriman, G. Porter, M.-C. Richoux, *Coord. Chem. Rev.* **1982**, *44*, 83–126.

[175] A. Nabiyan, J. B. Max, C. Neumann, M. Heiland, A. Turchanin, C. Streb, F. H. Schacher, *Chem. Eur. J.* **2021**, *27*, 16924–16929.

[176] S. Batool, S. P. Nandan, S. N. Myakala, A. Rajagopal, J. S. Schubert, P. Ayala, S. Naghdi, H. Saito, J. Bernardi, C. Streb, A. Cherevan, D. Eder, *ACS Catal.* **2022**, *12*, 6641–6650.

[177] X.-B. Fan, S. Yu, B. Hou, J. M. Kim, *Isr. J. Chem.* **2019**, *59*, 762–773.

[178] W.-W. Yong, H. Lu, H. Li, S. Wang, M.-T. Zhang, *ACS Appl. Mater. Interfaces* **2018**, *10*, 10828–10834.

[179] Y. Pellegrin, F. Odobel, *C. R. Chim.* **2017**, *20*, 283–295.

[180] Y. Tachibana, L. Vayssieres, J. R. Durrant, *Nat. Photonics* **2012**, *6*, 511–518.

[181] L. Duan, L. Tong, Y. Xu, L. Sun, *Energy Environ. Sci.* **2011**, *4*, 3296–3313.

[182] J. Schneider, D. W. Bahnemann, *J. Phys. Chem. Lett.* **2013**, *4*, 3479–3483.

[183] M. D. Kärkäs, O. Verho, E. V. Johnston, B. Åkermark, *Chem. Rev.* **2014**, *114*, 11863–12001.

[184] L. Velasco-Garcia, C. Casadevall, *Commun. Chem.* **2023**, *6*, 263.

[185] M. Burian, Z. Syrgiannis, G. La Ganga, F. Puntoriero, M. Natali, F. Scandola, S. Campagna, M. Prato, M. Bonchio, H. Amenitsch, A. Sartorel, *Inorganica Chim. Acta* **2017**, *454*, 171–175.

[186] B. Kirchhoff, S. Rau, C. Streb, *Eur. J. Inorg. Chem.* **2016**, 1425–1429.

[187] D. Ziegenbalg, A. Pannwitz, S. Rau, B. Dietzek-Ivanšić, C. Streb, *Angew. Chem. Int. Ed.* **2022**, *61*, e202114106.

[188] J.-M. Lehn, J.-P. Sauvage, *Nouv. J. Chim.* **1977**, *1*, 449–451.

[189] M. Kirch, J.-M. Lehn, J.-P. Sauvage, *Helv. Chim. Acta* **1979**, *62*, 1345–1384.

[190] V. Balzani, A. Juris, *Coord. Chem. Rev.* **2001**, *211*, 97–115.

[191] F. H. Burstall, *J. Chem. Soc.* **1936**, 173–175.

[192] F. E. Lytle, D. M. Hercules, *J. Am. Chem. Soc.* **1969**, *91*, 253–257.

[193] T. Schweizer, H. Kubach, T. Koch, *Automot. Engine Technol.* **2021**, *6*, 275–287.

[194] J. N. Demas, *J. Chem. Educ.* **1983**, *60*, 803–808.

[195] V. Balzani, S. Campagna, *Photochemistry and Photophysics of Coordination Compounds I. Topics in Current Chemistry*, Springer-Verlag, Berlin, Heidelberg, **2007**.

[196] V. Balzani, P. Ceroni, A. Juris, *Photochemistry and Photophysics: Concepts, Research, Applications*, Wiley-VCH Verlag, Weinheim, **2014**.

[197] E. Papaconstantinou, *Chem. Soc. Rev.* **1989**, *18*, 1–31.

[198] P. Dongare, B. D. B. Myron, L. Wang, D. W. Thompson, T. J. Meyer, *Coord. Chem. Rev.* **2017**, *345*, 86–107.

[199] O. Laporte, W. F. Meggers, *J. Opt. Soc. Am.* **1925**, *11*, 459–463.

[200] M.-B. S. Kirketerp, S. B. Nielsen, *Int. J. Mass Spectrom.* **2010**, *297*, 63–66.

[201] J. Ferguson, E. R. Krausz, M. Maeder, *J. Phys. Chem.* **1985**, *89*, 1852–1854.

[202] A. Basu, H. D. Gafney, T. C. Strekas, *Inorg. Chem.* **1982**, *21*, 2231–2235.

[203] K. M. Omberg, J. R. Schoonover, J. A. Treadway, R. M. Leasure, R. B. Dyer, T. J. Meyer, *J. Am. Chem. Soc.* **1997**, *119*, 7013–7018.

[204] J. V. Caspar, T. J. Meyer, *J. Am. Chem. Soc.* **1983**, *105*, 5583–5590.

[205] D. Hernández-Castillo, I. Eder, L. González, *Coord. Chem. Rev.* **2024**, *510*, 215819.

[206] S. Cerfontaine, L. Troian-Gautier, Q. Duez, J. Cornil, P. Gerbaux, B. Elias, *Inorg. Chem.* **2021**, *60*, 366–379.

[207] C. Creutz, M. Chou, T. L. Netzel, M. Okumura, N. Sutin, *J. Am. Chem. Soc.* **1980**, *102*, 1309–1319.

[208] Y. Kaizu, H. Ohta, K. Kobayashi, H. Kobayashi, K. Takuma, T. Matsuo, *J. Photochem.* **1985**, *30*, 93–103.

[209] D. W. Thompson, A. Ito, T. J. Meyer, *Pure Appl. Chem.* **2013**, *85*, 1257–1305.

[210] S. Yoon, P. Kukura, C. M. Stuart, R. A. Mathies, *Mol. Phys.* **2006**, *104*, 1275–1282.

[211] J.-L. Fillaut, *Coord. Chem. Rev.* **2024**, *518*, 216050.

[212] D. M. Arias-Rotondo, J. K. McCusker, in *Visible Light Photocatalysis in Organic Chemistry* (Eds.: C. R. J. Stephenson, T. P. Yoon, D. W. C. MacMillan), Wiley-VCH Verlag, Weinheim, **2018**, pp. 1–24.

[213] N. E. Tokel-Takvoryan, R. E. Hemingway, A. J. Bard, *J. Am. Chem. Soc.* **1973**,

95, 6582–6589.

[214] A. Dahiya, A. G. Gevondian, A. Selmani, F. Schoenebeck, *Org. Lett.* **2023**, *25*, 7209–7213.

[215] H. Zheng, K. Wang, D. Ji, X. Liu, C. Wang, Y. Jiang, Z. Jia, B. Xiong, Y. Ling, J. Miao, *Eur. J. Med. Chem.* **2024**, *279*, 116909.

[216] S. Bensaid, C. Ottone Melis, S. Hernández, M. Armandi, S. Esposito, G. Saracco, B. Bonelli, *Chem. Eng. J.* **2017**, *311*, 143–152.

[217] M. Hammonds, T.-T. Tran, Y. H. H. Tran, M.-H. Ha-Thi, T. Pino, *J. Phys. Chem. A* **2020**, *124*, 2736–2740.

[218] V. Balzani, P. Ceroni, A. Credi, M. Venturi, *Coord. Chem. Rev.* **2021**, *433*, 213758.

[219] E. Deponti, M. Natali, *Dalton Trans.* **2016**, *45*, 9136–9147.

[220] M. K. DeArmond, C. M. Carlin, *Coord. Chem. Rev.* **1981**, *36*, 325–355.

[221] A. Vaidyalingam, P. K. Dutta, *Anal. Chem.* **2000**, *72*, 5219–5224.

[222] R. F. Jones, D. J. Cole-Hamilton, *Inorganica Chim. Acta* **1981**, *53*, L3–L5.

[223] A. Soupart, F. Alary, J.-L. Heully, P. I. P. Elliott, I. M. Dixon, *Coord. Chem. Rev.* **2020**, *408*, 213184.

[224] A. Soupart, F. Alary, J. L. Heully, P. I. P. Elliott, I. M. Dixon, *Inorg. Chem.* **2020**, *59*, 14679–14695.

[225] J. Van Houten, R. J. Watts, *J. Am. Chem. Soc.* **1976**, *98*, 4853–4858.

[226] B. Limburg, E. Bouwman, S. Bonnet, *ACS Catal.* **2016**, *6*, 5273–5284.

[227] M. N. Iqbal, A. F. Abdel-Magied, H. N. Abdelhamid, P. Olsén, A. Shatskiy, X. Zou, B. Åkermark, M. D. Kärkäs, E. V. Johnston, *ACS Sustain. Chem. Eng.* **2017**, *5*, 9651–9656.

[228] B. Hasenknopf, *Front. Biosci.* **2005**, *10*, 275–287.

[229] S. A. Knoll, Organic-Inorganic Hybrid α_2-Dawson-type Molecular Metal Oxides in Photocatalysis and Energy Storage, Faculty of Natural Sciences, Ulm University, **2024**.

[230] L. Schwiedrzik, T. Rajkovic, L. González, *ACS Catal.* **2023**, *13*, 3007–3019.

[231] M. T. Pope, A. Müller, *Angew. Chem. Int. Ed. Engl.* **1991**, *30*, 34–48.

[232] M. T. Pope, *Heteropoly and Isopoly Oxometalates*, Springer-Verlag, Berlin, Heidelberg, New York, Tokyo, **1983**.

[233] M. T. Pope, A. Müller, *Polyoxometalate Chemistry From Topology via Self-Assembly to Applications*, Kluwer Academic Publishers, NewYork, Boston, Dordrecht, London, Moscow, **2001**.

[234] G. Patzke, *Vierteljahrsschrift der Naturforschenden Gesellschaft Zürich* **2013**, *158(1/2)*, 23–36.

[235] M. Nyman, *Dalton Trans.* **2011**, *40*, 8049–8058.

[236] C. P. Pradeep, D.-L. Long, L. Cronin, *Dalton Trans.* **2010**, *39*, 9443–9457.

[237] D.-L. Long, R. Tsunashima, L. Cronin, *Angew. Chem. Int. Ed.* **2010**, *49*, 1736–1758.

[238] G. A. Seisenbaeva, T. Mallah, V. G. Kessler, *Dalton Trans.* **2010**, *39*, 7774–7779.

[239] H. R. Allcock, E. C. Bissell, E. T. Shawl, *Inorg. Chem.* **1973**, *12*, 2963–2968.

[240] L. J. Batchelor, R. Shaw, S. J. Markey, M. Helliwell, E. J. L. McInnes, *Chem. Eur. J.* **2010**, *16*, 5554–5557.

[241] Y. Hayashi, *Coord. Chem. Rev.* **2011**, *255*, 2270–2280.

[242] H. Nakano, T. Ozeki, A. Yagasaki, *Acta Crystallogr.* **2002**, *C58*, m464–m465.

[243] H. T. Evans, *Inorg. Chem.* **1966**, *5*, 967–977.

[244] X. López, J. J. Carbó, C. Bo, J. M. Poblet, *Chem. Soc. Rev.* **2012**, *41*, 7537–7571.

[245] D.-L. Long, L. Cronin, *Dalton Trans.* **2012**, *41*, 9815–9816.

[246] Y. P. Jeannin, *Chem. Rev.* **1998**, *98*, 51–76.

[247] J. F. Keggin, *Nature* **1933**, *131*, 908–909.

[248] Y. Zhou, J. Yang, H. Su, J. Zeng, S. P. Jiang, W. A. Goddard, *J. Am. Chem. Soc.* **2014**, *136*, 4954–4964.

[249] B. Dawson, *Acta Crystallogr.* **1953**, *6*, 113–126.

[250] A. Blazevic, A. Rompel, *Coord. Chem. Rev.* **2016**, *307*, 42–64.

[251] D. E. Salazar Marcano, N. D. Savić, S. A. M. Abdelhameed, F. de Azambuja, T. N. Parac-Vogt, *JACS Au* **2023**, *3*, 978–990.

[252] J. Tucher, S. Schlicht, F. Kollhoff, C. Streb, *Dalton Trans.* **2014**, *43*, 17029–17033.

[253] A. Dolbecq, E. Dumas, C. R. Mayer, P. Mialane, *Chem. Rev.* **2010**, *110*, 6009–6048.

[254] A. Proust, R. Thouvenot, P. Gouzerh, *Chem. Commun.* **2008**, 1837–1852.

[255] S. Schönweiz, S. Knoll, M. Anjass, M. Braumüller, S. Rau, C. Streb, *Dalton Trans.* **2016**, *45*, 16121–16124.

[256] D.-L. Long, L. Cronin, *Chem. Eur. J.* **2006**, *12*, 3698–3706.

[257] S. Herrmann, C. Ritchie, C. Streb, *Dalton Trans.* **2015**, *44*, 7092–7104.

[258] Y.-F. Song, *Polyoxometalate-Based Assemblies and Functional Materials*, Springer, Cham, **2018**.

[259] S. Repp, M. Remmers, A. S. J. Rein, D. Sorsche, D. Gao, M. Anjass, M. Mondeshki, L. M. Carrella, E. Rentschler, C. Streb, *Nat. Commun.* **2023**, *14*, 5563.

[260] D.-L. Long, E. Burkholder, L. Cronin, *Chem. Soc. Rev.* **2007**, *36*, 105–121.

[261] L. Vilà-Nadal, A. Rodríguez-Fortea, J. M. Poblet, *Eur. J. Inorg. Chem.* **2009**, 5125–5133.

[262] L. Vilà-Nadal, E. F. Wilson, H. N. Miras, A. Rodríguez-Fortea, L. Cronin, J. M. Poblet, *Inorg. Chem.* **2011**, *50*, 7811–7819.

[263] E. Weidner, F. Ciesielczyk, *Materials* **2019**, *12*, 927.

[264] J. Aveston, *Inorg. Chem.* **1964**, *3*, 981–986.

[265] J. Livage, *Coord. Chem. Rev.* **1998**, *178–180*, 999–1018.

[266] O. F. Oyerinde, C. L. Weeks, A. D. Anbar, T. G. Spiro, *Inorganica Chim. Acta* **2008**, *361*, 1000–1007.

[267] A. Misra, K. Kozma, C. Streb, M. Nyman, *Angew. Chem. Int. Ed.* **2020**, *59*, 596–612.

[268] J. Forster, B. Rösner, R. H. Fink, L. C. Nye, I. Ivanovic-Burmazovic, K. Kastner, J. Tucher, C. Streb, *Chem. Sci.* **2013**, *4*, 418–424.

[269] M. Ammam, *J. Mater. Chem. A* **2013**, *1*, 6291–6312.

[270] F. Evangelisti, P.-E. Car, O. Blacque, G. R. Patzke, *Catal. Sci. Technol.* **2013**, *3*, 3117–3129.

[271] A. Müller, C. Serain, *Acc. Chem. Res.* **2000**, *33*, 2–10.

[272] J. M. Cameron, G. Guillemot, T. Galambos, S. S. Amin, E. Hampson, K. Mall Haidaraly, G. N. Newton, G. Izzet, *Chem. Soc. Rev.* **2022**, *51*, 293–328.

[273] A. Misra, I. Franco Castillo, D. P. Müller, C. González, S. Eyssautier-Chuine, A. Ziegler, J. M. de la Fuente, S. G. Mitchell, C. Streb, *Angew. Chem. Int. Ed.* **2018**, *57*, 14926–14931.

[274] A. R. Bagheri, N. Aramesh, J. Chen, W. Liu, W. Shen, S. Tang, H. K. Lee, *Anal. Chim. Acta* **2022**, *1209*, 339509.

[275] M. I. S. Veríssimo, D. V. Evtuguin, M. T. S. R. Gomes, *Front. Chem.* **2022**, *10*, 840657.

[276] A. Bijelic, M. Aureliano, A. Rompel, *Angew. Chem. Int. Ed.* **2019**, *58*, 2980–2999.

[277] A. Barba-Bon, N. I. Gumerova, E. Tanuhadi, M. Ashjari, Y. Chen, A. Rompel, W. M. Nau, *Adv. Mater.* **2024**, *36*, 2309219.

[278] D. E. Salazar Marcano, T. N. Parac-Vogt, *Coord. Chem. Rev.* **2024**, *518*, 216086.

[279] A. Misra, C. Zambrzycki, G. Kloker, A. Kotyrba, M. H. Anjass, I. F. Castillo, S. G. Mitchell, R. Güttel, C. Streb, *Angew. Chem. Int. Ed.* **2020**, *59*, 1601–1605.

[280] N. Aramesh, A. R. Bagheri, Z. Zhang, B. Yadollahi, H. K. Lee, *Coord. Chem. Rev.* **2024**, *507*, 215767.

[281] I. A. Weinstock, R. H. Atalla, R. S. Reiner, M. A. Moen, K. E. Hammel, C. J. Houtman, C. L. Hill, *New J. Chem.* **1996**, *20*, 269–275.

[282] Z.-X. Yang, F. Gong, D. Lin, Y. Huo, *Coord. Chem. Rev.* **2023**, *492*, 215205.

[283] J. M. Clemente-Juan, E. Coronado, A. Gaita-Ariño, *Chem. Soc. Rev.* **2012**, *41*, 7464–7478.

[284] E. Coronado, C. J. Gómez-García, *Chem. Rev.* **1998**, *98*, 273–296.

[285] L. Li, Y.-T. Yu, Y. Hua, X.-N. Li, H. Zhang, *Inorg. Chem. Front.* **2023**, *10*, 1965–1985.

[286] J. Xu, H. Volfova, R. J. Mulder, L. Goerigk, G. Bryant, E. Riedle, C. Ritchie, *J. Am. Chem. Soc.* **2018**, *140*, 10482–10487.

[287] K. Suzuki, N. Mizuno, K. Yamaguchi, *ACS Catal.* **2018**, *8*, 10809–10825.

[288] S.-S. Wang, G.-Y. Yang, *Chem. Rev.* **2015**, *115*, 4893–4962.

[289] Y. Ren, M. Wang, X. Chen, B. Yue, H. He, *Materials* **2015**, *8*, 1545–1567.

[290] Q. Hu, S. Chen, T. Wågberg, H. Zhou, S. Li, Y. Li, Y. Tan, W. Hu, Y. Ding, X. Han, *Angew. Chem. Int. Ed.* **2023**, *62*, e202303290.

[291] S. Amthor, S. Knoll, M. Heiland, L. Zedler, C. Li, D. Nauroozi, W. Tobaschus, A. K. Mengele, M. Anjass, U. S. Schubert, B. Dietzek-Ivanšić, S. Rau, C. Streb, *Nat. Chem.* **2022**, *14*, 321–327.

[292] M. Anjass, G. A. Lowe, C. Streb, *Angew. Chem. Int. Ed.* **2021**, *60*, 7522–7532.

[293] S. Zhang, R. Liu, C. Streb, G. Zhang, *Polyoxometalates* **2023**, *2*, 9140037.

[294] B. E. Petel, E. M. Matson, *Chem. Commun.* **2020**, *56*, 13477–13490.

[295] C. Streb, *Dalton Trans.* **2012**, *41*, 1651–1659.

[296] A. Sartorel, M. Carraro, G. Scorrano, R. De Zorzi, S. Geremia, N. D. McDaniel, S. Bernhard, M. Bonchio, *J. Am. Chem. Soc.* **2008**, *130*, 5006–5007.

[297] Y. V. Geletii, Z. Huang, Y. Hou, D. G. Musaev, T. Lian, C. L. Hill, *J. Am. Chem. Soc.* **2009**, *131*, 7522–7523.

[298] B. Schwarz, J. Forster, M. K. Goetz, D. Yücel, C. Berger, T. Jacob, C. Streb, *Angew. Chem. Int. Ed.* **2016**, *55*, 6329–6333.

[299] B. Schwarz, J. Forster, M. H. Anjass, S. Daboss, C. Kranz, C. Streb, *Chem. Commun.* **2017**, *53*, 11576–11579.

[300] Z. Huang, Z. Luo, Y. V. Geletii, J. W. Vickers, Q. Yin, D. Wu, Y. Hou, Y. Ding, J. Song, D. G. Musaev, C. L. Hill, T. Lian, *J. Am. Chem. Soc.* **2011**, *133*, 2068–2071.

[301] T. J. R. Weakley, H. T. Evans, J. Showell, G. F. Tourné, C. M. Tourné, *J. Chem. Soc., Chem. Commun* **1973**, *4*, 139–140.

[302] R. G. Finke, M. Droege, J. R. Hutchinson, O. Gansow, *J. Am. Chem. Soc.* **1981**, *103*, 1587–1589.

[303] Q. Yin, J. M. Tan, C. Besson, Y. V. Geletii, D. G. Musaev, A. E. Kuznetsov, Z. Luo, K. I. Hardcastle, C. L. Hill, *Science* **2010**, *328*, 342–345.

[304] J. W. Vickers, H. Lv, J. M. Sumliner, G. Zhu, Z. Luo, D. G. Musaev, Y. V. Geletii,

C. L. Hill, *J. Am. Chem. Soc.* **2013**, *135*, 14110–14118.

[305] H. N. Miras, J. Yan, D.-L. Long, L. Cronin, *Chem. Soc. Rev.* **2012**, *41*, 7403–7430.

[306] S. Goberna-Ferrón, J. Soriano-López, J. R. Galán-Mascarós, *Inorganics* **2015**, *3*, 332–340.

[307] R. Hernández-Molina, A. G. Sykes, *J. Chem. Soc., Dalton Trans.* **1999**, 3137–3148.

[308] R. Hernández-Molina, M. N. Sokolov, A. G. Sykes, *Acc. Chem. Res.* **2001**, *34*, 223–230.

[309] A. Müller, S. Sarkar, R. G. Bhattacharyya, S. Pohl, M. Dartmann, *Angew. Chem. Int. Ed. Engl.* **1978**, *17*, 535.

[310] A. Müller, W.-O. Nolte, B. Krebs, *Angew. Chem. Int. Ed. Engl.* **1978**, *17*, 279.

[311] E. Diemann, A. Müller, P. J. Aymonino, *Z. Anorg. Allg. Chem.* **1981**, *479*, 191–198.

[312] J. McAllister, N. A. G. Bandeira, J. C. McGlynn, A. Y. Ganin, Y.-F. Song, C. Bo, H. N. Miras, *Nat. Commun.* **2019**, *10*, 370.

[313] E. Cadot, B. Salignac, S. Halut, F. Sécheresse, *Angew. Chem. Int. Ed.* **1998**, *37*, 611–613.

[314] A. Elliott, H. N. Miras, *J. Coord. Chem.* **2022**, *75*, 1467–1493.

[315] E. Königer-Ahlborn, A. Müller, *Angew. Chemie* **1975**, *87*, 598.

[316] P. R. Fontenot, B. Shan, B. Wang, S. Simpson, G. Ragunathan, A. F. Greene, A. Obanda, L. A. Hunt, N. I. Hammer, C. E. Webster, J. T. Mague, R. H. Schmehl, J. P. Donahue, *Inorg. Chem.* **2019**, *58*, 16458–16474.

[317] B. R. Garrett, S. M. Polen, K. A. Click, M. He, Z. Huang, C. M. Hadad, Y. Wu, *Inorg. Chem.* **2016**, *55*, 3960–3966.

[318] E. I. Stiefel, in *Transition Metal Sulfur Chemistry* (Eds.: E. I. Stiefel, K. Matsumoto), American Chemical Society, Washington, DC, **1996**, pp. 2–38.

[319] B. Hinnemann, P. G. Moses, J. Bonde, K. P. Jørgensen, J. H. Nielsen, S. Horch, I. Chorkendorff, J. K. Nørskov, *J. Am. Chem. Soc.* **2005**, *127*, 5308–5309.

[320] C. G. Morales-Guio, X. Hu, *Acc. Chem. Res.* **2014**, *47*, 2671–2681.

[321] H. Li, C. Tsai, A. L. Koh, L. Cai, A. W. Contryman, A. H. Fragapane, J. Zhao, H. S. Han, H. C. Manoharan, F. Abild-Pedersen, J. K. Nørskov, X. Zheng, *Nat. Mater.* **2016**, *15*, 48–53.

[322] T. Wang, J. Zhuo, K. Du, B. Chen, Z. Zhu, Y. Shao, M. Li, *Adv. Mater.* **2014**, *26*, 3761–3766.

[323] T. F. Jaramillo, K. P. Jørgensen, J. Bonde, J. H. Nielsen, S. Horch, I. Chorkendorff, *Science* **2007**, *317*, 100–102.

[324] P. D. Tran, T. V. Tran, M. Orio, S. Torelli, Q. D. Truong, K. Nayuki, Y. Sasaki, S.

Y. Chiam, R. Yi, I. Honma, J. Barber, V. Artero, *Nat. Mater.* **2016**, *15*, 640–646.

[325] A. S. Cherevan, S. P. Nandan, I. Roger, R. Liu, C. Streb, D. Eder, *Adv. Sci.* **2020**, *7*, 1903511.

[326] T. F. Jaramillo, J. Bonde, J. Zhang, B.-L. Ooi, K. Andersson, J. Ulstrup, I. Chorkendorff, *J. Phys. Chem. C* **2008**, *112*, 17492–17498.

[327] Y. Lei, M. Yang, J. Hou, F. Wang, E. Cui, C. Kong, S. Min, *Chem. Commun.* **2018**, *54*, 603–606.

[328] M. Dave, A. Rajagopal, M. Damm-Ruttensperger, B. Schwarz, F. Nägele, L. Daccache, D. Fantauzzi, T. Jacob, C. Streb, *Sustain. Energy Fuels* **2018**, *2*, 1020–1026.

[329] M. Heiland, R. De, S. Rau, B. Dietzek-Ivansic, C. Streb, *Chem. Commun.* **2022**, *58*, 4603–4606.

[330] W. Li, S. Min, F. Wang, Z. Zhang, D. Gao, *Chem. Commun.* **2021**, *57*, 1121–1124.

[331] A. Rajagopal, F. Venter, T. Jacob, L. Petermann, S. Rau, S. Tschierlei, C. Streb, *Sustain. Energy Fuels* **2019**, *3*, 92–95.

[332] I. Romanenko, A. Rajagopal, C. Neumann, A. Turchanin, C. Streb, F. H. Schacher, *J. Mater. Chem. A* **2020**, *8*, 6238–6244.

[333] Y. Ji, J. Xu, H. Sun, J. Liu, *Chem. Res. Chinese Univ.* **2022**, *38*, 688–697.

[334] X. L. Ho, H. Shao, Y. Y. Ng, R. Ganguly, Y. Lu, H. Sen Soo, *Inorg. Chem.* **2019**, *58*, 1469–1480.

[335] C. Kranz, M. Wächtler, *Chem. Soc. Rev.* **2021**, *50*, 1407–1437.

[336] D. R. Whang, *Nano Converg.* **2020**, *7*, 37.

[337] H. Lv, Y. V. Geletii, C. Zhao, J. W. Vickers, G. Zhu, Z. Luo, J. Song, T. Lian, D. G. Musaev, C. L. Hill, *Chem. Soc. Rev.* **2012**, *41*, 7572–7589.

[338] B. Cornils, W. A. Herrmann, *J. Catal.* **2003**, *216*, 23–31.

[339] J. J. Stracke, R. G. Finke, *ACS Catal.* **2014**, *4*, 909–933.

[340] S. Fukuzumi, D. Hong, *Eur. J. Inorg. Chem.* **2014**, 645–659.

[341] Y. Zhou, Z. Guo, W. Hou, Q. Wang, J. Wang, *Catal. Sci. Technol.* **2015**, *5*, 4324–4335.

[342] X. Sala, I. Romero, M. Rodríguez, L. Escriche, A. Llobet, *Angew. Chem. Int. Ed.* **2009**, *48*, 2842–2852.

[343] Y. Zhou, G. Chen, Z. Long, J. Wang, *RSC Adv.* **2014**, *4*, 42092–42113.

[344] X. Wang, X. Shi, S. Yin, J. Zheng, Y. Song, H. Sun, *ACS Mater. Lett.* **2024**, *6*, 3770–3793.

[345] L. Nicole, L. Rozes, C. Sanchez, *Adv. Mater.* **2010**, *22*, 3208–3214.

[346] E. D. Koutsouroubi, I. T. Papadas, G. S. Armatas, *ChemPlusChem* **2016**, *81*, 947–

954.

[347] F. M. Toma, A. Sartorel, M. Iurlo, M. Carraro, P. Parisse, C. Maccato, S. Rapino, B. R. Gonzalez, H. Amenitsch, T. Da Ros, L. Casalis, A. Goldoni, M. Marcaccio, G. Scorrano, G. Scoles, F. Paolucci, M. Prato, M. Bonchio, *Nat. Chem.* **2010**, *2*, 826–831.

[348] A. Rajagopal, E. Akbarzadeh, C. Li, D. Mitoraj, I. Krivtsov, C. Adler, T. Diemant, J. Biskupek, U. Kaiser, C. Im, M. Heiland, T. Jacob, C. Streb, B. Dietzek, R. Beranek, *Sustain. Energy Fuels* **2020**, *4*, 6085–6095.

[349] D. Yue, X. Qian, Z. Zhang, M. Kan, M. Ren, Y. Zhao, *ACS Sustain. Chem. Eng.* **2016**, *4*, 6653–6658.

[350] X. Dong, X. Zhang, P. Wu, Y. Zhang, B. Liu, H. Hu, G. Xue, *ChemCatChem* **2016**, *8*, 3680–3687.

[351] Y. Liu, C. Tang, M. Cheng, M. Chen, S. Chen, L. Lei, Y. Chen, H. Yi, Y. Fu, L. Li, *ACS Catal.* **2021**, *11*, 13374–13396.

[352] B. Fabre, C. Falaise, E. Cadot, *ACS Catal.* **2022**, *12*, 12055–12091.

[353] K. Maeda, *J. Photochem. Photobiol. C: Photochem. Rev.* **2011**, *12*, 237–268.

[354] R. K. Hocking, R. Brimblecombe, L.-Y. Chang, A. Singh, M. H. Cheah, C. Glover, W. H. Casey, L. Spiccia, *Nat. Chem.* **2011**, *3*, 461–466.

[355] H. Wei, N. Shi, J. Zhang, Y. Guan, J. Zhang, X. Wan, *Chem. Commun.* **2014**, *50*, 9333–9335.

[356] T. R. Hellstern, J. Kibsgaard, C. Tsai, D. W. Palm, L. A. King, F. Abild-Pedersen, T. F. Jaramillo, *ACS Catal.* **2017**, *7*, 7126–7130.

[357] A. Chettri, J.-H. Kruse, K. Kumar Jha, L. Dröge, I. Romanenko, C. Neumann, S. Kupfer, A. Turchanin, S. Rau, F. H. Schacher, B. Dietzek, *Chem. Eur. J.* **2021**, *27*, 17049–17058.

[358] J.-H. Kruse, M. Langer, I. Romanenko, I. Trentin, D. Hernández-Castillo, L. González, F. H. Schacher, C. Streb, *Adv. Funct. Mater.* **2022**, *32*, 2208428.

[359] T. Çeper, M. Langer, N. Vashistha, B. Dietzek-Ivanšić, C. Streb, S. Rau, F. H. Schacher, *Macromol. Rapid Commun.* **2024**, *45*, 2300448.

[360] R. A. L. Jones, *Soft Condensed Matter*, Oxford University Press, New York, **2002**.

[361] R. L. Truby, J. A. Lewis, *Nature* **2016**, *540*, 371–378.

[362] M. Wei, Y. Gao, X. Li, M. J. Serpe, *Polym. Chem.* **2017**, *8*, 127–143.

[363] M. A. C. Stuart, W. T. S. Huck, J. Genzer, M. Müller, C. Ober, M. Stamm, G. B. Sukhorukov, I. Szleifer, V. V. Tsukruk, M. Urban, F. Winnik, S. Zauscher, I. Luzinov, S. Minko, *Nat. Mater.* **2010**, *9*, 101–113.

[364] F. H. Schacher, P. A. Rupar, I. Manners, *Angew. Chem. Int. Ed.* **2012**, *51*, 7898–7921.

[365] F. S. Bates, G. H. Fredrickson, *Phys. Today* **1999**, *52*, 32–38.

[366] T. P. Lodge, *Macromol. Chem. Phys.* **2003**, *204*, 265–273.

[367] J. Kund, J.-H. Kruse, A. Gruber, I. Trentin, M. Langer, C. Read, G. Neusser, D. Blaimer, U. Rupp, C. Streb, K. Leopold, F. H. Schacher, C. Kranz, *Angew. Chem. Int. Ed.* **2023**, *62*, e202217196.

[368] S. L. Haag, M. T. Bernards, *Gels* **2017**, *3*, 41.

[369] D. Yang, *Chem. Mater.* **2022**, *34*, 1987–1989.

[370] T. L. Sun, K. Cui, J. P. Gong, *Polym. Sci. Ser. C* **2017**, *59*, 11–17.

[371] K. M. Zurick, M. Bernards, *J. Appl. Polym. Sci.* **2014**, *131*, 40069.

[372] S. E. Kudaibergenov, N. Nuraje, V. V. Khutoryanskiy, *Soft Matter* **2012**, *8*, 9302–9321.

[373] G. S. Georgiev, E. B. Kamenska, E. D. Vassileva, I. P. Kamenova, V. T. Georgieva, S. B. Iliev, I. A. Ivanov, *Biomacromolecules* **2006**, *7*, 1329–1334.

[374] G. La Sorella, G. Strukul, A. Scarso, *Green Chem.* **2015**, *17*, 644–683.

[375] W. Jiang, Y. Zhu, G. Zhu, Z. Zhang, X. Chen, W. Yao, *J. Mater. Chem. A* **2017**, *5*, 5661–5679.

[376] A. V. Anyushin, A. Kondinski, T. N. Parac-Vogt, *Chem. Soc. Rev.* **2020**, *49*, 382–432.

[377] H. Wu, H.-K. Yang, W. Wang, *New J. Chem.* **2016**, *40*, 886–897.

[378] S. Chakraborty, A. Keightley, V. Dusevich, Y. Wang, Z. Peng, *Chem. Mater.* **2010**, *22*, 3995–4006.

[379] P. Judenstein, *Chem. Mater.* **1992**, *4*, 4–7.

[380] U. Tong, W. Chen, C. Ritchie, X. Wang, Y.-F. Song, *Chem. Eur. J.* **2014**, *20*, 1500–1504.

[381] A. Macdonell, N. A. B. Johnson, A. J. Surman, L. Cronin, *J. Am. Chem. Soc.* **2015**, *137*, 5662–5665.

[382] W.-K. Miao, Y.-K. Yan, X.-L. Wang, Y. Xiao, L.-J. Ren, P. Zheng, C.-H. Wang, L.-X. Ren, W. Wang, *ACS Macro Lett.* **2014**, *3*, 211–215.

[383] Y. Han, Y. Xiao, Z. Zhang, B. Liu, P. Zheng, S. He, W. Wang, *Macromolecules* **2009**, *42*, 6543–6548.

[384] J. Lesage de la Haye, P. Beaunier, L. Ruhlmann, B. Hasenknopf, E. Lacôte, J. Rieger, *ChemPlusChem* **2014**, *79*, 250–256.

[385] M. V. Vasylyev, S. Gatard, I. Bar-Nahum, L. Konstantinovski, E. J. Wachtel, R. Neumann, *J. Clust. Sci.* **2006**, *17*, 235–243.

[386] T. Lunkenbein, M. Kamperman, Z. Li, C. Bojer, M. Drechsler, S. Förster, U. Wiesner, A. H. E. Müller, J. Breu, *J. Am. Chem. Soc.* **2012**, *134*, 12685–12692.

[387] M. H. Anjass, M. Deisböck, S. Greiner, M. Fichtner, C. Streb, *ChemElectroChem* **2019**, *6*, 398–403.

[388] S. Jiao, X. Fu, S. Wang, Y. Zhao, *Energy Environ. Sci.* **2021**, *14*, 1722–1770.

[389] H. Sai, A. Erbas, A. Dannenhoffer, D. Huang, A. Weingarten, E. Siismets, K. Jang, K. Qu, L. C. Palmer, M. Olvera de la Cruz, S. I. Stupp, *J. Mater. Chem. A* **2020**, *8*, 158–168.

[390] A. S. Weingarten, R. V. Kazantsev, L. C. Palmer, M. McClendon, A. R. Koltonow, A. P. S. Samuel, D. J. Kiebala, M. R. Wasielewski, S. I. Stupp, *Nat. Chem.* **2014**, *6*, 964–970.

[391] I. Romanenko, M. Lechner, F. Wendler, C. Hörenz, C. Streb, F. H. Schacher, *J. Mater. Chem. A* **2017**, *5*, 15789–15796.

[392] A. Baloglou, M. Plattner, M. Ončák, M.-L. Grutza, P. Kurz, M. K. Beyer, *Angew. Chem. Int. Ed.* **2021**, *60*, 5074–5077.

[393] C.-H. Lee, S. Lee, Y.-K. Lee, Y. C. Jung, Y.-I. Ko, D. C. Lee, H.-I. Joh, *ACS Catal.* **2018**, *8*, 5221–5227.

[394] B. Seo, G. Y. Jung, S. J. Lee, D. S. Baek, Y. J. Sa, H. W. Ban, J. S. Son, K. Park, S. K. Kwak, S. H. Joo, *ACS Catal.* **2020**, *10*, 652–662.

[395] Z. Huang, W. Luo, L. Ma, M. Yu, X. Ren, M. He, S. Polen, K. Click, B. Garrett, J. Lu, K. Amine, C. Hadad, W. Chen, A. Asthagiri, Y. Wu, *Angew. Chem. Int. Ed.* **2015**, *54*, 15181–15185.

[396] J. A. Bau, A.-H. Emwas, P. Nikolaienko, A. A. Aljarb, V. Tung, M. Rueping, *Nat. Catal.* **2022**, *5*, 397–404.

[397] B. Seo, S. H. Joo, *Nano Converg.* **2017**, *4*, 19.

[398] J. A. Bau, R. Ahmad, L. Cavallo, M. Rueping, *ACS Energy Lett.* **2022**, *7*, 3695–3702.

[399] A. M. Appel, D. L. DuBois, M. Rakowski DuBois, *J. Am. Chem. Soc.* **2005**, *127*, 12717–12726.

[400] M. Pritzi, T. F. Pascher, M.-L. Grutza, P. Kurz, M. Ončák, M. K. Beyer, *Phys. Chem. Chem. Phys.* **2022**, *24*, 16576–16585.

[401] R. Zhang, K. Gong, F. Du, S. Cao, *Int. J. Hydrogen Energy* **2022**, *47*, 19570–19579.

[402] J. D. Benck, T. R. Hellstern, J. Kibsgaard, P. Chakthranont, T. F. Jaramillo, *ACS Catal.* **2014**, *4*, 3957–3971.

[403] S. Kozuch, J. M. L. Martin, *ACS Catal.* **2012**, *2*, 2787–2794.

[404] T. Bligaard, R. M. Bullock, C. T. Campbell, J. G. Chen, B. C. Gates, R. J. Gorte, C. W. Jones, W. D. Jones, J. R. Kitchin, S. L. Scott, *ACS Catal.* **2016**, *6*, 2590–2602.

[405] M. Yuan, H. Yao, L. Xie, X. Liu, H. Wang, S. M. Islam, K. Shi, Z. Yu, G. Sun, H. Li, S. Ma, M. G. Kanatzidis, *J. Am. Chem. Soc.* **2020**, *142*, 1574–1583.

[406] D. Yue, Z. Zhang, Z. Tian, T. Zhang, M. Kan, X. Qian, Y. Zhao, *Catal. Today* **2016**, *274*, 22–27.

[407] D. Yue, T. Zhang, M. Kan, X. Qian, Y. Zhao, *Appl. Catal. B Environ.* **2016**, *183*, 1–7.

[408] Y. Han, D. Yue, M. Kan, Y. Wu, J. Zeng, Z. Bian, Y. Zhao, X. Qian, *Appl. Catal. B Environ.* **2019**, *245*, 190–196.

[409] Z. Xin, J.-L. Liu, W. Wei, A.-Q. Jia, Q.-F. Zhang, *Inorg. Nano-Met. Chem.* **2023**, *53*, 1371–1379.

[410] W. Koch, M. C. Holthausen, *A Chemist`s Guide to Density Functional Theory*, Wiley-VCH Verlag, Weinheim, **2015**.

[411] W. G. Noid, *J. Chem. Phys.* **2013**, *139*, 090901.

[412] H. M. Senn, W. Thiel, *Angew. Chem. Int. Ed.* **2009**, *48*, 1198–1229.

[413] J. Frank, *Introduction to Computational Chemistry*, Wiley-VCH Verlag, Weinheim, **2017**.

[414] R. Dias, W. Filgueira de Azevedo Jr., *Curr. Drug Targets* **2008**, *9*, 1040–1047.

[415] Z. Zhang, L. Zhou, Y. Zhou, J. Liu, X. Xing, J. Zhong, G. Xu, Z. Khang, J. Liu, *Biomaterials* **2015**, *65*, 56–65.

[416] A. Nisar, Y. Lu, J. Zhuang, X. Wang, *Angew. Chem. Int. Ed.* **2011**, *50*, 3187–3192.

[417] Y. Yan, B. Li, Q. He, Z. He, H. Ai, H. Wang, Z. Yin, L. Wu, *Soft Matter* **2012**, *8*, 1593–1600.

[418] X. Wang, F. Li, S. Liu, M. T. Pope, *J. Inorg. Biochem.* **2005**, *99*, 452–457.

[419] B. Hu, C. Wang, J. Wang, J. Gao, K. Wang, J. Wu, G. Zhang, W. Cheng, B. Venkateswarlu, M. Wang, P. S. Lee, Q. Zhang, *Chem. Sci.* **2014**, *5*, 3404–3408.

[420] L. Yang, J. Lei, J.-M. Fan, R.-M. Yuan, M.-S. Zheng, J.-J. Chen, Q.-F. Dong, *Adv. Mater.* **2021**, *33*, 2005019.

[421] X. Chen, Y. Zhou, V. A. L. Roy, S.-T. Han, *Adv. Mater.* **2018**, *30*, 1703950.

[422] M. R. Horn, A. Singh, S. Alomari, S. Goberna-Ferrón, R. Benages-Vilau, N. Chodankar, N. Motta, K. (Ken) Ostrikov, J. MacLeod, P. Sonar, P. Gomez-Romero, D. Dubal, *Energy Environ. Sci.* **2021**, *14*, 1652–1700.

[423] M. Genovese, K. Lian, *Curr. Opin. Solid State Mater. Sci.* **2015**, *19*, 126–137.

[424] M. Bonchio, M. Carraro, M. Gardan, G. Scorrano, E. Drioli, E. Fontananova, *Top. Catal.* **2006**, *40*, 133–140.

[425] X. Zhang, P. Tanner, A. Graff, C. G. Palivan, W. Meier, *J. Polym. Sci. Part A: Polym. Chem.* **2012**, *50*, 2293–2318.

[426] F. H. Schacher, M. Ulbricht, A. H. E. Müller, *Adv. Funct. Mater.* **2009**, *19*, 1040–1045.

[427] F. H. Schacher, T. Rudolph, F. Wieberger, M. Ulbricht, A. H. E. Müller, *ACS Appl. Mater. Interfaces* **2009**, *1*, 1492–1503.

[428] J. J. Stracke, R. G. Finke, *J. Am. Chem. Soc.* **2011**, *133*, 14872–14875.

[429] M. Zhang, M. de Respinis, H. Frei, *Nat. Chem.* **2014**, *6*, 362–367.

[430] C.-W. Tang, C.-B. Wang, S.-H. Chien, *Thermochim. Acta* **2008**, *473*, 68–73.

[431] S. E. Kudaibergenov, *Polym. Adv. Technol.* **2021**, *32*, 906–918.

[432] U. Günther, L. V. Sigolaeva, D. V. Pergushov, F. H. Schacher, *Macromol. Chem. Phys.* **2013**, *214*, 2202–2212.

[433] J. B. Max, D. V. Pergushov, L. V. Sigolaeva, F. H. Schacher, *Polym. Chem.* **2019**, *10*, 3230.

[434] P. Biehl, M. von der Lühe, F. H. Schacher, *Macromol. Rapid Commun.* **2018**, *39*, 1800017.

[435] M. Billing, G. Festag, P. Bellstedt, F. H. Schacher, *Polym. Chem.* **2017**, *8*, 936–945.

[436] M. von der Lühe, A. Weidner, S. Dutz, F. H. Schacher, *ACS Appl. Nano Mater.* **2018**, *1*, 232–244.

[437] Y. Zhao, J. Kang, T. Tan, *Polymer* **2006**, *47*, 7702–7710.

[438] F. L. Huber, S. Amthor, B. Schwarz, B. Mizaikoff, C. Streb, S. Rau, *Sustain. Energy Fuels* **2018**, *2*, 1974–1978.

[439] U. S. Akhtar, E. L. Tae, Y. S. Chun, I. C. Hwang, K. B. Yoon, *ACS Catal.* **2016**, *6*, 8361–8369.

[440] M. Sender, F. L. Huber, M. C. G. Moersch, D. Kowalczyk, J. Hniopek, S. Klingler, M. Schmitt, S. Kaufhold, K. Siewerth, J. Popp, B. Mizaikoff, D. Ziegenbalg, S. Rau, *ChemSusChem* **2022**, *15*, e202200708.

[441] V. Marin, E. Holder, U. S. Schubert, *J. Polym. Sci. Part A: Polym. Chem.* **2004**, *42*, 374–385.

[442] V. Marin, E. Holder, R. Hoogenboom, U. S. Schubert, *Chem. Soc. Rev.* **2007**, *36*, 618–635.

[443] J. Eichhorn, Y. D. Gordievskaya, E. Y. Kramarenko, A. R. Khokhlov, F. H. Schacher, *Macromolecules* **2021**, *54*, 1976–1991.

[444] J.-H. Kruse, Catalytically Active Block Copolymer Membranes for Light-Driven Hydrogen Evolution and Water Oxidation, Friedrich Schiller University Jena, **2023**.

[445] M. Wu, L. Han, B. Yan, H. Zeng, *Supramol. Mater.* **2023**, *2*, 100045.

[446] G. Nandi, S. Sarkar, B. S. Reddy, T. Kim, K. M. Tripathi, *J. Mol. Struct.* **2021**, *1234*, 130138.

[447] A. L. Gushchin, Y. A. Laricheva, P. A. Abramov, A. V. Virovets, C. Vicent, M. N. Sokolov, R. Llusar, *Eur. J. Inorg. Chem.* **2014**, 4093–4100.

[448] H. Abul-Futouh, D. Costabel, K. Hotzel, P. Liebing, H. Görls, W. Weigand, K. Peneva, *Inorganica Chim. Acta* **2023**, *551*, 121469.

[449] D. N. Chirdon, R. F. Lalisse, J. Sun, S. Zhang, B. R. Garrett, C. M. Hadad, Y. Wu, *SN Appl. Sci.* **2020**, *2*, 889.

[450] A. L. Gushchin, Y. L. Laricheva, N. I. Alferova, A. V. Virovets, M. N. Sokolov, *J. Struct. Chem.* **2013**, *54*, 752–758.

[451] L. Chen, K. A. San, M. J. Turo, M. Gembicky, S. Fereidouni, M. Kalaj, A. M. Schimpf, *J. Am. Chem. Soc.* **2019**, *141*, 20261–20268.

[452] L. Chen, M. J. Turo, M. Gembicky, R. A. Reinicke, A. M. Schimpf, *Angew. Chem. Int. Ed.* **2020**, *59*, 16609–16615.

[453] Z. Ji, C. Trickett, X. Pei, O. M. Yaghi, *J. Am. Chem. Soc.* **2018**, *140*, 13618–13622.

[454] M. Bonchio, M. Carraro, G. Scorrano, E. Fontananova, E. Drioli, *Adv. Synth. Catal.* **2003**, *345*, 1119–1126.

[455] R. Neumann, *Inorg. Chem.* **2010**, *49*, 3594–3601.

[456] M. Lechner, K. Kastner, C. J. Chan, R. Güttel, C. Streb, *Chem. Eur. J.* **2018**, *24*, 4952–4956.

[457] D. Costabel, A. Skabeev, A. Nabiyan, Y. Luo, J. B. Max, A. Rajagopal, D. Kowalczyk, B. Dietzek, M. Wächtler, H. Görls, D. Ziegenbalg, Y. Zagranyarski, C. Streb, F. H. Schacher, K. Peneva, *Chem. Eur. J.* **2021**, *27*, 4081–4088.

[458] T. Ceper, D. Costabel, D. Kowalczyk, K. Peneva, F. H. Schacher, *ACS Appl. Mater. Interfaces* **2024**, *16*, 24796–24805.

[459] D. Costabel, A. Nabiyan, A. Chettri, F. Jacobi, M. Heiland, J. Guthmuller, S. Kupfer, M. Wächtler, B. Dietzek-Ivanšić, C. Streb, F. H. Schacher, K. Peneva, *ACS Appl. Mater. Interfaces* **2023**, *15*, 20833–20842.

[460] R. Leardi, *Anal. Chim. Acta* **2009**, *652*, 161–172.

[461] B. Dejaegher, Y. Vander Heyden, *J. Pharm. Biomed. Anal.* **2011**, *56*, 141–158.

[462] D. Kowalczyk, P. Li, A. Abbas, J. Eichhorn, P. Buday, M. Heiland, A. Pannwitz, F. H. Schacher, W. Weigand, C. Streb, D. Ziegenbalg, *ChemPhotoChem* **2022**, *6*, e202200044.

[463] R. Palkovits, S. Palkovits, *ACS Catal.* **2019**, *9*, 8383–8387.

[464] B. Limburg, E. Bouwman, S. Bonnet, *Coord. Chem. Rev.* **2012**, *256*, 1451–1467.

[465] A. W. Adamson, J. N. Demas, *J. Am. Chem. Soc.* **1971**, *93*, 1800–1801.

[466] M. Biner, H. B. Bürgi, A. Ludi, C. Röhr, *J. Am. Chem. Soc.* **1992**, *114*, 5197–5203.

[467] M. Langer, A. K. Mengele, R. Müller, J. C. Wetzel, J. Mayer, S. Rau, C. Streb, *Dalton Trans.* **2025**, *54*, 4861–4865.

[468] A. Lewandowska-Andralojc, D. E. Polyansky, *J. Phys. Chem. A* **2013**, *117*, 10311–10319.

[469] B. Durham, J. V. Caspar, J. K. Nagle, T. J. Meyer, *J. Am. Chem. Soc.* **1982**, *104*, 4803–4810.

6. Publications

Parts of this dissertation have already been published in the following peer-reviewed journals. The reprints of the publication articles, including the electronic supplementary information where applicable, are presented in the following chapters 6.1–6.5 and are reproduced with the permission of the respective publishers. The title and status of the publication, information about the journal, copyright details and the individual author contributions of each publication are given in the corresponding chapters.

6.1 {MLa-1}: Polyoxometalate-Soft Matter Composite Materials: Design Strategies, Applications, and Future Directions

Jan-Hendrik Kruse,‡ Marcel Langer,‡ Iuliia Romanenko, Ivan Trentin, David Hernández-Castillo, Leticia González, Felix H. Schacher,* and Carsten Streb*

‡ *Authors contributed equally to this work*

* *Corresponding authors*

Abstract: Soft matter chemistry and design strategies for the corresponding hybrid classes with molecular POMs were presented together with the progress in their experimental and theoretical characterization over the last decade, highlighting the challenges and advantages of complementary and auspicious analytical tools to assess integrity, stability and reactivity of POMs embedded in soft matter matrices. Applications and future directions in this interdisciplinary research area were also discussed using examples from the literature.

Published in: *Adv. Funct. Mater.* **2022**, *32*, 2208428.

Status: Published

Copyright: Reprinted with permission from "Polyoxometalate-Soft Matter Composite Materials: Design Strategies, Applications, and Future Directions", J.-H. Kruse,‡ M. Langer,‡ I. Romanenko, I. Trentin, D. Hernández-Castillo, L. González, F. H. Schacher,* and C. Streb,* *Adv. Funct. Mater.* **2022**, *32*, 2208428.
DOI: 10.1002/adfm.202208428.

© 2022, Battelle Memorial Institute, Advanced Functional Materials published by Wiley-VCH GmbH under the terms of the CC BY 4.0 license.

Author Contributions:

J.-H. Kruse	Writing and discussion of section 3.1. “Stimuli-Responsive Materials and Sensing Applications” and section 3.2. “Biomedical Applications”; Discussion and revision of the manuscript.
M. Langer	Writing and discussion of section 2.2. “Challenges in Characterizing Molecular Species Embedded in Heterogeneous Matrices. Key (In Situ/”Operando”) Techniques to Assess Reactivity, Stability, and Structural Integrity” and section 3.3. “Molecular Electronics”; Discussion and revision of the manuscript.
I. Romanenko	Writing and discussion of section 1.1.1. “Soft Matter”, section 1.1.2. “Hard and Soft Matter Composites” and section 2.1. “General Deposition Strategies”; Revision of the manuscript.
I. Trentin	Writing and discussion of section 1.1.3. “Polyoxometalates” and section 3.4. “Solar and Electrochemical Energy Conversion, Catalysis”; Revision of the manuscript.
D. H.-Castillo	Writing section 2.3. “Computational Studies on Polyoxometalates-Soft Matter Hybrid Materials”; Revision of the manuscript.
L. González	Supervision; Writing, discussion and revision of the corresponding section 2.3. of the manuscript.
F. H. Schacher	Conceptualization; Supervision; Writing and discussion of section 1. “Introduction” and section 4. “Outlook and Summary”; Writing, discussion and revision of the manuscript.
C. Streb	Conceptualization; Supervision; Writing and discussion of section 1. “Introduction” and section 4. “Outlook and Summary”; Writing, discussion and revision of the manuscript.

REVIEW

ADVANCED FUNCTIONAL MATERIALS
www.afm-journal.de

Polyoxometalate-Soft Matter Composite Materials: Design Strategies, Applications, and Future Directions

Jan-Hendrik Kruse, Marcel Langer, Iuliia Romanenko, Ivan Trentin, David Hernández-Castillo, Leticia González, Felix H. Schacher, and Carsten Streb**

Molecular metal oxides or polyoxometalates (POMs) offer unrivaled properties in areas ranging from catalysis and energy conversion through to molecular electronics, biomimetics, and theranostics. While POMs are ubiquitous metal oxide model systems studied in most areas of chemistry and materials science, their technological deployment is often hampered by their molecular nature, as this leads to increased degradation, leaching, and loss of reactivity, particularly when harsh applications, such as water electrolysis, thermal catalysis or highly basic/acidic reaction solutions are targeted. Therefore, immobilization of POMs on heterogeneous substrates has recently become a central theme in POM research. While early studies focused mainly on metal oxide and semiconductor supports, more recently, POM integration in soft matter matrices including polymers, conductive polymers, hydrogels, and stimuli-responsive matrices leads to breakthroughs in multifunctional composite design. This Review summarizes pioneering experimental and theoretical progress in this emerging field over the last decade, highlighting current challenges that need to be overcome to allow a more widespread technological deployment and providing the authors' view of some of the most promising future directions of the research field. In addition, the current understanding of correlations between structure (on the molecular, nano- and microscale) and reactivity in POM polymer composites is summarized, so that rational materials design can be further developed.

1. Introduction

The combination of hard and soft matter—often thought of as inorganic and organic components—can yield functional composites with unique and otherwise inaccessible properties. Prime examples are found in Nature, where biomineralization forms bones in vertebrates or shells in mollusks. These composites combine mechanical strength with flexibility and offer structural stabilization and protection. These materials are composed of hard inorganic components, e.g., calcium carbonate, $CaCO_3$ or hydroxy apatite, $Ca_5[OH(PO_4)_3]$, and polymeric soft matter, e.g., collagens, which are combined to give new structures and unique function.[1] In this Review, we will explore the combination of polymeric soft matter matrices with molecular metal oxides—polyoxometalates (POMs)—as a unique class of composites where structure, reactivity, and function can be controlled on the molecular level, while giving macroscopic materials suitable for technological device integration, e.g., as membranes, films, or gels.

J.-H. Kruse, I. Romanenko, F. H. Schacher
Institute of Organic Chemistry and Macromolecular Chemistry (IOMC)
Friedrich Schiller University Jena
Lessingstr. 8, 07743 Jena, Germany
E-mail: felix.schacher@uni-jena.de
M. Langer, I. Trentin, C. Streb
Institute of Inorganic Chemistry I
Ulm University
Albert-Einstein-Allee 11, 89081 Ulm, Germany
E-mail: carsten.streb@uni-mainz.de

The ORCID identification number(s) for the author(s) of this article can be found under https://doi.org/10.1002/adfm.202208428.

© 2022 Battelle Memorial Institute. Advanced Functional Materials published by Wiley-VCH GmbH. This is an open access article under the terms of the Creative Commons Attribution License, which permits use, distribution and reproduction in any medium, provided the original work is properly cited.

DOI: 10.1002/adfm.202208428

M. Langer, C. Streb
Department of Chemistry
Johannes Gutenberg University Mainz
Duesbergweg 10–14, 55128 Mainz, Germany
D. Hernández-Castillo, L. González
Institute of Theoretical Chemistry
Faculty of Chemistry
Währingerstr. 17, 1090 Vienna, Austria
D. Hernández-Castillo
Vienna Doctoral School in Chemistry (DoSChem)
University of Vienna
Währinger Str. 42, 1090 Vienna, Austria
F. H. Schacher
Jena Center for Soft Matter (JCSM)
Friedrich-Schiller-University Jena
Philosophenweg 7 07743, Jena, Germany

© 2022 Battelle Memorial Institute. Advanced Functional Materials published by Wiley-VCH GmbH

ADVANCED SCIENCE NEWS
www.advancedsciencenews.com

ADVANCED FUNCTIONAL MATERIALS
www.afm-journal.de

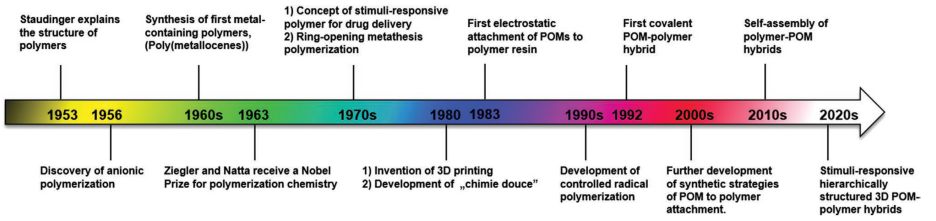


Figure 1. Historic overview of POM-polymer hybrid materials.

1.1. The Relevance of Embedding Molecular Metal Oxide Species in Soft Matter

1.1.1. Soft Matter

The 21st century may rightfully be called the era of soft matter.[2,3] The term "soft matter" was officially introduced in science by Pierre-Gilles de Gennes in his Nobel Prize lecture in 1991.[4] In contrast to hard matter, which is characterized by structural rigidity and strong (e.g., covalent or ionic) interactions, soft matter possesses properties in between solids and liquids and is dominated by weaker, intermolecular interactions (e.g., dipolar or hydrogen bonding interactions) between the constituents. These systems are flexible and are responsive to external forces or stimuli. Further, soft matter features structuring on different length scales from nano- to micrometers, and the macroscopic behavior of soft matter is dictated by non-covalent, intermolecular interactions. Based on these characteristics, polymers, colloids, surfactants, liquid crystals, vesicles, biological objects etc., are all examples of soft matter.[5]

Among those, polymers represent a thriving and promising field that was established about 100 years ago by Staudinger.[6] Later on, the discovery of living anionic polymerization in 1956[7] and stereo-regular polyolefins[8] provided facile access to materials on a large scale. The interest in polymers as industrial materials was also driven by the invention of 3D printing in the 1980s, which provided access to hierarchically complex architectures, which were not achievable by conventional manufacturing technologies.[2] In addition, the discovery of controlled polymerization techniques in the 1990s significantly increased the portfolio of accessible materials and functionalities.[9] Another break-through in soft matter was the development of block copolymers that chemically link two or more polymer-chains into one compound, resulting in unusual structure and new function.[10] In the last three decades the focus of polymer chemistry has shifted to stimuli-responsive or "smart" materials, which adapt to environmental changes by changes of structure or reactivity, enabling application in sensing, drug delivery, self-healing coatings, or tuneable catalyst supports.[11,12]

With the development of polymer chemistry, the interest to incorporate inorganic materials into polymers also emerged. Significant influence on development of such polymer–inorganic nanocomposites can be linked to the discovery of "chimie douce" in 1980s.[13] With that, sol–gel-based approaches were established as an alternative to traditional high-temperature "shake and bake" chemistry and the resulting composites often featured extended organic–inorganic interfaces. The combination of complementary properties of organic (soft) and inorganic (hard) matter opened up the way for materials with unique, sometimes even synergistic, characteristics.[14] This led to extensive applications in fields like sensing, bio-imaging, photovoltaics, or in catalysis (**Figure 1**).[3]

1.1.2. Hard and Soft Matter Composites

In the classical approach of catalytically active hybrid materials, a catalyst is often grafted or anchored on the surface of an inorganic support (e.g., silica, titania, or alumina). The obtained heterogeneous catalyst (hard matter composite) typically shows high thermal stability and good performance, and can be easily recycled.[15] The reverse approach, where inorganic catalytic species are attached to a (structured) polymeric surface (soft matter composite) is less common, presumably due to a (perceived) lower stability of soft matter. However, polymer-supported catalysts open avenues that would not be possible with classical inorganic supports. Soft matter offers superior local control of the catalyst environment, e.g., by careful selection of building blocks for nanostructured polymer matrices. This can even enable approaches where polymers model the well-defined reaction-spaces of biological systems, e.g. ‚enzymes.[16] In consequence, enhanced control over morphology, chain folding, and the presence of functional groups at the molecular level is possible, which could even result in the formation of artificial enzymes.[17] In addition, selection of a stimuli-responsive block allows to obtain smart catalytic materials in which the catalytic function can be controlled by external stimuli such as changes in pH, temperature, or light.[18] The selectivity and activity of the material can also be tuned by variation of local polarity in the vicinity of the catalytic center.[19] Currently, various inorganic materials have been used to design polymer–inorganic composites, however in this Review we focus only on hybrids based on polymers and molecular metal oxide clusters, so-called polyoxometalates (POMs).

1.1.3. Polyoxometalates

POMs are ideal molecular components for integration into soft matter matrices, based on their structural versatility combined with an enormous range of applications: POMs are molecular metal-oxide anions, typically based on early transition metals

© 2022 Battelle Memorial Institute. Advanced Functional Materials published by Wiley-VCH GmbH

16163028, 2022, 51, Downloaded from https://advanced.onlinelibrary.wiley.com/doi/10.1002/adfm.202208428 by Universitätsbibliothek Mainz, Wiley Online Library on [04/06/2025]. See the Terms and Conditions (https://onlinelibrary.wiley.com/terms-and-conditions) on Wiley Online Library for rules of use; OA articles are governed by the applicable Creative Commons License

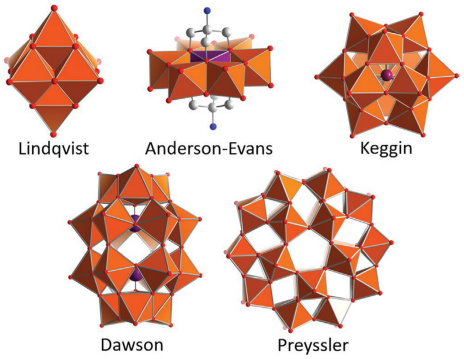


Figure 2. Prototype POM structures discussed in this review.

(group 5, 6) in their highest oxidation states (**Figure 2**).[20–22] POMs self-assemble spontaneously in solution by oligo-condensation reactions of oxometalate precursors (e.g., MoO_4^{2-}, WO_4^{2-}), sometimes in the presence of templating anions (e.g., halides, oxo-anions, etc.).[23] POMs contain between 2 and 368 metal centers are typically in the 1–5 nm size range and can feature several tens of negative charges.[20–22] POM structure formation is difficult to predict, but can be influenced by secondary reaction parameters including solvent, pH-value, temperature, pressure and others .[20] To-date, POM chemistry is dominated by W-, Mo- and V-based POMs, as these metals feature the ideal combination of high oxidation states, suitable ionic radius and availability of empty d-orbitals to stabilize terminal oxo ligands by d-p π-bonding.[20–22]

Over the last decades, advances in synthesis, characterization and mechanistic understanding have led to breakthroughs in POM applications ranging from (photo-)catalysis,[24,25] energy conversion/storage,[26] molecular magnetism and electronics[27,28] through to bio-medicine,[29–31] and artificial enzymes.[30] Of particular interest over the last decade was the development of POMs covalently functionalized with organic groups to merge the fields of metal oxide and organic chemistry.[32,33] Also, the redox-activity of POMs renders them ideal components for charge-transfer and storage as well as (photo-) redox catalysis. In addition, surface protonation of POMs makes them intriguing Brønsted acid catalysts.[34] Metal functionalization of the POM cluster shell can be used to further tune structure and reactivity.[23,35,36] The most commonly used POM structure types are summarized in Figure 2. Due to their molecular nature, POMs can easily be dissolved in various solvents, and solubility can be controlled by the type of counter-cation used.[37] This feature makes POMs amenable for solution-processing, so that incorporation in a wide variety of organic, bio-organic and inorganic heterogeneous matrices (including polymers, proteins, solid oxides) becomes possible.[38] Note that due to their facile synthesis, high stability under many typical operating conditions and ease of functionalization, Keggin- and Dawson-anions are the most widely used POMs in application-driven research.[23] However, care must be taken when deploying these systems to ensure their structural integrity, as POMs can degrade and form colloids or nanostructured metal oxides that might still show some of the targeted properties (e.g., redox-reactivity or catalytic activity).[39] Careful analysis as outlined below is therefore required to distinguish function derived from POM versus function derived from POM degradation products.[40]

2. POM-Soft Matter Embedding Strategies

2.1. General Deposition Strategies

Two general approaches can be identified for the integration of POMs in soft matter matrices, that is the use of covalent (so-called Class I hybrids) or non-covalent linkages (so-called Class II hybrids).[14] For POMs, non-covalent materials integration is synthetically more straight-forward. Thus, early studies focused in Class II POM-polymer hybrids. In 1983, Parmon and co-workers reported the first example of electrostatic POM integration in soft matter. The group immobilized $H_4[SiW_{12}O_{40}]$ or $H_3[PW_{12}O_{40}]$ on a poly(2-vinyl pyridine) anion exchange resin. However, the resulting composite did not show the proposed light-driven hydrogen evolution activity, possibly due to the absence of mobile protons in close proximity to the POM.[41] In contrast, the catalytic activity of POMs can also increase upon immobilization. For example, Wang and co-workers prepared $H_3[PW_{12}O_{40}]$-based polymers with different degrees of polymerization. The authors reported a dependence of the POM-catalyzed tetrahydrothiophene oxidation on the size of the polymer; the polymer featuring ten repeating units showed the highest catalytic activity, which was 2.5 times higher than unsupported POM cluster.[42]

2.1.1. Class I Hybrids

In class I POM-polymer hybrids, the components are linked covalently, which can have benefits in terms of stability of the POM-polymer linkage.[43] However, due to synthetic challenges in covalently linking POM and polymer, this materials class is still in its infancy. First, organo-functionalized POMs suitable for covalent linkage to polymers are required, which limits the number of suitable candidates, mainly to Keggin, Dawson, Anderson and Lindqvist ion derivatives.[32,33,44] These species can be modified by organic anchoring groups, typically using multidentate tethering groups such as phosphonate or silyl moieties.[33] Note that these linkages can be chemically labile and result in a lower overall stability of the cluster. In addition, given the large number of polymers available, no generalized strategies for POM-to-polymer attachment exist, and each system needs to be carefully tuned for optimum POM covalent attachment.[45] We also note that often, covalent modification of polymers with POMs significantly affects the resulting composite properties, often leading to decreased solubility in general,[46] which causes challenges for materials processing and application. However, when developed successfully, this approach gives access to new materials with synergistic and often unexpected properties. The covalently

© 2022 Battelle Memorial Institute. Advanced Functional Materials published by Wiley-VCH GmbH

16163028, 2022, 51, Downloaded from https://advanced.onlinelibrary.wiley.com/doi/10.1002/adfm.202208428 by Universitatsbibliothek Mainz, Wiley Online Library on [04/06/2023]. See the Terms and Conditions (https://onlinelibrary.wiley.com/terms-and-conditions) on Wiley Online Library for rules of use; OA articles are governed by the applicable Creative Commons License

ADVANCED SCIENCE NEWS
www.advancedsciencenews.com

ADVANCED FUNCTIONAL MATERIALS
www.afm-journal.de

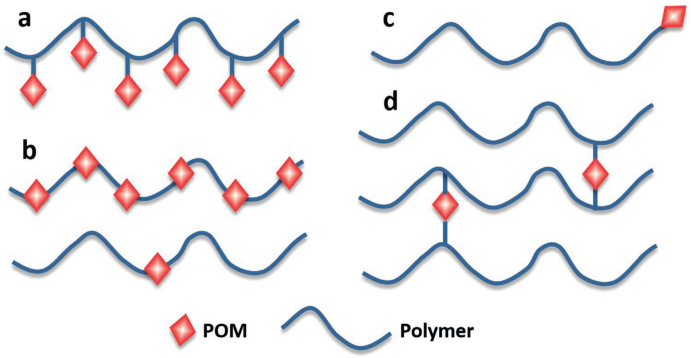


Figure 3. Main classes of POM-polymer hybrids based on their chain configuration: a) side-chain, b) backbone, c) head-tail POM-polymer hybrids, d) cross-linked networks. The red symbols represent the POM clusters.

linked POM-polymer hybrid materials can be separated into five main classes, based on the location of the POM (**Figure 3**). The POM can be incorporated a) into the polymer side-chain, b) into the polymer backbone, c) as chain end group, (so called head – tail hybrids), d) as crosslinking agent, and e) in dendrimeric structures.

Based on the synthetic method, covalently linked POM-polymer hybrids can be produced directly by polymerization of POM-modified monomers or by post-polymerization modification. The first covalently linked POM-polymer hybrid was obtained by P. Judeinstein and co-workers in 1992 by direct polymerization of organofunctionalized Keggin-type POMs $[(RSi)_2SiW_{11}O_{40}]^{4-}$ (R = vinyl, allyl, methacryl, styryl) using free radical polymerization. The reactivity of the POM-containing monomer increased in the order vinyl << allyl < methacryl < styryl, suggesting that the proximity of the cluster to the polymerizable group decreases the polymerization rate. Due to the presence of two polymerizable groups in one POM cluster, a mixture of branched and linear polymers was obtained, where the POM was located along the polymer backbone.[47]

POM-polymer hybrids where the POM is incorporated along the backbone are usually synthesized by step-growth polymerizations, e.g. polyaddition and polycondensation. One particularly interesting example of polyaddition was reported by Song and colleagues who performed photo-induced [2+2] cycloaddition of *bis*-coumarin modified Anderson POMs. The success of polymerization can be visually monitored by change of the color of polymer from colorless to red due to an increase of the chromophore system. Upon 90 min of irradiation, polymers with molar masses of 337 kDa and a dispersity of 1.60 were obtained.[48] Also, the use of CLICK chemistry (Cu-catalyzed alkyne-azide coupling) has been reported by Cronin and coworkers to access POM-oligomers based on suitably functionalized Anderson-POMs.[49] Here, the authors first designed POM-based "monomers" featuring terminal amine groups at either end of the POM molecule. Chain growth was then enabled by functionalizing the terminal groups with alkyne moieties that could then undergo further CLICK-linkage. This route can be repeated, leading to well-defined Mn-Anderson hybrids ranging from dimers to pentamers. Despite unprecedented control over the polymerization process, the proposed strategy is still limited due to the difficulties in synthesizing unsymmetrically functionalized POMs.

In one example, the integration of POMs into polymeric side-chains has been achieved by ring-opening polymerization of norbornene monomers modified with Dawson-POMs. The polymerization occurred nearly quantitatively and resulted in POM-polymer hybrids where $[H_4P_2V_3W_{15}O_{62}]^{5-}$ POM clusters are attached to well-defined polynorbornene backbones (**Figure 4**a). Molar masses up to 600 kDa and a low dispersity (PDI = 1.2) were reported, which corresponds to 100 POM-norbornene repeating units. The resulting composite showed catalytic activity for the oxidation of tetrahydrothiophene and could also be processed into thin films.[42] The same Dawson-type POM has also been used for the formation of head to tail type POM-polymer hybrids by ATRP (Figure 4b). Here, the macroinitiator was synthesized at first by ligand exchange between POM and bromofunctionalized tris-(hydroxymethyl)methane. This macroinitiator was then used in polymerization reactions, giving polystyrene-based head-to-tail hybrids with molar masses up to 119 kDa. Exchange of lipophilic NBu_4^+ cations with hydrophilic H^+ resulted in the formation of giant amphiphiles with hydrophilic POM headgroups and long hydrophobic tails, forming vesicles via self-assembly in aqueous media.[50] RAFT polymerization techniques have been used to access poly(*N*,*N*-diethylacrylamide) composites using trithiocarbonate-functionalized Dawson-type phosphotungstates as chain transfer agent and AIBN as initiator. Here, chain transfer agent (CTA) synthesis was performed through the formation of a lacunary POM with the next tin modification followed by azide-alkyne coupling (Figure 4c). This led to head to tail hybrid polymers with molecular weights in the range of 10 to 100 kDa and dispersities <1.5.

The covalent attachment of POMs to pre-formed dendrimers has been possible by post-polymerization modification. For example, $[H_4P_2V_3W_{15}O_{62}]^{5-}$ Dawson POMs have been directly attached to dendrimers featuring terminal tris(hydroxymethyl) groups through transesterification. The material obtained was

© 2022 Battelle Memorial Institute. Advanced Functional Materials published by Wiley-VCH GmbH

16163028, 2022, 51, Downloaded from https://advanced.onlinelibrary.wiley.com/doi/10.1002/adfm.202208428 by Universitätsbibliothek Mainz, Wiley Online Library on [04/06/2025]. See the Terms and Conditions (https://onlinelibrary.wiley.com/terms-and-conditions) on Wiley Online Library for rules of use; OA articles are governed by the applicable Creative Commons License

ADVANCED SCIENCE NEWS
www.advancedsciencenews.com

ADVANCED FUNCTIONAL MATERIALS
www.afm-journal.de

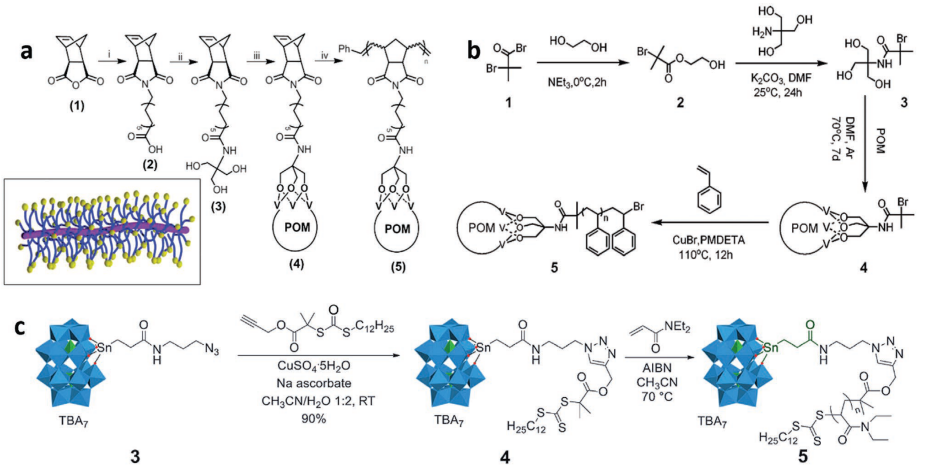


Figure 4. Selected examples for the utilization of controlled polymerization techniques: a) ROP. Reproduced with permission.[42] Copyright 2009, American Chemical Society. b) ATRP. Reproduced with permission.[50] Copyright 2014, American Chemical Society. c) RAFT for the formation of covalently linked POM-polymer hybrids. Reproduced with permission.[51] Copyright 2014, Wiley-VCH GmbH.

used as a catalyst for the tetrahydrothiophene oxidation using *t*BuOOH or H_2O_2 as oxidant. Catalyst recycling and reuse by precipitation and filtration-recovery has also been demonstrated.[52] Also, for Keggin-POMs, dendrimer attachment has been achieved by reaction of dendrimer-based amino groups with tin chloride-modified POM clusters.[53]

2.1.2. Class II Hybrids

The simplicity of electrostatic attachment of anionic POMs to cationic polymers has made it the most used approach for POM-in-polymer integration, and various polymers have been used, including quaternized poly(vinylpyridine), polyimidazole, polyaniline, protonated polylysine, polypyrrole, poly(vinylchloride), polyethylene-*block*-polydimethyl aminoethyl methacrylate, or polystyrene-*block*-poly(2-dimethylaminoethyl methacrylate).[54] Despite the facile composite preparation, non-covalent attachment can often lead to POM leakage under operation, particularly upon pH changes. Especially in case of electrostatic attachment, drastic changes in pH can lead to weakening of the interaction and removal of POM from the polymer matrix (e.g., by POM protonation). Nevertheless, reversible attachment upon changes in pH could be potentially used for metal recovery and polymer recycling. In addition, electrostatic attachment is the method of choice for the formation of hierarchically structured 1D–3D POM-polymer hybrid materials. Particularly, when block-copolymers with chemically different "blocks" (e.g., a hydrophilic and a hydrophobic block) are used, then access to POM-functionalized hierarchical structures including micelles, vesicles, thin films, membranes, fibers, or porous solids becomes possible (**Figure 5**). In addition to direct mixing of POM and polymer during the preparation, electrostatic POM-anchoring is also possible as a post-functionalization method of the pre-formed polymer. So far the direct mixing of POM with polymer is rather difficult as in this case all components should be well soluble in one solvent.[55] More often the attachment of POM is realized due to the electrostatic attachment of POM to polymers bearing an amino function, that also could be introduced in the commercial polymer network like poly(vinylidene difluoride) (PVDF) by plasma treatment.[56]

2.2. Challenges in Characterizing Molecular Species Embedded in Heterogeneous Matrices. Key (In Situ/"Operando") Techniques to Assess Reactivity, Stability, and Structural Integrity

The structural analysis of POM integrity within the soft matter matrix is most often performed using surface spectroscopic and microscopic techniques. In the following chapter, key techniques are presented, and their relevance is demonstrated by appropriate literature examples.

2.2.1. Fourier-Transform and Attenuated Total Reflectance Infrared Spectroscopy (FT-/ATR-IR)

FT-/ATR-IR are suitable solid-state methods to study materials such as powders, (hydro)gels,[57] films,[58] membranes,[59] etc., and to verify POM presence and integrity in a polymer matrix.[60,61] Note that ATR typically probes the sample surface, while FT-IR targets the sample bulk. POMs exhibit intense, characteristic metal-oxygen vibrational modes in the fingerprint region of 1000—500 cm^{-1}, which are highly sensitive to

© 2022 Battelle Memorial Institute. Advanced Functional Materials published by Wiley-VCH GmbH

16163928, 2022, 51, Downloaded from https://advanced.onlinelibrary.wiley.com/doi/10.1002/adfm.202208428 by Universitatsbibliothek Mainz, Wiley Online Library on [04/06/2023]. See the Terms and Conditions (https://onlinelibrary.wiley.com/terms-and-conditions) on Wiley Online Library for rules of use; OA articles are governed by the applicable Creative Commons License

ADVANCED SCIENCE NEWS
www.advancedsciencenews.com

ADVANCED FUNCTIONAL MATERIALS
www.afm-journal.de

16163928, 2022, 51, Downloaded from https://advanced.onlinelibrary.wiley.com/doi/10.1002/adfm.202208428 by Universitatsbibliothek Mainz, Wiley Online Library on [04/06/2025]. See the Terms and Conditions (https://onlinelibrary.wiley.com/terms-and-conditions) on Wiley Online Library for rules of use; OA articles are governed by the applicable Creative Commons License

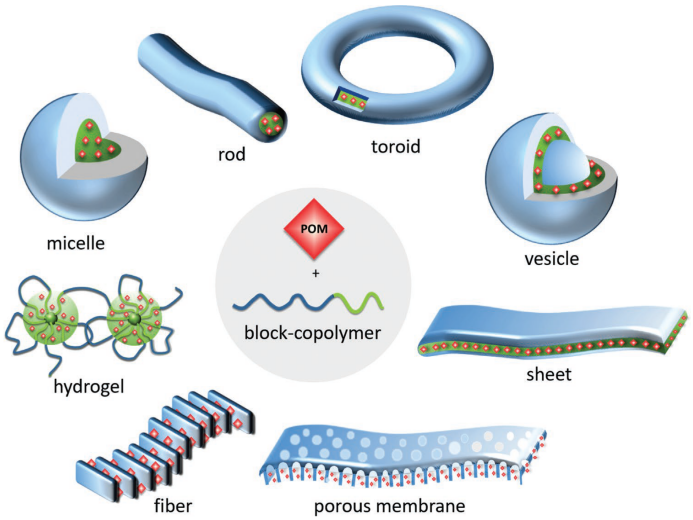


Figure 5. Overview of 1D, 2D, and 3D POM-polymer hybrid structures obtained using block copolymer self-assembly.

structural changes, degradation or interactions with the environment. Hence, IR-spectroscopy can be used, e.g., to assess POM stability or leaching in reactivity studies by analysis of POM-characteristic signals in the fingerprint region <1000 cm^{-1}.[62–64] In addition, POM-polymer interactions can be experimentally studied, including hydrogen bonding,[61] π-stacking,[65] electrostatic,[57,58] ionic[61] and covalent attachment[66,67] by analysis of the specific vibrational features.[61,65,68] IR spectroscopy (in combination with other methods) also allows to track the progress of a reaction by evaluating changes in vibrational intensities, as demonstrated by Judeinstein and co-workers for a (POM-methacrylate) polymerization reaction, where the intensity decrease of the polymer-based C=C-vibration is used as spectroscopic probe.[47]

2.2.2. Raman Spectroscopy

Raman spectroscopy is a vibrational spectroscopy method to characterize POM-polymer composites that offers higher signal resolution compared with conventional IR spectroscopy. However, it typically operates at high excitation laser power, which can cause damage to sensitive samples. In one example, Luis Vilas, Gutiérrez–Zorrilla and colleagues[69] used confocal Raman microscopy (CRM) to access depth profiles/cross sections of composite films containing POMs. The study highlighted that POM-identification within the films is possible at high spatial resolution, enabling the observation of homogeneous POM distribution. In another example, Jacob, Travaš-Sejdić, Streb and co-workers used "operando" Raman-spectro-electrochemistry to explore reversible redox-cycling of POM-conductive polymer composites.[70] Yang and colleagues used in situ Raman spectroscopy to assess structural changes, degradation, and substrate binding in a mesoporous POM-soft matter hybrid.[62]

2.2.3. X-Ray Photoelectron Spectroscopy (XPS)

XPS is a surface sensitive (top few nm) technique to quantify the elemental composition of solids under ultra-high vacuum. The technique can also be used to study POM or polymer surface-processes including structure changes, degradation, diffusion, or leaching.[71] In addition to the detection of characteristic binding energies and the assignment of metal oxidation states, changes in signal intensity ratios can be used to gain insights into chemical changes before and after specific reactions.[63,72]

2.2.4. Nuclear Magnetic Resonance (NMR) Spectroscopy

NMR spectroscopy can be used to probe the structural integrity of POMs and their interaction with polymers in solution and the solid state. In one example, Ikegami and co-workers studied a Keggin-phosphotungstate embedded in a copolymer matrix.[73] The authors used ^{31}P-NMR to verify cluster integrity and to explore the reactivity loss during recycling. Hill and colleagues[66] used the solid-state method Cross-Polarization Magic Angle Spinning (CP-MAS) ^{13}C-NMR to examine the presence of covalent bonds between polymer-anchored 1,3,5-benzenetricarboxamide linkers and polyoxovanadate clusters. The presence and integrity of the vanadate cluster itself was confirmed by solid-state MAS-^{51}V-NMR and solution ^{51}V-NMR.

© 2022 Battelle Memorial Institute. Advanced Functional Materials published by Wiley-VCH GmbH

ADVANCED SCIENCE NEWS
www.advancedsciencenews.com

ADVANCED FUNCTIONAL MATERIALS
www.afm-journal.de

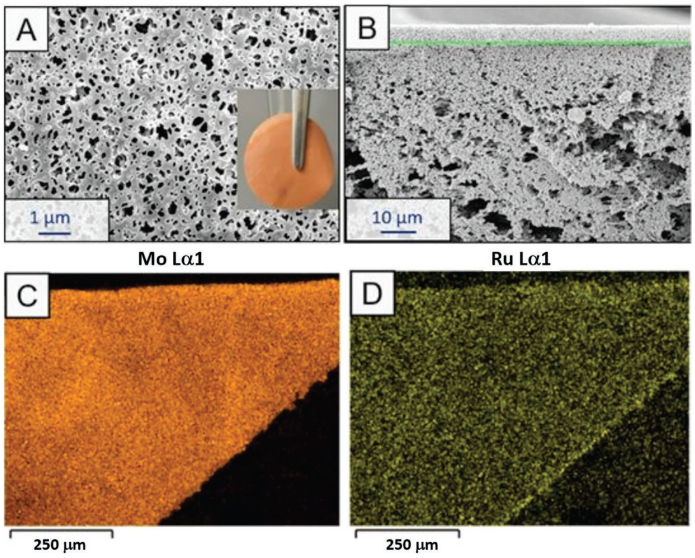


Figure 6. a,b) Top view and cross sectional SEM micrographs of a non-functionalized block copolymer membrane. Inset A: photograph of the functionalized membrane showing the characteristic color of the immobilized molecular species. c,d) EDX elemental mapping (Mo/Ru) mapping of functionalized membrane. Reproduced with permission.[79] Copyright 2020, RSC Publishing.

2.2.5. UV–vis Absorption and Emission Spectroscopies

UV–vis absorption and emission spectroscopies can be used to probe the presence and reactivity of POMs in soft matter.[64] In one example, Oms, Dessapt, Roger and co-workers[74] designed a polymer containing Anderson-type POM and organic spiropyran. The materials showed strong solid-state photochromism that was tuned by the POM loading amount. In another example, Zhang, Wan and colleagues[75] reported a pH-responsive POM-soft matter hydrogel unusual, POM-dependent luminescence properties.

2.2.6. Elemental Analysis

Elemental analysis allows the determination of metals and most non-metals in composite materials by CHN elemental analysis (EA) and inductively coupled plasma optical/atomic emission spectroscopy (ICP-OES/AES). This enables validation of elemental compositions,[76] determine POM- and organic contents,[63] and assess POM stability and leaching resistance.[63]

2.2.7. Scanning Electron Microscopy (SEM) and Energy-Dispersive X-Ray Spectroscopy (EDX)

SEM provides nanometer-resolution information of the morphology,[57] micro- and nanostructure of POM-soft matter systems. When combined with EDX, structural and elemental information can be obtained, e.g. to, study POM incorporation and distribution in soft matter matrices.[56,63,77] Bonchio, Carraro and co-workers used SEM-EDX to investigate the surface and cross-sectional morphology of a photocatalytically active POM-polymer membrane, and provide information on membrane changes during catalysis.[78] Streb, Schacher and colleagues reported light-driven hydrogen evolving nanoporous block copolymer membranes functionalized with a molecular photosensitizer ($[Ru(bpy)_3]^{2+}$) and a HER-active catalyst ($[Mo_3S_{13}]^{2-}$).[79] SEM-EDX was used to explore the distribution of the molecular components on the membrane surface (**Figure 6**).

2.2.8. High-Resolution Transmission Electron Microscopy (HR-TEM)

HR-TEM provides down-to atomic resolution analysis of thin samples. Due to the large difference in electron density, HR-TEM is particularly suitable for studying POM distributions in organic soft matter. In one example, Breu, Kamperman and co-workers showed that different nanostructures (micelles, networks, and vesicles) can be accessed in POM ($H_3[PMo_{12}O_{40}]$)/PB-b-PDMEAMA hybrids, depending on the POM-to-polymer ratio.[55]

2.2.9. Atomic Force Microscopy (AFM)

AFM can be performed under ambient conditions on non-pretreated (e.g., dried) samples. AFM gives access to surface topology

© 2022 Battelle Memorial Institute. Advanced Functional Materials published by Wiley-VCH GmbH

16163928, 2022, 51, Downloaded from https://advanced.onlinelibrary.wiley.com/doi/10.1002/adfm.202208428 by Universitatsbibliothek Mainz, Wiley Online Library on [04/06/2023]. See the Terms and Conditions (https://onlinelibrary.wiley.com/terms-and-conditions) on Wiley Online Library for rules of use; OA articles are governed by the applicable Creative Commons License

ADVANCED SCIENCE NEWS
www.advancedsciencenews.com

ADVANCED FUNCTIONAL MATERIALS
www.afm-journal.de

16163028, 2022, 51, Downloaded from https://advanced.onlinelibrary.wiley.com/doi/10.1002/adfm.202208428 by Universitätsbibliothek Mainz, Wiley Online Library on [04/06/2025]. See the Terms and Conditions (https://onlinelibrary.wiley.com/terms-and-conditions) on Wiley Online Library for rules of use; OA articles are governed by the applicable Creative Commons License

and roughness of POM-polymer hybrids. For example, Luis Vilas, Gutiérrez–Zorrilla and colleagues[69] used AFM to show that POMs of different size feature distinct distributions at polymer interfaces.

2.2.10. Thermogravimetric Analysis (TGA)

TGA can be used to quantify the POM-content in a POM-polymer hybrid by determining the amount of combustible components.[61] In addition, TGA provides information on the thermal stability[58] and degradation temperature[67] of the samples studied.

2.2.11. Dynamic Scanning Calorimetry (DSC)

DSC can further be used to identify melting/solidification behavior[65] and glass-transitions[76] in POM-soft matter composites, e.g., hydrogels.[57]

2.2.12. Electron Paramagnetic Resonance (EPR) Spectroscopy

EPR spectroscopy provides insights into the electronic states of POMs embedded in soft matter. In one example, Lalevée and co-workers[80] followed the catalytic performance and oxidative re-generation of POMs when embedded in a polymer matrix using EPR spectroscopy.

2.2.13. Electrochemical Analyses

Electrochemical analyses are ideal tools to study the redox-activity of POMs embedded in redox-active or conducting polymers. Voltammetric-, bulk electrolysis and related studies can provide critical information on the accessible oxidation states, changes in reversibility and electron storage/transfer capabilities of the materials studied.[67,76,81]

2.3. Computational Studies on Polyoxometalates-Soft Matter Hybrid Materials

Over the last two decades, the number of publications dedicated to computational studies of POMs has increased steadily. The rise on computational power alongside the appearance of novel theoretical methods has made possible to target transition metal compounds with high accuracy.[82] Recent reviews[83,84] have covered some of the applications of theory to POMs. However, the number of computational studies addressing POM-soft matter composites is far below those, which focus on computed properties of POMs. Here, we discuss computational studies of POM-soft matter hybrid materials, first pointing to the challenges associated with model POMs.

2.3.1. Computational Methods

Even though theory has been able to provide qualitative and quantitative descriptions of some of the properties of isolated POMs, this path has been far from straightforward and hindered by the many limitations of the available methods. Atomistic simulations can employ quantum mechanical (QM) methods (**Figure 7**, bottom), either based on ab initio wave function or density functional theory[85] (DFT). Whereas wave function methods quickly become unfeasible as the size of the molecular system increases, DFT has a better trade-off between cost and accuracy and is therefore more popular. DFT studies on POMs until 2012 can be found in the excellent review from Bo, Poblet and co-workers.[84] Recent examples, where DFT has aided the interpretation of experimental data or predicted POM properties include the calculation of redox potentials,[86–88] X-ray spectra,[89] reaction mechanisms,[88,90–92] and non-linear optical (NLO) properties.[93–95]

When studying the interactions of POMs and soft matter, the large dimensions of the global system requires the use of classical approximations. Most methods in this category involve molecular dynamics (MD) simulations based on parametrized force fields—also known as molecular mechanics (MM). In this fashion, atoms are considered as classical balls that follow Newton's equations in time. To recover QM effects and thus improve accuracy, hybrid QM/MM methods[96,97] divide the system in (at least) two regions, a small one that is treated quantum mechanically with high accuracy, and the rest that is described with a suitable force field. The different flavors of QM/MM methods depend on how the interaction between the QM and MM regions is described. The computational cost of QM/MM is roughly as expensive as that of the chosen QM method, and thus combined with MD, propagation time scales are shorter than those that can be achieved with MD only (see Figure 7). When the system is much larger than the computational feasibility of all-atom MD allows or propagations in the µs-ms regime are targeted, coarse-grained[98] modeling can reduce the number of degrees of freedom by defining a group of atoms in a so-called bead. Despite its lower resolution as compared with all-atom simulations, combined with MD coarse-grained modeling exhibits a computational speedup of the order of N^2, with N the number of particles.[99] To reach larger spatial and time scales, at the meso- or macroscale, supra coarse-grained MD strategies include one or more molecular units in one bead (see top of Figure 7). Furthermore, static information on the positioning or interaction modes between POMs and macromolecular systems can be addressed by means of molecular docking.[100]

2.3.2. Modeling POM Geometries

Before any molecular properties can be calculated, one requires an accurate prediction of the equilibrium geometry. If the system is flexible, one needs to sample and energetically rank all accessible conformers. Unlike for main group element-containing molecules, conformational energy benchmarks for transition metals are scarce and they lack the inclusion of POMs in their datasets.[102,103] It is worth noting that in recent times there have been major advances in the development of new density functionals that allow to routinely compute several hundreds of atoms, while conserving the accuracy of more computationally demanding counterparts.[104–108] Regarding

© 2022 Battelle Memorial Institute. Advanced Functional Materials published by Wiley-VCH GmbH

ADVANCED SCIENCE NEWS
www.advancedsciencenews.com

ADVANCED FUNCTIONAL MATERIALS
www.afm-journal.de

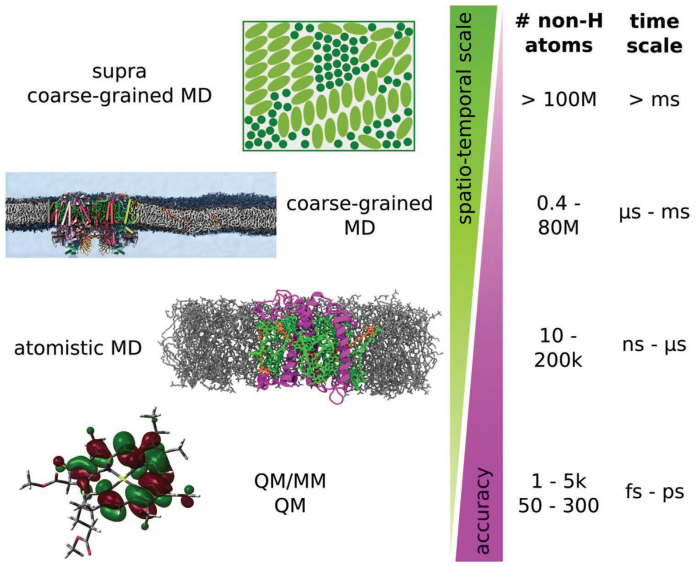


Figure 7. A general hierarchical scheme of different modeling approaches, including approximate time-scales and system sizes that can be studied with each method. Reproduced with permission (http://creativecommons.org/licenses/by/4.0/).[101] Copyright 2020, the Authors, published by Springer.

flexibility, Jahn-Teller (JT) effects and redox isomerism should also be considered when describing the conformational landscape of POMs. For example, the DFT studies of López, Poblet and co-workers[109] found that intrinsic geometrical distortions present in molybdates are due to pseudo JT distortions. Likewise, Irlet and colleagues[110] attributed JT distortions as the driving force for the molecular and electronic structure changes during super-reduction of a α-Keggin POM cluster. Very recently, some of us[111,112] showed that the position of JT axes influences the local reactivity in a Mn-based POM,[113] which is a synthetic mimic of the oxygen evolving complex in natural photosynthesis.

2.3.3. Modeling POM Electronic Properties

As POMs are composed of transition metals, they inherit the associated computational challenges of dealing with such atoms. If calculating relative energies of different spin states can be a difficult task in a transition metal complex, to do so in a POM is considerably more challenging as the many metal atoms increase the number of oxidation and spin states. Ideally, such problems are best treated with QM methods[] able to deal with the multi-configurational situations that most likely such structures incur. However, multi-configurational QM methods are computationally very demanding and applications to POMs are scarce.[115,116] Alternatively, the relative stability of high and low-spin states is often calculated with the cheaper broken-symmetry DFT approach.[117,118] In this framework, the low-spin manifold is accessed by a variational self-consistent-field optimization of a mono-configurational wave function, where the sign of the spin-density of an atomic center is inverted to represent a lower symmetry state compared to the high-spin state. One example of low-spin states calculated in this fashion is the computed redox potentials of a Mn-based POM,[88] but many more exist. Broken-symmetry DFT has also been employed to calculate magnetic properties of POMs.[119,120]

2.3.4. Modeling POMs Embedded in Polymers

Due to their large size, high conformational flexibility, and often amorphous structure, the choice of a computational technique to model polymers is far from trivial.[121] Particularly, for the study of POM-in-polymer integration, all-atom MD simulations and coarse-grained MD approaches are by far the most popular choices.

An example for a soft matter environment where POM-integration has been computationally studied are dendrimers. The POM@dendrimer systems are termed artificial dendrizymes,[122,123] as they are intended to have structural resemblance with natural metalloproteins and are to be applied as enhanced catalysts. Early studies by Volkmer, Kurth, Krebs and colleagues[123] on a heteropolytungstate cluster encapsulated in a shell of dendritically branching surfactants laid the foundations for later applications of all-atom MD simulations on POMs embedded in dendrimers.[124,125] Their study was mostly qualitative in nature, giving insights into the packing

© 2022 Battelle Memorial Institute. Advanced Functional Materials published by Wiley-VCH GmbH

16163928, 2022, 51, Downloaded from https://advanced.onlinelibrary.wiley.com/doi/10.1002/adfm.202208428 by Universitatsbibliothek Mainz, Wiley Online Library on [04/06/2023]. See the Terms and Conditions (https://onlinelibrary.wiley.com/terms-and-conditions) on Wiley Online Library for rules of use; OA articles are governed by the applicable Creative Commons License

ADVANCED SCIENCE NEWS
www.advancedsciencenews.com

ADVANCED FUNCTIONAL MATERIALS
www.afm-journal.de

16163928, 2022, 51, Downloaded from https://advanced.onlinelibrary.wiley.com/doi/10.1002/adfm.202208428 by Universitätsbibliothek Mainz, Wiley Online Library on [04/06/2025]. See the Terms and Conditions (https://onlinelibrary.wiley.com/terms-and-conditions) on Wiley Online Library for rules of use; OA articles are governed by the applicable Creative Commons License

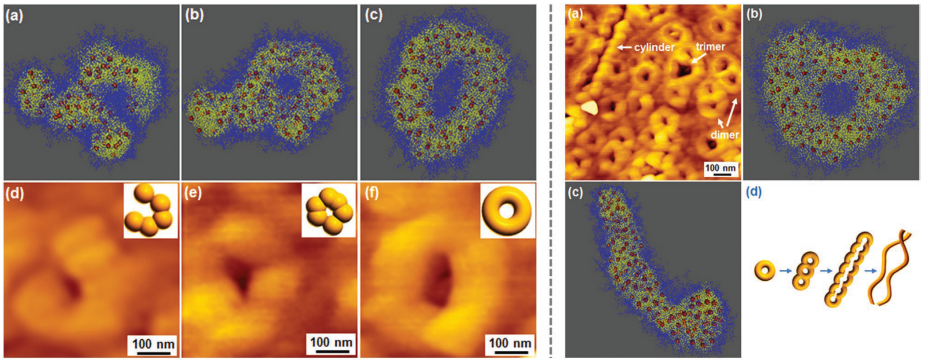


Figure 8. Left: a–c) coarse-grained MD snapshots of the micelles. d–f) AFM images of intermediate states during the formation of toroids. Right: a) AFM image of the coexisting shapes of the micelles, b) snapshot from the simulated early stage formation of the toroidal micelle, c) snapshot from the simulated evolution of the toroidal micelle into cylinder shape.[60] Reproduced with permission.[60] Copyright 2015, American Chemical Society.

arrangement of dendrons over the anionic metal cluster. More recently, several studies combining theory and experiment have been carried out on perfluorosulfonic acid polymers (PFSA) doped with heteropoly acids (HPAs), which is a subset family of POMs.[126–129] PFSAs are able to form proton exchange membranes, which upon doping with HPAs should see an increase in the proton conductivity capabilities. Maupin, Herring and co-workers[126] combined experiment and theory to study the PFSA membranes doped with $[H_3PW_{12}O_{40}]$ and $[H_4SiW_{12}O_{40}]$ HPAs. All atom MD simulations assisted the understanding of the observed enhanced proton conducting capabilities of the membranes, by addressing the solvent distribution. From their calculations, they concluded that enhanced proton conductivity was due to a trapping mechanism of solvent water molecules around the HPAs, resulting in a hydrogen-bonding network.[126] A study by the same group[127] followed a very similar modeling protocol to provide additional information regarding the balance between the loading of HPAs and the resulting conductivity. Relying solely on computer simulations, Mosavavian and co-workers[128] studied the doping of Nafion® 117 with $[H_3PW_{12}O_{40}]$, $[H_5IW_6O_{24}]$, $[H_9AlW_6O_{24}]$, and $[H_2W_6O_{19}]$. They applied MD simulations coupled with quantum mechanically derived proton hopping[130] to investigate the hydrogen bond network and structural diffusion of protons. This method allows to compute rate constants of proton hopping between water molecules, and to detect decreased activation energies in the proton migration between two adjacent water molecules when the POMs are integrated in the Nafion® 117. The same authors also employed all-atom MD simulations to investigate in more detail the creation of a change in the water network triggered by POMs through a detailed percolation analysis.[129]

Computational simulations of other mechanisms, such as co-assembly of POMs and polymers, requires accessing to time-scales much longer than those accessed by atomistic MD methods, e.g., using coarse-grained MD.[121] In this manner, Li, Quian, Wu and colleagues[60] showed the time evolution of a supramolecular star polymer with a Keggin-type POM cluster core ($[CoW_{12}O_{40}]^{5-}$) and blockcopolymers. The system was composed of a supramolecular star copolymer with the POM as a core and a solution of a block-copolymer. Their simulations showed the time evolution of the system going from the formation of toroidal micelles (**Figure 8**, left) to their assembly into cylindrical micelles (Figure 8, right), which nicely agreed with measured AFM images. Very recently, coarse-grained MD was also used to simulate the self-assembly mechanism of POM nanoparticles decorated with mobile polymer ligands (i.e., via electrostatic interactions),[131] providing designing rules for tailored self-assembly into lamellar, cylindrical, and spherical structures.

Complementary to the methods above, it is also possible to take truncated models of POM-polymer structures sufficiently small for QM calculations. For example, in a joint experimental and theoretical work, De Luca and co-workers[132] constructed a model system composed of: i) the Keggin POM $[PMo_{12}O_{40}]^{3-}$, ii) one and three acryloyloxyundecyltrimethyl ammonium bromide surfactant tails, and iii) 36 explicit water molecules, that was analyzed with DFT calculations, through a rather elaborate protocol. The computed non-covalent interaction energies among this Keggin POM, bromide ions, and the surfactant, as well as solvation energies provided insights into the bromide ion exchange process led by the POM. In another study, NLO properties were calculated in a POM cluster with attached polymeric chains as a pendant.[133] By creating a model system of one attached polymer chain with varying number of π-spacer units, time-dependent DFT calculations were performed to elucidate the structure/property relationship that leads to tuneable NLO properties.

2.3.5. Modeling POMs in Miscellaneous Soft Matter Environments

Although there are less examples, computational modeling has been also used to study the integration of POMs in lipid bilayer membranes and surfactants or to analyze self-aggregation processes. For example, a study from Aksimentiev and co-workers[134] made use of coarse-grained MD to propose a route

© 2022 Battelle Memorial Institute. Advanced Functional Materials published by Wiley-VCH GmbH

16163928, 2022, 51, Downloaded from https://advanced.onlinelibrary.wiley.com/doi/10.1002/adfm.202208428 by Universitatsbibliothek Mainz, Wiley Online Library on [04/06/2023]. See the Terms and Conditions (https://onlinelibrary.wiley.com/terms-and-conditions) on Wiley Online Library for rules of use; OA articles are governed by the applicable Creative Commons License

for spontaneous self-assembly of a POM nanocapsule into a phospholipid membrane. Polarz and colleagues[135] fabricated a novel surfactant by self-assembly of a Keggin-type polyoxometalate functionalized with anthraquinone via a π-conjugated chain. The supramolecular composite showed promising capabilities as an electron reservoir and frontier molecular orbitals were computed at the DFT level of theory to understand the electron confinement properties. In a recent study,[136] a surfactant-encapsulated POM was integrated into a polymerizable bicontinuous microemulsion to create a novel smart material for wastewater treatment. By using DFT QM/MM calculations, non-covalent binding energies between the POM and the surfactant tails were evaluated in order to analyze the stability of the supramolecular system.[136] Bo, Izzet and co-workers[137] prepared soft nanostructured materials through aggregation of dumbbell-like POM units joined by hybrid organic–inorganic linkers and DFT calculations were used to analyze the electronic configuration of the metal centers at the linkers; additional all-atom MD simulations provided further insights into the assembly mechanism.

3. Application-Driven POM-Soft Matter Composite Design

3.1. Stimuli-Responsive Materials and Sensing Applications

As described above, polyoxometalates are versatile compounds and of interest for various applications. It can be beneficial to enhance selectivity or tune solubility by combining POMs with stimuli-responsive materials such as polymers or biomolecules. In that way, a variety of different triggers can be used to activate specific properties of the POM that are required in different environments. The most common triggers for responsive materials are pH, heat, light and electricity. Due to their versatility, POMs can be responsive to all these triggers under suitable circumstances. With these different triggers, applications of responsive POM/organic hybrid systems in various fields such as theranostics,[138] sensors,[139] catalysis,[140] or redox systems[141] are possible. Decisive for the application of POMs in different soft matter matrices are the controlled accessibility of the POM and at the same time the sensible enhancement of the POM's properties.

For many applications the embedding of POMs in organic thin films is a suitable method. This provides a high stability of the resulting systems and functional polymers enhance the properties of the POMs. Different thin film formation methods are employed, including Langmuir–Blodgett deposition, spin-coating, as well as layer-by-layer (LbL) methods, where cationic and anionic layers are deposited in an alternating fashion (**Figure 9**a).[142] These deposition methods are ideally suited for the deposition of POMs and subsequent application in sensing and stimuli-responsive materials.[142] When integrated into electrochemical devices, redox-active POMs can be coupled to external electrical stimuli to trigger changes of their physicochemical properties, such as their redox-states. In one example, Volkmer and co-workers used LbL assembly to fabricate thin films containing the polycation poly(allylamine hydrochloride) (PAH) as positively charged layer and anionic layers composed of the polyanion poly(styrenesulfonate) (PSS) and the Preyssler-heteropolytungstate anion $[Eu(H_2O)P_5W_{30}O_{110}]^{12-}$.[143] Films with switchable electrochromism, short response times and high cyclic stability were reported.

Similar concepts have been used for the assembly of POM-based sensors, which often utilize the POM redox-activity to detect gases or toxins. In one example, Kurth and co-workers used LbL assembly to fabricate a POM-based sensor for nitrogen monoxide. To this end, alternating layers of the polyelectrolytes PSS and PAH were deposited on an ITO electrode, followed by the alternating adsorption of the cobalt containing Dawson based POM $[Co_4(H_2O)_2(P_2W_{15}O_{56})_2]^{16-}$ and PAH. The resulting multilayer assembly shows selective gas permeability and sensing selectivity. The deposition of a PSS/PAH/PSS surface layer was used to prevent anion (e.g., nitrite/nitrate) diffusion into the film, so as to prevent unwanted redox-reaction of the POM with these species. High sensitivity for NO detection (down to 1 nM) was reported.[147]

POMs can also be utilized in sensors by the embedding in thin films of conductive organic polymers. This allows substrates to access redox-active POMs that can be directly electrically addressed via the conductive polymer.[139] McCormac and colleagues prepared an electrochemical sensor for the detection of hydrogen peroxide based on a polypyrrole film with transition metal-substituted Dawson-POMs as dopant anions. These films were directly deposited on a glassy carbon electrode by electropolymerization from solutions containing pyrrole and the respective POM.[148]

Another approach to POM-based sensing materials is the use of lanthanide-functionalized POMs. These compounds can show excellent photoluminescent properties, such as long decay times and intense and sharp emission bands.[149] Wang and co-workers used the photoluminescent Preyssler anion $[EuP_5W_{30}O_{110}]^{12-}$ together with PAH for LbL film assembly.[150] Building on this principle, Ma, Yao, and colleagues immobilized Europium-containing polyoxometalates in agarose nanocomposite films to create photoluminescent sensors for gaseous acids and bases based on pH-dependent on/off switching of the europium-based red luminescence (Figure 9B).[145]

A related concept for the development of luminescent POM-polymer hybrids is the immobilization of POMs in hydrogels. This can lead to sensors with response mechanisms based on pH, light or humidity. Zhang, Wan, and co-workers used an ABA triblock copolymer and a $[Dy(W_5O_{18})_2]^{9-}$ POM for the reversible formation of a supramolecular hybrid hydrogel. The DMAEMA units of the hydrophilic $PDMAEMA_{35}$-*b*-PEO_{230}-*b*-$PDMAEMA_{35}$ triblock copolymer can be protonated. This has been used for the electrostatic co-assembly of protonated DMAEMA with anionic POMs. Notably, the emission behavior of the system changed significantly upon gelation, so that applications as smart, pH-sensitive materials can be envisaged.[75]

A similar approach has been established for carbon dioxide detection in solution using core-shell nanostructures based on PEO_{114}-*b*-$PDMAEMA_{16}$ diblock copolymers electrostatically functionalized with $Dy(W_5O_{18})_2]^{9-}$ POM. Also, here the DMAEMA units of the block copolymer are protonated during changes in pH. In this case, the pH change is induced by the acidic reaction of CO_2 in water. Due to the missing third block in the block copolymer, however, the mechanism for the change of fluorescence is different. The block copolymer and

© 2022 Battelle Memorial Institute. Advanced Functional Materials published by Wiley-VCH GmbH

ADVANCED SCIENCE NEWS
www.advancedsciencenews.com

ADVANCED FUNCTIONAL MATERIALS
www.afm-journal.de

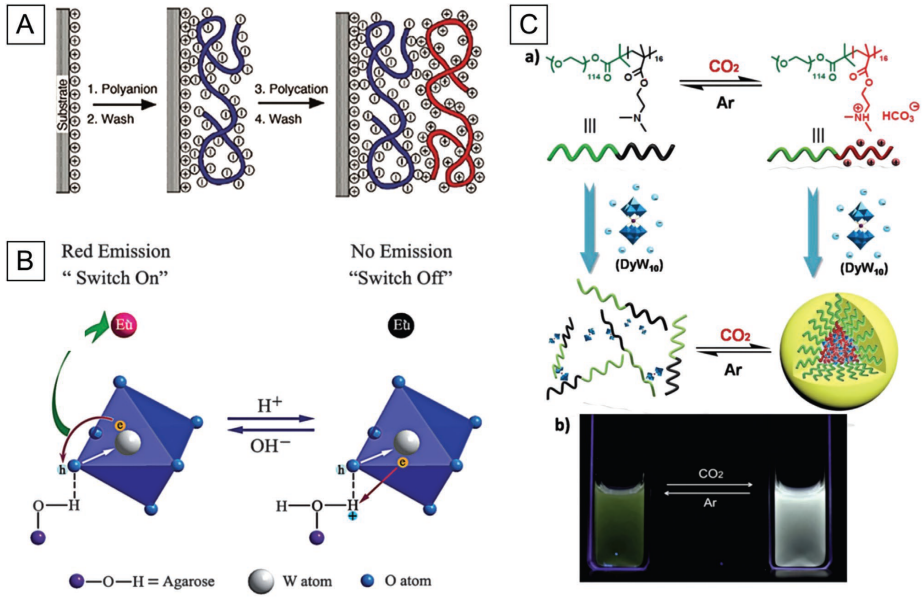


Figure 9. A) Working principle of the layer-by-layer deposition method. Reproduced with permission.[144] Copyright 1997, American Association for the Advancement of Science. B) Luminescent switch, illustration of the nanocomposite film ("e", electrons; "h", holes). Reproduced with permission.[145] Copyright 2010, RSC Publishing. C) Structural change of the PEO-*b*-PDMAEMA block copolymer and schematic representation of the reversible formation of a hybrid micelle after the reaction with CO_2 in aqueous medium. Reproduced with permission.[146] Copyright 2015, RSC Publishing.

the POM do not form hydrogels but complexes. When the pH is decreased by dissolved CO_2, the charged DMAEMA units assemble around the negatively charged POMs. This leads again to a change of the fluorescence color from weakly green to white. When the solution is then purged with inert gases, the CO_2 is removed from the solution, which leads to the disassembly of the complexes and the sensor can be used again (Figure 9C).[146]

3.2. . Biomedical Applications

POMs have been employed in a range of biomedical settings including antiviral, antimicrobial and anticancer applications.[31,151] However, for in vivo applications it is crucial to mediate their toxicity and increase the selectivity as well as their mode of action. Linking POMs to biologically inspired soft matter matrices is a method of choice to achieve these goals.

One approach has been reported by Wang and co-workers. The group combined POMs with lipids to generate liposome-encapsulated $[SiW_{11}TiO_{40}]^{6-}$. In these systems, the POMs were encapsulated in spherical lipid-bilayer vesicles (d = 15–60 snm), resulting in a significant drop in toxicity during in vivo anticancer studies. Further in vitro studies showed improved cell-membrane penetration and enhanced antitumor activity and stability in comparison to the pure POM.[152] Similar effects have also been reported when POMs were covalently attached to lipids. Liu and colleagues functionalized a Preyssler-POM with a long-chain organoalkoxysilane lipid. The amphiphilic POM hybrids spontaneously assembled into vesicles and exhibit significantly increased antitumor activity in comparison to the pure POMs. According to the authors, this difference is due to the improved cell-membrane binding and cell uptake of the functionalized POM (**Figure 10**A).[153]

A similar approach is the encapsulation of POM in chitosan, a polysaccharide copolymer of β-(1,4)-2-acetamido-D-glucose and β-(1,4)-2-amino-D-glucose. Chitosan is known to enhance in vivo drug delivery whilst reducing undesired side-effects.[37] These benefits have been explored in the encapsulation of POMs in chitosan matrixes, targeting bio-medical applications.[38] In one example, Nair and co-workers used a POM/chitosan hybrid as potential anti-cancer treatments. The group designed stable, monodisperse hybrid nanoparticles with a diameter of ≈200 nm by encapsulating the europium POM $[Cs{\subset}Eu_6As_6W_{63}O_{218}(H_2O)_{14}(OH)_4]^{25-}$ by a simple ionotropic gelation method. The hybrid was tested against a range of cancer cell-lines in vitro and showed a slow and sustained POM release, so that significantly lower doses of the hybrid were required (based in IC_{50} values) compared with the pure POM reference.[155]

© 2022 Battelle Memorial Institute. Advanced Functional Materials published by Wiley-VCH GmbH

10163928, 2022, 51, Downloaded from https://advanced.onlinelibrary.wiley.com/doi/10.1002/adfm.202208428 by Universitätsbibliothek Mainz, Wiley Online Library on [04/06/2025]. See the Terms and Conditions (https://onlinelibrary.wiley.com/terms-and-conditions) on Wiley Online Library for rules of use; OA articles are governed by the applicable Creative Commons License

ADVANCED SCIENCE NEWS
www.advancedsciencenews.com

ADVANCED FUNCTIONAL MATERIALS
www.afm-journal.de

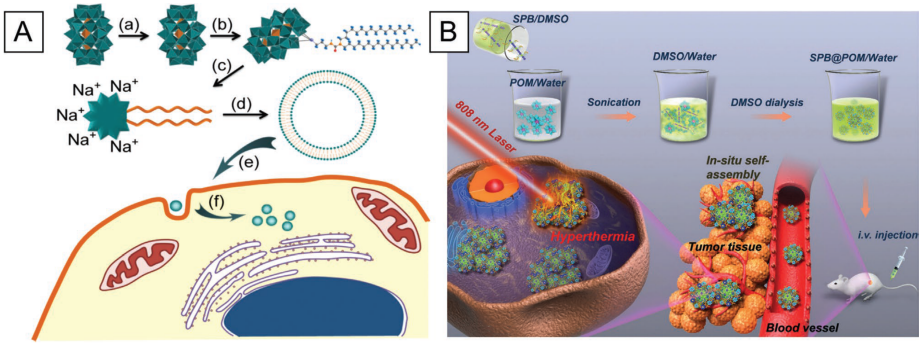


Figure 10. A: Illustration of the synthesis process of POM-based organic–inorganic hybrids, $[(C_{16}H_{33})_2NCONH(CH_2)_3SiNaP_5W_{29}O_{110}]^{14-}$ (Na-lipid-P_5W_{29}), and their vesicle formation in water/MeCN solution. The lacunary Preyssler-type ion, P_5W_{29}, is presented using a polyhedral model, and the organic part is presented using a ball and stick model (P, orange; W-O polyhedral, green; C, gray; N, yellow; H, blue; Si, purple). a) Synthesis of a lacunary Preyssler-type POM, b) covalent reaction between lacunary POM and organoalkoxysilane lipid, c) cation exchange, d) formation of micelles of Na-lipid-P_5W_{29}, e) entering the tumor cells, f) intracellular localization. Reproduced with permission[153] Copyright 2015, Wiley-VCH GmbH. B: Schematic of pH/GSH-responsive SPB@POM for tumor-specific self-assembly and phototheranostic enhancement. Reproduced with permission[154] Copyright 2018, Wiley-VCH GmbH.

A different approach to anti-tumor activity of POM-polymer hybrids has been reported by Wang, Chen and co-workers. The group used semiconducting polymer brushes and POM clusters that aggregated specifically to larger in the low pH, reducing microenvironment of a tumor. This led to enhanced retention of the particles in the tumor. Further, chemical reduction of the Mo-based POM resulted in enhanced NIR light absorption, enabling efficient use in hyperthermia-inducing photothermal therapy (Figure 10B).[154]

3.3. Molecular Electronics

The anchoring of electronically or magnetically active POMs[28,156,157] in functional polymers holds great promise for the design of unique composites, e.g., for molecular electronics, quantum computing, or spintronics. To-date, most studies in the field have focused on the deposition of POMs on metal or semiconductor surfaces, while POM-polymer composites have received little attention. This could in part be due to the challenging fabrication and processing of POM-polymer composites, particularly when sub-nanometer accuracy in the positioning of the POMs is required. For molecular electronics, this precision is needed, as electronic and magnetic interactions between neighboring POMs have major impact on their performance, e.g., in the context of the loss of information due to quantum decoherence effects.[28] In a pioneering example, Mallah, Wernsdorfer, Mialane, and co-workers embedded the single molecule magnet (SMM) POM $[Fe_4(H_2O)_2[FeW_9O_{34}]_2]^{10-}$ (= $[Fe_6W_{18}]$) into a gelatin biopolymer.[158] Magnetic analyses showed similar behavior between the pure POM compound, and the POM-gelatin-composite, highlighting that the sensitive magnetic properties of the POM were not affected by the (diamagnetic) gelatin matrix.

Redox-active POMs can also be used as reactive sites in molecular junctions, i.e., systems where molecules act as charge-transfer sites between two metal electrodes. Velessiotis, Glezos, and co-workers[159,160] demonstrated that POM-polymer composites can be used as active materials in molecular junctions. The group fabricated a PMMA-$[H_3PW_{12}O_{40}]$ composite and provided first insights into the electronic transport properties of the system. In particular, the authors report that POM-concentration as well as electrode geometry are two key factors for electron transport. Two distinct transport mechanisms (tunneling vs hopping) were reported depending on the electrode distances. The design of a POM-polymer composite for non-volatile, rewritable multilevel memories was reported by Zhang and colleagues.[161] The authors used Anderson-POMs covalently linked to the backbone of a PMMA polymer as active compound. The material showed three distinct redox states with long retention times. Resetting the material to enable re-writing was possible by careful choice of the redox potentials employed. Other POM-based applications in molecular electronics and related fields have recently been reviewed by Chen, Dong, and co-workers,[162] and Zhou, A. L. Roy, S.-T. Han, and co-workers.[163]

In summary, the use of POMs with controllable spin and/or redox states combined with the flexibility, processability and scalability of soft-matter polymers holds great promises to realize nanoscale devices for molecular electronics. Key for the further development is to understand how to control the POM distribution within such hybrid materials, ultimately tailoring the composite structure from nano- to microscale, as well as engineering robust and functional polymers that contribute to the device performance.

3.4. Solar and Electrochemical Energy Conversion, Catalysis

POM-polymer composites are key materials for energy conversion and storage, and have been used in batteries, supercapacitors, fuel cells, and electrocatalysis. The field has been reviewed recently, and is therefore not discussed in detail here.[139,164,165]

© 2022 Battelle Memorial Institute. Advanced Functional Materials published by Wiley-VCH GmbH

16163328, 2022, 51, Downloaded from https://advanced.onlinelibrary.wiley.com/doi/10.1002/adfm.202208428 by Universitatsbibliothek Mainz, Wiley Online Library on [04/06/2023]. See the Terms and Conditions (https://onlinelibrary.wiley.com/terms-and-conditions) on Wiley Online Library for rules of use; OA articles are governed by the applicable Creative Commons License

16163928, 2022, 51, Downloaded from https://advanced.onlinelibrary.wiley.com/doi/10.1002/adfm.202208428 by Universitätsbibliothek Mainz, Wiley Online Library on [14/06/2023]. See the Terms and Conditions (https://onlinelibrary.wiley.com/terms-and-conditions) on Wiley Online Library for rules of use; OA articles are governed by the applicable Creative Commons License

4. Outlook and Summary

POM-polymer composites are versatile materials merging the areas of organic and inorganic chemistry and overall benefit from improvements in both synthetic access to the respective building blocks as well as advances in analytical techniques. Over the last decades, they have opened new avenues to harness synergisms from these fields and develop applications in biomedicine, energy conversion/storage, molecular electronics, and other fields. Their characterization from the molecular to the macroscopic level is still challenging, and advanced methods are currently being developed to gain further understanding of the complex behavior of these systems, especially regarding a precise description of the surrounding of a single POM site within a given soft matter matrix, both from an experimental and a theoretical point of view. With that, it will be possible to address changes in reactivity or selectivity (e.g., in case of a catalytic process) upon matrix embedding of a given POM, or even to understand effects on long-term stability or cyclability if the soft matter environment provides local buffering, additional functional groups, or even competing ligands—the latter allowing for new and straightforward (covalent) anchoring strategies of suitable building blocks. In the future, the authors expect that combined experimental and theoretical studies will shed light on the correlation between structure, properties, and function, enabling the knowledge-based design of next-generation POM-polymer composites.

Acknowledgements

J.K. and M.L. contributed equally to this work. Financial support by the Deutsche Forschungsgemeinschaft DFG via the SFB/TRR 234 "CataLight" (projects A4, A5, B3, B5, C3; funding ID 364549901) is gratefully acknowledged. C.S. gratefully acknowledges funding by Ulm University, Johannes Gutenberg University Mainz, the Gutenberg Research College Mainz, and the Rheinland-Pfalz Research Initiative SusInnoScience. L.G. gratefully acknowledges financial support by the Austrian Science Fund FWF (project nos. I3987-N28, I611).

Conflict of Interest

The authors declare no conflict of interest.

Keywords

organic–inorganic hybrids, polymers, polyoxometalates, self-assemblies

Received: July 22, 2022
Revised: August 17, 2022
Published online: October 31, 2022

[1] L. A. Estroff, *Chem. Rev.* **2008**, *108*, 4329.
[2] R. L. Truby, J. A. Lewis, *Nature* **2016**, *540*, 371.
[3] A. C. Balazs, T. Emrick, T. P. Russell, *Science* **2006**, *314*, 1107.
[4] P. De Gennes, *Angew Chem Int Ed Engl* **1992**, *31*, 842.
[5] R. A. L. Jones, *Soft Condensed Matter*, Oxford University Press, New York **2002**.
[6] C. M. Bates, F. S. Bates, *Macromolecules* **2017**, *50*, 3.
[7] M. Szwarc, M. Levy, R. Milkovich, *J. Am. Chem. Soc.* **1956**, *78*, 2656.
[8] K. Ziegler, *Rubber Chem. Technol.* **1965**, *38*, 23.
[9] J. Pyun, K. Matyjaszewski, *Chem. Mater.* **2001**, *13*, 3436.
[10] F. S. Bates, G. H. Fredrickson, *Phys. Today* **1999**, *52*, 32.
[11] M. Wei, Y. Gao, X. Li, M. J. Serpe, *Polym. Chem.* **2017**, *8*, 127.
[12] M. A. C. Stuart, W. T. S. Huck, J. Genzer, M. Müller, C. Ober, M. Stamm, G. B. Sukhorukov, I. Szleifer, V. V. Tsukruk, M. Urban, F. Winnik, S. Zauscher, I. Luzinov, S. Minko, *Nat. Mater.* **2010**, *9*, 101.
[13] J. Livage, *Transition Metal Oxide Gels*, Springer, Netherlands, Dordrecht **1985**.
[14] L. Nicole, L. Rozes, C. Sanchez, *Adv. Mater.* **2010**, *22*, 3208.
[15] A. Corma, M. T. Navarro, J. P. Pariente, *J Chem Soc Chem Commun* **1994**, 147.
[16] D. Mathew, B. Thomas, K. S. Devaky, *Artif Cells Nanomed Biotechnol* **2019**, *47*, 1149.
[17] H. Rothfuss, N. D. Knöfel, P. W. Roesky, C. Barner-Kowollik, *J. Am. Chem. Soc.* **2018**, *140*, 5875.
[18] Y. Lu, Y. Mei, M. Drechsler, M. Ballauff, *Angew. Chem., Int. Ed.* **2006**, *45*, 813.
[19] G. L.a Sorella, G. Strukul, A. Scarso, *Green Chem.* **2015**, *17*, 644.
[20] M. T. Pope, *Heteropoly and Isopoly Oxometalates* **1983**.
[21] L. Cronin, A. Müller, *Chem. Soc. Rev.* **2012**, *41*, 7325.
[22] U. Kortz, T. Liu, *Eur. J. Inorg. Chem.* **2013**, *2013*, 1556.
[23] A. Kondinski, T. N. Parac-Vogt, *Front Chem* **2018**, *6*, 346.
[24] C. L. Hill, C. M. Prosser-McCartha, *Coord. Chem. Rev.* **1995**, *143*, 407.
[25] C. Streb, *Dalton Trans.* **2012**, *41*, 1651.
[26] Y. Ji, L. Huang, J. Hu, C. Streb, Y. Song, *Energy Environ. Sci.* **2015**, *8*, 776.
[27] A. Müller, P. Kögerler, *Coord. Chem. Rev.* **1999**, *182*, 3.
[28] J. M. Clemente-Juan, E. Coronado, A. Gaita-Ariño, *Chem. Soc. Rev.* **2012**, *41*, 7464.
[29] A. Bijelic, M. Aureliano, A. Rompel, *Angew. Chem., Int. Ed.* **2019**, *58*, 2980.
[30] K. Stroobants, E. Moelants, H. G. T. Ly, P. Proost, K. Bartik, T. N. Parac-Vogt, *Chem. Eur. J.* **2013**, *19*, 2848.
[31] M. B. Čolović, M. Lacković, J. Lalatović, A. S. Mougharbel, U. Kortz, D. Z. Krstić, *Curr. Med. Chem.* **2020**, *27*, 362.
[32] A. Proust, B. Matt, R. Villanneau, G. Guillemot, P. Gouzerh, G. Izzet, *Chem. Soc. Rev.* **2012**, *41*, 7605.
[33] A. V. Anyushin, A. Kondinski, T. N. Parac-Vogt, *Chem. Soc. Rev.* **2020**, *49*, 382.
[34] I. V. Kozhevnikov, *Chem. Rev.* **1998**, *98*, 171.
[35] A. Sartorel, M. Carraro, F. M. Toma, M. Prato, M. Bonchio, *Energy Environ. Sci.* **2012**, *5*, 5592.
[36] H. Lv, Y. V. Geletii, C. Zhao, J. W. Vickers, G. Zhu, Z. Luo, J. Song, T. Lian, D. G. Musaev, C. L. Hill, *Chem. Soc. Rev.* **2012**, *41*, 7572.
[37] A. Misra, K. Kozma, C. Streb, M. Nyman, *Angew. Chem., Int. Ed.* **2020**, *59*, 596.
[38] A. S. Cherevan, S. P. Nandan, I. Roger, R. Liu, C. Streb, D. Eder, *Adv. Sci.* **2020**, *7*, 1903511.
[39] M. H. Anjass, M. Deisböck, S. Greiner, M. Fichtner, C. Streb, *ChemElectroChem* **2019**, *6*, 398.
[40] D. Gao, I. Trentin, L. Schwiedrzik, L. González, C. Streb, *Molecules* **2020**, *25*, 157.
[41] S. S. Saidkhanov, A. I. Kokorin, E. N. Savinov, A. I. Vokov, V. N. Parmon, **1983**, *21*, 365.
[42] W.-K. Miao, Y.-K. Yan, X.-L. Wang, Y. Xiao, L.-J. L.-X. Ren, P. Zheng, C.-H. Wang, L.-J. L.-X. Ren, W. Wang, *ACS Macro Lett.* **2014**, *3*, 211.
[43] A. Pardiwala, S. Kumar, R. Jangir, *Dalton Trans.* **2022**, *51*, 4945.
[44] R. Jangir, R. Antony, R. Murugavel, *New J. Chem.* **2016**, *40*, 1004.
[45] H. Wu, H.-K. Yang, W. Wang, *New J. Chem.* **2016**, *40*, 886.

© 2022 Battelle Memorial Institute. Advanced Functional Materials published by Wiley-VCH GmbH

[46] S. Chakraborty, A. Keightley, V. Dusevich, Y. Wang, Z. Peng, *Chem. Mater.* **2010**, *22*, 3995.
[47] P. Judeinstein, *Chem. Mater.* **1992**, *4*, 4.
[48] U. Tong, W. Chen, C. Ritchie, X. Wang, Y. Song, *Chem. - Eur. J.* **2014**, *20*, 1500.
[49] A. Macdonell, N. A. B. Johnson, A. J. Surman, L. Cronin, *J. Am. Chem. Soc.* **2015**, *137*, 5662.
[50] Y. Han, Y. Xiao, Z. Zhang, B. Liu, P. Zheng, S. He, W. Wang, *Macromolecules* **2009**, *42*, 6543.
[51] J. Lesage De La Haye, P. Beaunier, L. Ruhlmann, B. Hasenknopf, E. Lacôte, J. Rieger, *ChemPlusChem* **2014**, *79*, 250.
[52] M. V. Vasylyev, S. Gatard, I. Bar-Nahum, L. Konstantinovski, E. J. Wachtel, R. Neumann, *J Clust Sci* **2006**, *17*, 235.
[53] H. Zeng, G. R. Newkome, C. L. Hill, *Angew. Chem., Int. Ed.* **2000**, *39*, 1771.
[54] M. Ammam, *J. Mater. Chem. A* **2013**, *1*, 6291.
[55] T. Lunkenbein, M. Kamperman, Z. Li, C. Bojer, M. Drechsler, S. Fo, U. Wiesner, A. H. E. Müller, J. Breu, *J. Am. Chem. Soc.* **2012**, *134*, 12685.
[56] E. Fontananova, L. Donato, E. Drioli, L. C. Lopez, P. Favia, R. Agostino, *Chem. Mater.* **2006**, *18*, 1561.
[57] Azizullah, M. A.l-R. , A. Haider, U. Kortz, S. A. Joshi, J. Iqbal, *ChemistrySelect* **2018**, *3*, 1472.
[58] H. Yun, M. Kuwabara, H. Zhou, I. Honma, *Thin Solid Films* **2007**, *515*, 2842.
[59] I. Romanenko, M. Lechner, F. Wendler, C. Hörenz, C. Streb, F. H. Schacher, *J. Mater. Chem. A* **2017**, *5*, 15789.
[60] D. Li, X. Jia, X. Cao, T. Xu, H. Li, H. Qian, L. Wu, *Macromolecules* **2015**, *48*, 4104.
[61] Y. Leng, P. Jiang, J. Wang, *Catal. Commun.* **2012**, *25*, 41.
[62] H. Yang, B. Jiang, Y. Sun, L. Zhang, Z. Huang, Z. Sun, N. Yang, *J. Hazard. Mater.* **2017**, *333*, 63.
[63] M. Blasco-Ahicart, J. Soriano-López, J. R. Galán-Mascarós, *ChemElectroChem* **2017**, *4*, 3296.
[64] M. A. Rezvani, M. A. N. Asli, M. Oveisi, R. Babaei, K. Qasemi, S. Khandan, *RSC Adv.* **2016**, *6*, 53069.
[65] D. Li, J. Wei, S. Dong, H. Li, Y. Xia, X. Jiao, T. Wang, D. Chen, *ACS Appl. Mater. Interfaces* **2018**, *10*, 1701.
[66] K. P. Sullivan, W. A. Neiwert, H. Zeng, A. K. Mehta, Q. Yin, D. A. Hillesheim, S. Vivek, P. Yin, D. L. Collins-Wildman, E. R. Weeks, T. Liu, C. L. Hill, *Chem. Commun.* **2017**, *53*, 11480.
[67] B. B. Xu, B. B. Xu, M. Lu, M. Lu, J. H. Kang, J. H. Kang, D. Wang, D. Wang, J. Brown, J. Brown, Z. H. Peng, Z. H. Peng, *Chem. Mater.* **2005**, *17*, 2841.
[68] S. Ma, J. Meng, J. Li, Y. Zhang, L. Ni, *J Memb Sci* **2014**, *453*, 221.
[69] S. Aguado-Ureta, J. Rodríguez-Hernández, A. del Campo, L. Perez-Álvarez, L. Ruiz-Rubio, J. L. Vilas, B. Artetxe, S. Reinoso, J. M. Gutiérrez-Zorrilla, *Nanomaterials* **2018**, *8*, 142.
[70] S. Herrmann, N. Aydemir, F. Nägele, D. Fantauzzi, T. Jacob, J. T. Sejdic, C. Streb, *Adv. Funct. Mater.* **2017**, *27*, 1700881.
[71] L. Ruiz-Rubio, B. Artetxe, L. Perez-Álvarez, J. Martín-Caballero, T. Ishihara, J. M. Gutiérrez-Zorrilla, J. L. Vilas-Vilela, *Molecules* **2019**, *24*, 2313.
[72] L. C. Lopez, M. G. Buonomenna, E. Fontananova, G. Iacoviello, E. Drioli, R. D`Agostino, P. Favia, *Adv. Funct. Mater.* **2006**, *16*, 1417.
[73] Y. M. A. Yamada, H. Tabata, M. Ichinohe, H. Takahashi, S. Ikegami, *Tetrahedron* **2004**, *60*, 4087.
[74] I. Bazzan, P. Bolle, O. Oms, H. Salmi, N. Aubry-Barroca, A. Dolbecq, H. Serier-Brault, R. Dassapt, P. Roger, P. Mialane, *J. Mater. Chem. C* **2017**, *5*, 6343.
[75] H. Wei, N. Shi, J. Zhang, Y. Guan, J. Zhang, X. Wan, *Chem. Commun.* **2014**, *50*, 9333.
[76] M. Lu, B. Xie, J. Kang, F. C. Chen, Y. Yang, Z. Peng, *Chem. Mater.* **2005**, *17*, 402.
[77] M. A. Rezvani, N. Khalafi, *Mater Today Commun* **2020**, *22*, 100730.
[78] M. Bonchio, M. Carraro, M. Gardan, G. Scorrano, E. Drioli, E. Fontananova, *Top. Catal.* **2006**, *40*, 133.
[79] I. Romanenko, A. Rajagopal, C. Neumann, A. Turchanin, C. Streb, F. H. Schacher, *J. Mater. Chem. A* **2020**, *8*, 6238.
[80] M. Ghali, C. Brahmi, M. Benltifa, F. Dumur, S. Duval, C. Simonnet-Jégat, F. Morlet-Savary, S. Jellali, L. Bousselmi, J. Lalevée, *J. Polym. Sci. Part A Polym. Chem.* **2019**, *57*, 1538.
[81] Y. Li, K. Shetye, K. Baral, L. Jin, J. D. Oster, D. Zhu, Z. Peng, *RSC Adv.* **2016**, *6*, 29909.
[82] E. Broćławik, T. Borowski, M. Radoń, in *Transition Metals in Coordination Environments*, (Eds.: E. Broclawik, T. Borowski, M. Radoń), Springer International Publishing, Cham **2019**, p. 1.
[83] X. López, P. Miró, J. J. Carbó, A. Rodríguez-Fortea, C. Bo, J. M. Poblet, *Theor. Chem. Acc.* **2011**, *128*, 393.
[84] X. López, J. J. Carbó, C. Bo, J. M. Poblet, *Chem. Soc. Rev.* **2012**, *41*, 7537.
[85] W. Koch, M. C. Holthausen, *A Chemist's Guide to Density Functional Theory*, John Wiley & Sons, Weinheim **2015**.
[86] S. Schönweiz, M. Heiland, M. Anjass, T. Jacob, S. Rau, C. Streb, *Chemistry* **2017**, *23*, 15370.
[87] J. Du, Z. L. Lang, Y. Y. Ma, H. Q. Tan, B. L. Liu, Y. H. Wang, Z. H. Kang, Y. G. Li, *Chem. Sci.* **2020**, *11*, 3007.
[88] G. Cárdenas, I. Trentin, L. Schwiedrzik, D. Hernández-Castillo, G. A. Lowe, J. Kund, C. Kranz, S. Klingler, R. Stach, B. Mizaikoff, P. Marquetand, J. J. Nogueira, C. Streb, L. González, *Chem. Sci.* **2021**, *12*, 12918.
[89] E. Falbo, C. D. Rankine, T. J. Penfold, *Chem. Phys. Lett.* **2021**, *780*, 138893.
[90] L. Lin, L. Gao, K. Xie, R. Jiang, S. Lin, *Phys. Chem. Chem. Phys.* **2020**, *22*, 7234.
[91] Z. L. Lang, G. C. Yang, N. N. Ma, S. Z. Wen, L. K. Yan, W. Guan, Z. M. Su, *Dalton Trans.* **2013**, *42*, 10617.
[92] T. T. Mihaylov, H. G. T. Ly, K. Pierloot, T. N. Parac-Vogt, *Inorg. Chem.* **2016**, *55*, 9316.
[93] A. Al-Yasari, N. Van Steerteghem, H. Kearns, H. El Moll, K. Faulds, J. A. Wright, B. S. Brunschwig, K. Clays, J. Fielden, *Inorg. Chem.* **2017**, *56*, 10181.
[94] A. Al-Yasari, P. Spence, H. El Moll, N. Van Steerteghem, P. N. Horton, B. S. Brunschwig, K. Clays, J. Fielden, *Dalton Trans.* **2018**, *47*, 10415.
[95] A. Al-Yasari, H. El Moll, R. Purdy, K. B. Vincent, P. Spence, J. P. Malval, J. Fielden, *Phys. Chem. Chem. Phys.* **2021**, *23*, 11807.
[96] H. M. Senn, W. Thiel, *Angew. Chem., Int. Ed.* **2009**, *48*, 1198.
[97] J. Frank, *Introduction to Computational Chemistry*, Wiley-VCH, Weinheim **2017**.
[98] W. G. Noid, *J. Chem. Phys.* **2013**, *139*, 090901.
[99] H. I. Ingólfsson, C. A. Lopez, J. J. Uusitalo, D. H. de Jong, S. M. Gopal, X. Periole, S. J. Marrink, *Wiley Interdiscip Rev Comput Mol Sci* **2014**, *4*, 225.
[100] R. Dias, W. de AzevedoJr, *Curr. Drug Targets* **2008**, *9*, 1040.
[101] N. Liguori, R. Croce, S. J. Marrink, S. Thallmair, *Photosynth. Res.* **2020**, *144*, 273.
[102] Y. Minenkov, D. I. Sharapa, L. Cavallo, *J. Chem. Theory Comput.* **2018**, *14*, 3428.
[103] M. Bursch, A. Hansen, P. Pracht, J. T. Kohn, S. Grimme, *Phys. Chem. Chem. Phys.* **2021**, *23*, 287.
[104] S. Grimme, J. G. Brandenburg, C. Bannwarth, A. Hansen, *J. Chem. Phys.* **2015**, *143*, 054107.
[105] S. Grimme, C. Bannwarth, P. Shushkov, *J. Chem. Theory Comput.* **2017**, *13*, 1989.
[106] J. G. Brandenburg, C. Bannwarth, A. Hansen, S. Grimme, *J. Chem. Phys.* **2018**, *148*, 064104.
[107] S. Grimme, A. Hansen, S. Ehlert, J. M. Mewes, *J. Chem. Phys.* **2021**, *154*, 064103.
[108] C. Bannwarth, E. Caldeweyher, S. Ehlert, A. Hansen, P. Pracht, J. Seibert, S. Spicher, S. Grimme, *WIREs Comput. Mol. Sci.* **2021**, *11*, e1493.

© 2022 Battelle Memorial Institute. Advanced Functional Materials published by Wiley-VCH GmbH

16163928, 2022, 51, Downloaded from https://advanced.onlinelibrary.wiley.com/doi/10.1002/adfm.202208428 by Universitatsbibliothek Mainz, Wiley Online Library on [04/06/2023]. See the Terms and Conditions (https://onlinelibrary.wiley.com/terms-and-conditions) on Wiley Online Library for rules of use; OA articles are governed by the applicable Creative Commons License

[109] X. López, L. Vilà-Nadal, X. Aparicio-Anglès, J. M. Poblet, *Phys Procedia* **2010**, *8*, 94.
[110] Y. Nishimoto, D. Yokogawa, H. Yoshikawa, K. Awaga, S. Irle, *J. Am. Chem. Soc.* **2014**, *136*, 9042.
[111] S. Mai, M. Holzer, A. Andreeva, L. González, *Chem. – A Eur. J.* **2021**, *27*, 17066.
[112] L. Schwiedrzik, V. Brieskorn, L. González, *ACS Catal.* **2021**, *11*, 13320.
[113] B. Schwarz, J. Forster, M. K. Goetz, D. Yücel, C. Berger, T. Jacob, C. Streb, *Angew. Chem., Int. Ed.* **2016**, *55*, 6329.
[114] S. Mai, L. González, *Angew. Chem., Int. Ed.* **2020**, *59*, 16832.
[115] X. López, C. De Graaf, J. M. Maestre, M. Bénard, M. M. Rohmer, C. Bo, J. M. Poblet, *J. Chem. Theory Comput.* **2005**, *1*, 856.
[116] D. Aravena, D. Venegas-Yazigi, E. Ruiz, *Inorg. Chem.* **2016**, *55*, 6405.
[117] L. Noodleman, *J. Chem. Phys.* **1981**, *74*, 5737.
[118] L. Noodleman, E. R. Davidson, *Chem. Phys.* **1986**, *109*, 131.
[119] J. M. Maestre, X. Lopez, C. Bo, J. M. Poblet, N. Casañ-Pastor, *J. Am. Chem. Soc.* **2001**, *123*, 3749.
[120] B. Yin, G. Xue, J. Li, L. Bai, Y. Huang, Z. Wen, Z. Jiang, *J Mol Model* **2012**, *18*, 2271.
[121] J. L. Bouvard, D. K. Ward, D. Hossain, S. Nouranian, E. B. Marin, M. F. Horstemeyer, *J Eng Mater Technol* **2009**, *131*, 0412061.
[122] C. Bolm, N. Derrien, A. Seger, *Chem. Commun.* **1999**, *0*, 2087.
[123] D. Volkmer, B. Bredenkötter, J. Tellenbröker, P. Kögerler, D. G. Kurth, P. Lehmann, H. Schnablegger, D. Schwahn, M. Piepenbrink, B. Krebs, *J. Am. Chem. Soc.* **2002**, *124*, 10489.
[124] R. Brodbeck, T. Tönsing, D. Andrae, D. Volkmer, *J. Phys. Chem. B* **2008**, *112*, 5153.
[125] R. Brodbeck, D. Andrae, *High Performance Computing in Science and Engineering, Garching/Munich 2007*, Eds.: S. Wagner, M. Steinmetz, A. Bode, M. Brehm, Springer, Berlin, Heidelberg **2009**, pp. 129–142.
[126] Y. Liu, S. V. Sambasivarao, J. L. Horan, Y. Yang, C. M. Maupin, A. M. Herring, *J. Phys. Chem. C* **2014**, *118*, 854.
[127] S. V. Sambasivarao, Y. Liu, J. L. Horan, S. Seifert, A. M. Herring, C. M. Maupin, *J. Phys. Chem. C* **2014**, *118*, 20193.
[128] S. Akbari, M. T. Hamed Mosavian, F. Moosavi, A. Ahmadpour, *Compos. Part B Eng.* **2019**, *161*, 402.
[129] S. Akbari, M. T. H. Mosavian, F. Moosavi, A. Ahmadpour, *Phys. Chem. Chem. Phys.* **2019**, *21*, 25080.
[130] M. A. Lill, V. Helms, *J. Chem. Phys.* **2001**, *115*, 7993.
[131] F. R. Xu, R. Shi, X. M. Jia, S. C. Chai, H. L. Li, H. J. Qian, Z. Y. Lu, *Soft Matter* **2021**, *17*, 5897.
[132] G. De Luca, F. Bisignano, A. Figoli, F. Galiano, E. Furia, R. Mancuso, O. Saoncella, M. Carraro, M. Bonchio, B. Gabriele, *J. Phys. Chem. B* **2014**, *118*, 2396.
[133] M. R. S. A. Janjua, M. U. Khan, B. Bashir, M. A. Iqbal, Y. Song, S. A. R. Naqvi, Z. A. Khan, *Comput. Theor. Chem.* **2012**, *994*, 34.
[134] R. Carr, I. A. Weinstock, A. Sivaprasadarao, A. Müller, A. Aksimentiev, *Nano Lett.* **2008**, *8*, 3916.
[135] A. Klaiber, T. Kollek, S. Cardinal, N. Hug, M. Drechsler, S. Polarz, *Adv. Mater. Interfaces* **2018**, *5*, 1701430.
[136] F. Galiano, R. Mancuso, M. Carraro, J. Bundschuh, J. Hoinkis, M. Bonchio, G. De Luca, B. Gabriele, A. Figoli, *Appl. Mater. Today* **2021**, *23*, 101002.
[137] M. S. Centellas, M. Piot, R. Salles, A. Proust, L. Tortech, D. Brouri, S. Hupin, B. Abécassis, D. Landy, C. Bo, G. Izzet, *Chem. Sci.* **2020**, *11*, 11072.
[138] Z. Zhang, L. Zhou, Y. Zhou, J. Liu, X. Xing, J. Zhong, G. Xu, Z. Kang, J. Liu, *Biomaterials* **2015**, *65*, 56.
[139] S. Herrmann, C. Ritchie, C. Streb, *Dalton Trans.* **2015**, *44*, 7092.
[140] A. Nisar, Y. Lu, J. Zhuang, X. Wang, *Angew. Chem., Int. Ed.* **2011**, *50*, 3187.
[141] Y. Yan, B. Li, Q. He, Z. He, H. Ai, H. Wang, Z. Yin, L. Wu, *Soft Matter* **2012**, *8*, 1593.
[142] S.-M. Wang, J. Hwang, E. Kim, *J. Mater. Chem. C* **2019**, *7*, 7828.
[143] S. Liu, D. G. Kurth, H. Möhwald, D. Volkmer, *Adv. Mater.* **2002**, *14*, 225.
[144] G. Decher, *Science* **1997**, *277*, 1232.
[145] Z. Wang, R. Zhang, Y. Ma, A. Peng, H. Fu, J. Yao, *J. Mater. Chem.* **2010**, *20*, 271.
[146] H. Wei, J. Zhang, N. Shi, Y. Liu, B. Zhang, J. Zhang, X. Wan, *Chem. Sci.* **2015**, *6*, 7201.
[147] S. Liu, D. Volkmer, D. G. Kurth, *Anal. Chem.* **2004**, *76*, 4579.
[148] N. Anwar, M. Vagin, F. Laffir, G. Armstrong, C. Dickinson, T. McCormac, *Analyst* **2012**, *137*, 624.
[149] J. Zhang, Y. Liu, Y. Li, H. Zhao, X. Wan, *Angew. Chem., Int. Ed.* **2012**, *51*, 4598.
[150] L. Xu, H. Zhang, E. Wang, D. G. Kurth, Z. Li, *J. Mater. Chem.* **2002**, *12*, 654.
[151] A. Bijelic, A. Rompel, M. Aureliano, *Angew Chem Int Ed Engl* **2019**, *58*, 2980.
[152] X. Wang, F. Li, S. Liu, M. T. Pope, *J. Inorg. Biochem.* **2005**, *99*, 452.
[153] L. Fu, H. Gao, M. Yan, S. Li, X. Li, Z. Dai, S. Liu, *Small* **2015**, *11*, 2938.
[154] Z. Yang, W. Fan, W. Tang, Z. Shen, Y. Dai, J. Song, Z. Wang, Y. Liu, L. Lin, L. Shan, Y. Liu, O. Jacobson, P. Rong, W. Wang, X. Chen, *Angew. Chem., Int. Ed.* **2018**, *57*, 14101.
[155] D. Menon, R. T. Thomas, S. Narayanan, S. Maya, R. Jayakumar, F. Hussain, V.-K. Lakshmanan, S. V. Nair, *Carbohydr. Polym.* **2011**, *84*, 887.
[156] C. Boskovic, *Acc. Chem. Res.* **2017**, *50*, 2205.
[157] E. Coronado, *Nat. Rev. Mater.* **2020**, *5*, 87.
[158] W. Salomon, Y. Lan, E. Rivière, S. Yang, C. Roch-Marchal, A. Dolbecq, C. Simonnet-Jégat, N. Steunou, N. Leclerc-Laronze, L. Ruhlmann, T. Mallah, W. Wernsdorfer, P. Mialane, *Chem. - Eur. J.* **2016**, *22*, 6564.
[159] D. Velessiotis, N. Glezos, V. Ioannou-Sougleridis, *J. Appl. Phys.* **2005**, *98*, 084503.
[160] N. Glezos, P. Argitis, D. Velessiotis, C. D. Diakoumakos, *Appl. Phys. Lett.* **2003**, *83*, 488.
[161] B. Hu, C. Wang, J. Wang, J. Gao, K. Wang, J. Wu, G. Zhang, W. Cheng, B. Venkateswarlu, M. Wang, P. S. Lee, Q. Zhang, *Chem. Sci.* **2014**, *5*, 3404.
[162] L. Yang, J. Lei, J. M. Fan, R. M. Yuan, M. Sen Zheng, J. J. Chen, Q. F. Dong, *Adv. Mater.* **2021**, *33*, 2005019.
[163] X. Chen, Y. Zhou, V. A. L. Roy, S.-T. Han, *Adv. Mater.* **2018**, *30*, 1703950.
[164] M. R. Horn, A. Singh, S. Alomari, S. Goberna-Ferrón, R. Benages-Vilau, N. Chodankar, N. Motta, K. (Ken) Ostrikov, J. MacLeod, P. Sonar, P. Gomez-Romero, D. Dubal, *Energy Environ. Sci.* **2021**, *14*, 1652.
[165] M. Genovese, K. Lian, *Curr. Opin. Solid State Mater. Sci.* **2015**, *19*, 126.

© 2022 Battelle Memorial Institute. Advanced Functional Materials published by Wiley-VCH GmbH

16163028, 2022, 51, Downloaded from https://advanced.onlinelibrary.wiley.com/doi/10.1002/adfm.202208428 by Universitätsbibliothek Mainz, Wiley Online Library on [14/06/2025]. See the Terms and Conditions (https://onlinelibrary.wiley.com/terms-and-conditions) on Wiley Online Library for rules of use; OA articles are governed by the applicable Creative Commons License



Felix H. Schacher studied chemistry at the Universities of Bayreuth (Germany) and Lund (Sweden) and obtained his PhD in 2009. After joining the University of Bristol as DAAD postdoctoral fellow, he was appointed junior professor at the Friedrich-Schiller-Universität Jena in 2010 and became Full Professor at this institution in 2015. His scientific interests include controlled/living polymerization techniques, block copolymers, polyelectrolytes, and polyampholytes—all in the context of self-assembly processes for material design in the fields of membranes, hybrid materials, and biomedicine.



Carsten Streb is Professor for Inorganic Chemistry at Johannes Gutenberg University Mainz. His research interests are focused on designing polyoxometalate-based materials and composites to address global challenges in energy, catalysis, sustainability, and public health.

© 2022 Battelle Memorial Institute. Advanced Functional Materials published by Wiley-VCH GmbH

16163028, 2022, 51, Downloaded from https://advanced.onlinelibrary.wiley.com/doi/10.1002/adfm.202208428 by Universitatsbibliothek Mainz, Wiley Online Library on [04/06/2023]. See the Terms and Conditions (https://onlinelibrary.wiley.com/terms-and-conditions) on Wiley Online Library for rules of use; OA articles are governed by the applicable Creative Commons License

6.2 {MLa-2}: Multimodal Analysis of Light-Driven Water Oxidation in Nanoporous Block Copolymer Membranes

Julian Kund,‡ Jan-Hendrik Kruse,‡ Andreas Gruber, Ivan Trentin, Marcel Langer, Clarissa Read, Gregor Neusser, Dominik Blaimer, Ulrich Rupp, Carsten Streb,* Kerstin Leopold, Felix H. Schacher,* and Christine Kranz*

‡ *Authors contributed equally to this work*

* *Corresponding authors*

Abstract: Nanoporous block copolymer membranes functionalized with the OEC $\{Co_4\}$ and the PS $[Ru(bpy)_3]^{2+}$ by non-covalent interactions were investigated for their activity in light-driven WOC. Time-resolved *operando* SECM measurements were performed to assess their functionality. The stability and spatial distribution of the molecular components within the membrane before and after catalysis were thoroughly examined using *ex situ* μXRF, TXRF, STEM/EDX, HR-CS-GFAAS and ATR-FTIR analyses.

Published in: *Angew. Chem. Int. Ed.* **2023**, *62*, e202217196.

Status: Published

Copyright: Reprinted with permission from "Multimodal Analysis of Light-Driven Water Oxidation in Nanoporous Block Copolymer Membranes", J. Kund,‡ J.-H. Kruse,‡ A. Gruber, I. Trentin, M. Langer, C. Read, G. Neusser, D. Blaimer, U. Rupp, C. Streb,* K. Leopold, F. H. Schacher,* and C. Kranz,* *Angew. Chem. Int. Ed.* **2023**, *62*, e202217196. **DOI:** 10.1002/anie.202217196.

© 2023, The Authors, Angewandte Chemie International Edition published by Wiley-VCH GmbH under the terms of the CC BY-NC 4.0 license.

Author Contributions:

J. Kund	Performing *operando* SECM experiments; Design of the electrochemical flow cell; Conducting ATR-IR experiments; Discussion of results; Writing, discussion and revision of the manuscript.
J.-H. Kruse	Synthesis and characterization of the block copolymer; Fabrication of the block copolymer membrane; Conducting TGA, SEC and NMR analyses; Writing the synthesis part of the manuscript; Revision of the manuscript.
A. Gruber	Conducting μXRF and TXRF experiments; Data analysis; Writing the corresponding part of the manuscript; Revision of the manuscript.
I. Trentin	Membrane functionalization.
M. Langer	Synthesis and characterization of {Co_4}; Functionalization of the membrane; Discussion of results, including the evaluation of POM degradation; Revision of the manuscript.
C. Read	TEM and STEM/EDX analyses.
G. Neusser	TEM and STEM/EDX analyses.
D. Blaimer	HR-CS-GFAAS measurements.
U. Rupp	TEM and STEM/EDX analyses.
C. Streb	Conceptualization; Supervision; Discussion of the results; Revision of the manuscript.
K. Leopold	Conceptualization; Supervision; Discussion of the results; Revision of the manuscript.
F. H. Schacher	Conceptualization; Supervision; Discussion of the results; Revision of the manuscript.
C. Kranz	Conceptualization; Supervision; Discussion of the results; Writing, discussion and revision of the manuscript.

GDCh Research Articles Angewandte International Edition Chemie www.angewandte.org

Check for updates

How to cite: *Angew. Chem. Int. Ed.* **2023,** *62,* e202217196
International Edition: doi.org/10.1002/anie.202217196
German Edition: doi.org/10.1002/ange.202217196

Water Oxidation Catalysis

Multimodal Analysis of Light-Driven Water Oxidation in Nanoporous Block Copolymer Membranes**

Julian Kund[+], Jan-Hendrik Kruse[+], Andreas Gruber, Ivan Trentin, Marcel Langer, Clarissa Read, Gregor Neusser, Dominik Blaimer, Ulrich Rupp, Carsten Streb, Kerstin Leopold, Felix H. Schacher,* and Christine Kranz**

Abstract: Heterogeneous light-driven catalysis is a cornerstone of sustainable energy conversion. Most catalytic studies focus on bulk analyses of the hydrogen and oxygen evolved, which impede the correlation of matrix heterogeneities, molecular features, and bulk reactivity. Here, we report studies of a heterogenized catalyst/photosensitizer system using a polyoxometalate water oxidation catalyst and a model, molecular photosensitizer that were co-immobilized within a nanoporous block copolymer membrane. Via operando scanning electrochemical microscopy (SECM), light-induced oxygen evolution was determined using sodium peroxodisulfate ($Na_2S_2O_8$) as sacrificial electron acceptor. Ex situ element analyses provided spatially resolved information on the local concentration and distribution of the molecular components. Infrared attenuated total reflection (IR-ATR) studies of the modified membranes showed no degradation of the water oxidation catalyst under the reported light-driven conditions.

Introduction

Heterogeneous catalysis is a cornerstone of modern chemical research, and most industrial chemical processes use one or more heterogeneous catalysts.[1] More recently, the field of sustainable energy has become one of the main drivers of heterogeneous catalyst development, as the splitting of water into hydrogen (H_2) and oxygen (O_2) is one of the major paths to carbon-neutral fuels.[2] One particularly promising approach to this end is artificial photosynthesis where chemical and materials solutions for light-driven water splitting are developed.[3] The concept relies on highly active and stable catalysts for the hydrogen evolution reaction (HER) and water oxidation catalysis (WOC).[4] Specifically, the 4-proton-4-electron WOC is a bottleneck, as suitable catalysts must combine high redox-activity and oxidative/hydrolytic stability with economic viability.[5] This has led to materials design approaches ranging from single-atom catalysts[6] to molecules,[7] clusters,[8] nanoparticles[9] and bulk materials.[5,10] Independent of the type of catalyst, there is common consensus that photo(electro)catalytic water splitting schemes require the use of heterogeneous or heterogenized catalysts to ensure their compatibility with large-scale technological deployments.[11] Thus, high-performance heterogeneous WOCs based on earth-abundant components,[4a,12] embedded in suitable supports are developed. To-date, most heterogeneous or heterogenized WOC relies on bulk reactivity analyses, such as quantification of the evolved O_2 in solution and/or the gas phase using fluorescence-based oxygen sensors,[13] head-space gas chromatography, or Clark-type electrodes.[14] While these approaches provide viable averaged (bulk) information on the performance of the catalyst (i.e. amount of O_2 evolved per gram of catalyst material), no information, e.g., regarding possible heterogeneity of the matrix, or distribution and

[*] J. Kund,[+] A. Gruber, Dr. G. Neusser, D. Blaimer, Prof. Dr. K. Leopold, Prof. Dr. C. Kranz
Ulm University, Institute of Analytical and Bioanalytical Chemistry
Albert-Einstein-Allee 11, 89081 Ulm (Germany)
E-mail: christine.kranz@uni-ulm.de

J.-H. Kruse,[+] Prof. Dr. F. H. Schacher
Friedrich-Schiller University Jena, Institute of Organic Chemistry and Macromolecular Chemistry
Lessingstraße 8, 07743 Jena (Germany)
and
Jena Center for Soft Matter (JCSM)
Philosophenweg 7, 07743 Jena (Germany)
E-mail: felix.schacher@uni-jena.de

Dr. I. Trentin, M. Langer, Prof. Dr. C. Streb
Ulm University, Institute of Inorganic Chemistry
Albert-Einstein-Allee 11, 89081 Ulm (Germany)

M. Langer, Prof. Dr. C. Streb
Johannes Gutenberg University Mainz, Department of Chemistry
Duesbergweg 10–14, 55128 Mainz (Germany)
E-mail: carsten.streb@uni-mainz.de

Dr. C. Read, Dr. U. Rupp
Ulm University, Central Facility of Electron Microscopy
Albert-Einstein-Allee 11, 89081 Ulm (Germany)

[+] These authors contributed equally to this work.

[**] A previous version of this manuscript has been deposited on a preprint server (https://doi.org/10.5281/zenodo.5722330).

© 2023 The Authors. Angewandte Chemie International Edition published by Wiley-VCH GmbH. This is an open access article under the terms of the Creative Commons Attribution Non-Commercial License, which permits use, distribution and reproduction in any medium, provided the original work is properly cited and is not used for commercial purposes.

© 2023 The Authors. Angewandte Chemie International Edition published by Wiley-VCH GmbH

15213773, 2023, 22, Downloaded from https://onlinelibrary.wiley.com/doi/10.1002/anie.202217196 by Universitatsbibliothek Mainz, Wiley Online Library on [04/06/2025]. See the Terms and Conditions (https://onlinelibrary.wiley.com/terms-and-conditions) on Wiley Online Library for rules of use; OA articles are governed by the applicable Creative Commons License

molecule-in-matrix stability of catalysts is obtained. Critical insights into the catalytic performance of reactive sites, e.g., photosensitizer molecules or water oxidation sites, are not accessible by bulk methods. In addition, fundamental limitations of the material, e.g., poor light-penetration into the bulk materials, inaccessibility of catalytic sites, inhomogeneous distribution of the active compounds, or major mass-transport limitations cannot be extracted from these bulk measurements. In this regard, we use scanning electrochemical microscopy (SECM) to measure locally the O_2 evolution and correlate the SECM data with micro-X-ray fluorescence spectroscopy (μXRF) and scanning transmission electron microscopy/energy-dispersive X-ray spectroscopy (STEM/EDX) data that reveal the element distribution within the matrix at different length scales. By this approach, we demonstrate how spatially and temporally resolved in situ/operando WOC reactivity data and ex situ information on spatial distribution can be obtained for molecular photosensitizer and molecular WOC systems heterogenized within nanoporous block copolymer membranes. The concept is inspired by studies where SECM has been employed for H_2/O_2 quantification at the surface of photocatalytic systems including $BiVO_4$-based semiconductors,[15] photoanodes,[16] cobaloxime HER catalysts,[17] and manganese-based WOC electrocatalysts.[18]

We use SECM to locally determine the O_2 evolution rate for light-driven heterogenized WOC, using the prototype ruthenium photosensitizer $[Ru(bpy)_3]^{2+}$ (=Ru-PS; bpy=2,2′-bipyridine),[19] which features well-understood photophysics and is characterized by high oxidative redox-potentials capable of driving many WOCs. As WOC, we chose the polyoxometalate (POM) cluster $[Co_4(H_2O)_2(PW_9O_{34})_2]^{10-}$ (=POM-WOC),[20] whose WOC activity under a range of photochemical and electrochemical conditions has been explored. So far, the POM-WOC has been mainly embedded in polymeric membranes for electrocatalytic anodes.[21] Here, we demonstrate the heterogenization of the active components using nanoporous membranes based on polystyrene-*block*-poly(2-(dimethylamino)ethyl methacrylate) (PS-*b*-DMAEMA), where hydrophilic PDMAEMA units can be positively charged by protonation[22] to facilitate POM-WOC immobilization. The hydrophobic polystyrene (PS) block provides a mechanically rigid membrane scaffold (Figure 1a). The light-induced reaction Scheme using $Na_2S_2O_8$ as sacrificial electron acceptor is depicted in Figure 1b.

The resulting PS-*b*-PDMAEMA block copolymers were then used to prepare nanoporous membranes via the so-called NIPS (non-solvent induced phase separation) process.[23] This type of membrane has recently been successfully applied for the heterogenization of POM-based oxidation catalysts for the oxidation of organic compounds like anthracene or tetrahydrothiophene,[24] as well as Ru-PS and thiomolybdate catalysts for light-driven hydrogen evolution.[25] Anchoring of the photoactive components can be achieved through electrostatic[26] or covalent interactions.[27]

To the best of our knowledge, the present study reports the first spatially and temporally operando O_2 measurements of soft matter-embedded molecular photoactive

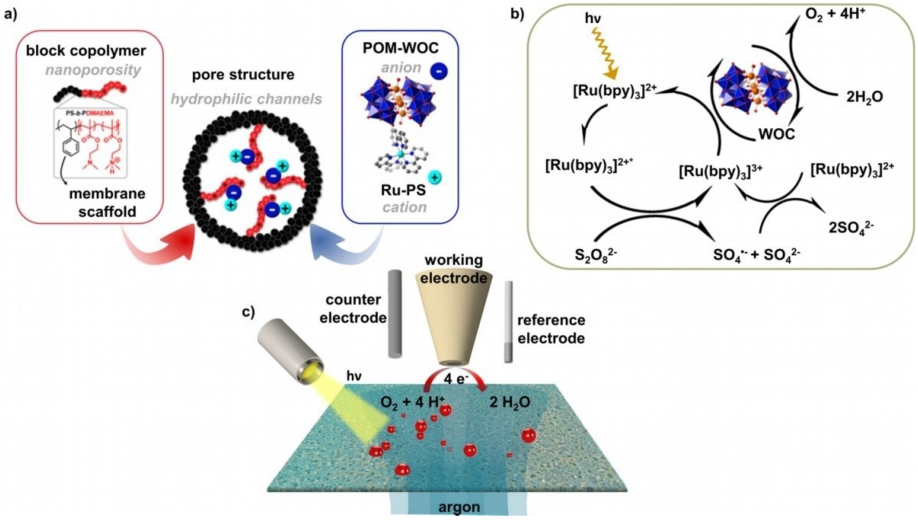


Figure 1. a) Illustration of the nanoporous block copolymer and heterogenized PS and WOC through electrostatic interactions. b) Depiction of the reactions of the light-driven O_2 evolution and c) illustration of local operando O_2 measurements at a nanoporous block copolymer membrane (SEM image in false colours) using SECM.

© 2023 The Authors. Angewandte Chemie International Edition published by Wiley-VCH GmbH

components, i.e., hereafter referred to as WOCbranes. Conventionally used bulk photocatalytic measurements may result in lower apparent O_2 values, due to O_2 entrapment within the porous nanostructured membrane. SECM enables the time-resolved quantification of dissolved O_2 in close proximity to the membrane surface using a customized SECM setup that allowed gentle purging of the membrane with Argon (Ar) to drive produced O_2 out of the membrane. In combination with ex situ element analysis by STEM/EDX, μXRF, total reflection X-ray fluorescence (TXRF) and high resolution-continuum source-graphite furnace atomic absorption spectrometry (HR-CS-GFAAS), quantitative analysis of Co and Ru could be achieved along with correlated information on homogeneity, morphology and molecular distribution of photosensitizer and catalyst.

Results and Discussion

The Ru-PS and POM-WOC were immobilized in PS-*b*-PDMAEMA block copolymer membranes via electrostatic interactions. In contrast to the reported two-step synthesis procedure of PS-*b*-PDMAEMA by anionic polymerization,[28] we utilized here stepwise nitroxide-mediated polymerization (NMP, Figure S1). In brief, the hydrophobic block was prepared via NMP of styrene forming the membrane scaffold as depicted in Figure S1. In a second step, the PS macroinitiator was used for the NMP of DMAEMA, which led to the final block copolymer PS_{304}-*b*-$PDMAEMA_{71}$ ($M_n = 42{,}900\ g\,mol^{-1}$, $Đ = 1.20$, Figure S2a); the subscripts denote the degree of polymerization in the respective segment. Nuclear magnetic resonance (NMR) measurements (Figure S2b) resulted in a weight fraction of 26–29 wt% of DMAEMA for different WOCbrane batches, which has an increased hydrophilic fraction compared to earlier studies.[22,25,29] Figure S3 shows SEM images of the block copolymer membrane, where the nanoporous nature is clearly visible. The anionic POM-WOC was anchored to the positively charged DMAEMA units by immersion of the membrane into an aqueous POM-WOC-containing solution (see Supporting Information). The anionic POM units (POM-WOC charge: −10) facilitate the subsequent immobilization of the cationic Ru-PS (see Figure 1a and Supporting Information for details). Thermogravimetric analysis gave approximately 38.8 wt% POM-WOC and ca. 3.7 wt% Ru-PS (Figure S2c). Based on earlier results and electrostatic considerations,[25] we assume that the relatively low Ru-PS loading observed is due to repulsive electrostatic interactions between Ru-PS and cationic PDMAEMA chains (Figure 1a).

Scanning electron microscopy (SEM) and transmission electron microscopy (TEM), respectively (see Figure S3 and Figure S4) show the "sponge-like" morphology of the membrane with pores of varying size up to 20–30 μm (blue arrows, Figure S4a, c), and varying shapes and density, which is in line with literature reports for this type of block copolymer membranes.[23a,24,30] The "finger-like" or "rod-like" features with a thickness of ca. 50–60 nm (red arrows, Figure S4b, d) are associated with the block copolymer. The thickness of the membrane can be tuned during fabrication and is typically in the range of approx. 52.5 to 55.4 μm, as determined via SEM and TEM cross-sectional images, however thicker, more rigid membranes up to 100 μm can be obtained. For high-resolution STEM/EDX mapping of the distribution of Ru-PS and POM-WOC within the inner pores of the membrane, the WOCbranes were embedded within an EPON™ epoxy resin.[31] Thereby, artifacts due to sample preparation (e.g., vacuum drying) are avoided (for details see Supporting Information).

The dark fringes adjacent to the rod-like polymeric structures evident in the STEM image (Figure 2) and TEM images (Figure S4) reveal the presence of heavy elements, which originate from the POM-WOC (W and Co) and from the Ru-PS (Ru). These are also clearly discernible in the EDX maps surrounding the rod-like features (i.e., the carbon EDX map shown in Figure S5 reflects the high carbon content of the rod-like polymer structures). The EDX maps show the high oxygen content originating from $[Co_4(H_2O)_2(PW_9O_{34})_2]^{10-}$. The rod-shape and round features visible in the STEM image are related to the orientation of the polymer within the EPON resin and differences in the intensities of the dark fringes are likely related to the orientation as well as sectioning artifacts. The distribution of the mapped elements at the edges of the rod-like structures shows the successful immobilization through electrostatic interactions between positively charged PDMAEMA and the negatively charged POM-WOCs. The element ratio of 0.26 for Co:W derived from the EDX data is in excellent agreement with the element ratio of the POM-WOC itself (Co:W = 0.22). For Ru ($[Ru(bpy)_3]^{2+}$), an unambiguous quantification from EDX data is difficult due to an overlap of the Ru and Cl signals. The difference in energy between Cl (2.62 keV) and Ru (2.58 keV) is only 40 eV. Hence, with a detector resolution of around 130 eV, a clear distinction is impeded.[32] The observed Cl signal (see Figure S5) originates from the $[Ru(bpy)_3]Cl_2$ counter-anions or may originate from residual NaCl used in the POM-WOC crystallization.[20a] Consequently, the Ru content within the modified block copolymer membranes was determined via HR-CS-GFAAS after digestion of small amounts of the WOCbranes. Low Ru concentrations were found, varying among different immobilization batches and storage times of the membranes (see Table S1). A possible explanation for these low concentrations is that the positively charged DMAEMA fraction of the block copolymer partially counteracts the attractive electrostatic interaction of the photosensitizer with the catalyst.

Typically, heterogeneous WOC is predominantly characterized by bulk O_2 detection, which provides no spatially resolved information on the local performance of complex heterogeneous catalysts. Hence, SECM is an attractive alternative for operando O_2 detection, as measurements can be performed in close vicinity to the WOCbranes for determining light-driven WOC activity during illumination. Electrochemical O_2 measurements using microelectrodes have been recently demonstrated to determine photocatalytic WOC activity of the semiconductor strontium titanate ($SrTiO_3$) doped with aluminium,[33] however have not yet

© 2023 The Authors. Angewandte Chemie International Edition published by Wiley-VCH GmbH

15213773, 2023, 22, Downloaded from https://onlinelibrary.wiley.com/doi/10.1002/anie.202217196 by Universitatsbibliothek Mainz, Wiley Online Library on [04/06/2025]. See the Terms and Conditions (https://onlinelibrary.wiley.com/terms-and-conditions) on Wiley Online Library for rules of use; OA articles are governed by the applicable Creative Commons License

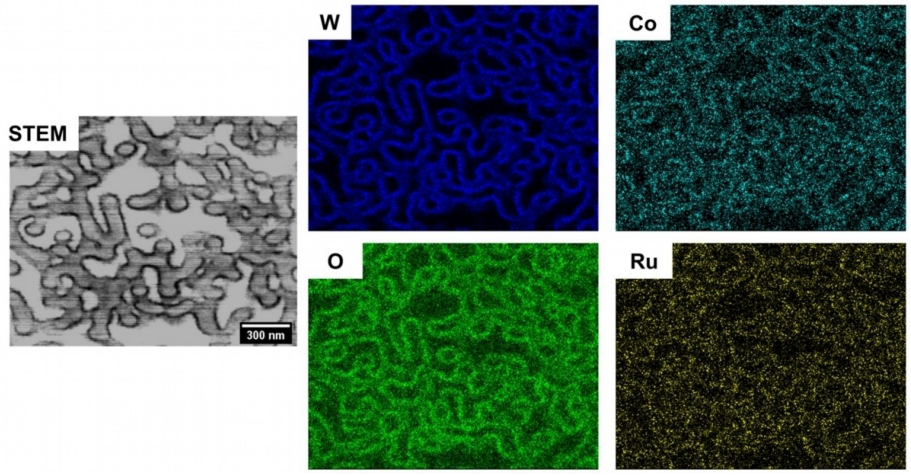


Figure 2. STEM/EDX mapping of the elemental distribution of tungsten (W), cobalt (Co), oxygen (O), and ruthenium (Ru).

been shown for heterogenized molecular water oxidation catalysts. Here, we used static SECM measurements using Pt microelectrodes to quantitatively analyse the light-driven evolution of O_2 (for details on positioning the microelectrode at the membrane, see Figure S6a). A customized SECM cell facilitates illumination of the membrane with a fiber-coupled LED ($\lambda = 470$ nm) and allows simultaneously purging of the membrane with Ar. Current-time (i-t) curves depicting the current response when the membrane is purged either with air (magenta) or Ar (grey) are shown schematically and experimentally in Figure S6b,c. The membranes were purged with Ar (for approx. 15 min) prior to irradiation to remove any O_2 (below the detection limit of our measurements) trapped within the membrane. During the light-driven O_2 measurements, a continuous Ar flow of 1 mL min^{-1} was maintained to drive the produced O_2 out the membrane. Operando O_2 measurements were performed in O_2-free borate buffer solution (pH 8.05) with $Na_2S_2O_8$ as sacrificial electron acceptor[34] in substrate generation/tip collection mode[35] applying a potential of −500 mV vs. Ag/AgCl at the SECM tip.

The pH dependence of the permeability of PDMAEMA membranes has been previously reported.[23a] According to the pore size, O_2 bubbles in the size range around 15 nm should completely pass the membranes at pH 6–10. It has been reported that during homogeneous catalysis, in dependence of the concentrations of the catalyst $[Co_4(H_2O)_2(PW_9O_{34})_2]^{10-}$, the amount of O_2 concentration reached a plateau after 5—15 min of illumination.[36] Three different immobilization batches from two independently synthesized membranes were investigated (in the following termed WOCbrane 1–3). WOCbrane 1 and WOCbrane 2 were illuminated by 60 s intervals separated by 60 s dark intervals. Samples from WOCbrane 3 were constantly illuminated to explore the effect of different irradiation conditions on the photocatalytic performance.[37]

Figure 1c shows schematically the O_2 measurements under irradiation and Figure 3a exemplarily depicts the increase of cathodic current measured at the SECM tip originating from the reduction of O_2 during the individual irradiation steps (chopped illumination, green curve). The same experiments were carried out under dark conditions (magenta curve) and resulted, as expected, in a constant background current.

The current response reveals an initially slow increase in O_2 evolution with a delay of 60 s to 180 s, corresponding to one to three illumination steps, after which an exponential increase of the current with the illumination time is observed for most of the examined WOCbranes (Figure 3b). This behaviour is in contrast to homogeneous photocatalysis of the WOC-POM reported in the literature using the same sacrificial electron acceptor and photosensitizer,[36] although the reported O_2 measurements were obtained via headspace gas chromatography (GC). We hypothesize that the observed delayed onset is mainly attributed to diffusion limitations within the membrane, which is dependent on the actual investigated area. The variation in onset of the O_2 detection for chopped illumination is depicted in Figure 4a. Areas with high polymer density and thus smaller pores may lead to the observed longer delay. It should be noted that the two different WOCbrane 1 and WOCbrane 2 were stored in ultrapure water for different times prior to the SECM measurements and for further ex situ analytical characterization (see Supporting Information).

In addition to the chopped illumination experiments, continuous illumination experiments were carried out for

© 2023 The Authors. Angewandte Chemie International Edition published by Wiley-VCH GmbH

15213773, 2023, 22, Downloaded from https://onlinelibrary.wiley.com/doi/10.1002/anie.202217196 by Universitatsbibliothek Mainz, Wiley Online Library on [04/06/2025]. See the Terms and Conditions (https://onlinelibrary.wiley.com/terms-and-conditions) on Wiley Online Library for rules of use; OA articles are governed by the applicable Creative Commons License

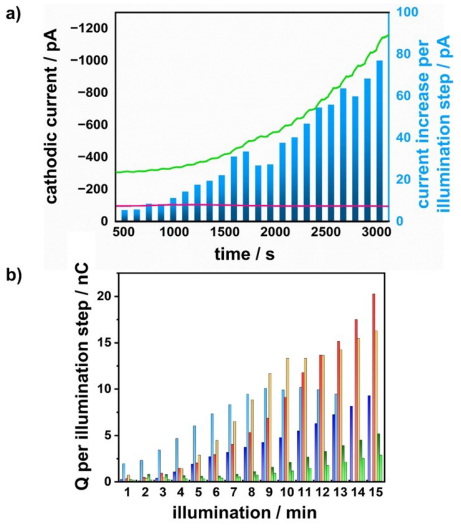


Figure 3. a) Exemplary current response recorded at the microelectrode during illumination (green, illumination was started after 500 s) and under dark conditions (magenta) in 5 mM $Na_2S_2O_8$/100 mM borate buffer solution (see Table S2, measurement membrane 2.2). The cathodic current increase per illumination step is shown by the blue bars. b) Charge evolution during 15 individual irradiation steps (60 s) measured at 6 individual WOCbranes (WOCbrane 1 and 2—two immobilization batches (M1.1 dark blue, M1.2 light blue, M2.1 red, M2.2 orange, M3.1 light green, M3.2 dark green).

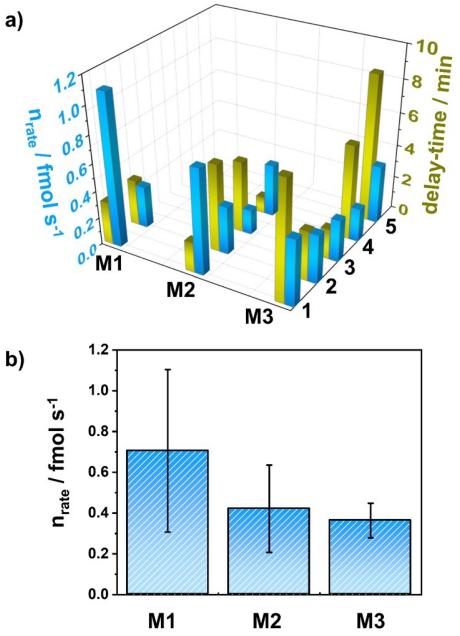


Figure 4. a) Bar diagram showing the reaction rate (blue) and delay time in O_2 evolution (green) for the different membrane batches. b) Amount of O_2 per second (blue bars) of three different immobilization batches from two membranes (M1: $n=2$; M2: $n=4$; M3: $n=6$).

WOCbrane 3 immediately after WOC-POM/Ru-PS loading (i-t curve is shown in Figure S7a**)**. The observed prolonged delay time up to 9 minutes (Figure 4a) observed for WOCbrane 3 may be related to the increased thickness (thickness = 104 µm), which is twice the thickness of WOCbrane 1 and 2. Interestingly, the investigated batches of WOCbrane 3 exhibit a prolonged activity time in the range of 38 minutes up to 66 minutes compared to WOCbrane 1 and 2, where 66 % of the studied patches showed no activity after 15 min of illumination. One sample of WOCbrane 3 was also illuminated under comparable conditions as carried out for WOCbrane 1 and 2 (chopped illumination, Figure S7b). Over a period of 60 illumination steps, this sample exhibits an O_2 evolution-rate of 0.28 fmol s^{-1}, which is in good agreement with the continuously illuminated samples (see Table S2). After storage of the illuminated WOCbranes for several hours in ultrapure water, bubbles of O_2 were observed at the WOCbrane surface as shown in Figure S7c, which may be associated with trapped oxygen.

Figure 4b summarizes the O_2 evolution rate (amount of produced O_2 per second), which was in the range of 0.18 to 1.10 fmol s^{-1} (Table S2) for the different WOCbranes. The apparent variabilities are related to the fact that different areas were probed, which may reflect the heterogeneity in terms of pore space and pore size distribution. Figure S8 shows the change in cathodic current of the three investigated WOCbranes within 15 min illumination, non-modified block copolymer membranes and measurements at the WOCbrane under dark conditions, clearly indicating the photocatalytic activity of the WOCbrane. We performed further studies with respect to the immobilized POM-WOC and Ru-PS content to exclude that this variability in the current response and the time of photocatalytic activity is related to degradation and loss of the WOC. We investigated WOCbranes via EDX prior and after the operando light-driven measurements, as shown in Figure S9. The EDX data show some decrease of W and Co content after illumination which may originate from minor degradation of the WOC or again reflects the heterogeneity of the WOCbrane. Although the same WOCbrane was investigated before and after illumination, the investigated area of the WOCbrane was likely not the same for the EDX measurements. A standard-less quantification of the EDX spectra before and after photocatalytic conditions was used to estimate the ratio between W and Co content. The trend reveals a slight decrease of approximately 4 % in the W signal. This is in line with our TXRF measurements in

© 2023 The Authors. Angewandte Chemie International Edition published by Wiley-VCH GmbH

15213773, 2023, 22, Downloaded from https://onlinelibrary.wiley.com/doi/10.1002/anie.202217196 by Universitatsbibliothek Mainz, Wiley Online Library on [04/06/2025]. See the Terms and Conditions (https://onlinelibrary.wiley.com/terms-and-conditions) on Wiley Online Library for rules of use; OA articles are governed by the applicable Creative Commons License

15213773, 2023, 22, Downloaded from https://onlinelibrary.wiley.com/doi/10.1002/anie.202217196 by Universitatsbibliothek Mainz, Wiley Online Library on [04/06/2025]. See the Terms and Conditions (https://onlinelibrary.wiley.com/terms-and-conditions) on Wiley Online Library for rules of use; OA articles are governed by the applicable Creative Commons License

leaching experiments, as discussed in the last paragraph and shown in Figure S12.

Degradation of the POM ($[Co_4(H_2O)_2(PW_9O_{34})_2]^{10-}$) was reported for electrochemically driven water oxidation.[38] Thus, to gain insights into POM-WOC stability under the given conditions, the POM-WOC and WOCbranes were spectroscopically investigated before and after illumination. We used infrared attenuated total reflection spectroscopy (IR-ATR) to detect any degradation induced by the immobilization process or photocatalysis. The IR spectra (Figure S10) show the characteristic bands of the pure POM-WOC (blue spectrum) (P–O stretching at 1020 cm^{-1}, W–O stretching at 941 cm^{-1}, W–O–W bending at 872 cm^{-1} and 783 cm^{-1}) and the WOCbrane before (grey spectrum) and after illumination (red spectrum).[20a] Upon immobilization, a shift of the W–O–W bands to higher wavenumbers (from 872 cm^{-1} to 890 cm^{-1} and from 783 cm^{-1} to 795 cm^{-1}, respectively) was observed, which is expected due to the molecular interaction with the block copolymer membrane. More importantly, after illumination, only a small shift of approx. 4–5 cm^{-1} from 795 cm^{-1} to 790 cm^{-1} and 890 cm^{-1} to 886 cm^{-1} of the W–O–W bands was observed indicating no major changes of the molecular structure. Also, no characteristic bands for CoO_x species (e.g., at 510 cm^{-1}, 661 cm^{-1}, 690 cm^{-1}, 840 cm^{-1} and 1013 cm^{-1}) were observed by IR spectroscopy at observable concentrations under the given conditions.[39] Based on this data, we do not observe degradation of the POM-WOC into CoO_x species, either upon immobilization or after 30 min of illumination. This is in line with previous studies, where similar behaviour was reported by Schiwon et al.[40] However, we cannot rule out that small amounts of CoO_x are formed during light-driven catalysis, given the limit of detection (LOD) of our IR-ATR measurements. As expected, also no shift of the characteristic bands of the polystyrene-based block copolymer was observed.

Although, high-resolution STEM/EDX mappings (Figure 2) clearly show a quite uniform presence of POM-WOC, the probed sample sections in these high-resolution maps cover an area of less than 2 μm^2, which is not representative for statistically meaningful evaluation of the macroscopic, homogeneous distribution of WOC and Ru-PS in these molecule-in-matrix systems. This information is crucial for optimization of synthesis and loading procedures of the nanoporous block copolymer membranes to achieve high photocatalytic activity. Moreover, heterogeneities on a larger scale may explain the variations in the observed O_2 evolution, as the probed membrane volume in the SECM experiment is approx. 0.025 mm^3 to 0.05 mm^3 (in dependence of the membrane thickness) giving the overall dimension of the microelectrode (i.e., assuming a cylindrical configuration). As a novel non-destructive 2D elemental mapping method, µXRF remains rarely used for soft materials.[41] However, the technique is ideally suited to study the element distribution of WOC-POM within the membranes on a macroscopic scale, as it gives access to element distribution maps of sample areas up to 20×30 cm, in a concentration range from low ppm up to wt.-%, and with a spatial resolution of about 25 µm. Figure 5 presents exemplary intensity maps of W and Co of WOCbranes from membrane 1 and 3. W and Co were detected in all three investigated WOCbrane batches and evaluation of intensities revealed quite uniform distributions.

To evaluate whether the observed minute variations in the element maps may influence the observed O_2 evolution, the resolution of the electrochemical measurement—providing a probing volume of 0.025–0.05 mm^3 taking the thickness of the membranes into account—was translated to this experiment by summing up of the corresponding µXRF probing volumes. The intensity variation along a marked line (Figure 5a, c) was evaluated by calculation of mean intensities in SECM-analogous probing volumes (Figure 5a,c red squares). As can be seen from the insets in Figure 5a and 5c, the relative intensities differ for Co between 34 and 38 a.u. and for W between 120 and 135 a.u. Intensity variation at blank level (2σ) are 3 a.u. for Co and 5 a.u. for W. Assuming comparable variance in presence of the analyte, these data reveal minor distribution inhomogeneities which may add to the observed variations in O_2 generation. However, most likely other effects, such as inhomogeneity in pore connectivity and/or limitations in diffusion will have a more pronounced effect.

The impact of long-term illumination up to 110 min under photocatalytic conditions was also studied by recording element maps of Co and W in WOCbrane 3. Figure 5b (Co) and 5d (W) show pieces of WOCbrane 3, which were used in SECM experiments and illuminated for 60 min, 110 min, 60 min, and 60 min (left to right) compared to a pristine WOCbrane piece kept in the dark in ultrapure water for storage. Signal intensities for W as well as for Co are on a comparable level for all investigated membrane pieces revealing no significant changes of W and Co load after photocatalysis.

Quantification of Co as catalytically active element, as well as of Ru (photosensitizer) were achieved in digests of WOCbrane pieces via TXRF and HR-CS-GFAAS, respectively. The results are presented in Table S1.

The Co and Ru content of the three investigated replicate samples from WOCbrane 1 and 3 resulted in similar concentrations for Co and Ru, respectively. The found mean Co content for WOCbrane 1 is in the range of 228.0 ± 68.9 to 271.3 ± 65.4 nmol mm^{-3}, whereas as expected, a much lower Ru content of 1.1 ± 0.3 to 1.3 ± 0.4 nmol mm^{-3} was determined (see Table S1). The more rigid WOCbrane 3 (thickness of 104 µm) resulted overall in a lower Co content and a Ru content below the detection limit of 0.1 nmol mm^{-3}, which may be associated with the increased thickness of the membrane. However, the reaction rate is not significantly lower compared to e.g., WOCbrane 2 (M.2.2, see Table S2).

To understand possible effects occurring due to storage, we also studied leaching of Co, W and Ru from WOCbranes 1 and 3 stored in ultrapure water for up to six days. Element contents in the storage solutions were quantified using HR-CS-GFAAS and TXRF, respectively, and were related to the element loss in a membrane volume of 1 mm^3. WOCbrane 1, which had a 3 times higher content of POM and Ru-PS also showed significantly higher leaching com-

© 2023 The Authors. Angewandte Chemie International Edition published by Wiley-VCH GmbH

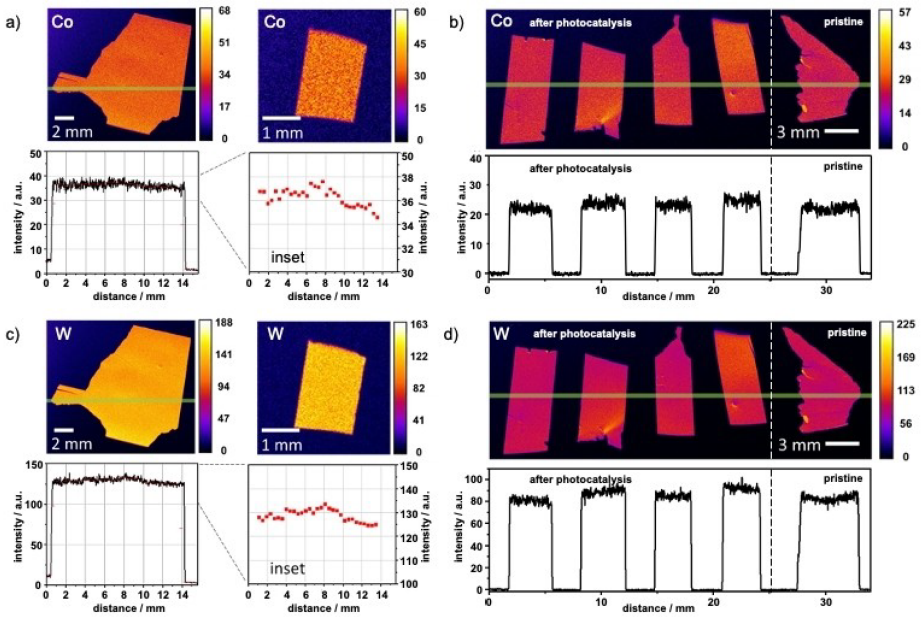


Figure 5. Exemplary element maps (each at the top part) and corresponding intensity distribution along the marked line (each lower part) of cobalt (a, b) and tungsten (c, d) in pieces of WOCbrane 1 (a, c) and WOCbrane 3 (b, d). WOCbrane 1 (a, c) was investigated after preparation and storage in pure water. WOCbrane 3 was investigated either after preparation and storage in pure water (pristine; very right) or after photocatalysis, i.e., immersed in 5 mM $Na_2S_2O_8$/100 mM borate buffer solution and illuminated for 60 min, 110 min, 60 min, and 60 min, respectively. (Resolution in maps and line scans ca. 25 µm; Insets in a, c): red squares are mean values at 400 µm resolution corresponding to SECM probing volume. Line scans in b, d are baseline corrected).

pared to WOCbrane 3 (Figure S11). WOCbrane 3 was investigated directly after immobilization within a period of six days. For the photosensitizer, Ru leaching was observed within the first three days after which the amount of Ru leaching remained constant.

The element ratios of W and Co with ratios between 4.1 and 4.3, as determined by µXRF (WOCbrane 1), fit well with the theoretical value of 4.5. The found molar ratio of Co to Ru of 210 to 219 suggests that only approx. every 50th WOC-POM interacts electrostatically with a photosensitizer molecule, which may be associated with the positively charged PDMAEMA that counteracts the electrostatic interaction of the photosensitizer with the catalyst. Despite the unfavorable ratio of POM-WOC/Ru-PS, and the fact that the heterogenized system suffers from reduced light-penetration of the WOCbrane, as shown in Table S3, the significant light-driven catalytic activity as demonstrated by our SECM measurements, may indicate a favorable, synergistic effect of the molecule-in-matrix system, compensating the relatively low loading of Ru-PS. This is also indicated by the prolonged catalytic activity compared to previous results.[36] It should be noted that for homogeneous photocatalysis in solution typically a significant excess of Ru-PS is used and typical concentration ratios of 0.002–0.01 CAT/Ru-PS are employed.[42]

We also studied possible WOC leaching under photocatalytic conditions that may influence the light-driven activity of the WOCbrane over time. W leaching into the buffer solution was observed under irradiation as well as under dark conditions at a quite low level (see Figure S12) resulting in a maximum W loss of approximately 0.11 pmol mm^{-3} after 120 min. Based on our IR-ATR measurements, we assumed leaching of intact POM with a W to Co atomic ratio of 18 to 4. Thus, Co leaching should be 4.5 times lower than W leaching. In fact, Co concentration in the studied buffer solution was below the limit of detection in all samples. In relation to the initial content of Co in this WOCbrane (89–101 nmol mm^{-3}), we can therefore approximate maximum possible leaching of POM to be in the range of only 0.02 % after 120 min under photocatalytic conditions.

© 2023 The Authors. Angewandte Chemie International Edition published by Wiley-VCH GmbH

15213773, 2023, 22, Downloaded from https://onlinelibrary.wiley.com/doi/10.1002/anie.202217196 by Universitatsbibliothek Mainz, Wiley Online Library on [04/06/2025]. See the Terms and Conditions (https://onlinelibrary.wiley.com/terms-and-conditions) on Wiley Online Library for rules of use; OA articles are governed by the applicable Creative Commons License

15213773, 2023, 22, Downloaded from https://onlinelibrary.wiley.com/doi/10.1002/anie.202217196 by Universitatsbibliothek Mainz, Wiley Online Library on [04/06/2025]. See the Terms and Conditions (https://onlinelibrary.wiley.com/terms-and-conditions) on Wiley Online Library for rules of use; OA articles are governed by the applicable Creative Commons License

Conclusion

In conclusion, we demonstrated that POM-WOC catalysts and $[Ru(bpy)_3]^{2+}$ photosensitizers can be immobilized within nanoporous block copolymer membranes via electrostatic interactions resulting in active hybrid materials for light-driven water oxidation. Such block copolymer membranes are highly suitable matrices, as the degree of protonation of PDMAEMA and therefore POM-WOC/Ru-PS loadings can be controlled. A thorough characterization of these complex materials based on complementary analysis techniques facilitated obtaining unprecedented insight into the distribution of the WOC-POM and Ru-PS along with quantitative data on membrane loading and photocatalytic activity. SECM is ideally suited for performing spatially resolved, operando measurements of dissolved O_2 at WOCbranes probing sub-millimetre sized areas. Thus, obtained information on variations in O_2 evolution offered insight on the membrane heterogeneity and on possible heterogeneity in WOC-POM/Ru-PS loading, demonstrating that the membrane structure such as distribution of pores may have a significant impact on the observed variations. For high-performance heterogeneous WOCs, the macroscopic uniformity of the CAT/PS distribution is a prerequisite. μXRF element mapping provides access to the homogeneity of WOC elements within the membranes on a macroscopic scale. It was also shown that leaching effects need to be considered during extended storage periods. IR-ATR studies suggest that the immobilized POM stays mainly intact over the duration of the measurements and only small amounts of CoO_x (below the detection limit of our measurements) may be formed. Reduced leaching and prolonged light-driven activity were observed for more rigid (i.e., thicker) membranes, even so these membranes showed lower catalyst loading, which indicates a stabilizing effect by embedding the molecular components into the matrix. We herein present the first successful in situ, local measurements on such heterogenized WOC-POM modified nanoporous block copolymer membranes and to our best knowledge, no bulk measurements of such hybrid materials have been reported so far.

Acknowledgements

The authors acknowledge Prof. Dr. Paul Walther at the Central Facility for Electron Microscopy, Ulm University for his support. The authors thank Riccarda Müller, Ulm University for her assistance with μXRF measurements and data evaluation. The authors acknowledge funding by the German Science Foundation (DFG)—Transregio-SFB—TRR234 "CataLight" (project no: 364549901), projects C4 and B3. Open Access funding enabled and organized by Projekt DEAL.

Conflict of Interest

The authors declare no conflict of interest.

Data Availability Statement

The data that support the findings of this study are available from the corresponding author upon reasonable request.

Keywords: Light-Driven Catalysis · Nanoporous Block Copolymer · SECM · μXRF

[1] R. Schlögl, *Angew. Chem. Int. Ed.* **2015**, *54*, 3465–3520.
[2] a) Q. Wang, K. Domen, *Chem. Rev.* **2020**, *120*, 919–985; b) J. Wang, W. Cui, Q. Liu, Z. Xing, A. M. Asiri, X. Sun, *Adv. Mater.* **2016**, *28*, 215–230.
[3] a) I. Roger, M. A. Shipman, M. D. Symes, *Nat. Chem. Rev.* **2017**, *1*, 0003; b) A. Listorti, J. Durrant, J. Barber, *Nat. Mater.* **2009**, *8*, 929–930; c) T. Faunce, S. Styring, M. R. Wasielewski, G. W. Brudvig, A. W. Rutherford, J. Messinger, A. F. Lee, C. L. Hill, H. DeGroot, M. Fontecave, D. R. MacFarlane, B. Hankamer, D. G. Nocera, D. M. Tiede, H. Dau, W. Hillier, L. Wang, R. Amal, *Energy Environ. Sci.* **2013**, *6*, 1074–1076.
[4] a) P. Du, R. Eisenberg, *Energy Environ. Sci.* **2012**, *5*, 6012–6021; b) Q. Yin, C. L. Hill, *Nat. Chem.* **2018**, *10*, 6–7.
[5] J. Li, C. A. Triana, W. Wan, D. P. Adiyeri Saseendran, Y. Zhao, S. E. Balaghi, S. Heidari, G. R. Patzke, *Chem. Soc. Rev.* **2021**, *50*, 2444–2485.
[6] X.-F. Yang, A. Wang, B. Qiao, J. Li, J. Liu, T. Zhang, *Acc. Chem. Res.* **2013**, *46*, 1740–1748.
[7] S. Berardi, S. Drouet, L. Francàs, C. Gimbert-Suriñach, M. Guttentag, C. Richmond, T. Stoll, A. Llobet, *Chem. Soc. Rev.* **2014**, *43*, 7501–7519.
[8] A. Sartorel, M. Bonchio, S. Campagna, F. Scandola, *Chem. Soc. Rev.* **2013**, *42*, 2262–2280.
[9] S. Ye, C. Ding, M. Liu, A. Wang, Q. Huang, C. Li, *Adv. Mater.* **2019**, *31*, 1902069.
[10] C. Costentin, D. G. Nocera, *Proc. Natl. Acad. Sci. USA* **2017**, *114*, 13380–13384.
[11] S. Jiao, X. Fu, S. Wang, Y. Zhao, *Energy Environ. Sci.* **2021**, *14*, 1722–1770.
[12] B. M. Hunter, H. B. Gray, A. M. Müller, *Chem. Rev.* **2016**, *116*, 14120–14136.
[13] F. L. Huber, S. Amthor, B. Schwarz, B. Mizaikoff, C. Streb, S. Rau, *Sustainable Energy Fuels* **2018**, *2*, 1974–1978.
[14] A. Indra, P. W. Menezes, M. Driess, *C. R. Chim.* **2018**, *21*, 909–915.
[15] H. Ye, H. S. Park, A. J. Bard, *J. Phys. Chem. C* **2011**, *115*, 12464–12470.
[16] a) S. Chen, S. Prins, A. Chen, *ACS Appl. Mater. Interfaces* **2020**, *12*, 18065–18073; b) F. Conzuelo, K. Sliozberg, R. Gutkowski, S. Grützke, M. Nebel, W. Schuhmann, *Anal. Chem.* **2017**, *89*, 1222–1228.
[17] E. Oswald, A. Gaus, J. Kund, M. Küllmer, J. Romer, S. Weizenegger, T. Ullrich, A. K. Mengele, L. Petermann, R. Leiter, P. R. Unwin, U. Kaiser, S. Rau, A. Kahnt, A. Turchanin, M. Delius, C. Kranz, *Chem. Eur. J.* **2021**, *27*, 16896–16903.
[18] Z. Jin, A. J. Bard, *Angew. Chem. Int. Ed.* **2021**, *60*, 794–799.
[19] a) A. W. Adamson, J. N. Demas, *J. Am. Chem. Soc.* **1971**, *93*, 1800–1801; b) V. Balzani, P. Ceroni, A. Credi, M. Venturi, *Coord. Chem. Rev.* **2021**, *433*, 213758.
[20] a) Q. Yin, J. M. Tan, C. Besson, Y. V. Geletii, D. G. Musaev, A. E. Kuznetsov, Z. Luo, K. I. Hardcastle, C. L. Hill, *Science* **2010**, *328*, 342–345; b) N. Li, J. Liu, B. Dong, Y. Lan, *Angew. Chem. Int. Ed.* **2020**, *59*, 20779–20793; c) D. Gao, I. Trentin, L. Schwiedrzik, L. González, C. Streb, *Molecules* **2020**, *25*, 157.

© 2023 The Authors. Angewandte Chemie International Edition published by Wiley-VCH GmbH

15213773, 2023, 22, Downloaded from https://onlinelibrary.wiley.com/doi/10.1002/anie.202217196 by Universitatsbibliothek Mainz, Wiley Online Library on [04/06/2025]. See the Terms and Conditions (https://onlinelibrary.wiley.com/terms-and-conditions) on Wiley Online Library for rules of use; OA articles are governed by the applicable Creative Commons License

[21] a) S. Herrmann, C. Ritchie, C. Streb, *Dalton Trans.* **2015**, *44*, 7092–7104; b) M. Blasco-Ahicart, J. Soriano-López, J. R. Galán-Mascarós, *ChemElectroChem* **2017**, *4*, 3296–3301.
[22] F. Schacher, T. Rudolph, F. Wieberger, M. Ulbricht, A. H. E. Müller, *ACS Appl. Mater. Interfaces* **2009**, *1*, 1492–1503.
[23] a) F. Schacher, M. Ulbricht, A. H. E. Müller, *Adv. Funct. Mater.* **2009**, *19*, 1040–1045; b) K.-V. Peinemann, V. Abetz, P. F. W. Simon, *Nat. Mater.* **2007**, *6*, 992–996.
[24] I. Romanenko, M. Lechner, F. Wendler, C. Hörenz, C. Streb, F. H. Schacher, *J. Mater. Chem. A* **2017**, *5*, 15789–15796.
[25] I. Romanenko, A. Rajagopal, C. Neumann, A. Turchanin, C. Streb, F. H. Schacher, *J. Mater. Chem. A* **2020**, *8*, 6238–6244.
[26] a) M. Bonchio, M. Carraro, M. Gardan, G. Scorrano, E. Drioli, E. Fontananova, *Top. Catal.* **2006**, *40*, 133–140; b) M. Bonchio, M. Carraro, G. Scorrano, E. Fontananova, E. Drioli, *Adv. Synth. Catal.* **2003**, *345*, 1119–1126.
[27] X. Zhang, P. Tanner, A. Graff, C. G. Palivan, W. Meier, *J. Polym. Sci. Part A* **2012**, *50*, 2293–2318.
[28] W. A. Phillip, R. M. Dorin, J. Werner, E. M. V. Hoek, U. Wiesner, M. Elimelech, *Nano Lett.* **2011**, *11*, 2892–2900.
[29] C. Hörenz, C. Pietsch, A. S. Goldmann, C. Barner-Kowollik, F. H. Schacher, *Adv. Mater. Interfaces* **2015**, *2*, 1500042.
[30] Y. Wang, *Acc. Chem. Res.* **2016**, *49*, 1401–1408.
[31] E. Blaauw, J. Oosterbaan, J. Schakenraad, *Biomaterials* **1989**, *10*, 356–358.
[32] J. J. Friel, *X-Ray and Image Analysis in Electron Microscopy*, 2nd Ed. Princeton Gamma-Tech, **2003**.
[33] T. Kosaka, Y. Teduka, T. Ogura, Y. Zhou, T. Hisatomi, H. Nishiyama, K. Domen, Y. Takahashi, H. Onishi, *ACS Catal.* **2020**, *10*, 13159–13164.
[34] A. L. Kaledin, Z. Huang, Y. V. Geletii, T. Lian, C. L. Hill, D. G. Musaev, *J. Phys. Chem. A* **2010**, *114*, 73–80.
[35] L. Johnson, D. A. Walsh, *J. Electroanal. Chem.* **2012**, *682*, 45–52.
[36] Z. Huang, Z. Luo, Y. V. Geletii, J. W. Vickers, Q. Yin, D. Wu, Y. Hou, Y. Ding, J. Song, D. G. Musaev, C. L. Hill, T. Lian, *J. Am. Chem. Soc.* **2011**, *133*, 2068–2071.
[37] D. Ziegenbalg, A. Pannwitz, S. Rau, B. Dietzek-Ivanšić, C. Streb, *Angew. Chem. Int. Ed.* **2022**, *61*, e202114106.
[38] J. J. Stracke, R. G. Finke, *J. Am. Chem. Soc.* **2011**, *133*, 14872–14875.
[39] a) M. Zhang, M. de Respinis, H. Frei, *Nat. Chem.* **2014**, *6*, 362–367; b) C.-W. Tang, C.-B. Wang, S.-H. Chien, *Thermochim. Acta* **2008**, *473*, 68–73.
[40] R. Schiwon, K. Klingan, H. Dau, C. Limberg, *Chem. Commun.* **2014**, *50*, 100–102.
[41] a) J.-C. Müller, M. Horstmann, L. Traeger, A. U. Steinbicker, M. Sperling, U. Karst, *J. Trace Elem. Med. Biol.* **2019**, *52*, 166–175; b) A. Mijovilovich, F. Morina, S. N. Bokhari, T. Wolff, H. Küpper, *Plant Methods* **2020**, *16*, 82.
[42] a) B. Schwarz, J. Forster, M. K. Goetz, D. Yücel, C. Berger, T. Jacob, C. Streb, *Angew. Chem. Int. Ed.* **2016**, *55*, 6329–6333; b) J. W. Vickers, H. Lv, J. M. Sumliner, G. Zhu, Z. Luo, D. G. Musaev, Y. V. Geletii, C. L. Hill, *J. Am. Chem. Soc.* **2013**, *135*, 14110–14118.

Manuscript received: November 22, 2022
Accepted manuscript online: March 6, 2023
Version of record online: April 25, 2023

© 2023 The Authors. Angewandte Chemie International Edition published by Wiley-VCH GmbH

Angewandte Chemie
Eine Zeitschrift der Gesellschaft Deutscher Chemiker

Supporting Information

Multimodal Analysis of Light-Driven Water Oxidation in Nanoporous Block Copolymer Membranes

J. Kund, J.-H. Kruse, A. Gruber, I. Trentin, M. Langer, C. Read, G. Neusser, D. Blaimer, U. Rupp, C. Streb, K. Leopold, F. H. Schacher*, C. Kranz**

WILEY-VCH

SUPPORTING INFORMATION

Supporting Information

Table of Contents

Experimental Procedures **2**
Block copolymer synthesis 2
Membrane fabrication 2
Functionalization of the block copolymer membrane 2
Sample preparation for (S)TEM/EDX analysis 2
"WOCbrane" digestion 3
Leaching experiment under photocatalytic conditions 3
Scanning electrochemical microscopy (SECM) 3
Nuclear magnetic resonance spectroscopy (NMR) 3
Size exclusion chromatography (SEC) 3
Thermogravimetric analysis (TGA) 3
Scanning electron microscopy (SEM) 3
Transmission electron microscopy (TEM) 4
Micro-X-ray fluorescence spectrometry (μ-XRF) 4
Total reflection X-ray fluorescence spectrometry (TXRF) 4
High resolution-continuum source-graphite furnace atomic absorption spectrometry (HR-CS-GFAAS) 4
Infrared attenuated total reflection spectroscopy (IR-ATR) 4

Results and Discussion **4**
Figure S1: Stepwise synthesis of the diblock copolymer PS-*b*-PDMAEMA via NMP 5
Figure S2: SEC, NMR and TGA analysis 5
Figure S3: SEM image of pristine nanoporous block copolymer membrane 6
Figure S4: TEM image of EPON-embedded nanoporous block copolymer 6
Figure S5: EDX maps of carbon and chlorine 7
Table S1: Element content of WOCbranes 7
Figure S6: SECM approach curve and schematic of *operando* SECM measurements 7
Figure S7: Control experiments (i-t curves) 8
Figure S8: Current change measured for the first 15 minutes of illumination 8

WILEY-VCH

SUPPORTING INFORMATION

Table S2: O_2 amounts determined at POM/photosensitizer-embedded nanoporous block copolymer membranes 8
Figure S9: EDX data prior and after illumination 9
Figure S10: IR-ATR measurements of pristine and illuminated membrane 9
Table S3: Change in light intensity through WOCbranes..... 10
Figure S11: Leaching experiments of Co, W and Ru 10
Figure S12: Leaching experiments (W) under dark and photocatalytic conditions 10

References **11**

Author Contribution **11**

Experimental Procedures

Sodium borate tetrahydrate and sodium peroxodisulfate were purchased from Sigma-Aldrich (St. Louis, MO, USA). Boric Acid, potassium chloride (KCl) and hexaammineruthenium (III) chloride ($[Ru(NH_3)_6]Cl_3$) were purchased from Merck, (Darmstadt, Germany). Tris(2,2'-bipyridyl)ruthenium(II)chloride, ($[Ru(bpy)_3]Cl_2$]) was purchased from Acros Organics (Fair Lawn, NJ, USA). High purity water 18.1 MΩcm, Barnstead Nanopure – Thermo Fisher Scientific (Dubuque, IA, USA) was used for all solutions. Track-etched polycarbonate membranes (pore diameter: 2 µm) were purchased from Osmonic Incs. (Minnetonka, MN, USA). All chemicals and analytical grade solvents were purchased from Sigma-Aldrich Chemie GmbH (Munich, Germany). BlocBuilder MA was kindly donated by Sylvain Bourrigaud of Arkema and used as received. Styrene and 2-(dimethylamino)ethyl methacrylate and analytical grade solvents were purchased from Sigma-Aldrich Chemie GmbH (Munich, Germany). BlocBuilder MA was kindly donated by Sylvain Bourrigaud from Arkema (Colombes, France) and used as received.

Block copolymer synthesis

For the synthesis of the polystyrene (PS) macroinitiator the initiator BlocBuilder MA (106 mg, 0.28 mmol) was dissolved in 32 mL styrene ([M]/[I]=1000). The oxygen was removed from the reaction mixture by three freeze-pump-thaw cycles and the reaction vessel was subsequently filled with argon. The reaction mixture was heated at 110 °C for 21 h. Afterwards, the mixture was cooled down in liquid nitrogen. The resulting polymer was precipitated twice in cold methanol (M_n= 31.700 g mol^{-1}, Đ=1.08).
In the second step, 1.2 g of the macroinitiator PS (M_n= 31.700 g mol^{-1}) were dissolved in a solution of 10 mL tetrahydrofuran (THF) and DMAEMA (2.86 mL, [M]/[I]=450). The reaction mixture was subsequently degassed by three freeze-pump thaw-cycles. Afterwards the reaction vessel was filled with argon and heated at 110°C for 1.5 h. The stabilizer of DMAEMA was removed by passing through a short column of basic alumina. After the polymerization, the reaction mixture was cooled down to room temperature and precipitated three times in hexane (M_n= 42.900 g mol^{-1}, Đ=1.20).

Membrane fabrication

Membranes were prepared via the NIPS process as described previously:[1] Films were cast onto glass substrates from 15 wt% block copolymer solution in THF/ *N,N*-dimethylformamide (DMF) (70/30 wt%) solvent mixtures using a 200 mm gate height doctor blade. The film casting was carried out in a climate chamber from Plas-Labs (Lansing, MI, USA) at controlled humidity (50%) and temperature (22 °C). After casting, the membrane was exposed to air for 30 s (so called “open time”), followed by fast immersion into a coagulation water bath. The membranes were lifted off from the glass substrates, and then stored in deionized water.

Functionalization of the block copolymer membrane

The functionalization of the membranes was carried out in deionized water. For every unit of DMAEMA in the block copolymer, a unit of POM was added to the solution. $[Co_4(H_2O)_2(PW_9O_{34})_2]^{10-}$ was prepared following the synthesis by Hill and co-workers.[2] Catalyst and photosensitizer immobilization was achieved in a facile two-step process. All steps were carried out in a round bottom flask having a round mesh (polyamide mesh-Nylon) to protect the membrane from damages through the magnetic stir bar. A round piece of membrane (ca. 450 mm^2) was immersed in 20 mL of a 0.64 mmol L^{-1} $Na_{10}[Co_4(H_2O)_2(PW_9O_{34})_2]$ x $27H_2O$ aqueous solution for 24 hours kept under stirring. The solution was then exchanged with deionized water and stirred for 24 hours to remove possible excess of the catalyst. Following, the membrane was immersed in an aqueous solution of the 1.2 mmol L^{-1} $[Ru(bpy)_3]Cl_2$ and kept under stirring for 24 hours. Another washing step in deionized water was carried out for 24 hours and the modified membrane was stored in ultrapure water prior to use.

Sample preparation for (S)TEM/EDX analysis

The “WOCbranes” were embedded into EPON resin (Sigma-Aldrich Chemie GmbH, Munich, Germany) to avoid a possible reduction of the pore size during drying processes, avoiding thus morphological changes of the membrane. Embedding was performed following a protocol of Walter et al.[3] During this process, the water content of the wet membrane was substituted with propanol and EPON resin. For embedding, samples were incubated successively for one hour in 33%, 50% and 67% EPON resin in isopropanol, then overnight in 100% EPON and polymerized for 48 h at 60 °C. A Leica Ultracut UC7 ultramicrotome was used to prepare the ultrathin cross-sections

(30 nm thickness for EDX mapping, 70 nm for TEM), which were then mounted on carbon-coated Formvar (Plano GmbH, Wetzlar, Germany) films on a 300-mesh cupper TEM grid.

"WOCbrane" digestion

For quantification of Ru, Co, and W content of the membranes via GFAAS, six samples of a few mm^2 each were taken from two individual immobilization batches using a scalpel (for each batch n=3). Each membrane piece was transferred to a micro-centrifuge tube, precleaned by subboiling distillation (dst1000, Salvillex Corporation, USA) and 100 µL of nitric acid (HNO_3, 63% AnalR Normapur, VWR International GmbH, Darmstadt, Germany) were added for digestion. Subsequently, the samples were treated in an ultrasonic bath for 10 min at 40 °C followed by mixing for 60 s at 2500 rpm. Ultra-sonication and mixing steps were repeated two more times. After that, 1000 µL of ultrapure water (obtained from ultrapure water purification system Sartorius AG, Göttingen, Germany) were added and the resulting suspension was vortexed for another 60 s at 2500 rpm. All steps of this sample preparation procedure were performed in a laminar flow box (Susi Super Silent, Spetec GmbH, Erding, Germany) in order to minimize possible trace contamination. Micro-centrifuge tubes (VWR International GmbH, Darmstadt, Germany) and pipette tips (Brandt GmbH & Co KG, Wertheim, Deutschland) were precleaned by immersion in 10% sub-boiled HNO_3 for at least 24 h and subsequent storage in 0.5% sub-boiled HNO_3.

Leaching experiment under photocatalytic conditions

For quantification of possible loss of Ru, Co, and W from membranes into buffer solutions, membrane pieces of WOCbrane 3 of a few mm^2 each were taken using a scalpel and immersed in two 1-mL-batches of 5 mmol L^{-1} sodium peroxodisulfate in 100 mmol L^{-1} borate buffer solution. Sample aliquots of 100 µL were taken after 30, 60, 90, 120 min. One batch was illuminated using a 21.8 mW blue LED (M470F3, Thorlabs GmbH, Bergkirchen, Germany) which was placed 1 cm above the membrane mimicking the set-up used in SECM experiments for localized measurement of O_2 evolution. The other batch was kept in the dark. Quantification of elements in the samples was achieved using TXRF and GFAAS (details see below).

Instrumentation

Scanning electrochemical microscopy (SECM)

A custom-built SECM setup (software: G. Wittstock, University Oldenburg, Oldenburg, Germany) was used to study the O_2 evolution at "WOCbranes" using Pt UMEs. Approach curves were recorded in 5 mmol L^{-1} hexaammineruthenium (III) chloride/0.1 mol L^{-1} KCl solution. A customized electrochemical flow cell was designed that allowed purging of the WOCbrane with Ar. Photocatalytic studies were carried out in 5 mmol L^{-1} sodium peroxodisulfate in 100 mmol L^{-1} borate buffer solution (pH 8.05). To ensure a constant argon flow, a flow rate of 1 mL min^{-1} was applied using a mass flow controller (MFC) (Bronkhorst GmbH, Kamen, Germany). Track-etched polycarbonate membranes with a pore size of 2 µm and a pore density of $2x10^6$ pores/cm^2 were used as support for the soft membranes and allowing a uniform Ar stream. The photocatalytic measurements of membrane B were performed within two days after modification, and of membrane A within a time period of four days after modification. A 400-µm optical fiber (MT-28L01, Thorlabs GmbH, Bergkirchen, Germany) connected to a 21.8 mW blue LED (M470F3, Thorlabs GmbH) was attached to the tip holder and placed 1 cm above the membrane. All electronic devices were placed outside of the Faraday cage.

Pt microelectrodes (ME) were fabricated with an RG value of 30. A Pt wire (10 µm diameter, Goodfellow, Bad Nauheim, Germany) was melted into borosilicate glass (glass capillaries were purchased from Hilgenberg, Malsfeld, Germany). The electrodes were then polished using diamond lapping films (Allied High-Tech Products, Rancho Dominguez, CA, USA) and aluminum oxide suspensions (LECO, St. Joseph, MO, USA). The electrochemical characterization of the UME was performed in a three-electrode setup, with an Ag/AgCl/3M reference electrode (RE), a Pt counter electrode (CE) and the ME as working electrode in a 5 mmol L^{-1} hexaammineruthenium (III) chloride/0.1 mol L^{-1} KCl solution.

Nuclear magnetic resonance spectroscopy (NMR)

^{1}H-NMR spectra were measured on a 300 MHz Bruker AVANCE spectrometer using $CDCl_3$, as deuterated solvent at a temperature of 298 K. The solvent residual peak $CDCl_3$ was used as standard.

Size exclusion chromatography (SEC)

SEC measurements in THF were performed on an Agilent system equipped with G1310A pump, a G1362A refractive index detector, and both a PSS Gram30 and a PSS Gram1000 column in series. THF was applied as eluent at 1 mL min^{-1} flow rate and the column oven was set to 40 °C. For calibration PS standards were used.

Thermogravimetric analysis (TGA)

TGA was performed on a Perkin-Elmer-TGA 8000 instrument under airflow (20 mL min^{-1}) at a heating rate of 10 °C min^{-1}.

Scanning electron microscopy (SEM)

SEM was performed on a Zeiss (Oberkochen, Germany) (LEO) 1530 Gemini FESEM operating at 5 to 10 kV using an InLens detector. Previously, the samples were coated with gold (~5 nm) using a SCD005 sputtering device BAL-TEC (Balzers, Liechtenstein).

SUPPORTING INFORMATION

Transmission electron microscopy (TEM)

TEM investigations were carried out using JoelTEM 1400 with an accelerating voltage of 110 kV. EDX mapping was performed at a Hitachi S-5200 field emission scanning electron microscope (FESEM) equipped with a scanning transmission electron microscopy (STEM)-detector (Hitachi High-Tech Corp., Tokyo, Japan) and an EDAX Phoenix X-ray detector system with a 30 mm^2 SUTW window (AMETEK GmbH, Weiterstadt, Germany). Acceleration voltage of 30 kV and a current of 20 µA were used for the measurements.

Micro-X-ray fluorescence spectrometry (µ-XRF)

Elemental maps of W and Co in the loaded membranes were recorded using micro-X-ray fluorescence spectrometer M4 Tornado (Bruker Nano GmbH, Berlin, Germany). For this purpose, membranes were dried for 1 h at room temperature and placed on an Ultralene ® foil (SPEX Sample Prep, Metuchen, NJ, USA) stretched on 31 mm open-ended X-cells (SPEX Sample Prep). The X-cells were fixed in a house-made holder attached to the M4 Tornado sample stage. The instrument is equipped with an Rh X-ray tube which was operated at maximum power (50 kV, 600 µA). The polychromatic beam is focused via poly capillary lenses to a spot size of 25 µm. The dwell time per pixel was set to 10 ms. Detection of the fluorescence quants takes place at a XFlash 430-PA detector with an active area of 30 mm^2 and a resolution of <145 eV for Mn-Kα. Fiji software (1.53k 07/06/2021) was used for both data visualization via Fire lookup table and interpretation of the intensity distribution.

Total reflection X-ray fluorescence spectrometry (TXRF)

Quantification of Co and W in the membrane digests and analysis of the storage and buffer solution of membranes was performed using TXRF Picofox S2 high-efficiency module (Bruker Nano GmbH, Berlin, Germany). The Picofox S2 is equipped with a Mo X-ray tube, operated with a voltage of 50 kV and a current of 600 µA. 50 µL of each digest were diluted in 1000 µL of ultrapure water and mixed with 10 µL of Ti standard solution (100 mg L^{-1} in 2% HNO_3, Sigma Aldrich, Darmstadt, Germany) as internal standard. For investigation of buffer solutions, 100 µL were taken and 100 µL of Ti standard solution (see above) added. To investigate the leaching into storage solution (UPW), 1 mL aliquotes were taken and used for GFAAS and TXRF measurements. For quantification by TXRF, 10 µL of Cr standard solution (100 mg L^{-1} in 2% HNO_3, Carl Roth GmbH + Co. KG, Karlsruhe, Germany) is added to 500 µL as an internal standard. After thorough mixing for 60 s at 2500 rpm, 10 µL were applied to a siliconized (silicone solution, SERVA electrophoresis GmbH, Heidelberg, Germany) sample carrier (Bruker Nano GmbH, Berlin, Germany). For each sample three sample carriers were prepared and dried at 60°C for 30 min on a hot plate (n=3). The lifetime per sample carrier was set to 1000 seconds.

High resolution-continuum source-graphite furnace atomic absorption spectrometry (HR-CS-GFAAS)

Quantification of Ru in the digested membranes was performed using HR-CS-GFAAS. A ContrAA 600 spectrometer (Analytik Jena GmbH, Germany) equipped with a graphite furnace atomization unit and solid sampling SSA 600 auto sampler was used. As purge and protective gas argon with a purity of 99.996% (MTI, Germany) was applied. For atomic absorption measurement the most sensitive line of Ru (349.895 nm) was selected, and a spectral range of 0.36 nm (200 pixels) was observed. Pixel 164 (349.895 nm) was evaluated by manually integration of the absorbance signal with the software OriginPro 2019b (OriginLab Corporation, USA). Three replicate measurements were performed by applying 10 µL of the digest onto a pyrolytic graphite-coated sample platform (Analytik Jena GmbH). Platforms are transferred automatically into the pyrolytic graphite-coated tube and the standard temperature program as suggested by the instrument's software was started. Ru concentration was determined using external calibration. For this purpose, a Ru stock standard solution of 15 µg L^{-1} was prepared by dilution of adequate volume of Ru standard solution (1000 mg L^{-1} in 5% HCl, VWR International GmbH, Germany) in 0.5 mol L^{-1} sub-boiled HNO_3. Subsequently, different volumes of the stock standard solution were pipetted on the platform and the atomization signal at 349.895 nm was integrated.

Infrared attenuated total reflection spectroscopy (IR-ATR)

IR spectra were recorded using a Fourier-transform infrared (FT-IR) spectrometer (Alpha I, Bruker Optik GmbH, Ettlingen, Germany) equipped with a diamond single-bounce attenuated total reflection (ATR) accessory. The spectra were collected at a spectral resolution of 2 cm^{-1} averaging 64 spectra per measurement. For measurement, the wet membrane was placed onto the ATR crystal to achieve a flat and non-destroyed membrane for the maximum interaction between diamond ATR crystal and membrane. Afterwards the membrane was dried over period of 60 minutes under ambient conditions.

Results and Discussion

The *PS-b*-PDMAEMA diblock copolymer for the preparation of the membranes was synthesized in a two-step procedure. In the first step, the hydrophobic block was prepared via nitroxide-mediated polymerization (NMP) of styrene (Figure S1). This block forms the membrane scaffold and is therefore larger than the hydrophilic block. The resulting PS polymer has an average molar mass (M_n) of 31.700 g mol^{-1} and a polydispersity (Đ) of 1.08 (Figure S2b). In the second step, the PS macroinitiator is used for the NMP of DMAEMA, which led to the final diblock copolymer PS_{304}-*b*-$PDMAEMA_{71}$ (Mn= 42.900 g mol^{-1}, Đ=1.20), the subscripts denote the number of repeating units of each monomer. The weight share of DMAEMA of the overall polymer is 26% and was calculated via nuclear magnetic resonance (NMR) measurements (Figure S2a).

SUPPORTING INFORMATION

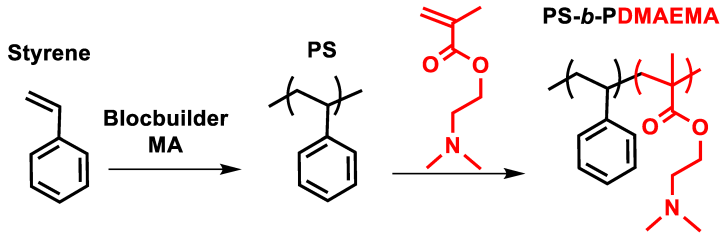


Figure S1. Stepwise synthesis of the diblock copolymer PS-*b*-PDMAEMA via NMP.

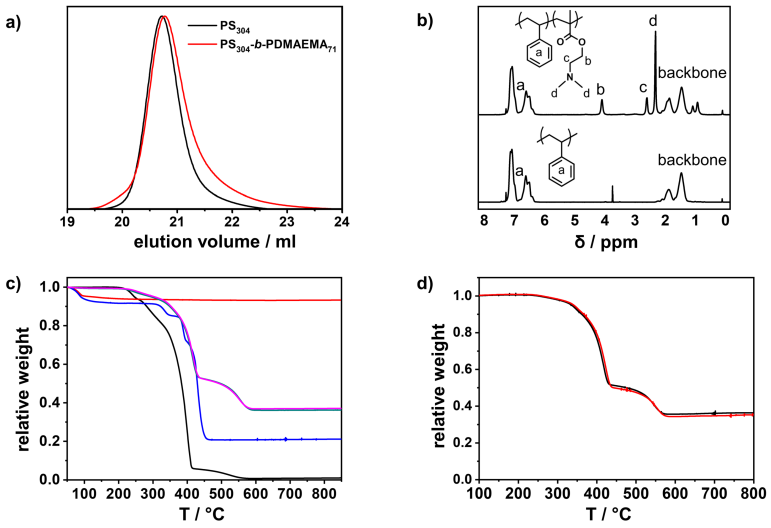


Figure S2. a) SEC elution traces of PS standard (black) and PS-*b*-PDMAEMA (red), THF was used as solvent; b) NMR of PS-*block*-poly(*N,N*-dimethylaminoethyl methacrylate); c) TGA graph of membrane before functionalization (black), pure $[Co_4(H_2O)_2(PW_9O_{34})_2]^{10-}$ WOC (red), the pure $Ru(bpy)_3Cl_2$ photosensitizer (blue), the membrane functionalized with the $[Co_4(H_2O)_2(PW_9O_{34})_2]^{10-}$ (green) and the membrane functionalized both with the $[Co_4(H_2O)_2(PW_9O_{34})_2]^{10-}$ the $Ru(bpy)_3^{2+}$ photosensitizer (magenta). d) TGA graph of the modified membrane before (black) and after illumination (red) for 2 h under photocatalytic conditions (5 mM $Na_2S_2O_8$/0.1 M borate buffer solution, pH 8.0, red).

SUPPORTING INFORMATION

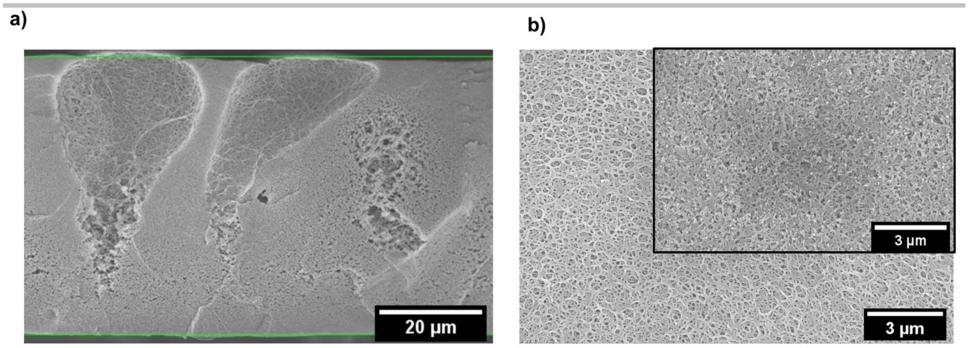


Figure S3. SEM image of a pristine nanoporous block copolymer membrane; a) cross-section; b) top view of both sides of the membrane.

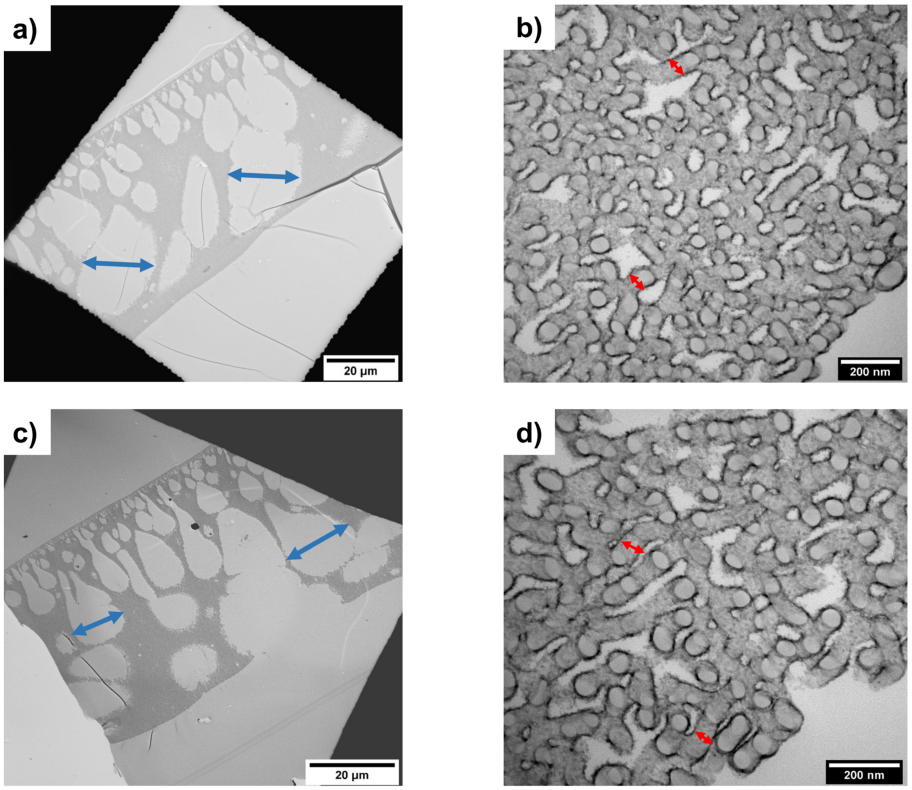


Figure S4. TEM image of an EPON-embedded nanoporous block copolymer membrane. a) Cross-section of an EPON-embedded modified nanoporous block copolymer membrane; b) zoomed view; c) cross-section of an EPON-embedded nanoporous block copolymer membrane (after illumination in 5 mM $Na_2S_2O_8$/100 mM borate buffer solution for 30 min); d) zoomed view (after illumination in 5 mM $Na_2S_2O_8$/100 mM borate buffer solution).

SUPPORTING INFORMATION

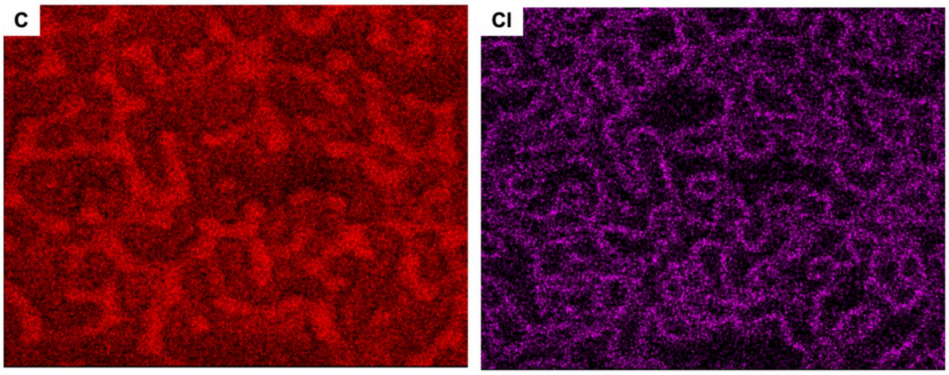


Figure S5. STEM/EDX mappings of the elemental distribution of carbon (C) and chlorine (Cl) of the modified block copolymer membrane.

Table S1. Concentrations of Co and Ru determined *via* TXRF and GFAAS measurement, respectively, in digests of pieces of WOCbrane 1 and WOCbrane 3. (Uncertainties given as ± one standard deviation with n=4.)

Sample	Sample volume [mm³]			Concentration [nmol mm⁻³]	
				Co	Ru
1.1	0.160	±	0.027	271.3 ± 65.4	1.3 ± 0.4
1.2	0.181	±	0.030	228.0 ± 68.9	1.1 ± 0.3
1.3	0.302	±	0.049	260.1 ± 74.7	1.2 ± 0.3
3.1	3.718	±	0.599	88.9 ± 20.5	< 0.1
3.2	2.721	±	0.441	92.9 ± 21.5	< 0.1
3.3	3.057	±	0.494	100.9 ± 23.2	< 0.1

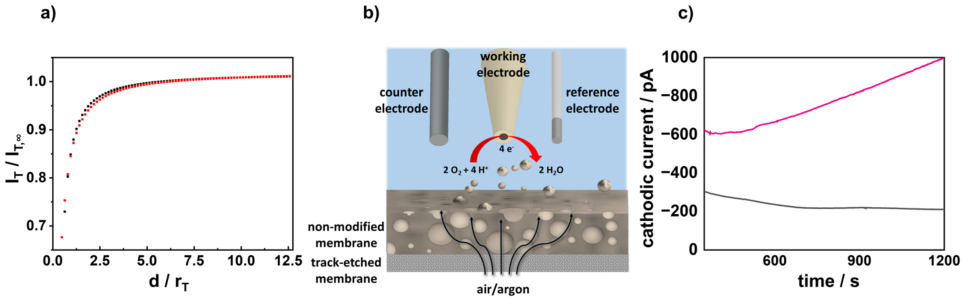


Figure S6. a) Exemplary SECM approach curve recorded with a Pt microelectrode in 5 mmol L^{-1} hexaammineruthenium (III) chloride / 0.1 mol L^{-1} KCl solution. Et_{ip} = -300 mV vs. QRE with an approach velocity 1 µm s^{-1}; black dotted line is the experimental curve showing negative feedback current; red dotted line is the theoretical approach curve using the fitting approach of Amphlett and Denuault[4]; b) Schematic of the track-etched membrane supported setup and the purging

using Argon during illumination experiments or purging with air for testing the SECM set-up. c) i-t curve recorded at the microelectrode positioned at a non-modified membrane purging with air (magenta) of Argon (grey).

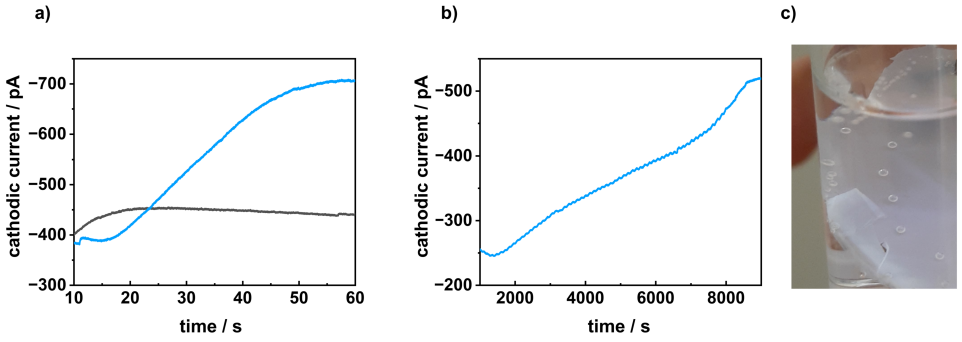


Figure S7. Exemplary current response recorded at the SECM tip during a) continuously illumination (blue, illumination was started after 660 s) and under dark conditions (grey) (see Table S2, measurement membrane 3.1) and b) chopped illumination in 5 mM $Na_2S_2O_8$/100 mM borate buffer solution (see Table S2, measurement membrane 3.6). c) Photograph of air bubbles at the surface of WOCbrane after illumination in 5 mM $Na_2S_2O_8$/100 mM borate buffer solution.

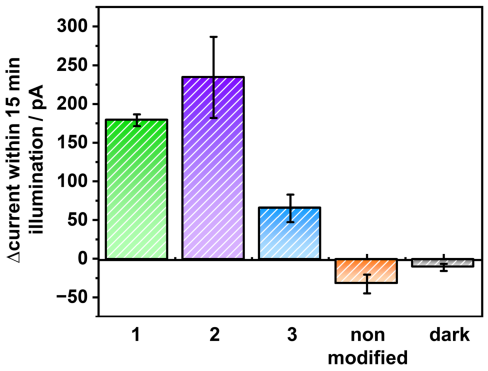


Figure S8. Overall current change measured for the first 15 minutes of illumination at non-modified block copolymer membrane (orange, n = 4), at WOCbranes from three immobilization batches (green, n =2; purple, n = 4; blue, n = 6) and dark condition (grey, n =5).

Table S2. Calculated amount of O_2 per seconds of WOC/photosensitizer-embedded nanoporous block copolymer membrane after illumination in 5 mM $Na_2S_2O_8$/100 mM borate buffer solution. 12 different samples from three batches were investigated.

Amount of O_2 per second [fmol s^{-1}]											
M 1.1	M 1.2	M2.1	M 2.2	M2.3	M2.4	M3.1	M 3.2	M3.3	M 3.4	M 3.5	M 3.6
1.10	0.31	0.77	0.35	0.18	0.38	0.49	0.36	0.31	0.24	0.42	0.28

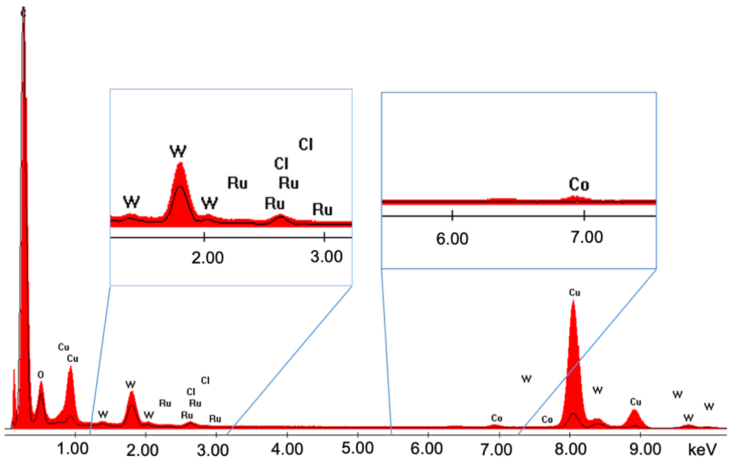


Figure S9. EDX spectra (red) of a non-illuminated WOCbrane and after 30 min of illumination in 5 mM $Na_2S_2O_8$/100 mM borate buffer solution (black line); intensity normalized to C peak. It should be noted that the Cu signal in the EDX spectra comes from the Cu TEM grid. Electrons scattered in the sampled membrane may hit the Cu grid producing Cu X-ray. The number of scattered electrons correlates with the density of the sampled volume and therefore on the concentration of W.

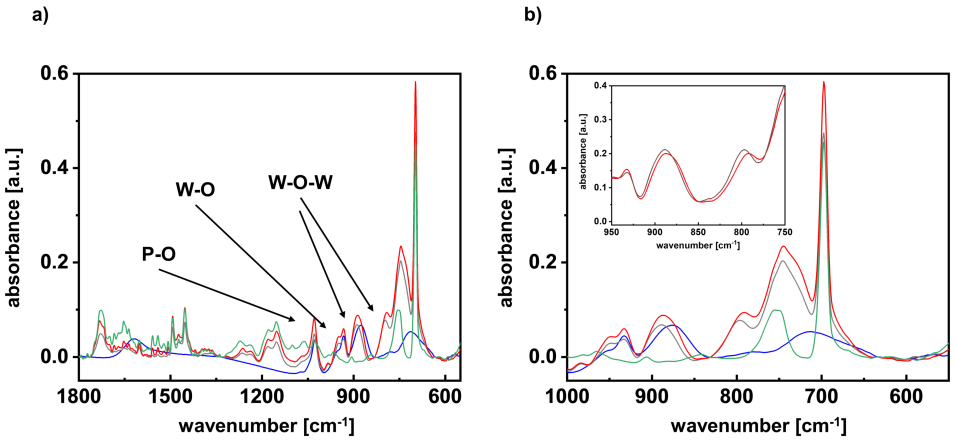


Figure S10. IR spectra of $[Co_4(H_2O)_2(PW_9O_{34})_2]^{10-}$(blue), WOC-modified membrane (grey), illuminated WOC-modified membrane after 30 min of illumination in 5 mM $Na_2S_2O_8$/100 mM borate buffer solution (red), non-modified membrane (green); b) inset show normalized IR spectra of WOC-modified membrane before illumination (grey), after illumination in 5 mM $Na_2S_2O_8$/100 mM borate buffer solution (red).

SUPPORTING INFORMATION

Table S3. Light intensity measured at the bottom of the membranes at a fixed distance of 1 cm using a 400-µm optical fiber connected to a 21.8 mW blue LED

Membrane Thickness [µm]	Power [mW]	Absorbance [%]
Without membrane	8.63	-
Membrane: 52.5 µm	3.01	65
(M1&M2 Membrane: 104.1 µm (M3)	1.22	86

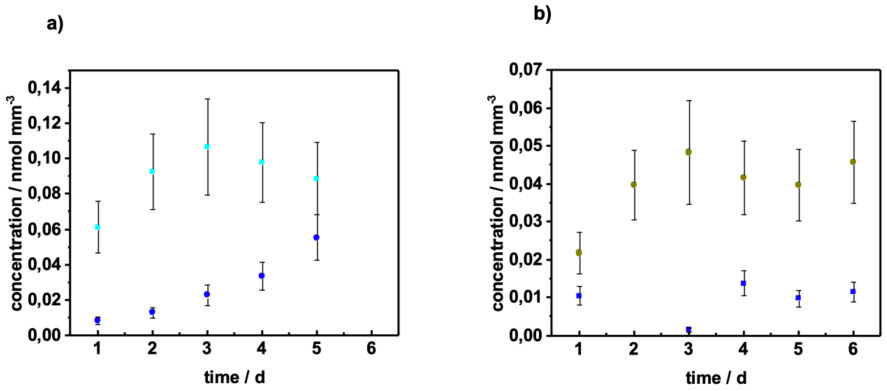


Figure S11. Leaching experiments over 6 days of WOCbrane 1 (a) and WOCbrane 3 (b). Quantification of W (dark blue), Co (light blue) and Ru (olive) in the storage water were performed via TXRF (W, Co) and GF-AAS (Ru), respectively. *Note:* In a) no Ru quantification was performed; In b) Co contents were below the detection limit of 1.6 $\cdot 10^{-6}$ nmol mm^{-3}. Error bars result from gaussian error propagation of determination of area and thickness of membranes (volumes) as well as from replicate sample preparation and measurement of element contents. Furthermore, it should be taken into account that concentrations are in the sub µg L^{-1} level and significant re-adsorption of Co, W, and Ru onto container walls is to be expected. This, however, cannot be avoided by addition of stabilizers in the present experimental set-up because membranes were supposed to be kept in pure water only.

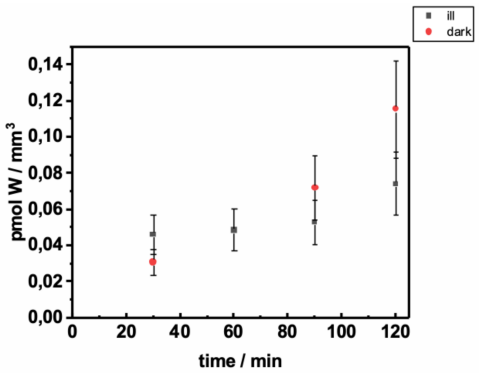


Figure S12. Leaching experiments with WOCbrane 3 under dark (blue) and photocatalytic conditions (orange) in 5 mM $Na_2S_2O_8$/100 mM borate buffer solution within a period of 2 h irradiation. W was quantified in the buffer solution by TXRF and related to the loss of W in a volume of 1 mm^3 of membrane. Co contents were below the detection limit of 1.6 $\cdot 10^{-6}$ nmol mm^{-3}. Error bars result from gaussian error propagation of determination of area and thickness of membranes (volumes) as well as from replicate sample preparation and measurement of element contents.

References

[1] F. Schacher, M. Ulbricht, A. H. E. Müller, *Adv. Funct. Mater.* **2009**, *19*, 1040–1045.
[2] Q. Yin, J. M. Tan, C. Besson, Y. V Geletii, D. G. Musaev, A. E. Kuznetsov, Z. Luo, K. I. Hardcastle, C. L. Hill, *Science* **2010**, *328*, 342–345.
[3] P. Walther, A. Ziegler, *J. Microsc.* **2002**, *208*, 3–10.
[4] J. L. Amphlett, G. Denuault, *J. Phys. Chem. B* **1998**, *102*, 9946–9951.

Author Contributions

Julian Kund performed the *in-situ* SECM experiments, designed the electrochemical flow cell, carried out IR-ATR experiments, and wrote the draft manuscript. Jan Kruse synthesized the block copolymer, fabricated the block copolymer membrane, carried out the TGA, SEC and NMR analysis and wrote the synthesis part of the draft manuscript. Ivan Trentin, Marcel Langer performed the membrane functionalization. Gregor Neusser, Clarissa Read and Ulrich Rupp carried out the TEM and STEM/EDX analysis. Andreas Gruber carried out the µ-XRF and TXRF experiments and data analysis and wrote the corresponding part of the draft manuscript. Dominik Blaimer performed the HR-CS-GFAAS measurements. Christine Kranz, Felix Schacher, Carsten Streb and Kerstin Leopold designed and supervised the experiments and revised the manuscript. All authors have read and agreed to the version of the manuscript.

6.3 {MLa-4}: Thiomolybdate Clusters: From Homogeneous Catalysis to Heterogenization and Active Sites

Samar Batool,‡ Marcel Langer,‡ Stephen N. Myakala, Magdalena Heiland, Dominik Eder, Carsten Streb,* and Alexey Cherevan*

‡ *Authors contributed equally to this work*

* *Corresponding authors*

Abstract: The relevance of thiomolybdates as molecular models for a-MoS_x, their photocatalytic properties and their principal HER reactivity were underpinned by seminal reports from the literature. State-of-the-art studies on their reactivity and stability as well as the identification of HER mechanisms at different active sites were critically evaluated with respect to the exact reaction conditions used. Deposition strategies on functional substrates were briefly outlined and their pioneering and emerging applications, with particular emphasis on electro- and photocatalysis, were discussed in detail using appropriate performance indicators.

Published in: *Adv. Mater.* **2024**, *36*, 2305730.

Status: Published

Copyright: Reprinted with permission from “Thiomolybdate Clusters: From Homogeneous Catalysis to Heterogenization and Active Sites”, S. Batool,‡ M. Langer,‡ S. N. Myakala, M. Heiland, D. Eder, C. Streb,* and A. Cherevan,* *Adv. Mater.* **2024**, *36*, 2305730.
DOI: 10.1002/adma.202305730.

© 2023, The Authors, Advanced Materials published by Wiley-VCH GmbH under the terms of the CC BY 4.0 license.

Author Contributions:

S. Batool	Writing and discussion of section 3.2. “Photocatalysis”; Discussion and revision of the manuscript.
M. Langer	Writing and discussion of section 2.2. “Identification of Active Sites in Thiomolybdates”; Discussion and revision of the manuscript.
S. N. Myakala	Writing and discussion of section 3.1. “Electrocatalysis”; Revision of the manuscript.
M. Heiland	Writing and discussion of section 2.1. “Catalytic Properties”; Revision of the manuscript.
D. Eder	Revision of the manuscript.
C. Streb	Conceptualization; Supervision; Writing section 1.1. “Thiometalates: Structure and Recent Developments”, section 2. “Catalytic Performance and Active Sites” and section 4. “Conclusion and Outlook”; Writing, discussion and revision of the manuscript.
A. Cherevan	Conceptualization; Supervision; Writing section 1. “Introduction”, section 2.3. “Heterogenization of Thiometalates”; section 3. “Applications of Heterogenized Thiomolybdate Clusters”, section 3.3. “Other Applications” and section 4. “Conclusion and Outlook”; Writing, discussion and revision of the manuscript.

Check for updates

REVIEW

ADVANCED MATERIALS
www.advmat.de

Thiomolybdate Clusters: From Homogeneous Catalysis to Heterogenization and Active Sites

Samar Batool, Marcel Langer, Stephen Nagaraju Myakala, Magdalena Heiland, Dominik Eder, Carsten Streb, and Alexey Cherevan**

Thiomolybdates are molecular molybdenum-sulfide clusters formed from Mo centers and sulfur-based ligands. For decades, they have attracted the interest of synthetic chemists due to their unique structures and their relevance in biological systems, e.g., as reactive sites in enzymes. More recently, thiomolybdates are explored from the catalytic point of view and applied as homogeneous and molecular mimics of heterogeneous molybdenum sulfide catalysts. This review summarizes prominent examples of thiomolybdate-based electro- and photocatalysis and provides a comprehensive analysis of their reactivities under homogeneous and heterogenized conditions. Active sites of thiomolybdates relevant for the hydrogen evolution reaction are examined, aiming to shed light on the link between cluster structure and performance. The shift from solution-phase to surface-supported thiomolybdates is discussed with a focus on applications in electrocatalysis and photocatalysis. The outlook highlights current trends and emerging areas of thiomolybdate research, ending with a summary of challenges and key takeaway messages based on the state-of-the-art research.

1. Introduction

Extraction, processing, and combustion of fossil fuels are the cornerstones of our modern global economy. However, fossil feedstocks are finite, and their use is the main driver of greenhouse gas emissions and climate change. The continuously increasing energy demand poses massive challenges for the global economy and underlines the need to transition from fossil to renewable energy systems. One promising alternative fuel is hydrogen (H_2) as it has a high gravimetric energy density and can be produced from water by chemical, photochemical, and electrochemical means. However, traditional methods of H_2 production, such as steam reforming, need to be replaced with sustainable technologies including water electrolysis or photocatalysis, which enable the direct production of "green", sustainable H_2 using renewable energy. Thus, the development of efficient and robust catalytic systems for the splitting of water is one of the grand current challenges in chemistry. Cooperative and interdisciplinary research efforts are required to design earth-abundant and high-performance electro- and photocatalysts able to perform the hydrogen evolution reaction (HER) with high efficiency, selectivity, and stability.

HER involves the proton-coupled transfer of two electrons and occurs in two steps. The first step of HER is the Volmer reaction, which involves electron transfer to adsorbed H^+ ions to form hydrogen intermediates (H*) bound to the catalyst. After this, the formation of molecular H_2 can occur via two reaction pathways, depending on the surface coverage of H*. If the surface coverage is low, the H_2 formation will proceed by electrochemical hydrogen desorption—termed as Heyrovsky reaction—where a proton-coupled electron transfer (PCET) results in the formation and release of H_2 (**Scheme 1**a). In contrast, if the surface coverage of H* is high, this second step proceeds via the Tafel reaction, where two neighboring surface-bound hydrogen atoms H* are coupled to give dihydrogen (**Scheme** 1b). Independent of the reaction mechanism, it is evident that H* is involved in all reaction steps, hence the Gibbs free energy of hydrogen adsorption (ΔG_{H^*}) becomes an important indicator for an efficient HER catalyst. As postulated in the Sabatier principle,[1] and practically demonstrated by Nørskov et al.[2,3] the bonding strength between the catalyst surface and hydrogen atoms should neither be too weak nor too strong, implying that optimal bonding is a key to achieving optimized HER rates.

Many compounds have demonstrated HER activity, including noble metals, metal oxides, nitrides, and sulfides.[4] In this

S. Batool, S. N. Myakala, D. Eder, A. Cherevan
Institute of Materials Chemistry
TU Wien
Getreidemarkt 9/BC/02, Vienna 1060, Austria
E-mail: alexey.cherevan@tuwien.ac.at
M. Langer, M. Heiland, C. Streb
Institute of Inorganic Chemistry I
Ulm University
Albert-Einstein-Allee 11, 89081 Ulm, Germany
E-mail: carsten.streb@uni-mainz.de
M. Langer, M. Heiland, C. Streb
Department of Chemistry
Johannes Gutenberg University Mainz
Duesbergweg 10-14, 55128 Mainz, Germany

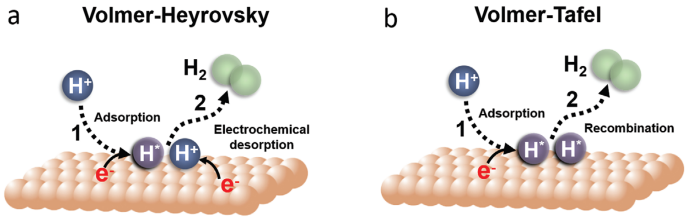
The ORCID identification number(s) for the author(s) of this article can be found under https://doi.org/10.1002/adma.202305730

© 2023 The Authors. Advanced Materials published by Wiley-VCH GmbH. This is an open access article under the terms of the Creative Commons Attribution License, which permits use, distribution and reproduction in any medium, provided the original work is properly cited.

DOI: 10.1002/adma.202305730

ADVANCED SCIENCE NEWS
www.advancedsciencenews.com

ADVANCED MATERIALS
www.advmat.de



Scheme 1. Simplified HER pathways taking place under acidic conditions. a) Volmer–Heyrovsky mechanism in which H_2 formation proceeds via PCET and electrochemical desorption steps, b) Volmer–Tafel mechanism in which two surface-adsorbed hydrogen atoms (H*) recombine to form H_2.

respect, molybdenum sulfides (MoS_2) have emerged as promising earth-abundant alternatives to the state-of-the-art Pt HER catalysts. MoS_2-based catalysts are long known as a class of industrial catalysts widely used in the world for petroleum refining processes such as hydrodesulfurization (HDS), hydrodeoxygenation (HDO), and hydrodemetallization (HDM) reactions.[5] Importantly, these processes share the dihydrogen activation steps required for the following hydrogenation or hydrogenolysis reactions, which highlights the H_2 activation reactivity of MoS_2 with relevance for HER. Despite these widespread commercial applications of MoS_2-based catalysts, early experiments using bulk crystalline MoS_2 revealed poor HER performance.[6] However, later studies showed that nanostructuring of MoS_2 results in HER activity levels approaching those of Pt.[7] Also, amorphous molybdenum sulfides (a-MoS_x) as well as nonstoichiometric molybdenum sulfides ($MoS_{2\pm x}$) have been shown to exhibit suitable hydrogen adsorption centers and promising HER performance.[8,9] The demonstration that edge-sites of MoS_2 sheets are likely HER active sites[10] triggered further interest in thiomolybdate clusters, which can be seen as molecular analogs of MoS_2. Their well-defined molecular structure and composition make it possible to probe their active centers and study their (de)activation pathways, ultimately delivering atomistic insights on the performance of a variety of MoS_2-based catalysts. This is nicely exemplified by early developments in inorganic molecular thiochemistry, which were stimulated by the needs of the petrochemical industries. In this context, molecular transition metal sulfides have been studied to gain insights into reactions that occur on the surfaces of heterogeneous catalysts. These studies involve the investigation of model feedstock molecules and the activation of dihydrogen with transition metal sulfur sites, shedding light on potential modes of binding for H_2 and thiophenes.[11]

Research progress in thiomolybdate HER activity until 2018 has been summarized by Streb and colleagues in their recent review.[12] The authors pointed out that thiomolybdates can act as models for two proposed active site mechanisms. The "sulfide/disulfide" mechanism proceeds via a Volmer–Heyrovsky process based on protonated sulfide/disulfide ligands. The "molybdenum hydride" mechanism proceeds via the formation of a Mo^V—H moiety, so that Mo-centered redox processes are involved in the hydrogen evolution.[13] It was pointed out that careful design of thiomolybdate complexes can provide crucial information on the active sites and limitations of MoS-based HER catalysis.

Previous reviews and book chapters have already provided a systematic look into the structure and synthesis of thiomolybdates and related inorganic compounds,[14–16] described methodologies that have been used to construct oxothiometalate-based materials[17,18] and reviewed early application of transition-metal complexes with sulfide ligand and thiomolybdate clusters in catalysis[19] and petrochemical industry.[5] This progress report will put a particular focus on the latest developments in thiomolybdate-based electro- and photocatalysts, especially with regard to combined experimental and theoretical studies to shed light on reaction mechanisms, active sites, and possible degradation and repair paths, as well as emerging strategies for heterogenization on functional substrates. Section 2 will introduce thiomolybdates from the perspective of their origin, structural variety and highlight some of the recent developments. Section 3.1 will provide a comprehensive look into the catalytic properties of thiomolybdates under homogeneous conditions in solution. Section 3.2 will examine state-of-the-art research related to the identification of active sites of molecularly dissolved and surface-supported thiomolybdate clusters. Section 4.1 will explore a variety of thiomolybdate compounds, including $[Mo_2S_{12}]^{2-}$, $[Mo_3S_{13}]^{2-}$, $[Mo_3S_4]^{4+}$, their analogs and derivatives, as HER electrocatalysts and will provide insights into the activity comparisons of the clusters compared to other MoS_x-based nanostructures. Section 4.2 will document the successful implementation of basic thiomolybdate clusters as HER co-catalysts by combining them with a range of oxide, nitride, sulfide, and microporous supports exhibiting inorganic, organic as well as hybrid nature. Section 5 will provide a short summary of our findings and present our broad outlook aiming to provide directions for the future research.

1.1. Thiometalates: Structure and Recent Developments

Pioneering work in the field of (poly)thiometalates—all-inorganic molecular metal sulfide clusters formed by several metal centers and sulfur-containing ligands—was in part inspired by bioinorganic studies of the enzymes nitrogenase and hydrogenase, where metal sulfide clusters were identified as active sites.[20,21] This insight has triggered major research into the design of artificial, biomimetic analogs.[22–26] In ground-breaking studies in the late 1970s, Müller and co-workers reported the structure and characterization of the two prototype anions $[Mo^V{}_2S_{12}]^{2-}$ (**Mo_2**)[27] and $[Mo^{IV}{}_3S_{13}]^{2-}$ (**Mo_3**)[28] as the respective ammonium

© 2023 The Authors. Advanced Materials published by Wiley-VCH GmbH

15214095, 2024, 7, Downloaded from https://advanced.onlinelibrary.wiley.com/doi/10.1002/adma.202305730 by Universitatsbibliothek Mainz, Wiley Online Library on [04/06/2025]. See the Terms and Conditions (https://onlinelibrary.wiley.com/terms-and-conditions) on Wiley Online Library for rules of use; OA articles are governed by the applicable Creative Commons License

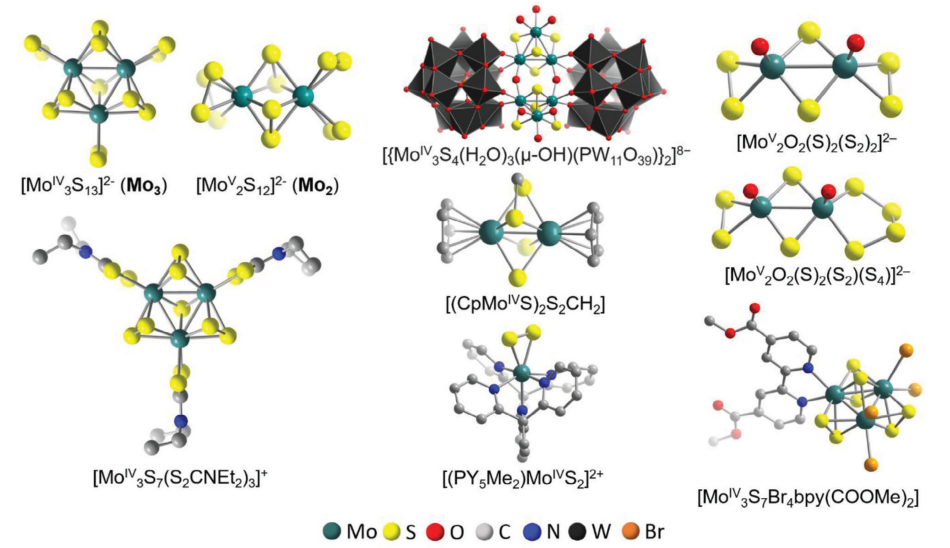


Figure 1. Structure illustrations of the thiomolybdate compounds described in this Review.

salts. Both clusters are formed by reduction of Mo^{VI} precursors (originally, ammonium heptamolybdate, $(NH_4)_6[Mo_7O_{24}]$) in (poly)sulfide-containing aqueous solutions resulting in the isolation of crystalline products. As shown in **Figure 1** (left), $Mo^{V/IV}$ centers in both thiomolybdate anions are coordinated by terminal and bridging disulfide (S_2^{2-}) ligands, however, the **Mo_3** cluster also contains an apical μ_3-S^{2-} ligand, which has been shown to allow initial **Mo_3** dimerization and stacking on the way to its thermal transformation to the hexagonal MoS_2 lattice.[29] Several extensive reviews published soon after this initial work provide a comprehensive overview of the synthesis, structural archetypes, electronic configurations, and spectroscopic characteristics of these and similar anionic clusters, in particular with a focus on their relevance as bioinspired models for the active sites of nitrogenase and hydrogenase enzymes.[30,31]

Although **Mo_2** and **Mo_3** can be seen as major representatives of prototypical all-inorganic thiomolybdates, several other groups of Mo-S-related molecular clusters and compounds are of high relevance to this review. As such, thiomolybdates can be modified to introduce O-containing ligands, leading to a larger group of oxothiometalate clusters (Figure 1, right).[32] On the other hand, stable thiometalates with structurally similar tungsten cores, such as $[W_2O_2S_8]^{2-}$ or $[W_3S_9]^{2-}$,[32,33] can be studied to gain deeper understanding of the roles of sulfide/disulfide ligands and metal centers on structural and catalytic aspects of such clusters. In recent years, studies in thiometalate chemistry have moved from individual molecules to extended structures, so that 1D chains,[34] metal–organic frameworks (MOFs),[35] and coordination polymers[36] with exciting reactivity have been reported. This opens new avenues to the design and implementation of more complex thiomolybdate (nano)structures.

Although thiomolybdates and their derivatives have been long-known in the literature, the main interest was initially focused on their synthesis, structure, principal chemistry, and bioinorganic relevance. The in-depth study of their hydrogen evolution activity was only triggered in 2008, when Chorkendorff and colleagues reported the electrochemical HER activity of the cubane-type $[Mo_3S_4(H_2O)_9]^{4+}$.[37,38] These groundbreaking studies have now led to a plethora of research activities, both in homogeneous and heterogeneous catalysis.

2. Catalytic Performance and Active Sites

In this section, we will explore the catalytic performance of prototype thiomolybdates and their derivatives under homogeneous conditions and when deposited as molecular species on heterogeneous supports and discuss proposed active sites of these species. Molecular thiomolybdate systems are ideally suited to deploy a wide range of modern analytical methods, including in situ and operando spectroscopies, to gain atomic-level understanding of active species, reaction mechanisms, and degradation pathways. Over the last decade, pioneering mechanistic studies have utilized thiomolybdates as molecular models able to shed light on the underlying processes which govern reactivity and stability of these and more complex molybdenum sulfide-based nanostructures. Most of these studies were focused on electrochemical or light-driven catalysis by the prototype **Mo_3** cluster (Figure 1, left).

© 2023 The Authors. Advanced Materials published by Wiley-VCH GmbH

15214095, 2024, 7, Downloaded from https://advanced.onlinelibrary.wiley.com/doi/10.1002/adma.202305730 by Universitätsbibliothek Mainz, Wiley Online Library on [04/06/2025]. See the Terms and Conditions (https://onlinelibrary.wiley.com/terms-and-conditions) on Wiley Online Library for rules of use; OA articles are governed by the applicable Creative Commons License

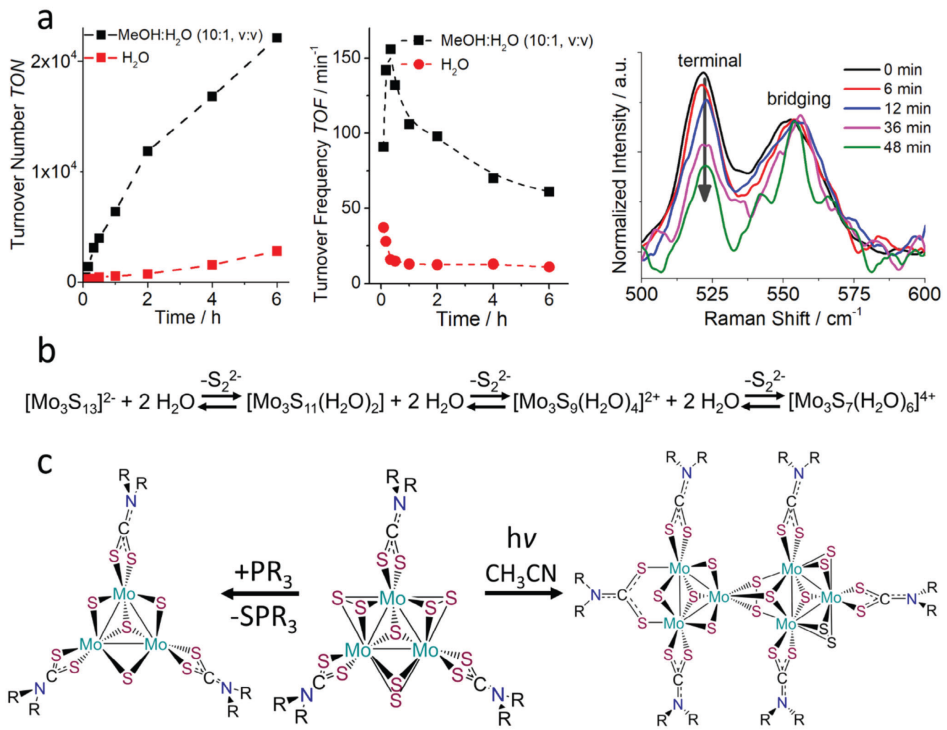


Figure 2. Catalytic performance under homogeneous conditions. a) Effect of solvent mixtures on light-driven HER: turnover numbers (TONs, left) and turnover frequencies (TOFs, center) during HER catalysis indicate faster deactivation of Mo_3 in aqueous conditions and suggest exchange of ligands followed by in situ generation of a catalytically more active species, also confirmed with in situ Raman spectroscopy (right). b) Schematic of disulfide ligand exchange with water ligands. c) Conversion of $\{Mo_3S_7\}$-core to $\{Mo_3S_4\}$-core containing clusters. R: methyl, ethyl, i-butyl, benzyl. (a,b) Reproduced with permission.[40] Copyright 2018, Royal Society of Chemistry. (c) Adapted with permission.[44] Copyright 2019, American Chemical Society.

In the following, we will explore the principal HER reactivity of thiomolybdates in Section 3.1, while active site insights will be discussed in Section 3.2.

2.1. Catalytic Properties

In 2018, the groups of Min[39] and Streb[40] independently reported the first studies into the light-driven HER by **Mo_3** under homogeneous conditions. Both groups observed high catalytic activity when combining **Mo_3** with $[Ru(bpy)_3]^{2+}$ as a photosensitizer (PS) and provided initial mechanistic understanding of the catalyst deactivation. Theoretical modeling of the HER process was used to rationalize the experimental data.

Streb and co-workers focused on understanding the structural changes and deactivation pathways of **Mo_3**. The group used Raman spectroscopy to propose the exchange of the terminal disulfide ligands of **Mo_3** by water ligands when operating in methanol/water ($MeOH/H_2O$) mixtures (**Figure 2**a,b). Catalytic analyses and theoretical calculations indicated that the resulting **Mo_3**-derivatives have different HER activity, depending on the number of water ligands. This insight was used to optimize the water content of the reaction mixture, so that the most active species were stabilized, leading to turnover numbers (TONs) > 20000. The group also observed decreasing TONs with increasing **Mo_3** concentration, which was assigned to ion pairing and colloid formation by aggregation of the anionic **Mo_3** with the cationic PS $[Ru(bpy)_3]^{2+}$. In a follow-up study using the **Mo_3**/$[Ru(bpy)_3]^{2+}$/ascorbic acid solutions, the authors reported an unusual effect of ammonium ions (NH_4^+) in enhancing the overall HER performance of the photosystem.[41] The authors performed a range of mechanistic studies and suggested that NH_4^+ is capable of increasing the lifetime of the photosensitizer excited state. Other contributions, including hydrogen bonding or proton management during HER, were also discussed, and the effect was demonstrated to be more general and

 © 2023 The Authors. Advanced Materials published by Wiley-VCH GmbH

15214095, 2024, 7, Downloaded from https://advanced.onlinelibrary.wiley.com/doi/10.1002/adma.202305730 by Universitatsbibliothek Mainz, Wiley Online Library on [04/04/2025]. See the Terms and Conditions (https://onlinelibrary.wiley.com/terms-and-conditions) on Wiley Online Library for rules of use; OA articles are governed by the applicable Creative Commons License

ADVANCED SCIENCE NEWS
www.advancedsciencenews.com

ADVANCED MATERIALS
www.advmat.de

15214095, 2024, 7, Downloaded from https://advanced.onlinelibrary.wiley.com/doi/10.1002/adma.202305730 by Universitätsbibliothek Mainz, Wiley Online Library on [04/06/2025]. See the Terms and Conditions (https://onlinelibrary.wiley.com/terms-and-conditions) on Wiley Online Library for rules of use; OA articles are governed by the applicable Creative Commons License

relevant to other PS, HER-catalysts, solvents, and sacrificial electron donors.

At the same time, Min and co-workers analyzed the effects of varying reaction parameters on the catalytic activity of **Mo$_3$**, including catalyst and photosensitizer concentration and their molar ratio. The authors also screened commonly used sacrificial electron donors such as organic amines or organic carboxylic acids. The highest light-driven HER activity was observed for ascorbic acid, which the authors explained by its dual function as proton and electron donor. Also, the authors reported that exchange of the original PS $[Ru(bpy)_3]^{2+}$ with the organic dye Eosin Y resulted in a complete loss of HER activity, possibly due to weak excited-state interactions of the PS and ascorbic acid, so that no electron transfer between the species occurs. Emission quenching studies demonstrated that ascorbic acid acts as a reductive quencher, while **Mo$_3$** acts as an oxidative quencher for the excited state of $[Ru(bpy)_3]^{2+}$. In a subsequent study, Min and co-workers combined **Mo$_3$** with the polyoxometalate (POM) $[H_4SiW_{12}O_{40}]$ as a UV-active photosensitizer.[42] In the presence of ethanol as a sacrificial agent, and under irradiation with UV light, the POM forms a two-electron-reduced species capable of electron transfer to **Mo$_3$**. Sustained hydrogen evolution over periods of 40 h with maximum TONs of≈6900 was reported for this molecular photosystem.

$[Mo_2S_{12}]^{2-}$ (**Mo$_2$**) is a smaller pure thiomolybdate cluster structurally closely related to **Mo$_3$** (Figure 1, left). Streb and co-workers explored the light-driven homogeneous HER of this complex[43] when combined with a PS and a sacrificial electron/proton donor. The group observed that catalyst reactivity is highly dependent on the solvent mixture used. Lower HER activity compared with **Mo$_3$** was reported, with TONs ≈ 1600. Notably, **Mo$_2$** shows the highest activity in pure methanol, and HER activity decreases with increasing water content of the solvent. This was rationalized by emission quenching studies which showed that increasing solvent water content leads to a less effective quenching of the $[Ru(bpy)_3]^{2+}$ PS by **Mo$_2$**. The authors did not observe the exchange of the terminal disulfide ligands of **Mo$_2$** under reaction conditions, which had been described as a major deactivation path for the reference **Mo$_3$** cluster. Analysis of the main reasons for the loss of catalytic activity (studied after ca. 6 h of irradiation) showed significant PS degradation, so the addition of a second PS aliquot after the initial irradiation period could be used to re-establish HER activity. These early results emphasize the need for replacing molecular photosensitizers with more redox-stable absorbers—a strategy that will be discussed in Section 3.3.

In addition to studies using pure thiomolybdates such as **Mo$_2$** and **Mo$_3$**, other thiomolybdate derivatives have been explored under homogeneous conditions. Donahue, Schmehl and colleagues investigated the light-driven HER activity for dithiocarbamate-functionalized **Mo$_3$** (Figure 1, left).[44] In these systems, the $\{Mo_3S_4\}$-core of native **Mo$_3$** is retained, while the terminal disulfides are substituted by dithiocarbamate ligands, e.g., diethyl dithiocarbamate, $NEt_2CS_2^-$. The authors used MALDI mass spectrometry to gain understanding of structural changes during catalysis. Within a few minutes of irradiation, the original species $[Mo_3S_7(S_2CNEt_2)_3]^+$ (Figure 1, left) disappears and a new species, $[Mo_3S_4(S_2CNEt_2)_3]^+$ arises. The authors propose that this new species is formed from the original cluster by exchange of the bridging disulfide ligands (S_2^{2-}) with sulfide ligands (S^{2-}), so that under catalytic conditions, $[Mo_3S_7(S_2CNEt_2)_3]^+$ acts as pre-catalyst, forming $[Mo_3S_4(S_2CNEt_2)_3]^+$ as the initial HER-active species. During catalysis, further speciation is observed, including the formation of dimeric species where a $[Mo_3S_7(S_2CNEt_2)_3]^+$ and a $[Mo_3S_4(S_2CNEt_2)_3]^+$ moiety are linked by a bridging sulfide ligand (Figure 2c). This observation is further evidence of the highly dynamic behavior and coordination chemistry of organo-functionalized thiomolybdates, which has been previously discussed for the parent **Mo$_3$** (vide supra).[40]

In a related study, Cadot and co-workers used the $\{Mo_3S_4\}$-core as an HER-active site for homogeneous, light-driven hydrogen evolution.[45] The authors stabilized two $[Mo_3S_4(H_2O)_3(\mu\text{-}OH)]^{3+}$ species with two $[PW_{11}O_{39}]^{8-}$ polyoxometalate clusters (Figure 1, middle), and reported the light-driven homogeneous HER of this compound using an Ir-based PS and triethanolamine as sacrificial electron donor. The authors showed that the covalent–coordinate linkage between thiomolybdate and polyoxometalate is required for high HER activity, while physical mixtures of both components only result in low hydrogen evolution. Mechanistic studies based on steady-state and time-resolved optical absorption and emission spectroscopies suggested that the Ir-based PS is reductively quenched by the electron donor and can subsequently transfer electrons to the catalyst at a high rate. Notably, high catalyst concentrations led to decreasing HER activity. The authors propose that the **Mo$_3$**-derived catalyst can absorb significant amounts of the incident photons, leading to overall suppressed rates of light-driven HER.

These studies document the intrinsic reactivity of a variety of thiomolybdate species towards light-driven HER under strictly homogeneous conditions and provide initial molecular-level insights about their activity and stability. The following chapter will examine mechanistic insights on the type of active sites in thiomolybdate HER catalysts.

2.2. Identification of Active Sites in Thiomolybdates

Mechanistic studies on amorphous materials are notoriously challenging due to a lack of information on the material structure at the atomic level, as well as the possible presence of multiple reactive sites. However, identifying the active site and rationalizing the resulting HER mechanism are critical for advancing catalyst development, as the nature of the active site is a key factor that determines the energetics, kinetics, and stability of a catalyst.

The study of thiomolybdate clusters as molecular models for a-MoS_x catalysts was fueled by a pioneering study by Tran, Artero and colleagues, who proposed that a-MoS_x with high HER activity is composed of polymeric chains of **Mo$_3$**.[46] This report has led to massive interest in exploring thiomolybdate reactivity and rationalizing HER mechanisms along with the nature of the active sites in molybdenum sulfide hydrogen evolving catalysts. However, even for molecularly well-defined systems such as thiomolybdates, identification of catalytically active sites is not straightforward, as active sites can depend on the reaction conditions applied (e.g., photochemical versus electrochemical processes, type of solvent, pH value, etc.).

In addition, it has been reported that thiomolybdates show highly dynamic behavior and undergo ligand exchange under typical catalytic conditions, so that different species can be

 © 2023 The Authors. Advanced Materials published by Wiley-VCH GmbH

present and the catalyst composition can change as a function of time (vide infra). As a result, different reactivity mechanisms are currently described in the literature based on experimental methods (e.g., spectroscopic investigations), theoretical calculations (e.g., DFT studies) and combinations of both. In the following section, we will discuss recent findings and summarize the current understanding of HER mechanisms and active sites in thiomolybdates. In addition, the summary presented in **Table 1** aims at correlating catalyst type, experimental condition and proposed active site.

2.2.1. Sulfide/Disulfide Mechanisms

Experimental and theoretical evidence highlighting the importance of the disulfide ligands were reported by Fantauzzi, Jacob, Streb and colleagues, who studied the light-driven HER using $\mathbf{Mo_3}$ as a catalyst.[40] The authors showed that under catalytic conditions in the presence of water, partial or complete exchange of terminal disulfide ligands with water ligands leads to several $\mathbf{Mo_3}$ derivatives (which can be described as $[Mo_3S_{13-x}(H_2O)_x]^{(2-x)-}$) that coexist in the reaction solution (Figure 2b). Experimental and theoretical analyses indicated that the number of water ligands in such a cluster controls the HER activity: while the fully exchanged species $[Mo_3S_7(H_2O)_6]^{4+}$ showed only marginal HER activity, Mo_3-core surrounded by a mixture of terminal disulfide and water ligands showed the highest reactivity. The introduction of terminal halide ligands also resulted in species with low HER activity. The study further used DFT calculations to explore the energetics of hydrogen evolution on the different water-substituted $\mathbf{Mo_3}$ species. The authors concluded that the energetics of the Volmer step for hydrogen adsorption at bridging disulfide ligands and for forming Mo-hydride species are similar, suggesting that both mechanistic paths are energetically feasible. These results could be interpreted as a first theoretical indication that $\mathbf{Mo_3}$ species are capable of undergoing sulfide/disulfide as well as molybdenum hydride mechanisms in HER catalysis Section 3.

Supporting evidence for a terminal disulfide ligand exchange mechanism was reported by Ončák and co-workers.[47] The groups combined mass spectrometric collision-induced dissociation (CID) experiments with theoretical DFT calculations to examine possible paths to $\mathbf{Mo_3}$ HER activity. The authors observed that even under low energy CID conditions, a range of sulfur/sulfide fragments could be generated from $\mathbf{Mo_3}$. The authors also note that the $\mathbf{Mo_3}$-based species created by CID show high reactivity with water, as observed by the formation of oxothiomolybdates as secondary species. As the mass spectrometric analyses did not allow unambiguous assignment of the type of sulfide ligands removed, the authors performed a subsequent study employing $\mathbf{Mo_3}$ derivatives where all terminal disulfides were replaced by halides (chloride, bromide, and iodide). Gas-phase fragmentation studies showed that loss of the terminal halides is the energetically most feasible fragmentation route, lending further support to the concept of preferred exchange at the terminal ligand sites.[48] In a follow-up work, Ončák and colleagues further linked thermochemical data calculated by DFT to experimental Fourier-transform ion-cyclotron resonance mass spectrometry (FT-ICR MS) and infrared multiple photon dissociation (IRMPD) spectroscopy data measured for a singly protonated $[HMo_3S_{13}]^-$ species.[49] The authors reported that under their conditions (in the gas phase), only the $\mathbf{Mo_3}$-based species with a singly protonated terminal disulfide ligand is observed. Calculations show that this species is thermochemically significantly more stable (by more than 1 eV) compared with $\mathbf{Mo_3}$ isomers where protonation occurs on the bridging disulfide or the apical sulfide position (**Figure 3**b). This study, therefore, suggests that protonated terminal disulfides are key HER intermediates. However, the authors also point out that these gas-phase studies cannot be directly compared with solution analyses, as many effects in the condensed phase can impact the stability and formation pathways of the intermediate and catalytic species.

In contrast to this series of studies focusing on terminal disulfide-based HER reactivity for thiomolybdate-derived catalysts, Joh and colleagues proposed that bridging sulfur ligands play a key role as HER active sites in heterogeneous systems accessed by thermal treatment of $\mathbf{Mo_3}$.[50] The authors used a combination of thermogravimetric analysis (TGA) and X-ray photoelectron spectroscopy (XPS) to link weight loss under heating to changes of the deconvoluted sulfur XPS signal to differentiate between apical/bridging and terminal sulfur positions. The authors propose that upon heating, first the apical sulfide ligand is removed, followed by the loss of the bridging ligands. Catalytic analyses of the resulting materials (supported on carbon nanotubes [CNTs]) showed that higher thermal treatment leads to lower electrocatalytic HER activity. However, further studies are required to fully appreciate the impact of sulfur removal versus structural/morphological changes caused by the heat treatment. Careful electrochemical studies, e.g., using electrochemical impedance spectroscopy or electrochemically active surface area determinations, could help to shed light on this intriguing result.

Very recently, Cherevan and colleagues reported a one-step deposition of $\mathbf{Mo_3}$ on TiO_2 particles for light-driven HER. The authors assigned the stable attachment to the formation of Mo—O—Ti bonds accompanied by the loss of most of the terminal disulfide ligands of $\mathbf{Mo_3}$.[51] Using XPS and thermal analyses together with pre- and postcatalytic materials comparison, the authors concluded that molybdenum centers with vacant coordination sites, Mo-oxo species or bridging disulfides are likely HER-active sites. In addition, the authors note that under catalytic conditions, polymerization of individual $\mathbf{Mo_3}$ species on the TiO_2 surface is observed, highlighting that operando studies are required to follow the temporal development of these catalysts as the reaction progresses.

Yeo and co-workers used operando Raman spectroelectrochemistry to assess possible active sites in a-MoS_2 films synthesized using $\mathbf{Mo_3}$ as precursor.[52] The group observed a characteristic Raman signal assigned to the S—H stretching of a Mo—S—H moiety. The assignment was supported by H/D isotope labeling and DFT calculations. Furthermore, the authors did not observe any Mo-hydride vibrations, which could be expected for a molybdenum hydride HER mechanism. Following a similar approach, Park and colleagues emphasize the importance of Mo=O intermediates in HER catalysis for a-MoS_x derived from thiomolybdate chains.[53] The heterogeneous material was obtained by simple polymerization of monomeric thiomolybdate $[MoS_4]^{2-}$ species. Resonance Raman spectroscopy and extended

© 2023 The Authors. Advanced Materials published by Wiley-VCH GmbH

15214095, 2024, 7, Downloaded from https://advanced.onlinelibrary.wiley.com/doi/10.1002/adma.202305730 by Universitatsbibliothek Mainz, Wiley Online Library on [04/04/2025]. See the Terms and Conditions (https://onlinelibrary.wiley.com/terms-and-conditions) on Wiley Online Library for rules of use; OA articles are governed by the applicable Creative Commons License

ADVANCED SCIENCE NEWS
www.advancedsciencenews.com

ADVANCED MATERIALS
www.advmat.de

Table 1. Active sites of Mo-sulfides: summary of conditions used and HER mechanisms proposed.

Proposed active sites	Catalyst	Experimental conditions	Year	Ref.
Terminal disulfides				
terminal S_2^{2-} (based on experimental data), possible role of Mo-H mechanism (based on theory)	Mo_3	Homogeneous, photochemical	2018	[40]
Terminal S_2^{2-}	Mo_3 and protonated species $([HMo_3S_{13}]^-$, $[H_3Mo_3S_{13}]^+)$	Homogeneous, gas-phase CID and FT-ICR $MS^{[47]}$/IRMPD[49]	2018, 2020	[47,49]
Bridging (di-)sulfides				
Bridging S_2^{2-}	Mo_3	Heterogeneous, electrochemical, deposited on O-CNT, low-temperature heat treatment	2018	[50]
Bridging S_2^{2-}, vacant coordination sites at Mo centers	Mo_3	Heterogeneous, photochemical, deposited on TiO_2	2022	[51]
Bridging S_2^{2-}	a-MoS_x, Mo-precursor: $(NH_4)_2[MoS_4]$	Heterogeneous, electrochemical, deposited on Mo or GC electrodes	2016	[52]
Bridging S^{2-} and Mo=O intermediates	Amorphous MoS_3, Mo-precursor: $(NH_4)_2[MoS_4]$	Heterogeneous, electrochemical, deposited on CP	2020	[53]
Bridging S_2^{2-}	Mo_2	Heterogeneous, electrochemical, deposited on FTO or GC electrodes	2015	[54]
Mo-centered				
Mo^{IV}-centered mechanism (Mo-hydride)	a-MoS_x, Mo-precursor: $(NH_4)_2[MoS_4]$	Heterogeneous, electrochemical, deposited on FTO electrodes	2016	[46]
Trapped Mo^{III}-H	Precatalytic a-MoS_x, Mo-precursor: $(NH_4)_2[MoS_4]$	Heterogeneous, electrochemical, deposited on a planar Au[55] or GC[56] electrode	2022	[55,56]
Others				
S_2^{2-}-centered mechanism	$[Mo^{IV}S_2(2,6\text{-}bis\{1,1\text{-}bis(2\text{-}pyridyl(ethyl)pyridine)\}^{2+}$	Heterogeneous, electrochemical, deposited on GC or Hg drop electrodes	2012	[58]
Protonated S_2^{2-}, Mo=O (as proton relay)	$[Mo^{VI}O(S_2)_2L]^-$/$[Mo^{VI}O(S_2)_2L]$ (L = pic[59] pym,[59] bpyR (R = H,[60,61] ^tBu,[60] $OMe^{[60]}$))	Homogeneous, electrochemical[59]	2016, 2017	[59–61]
Mo^{IV}—H mechanism and neighboring bridging hydrosulfide intermediates	$[Mo_3(\mu_3\text{-}S)(\mu_2\text{-}S_2)_3(S_2CNR_2)_3]$ (R = Me, Et, ^tBu, $CH_2C_6H_5$)	Homogeneous, photochemical	2019	[44]
S-centered mechanism	$[Mo_2O_2S_y]^{2-}$; $[(H)Mo_2O_2S_y]^-$ (y = 6, 5; x = 6, 5, 4)	Homogeneous, gas phase CID and FT-ICR MS	2022	[62]
S-centered mechanism, PCET	$[M_2O_2(\mu\text{-}S)_2(S_2)_2]^{2-}$ (M = Mo, W; x = 2, 4)	Heterogeneous, electrochemical, deposited on GC electrodes	2019	[32]

Notes: PCET: proton-coupled electron transfer; pic: picolinate; pym: pyrimidine-2-carboxylate; bpy: 2,2′-bipyridine; CID: collision-induced dissociation; FT-ICR MS: Fourier transform ion cyclotron resonance mass spectrometry; IRMPD: infrared multiple photon dissociation; O-CNT: oxidized multiwalled carbon nanotubes; GC: glassy carbon; CP: carbon paper; FTO: fluorine-doped tin oxide.

© 2023 The Authors. Advanced Materials published by Wiley-VCH GmbH

15214095, 2024, 7, Downloaded from https://advanced.onlinelibrary.wiley.com/doi/10.1002/adma.202305730, by Universitätsbibliothek Regensburg, Wiley Online Library on [04/06/2025]. See the Terms and Conditions (https://onlinelibrary.wiley.com/terms-and-conditions) on Wiley Online Library for rules of use; OA articles are governed by the applicable Creative Commons License

ADVANCED SCIENCE NEWS
www.advancedsciencenews.com

ADVANCED MATERIALS
www.advmat.de

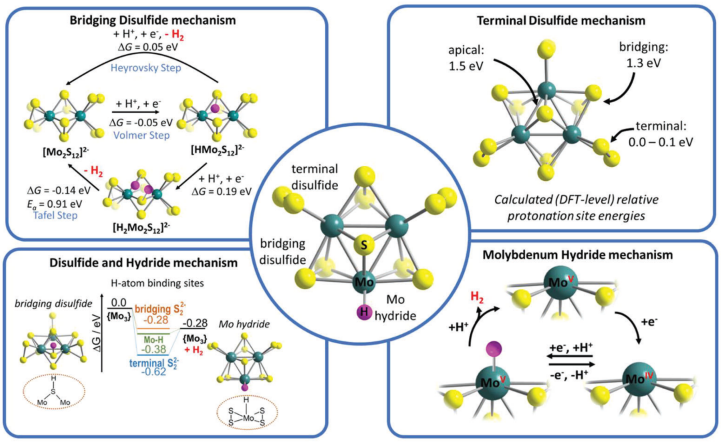


Figure 3. Illustration of possible active sites in the thiomolybdate prototype Mo_3, and proposed mechanisms at these active sites.

X-ray absorption fine structure (EXAFS) analyses showed that under catalytic conditions, formation of $Mo(O)_x$ species ($x = 1, 2$) is observed. The authors suggest that both, the presence of these $Mo(O)_x$ species and the presence of Mo^V units are important for binding and stabilizing protons on the reactive Mo—S site. They propose that the molybdenum-oxo groups could be responsible for proton management, e.g., by stabilizing hydrogen-bound intermediates via hydrogen bonding and by facilitating hydrogen atom transfer to the reactive disulfide ligands.

Chen and co-workers used the small $\mathbf{Mo_2}$ thiomolybdate as a model HER electrocatalyst by drop-casting $\mathbf{Mo_2}$ on electrode surfaces.[54] The authors used DFT calculations to study the high HER activity observed for $\mathbf{Mo_2}$. Their theoretical analyses show a calculated Gibbs free energy for hydrogen atom adsorption to the bridging disulfide ligands (−0.05 eV), which is close to the thermoneutral optimum of 0 eV. Experimental electrochemistry (Tafel slope analysis) and theoretical calculations both support that H_2 formation proceeds via a Volmer–Heyrovsky mechanism, while high activation barriers are calculated for the alternative Volmer–Tafel mechanism (Figure 3a; Scheme 1).

2.2.2. Mo-Hydride Mechanisms

In contrast to these sulfur-based mechanisms, Tran et al. proposed a Mo-based HER mechanism, based on electrochemistry, resonance Raman spectroscopy, and electron paramagnetic resonance (EPR) spectroscopy as well as DFT calculations.[46] The authors studied samples of $\mathbf{Mo_3}$ as nanoparticles or a-MoS_x films deposited on electrodes. Based on their results, they propose that under reductive electrochemical conditions, a pre-catalytic electrochemical activation occurs where Mo^{IV} centers with a vacant coordination site are generated on $\mathbf{Mo_3}$. These Mo^{IV} centers are reported to represent the catalytically active site (Figure 3d). Theoretical studies support the possibility of Mo^{IV}-hydride moieties as active sites of $\mathbf{Mo_3}$-derived amorphous MoS_x films. In addition, the authors reported that during HER electrocatalysis, resonance Raman data show that the signal intensity for bridging disulfide ligands is reduced, and the signal for terminal disulfides is completely lost. Also, the apical sulfide ligand signal is shifted, and the formation of Mo-oxide species is observed. Thus, the authors suggest that the resulting amorphous materials are best described by the formula MoS_{2+x}.

Very recently, Bau et al. reported the presence of Mo^{III} hydride species in $\mathbf{Mo_3}$-derived a-MoS_x deposited on electrode surfaces.[55] The authors report the observation of isotropic EPR spectra, which can be interpreted as a Mo^{III}-H species formed by electrochemical reduction starting from Mo^{IV}-based amorphous molybdenum sulfide. In-depth (in situ/operando) analyses, e.g., using X-ray absorption spectroscopy (XAS) methods are expected to provide further evidence for this striking initial hypothesis. The authors built on this work and proposed that Mo^{III} hydrides play an important role in many molybdenum-based HER electrocatalysts. Their hypothesis is based on experimental and theoretical analysis of a range of catalytic systems. The authors propose that (partial) oxidation of the Mo centers is a key deactivation mechanism, since Mo^{III}-oxo species are difficult to reduce to the active Mo^{III}-centers, and oxo ligands also limit proton diffusion to the Mo site.[56]

2.2.3. Organo-Functionalized Thiomolybdate Derivatives

Research has also focused on systems beyond pure molybdenum sulfides. In particular, modification of thiomolybdates with organic ligands has been used to control reactivity. In pioneering work, Appell et al. reported the electrocatalytic homogeneous HER of binuclear $[(CpMoS)_2S_2CH_2]$ and related species at nearly 100% current efficiency and low overpotentials (Figure 1, middle).[57] In mechanistic studies, the author team proposed

© 2023 The Authors. Advanced Materials published by Wiley-VCH GmbH

15214095, 2024, 7, Downloaded from https://advanced.onlinelibrary.wiley.com/doi/10.1002/adma.202305730 by Universitatsbibliothek Mainz, Wiley Online Library on [04/06/2025]. See the Terms and Conditions (https://onlinelibrary.wiley.com/terms-and-conditions) on Wiley Online Library for rules of use; OA articles are governed by the applicable Creative Commons License

15214095, 2024, 7, Downloaded from https://advanced.onlinelibrary.wiley.com/doi/10.1002/adma.202305730 by Universitätsbibliothek Mainz, Wiley Online Library on [04/06/2025]. See the Terms and Conditions (https://onlinelibrary.wiley.com/terms-and-conditions) on Wiley Online Library for rules of use; OA articles are governed by the applicable Creative Commons License

that the rate-determining step appears to be the elimination of dihydrogen which can occur via neighboring hydrosulfide ligands or mixed hydrosulfido/Mo-hydride species.

Chang and co-workers explored the electrocatalytic homogeneous HER activity of the complex $[(PY_5Me_2)Mo^{IV}S_2]^{2+}$ (PY_5Me_2 = 2,6-*bis*(1,1-*bis*(2-pyridyl)ethyl)pyridine), which is a molecular model for the terminal Mo-disulfide moiety (Figure 1, middle).[58] The authors observed that the complex can be reduced by at least two electrons. In the presence of protons under reductive electrochemical conditions, a strong catalytic wave, and H_2 evolution at nearly 100% Faradaic efficiency is observed. Voltammetric analyses show that the first reduction of the complex is proton-coupled, allowing the authors to propose that this process corresponds either to the formation of a protonated, one-electron-reduced Mo-disulfide species, or the breaking of a Mo—S bond between the molybdenum center and the disulfide ligand. Notably, reference experiments with the species $[(PY_5Me_2)MoO]^{2+}$ where the disulfide ligand is replaced with a terminal oxo group show much lower HER activity, highlighting the importance of the disulfide ligand, either as an active site or as a modulator to facilitate reduction of the complex.

A different, elegant model system has been reported by Wu and co-workers.[59–61] The group developed a mononuclear species, $[Mo^{IV}O(S_2)_2L]$ (L = organic ligand, e.g., picolinate,[59] pyrimidine-2-carboxylate or 2,2′-bipyridine-derivatives[60,61]), as an active-site model for a-MoS_x. For the 2,2-bipyridine-derivative, the authors propose an electrocatalytic Volmer-Heyrovsky type HER mechanism, which proceeds by two-electron reduction and protonation of a disulfide (to yield a sulfide, S^{2-} and a hydrosulfide, HS^-).[61] The hydrosulfide ligand acts as a "hydride" mimic and reacts with a second proton in a Mo-oxo-mediated Heyrovsky step, resulting in H_2 evolution and regeneration of the original catalyst. In a subsequent study, the group demonstrated the importance of the organic 2,2-bipyridine (bpy) ligand. Modification of the electronic structure of the ligand by attaching electron donating groups had a direct impact on the nucleophilicity of the disulfide ligands on the Mo center. This, in turn, modulated the protonation affinity of the disulfides, which affected the HER performance. The authors also demonstrate that the disulfide ligands are the redox-active sites in this system, while the molybdenum center retains its oxidation state (+IV) even under highly reductive conditions. This could be explained by the presence of the electronegative oxo ligand, which prevents further Mo reduction.

Schmehl and colleagues studied a **Mo_3** derivative, in which the three terminal disulfide ligands were selectively replaced with organic dithiocarbamates (Figure 2c).[44] This model compound is well suited to explore light-driven homogeneous HER activity in the absence of terminal disulfides. The authors used mass spectrometry to follow changes in the catalyst composition under turnover conditions and observed that the actual catalytic species is formed by conversion of the bridging disulfides to sulfide ligands. Catalyst "poisoning" experiments using strongly coordinating solvents such as DMF showed that at least one vacant coordination site at a Mo center is required for HER to proceed. Based on this observation and DFT calculations, the authors propose a species featuring a Mo^{IV} hydride and adjacent bridging hydrosulfide as the most likely intermediate formed before H_2 release.

2.2.4. Mixed Oxothiomolybdates

The introduction of oxo-ligands in thiomolybdates has a major impact on the reactivity of the resulting oxothiomolybdates (vide supra),[47,51,53] which led to seminal studies exploring their HER-function. Following the suggestion that protonated terminal disulfides are important HER intermediates for **Mo_3**, Ončák and colleagues used theoretical calculations to study potential H atom binding sites to $[Mo_2O_2S_x]^{n-}$ in different charge states together with H_2 elimination pathways. The authors identified several H atom adsorption sites as well as energetically favored H_2 elimination pathways. This flexibility, combined with the ease of electron attachment and removal, appears to be the crucial property that makes molybdenum oxysulfides such good HER catalysts.[62] Miras and co-workers reported the electrocatalytic HER activity of the dinuclear compounds $[Mo_2O_2(S)_2(S_2)(S_x)]^{2-}$ (x = 2, 4; Figure 1) when deposited on GC electrodes.[32] Computational analysis of the systems suggested a Volmer–Heyrovsky mechanism where proton-coupled two-electron-reduction leads to a reductive cleavage of a disulfide ligand and the formation of two hydrosulfides. The authors note that the exact mechanism of the Heyrovsky step in these models is still not fully understood, so a complete rationalization of the H_2 release requires further studies. In addition, DFT calculations suggest that the oxo ligand plays an important role in stabilizing the reduced catalyst species by accepting negative charge density due to the high electronegativity of the oxygen atom. In addition, Nadjo and co-workers explored the electrocatalytic homogeneous HER activity of mixed oxothiomolybdate rings, such as $[Mo_8S_8O_8(OH)_8(oxalate)]^{2-}$.[63] The group reported electrochemical studies where catalytic hydrogen evolution was observed under reducing conditions in DMF solution in the presence of strong as well as weak acids.

As shown in Table 1, when summarizing the findings from Section 3.2, there is a general trend that under homogeneous conditions, most reports favor terminal disulfide active sites, while under heterogenized conditions, bridging disulfides are mainly discussed as active sites. Mo-hydride species are most often described when amorphous a-MoS_x is studied, while for thiomolybdates featuring organic ligands, a variety of possible active sites have been reported. While each individual study provides a huge contribution to improve the general understanding of underlying mechanistic processes, stability and identification of catalytically active sites, many of the studies seem contradictory, and there is no general consensus in the field in terms of the true reaction mechanism (or mechanisms). This is due to the fact that the molybdenum sulfide HER mechanism is highly dependent on the exact reaction conditions, the type of support used, and on the exact structure of the cluster. Hence, further work including the design of suitable model systems, as well as combined experimental and theoretical studies—ideally involving in situ and operando investigations—are required to fully understand the complex mechanisms involved in hydrogen evolution by thiomolybdates.

2.3. Heterogenization of Thiometalates

In this section, we will pick up on initial discussions from Sections 3.1 and 3.2 concerning the prospects and benefits of

 © 2023 The Authors. Advanced Materials published by Wiley-VCH GmbH

15214095, 2024, 7, Downloaded from https://advanced.onlinelibrary.wiley.com/doi/10.1002/adma.202305730 by Universitatsbibliothek Mainz, Wiley Online Library on [04/06/2025]. See the Terms and Conditions (https://onlinelibrary.wiley.com/terms-and-conditions) on Wiley Online Library for rules of use; OA articles are governed by the applicable Creative Commons License

thiometalate heterogenization. In this context, heterogenization describes either the anchoring of individual thiometalate clusters on the surface of solid-state supports, the incorporation of thiometalates within (micro)porous matrices or the deposition of clusters followed by their chemical conversion into nanostructured amorphous or crystalline particles. Similar to the case of other molecular inorganics such as polyoxometalates,[64] surface-anchoring of thiometalate clusters can rely on electrostatic (due to their ionic charge), covalent (due to exchange of the sulfide/disulfide ligands), or weaker noncovalent interactions between cluster and the support surface. From the synthetic point of view, heterogenization can be achieved using a range of immobilization techniques including dip-coating, solvothermal deposition, layer-by-layer assembly, and electrodeposition.[64] Note that depending on the deposition methods and conditions used, the conversion of molecular thiomolybdates into more complex nanostructures—often a-MoS_x—is possible and should be critically assessed when studying and reporting thiomolybdate-based electrocatalysts.

Heterogenization of thiomolybdates is a fast-moving research direction due to several reasons: deposition of thiomolybdates on electrically conductive substrates or semiconductors facilitates their use in (photo)electrochemical HER as heterogeneous materials, which is an advantage for scaling and technological processing. Furthermore, heterogenization could lead to a stabilization of the thiomolybdate clusters, e.g., by preventing fast ligand exchange or providing structural stabilization during the catalytic redox cycles. In addition, molecule–support interactions could be used to further fine-tune reactivity and stability of thiomolybdates, e.g., by utilizing the supports for managing proton and/or electron transfer. Finally, the use of semiconductors as supports opens new avenues to combine heterogenization and photosensitization in one material, making the traditional use of noble metal-based photosensitizers (e.g., $[Ru(bpy)_3]^{2+}$) obsolete. These and other aspects of thiomolybdate heterogenization will be next discussed from the application point of view in Section 4.

3. Applications of Heterogenized Thiomolybdate Clusters

This section aims to scrutinize the applications of surface-anchored thiomolybdate clusters. The analysis focuses on the catalytic performance as well as on details of the surface-anchoring, the stability of the resulting system, and the fate of the cluster, from deposition through to catalysis. In particular, we highlight the emerging use of in situ/operando analyses as well as the combination of experiment and theory to rationalize the observed reactivity trends. In Section 3.1, we focus on electrocatalysis, while Section 3.2 describes selected examples of photocatalytic deployment. In Section 3.3, recent examples where heterogenized thiomolybdates were used for reactions and processes other than HER are summarized.

3.1. Electrocatalysis

Solid-state molybdenum sulfides are well known for their excellent electrocatalytic HER performance and are discussed as replacements for platinum-based HER catalysts. In particular, MoS_{2+x} systems with an S-to-Mo ratio higher than two have been reported to be excellent electrocatalysts for the HER.[65] This section explores how thiomolybdate-based heterogeneous materials are designed, tuned and deployed as high-performance HER electrocatalysts.

Along with TONs that are indicative of the catalyst stability, turnover frequencies (TOFs)—a measure of the rate of catalysis per active site—are key figure of merits for the HER performance and will be used throughout this section as an indicator for the intrinsic HER activity measured for the thiomolybdate clusters. Note that for most of the heterogenized catalysts discussed here, the calculation of TOFs and TONs assumes that every cluster present in the catalyst is available for the reaction. Thus, the use of TON and TOF—particularly in heterogenized systems, requires careful thought and critical analysis of the system studied.[66–68] Also note that all potentials mentioned throughout this chapter (and those in **Table 2**) are reported versus the reversible hydrogen electrode (RHE) and all overpotentials are reported at the current density of 10 mA cm^{-2} unless stated otherwise. Nevertheless, we strongly advise the reader to always be aware of the substrate used for the electrode, as different supporting materials can have varied electrochemical surface areas for the same geometric surface area, thus affecting the reported performance indicators. The challenges of benchmarking electrocatalytic reactions have been comprehensively reviewed by Jaramillo and co-workers.[69]

Further, throughout this section we will use Tafel slope analysis as a tool to gain insights into the rate-limiting steps in electrocatalytic HER. For example, a Tafel slope below 30 mV dec^{-1} is indicative of the Tafel reaction (H* recombination) to be the rate-limiting step. Similarly, a Tafel slope around 40 or 120 mV dec^{-1} suggests Heyrovsky (electrochemical H_2 desorption) or Volmer (discharge) step be the rate-limiting step, respectively (Scheme 1).[70]

3.1.1. Electrocatalytic HER Activity of Heterogenized Thiomolybdates

This section summarizes the initial reports on molecular mimics of MoS_2 electroactive toward HER, along with factors affecting their performance. Chorkendorff and co-workers were the first to test cubane-type $[Mo_3S_4]^{4+}$ clusters supported on carbon materials (Vulcan xc72 and highly oriented pyrolytic graphite [HOPG]) for the electrocatalytic HER.[38] For $[Mo_3S_4]^{4+}$/Vulcan system, the authors reported a low HER onset potential of ≈150 mV, similar to that of nanoparticulate MoS_2. However, the authors observed drops in current density upon multiple scans without any change in onset potential, which they attribute to possible dissolution of the clusters. Further investigation using scanning tunneling microscopic (STM) imaging was conducted for the drop-cast $[Mo_3S_4]^{4+}$/HOPG system revealing agglomeration mounds—possibly corresponding to cluster deposits or products of its degradation—which the authors related to the weak interactions between the clusters and the substrate surface. This assumption was further strengthened based on postcatalytic XPS analysis of $[Mo_3S_4]^{4+}$/HOPG, which revealed almost no peaks corresponding to the Mo 3d of the pristine cluster suggesting

 © 2023 The Authors. Advanced Materials published by Wiley-VCH GmbH

ADVANCED SCIENCE NEWS
www.advancedsciencenews.com

ADVANCED MATERIALS
www.advmat.de

Table 2. Supported thiomolybdates in electrocatalytic HER: summary table showing prominent examples of thiomolybdate clusters implementation, along with the supports used, deposition applied, and HER performance indicators including Tafel slopes, overpotentials, TOF values as well as major experimental conditions.

Cluster	Support	Deposition technique	Experimental conditions	Tafel slope [mV dec^{-1}]	Overpotential at 10 mA cm^{-2} vs RHE [mV]	TOF at 200 mV [s^{-1}]	Year	Ref.
MoS_2								
MoS_2 NPs	Au(111)	PVD of Mo in H_2S background	H_2SO_4, pH 0.2	55	–	0.02	2007	[10]
MoS_2	rGO | GCE	Drop casting	0.5 M H_2SO_4	41	–	–	2011	[85]
Monodispersed MoS_2	Au[110]	Incubation	0.5 M H_2SO_4	69	180–190	–	2013	[86]
		Drop casting		100	–		2013	[86]
Mo_xS_4								
$[Mo_3S_4]^{4+}$	C-xc72	Drop casting	0.5 M H_2SO_4, pH 0.4	120	200	0.07	2008	[38]
$CuMoS_4$	GCE	Drop casting	0.1 M H_3PO_4, pH 7	–	–	–	2012	[87]
$Mo_2/Mo_3/W_2$								
Mo_3	GP/HOPG	Drop casting	0.5 M H_2SO_4	40/57	180	1	2014	[71]
Mo_3	Au | GC	Spray coating	0.1 M $HClO_4$	58	–	0.47	2017	[72]
Mo_3	Ag | GC			48	–	0.27	2017	[72]
Mo_3	GC			45	–	0.15	2017	[72]
Mo_3	Cu | GC			66	–	0.045	2017	[72]
Mo_3	rGO-CNTs	Solvothermal	0.5 M H_2SO_4	67.4	179	–	2017	[76]
Mo_3	HOPG	Electrodeposition	0.5 M H_2SO_4	37	200	–	2017	[78]
Mo_3	O-CNTs	Physical mixture	0.5 M H_2SO_4	40	137	2.5 at 250 mV	2018	[50]
Mo_2	FTO	Drop casting	0.5 M H_2SO_4	39	161	1.6	2015	[54]
$[Mo_2O_2S_6]^{2-}$	GCE	Drop casting	1 M H_2SO_4	52	114	0.12	2019	[32]
$[Mo_2O_2S_8]^{2-}$			1 M H_2SO_4	55	116	0.12	2019	[32]
$[W_2O_2S_8]^{2-}$			1 M H_2SO_4	100	227	0.13	2019	[32]
MoS_3								
a-MoS_3-Mo_1-derived	Carbon paper	Drop casting	0.5 M H_2SO_4	46	167	0.01	2020	[53]
a-MoS_3-Mo_2-derived			0.5 M H_2SO_4	47	170	0.004	2020	[53]
a-MoS_3-Mo_3-derived			0.5 M H_2SO_4	52	196	0.0006	2020	[53]
MoS_3	FTO	Spray casting	1 M H_2SO_4	45	190	–	2011	[88]
MoS_3	FTO	Drop casting	1 M H_2SO_4, pH 0	61	200	–	2011	[88]
MoS_3	GCE	Drop casting	1 M H_2SO_4	50	200	–	2011	[88]
Others/composites								
bachera-MoS_2/MWCNT	Ag	Drop casting + in situ reduction of MoS_3	1 M H_2SO_4	40	–	–	2013	[89]
Ni-P/MoS_x	FTO	Electrodeposition	1 M KOH	64	140	–	2017	[90]
MoS_x	FTO	Electrodeposition	1 M KOH	140	260	–	2017	[90]
MoS_2/MWCNT	GCE	Drop casting	0.5 M H_2SO_4	62	–	–	2016	[91]
MoS_2/CO	GCE	Drop casting	0.5 M H_2SO_4	60	180	0.94 at 220 mV	2016	[92]
Pd-MoS_2/MWCNT	GCE	Drop casting	0.5 M H_2SO_4	54	120	0.05 at 30 mV	2017	[93]
MoS_2/CN_x	GCE	Drop casting	0.5 M H_2SO_4	52	158	–	2017	[94]

Notes: NPs: nanoparticles; PVD: physical vapor deposition; rGO: reduced graphene oxide; GCE: glassy carbon electrode; C-xc72: vulcan carbon; GP: graphite paper; HOPG: highly oriented pyrolytic graphite; O-CNTs: oxidized carbon nanotubes; FTO: fluorine-doped tin oxide; MWCNT: multiwalled carbon nanotubes.

© 2023 The Authors. Advanced Materials published by Wiley-VCH GmbH

15214095, 2024, 7, Downloaded from https://advanced.onlinelibrary.wiley.com/doi/10.1002/adma.202305730, by Universitatsbibliothek Munster, Wiley Online Library on [14/06/2024]. See the Terms and Conditions (https://onlinelibrary.wiley.com/terms-and-conditions) on Wiley Online Library for rules of use; OA articles are governed by the applicable Creative Commons License

ADVANCED SCIENCE NEWS
www.advancedsciencenews.com

ADVANCED MATERIALS
www.advmat.de

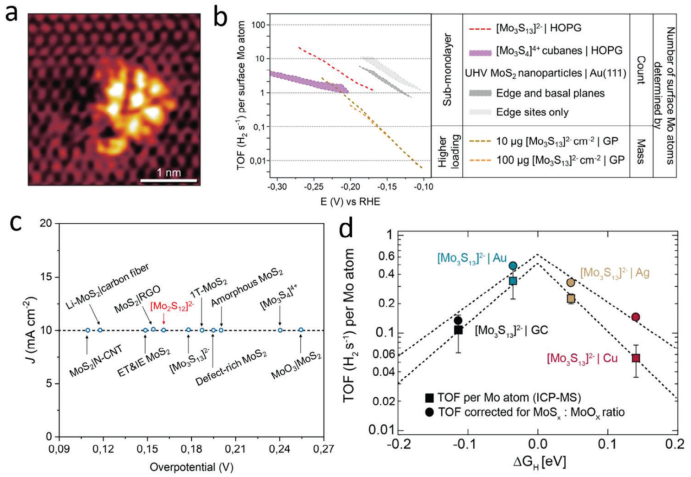


Figure 4. Supported thiometalates in electrocatalysis. a) Scanning tunneling microscopy (STM) image of a single Mo_3 cluster on HOPG support. b) TOF plot comparing electrochemical HER performance of Mo_3/HOPG and Mo_3/GP with other MoS_x catalysts. c) Overpotential comparison between various Mo—S based catalysts. d) HER volcano plot showing TOF_{MoOx} corrected using ICP-MS. (a,b) Reproduced and adapted with permission.[71] Copyright 2014, Nature Chemistry. (c) Adapted with permission.[54] Copyright 2015, Wiley-VCH GmbH. (d) Reproduced with permission.[72] Copyright 2017, American Chemical Society.

unstable nature of its attachment. To circumvent this issue, HOPG surface was activated by electrochemical oxidation to introduce —OH and —COOH groups able to act as anchoring sites for $[Mo_3S_4]^{4+}$ cations. Combining this strategy with STM imaging to reveal the surface density of the clusters, the authors reached a TOF of 0.07 s^{-1} per $[Mo_3S_4]^{4+}$ molecule, as compared to 0.02 s^{-1} (per edge site determined via STM imaging) measured for the reference MoS_2 sample.

Almost half a decade later, Besenbacher and co-workers reported excellent electrocatalytic performance by **Mo_3** which was drop-cast onto an anodized HOPG surface (**Figure 4a**). XPS analysis confirmed stable attachment of the clusters onto the surface without any transformation.[71] **Mo_3** dispersed over HOPG exhibited a low overpotential of ≈180 mV and a Tafel slope of ≈57 mV dec^{-1}, indicating H* recombination to be the rate-determining step (Scheme 1). However, to obtain a better comparison to reported literature, the authors loaded the clusters onto graphite paper (GP) increasing the loading from 10 to 100 µg cm^{-2}. They observed all Tafel slopes to be around 38–40 mV dec^{-1}, which indicates the Heyrovsky (desorption) step to be rate limiting. To further elucidate the reason for the change in HER mechanism and avoid any effects due to the change in support, the authors measured the Tafel slopes of different loadings of clusters onto a single support, glassy carbon (GC). They observed a Tafel slope of 40 mV dec^{-1} at higher loadings whereas a Tafel slope of ≈60 mV dec^{-1} was observed for very low loadings similar to the case of HOPG. Therefore, the authors suggested this change in the mechanism is independent of the support and rather could be due to closer packing of the cluster (and thus active sites) which affects the H-adsorption and chemical rearrangement of the intermediate steps during HER. As to the intrinsic HER activity of the clusters, the authors reported a high TOF of 3 s^{-1} per Mo atom (i.e., 1 s^{-1} per **Mo_3**) at −200 mV for the **Mo_3**/HOPG architecture (Figure 4b). However, they did observe a fivefold lower TOF when depositing higher loadings of the clusters onto GP, which they attributed to shielding of the catalytic sites due to cluster agglomeration. As an important contrast to the $[Mo_3S_4]^{4+}$ work conducted by Chorkendorff and coworkers,[38] here the authors observed no loss in catalytic performance, which suggests a more stable binding of **Mo_3** to anodized HOPG compared with $[Mo_3S_4]^{4+}$. As a consequence, upon accelerated HER testing (1000 cyclic voltammetry (CV) cycles between −0.3 and +0.2 V), the **Mo_3**/HOPG composite showed only a slight decrease in current density and a small increase in total impedance.

Building on these results, Wu and co-workers explored the electrochemical performance of the dimeric **Mo_2** deposited onto FTO substrate via layer-by-layer assembly (involving positively charged polyquaternium-6 interlayer) and drop-casting, aiming for sub-monolayers and higher catalyst loading, respectively.[54] They reported an even higher TOF of 3.2 s^{-1} per Mo atom (which could be translated to 1.6 s^{-1} per **Mo_2** cluster based on total **Mo_2** loading) at −200 mV, while the overpotential required to reach a current density of 10 mA cm^{-2} for **Mo_2** was found to be only 161 mV, outcompeting both previously mentioned $[Mo_3S_4]^{4+}$ and **Mo_3** that showed an overpotential of 240 and 180 mV, respectively, when deposited on HOPG (Figure 4c). To explain this difference in performance, the authors theoretically modeled H adsorption on the unsupported clusters in question. They calculated the change in free energy for **Mo_2** and **Mo_3** as −0.05 and

© 2023 The Authors. Advanced Materials published by Wiley-VCH GmbH

15214095, 2024, 7, Downloaded from https://advanced.onlinelibrary.wiley.com/doi/10.1002/adma.202305730 by Universitatsbibliothek Mainz, Wiley Online Library on [04/06/2025]. See the Terms and Conditions (https://onlinelibrary.wiley.com/terms-and-conditions) on Wiley Online Library for rules of use; OA articles are governed by the applicable Creative Commons License

ADVANCED SCIENCE NEWS
www.advancedsciencenews.com

ADVANCED MATERIALS
www.advmat.de

15214095, 2024, 7, Downloaded from https://advanced.onlinelibrary.wiley.com/doi/10.1002/adma.202305730 by Universitätsbibliothek Mainz, Wiley Online Library on [04/06/2025]. See the Terms and Conditions (https://onlinelibrary.wiley.com/terms-and-conditions) on Wiley Online Library for rules of use; OA articles are governed by the applicable Creative Commons License

−0.08 eV, respectively: these values are significantly closer to the theoretical optimum (0.0 eV) compared with data reported earlier for $[Mo_3S_4]^{4+}$ (0.4 eV).[54] Therefore, based on these initial works, dimeric **Mo_2** seems to outperform the previously reported MoS_x-based HER electrocatalysts due to favourable adsorption-desorption thermodynamics. However, more studies and direct comparison between **Mo_2** and **Mo_3** under identical experimental conditions is necessary to identify their active HER sites and unravel structural features which control their HER performance.

3.1.2. Catalyst–Support Interactions

The choice of the substrate is essential for providing robust anchoring and improved electronic coupling between catalyst and substrate. A bulk of earlier work on supported MoS_2-based catalytic phases for HDS, HDO and HDM catalysis already demonstrated a synergistic effect between the two components and importance of the support choice.[73,74] In this section, we discuss the current understanding of how the choice of substrates affects the stability and electrocatalytic performance of heterogenized thiomolybdates.

Building on their earlier studies on **Mo_3**, Jaramillo and co-workers carried out a follow up study correlating the HER activity of **Mo_3** with the type of support material used.[72] The group studied electrocatalytic HER performance of a thin layer of cluster deposited on four substrates, i.e., pristine glassy carbon (GC), Cu on GC (Cu/GC), Ag on GC (Ag/GC), and Au on GC (Au/GC). The authors deliberately kept the catalyst loading low to be able to observe the effects of the catalyst–support interactions as these tend to have a short range.[75] By keeping the catalyst loading low the authors also avoided any detrimental effects related to cluster aggregation. The results of XPS analyses of the supported catalysts were virtually identical to the pure **Mo_3** precursors, suggesting that the heterogenization did not majorly affect the structure of the deposited **Mo_3**. Tafel slope analyses for all samples were in the range of 40 to 60 mV dec^{-1}, so that no clear insights into the difference in underlying rate-determining steps were possible. In contrast, a marked impact of the substrate on the TOF was observed, and the resulting TOF values at −200 mV were measured to be 0.47 s^{-1} (Au/GC), 0.27 s^{-1} (Ag/GC), 0.15 s^{-1} (GC), and 0.045 s^{-1} (Cu/GC), respectively (Figure 4d). The authors carried out DFT calculations considering long range van der Waals forces to account for the effect of the strength of the cluster adhesion on the support on its activity.[75] They correlate the observed TOFs to changes in Gibbs free energy for hydrogen adsorption on the cluster (for each support) and arrived at the conclusion that the relationship between the two follows a volcano-plot trend well known for other HER electrocatalysts.[2]

Following similar concepts, Gao and co-workers reported an increase in electrocatalytic HER performance at low catalyst loadings when immobilizing **Mo_3** onto highly conductive reduced graphene oxide (rGO)–CNT aerogels (**Figure 5a**),[76] reporting an HER overpotential of 179 mV. Attachment of the clusters to the aerogels was demonstrated using multiple techniques including EDS mapping and Raman spectroscopy. The authors reported a low Tafel slope of 60–70 mV dec^{-1}, similar to the case reported by Jaramillo and co-workers in the best-performing **Mo_3** on Au/GC and Cu/GC.[72] The authors employed zeta potential measurements and XPS analyses to gain insights into the immobilization mechanism. Zeta potential measurements revealed a negatively charged rGO-CNT surface, which—considering the anionic **Mo_3** clusters in solution—renders electrostatic attachment unlikely. XPS analysis showed a characteristic S—O binding peak allowing the authors to suggest strong cluster attachment via covalent linkage to the O-containing functional groups on the nanocarbon surface. However, we note that molybdenum sulfides and thiomolybdates can feature oxidized sulfur species (e.g., sulfate) left from the synthesis or formed during catalysis.[77] Thus, care must be taken when interpreting the origin of any S—O signals, e.g., in XPS. Thus, further studies might be required to fully appreciate the type of attachment present in the **Mo_3**/rGO-CNT composites. For example, an alternative attachment scenario could take place via the **Mo_3** ligand exchange mechanism discussed in Section 3, which shows that charge-neutral or even cationic cluster species could be accessed. As to the electrocatalytic performance of the **Mo_3**/rGO-CNT composite, although the authors did not report the TOF values, the small Tafel slope, low charge transfer, and dispersion resistances indicate a fast reaction rate corresponding to efficient HER performance and low overpotentials. Moreover, the authors report a negligible change in activities even after 1000 CV cycles, further confirming the robust nature of the **Mo_3**/rGO-CNT electrocatalyst (Figure 5a).

Li and co-workers took a different approach to strengthen the linkage between the cluster and substrate.[78] Contrary to using drop-casting or impregnation methods, they electrodeposited **Mo_3** onto HOGP in the form of flakes of varying thicknesses by changing the deposition times. Note that under mild electrodeposition conditions, anionic **Mo_3** clusters can transform into an amorphous MoS-like structure that is largely made up of the original $\{Mo_3S_7\}$ subunits.[79] In line with this, XPS analysis complemented by atomic emission spectroscopy and XAS measurements, confirmed the structural integrity of the cluster after deposition. At optimized film thicknesses (beyond 1500 s when through-film resistance starts dominating the process), the as-derived **Mo_3**/HOPG attained an onset potential of 130 mV with a Tafel slope of 37 mV dec^{-1} and showed no signs of Mo leaching even after 3000 CV cycles, thereby confirming the durability of the supported electrocatalyst. Compared to simple drop-cast films, electrodeposited **Mo_3**/HOPG electrodes showed a much lower charge transfer resistance demonstrating remarkable electron transport.

In addition, Assaud and co-workers reported an interesting study demonstrating the effect of thiomolybdate cluster interactions with carbon-based supports commonly used in PEM water electrolysis.[80] They observed a strong decrease in onset potential from −439 to −124 mV when moving from graphene- to Vulcan-supported $[Mo_3S_4]^{4+}$-based clusters. Furthermore, the authors also reported a much lower overpotential required for $[Mo_3S_4]^{4+}$/Vulcan as compared to $[Mo_3S_4]^{4+}$/graphene to reach a current density of 30 mA cm^{-2}. Since these overpotentials already consider surface roughness characteristics of the two supports and the current densities were already normalized per electrochemically active surface area, the authors proposed that this difference in performance is due to stronger physisorption of $[Mo_3S_4]^{4+}$ on the Vulcan surface.

© 2023 The Authors. Advanced Materials published by Wiley-VCH GmbH

ADVANCED SCIENCE NEWS
www.advancedsciencenews.com

ADVANCED MATERIALS
www.advmat.de

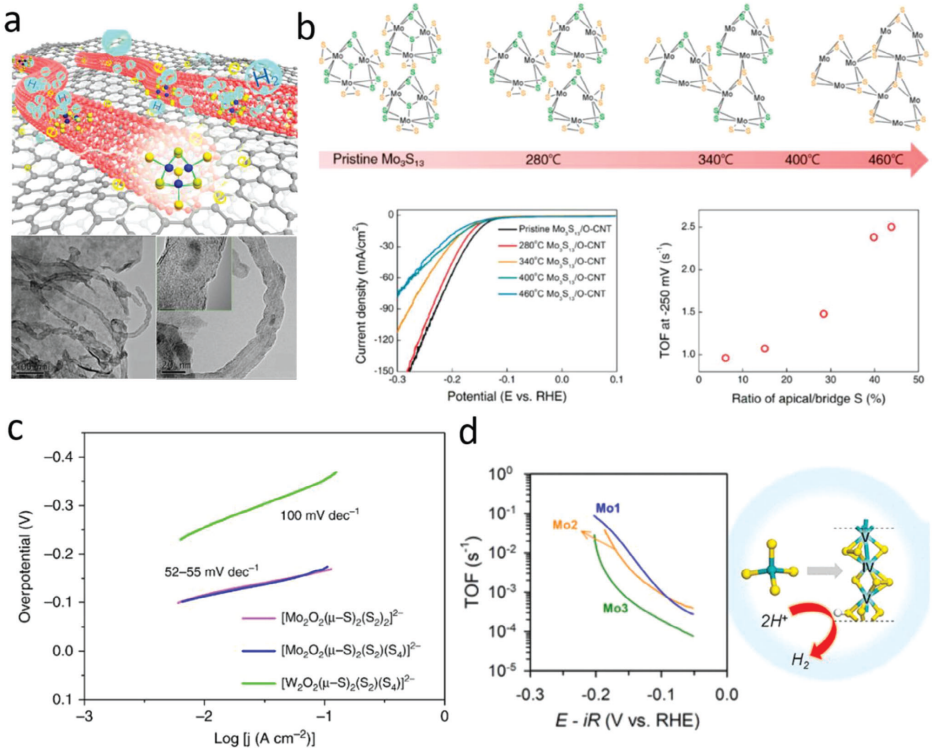


Figure 5. Supported thiometalates in electrocatalysis. a) Schematic representation of the Mo_3/rGO-CNTs composite structure with TEM images of Mo_3/rGO-CNT taken after 1000 HER cycles. b) Proposed structural evolution and electrochemical HER performance with TOFs of thermally annealed Mo_3/CNT composites at 280, 340, 400, and 460 °C. c) Tafel plots of different Mo- and W-based oxothiometalate clusters. d) TOFs of Mo_1-, Mo_2-, and Mo_3-derived MoS_3 (its model on the right). (a) Reproduced with permission.[76] Copyright 2017, American Chemical Society. (b) Reproduced with permission.[50] Copyright 2018, American Chemical Society. (c) Reproduced with permission.[32] Copyright 2019, Nature Communications. (d) Reproduced with permission.[53] Copyright 2020, American Chemical Society.

3.1.3. Role of Cluster Structure

Finally, this section outlines the studies performed to gain an in-depth understanding of how the composition, structure, and origin of the thiomolybdate species can be linked to their HER performance.

Traditionally, **Mo_3** clusters have been synthesized from $(NH_4)_6[Mo_7O_{24}]$ precursor via a method reported by Müller and co-workers.[27,28,81] However, there are several other synthetic methods of **Mo_3** formation using molybdenum trisulfide (MoS_3) as proposed by Müller and Weber.[82,83] Building on this, Joh and co-workers investigated electrochemical HER activity of MoS_3-derived **Mo_3** by supporting it onto oxidized multiwalled carbon nanotubes.[50] The authors observe an overpotential of 137 mV and a Tafel slope of 40 mV dec^{-1}. To further understand the role of each component they next explored the possibility of **Mo_3** cluster polymerization by studying the effect of thermally assisted conversion of **Mo_3**. The authors demonstrated that heat-treatment of **Mo_3** at different temperatures up to 460 °C results in materials which show variable TOFs in the electrocatalytic HER reaction (Figure 5b). Based on these catalytic data and complemented by DFT studies, the authors proposed bridging disulfide ligands to be the likely active HER site, as was detailed in Section 3.2.1. We note that the authors propose that the heat treatment at specific temperatures can be used to trigger selective structural changes (e.g., loss of the apical sulfide ligands). However, this level of assignment requires further detailed analysis, e.g., by vibrational spectroscopy or mass spectrometry to verify this hypothesis. Alternative processes might include (partial) cluster degradation and conversion into amorphous molybdenum sulfides.

© 2023 The Authors. Advanced Materials published by Wiley-VCH GmbH

15214095, 2024, 7, Downloaded from https://advanced.onlinelibrary.wiley.com/doi/10.1002/adma.202305730 by Universitatsbibliothek Mainz, Wiley Online Library on [04/04/2025]. See the Terms and Conditions (https://onlinelibrary.wiley.com/terms-and-conditions) on Wiley Online Library for rules of use; OA articles are governed by the applicable Creative Commons License

15214095, 2024, 7, Downloaded from https://advanced.onlinelibrary.wiley.com/doi/10.1002/adma.202305730 by Universitätsbibliothek Mainz, Wiley Online Library on [04/06/2025]. See the Terms and Conditions (https://onlinelibrary.wiley.com/terms-and-conditions) on Wiley Online Library for rules of use; OA articles are governed by the applicable Creative Commons License

In another prominent work, Miras and co-workers investigated the impact of the structural and stoichiometric ratio of the chalcogen to transition metal on HER performance by examining a broader set of oxothiometalate clusters.[32] Focusing specifically on the thiomolybdates, the authors compared $[Mo_2O_2(S)_2(S_2)_2]^{2-}$ and $[Mo_2O_2(S)_2(S_2)(S_4)]^{2-}$ (Figure 1, right) drop-cast onto GC electrodes. Both clusters exhibited similar Tafel slopes in the range of 52–54 mV dec^{-1} and a low overpotential of about 114 mV, which demonstrates a negligible effect of the terminal sulfide groups in the cluster on the HER mechanism and performance (Figure 5c). On contrary to this conclusion, the authors estimated a TOF of 0.12 s^{-1} for both oxothiometalates. This value is significantly lower as compared to TOFs reported for other similar clusters (Table 2), thus still leaving an open question to the stability and potential transformation of oxothiometalates under turnover conditions.

Joo and co-workers explored the effect of Mo oxidation state in the MoS_x family of clusters on the overall HER.[53] They prepared amorphous MoS_3 polymeric chains using $[MoS_4]^{2-}$, **Mo_2**, and **Mo_3** as monoatomic, diatomic, and triatomic Mo precursors, respectively. The electrodes were prepared by drop casting the precursors onto carbon paper, followed by thermal treatment at 120 °C to initiate polymerization. The samples were labeled as Mo_1-, Mo_2-, and Mo_3-derived MoS_3, depending on the precursor chemistry. After the synthesis, Mo_1-derived films showed the lowest overpotential of 167 mV, closely followed by 170 mV for Mo_2-derived and the highest overpotential of 196 mV for Mo_3-derived electrocatalysts. However, Tafel slopes for each of them was within the range of 46–52 mV dec^{-1}. Further characterization revealed that Mo_1-derived MoS_3 had a higher electrochemical active surface area as compared to other electrocatalysts, thus justifying its superior HER performance amongst the three (Figure 5d). Since both **Mo_2** and **Mo_3** clusters have been used as precatalysts (precursors) in this work, no further conclusion about the impact of thiomolybdate molecular structure on HER activity could be drawn from the results. However, this work demonstrates that thiomolybdates can be used as precursors which allow to obtain a variety of structurally different MoS_x electrocatalysts.

Overall, Table 2 highlights, that the HER performance of thiomolybdates depends strongly on the type of the cluster and type of the support used with overpotential values reported in the range between 120 and 200 mV (at 10 mA cm^{-2} current density). This range is generally higher when compared to molybdenum carbides or phosphides; however, MoS_2-based nanostructures are known for higher intrinsic activity (i.e., TOF values)[84] still making thiomolybdates and their derivatives attractive.

3.2. Photocatalysis

Soon after the first studies on thiomolybdate HER electrocatalysis, the light-driven catalysis community started exploring these cluster species as molecular co-catalysts. Starting with the most common UV-active TiO_2 as a photoactive support, a range of narrow-band semiconductors and (micro)porous hosts have been employed to design efficient and robust heterogeneous photoactive composites (**Figure 6**a). Section 4.2.1 discusses these studies with a focus on photocatalytic HER by thiomolybdate anchored on TiO_2 semiconductors, while Section 4.2.2 focuses on visible-light-active semiconductor supports. In Section 4.2.3, the photoreactivity of thiomolybdates heterogenized in porous matrices is discussed.

3.2.1. Thiomolybdate Clusters as HER Co-Catalysts

Several prominent works have been reported over the past years, in which heterogenized thiomolybdates have been used for light-driven HER. In 2014, Llusar and co-workers reported the use of $[Mo_3S_7]^{4+}$ fragments which were heterogenized onto TiO_2 to act as a co-catalyst for photocatalytic HER.[95] To facilitate covalent anchoring of the cluster on the oxide surface, the authors employed the $\{Mo_3S_7\}$-core-containing complex $[Mo_3S_7Br_4bpy(CO_2Me)_2]$, ($bpy(CO_2Me)_2$ = 4,4′-dimethyldicarboxylate-2,2′-bipyridine, see Figure 1, right). Based on electrochemical and spectroscopic measurements, the authors suggest that the molecular species serves as a precatalyst and is reductively converted to a more active catalyst species when in contact with sulfite/sulfide species in the reaction solution. The nature of these reduced species was unraveled by XPS analysis, according to which the final electroactive material is composed of Mo^{IV} atoms coordinated to S^{2-} moieties, suggesting a MoS_2-based compound. The resulting MoS_2/TiO_2 composite showed promising visible light-driven HER with no performance loss even after 8 h of operation (Figure 6b).

More recently, Cherevan and colleagues investigated the attachment modes and loading-dependent photocatalytic HER performance of the non-modified **Mo_3** cluster which was anchored onto TiO_2.[51] The authors proposed that **Mo_3** deposition follows a monolayer adsorption and involves the formation of Mo—O—Ti coordinative bonds while maintaining the overall molecular structure of **Mo_3**. The authors further explored the photocatalytic HER performance of **Mo_3**/TiO_2 composites with different cluster loadings revealing optimal activity at around 3 wt% of **Mo_3** (Figure 6c). As revealed by radical-trapping photoluminescence (PL) spectroscopy, the drop for higher loading values is related to the availability of the support-solution interface required for the efficient hole scavenging. The authors also performed long-term HER studies which showed stable photocatalytic H_2 evolution rates. These results are in strong contrast to the work discussed previously[95] and suggest that native thiomolybdates without any organo-functionalization are able to undergo direct binding with oxide-based supports and further act as structurally stable co-catalysts for HER.

In related studies, Du and colleagues explored the surface attachment, optical properties, photocatalytic HER performance and stability of **Mo_2** as a co-catalyst when deposited onto anatase-type TiO_2.[97] XPS analyses indicated that **Mo_2** attaches covalently to the TiO_2 support by replacement of the terminal S_2^{2-} ligands. Optimum HER activity was achieved at 3 wt% loading. The authors additionally reported PL data for **Mo_2**/TiO_2 composites, which documented improvement in charge separation (low PL intensity and higher excited state lifetime when compared to pure TiO_2), while complementary photoelectrochemical measurements showed higher photocurrent for the optimum **Mo_2**/TiO_2 composite, which further confirms improved charge

 © 2023 The Authors. Advanced Materials published by Wiley-VCH GmbH

ADVANCED SCIENCE NEWS
www.advancedsciencenews.com

ADVANCED MATERIALS
www.advmat.de

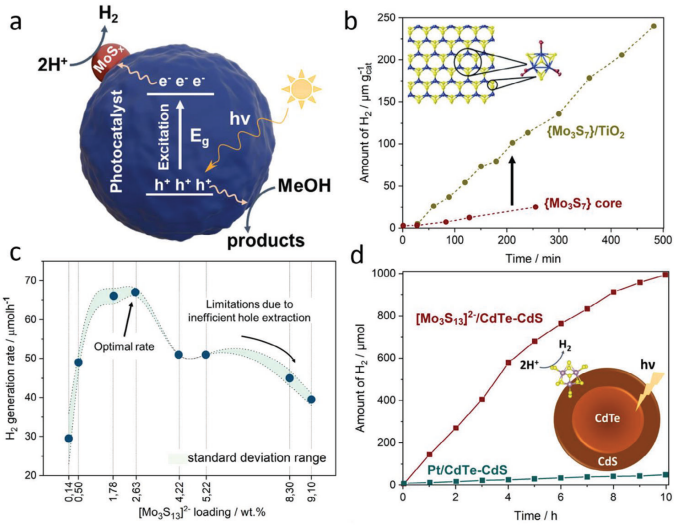


Figure 6. Supported thiometalates in photocatalysis. a) Illustration of charge transfer from photocatalyst to the thiometalate co-catalyst upon light illumination. E_g: energy bandgap; MoS_x: any thiometalate cluster. b) Hydrogen generation profiles of heterogenized $\{Mo_3S_7\}/TiO_2$ (5 wt% cluster loading, 1 g L^{-1}) and $\{Mo_3S_7\}$-core containing complex (homogeneous, 0.31 g L^{-1}) in acetone/H_2O mixture obtained in the presence of 0.1 M Na_2S and 0.02 M Na_2SO_3. c) Hydrogen evolution rate plotted against the Mo_3 cluster loading on TiO_2: volcano type profile is highlighted. d) Amount of hydrogen produced by Mo_3/CdTe@CdS (Mo_3 concentration: 4.6 × 10^{-6} M) and Pt/CdTe-CdS under optimal reaction conditions of pH = 2.5 from 20 mg mL^{-1} ascorbic acid aqueous solution (20 mL). (b) Adapted with permission.[95] Copyright 2015, Wiley-VCH. (c) Reproduced with permission.[51] Copyright 2022, American Chemical Society. (d) Adapted with permission.[96] Copyright 2016, American Chemical Society.

separation dynamics and suggests efficient charge extraction by the surface-bound **Mo_2** species.

3.2.2. Extension to Visible-Light-Active Supports

For light-driven HER, it is crucial to investigate support materials that can maximize the absorption of solar light.[98] One of the most promising classes to this end are semiconducting CdX (X = S, Se, Te) quantum dots (QDs), as their light absorption properties can be fine-tuned by modulating their dimensions and composition. Zhao and co-workers employed CdTe/CdS core/shell QDs as support for **Mo_3** and verified the cluster anchoring by a combination of high-resolution transmission electron microscopy (HRTEM) and XPS analyses.[96] The authors proposed that the adsorption of **Mo_3** occurs via the Cd-terminated faces as well as surface defects, including Cd adatoms and S vacancies of QDs. The HER activity of **Mo_3**/CdTe-CdS composite was almost constant over more than 10 h of illumination. The authors also report the HER performance to be significantly higher compared with a benchmark Pt co-catalyst loaded on CdTe-CdS QDs (Figure 6d). However, the team also emphasized that the **Mo_3**/CdTe-CdS composites were not stable below the optimal pH of 2.5 triggered by the precipitation of QDs and the weakened interaction between the two components. Also, the study reports that increasing **Mo_3** loading above a certain level results in the drop of HER activity, most likely due to light blocking by the catalyst.

Carbon nitride (CN_x) is another promising narrow band gap semiconductor often used by the community as an efficient metal-free heterogeneous light absorber. Driven by the idea to utilize the anionic charge of **Mo_3** for the attachment, Wang and co-workers used melon-derived mesoporous CN_x—that was rendered positively charged via facile protonation[99]—as a support for the attachment.[100] The **Mo_3**/CN_x composite was characterized using TEM and XPS measurements, which confirmed the monodispersed nature of the clusters. Similar to the works discussed above, the authors found **Mo_3** to act as efficient HER co-catalyst (**Figure 7**a): (a) when supported on insulating SiO_2, **Mo_3** was unable to generate any H_2 and (b) when neat (uncharged) CN_x was used as a support, much lower HER activities were recorded. These data correlate well with the conclusions drawn in Section 4.1 and strongly suggest the importance of strong (electrostatic) interaction between catalyst and support, which is critical to achieve optimal HER performance.

While many photosystems have demonstrated that **Mo_3** can act as co-catalysts for light-driven HER, Streb and colleagues provided a unique perspective on the electrostatically assembled **Mo_3**/CN_x—using amorphous carbon nitride support—aiming to shed light on the charge transfer dynamics between the

© 2023 The Authors. Advanced Materials published by Wiley-VCH GmbH

15214095, 2024, 7, Downloaded from https://advanced.onlinelibrary.wiley.com/doi/10.1002/adma.202305730 by Universitatsbibliothek Mainz, Wiley Online Library on [04/06/2025]. See the Terms and Conditions (https://onlinelibrary.wiley.com/terms-and-conditions) on Wiley Online Library for rules of use; OA articles are governed by the applicable Creative Commons License

ADVANCED SCIENCE NEWS
www.advancedsciencenews.com

ADVANCED MATERIALS
www.advmat.de

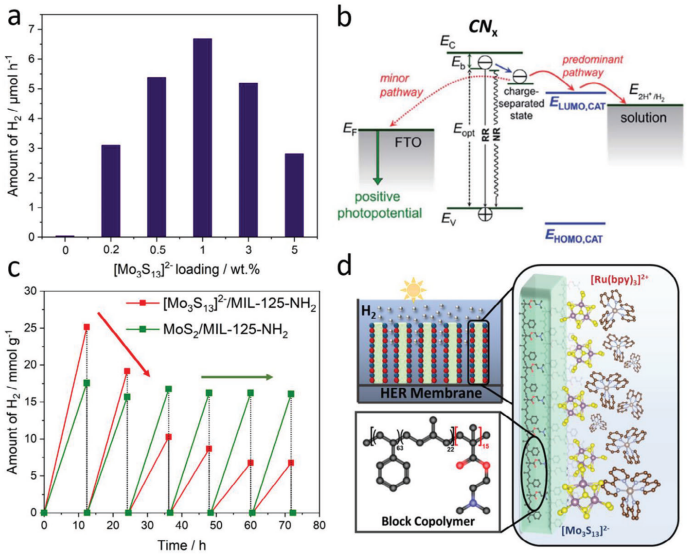


Figure 7. Supported thiometalates in photocatalysis. a) Effect of different loadings of Mo_3 in Mo_3/CN_x composite on the amount of hydrogen produced. b) Scheme showing the change in photopotential at FTO/CN_x photoelectrode surface in the presence of Mo_3 catalyst. E_c: conduction band edge; and E_v: valence band edge; RR: radiative recombination from emissive (band-edge) states; NR: nonradiative recombination from nonemissive (shallow-trap) excitonic states; E_{opt}: optical bandgap of CN_x; E_b: exciton binding energy; CAT: Mo_3 catalyst. c) Comparison of Mo_3/MIL-125-NH_2 and MoS_2/MIL-125-NH_2 in terms of their stability under HER experimental conditions. d) Design of photocatalytic hydrogen evolution system based on nanoporous block copolymer membrane that is electrostatically co-anchoring Mo_3 catalyst and $[Ru(bpy)_3]^{2+}$ photosensitizer. (a) Adapted with permission.[100] Copyright 2017, Royal Society of Chemistry. (b) Reproduced with permission.[101] Copyright 2020, Royal Society of Chemistry. (c) Adapted with permission.[102] Copyright 2018, American Chemical Society. (d) Adapted with permission.[77] Copyright 2020, Royal Society of Chemistry.

two components as well as unravel the reaction kinetics under turnover conditions.[101] The authors utilized steady-state and time-resolved PL spectroscopy to reveal that increasing cluster loading in $\mathbf{Mo_3}/CN_x$ composites leads to enhanced charge separation at the interface. As such, for smaller cluster loadings, $\mathbf{Mo_3}$ seems to selectively bind to the amine groups. As these are associated with shallow trap states, this binding tends to repopulate the emissive excitonic states, thereby increasing the PL intensity and lifetime. Higher cluster loadings, on the other hand, increase the nonradiative decay, which dissociates the shallow trapped excitons into charge carriers and leads to improved charge separation, causing the PL emission intensity and lifetime to decrease. These findings provide a valuable perspective to explain the loading-dependent HER performance observed in this and other works. The second relevant observation was delivered by the transient photopotential measurements able to elaborate the effect of $\mathbf{Mo_3}$ co-catalyst on the charge separation extent. As shown in Figure 7b, the photopotential is negative for the FTO-supported CN_x, which the authors attributed to its insulating behavior and the poor electrical connection between CN_x and FTO. Conversely, a positive photopotential was recorded when $\mathbf{Mo_3}$ was attached to the CN_x surface, suggesting the efficient extraction of photoexcited electrons by the cluster. These data suggest that surface-anchored $\mathbf{Mo_3}$ strongly affects the exciton dissociation and mediates the transfer of trapped electrons from CN_x to the reactants. However, as the addition of $\mathbf{Mo_3}$ had no impact on the ultrafast (sub-ns) photoinduced kinetics in the CN_x, the authors also note that the electron extraction to $\mathbf{Mo_3}$ occurs on a relatively longer (ns-s) time scale.

3.2.3. Thiomolybdates within Porous Hosts

Metal–organic frameworks (MOFs) have recently attracted the attention of the community as organic–inorganic hybrid materials comprised of metal ions or metal-oxo clusters linked by bridging organic ligands to form multidimensional solid-state networks. Their modular assembly and tunable pore structure and pore size makes them ideally suited for heterogenization of thiomolybdate HER catalysts.[103] This principle has been explored by Stylianou and colleagues who used the visible-light-active MIL-125-NH_2 MOF as a support to compare (co-)catalytic HER performance of $\mathbf{Mo_3}$ and 1T-MoS_2 nanoparticles (Figure 7c).[102] Their data suggest $\mathbf{Mo_3}$/MOF to be more active compared to MoS_2/MOF when similar co-catalyst loadings were used. The authors attributed this observation to the improved interaction of molecular

© 2023 The Authors. Advanced Materials published by Wiley-VCH GmbH

15214095, 2024, 7, Downloaded from https://advanced.onlinelibrary.wiley.com/doi/10.1002/adma.202305730 by Universitätsbibliothek Mainz, Wiley Online Library on [04/06/2025]. See the Terms and Conditions (https://onlinelibrary.wiley.com/terms-and-conditions) on Wiley Online Library for rules of use; OA articles are governed by the applicable Creative Commons License

clusters with the MOF surface along with their inherently higher catalytic activity discussed previously in Section 4.1. However, the authors also found Mo_3/MOF to be less stable in long-term photocatalytic tests compared to 1T-MoS_2/MOF composites, which could be attributed to structural instability of the Mo_3 under alkaline pH conditions.[100,101] More investigations are required to elaborate on this important issue.

In another prominent example, Streb and co-workers were the first to use soft-matter-based nanoporous block copolymer membranes with cationic surface groups as heterogeneous supports for electrostatic anchoring of Mo_3 catalyst and $[Ru(bpy)_3]^{2+}$ photosensitizer for light-driven HER (Figure 7d).[77] The functionalized polymer membranes were analyzed using scanning electron microscopy (SEM), energy dispersive X-ray spectroscopy (EDX), and XPS analyses, which suggest that one of the terminal S_2^{2-} ligands is replaced with a water ligand after attachment to the membrane, in line with the behavior observed previously.[40] The copolymer-supported Mo_3/$[Ru(bpy)_3]^{2+}$ photosystem generated H_2 for at least 20 h of illumination. However, the authors also observed that a considerable amount of H_2 was stored in the pores of the polymer membrane and could be recovered after the catalytic process. The authors further reported that Mo_3 did not leach from the membrane; however, they noted significant loss of the photosensitizer after 10 h of irradiation. Their data suggest that even at low Ru-photosensitizer loadings, the membrane is able to preserve its HER activity, possibly by mediating the electron transfer between photosensitizer and catalyst within the membrane.

3.3. Other Applications

Apart from electrocatalytic and photocatalytic applications involving thiometalates, most recent works have been exploring the heterogenized clusters in thermal catalysis, and selective ion capture. As such, Zhang and co-workers have immobilized Mo_2 and Mo_3 on mesoporous SiO_2 (SBA-15) and applied the composites for thiophene hydrodesulfurization (HDS), a process used to remove sulfur-containing compounds from petroleum.[104] The results showed that both thiomolybdates can be successfully deposited on SBA-15, while maintaining their structure. The stability of the supported catalysts was assessed through TGA, which revealed that Mo_2/Mo_3 are likely to retain their sulfur ligands during catalysis. The composites were also tested for hydrogen adsorption using temperature-programmed reduction, which indicated the hydrogenation of terminal and bridging sulfur species to be the likely intermediate step of the HDS process. Overall, the study demonstrates the successful loading and effective catalytic performance of the thiomolybdates in HDS. The findings further provide insights into the role of sulfur species in the catalytic process and contribute to the development of supported thiometalate clusters for other catalytic applications.

In another outstanding study, Ma, Kanatzidis and colleagues used Mo_3 to prepare composites for the selective extraction of silver from copper-rich minerals.[105] The authors incorporated Mo_3 into the matrix of a conjugated polypyrrole (ppy) backbone by ion-exchange reaction and demonstrated exceptional selectivity and high efficiency of the resulting Mo_3/ppy in capturing Ag^+ and Hg^{2+} ions at concentration levels <1 ppb. The mechanism for silver removal involves two synergistic pathways: direct binding and in situ reduction. In the former, the Mo_3 clusters release S^{2-} ions, which bind with Ag ions to form Ag_2S complexes, effectively removing Ag from the solution. In the latter, the Mo^{IV} ions in Mo_3 act as reducing agents, converting Ag^+ ions to metallic silver while being oxidized to Mo^{VI}. This reduction reaction occurs alongside the binding of Ag^+ ions to S^{2-} ions, resulting in the deposition of silver crystals on the Mo_3/ppy composite surface. The results suggest that composites based on Mo_3—and, potentially, other thiometalates—can offer a promising approach for selective silver extraction and removal of toxic metal ions from complex aqueous environments.

Parallel to the implementation of thiometalates as reduction co-catalysts for HER, several works have employed composites containing such clusters to promote various oxidation reactions. In an early set of studies, Mo_3 was employed as co-catalyst for photocatalytic dye degradation using visible-light-active BiOBr and Bi_2WO_6 substrates prepared through a hydrothermal method. Both nanocomposites demonstrated excellent photocatalytic activity—comparable to state-of-the-art Pt co-catalysts—which was primarily attributed to the ability of Mo_3 to efficiently promote the extraction of photoexcited electrons thus indirectly affecting the lifetimes of electron-hole pairs and hole utilization efficiency.[106,107] In addition to this, the authors highlighted that, compared to commonly used Pt, Mo_3 shows enhanced sulfur tolerance and can thus be used effectively in processes involving sulfur species, such as in desulfurization or sulfur-containing wastewater remediation.

In a more recent example of thiomolybdate application, Xufang and co-workers fabricated a novel Mo_3/TiO_2 photocatalyst for the oxidation of acetone to CO_2.[108] The CO_2 production was investigated with Mo_3/TiO_2 composites containing different loadings of Mo_3: 0.6, 1.1, 1.7, and 3.4 wt%. The authors found that among these composites, the highest amount of CO_2 was produced with 1.7Mo_3/TiO_2, which was ascribed to the optimal loading of clusters over titania surface promoting better photoinduced charge separation. Importantly for benchmarking, the 1.7Mo_3/TiO_2 photocatalyst was found to be more active for acetone mineralization compared to the benchmark Pt/TiO_2 photocatalyst exhibiting a similar co-catalyst loading value. In addition, the solution of 1.7$Mo_3$$TiO_2$ composite sprayed onto polypropylene nonwoven fabric produced higher CO_2 amounts compared to the pristine TiO_2/fabric, which one more time highlights the effect of Mo_3 in the structure. These polypropylene-coated nonwoven fabrics coated with Mo_3/TiO_2 composite have been used as an efficient photocatalyst for indoor air purification.

4. Conclusions and Outlook

This review placed special emphasis on recent developments in thiomolybdate catalysis, particularly with respect to combined experimental and theoretical studies that shed light on reaction mechanisms, active sites and potential degradation pathways, as well as on new strategies for thiometalate heterogenization on functional substrates and their emerging applications. Two comprehensive summary Tables were provided to highlight the current state-of-the-art: Table 1 examines active sites of thiomolybdate clusters, Table 2 documents that heterogenized thiomolybdates are highly active, structurally versatile HER promoters and

© 2023 The Authors. Advanced Materials published by Wiley-VCH GmbH

15214095, 2024, 7, Downloaded from https://advanced.onlinelibrary.wiley.com/doi/10.1002/adma.202305730 by Universitatsbibliothek Mainz, Wiley Online Library on [04/04/2025]. See the Terms and Conditions (https://onlinelibrary.wiley.com/terms-and-conditions) on Wiley Online Library for rules of use; OA articles are governed by the applicable Creative Commons License

15214095, 2024, 7, Downloaded from https://advanced.onlinelibrary.wiley.com/doi/10.1002/adma.202305730 by Universitätsbibliothek Mainz, Wiley Online Library on [04/06/2025]. See the Terms and Conditions (https://onlinelibrary.wiley.com/terms-and-conditions) on Wiley Online Library for rules of use; OA articles are governed by the applicable Creative Commons License

that their molecular nature can be used as a tool to tune their activity.

Despite a number of proof-of-concept demonstrations and promising results that are already been recorded, the authors of this perspective have identified a list of critical points that will hopefully help shaping future research directions in the field:

We suggest that more in-depth mechanistic studies are required to fully understand how thiomolybdates are anchored to heterogeneous supports, and to explore the role of catalyst–support interactions for electrocatalytic and photocatalytic HER. Also, understanding the physical and electronic structure of the catalytically active state of the clusters under turnover conditions is critical for a knowledge-based development of the field. These themes have been the focus of two recent studies which used time-resolved methods to gain further insights into thiomolybdate reactivity: Ha-Thi and colleagues revealed the mechanism of light-driven catalysis of a $\{Mo_3S_4\}$-core containing cluster in solutions,[45] while Streb and co-workers provided important insights into the charge transfer dynamics of surface-supported $\mathbf{Mo_3}$.[101] In another pioneering example, Bozheyev and colleagues used transient surface photovoltage spectroscopy to unravel the electronic properties of WSe_2-anchored $\mathbf{Mo_3}$ heterostructures.[109]

Another critical aspect when considering thiomolybdate heterogenization is the stability and fate of the molecules under deposition and reaction conditions. Many studies deliberately use thiomolybdates as molecular precursors for the preparation of MoS_x nanostructures or films. However, in other cases, this molecule-to-solid-state compound conversion might occur unintentionally. In both cases, the resulting material needs to be thoroughly characterized, and clear evidence must be provided if the respective manuscript claims that the material used for catalysis is still a molecular species. This can be challenging, particularly when the conversion occurs in situ, under catalytic conditions. Thus, comprehensive pre- and postcatalytic analyses—ideally supported by in situ/operando studies—are required to assess the complex processes occurring in this compound class. Key aspects to be focused on are ligand loss/exchange, chemical interaction with the surface, oligo- and polymerization of individual clusters and formation of MoS_x fragments. As outlined in Sections 2 and 3, there is still much room to explore these questions and provide more insights into improvement when analyzing and reporting these aspects.

In addition to the chemical and structural considerations outlined above, there is an urgent need to provide fundamental insights into the differences in reactivity of different thiomolybdate prototypes, particularly when deposited on identical supports. This would allow the research community to engage in knowledge-based advanced materials design, based on a full understanding of the underlying reaction and stability mechanisms.

Apart from these critical notes, the authors of this perspective would like to suggest directions of future research:

A current limitation in the field is that most HER research has been focused on the use of a limited number of prototype thiomolybdates, mainly $\mathbf{Mo_2}$ and $\mathbf{Mo_3}$. While these studies have provided ground-breaking new insights and materials, we propose expanding the compound base and exploring the reactivity of advanced cluster types. This includes research on other types of thiometalates, such as thiotungstates,[33] mixed-ligand clusters, e.g., featuring oxo- or organic ligands in addition to thio groups,[17] as well as selenide-containing derivatives.[110] While these areas are highly promising, they have thus far not received the attention to allow us to draw any final conclusions on the component suitability for HER studies.

State-of-the-art thiomolybdate catalysis research is mainly focused on electrocatalytic or light-driven HER. However, based on earlier research and on selected recent publications, we suggest that other (thermal) catalytic processes including reductions, oxidations and small molecule activations are intriguing areas to be explored using thiometalates. In a recent example, Llusar and colleagues have combined experimental and theoretical methods to explore the catalytic hydrogenation of azobenzene using cuboidal $\{Mo_3S_4\}$-containing clusters.[111] The results suggest a mechanism involving homolytic activation of hydrogen at bridging sulfur atoms in the cluster, followed by consecutive hydrogen transfers to azobenzene, resulting in the formation of aniline. The authors also explored the effects of different organic ligands on the catalytic activity of the clusters and provided evidence supporting the sulfur-centered mechanism, which contributes strongly to a better understanding of the catalytic properties of these and structurally similar thiomolybdates. Along similar lines, mechanistic comparison between HER and hydrodesulfurization catalysis studies can offer a new insight into the function of thiomolybdates. In one example, Suman and co-workers studied an oxothiomolybdate complex $[(Mo_2O_2S_4)(en)(dmf)]$ and suggested an oxidative addition/reductive elimination mechanism or a ligand-based insertion reaction—in which sulfur inserts either into the terminal S—S bond or into the Mo—S bond—as possible reaction pathways.[112]

Finally, the merging of thiomolybdates with functional support materials such as polymers, MOFs, and narrow bandgap semiconductors is also an area which can lead to advanced composites. In one example, Chane-Ching and colleagues recently immobilized $\mathbf{Mo_2}$ derivatives on 2D WS_2 photoelectrodes to drive photoelectrocatalytic water splitting.[113] In MOF-chemistry, Yaghi and co-workers were able to build thiomolybdate-based porous frameworks and demonstrate the HER performance of these pioneering materials.[35] We believe that many more functional molecular, hybrid, and solid-state materials could be realized using thiometalates and their derivatives.

Acknowledgements

S.B. and M.L. contributed equally to the work. The authors gratefully acknowledge financial support by the Austrian Science Fund (FWF, Project No. P32801 and Cluster of Excellence MECS) and Deutsche Forschungsgemeinschaft [Project No. 364549901 (TRR 234 CataLight, Project Nos. A4, A5, and B3)]. M.H. gratefully acknowledges the Alexander von Humboldt Foundation for a postdoctoral fellowship. C.S. gratefully acknowledges financial support by Johannes Gutenberg University Mainz, the Gutenberg Research College GRC, and the state of Rheinland-Pfalz (top-level research area SusInnoScience, and "Spitzenforscher" funds).

Open access funding enabled and organized by Projekt DEAL.

Conflict of Interest

The authors declare no conflict of interest.

© 2023 The Authors. Advanced Materials published by Wiley-VCH GmbH

Keywords

electrocatalysis, heterogenization, hydrogen evolution, molybdenum sulfide, photocatalysis, thiomolybdate

Received: June 14, 2023
Revised: October 9, 2023
Published online: December 2, 2023

[1] H. Ooka, J. Huang, K. S. Exner, *Front. Energy Res.* **2021**, *9*, 654460.
[2] J. K. Nørskov, T. Bligaard, A. Logadottir, J. R. Kitchin, J. G. Chen, S. Pandelov, U. Stimming, *J. Electrochem. Soc.* **2005**, *152*, 1.
[3] Z. W. Seh, J. Kibsgaard, C. F. Dickens, I. Chorkendorff, J. K. Nørskov, T. F. Jaramillo, *Science* **2017**, *355*, 4998.
[4] M. G. Walter, E. L. Warren, J. R. Mckone, S. W. Boettcher, Q. Mi, E. A. Santori, N. S. Lewis, *Chem. Rev.* **2010**, *110*, 6446.
[5] E. I. Stiefel, *Transition Metal Sulfur Chemistry*, American Chemical Society, Washington, DC, pp. 2–38.
[6] H. Tributsch, J. C. Bennett, *J. Electroanal. Chem. Interfacial Electrochem.* **1977**, *81*, 97.
[7] B. Hinnemann, P. G. Moses, J. Bonde, K. P. Jørgensen, J. H. Nielsen, S. Horch, I. Chorkendorff, J. K. Nørskov, *J. Am. Chem. Soc.* **2005**, *127*, 5308.
[8] C. G. Morales-Guio, X. Hu, *Acc. Chem. Res.* **2014**, *47*, 2671.
[9] H. Li, C. Tsai, A. L. Koh, L. Cai, A. W. Contryman, A. H. Fragapane, J. Zhao, H. S. Han, H. C. Manoharan, F. Abild-Pedersen, J. K. Nørskov, X. Zheng, *Nat. Mater.* **2016**, *15*, 364.
[10] T. F. Jaramillo, K. P. Jørgensen, J. Bonde, J. H. Nielsen, S. Horch, I. Chorkendorff, *Science* **2007**, *317*, 100.
[11] K. Herbst, M. Monari, M. Brorson, *Inorg. Chem.* **2002**, *41*, 1336.
[12] M.-L. Grutza, A. Rajagopal, C. Streb, P. Kurz, *Sustainable Energy Fuels* **2018**, *2*, 1893.
[13] B. Seo, S. H. Joo, *Nano Convergence* **2017**, *4*, 19.
[14] T. Shibahara, *Coord. Chem. Rev.* **1993**, *123*, 73.
[15] M. G. Kanatzidis, S.-P. Huang, *Coord. Chem. Rev.* **1994**, *130*, 509.
[16] E. Cadot, M. N. Sokolov, V. P. Fedin, C. Simonnet-Jégat, S. Floquet, F. Sécheresse, *Chem. Soc. Rev.* **2012**, *41*, 7335.
[17] F. Sécheresse, E. Cadot, *World Scientific Series in Nanoscience and Nanotechnology*, World Scientific, Singapore **2013**, pp. 243–304.
[18] A. Elliott, H. N. Miras, *J. Coord. Chem.* **2022**, *75*, 1467.
[19] M. R. Dubois, *Chem. Rev.* **1989**, *89*, 1.
[20] R. Hernández-Molina, A. G. Sykes, *J. Chem. Soc., Dalton Trans.* **1999**, 3137.
[21] R. Hernandez-Molina, M. N. Sokolov, A. G. Sykes, *Acc. Chem. Res.* **2001**, *34*, 223.
[22] A. Mcskimming, D. L. M. Suess, *Nat. Chem.* **2021**, *13*, 666.
[23] Y. Ohki, K. Munakata, Y. Matsuoka, R. Hara, M. Kachi, K. Uchida, M. Tada, R. E. Cramer, W. M. C. Sameera, T. Takayama, Y. Sakai, S. Kuriyama, Y. Nishibayashi, K. Tanifuji, *Nature* **2022**, *607*, 86.
[24] Y. Hou, B. L. Abrams, P. C. K. Vesborg, M. E. Björketun, K. Herbst, L. Bech, A. M. Setti, C. D. Damsgaard, T. Pedersen, O. Hansen, J. Rossmeisl, S. Dahl, J. K. Nørskov, I. Chorkendorff, *Nat. Mater.* **2011**, *10*, 434.
[25] M. G. Basallote, M. J. Fernández-Trujillo, J. Á. Pino-Chamorro, T. F. Beltrán, C. Corao, R. Llusar, M. Sokolov, C. Vicent, *Inorg. Chem.* **2012**, *51*, 6794.
[26] S. W. Seo, S. Park, H.-Y. Jeong, S. H. Kim, U.k Sim, C. W. Lee, K. T. Nam, K. S. Hong, *Chem. Commun.* **2012**, *48*, 10452.
[27] A. Müller, W.-O. Nolte, B. Krebs, *Angew. Chem., Int. Ed. Engl.* **1978**, *17*, 279.
[28] A. Müller, S. Sarkar, R. G. Bhattacharyya, S. Pohl, M. Dartmann, *Angew. Chem., Int. Ed. Engl.* **1978**, *17*, 535.
[29] E. Diemann, A. Müller, P. J. Aymonino, *Z. Anorg. Allg. Chem.* **1981**, *479*, 191.
[30] A. Müller, R. Jostes, F. A. Cotton, *Angew. Chem., Int. Ed. Engl.* **1980**, *19*, 875.
[31] A. Müller, E. Diemann, R. Jostes, H. Bögge, *Angew. Chem., Int. Ed. Engl.* **1981**, *20*, 934.
[32] J. Mcallister, N. A. G. Bandeira, J. C. Mcglynn, A. Y. Ganin, Y.-F. Song, C. Bo, H. N. Miras, *Nat. Commun.* **2019**, *10*, 370.
[33] E. Königer-Ahlborn, A. Müller, *Angew. Chem.* **1975**, *87*, 598.
[34] N. E. Horwitz, J. Xie, A. S. Filatov, R. J. Papoular, W. E. Shepard, D. Z. Zee, M. P. Grahn, C. Gilder, J. S. Anderson, *J. Am. Chem. Soc.* **2019**, *141*, 3940.
[35] Z. Ji, C. Trickett, X. Pei, O. M. Yaghi, *J. Am. Chem. Soc.* **2018**, *140*, 13618.
[36] J. Xie, L. Wang, J. S. Anderson, *Chem. Sci.* **2020**, *11*, 8350.
[37] T. Shibahara, H. Kuroya, *Polyhedron* **1986**, *5*, 357.
[38] T. F. Jaramillo, J. Bonde, J. Zhang, B.-L. Ooi, K. Andersson, J. Ulstrup, I. Chorkendorff, *J. Phys. Chem. C* **2008**, *112*, 17492.
[39] Y. Lei, M. Yang, J. Hou, F. Wang, E. Cui, C. Kong, S. Min, *Chem. Commun.* **2018**, *54*, 603.
[40] M. Dave, A. Rajagopal, M. Damm-Ruttensperger, B. Schwarz, F. Nägele, L. Daccache, D. Fantauzzi, T. Jacob, C. Streb, *Sustainable Energy Fuels* **2018**, *2*, 1020.
[41] M. Heiland, R. De, S. Rau, B. Dietzek-Ivansic, C. Streb, *Chem. Commun.* **2022**, *58*, 4603.
[42] W. Li, S. Min, F. Wang, Z. Zhang, D. Gao, *Chem. Commun.* **2021**, *57*, 1121.
[43] A. Rajagopal, F. Venter, T. Jacob, L. Petermann, S. Rau, S. Tschierlei, C. Streb, *Sustainable Energy Fuels* **2018**, *3*, 92.
[44] P. R. Fontenot, B. Shan, B.o Wang, S. Simpson, G. Ragunathan, A. F. Greene, A. Obanda, L. A. Hunt, N. I. Hammer, C. E. Webster, J. T. Mague, R. H. Schmehl, J. P. Donahue, *Inorg. Chem.* **2019**, *58*, 16458.
[45] Y. Smortsova, C. Falaise, A. Fatima, M.-H. Ha-Thi, R. Méallet-Renault, K. Steenkeste, S. Al-Bacha, T. Chaib, L. Assaud, M. Lepeltier, M. Haouas, N. Leclerc, T. Pino, E. Cadot, *Chemistry* **2021**, *27*, 17094.
[46] P. D. Tran, T. V. Tran, M. Orio, S. Torelli, Q. D. Truong, K. Nayuki, Y. Sasaki, S. Y. Chiam, R. Yi, I. Honma, J. Barber, V. Artero, *Nat. Mater.* **2016**, *15*, 640.
[47] A. Baloglou, M. OncK, M.-L. Grutza, C. Van Der Linde, P. Kurz, M. K. Beyer, *J. Phys. Chem. C* **2019**, *123*, 8177.
[48] M. Pritzi, T. F. Pascher, M.-L. Grutza, P. Kurz, M. OncK, M. K. Beyer, *J. Am. Soc. Mass Spectrom.* **2022**, *33*, 1753.
[49] A. Baloglou, M. Plattner, M. OncK, M.-L. Grutza, P. Kurz, M. K. Beyer, *Angew. Chem., Int. Ed.* **2021**, *60*, 5074.
[50] C.-H. Lee, S. Lee, Y.-K. Lee, Y. C. Jung, Y.-I. Ko, D. C. Lee, H.-I. Joh, *ACS Catal.* **2018**, *8*, 5221.
[51] S. Batool, S. P. Nandan, S. N. Myakala, A. Rajagopal, J. S. Schubert, P. Ayala, S. Naghdi, H. Saito, J. Bernardi, C. Streb, A. Cherevan, D. Eder, *ACS Catal.* **2022**, *12*, 6641.
[52] Y. Deng, L. R. L. Ting, P. H. L. Neo, Y.-J. Zhang, A. A. Peterson, B. S. Yeo, *ACS Catal.* **2016**, *6*, 7790.
[53] B. Seo, G. Y. Jung, S. J. Lee, D. S. Baek, Y. J. Sa, H. W. Ban, J. S. Son, K. Park, S. K. Kwak, S. H. Joo, *ACS Catal.* **2020**, *10*, 652.
[54] Z. Huang, W. Luo, L. Ma, M. Yu, X. Ren, M. He, S. Polen, K. Click, B. Garrett, J. Lu, K. Amine, C. Hadad, W. Chen, A. Asthagiri, Y. Wu, *Angew. Chem., Int. Ed.* **2015**, *54*, 15181.
[55] J. A. Bau, A.-H. Emwas, P. Nikolaienko, A. A. Aljarb, V. Tung, M. Rueping, *Nat. Catal.* **2022**, *5*, 397.
[56] J. A. Bau, R. Ahmad, L. Cavallo, M. Rueping, *ACS Energy Lett.* **2022**, *7*, 3695.
[57] A. M. Appel, D. L. Dubois, M. R. Dubois, *J. Am. Chem. Soc.* **2005**, *127*, 12717.

© 2023 The Authors. Advanced Materials published by Wiley-VCH GmbH

15214095, 2024, 7, Downloaded from https://advanced.onlinelibrary.wiley.com/doi/10.1002/adma.202305730 by Universitatsbibliothek Mainz, Wiley Online Library on [04/06/2025]. See the Terms and Conditions (https://onlinelibrary.wiley.com/terms-and-conditions) on Wiley Online Library for rules of use; OA articles are governed by the applicable Creative Commons License

[58] H. I. Karunadasa, E. Montalvo, Y. Sun, M. Majda, J. R. Long, C. J. Chang, *Science* **2012**, *335*, 698.
[59] B. R. Garrett, K. A. Click, C. B. Durr, C. M. Hadad, Y. Wu, *J. Am. Chem. Soc.* **2016**, *138*, 13726.
[60] B. R. Garrett, S. M. Polen, K. A. Click, M. He, Z. Huang, C. M. Hadad, Y. Wu, *Inorg. Chem.* **2016**, *55*, 3960.
[61] B. R. Garrett, S. M. Polen, M. Pimplikar, C. M. Hadad, Y. Wu, *J. Am. Chem. Soc.* **2017**, *139*, 4342.
[62] M. Pritzi, T. F. Pascher, M.-L. Grutza, P. Kurz, M. OncK, M. K. Beyer, *Phys. Chem. Chem. Phys.* **2022**, *24*, 16576.
[63] B. Keita, S. Floquet, J.-F. Lemonnier, E. Cadot, A. Kachmar, M. Bénard, M.-M. Rohmer, L. Nadjo, *J. Phys. Chem. C* **2008**, *112*, 1109.
[64] A. S. Cherevan, S. P. Nandan, I. Roger, R. Liu, C. Streb, D. Eder, *Adv. Sci.* **2020**, *7*, 1903511.
[65] T. Wang, J. Zhuo, K. Du, B. Chen, Z. Zhu, Y. Shao, M. Li, *Adv. Mater.* **2014**, *26*, 3761.
[66] S. Kozuch, J. M. L. Martin, *ACS Catal.* **2012**, *2*, 2787.
[67] T. Bligaard, R. M. Bullock, C. T. Campbell, J. G. Chen, B. C. Gates, R. J. Gorte, C. W. Jones, W. D. Jones, J. R. Kitchin, S. L. Scott, *ACS Catal.* **2016**, *6*, 2590.
[68] D. Ziegenbalg, A. Pannwitz, S. Rau, B. Dietzek-Ivansic, C. Streb, *Angew. Chem., Int. Ed.* **2022**, *61*, e202114106.
[69] J. D. Benck, T. R. Hellstern, J. Kibsgaard, P. Chakthranont, T. F. Jaramillo, *ACS Catal.* **2014**, *4*, 3957.
[70] S. Anantharaj, S. Noda, *Mater. Today Energy* **2022**, *29*, 101123.
[71] J. Kibsgaard, T. F. Jaramillo, F. Besenbacher, *Nat. Chem.* **2014**, *6*, 248.
[72] T. R. Hellstern, J. Kibsgaard, C. Tsai, D. W. Palm, L. A. King, F. Abild-Pedersen, T. F. Jaramillo, *ACS Catal.* **2017**, *7*, 7126.
[73] P. Faye, E. Payen, D. Bougeard, in *Hydrotreatment and Hydrocracking of Oil Fractions* (Eds: G. F. Froment, B. Delmon, P. Grange), Elsevier, Amsterdam **1997**, pp. 281–292.
[74] M. A. Domínguez-Crespo, E. M. Arce-Estrada, A. M. Torres-Huerta, L. Díaz-García, M. T. Cortez De La Paz, *Mater. Charact.* **2007**, *58*, 864.
[75] C. Tsai, F. Abild-Pedersen, J. K. Nørskov, *Nano Lett.* **2014**, *14*, 1381.
[76] Y. Shang, X. Xu, B. Gao, Z. Ren, *ACS Sustainable Chem. Eng.* **2017**, *5*, 8908.
[77] I. Romanenko, A. Rajagopal, C. Neumann, A. Turchanin, C. Streb, F. H. Schacher, *J. Mater. Chem. A* **2020**, *8*, 6238.
[78] K. Du, L. Zheng, T. Wang, J. Zhuo, Z. Zhu, Y. Shao, M. Li, *ACS Appl. Mater. Interfaces* **2017**, *9*, 18675.
[79] O. Mabayoje, Y. Liu, M. Wang, A. Shoola, A. M. Ebrahim, A. I. Frenkel, C. B. Mullins, *ACS Appl. Mater. Interfaces* **2019**, *11*, 32879.
[80] J. A.l Cheikh, R. Zakari, A. C. Bhosale, A. Villagra, N. Leclerc, S. Floquet, P. C. Ghosh, A. Ranjbari, E. Cadot, P. Millet, L. Assaud, *Mater. Adv.* **2020**, *1*, 430.
[81] A. Müller, S. Pohl, M. Dartmann, J. P. Cohen, J. M. Bennett, R. M. Kirchner, *Z. Naturforschung, B* **1979**, *34*, 434.
[82] A. Müller, E. Diemann, E. Krickemeyer, H. J. Walberg, H. Bögge, A. Armatage, *Eur. J. Solid State Inorg. Chem.* **1993**, *30*, 565.
[83] T. Weber, J. C. Muijsers, J. W. Niemantsverdriet, *J. Phys. Chem.* **1995**, *99*, 9194.
[84] J. N. Hansen, H. Prats, K. K. Toudahl, N. Mørch Secher, K. Chan, J. Kibsgaard, I. Chorkendorff, *ACS Energy Lett.* **2021**, *6*, 1175.
[85] Y. Li, H. Wang, L. Xie, Y. Liang, G. Hong, H. Dai, *J. Am. Chem. Soc.* **2011**, *133*, 7296.
[86] T. Wang, L. Liu, Z. Zhu, P. Papakonstantinou, J. Hu, H. Liu, M. Li, *Energy Environ. Sci.* **2013**, *6*, 625.
[87] P. D. Tran, M. Nguyen, S. S. Pramana, A. Bhattacharjee, S. Y. Chiam, J. Fize, M. J. Field, V. Artero, L. H. Wong, J. Loo, J. Barber, *Energy Environ. Sci.* **2012**, *5*, 8912.
[88] H. Vrubel, D. Merki, X. Hu, *Energy Environ. Sci.* **2012**, *5*, 6136.
[89] T.-W. Lin, C.-J. Liu, J.-Y. Lin, *Appl. Catal., B* **2013**, *134*, 75.
[90] G.-Q. Han, X. Li, J. Xue, B. Dong, X. Shang, W.-H. Hu, Y.-R. Liu, J.-Q. Chi, K.-L. Yan, Y.-M. Chai, C.-G. Liu, *Int. J. Hydrogen Energy* **2017**, *42*, 2952.
[91] S. Reddy, R. Du, L. Kang, N. Mao, J. Zhang, *Appl. Catal., B* **2016**, *194*, 16.
[92] W.-H. Hu, X. Shang, G.-Q. Han, B. Dong, Y.-R. Liu, X. Li, Y.-M. Chai, Y.-Q. Liu, C.-G. Liu, *Carbon* **2016**, *100*, 236.
[93] E. Heydari-Bafrooei, S. Askari, *Int. J. Hydrogen Energy* **2017**, *42*, 2961.
[94] X. Zhang, P. Ding, Y. Sun, Y. Wang, J. Li, J. Guo, *Mater. Lett.* **2017**, *197*, 41.
[95] D. Recatalá, R. Llusar, A. L. Gushchin, E. A. Kozlova, Y. A. Laricheva, P. A. Abramov, M. N. Sokolov, R. Gómez, T. Lana-Villarreal, *ChemSusChem* **2015**, *8*, 148.
[96] D. Yue, X. Qian, Z. Zhang, M. Kan, M. Ren, Y. Zhao, *ACS Sustainable Chem. Eng.* **2016**, *4*, 6653.
[97] R. Zhang, K. Gong, F. Du, S. Cao, *Int. J. Hydrogen Energy* **2022**, *47*, 19570.
[98] Z. Wang, C. Li, K. Domen, *Chem. Soc. Rev.* **2019**, *48*, 2109.
[99] Y. Zhang, A. Thomas, M. Antonietti, X. Wang, *J. Am. Chem. Soc.* **2009**, *131*, 50.
[100] F. Guo, Y. Hou, A. M. Asiri, X. Wang, *Chem. Commun.* **2017**, *53*, 13221.
[101] A. Rajagopal, E. Akbarzadeh, C. Li, D. Mitoraj, I. Krivtsov, C. Adler, T. Diemant, J. Biskupek, U. Kaiser, C. Im, M. Heiland, T. Jacob, C. Streb, B. Dietzek, R. Beranek, *Sustainable Energy Fuels* **2020**, *4*, 6085.
[102] T.u N. Nguyen, S. Kampouri, B. Valizadeh, W. Luo, D. Ongari, O. M. Planes, A. Züttel, B. Smit, K. C. Stylianou, *ACS Appl. Mater. Interfaces* **2018**, *10*, 30035.
[103] J. Wang, A. S. Cherevan, C. Hannecart, S. Naghdi, S. P. Nandan, T. Gupta, D. Eder, *Appl. Catal., B* **2021**, *283*, 119626.
[104] Z. Xin, J.-L. Liu, W. Wei, A.-Q. Jia, Q.-F. Zhang, *Inorg. Nano-Met. Chem.* **2021**, https://www.tandfonline.com/doi/full/10.1080/24701556.2021.1988975.
[105] M. Yuan, H. Yao, L. Xie, X. Liu, H. Wang, S. M. Islam, K. Shi, Z. Yu, G. Sun, H. Li, S. Ma, M. G. Kanatzidis, *J. Am. Chem. Soc.* **2020**, *142*, 1574.
[106] D. Yue, T. Zhang, M. Kan, X. Qian, Y. Zhao, *Appl. Catal., B* **2016**, *183*, 1.
[107] D. Yue, Z. Zhang, Z. Tian, T. Zhang, M. Kan, X. Qian, Y. Zhao, *Catal. Today* **2016**, *274*, 22.
[108] Y.u Han, D. Yue, M. Kan, Y. Wu, J. Zeng, Z. Bian, Y. Zhao, X. Qian, *Appl. Catal., B* **2019**, *245*, 190.
[109] F. Bozheyev, S. Fengler, J. Kollmann, T. Klassen, M. Schieda, *ACS Appl. Mater. Interfaces* **2022**, *14*, 22071.
[110] A. Elliott, J. Mcallister, L. Masaityte, M. Segado-Centellas, D.-L. Long, A. Y. Ganin, Y.-F. Song, C. Bo, H. N. Miras, *Chem. Commun.* **2022**, *58*, 6906.
[111] E. Guillamón, M. Oliva, J. Andrés, R. Llusar, E. Pedrajas, V. S. Safont, A. G. Algarra, M. G. Basallote, *ACS Catal.* **2021**, *11*, 608.
[112] B. O. Birgisson, L. J. Monger, K. K. Damodaran, S. G. Suman, *Inorg. Chim. Acta* **2020**, *501*, 119272.
[113] J. Barros Barbosa, P. L. Taberna, V. Bourdon, I. C. Gerber, R. Poteau, A. Balocchi, X. Marie, J. Esvan, P. Puech, A. Barnabé, L. Da Gama Fernandes Vieira, I.-T. Moraru, J. Y. Chane-Ching, *Appl. Catal., B* **2020**, *278*, 119288.

© 2023 The Authors. Advanced Materials published by Wiley-VCH GmbH

15214095, 2024, 7, Downloaded from https://advanced.onlinelibrary.wiley.com/doi/10.1002/adma.202305730 by Universitätsbibliothek Mainz, Wiley Online Library on [04/06/2025]. See the Terms and Conditions (https://onlinelibrary.wiley.com/terms-and-conditions) on Wiley Online Library for rules of use; OA articles are governed by the applicable Creative Commons License



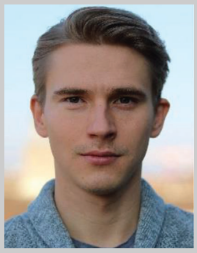
Samar Batool received her bachelor's degree in 2017 from Quaid-I-Azam University Islamabad, Pakistan. The same year she was awarded a scholarship from the Graduate School of Science and Engineering of Bilkent University and moved to Turkey to pursue her master's degree in chemistry, which she completed in 2020. She was then offered a Ph.D. fellowship from Vienna University of Technology, Austria, where she currently works as project assistant at the Institute of Materials Chemistry. Her research interests involve the combination of solid-state (heterogeneous) photocatalysts with molecular-sized artificial homogeneous photosystems.



Marcel Langer received his bachelor's degree from the University of Ulm in 2017. During his master's, which he completed in 2020, he worked in the group of Johan Boman in Gothenburg, Sweden, in the field of analytical chemistry. Marcel is currently a Ph.D. student in the Streb group at Johannes Gutenberg University Mainz, and—at the time of writing this Review—on a research visit to the group of Alina Schimpf at University of California San Diego. He is interested in embedding light-driven molecular catalysts for water oxidation and hydrogen evolution in soft matter membranes to harness synergistic reactivity.



Carsten Streb is professor of inorganic chemistry at Johannes Gutenberg University Mainz. His current research is focused on designing functional molecular and nanoscale materials and composites to address global chemical challenges with a focus on energy conversion and energy storage. He is interested in using in situ/operando methods to study reactivity and stability of homogeneous and heterogeneous catalysts.



Alexey Cherevan is an assistant professor and subgroup leader at the Institute of Materials Chemistry, TU Wien, Austria. He received his master's degree from Moscow State University in 2010 and a Ph.D. from the University of Münster in 2014. Joining TU Wien in 2015, he specializes in materials chemistry, particularly functional inorganic nanomaterials for energy applications. He develops innovative tools that combine heterogeneous and homogeneous branches of photocatalysis. As of 2023, he holds a tenure track assistant professor position and is a PI of the FWF Cluster of Excellence "Materials for Energy Conversion and Storage."

 © 2023 The Authors. Advanced Materials published by Wiley-VCH GmbH

15214095, 2024, 7, Downloaded from https://advanced.onlinelibrary.wiley.com/doi/10.1002/adma.202305730 by Universitatsbibliothek Mainz, Wiley Online Library on [04/06/2025]. See the Terms and Conditions (https://onlinelibrary.wiley.com/terms-and-conditions) on Wiley Online Library for rules of use; OA articles are governed by the applicable Creative Commons License

6.4 {MLa-5}: Poly(dehydroalanine)-Based Hydrogels as Efficient Soft Matter Matrices for Light-Driven Catalysis

Tolga Çeper,‡ Marcel Langer,‡ Nikita Vashistha, Benjamin Dietzek-Ivanšić, Carsten Streb, Sven Rau, and Felix H. Schacher*

‡ *Authors contributed equally to this work*

* *Corresponding author*

Abstract: Novel pH-responsive and polyampholytic hydrogels based on crosslinked poly(dehydroalanine) were developed and tested for their swelling behavior. The soft matter matrices were electrostatically functionalized with $[Ru(bpy)_3]^{2+}$, combined with either $\{Mo_3\}$ or $\{Co_4\}$ catalysts and examined in proof-of-principle studies for their reactivity and selectivity in light-driven HER and WOC. The stability of PS, catalysts and hydrogel scaffold was investigated in a series of photocatalytic studies and a possible self-repair approach of the molecular building blocks was explored by the reversible adsorption of the dye upon pH changes.

Published in: *Macromol. Rapid. Commun.* **2024**, *45*, 2300448.

Status: Published

Copyright: Reprinted with permission from "Poly(dehydroalanine)-Based Hydrogels as Efficient Soft Matter Matrices for Light-Driven Catalysis", T. Çeper,‡ M. Langer,‡ N. Vashistha, B. Dietzek-Ivanšić, C. Streb, S. Rau, and F. H. Schacher,* *Macromol. Rapid. Commun.* **2024**, *45*, 2300448. **DOI:** 10.1002/marc.202300448.

© 2024, The Authors, Macromolecular Rapid Communications published by Wiley-VCH GmbH under the terms of the CC BY 4.0 license.

Author Contributions:

T. Çeper	Conceptualization; Synthesis and characterization of hydrogels; FTIR, UV-Vis and Fluorescence spectroscopic analyses; Rheological characterization; Preparation of hydrogel composites; Conducting photocatalytic H_2 and O_2 evolution studies; Data analysis; Results discussion; Writing, discussion and revision of the manuscript.
M. Langer	Imparting general knowledge and assistance of the methodology for performing oxygen evolution catalysis and its corresponding data analysis; Discussion of results in section 2.5. “Light-Driven OER”; Synthesis and characterization of $\{Co_4\}$ and writing the corresponding part in the supplementary information; Discussion and revision of the manuscript.
N. Vashistha	Nanosecond time-resolved emission spectroscopic measurements; Revision of the manuscript.
B. Dietzek-Ivanšić	Discussion and revision of the manuscript.
C. Streb	Discussion and revision of the manuscript.
S. Rau	Discussion and revision of the manuscript.
F. H. Schacher	Conceptualization; Supervision; Discussion of results; Writing, discussion and revision of the manuscript.

RESEARCH ARTICLE

Macromolecular Rapid Communications
www.mrc-journal.de

Poly(dehydroalanine)-Based Hydrogels as Efficient Soft Matter Matrices for Light-Driven Catalysis

*Tolga Çeper, Marcel Langer, Nikita Vashistha, Benjamin Dietzek-Ivanšić, Carsten Streb, Sven Rau, and Felix H. Schacher**

Soft matter integration of photosensitizers and catalysts provides promising solutions to developing sustainable materials for energy conversion. Particularly, hydrogels bring unique benefits, such as spatial control and 3D-accessibility of molecular units, as well as recyclability. Herein, the preparation of polyampholyte hydrogels based on poly(dehydroalanine) (PDha) is reported. Chemically crosslinked PDha with bis-epoxy poly(ethylene glycol) leads to a transparent, self-supporting hydrogel. Due to the ionizable groups on PDha, this 3D polymeric matrix can be anionic, cationic, or zwitterionic depending on the pH value, and its high density of dynamic charges has a potential for electrostatic attachment of charged molecules. The integration of the cationic molecular photosensitizer $[Ru(bpy)_3]^{2+}$ (bpy = 2,2′-bipyridine) is realized, which is a reversible process controlled by pH, leading to light harvesting hydrogels. They are further combined with either a thiomolybdate catalyst ($[Mo_3S_{13}]^{2-}$) for hydrogen evolution reaction (HER) or a cobalt polyoxometalate catalyst ($Co_4POM = [Co_4(H_2O)_2(PW_9O_{34})_2]^{10-}$) for oxygen evolution reaction (OER). Under the optimized condition, the resulting hydrogels show catalytic activity in both cases upon visible light irradiation. In the case of OER, higher photosensitizer stability is observed compared to homogeneous systems, as the polymer environment seems to influence decomposition pathways.

1. Introduction

Constantly increasing global energy consumption continues to trigger new studies on sustainable and clean alternatives for fossil fuels.[1–3] Inspired by light-driven biological photosynthesis, photocatalytic water splitting into hydrogen and oxygen has become a key concept for simple and cost-effective solar energy conversion.[4–6] In plants, light is absorbed by chlorophyll and other pigments, and for the synthesis of biomass, a series of essential processes, such as charge separation, charge transfers, and redox reactions, are carried out in a variety of organelles.[4,7] These complex proteins are individually located on the stacked lipid bilayers called thylakoid membranes forming a physically continuous 3D network that provides spatial orientation of all essential building blocks, enabling efficient light-induced catalysis and contact with water.[8] This physical separation is key to controlling the flow of energy and charges within the membrane so that kinetic differences can be matched during photosynthesis.[9] Since excess excitation energy and harmful side products of water splitting could damage the reaction centers of organelles, plants have evolved several

T. Çeper, F. H. Schacher
Institute of Organic Chemistry and Macromolecular Chemistry
Friedrich Schiller University Jena
Humboldtstraße 10, D-07743 Jena, Germany
E-mail: felix.schacher@uni-jena.de
T. Çeper, F. H. Schacher
Jena Center for Soft Matter (JCSM)
Friedrich Schiller University Jena
Philosophenweg 7, D-07743 Jena, Germany

The ORCID identification number(s) for the author(s) of this article can be found under https://doi.org/10.1002/marc.202300448

© 2024 The Authors. Macromolecular Rapid Communications published by Wiley-VCH GmbH. This is an open access article under the terms of the Creative Commons Attribution License, which permits use, distribution and reproduction in any medium, provided the original work is properly cited.

DOI: 10.1002/marc.202300448

T. Çeper, F. H. Schacher
Center for Energy and Environmental Chemistry Jena (CEEC)
Friedrich Schiller University Jena
Philosophenweg 7a, 07743 Jena, Germany
M. Langer, C. Streb
Department of Chemistry
Johannes Gutenberg University Mainz
Duesbergweg 10–14, 55128 Mainz, Germany
N. Vashistha, B. Dietzek-Ivanšić
Institute of Physical Chemistry
Friedrich-Schiller-University Jena
Helmholtzweg 4, D-07743 Jena, Germany
N. Vashistha, B. Dietzek-Ivanšić
Leibniz Institute of Photonic Technology Jena
Department of Functional Interfaces
Albert Einstein Allee 9, D-07745 Jena, Germany
S. Rau
Institute of Inorganic Chemistry I
Ulm University
Albert-Einstein-Allee 11, 89081 Ulm, Germany

concepts of repair which might be mimicked in artificial photosynthesis.[10,11] Furthermore, the soft matter membrane integration is pivotal in the creation of a proton gradient across the thylakoid membranes which leads to ATP formation and aids repair.[12] To accommodate photosensitizers and catalysts developed for artificial photosynthesis systems with spatial control, new materials mimicking the thylakoid membrane are urgently required. Soft materials, such as vesicles, micelles, and block copolymer membranes, are particularly rewarding and of growing interest because they can be subjected to chemical modification to tailor versatile functions and can facilitate the compartmentalization of light harvesting units and catalysts within a 3D network.[13–24] For instance, Okeyoshi et al. have developed hydrogen and oxygen-generating gel systems based on copolymers consisting of temperature-responsive and photosensitizing monomer units.[25–28] Since the charge separation and migration, as well as surface reaction processes, are rate-determining and lead to low quantum efficiencies, 3D structured photoactive membranes are considered efficient solutions to overcome these challenges.[29] To access this materials class, photoactive molecular units can either be embedded in a 3D network structure or supporting networks can be surface-decorated with the photoactive species. This promotes maximum accessibility of these units for the reaction environment and can help to reduce the aggregation of subunits. The specific surface area, pore size, adsorptive properties, structural stability, and low gas resistance are just some of the important design parameters for such 3D networks as they provide more catalytically active sites and facilitate the spatial separation of reactive subunits.[29]

Polyampholyte hydrogels are appealing materials bearing both anionic and cationic functional groups that can be used for a wide range of applications, such as tissue engineering and drug delivery, as well as separation and purification technologies.[30,31] Net charge and charge density can be dynamic upon changes in pH and used to tune their mechanical and structural properties when the polyampholyte consists of weak acid and base.[32] They also feature tuneable isoelectronic points (IEP) at which charge neutrality and presumably the most compact structure are present, as well as excess anionic or cationic charge depending on the pH value, where electrostatic repulsions are dominant.[33] Due to these repulsive forces between similar charges, these hydrogels can expand, resulting in larger mesh sizes and higher swelling ratio.[34] In contrast, they tend to shrink near the IEP due to electrostatic attraction between opposite charges. These charges can be compensated by the addition of salts which restrict the attractive interactions, leading to reswelling which is also known as the anti-polyelectrolyte effect.[35] As a subclass of polyampholytes, polyzwitterionic hydrogels feature oppositely charged moieties or ionizable groups within the same repeating unit. They can bind large amounts of water, leading to antifouling properties and rendering materials very promising for biomedical and coating applications.[36–38] Besides, they can also be used in heavy metal ion removal,[39] ultrafiltration,[40] and battery applications.[41–43] Although there is great potential for polyampholyte/polyzwitterionic hydrogels as scaffolds for the immobilization of photosensitizers, polymer-metal complexes, metal nanoparticles, metal oxides, or enzymes, there are still rather few examples of such strategies in the literature.

Polyampholytes are commonly synthesized by two approaches: 1) Two different monomers (e.g., of anionic and cationic charge) can be copolymerized resulting in charges on different repeating units,[44] or 2), for polyzwitterions zwitterionic monomers can either directly be polymerized, or obtained by subsequent post-polymerization modification of precursor polymers.[45,46] Functional groups of polyzwitterions commonly include cationic ammonium groups, as well as anionic sulfonates, carboxylates, phosphates, phosphonates, or phosphinates, and various synthetic methods can be applied for the polymerization.[47] In general, free radical polymerization of their acrylic or vinylic derivatives in the presence of crosslinkers could be reasonable for polyzwitterionic hydrogel synthesis.[45] However, this strategy might encounter difficulties due to the presence of ionic groups and solubility limitations.[48] As an alternative, either the polymerization of protected monomers and subsequent deprotection or the chemical crosslinking of hydrophilic macromolecules can be useful strategies for hydrogel synthesis.[49] Various synthetic strategies have been already demonstrated for chemical crosslinking, such as Michael addition, CLICK reaction (azide-alkyne), or epoxide coupling, in the presence of suitable functional groups (—COOH, —OH, or —NH_2).[50,51] Further crosslinking reactions are readily available and commonly used in the field of bioconjugation.[48]

Polydehydroalanine (PDha) has been introduced as a pH-responsive polyampholyte with high charge density.[52] PDha bears weak acid and base moieties (—COOH and —NH_2) within each repeating unit, and net charge, as well as charge density, are controlled by pH so that PDha can in principle exist as polycation, polyanion, or polyzwitterion.[52] Because of the captodative nature of the monomer, typically precursor polymers featuring protective groups are synthesized, and subsequently subjected to deprotection reactions.[53] So far, *tert*-butoxycarbonylaminomethylacrylate (*t*BAMA) has been successfully polymerized using free-radical polymerization (FRP), atom transfer radical polymerization (ATRP), and nitroxide-mediated radical polymerization (NMP).[47,52,54–57] Alternative protecting groups could also be utilized especially in case milder deprotection reaction conditions are necessary.[53] PDha coated on magnetic nanoparticles has been so far biocompatible and can reversibly adsorb charged small molecules and macromolecules.[52,55,57] In addition, it has been recently shown that the chemical modification of PDha is possible via reactive amines present on the polymeric backbone, and the resulting graft copolymers are already used as dispersants for carbon nanotubes and as compatibilizers for photocatalytic reactions.[47,58]

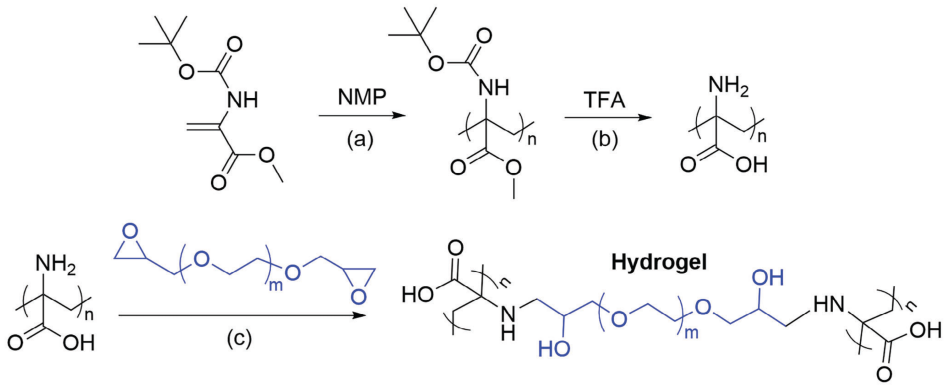
In the present work, we demonstrate a synthetic route for the design of stimuli-responsive hydrogels with a dynamic charge based on PDha. P*t*BAMA was first synthesized by controlled-radical polymerization (CRP) techniques as precursor polymer, subsequently hydrolyzed to obtain PDha, and afterward chemically crosslinked using bis-glycidyl ethers. Gelation parameters were optimized according to the molecular weight (M_n) of PDha and the crosslinker, polymer concentrations, crosslinker ratio, and reaction time. We investigated the swelling properties of such hydrogels at different pH and salinity and could further show that reversible adsorption of a cationic model complex was possible upon changes in pH. In this light, PDha-based hydrogels represent a promising scaffold for photocatalytic reactions by

 © 2024 The Authors. Macromolecular Rapid Communications published by Wiley-VCH GmbH

15213927, 2024, 5, Downloaded from https://onlinelibrary.wiley.com/doi/10.1002/marc.202300448 by Universitatsbibliothek Mainz, Wiley Online Library on [04/06/2025]. See the Terms and Conditions (https://onlinelibrary.wiley.com/terms-and-conditions) on Wiley Online Library for rules of use; OA articles are governed by the applicable Creative Commons License

ADVANCED SCIENCE NEWS
www.advancedsciencenews.com

Macromolecular Rapid Communications
www.mrc-journal.de



Scheme 1. Synthesis route of PDha-based hydrogel including a) polymerization of *t*BAMA, b) deprotection of P*t*BAMA to yield PDha, and c) hydrogel synthesis with a PEG-based crosslinker bearing epoxide groups.

immobilizing both photosensitizer dyes and catalysts in close proximity, facilitating e^- transfer steps and allowing other additives and products to move freely through the pores of the hydrogel. Our main focus herein is to demonstrate that by a smart choice of the building blocks for light-driven catalysis, such hydrogels can be used for both hydrogen and oxygen evolution reactions (HER and OER).

2. Results and Discussion

2.1. Hydrogel Synthesis

Herein, we introduce a straightforward strategy for the preparation of polyampholytic hydrogels comprising three steps; 1) the controlled radical polymerization of *t*BAMA, 2) deprotection of P*t*BAMA to yield PDha, and 3) the chemical crosslinking of PDha using bis-epoxy poly(ethylene glycol). As shown in **Scheme 1**, P*t*BAMA was synthesized by NMP according to a literature protocol,[52] leading to moderately narrow dispersity (*Đ*). The sample was treated with trifluoroacetic acid (TFA) for deprotection of the amine and carboxylic acid groups to give PDha.[52] After 1.5 h of treatment, the complete removal of Boc groups was observed, but around 8% of methoxy groups remained (Figure S1, Supporting Information). The leftover methoxy groups can be cleaved under basic conditions,[47] in our case during crosslinking and gelation in alkaline media. Two different P*t*BAMAs were synthesized with the average degree of polymerization (DP) 40 and 180 to determine the effect of M_n on crosslinking and hydrogel properties. *Đ* of polymers were 1.6 and 1.5, respectively (Figure S2, Supporting Information, for SEC results showing relative M_n of polymer and dispersity). For later sections, polymers were named based on the DP of P*t*BAMA as $PDha_{40}$ and $PDha_{180}$.

Hydrogel synthesis was performed using a pre-polymer mixture of PDha and poly(ethylene glycol) diglycidyl ether (PEGDGE) as a crosslinker, via the ring-opening reaction of epoxides with the amines of PDha. The crosslinking reaction was optimized via kinetic studies using $PDha_{40}$ and $PDha_{180}$ at different PDha concentrations and PDha-to-crosslinker ratios (PCR, w/w, shown in Table S1, Supporting Information). PEGDGE with 2000 g mol^{-1} of M_n ($PEGDGE^2$) was used as a crosslinker in optimization, thus leading to $PDha_{PEG2}$ hydrogels. Precursors were first dissolved in 0.1 M KOH solution, and the crosslinker was subsequently added. The solution was stirred at 60 °C yielding a clear hydrogel (**Figure 1a**), and unreacted crosslinker and PDha were removed by dialysis (Figure S3, Supporting Information, FTIR spectra of dialysates). The solubility of $PDha_{40}$ was limited to 33 mg mL^{-1} and a minimum of 25 mg mL^{-1} was required for gelation. Solutions of $PDha_{180}$ could be prepared at 20 mg mL^{-1}, already being more viscous compared to $PDha_{40}$. The minimum PCR for gelation of $PDha_{180}$ was w/w 1:1, and we also observed that $PDha_{180}$ led to faster gelation if compared to $PDha_{40}$. While at least 18 h were needed for $PDha_{40}$ according to the tube inversion test, this time is reduced to about 2 h in the case of $PDha_{180}$ (Table S2, Supporting Information, entries 4 and 6). We assume that higher M_n promotes crosslinking due to a larger extent of chain entanglements.

^{13}C cross-polarization magic angle spinning (CP-MAS) NMR spectra of the dry gel and PDha also verify the successful crosslinking reaction (Figure 1b), with the broad peak at 70 ppm assigned to the PEG-backbone. In addition, the methyl ester carbon signal at 55 ppm was no longer present after crosslinking, indicating that the remaining methyl esters were completely hydrolyzed during the gelation. The PDha content of the resulting hydrogels was calculated using the [C]/[N] ratio obtained from elemental analysis after drying the respective samples. The dry gel was also analyzed by FTIR and compared to the FTIR spectra of the precursors PDha and PEGDGE. The presence of a peak at 1098 cm^{-1} on the spectrum of the dry hydrogel is characteristic of the stretching vibration of the C—O bond of an aliphatic ether, corresponding to the successful incorporation of the crosslinker (Figure S4, Supporting Information).

Polymer crosslinking is an approach to hydrogel synthesis by which the mesh size of the hydrogel, which has an impact on

 © 2024 The Authors. Macromolecular Rapid Communications published by Wiley-VCH GmbH

15213927, 2024, 5, Downloaded from https://onlinelibrary.wiley.com/doi/10.1002/marc.202300448 by Universitätsbibliothek Mainz, Wiley Online Library on [04/06/2025]. See the Terms and Conditions (https://onlinelibrary.wiley.com/terms-and-conditions) on Wiley Online Library for rules of use; OA articles are governed by the applicable Creative Commons License

ADVANCED SCIENCE NEWS
www.advancedsciencenews.com

Macromolecular Rapid Communications
www.mrc-journal.de

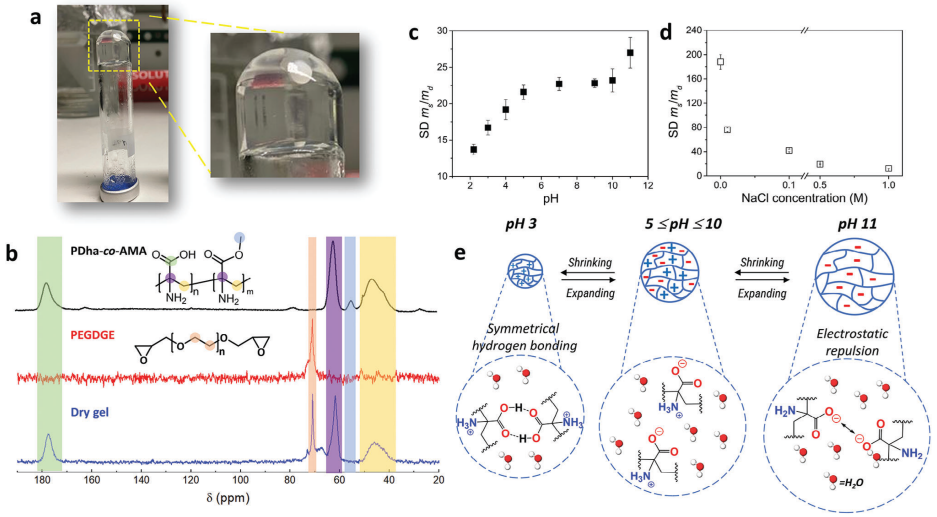


Figure 1. a) Hydrogel formed by crosslinking of PDha with poly(ethylene glycol) diglycidyl ether (PEGDGE), b) the comparison of ^{13}C CP-MAS NMR spectra of the dry gel, PDha, and PEGDGE, c) swelling degrees of $PDha_{PEG2}$ with respect to pH, d) swelling degrees of $PDha_{PEG2}$ at increasing salinity, and e) illustration of pH-dependent swelling behavior of PDha-based hydrogels with possible dominant interactions.

swelling and diffusion properties, can be tuned by using different M_n of crosslinkers.[59] Therefore, hydrogels with smaller and larger mesh sizes were also formed using $PDha_{180}$ and PEGDGE with 1000 and 6000 g mol^{-1} of M_n (PEGDGE[1] and PEGDGE[6]), employing a PCR of 1:8. Having a range of hydrogels with different mesh sizes is essential not only to adjust swelling properties, it will also be beneficial for tuning mechanics and durability. If compared to PEGDGE[1] and PEGDGE[6], PEGDGE[2] led to self-supporting hydrogels, thereby facilitating handling, cutting, or transferring steps. Therefore, we decided to use $PDha_{PEG2}$ in most of the following experiments.

2.2. Swelling Properties of Hydrogels

Deionized water (pH 7) was used to determine how the actual PDha content affects the swelling degree, which increased with increasing PDha ratio (Table S2, Supporting Information) and decreasing M_n of PDha (Table S2, Supporting Information, entries 1 and 6). This result is in good agreement with the fact that zwitterionic polymers often have a stronger binding ability for water if compared to PEG.[60] Regarding the pH-dependent charge of PDha,[56] the resulting hydrogels are anticipated to exhibit excess negative charge at high pH, excess positive charge at low pH, and be overall charge neutral close to the IEP of PDha.

The swelling was investigated in a pH range between 2.2 and 11, and solutions were prepared using three different buffers while maintaining comparable ionic strength. Three different trends could be observed (Figure 1c), with the minimum swelling degree (DS) for $PDha_{PEG2}$ of 13.7 ± 1 at pH 2.2. The DS gradually increased with increasing pH up to pH 5, presumably due to changes in dominant interactions within the hydrogel. FTIR spectra showed the presence of the deprotonated carboxylate groups from hydrogel samples freeze-dried at pH 6 and 11, with the stretching vibration at 1609 cm^{-1} (Figure S5, Supporting Information). Before deprotonation, we assumed that H-bonding between different carboxylic acid groups was one of the driving forces rather than just electrostatic repulsion, leading to smaller volume and mesh size. With increasing pH value, the dominant charge within the hydrogels should be anionic due to the presence of carboxylates, thereby also leading to an increase in hydrophilicity. $PDha_{PEG2}$ was able to swell at pH values ranging from 5 to 10, where PDha is zwitterionic,[52] and had slightly increasing swelling degree 21.6 ± 1 at pH 5, 22.7 ± 0.8 at pH 7, 22.8 ± 0.5 at pH 9, and 23.2 ± 1.5 at pH 10. PDha is supposed to exist as polyanion at pH values higher than 10 because the pK_a of the protonated amine of PDha is around 9.45.[52] In hydrogel form, it must be considered that the effective pK_a might vary due to the surrounding media and steric constraints. Similarly, the pK_a values of PDha are shifted compared to the pK_a values of small molecule L-alanine containing the same functional groups.[61,62] The presence of a charge, either positive or negative, contributes to swelling in hydrogels due to electrostatic repulsion.[63] The swelling degree for $PDha_{PEG2}$ was 27 ± 2 at pH 11 indicating that repulsive forces have a major influence on swelling. By changing local pH, we assume changes in hydrogel charge state and swelling as shown in Figure 1e.[55,57] The hydrogel structure and DS are also dependent on the ionic strength (Figure 1d),

 © 2024 The Authors. Macromolecular Rapid Communications published by Wiley-VCH GmbH

15213927, 2024, 5, Downloaded from https://onlinelibrary.wiley.com/doi/10.1002/marc.202300448 by Universitatsbibliothek Mainz, Wiley Online Library on [04/06/2025]. See the Terms and Conditions (https://onlinelibrary.wiley.com/terms-and-conditions) on Wiley Online Library for rules of use; OA articles are governed by the applicable Creative Commons License

ADVANCED SCIENCE NEWS
www.advancedsciencenews.com

Macro-olecular Rapid Communications
www.mrc-journal.de

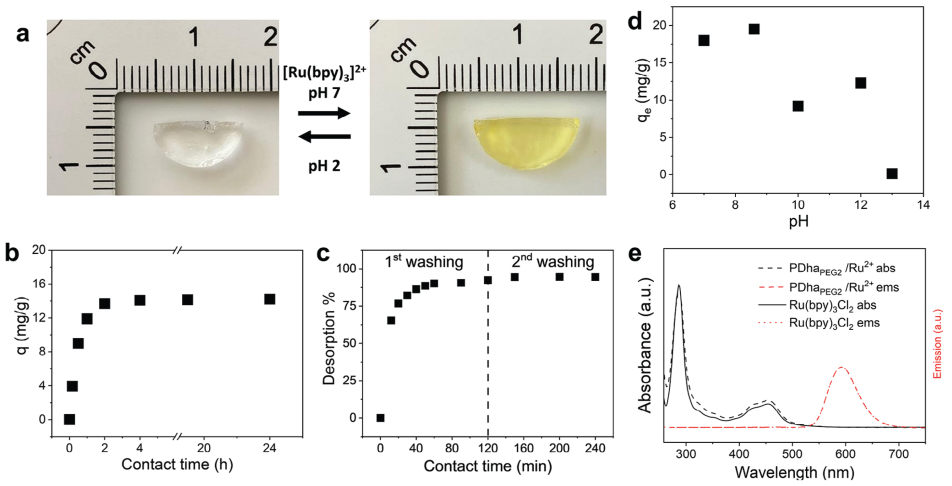


Figure 2. a) pH-controlled reversible adsorption of $[Ru(bpy)_3]^{2+}$ by PDha-based hydrogels; b) adsorption capacity (q) of $PDha_{PEG6}$ for $[Ru(bpy)_3]^{2+}$ at pH: 7 (initial dye concentration: 0.07 mM), c) desorption percentage of adsorbed $[Ru(bpy)_3]^{2+}$ with respect to time (hydrogel used in adsorption study in (b) was washed twice with aqueous solution at pH 2, fresh solution was used for the second washing step), d) adsorption capacity of $PDha_{PEG6}$ for $[Ru(bpy)_3]^{2+}$ at equilibrium at different pH values (qe, initial dye concentration: 0.085 mM), and e) absorption and emission spectra of $[Ru(bpy)_3]^{2+}$ in water and within PDha-based hydrogel.

and when $PDha_{PEG2}$ was soaked in aqueous NaCl solutions, the swelling degree gradually decreased. For polyzwitterionic hydrogels, ionic strength reduces inter- and intra-chain attractions between opposite charges leading to a stretching of the hydrogel called anti-polyelectrolyte effect.[64] In contrast, ions screen the charges on the polyampholytic PDha and lead to lower DS values. This effect should not be seen as polyelectrolyte or salting-out effect seen in polyelectrolyte-based (either positively or negatively charged) hydrogels which collapse in high ionic strength media because repulsive forces are reduced due to charge screening.[65] We also noted that the PDha-based hydrogels were able to swell in highly polar solvents other than water, such as dimethylformamide, acetonitrile, methanol, and acetone, however, water led to a higher swelling degree (Figure S6, Supporting Information).

2.3. Reversible Attachment of $[Ru(bpy)_3]^{2+}$

Since the herein synthesized polyampholytic hydrogel features pH-controlled net charge and charge density, it enables reversible adsorption of charged photosensitizer and/or catalyst building blocks. In this regard, the adsorption of $[Ru(bpy)_3]^{2+}$ by PDha-hydrogel and the absorption and emission properties of the resultant light-harvester hydrogel were investigated. In a typical experiment, the swollen hydrogel was placed in an aqueous $[Ru(bpy)_3]Cl_2$ solution. First, we tested the effect of contact time on adsorption in 2.5 mL of 0.07 mM dye solution at pH 7 using $PDha_{PEG6}$. Dye adsorption was optically monitored by the color change of the hydrogel since the dye complex has an absorption band in the visible range (**Figure 2a**). Dye adsorption was quantified using the extinction coefficient of $[Ru(bpy)_3]Cl_2$ unless otherwise indicated, and the drop of absorbance of the supernatant was followed by UV–vis spectroscopy (Figure S7a, Supporting Information). $PDha_{PEG6}$ exhibited an adsorption capacity (q) for $[Ru(bpy)_3]^{2+}$ of ≈14 mg g^{-1} within 4 h, without further significant change during prolonged storage of up to 24 h (Figure 2b). Therefore, the remaining experiments were carried out for 4 h. By changing the initial dye concentration from 0.07 to 0.6 mM, the equilibrium adsorption (q_e) increased from 18.3 to 50.1 mg g^{-1} after 24 h (Figure S7b, Supporting Information). Adsorption isotherms and diffusion kinetics of $[Ru(bpy)_3]^{2+}$ were further studied and indicate that ligand stacking, as well as electrostatic interactions between the dye complex and the hydrogel, are contributing to the dye binding (see additional discussion and Figures S8 and S9, Supporting Information).

Hydrogel samples were washed with DI water and the resulting solution was analyzed by UV–vis spectroscopy to test the adsorption stability. When the initial dye concentration was up to 0.1 mM, we noted the dye molecules were stably incorporated in the hydrogel because we observed no dye absorption in the supernatant solution. At higher concentrations, some dye leaching was observed, although we assume that these are mainly complex molecules loosely adsorbed within the polymeric network. After adsorption at pH 7, $PDha_{PEG6}$ was placed in 2 mL of aqueous solution at pH 2 for the controlled desorption of the complex. Before that, the hydrogel sample was washed in deionized water several times to remove excess dye. At pH 2, we observed around 90% of desorption in the initial 60 min (Figure 2c), and further desorption to 92% in the following 60 min, attributed to the equilibrium point. The supernatant was removed and fresh

 © 2024 The Authors. Macromolecular Rapid Communications published by Wiley-VCH GmbH

15213927, 2024, 5, Downloaded from https://onlinelibrary.wiley.com/doi/10.1002/marc.202300448 by Universitätsbibliothek Mainz, Wiley Online Library on [04/06/2025]. See the Terms and Conditions (https://onlinelibrary.wiley.com/terms-and-conditions) on Wiley Online Library for rules of use; OA articles are governed by the applicable Creative Commons License

ADVANCED SCIENCE NEWS
www.advancedsciencenews.com

Macromolecular Rapid Communications
www.mrc-journal.de

aqueous solution at pH 2 was subsequently added, resulting in further desorption up to 95% of the attached dye within 30 min. Afterward, no further release could be detected.

At pH 2, the charge characteristics of $PDha_{PEG6}$ are completely inverted to be cationic, leading to repulsive forces toward the model dye.[55] Given this reversible adsorption, PDha-based hydrogels might be of interest for the recycling of $[Ru(bpy)_3]^{2+}$ or even the repair/exchange of degraded molecular units. We further investigated the effect of pH value on adsorption in a pH range of 7–13 in 2.5 mL of 0.085 mM $[Ru(bpy)_3]^{2+}$ (Figure 2d). $PDha_{PEG6}$ featured maximum adsorption of 18 and 19.5 mg g^{-1} at pH 7 and 8.6, respectively. The adsorption capacity decreased at pH 10, 12, and 13 to 9.2, 12.3, and 0.13 mg g^{-1}, respectively, which we believe, particularly at pH 13, stemmed from the occupation of the binding sites by cation of the base. Hence, the adsorption of dye complexes was performed at pH 7 for further studies.

Besides pH, the adsorption capacity also depends on the used crosslinker (Figure S7c, Supporting Information). Compared to $PDha_{PEG2}$ with $PDha_{PEG6}$, which both contain the same amount of PDha, we assume that the inner free volume of the hydrogel increases, and the dye cations freely move within the hydrogel. $PDha_{PEG1}$ featured comparable dye adsorption of 13.8 mg g^{-1} despite the smaller mesh size. In our opinion, it can be attributed that $PDha_{PEG1}$ contains an overall higher amount of PDha (24%), which seems to be mainly responsible for dye adsorption. As herein described hydrogels were able to act as a host matrix for $[Ru(bpy)_3]^{2+}$ model complexes through reversible adsorption, during the next steps, we investigated their use as a soft matter matrix for light-driven catalysis.

Absorption and emission spectra of $[Ru(bpy)_3]^{2+}$ immobilized in the hydrogel were identical to those observed in water,[66] implying similar photophysical characteristics (Figure 2e).[67] Both spectra were taken for hydrogels in the swollen state. The charge transfer band for $[Ru(bpy)_3]^{2+}$ can be shifted by several factors, such as solvent, ionic strength, and ion pairing,[68] and in this context, PDha-based hydrogels might impose additional effects. Here, we aimed to use this hybrid hydrogel ($PDha_{PEG2}/[Ru(bpy)_3]^{2+}$) as a photosensitizer for light-driven HER or OER applications.[69–74] These processes rely on an efficient e^- transfer between $[Ru(bpy)_3]^{2+}$ and the sacrificial electron donor or acceptor agents and the respective catalyst, each requiring close spatial proximity. In this context, the emission quenching in hybrid hydrogels ($PDha_{PEG2}/[Ru(bpy)_3]^{2+}$) by varying the concentration of quenchers (Co_4POM and $[Mo_3S_{13}]^{2-}$) was studied by recording emission spectra at varying time delays using nanosecond transient emission spectroscopy (Figures S10–S12, Supporting Information).

The samples were prepared by adding catalyst solutions into hybrid hydrogels with the $[Ru(bpy)_3]^{2+}$ concentration fixed at 95 µM and excited at 500 nm. For this, aqueous solutions of Co_4POM (ranging from 2.5 to 20 µM) were added, while in independent quenching experiments the concentration of $[Mo_3S_{13}]^{2-}$ was varied from 0.267 to 2.136 µM in a 1:1 MeOH/water mixture. However, for calculating the catalyst concentrations within the hydrogel, we used the solvent amounts in the swollen hydrogel with the assumption that all catalysts are adsorbed, leading to concentrations of 17.2 to 133 µM for Co_4POM and 2 to 16 µM for $[Mo_3S_{13}]^{2-}$. Figure S10, Supporting Information, shows the emission spectra of the hybrid hydrogel with and without Co_4POM at different time delays on which the fluorescence maximum appears at 610 nm irrespective of the sample. Figures S11 and S12, Supporting Information, exhibit the fluorescence quenching behavior of the hybrid hydrogel at a varying concentration of quencher (Co_4POM and $[Mo_3S_{13}]^{2-}$) at the fixed delay time (1 µs).

For $PDha_{PEG2}/[Ru(bpy)_3]^{2+}$ with Co_4POM as a quencher, the fluorescence intensity decays nonlinearly upon linearly increasing the Co_4POM concentration (Figure S11, Supporting Information). A Stern–Volmer analysis (Figure S13, Supporting Information) reveals a strongly nonlinear behavior indicating a complex quenching behavior within the likely very heterogeneous sample.[75,76] Figure S14, Supporting Information, reveals that the emission intensity of the hydrogel samples upon addition of $[Mo_3S_{13}]^{2-}$ show a rise in emission intensity which we attributed to the instability of the sample in the air during the measurement (Figures S12 and S14, Supporting Information), which dried during the time-resolved emission measurements.

2.4. Light-Driven HER

We first investigated light-driven HER using a combination of $PDha_{PEG2}/[Ru(bpy)_3]^{2+}$ hydrogels and $[Mo_3S_{13}]^{2-}$ as the catalyst. In a typical experiment, $[Mo_3S_{13}]^{2-}$ and a sacrificial e^- donor (see below) were added to $PDha_{PEG2}/[Ru(bpy)_3]^{2+}$ in solution, followed by irradiation using a customized photoreactor with blue LED light (453 nm, see experimental part for light intensity and the details about the photoreactor) and H_2 production was observed as quantified by gas chromatography. Given that $PDha_{PEG2}/[Ru(bpy)_3]^{2+}$ contains some cationic charges ($-NH_3^+$) along the PDha backbone, and considering the presence of $[Ru(bpy)_3]^{2+}$ complexes, our hypothesis suggests that the incorporation of negatively charged $[Mo_3S_{13}]^{2-}$ into the hydrogel is feasible, facilitating charge transfer. This has previously been reported for related soft matter systems.[58] We initially selected ascorbic acid (AA), triethanolamine (TEOA), and triethylamine (TEA) as sacrificial e^- donor to check their effect on the electrostatic attachment stability of $[Ru(bpy)_3]^{2+}$. We observed that the use of AA solution adjusted to pH 5.5 led to some leaching of $[Ru(bpy)_3]^{2+}$. Presumably, AA can act as a competing partner for the $[Ru(bpy)_3]^{2+}$ complexes and, therefore, we mainly used TEA as a sacrificial e^- donor. HER experiments were carried out in an H_2O/MeOH mixture due to the rather poor water solubility of TEA. Also, it has been reported that the presence of MeOH increases the stability and the HER performance of $[Mo_3S_{13}]^{2-}$ in aqueous solutions.[72]

Since $[Mo_3S_{13}]^{2-}$ is prone to aggregation in water,[19] we examined the effect of catalyst loading conditions on the resulting HER activity by varying the amount of MeOH as co-solvent or using either swollen or freeze-dried gels. Table S5, Supporting Information, shows H_2 amounts evolved within PDha-based hydrogels and by benchmarks containing the same amounts of catalyst and dye (0.267 $[Mo_3S_{13}]^{2-}$ and 20 µM $[Ru(bpy)_3]^{2+}$) in solution without hydrogel. We observed relatively low H_2 production within hydrogels compared to the benchmark solutions, decreasing from 0.79 to 0.57 µmol, which probably arises from the limited release of H_2 bubbles from the hydrogel. We also noted higher hydrogen evolution values of samples prepared within swollen hydrogels if

 © 2024 The Authors. Macromolecular Rapid Communications published by Wiley-VCH GmbH

15213927, 2024, 5, Downloaded from https://onlinelibrary.wiley.com/doi/10.1002/marc.202300448 by Universitatsbibliothek Mainz, Wiley Online Library on [04/06/2025]. See the Terms and Conditions (https://onlinelibrary.wiley.com/terms-and-conditions) on Wiley Online Library for rules of use; OA articles are governed by the applicable Creative Commons License

ADVANCED SCIENCE NEWS
www.advancedsciencenews.com

Macromolecular Rapid Communications
www.mrc-journal.de

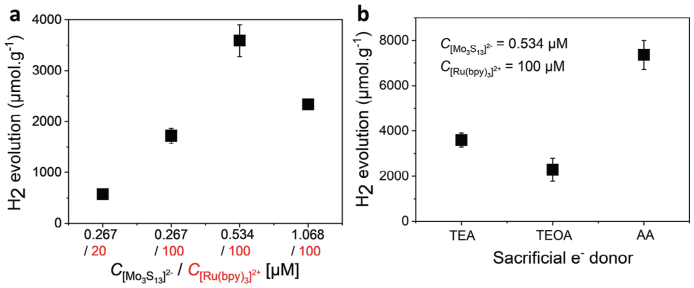


Figure 3. Amounts of evolved H_2 per gram dry gel; a) the effect of catalyst and dye concentrations, and b) the effect of sacrificial e^- donors ([TEA]: 0.9 M, [TEOA]: 0.9 M, [AA]: 0.1 M) on H_2 evolution performance.

compared to freeze-dried gels. Lowering the MeOH ratio from 70% to 50% in $PDha_{PEG2}$ hydrogels resulted in an increase in H_2 production which we believe mainly stems from increased swelling of the hydrogels. However, when less MeOH was used (30%), H_2 production decreased due to the solubility of TEA, and the catalyst degraded if only water was used as a solvent for catalyst loading. We also noted a decrease in H_2 production by adding MeOH a short time after catalyst loading in water. From these findings, we conclude that the swelling degree in H_2O/MeOH mixtures may not be the only dominating factor for photocatalytic HER but also the presence of MeOH increasing the solubility of TEA and the stability of the catalyst. This implies that 50% MeOH was reasonable, as well as using the swollen $PDha_{PEG2}$ hydrogels. Therefore, both conditions were chosen in the following HER studies.

To get better insight into the diffusion limitations, catalyst and dye amounts were varied in 50% MeOH aqueous solution containing 0.9 M TEA. **Figure** 3a shows evolved H_2 amounts normalized by gel amount and the effects of concentration of dye and catalyst on light-driven HER performance. The initial H_2 production amount was 570 µmol g^{-1} under the aforementioned conditions. We observed that it increased to 1720 µmol g^{-1} in case the fivefold amount of $[Ru(bpy)_3]^{2+}$ (100 µM) was used by keeping the $[Mo_3S_{13}]^{2-}$ amount constant as 0.267 µM, increasing turnover numbers (TON-Mo) from 951 to 2852. It should be noted that such TON values were calculated based on the overall catalyst amount by the assumption that all catalysts participated in HER. Afterward, we started increasing $[Mo_3S_{13}]^{2-}$ from 0.267 to 1.068 µM keeping $Ru(bpy)_3]^{2+}$ constant at 100 µM, resulting in an increase in H_2 production at 0.534 µM reaching 3590 µmol g^{-1} which is equivalent to a TON of 2983. Interestingly, a further increase of $[Mo_3S_{13}]^{2-}$ to 1.086 µM led to a decline in H_2 production to 2340 µmol g^{-1}, corresponding to a TON of 1037. While the increasing trend in the amount of evolved H_2 with increasing $[Mo_3S_{13}]^{2-}$ concentration is to a large extent in solution-based systems,[73] the results indicate that H_2 production within $PDha_{PEG2}$ hydrogels is not only limited by catalyst concentration but also the diffusion of catalyst into the hydrogel in our case, which was probably caused by the accumulation of $[Mo_3S_{13}]^{2-}$ on the hydrogel surface at such high concentration. Using 0.534 µM $[Mo_3S_{13}]^{2-}$ and 100 µM $[Ru(bpy)_3]^{2+}$, we repeated HER with 0.9 M TEOA and 0.1 M AA as the sacrificial e^- donor. While a lower amount of H_2 was evolved with TEOA giving 2280 µmol g^{-1} if compared to TEA, we found that H_2 production dramatically increased with AA reaching 7360 µmol g^{-1} although dye molecules were leached out to a certain extent (Figure 3b). However, we suppose this problem could be solved using covalently attached photosensitizers while retaining close proximity to the catalyst for sustained HER in further studies, but this is beyond the scope of this work.

2.5. Light-Driven OER

Besides HER, the polyampholytic $PDha_{PEG2}$/$[Ru(bpy)_3]^{2+}$ platform can also be employed for heterogeneous light-driven OER using the well-known $[Co_4(H_2O)_2(PW_9O_{34})_2]^{10-}$ (Co_4POM)[69] polyoxometalate as catalyst. Hereby, we aimed at loading Co_4POM via attractive electrostatic interactions and investigated subsequent light-driven OER. We performed OER using 5 mM $Na_2S_2O_8$ as a sacrificial e^- acceptor under visible light in 80 mM sodium borate buffer at an initial pH of 8. If mixed directly in aqueous media, Co_4POM and $[Ru(bpy)_3]^{2+}$ form electrostatic complexes and precipitate, which is observable with red shift of the main peak in the UV spectrum (Figure S15, Supporting Information).[71] Therefore, in experiments, Co_4POM and $[Ru(bpy)_3]^{2+}$ were loaded into swollen $PDha_{PEG2}$ in DI water to avoid ion-pairing before their diffusion into the hydrogel. After adding $Na_2S_2O_8$ and buffer solution, we started to illuminate the sample and record O_2 production rates using a contactless O_2 detector. Note that some evolved O_2 molecules could be trapped within the hydrogel so they are not included in our calculation. We observed colorless supernatant solutions after dye loading, implying that the majority of molecular units were integrated into $PDha_{PEG2}$ hydrogels. Since we used catalytic amounts of Co_4POM, only qualitative detection of Co_4POM was performed by SEM-EDX from the cross-section of the gel (**Figure** 4a) so we assumed all catalysts were also placed inside hydrogel and involved in light-driven OER.

We initially performed light-driven OER within $PDha_{PEG2}$ hydrogel (corresponding to 10 mg dry gel) with 5 µM Co_4POM and 100 µM $[Ru(bpy)_3]^{2+}$, and we noted that the rate of O_2 generation

 © 2024 The Authors. Macromolecular Rapid Communications published by Wiley-VCH GmbH

15213927, 2024, 5, Downloaded from https://onlinelibrary.wiley.com/doi/10.1002/marc.202300448 by Universitätsbibliothek Mainz, Wiley Online Library on [04/06/2025]. See the Terms and Conditions (https://onlinelibrary.wiley.com/terms-and-conditions) on Wiley Online Library for rules of use; OA articles are governed by the applicable Creative Commons License

ADVANCED SCIENCE NEWS
www.advancedsciencenews.com

Macromolecular Rapid Communications
www.mrc-journal.de

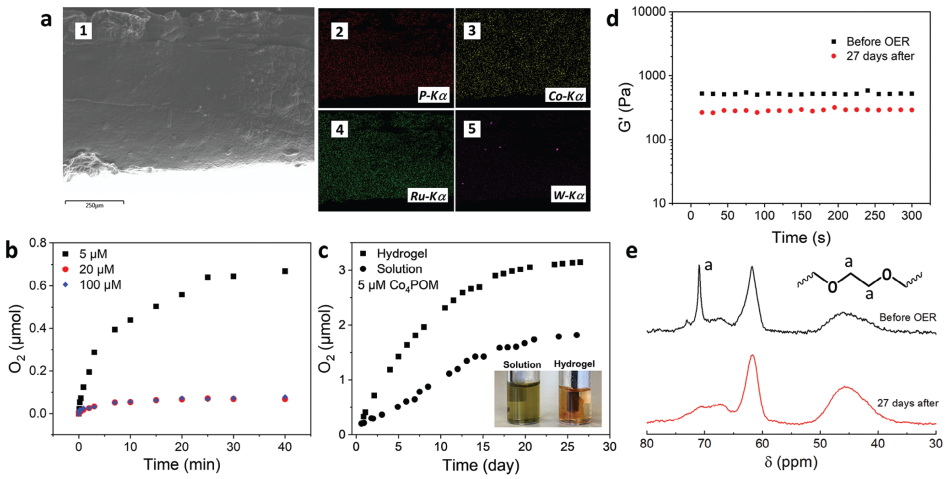


Figure 4. a) 1) Scanning electron microscopy (SEM) in cross-section of dry gel after loaded by $[Ru(bpy)_3]^{2+}$ and Co_4POM, 2–5) energy dispersive X-ray spectroscopy (EDX) elemental mapping (P, Co, Ru, and W), b,c) the amounts of evolved O_2; b) the effect of catalyst concentration on O_2 evolution within hydrogel in 40 min, c) the comparison between OER in hydrogel and OER in solution for long-term O_2 evolution, and (inset c) the pictures of corresponding samples after OER (5 mM NaS_2O_8, 80 mM sodium borate buffer), d) dynamic oscillatory time sweep measuring storage modulus (G') of the hydrogel after OER (measured applying 6.28 rad s^{-1} angular frequency in the linear viscoelastic region (LVR)), and e) ^{13}C CP-MAS NMR spectra of the dry gel before and after OER.

gradually increased and reached a plateau after 40 min, where around 0.7 μmol O_2 was produced which corresponds to a TON of 70 based on the catalyst loading (Figure 4b). 80 mM of sodium borate buffer was able to maintain the pH with a decrease of only 0.06 pH by the end of the reaction. To compare with the O_2 production within $PDha_{PEG2}$ hydrogels, control experiments in solution were carried out using 5 μM Co_4POM and different concentrations of $[Ru(bpy)_3]^{2+}$. We observed a large variance in light-driven O_2 production, which were 0.48 μmol for 1 mM $[Ru(bpy)_3]^{2+}$ and 0.1 μmol for 100 μM $[Ru(bpy)_3]^{2+}$ within 30 min, from earlier reported values that were around 2.5 μmol within 15 min.[69] We believe that this might have been caused by experimental differences such as light intensity, sample preparation, or quantification. The results indicate that charge transfer within the $PDha_{PEG2}$ hydrogel resulted in a more efficient O_2 production despite the lower dye concentration used and some trapping of formed O_2. In this study, we were inspired by the earlier report regarding the oxygen evolution performance of the $Co_4POM/[Ru(bpy)_3]^{2+}$ system in solution to decide the concentration of the catalyst for our first trials.[69] Since the increased Co_4POM concentration is leading to enhanced catalytic performance,[69] we also tend to increase the catalyst concentration for our hydrogel-based system. Figure 4b shows the effect of Co_4POM concentration on O_2 production at 100 μM $[Ru(bpy)_3]^{2+}$. When we used an excess amount of catalyst, such as 20 and 100 μM, we observed that the resulting O_2 amount significantly decreased to 0.07 and 0.08 μmol, respectively. During dye loading, we recognized that for $PDha_{PEG2}$ hydrogels featuring an excess of Co_4POM lower amounts of $[Ru(bpy)_3]^{2+}$ could be immobilized without precipitation being observed. On the other hand, when we prepared stoichiometric solutions of Co_4POM and $[Ru(bpy)_3]^{2+}$, direct precipitation occurred. These results show that diffusion of Co_4POM into hydrogels might not be the limiting factor for light-driven OER, however, an increasing concentration of Co_4POM can limit $[Ru(bpy)_3]^{2+}$ integration into hydrogels resulting in lower O_2 production.

It is well-known that $[Ru(bpy)_3]^{2+}$ photosensitizers can decompose over time (typically by loss of bpy ligands), when irradiated with visible light, leading to a loss of catalytic performance.[77,78] Under photocatalytic OER conditions with $Na_2S_2O_8$ as an electron acceptor, very fast and efficient degradation of the PS by the attack of reactive sulfate species has recently been proposed as a key deactivation pathway.[79] To see the effect of $PDha_{PEG2}$ hydrogel on the decomposition of photosensitizer and O_2 production during a longer period, we kept tracking the evolved O_2 amount of the sample having 5 μM Co_4POM and 100 μM $[Ru(bpy)_3]^{2+}$ for 27 days. Figure 4b shows the difference in the O_2 production rate of a comparative sample in solution and within a hydrogel. We observed that the O_2 production gradually increased and reached a plateau for both samples, where we detected 3.2 μmol O_2 (TON of 320) within $PDha_{PEG2}$ hydrogel, and 1.9 μmol O_2 (TON of 190) in solution. These values made around 63% and 38% of chemical yields for hydrogel and solution, respectively, based on the theoretical maximum chemical yield calculated by the amount of added $Na_2S_2O_8$. After one day of irradiation, we noted a color change in both samples to dark orange indicating the

 © 2024 The Authors. Macromolecular Rapid Communications published by Wiley-VCH GmbH

15213927, 2024, 5, Downloaded from https://onlinelibrary.wiley.com/doi/10.1002/marc.202300448 by Universitatsbibliothek Mainz, Wiley Online Library on [04/06/2025]. See the Terms and Conditions (https://onlinelibrary.wiley.com/terms-and-conditions) on Wiley Online Library for rules of use; OA articles are governed by the applicable Creative Commons License

ADVANCED SCIENCE NEWS
www.advancedsciencenews.com

Macro-olecular Rapid Communications
www.mrc-journal.de

15213927, 2024, 5, Downloaded from https://onlinelibrary.wiley.com/doi/10.1002/marc.202300448 by Universitätsbibliothek Mainz, Wiley Online Library on [04/06/2025]. See the Terms and Conditions (https://onlinelibrary.wiley.com/terms-and-conditions) on Wiley Online Library for rules of use; OA articles are governed by the applicable Creative Commons License

decomposition of $[Ru(bpy)_3]^{2+}$. Interestingly, during the following days (up to day 27) the color of the hydrogel remained dark orange, while the color of the solution turned green (Figure 4b inset). To gain information regarding this issue, both solutions were characterized by UV–vis spectrophotometry, and the results were compared to the spectra of the solution and the hydrogel taken before OER. The results show that the characteristic MLCT absorption bands of $[Ru(bpy)_3]^{2+}$ disappeared upon irradiation of the samples during OER (Figure S16, Supporting Information). Post-catalytic analyses show that after OER, two new absorption bands appear at 467 and 663 nm for the homogeneous solution sample, while only one new absorption band appears at 467 nm for the hydrogel sample. In photocatalytic water oxidation employing light-$[Ru(bpy)_3]^{2+}$-catalyst and $S_2O_8^{2-}$ as sacrificial e^- acceptor, different mechanisms of deactivation are discussed, depending on the utilized catalyst.[78] Furthermore, Yoon et al. proposed decomposition pathways of $[Ru(bpy)_3]^{2+}$ during photocatalytic water oxidation with $S_2O_8^{2-}$ as a sacrificial e^- acceptor.[77] They isolated orange and blue dimers and trimers as decomposition products of $[Ru(bpy)_3]^{2+}$ and showed their absorption bands and catalytic activities for OER. They also claimed that decomposition products containing Ru_n $n \geq 3$ are catalytically inactive for OER. Based on this assessment, we propose that the decomposition products within the $PDha_{PEG2}$ hydrogel are mainly $[Ru_2]$ dimers. We speculate that the formation of these dimers is due to limited diffusion of the degradation products within the hydrogel and could be the reason for the higher O_2 evolution observed. In sum, the findings suggest that the reported hydrogel is an attractive matrix for light-driven OER, and further could have a stabilizing effect on O_2 evolution by influencing possible decomposition pathways of $[Ru(bpy)_3]^{2+}$. Operando spectroscopic studies will be performed in the future to assess the exact mechanism of photosensitizer degradation within the hydrogel.

On the other hand, since Co_4POM-based catalysts might also oxidize organic molecules other than photosensitizers in OER media, the stability of the herein-used hydrogels was also of interest in our work. We examined the swelling degree and mechanics of the hydrogel by rheological analysis after long-term OER. We performed oscillatory time sweep analysis of the hydrogel ($PDha_{PEG2}$/$[Ru(bpy)_3]^{2+}$/Co_4POM with sacrificial e^- acceptor and buffer solution) before and after OER for 5 min in the predetermined linear viscoelastic region (LVR). We observed that the storage modulus (G') of the hydrogel decreased by 45% after 27 days under irradiation (Figure 4d), and in parallel, we noted an increase in swelling degree by around 20%. These results indicate that the crosslink density decreased during light-driven OER. In addition, we did some structural analyses using ^{13}C CP-MAS NMR, showing that the rather sharp PEG signal at around 70 ppm partially disappeared, which we believe implies oxidative degradation during OER (Figure 4e). The results show that soft matter integration of catalyst and dye for light-driven OER might face a trade-off between mechanical integrity and (long-term) catalytic performance. Future studies for sustainable systems might involve the use of alternative crosslinkers which tend to be more stable in OER media while retaining mechanical, optical, and chemical properties, and the use of a gas flowing through the hydrogel to further facilitate the mass transfer.

3. Conclusion

We developed a novel pH-responsive and polyampholytic soft matter matrix based on crosslinked poly(dehydroalanine) hydrogels and demonstrated that these materials can be used as scaffolds for both light-driven HER and OER. Electrostatic adsorption allowed for reversible immobilization of the respective photosensitizer and catalyst, and by that providing close spatial proximity for subsequent light-driven processes. It could further be shown that photosensitizer ($[Ru(bpy)_3]^{2+}$) attachment was reversible upon changes in pH value, and therefore this system is also attractive concerning catalyst/photosensitizer repair approaches. The herein documented proof-of-principle studies showed that the resulting hybrid materials are an interesting platform for light-driven catalysis, presenting a range of set screws to influence reactivity and selectivity (e.g., by varying the degree of swelling), and in the case of OER even leading to prolonged catalytic activity and changes in photosensitizer decomposition, although the latter process is far from being completely understood at this point. In addition, especially, the OER conditions also seem to influence hydrogel structure and integrity upon prolonged exposure. Nevertheless, this work in our opinion opens up an avenue toward tailor-made responsive soft matter matrices for light-driven catalysis, enabling superior control over the positioning of different building blocks and allowing electrostatically mediated exchange and repair approaches.

4. Experimental Section

Materials: All reagents were used as received unless otherwise stated. *t*BAMA was synthesized according to an earlier report.[57] Methanesulfonyl chloride (≥99.7%), PEGDGE (1000, 2000, and 6000 g mol^{-1}), tris(2,2′-bipyridyl)dichlororuthenium(II) hexahydrate, TEA (≥99.5%), TEOA (≥99%), and L-ascorbic acid (≥99%) were purchased from Sigma-Aldrich Chemie GmbH. TFA (≥99.9%) was purchased from Roth and sodium peroxodisulfate (≥98%) was purchased from Acros Organics. BlocBuilder and SG-1 were synthesized following a procedure reported in the literature.[52,53,80,81] Catalysts were synthesized and characterized as reported previously (see details in the Supporting Information).[72,82] Methanol used for HER was redistilled with a rotary evaporator before catalysis.

Characterization: ^1H NMR was performed in $CDCl_3$ and D_2O/NaOD using Bruker AC 300 MHz-spectrometer with Fourier/Avance I console at 298 °K. The spectra were referenced to the residual deuterated solvent signal. ^{13}C solid-state magic angle spinning (ssMAS) NMR spectra using cross-polarization (CP) with 2 ms contact time and 14 kHz spinning frequency were obtained from Bruker 400 MHz-Avance III HP-spectrometer at 25 °C with a 4 mm probe head. Size exclusion chromatography (SEC) traces in THF were measured using an Agilent 1260 Infinity system equipped with a 1260 IsoPump (G1310B), a 1260 ALS (G1310B) autosampler, and three consecutive PSS SDV, 5 µm, 8●300 mm, columns. The eluent flow rate was set to 1 mL min^{-1} and the column oven was set to 40 °C. Signals were detected using a 1260 DAD VL (G1329B) and a 1260 RID (G1315D) detector. The system was calibrated using PMMA (Mp: 2.2M-800 Da) standards. Elemental analysis was performed on a Vario El III (Elementar) elemental analyzer. Infrared spectra were measured on a Perkin Elmer Frontier FT-IR/NIR spectrometer equipped with a Golden Gate ATR unit from Sepcac. The spectra were recorded using 40 scans at a resolution of 4 wavenumbers between 4000 and 400 cm^{-1}. UV–vis spectra in solution were recorded on an Agilent Cary 60 in a Hellma quartz glass cuvette with a path length of 10 mm at room temperature. The absorbance was measured in a range from 200 to 800 nm in 5 nm steps.

 © 2024 The Authors. Macromolecular Rapid Communications published by Wiley-VCH GmbH

ADVANCED SCIENCE NEWS
www.advancedsciencenews.com

Macromolecular Rapid Communications
www.mrc-journal.de

Emission analysis was carried out in solution using a laser source operating at 458 nm on a Jasco FP-8300 fluorescence spectrometer with both emission and excitation slits of 5 nm. Gel samples with adsorbed dye were placed in a corresponding cuvette for recording absorbance and emission spectra. SEM images were acquired on a Zeiss Sigma VP at an acceleration voltage of 14 kV with an SE2 detector. EDX investigations were performed on an Oxford AztecEnergy Standard system with SDD detector X-MaxN50 and an energy resolution of < 127 eV at Mn$K\alpha$.

Hydrogel Synthesis: PDha$_{PEGX}$ (X = 1, 2, 6): Hydrogels were prepared by chemical crosslinking of polydehydroalanine (PDha); 50 mg PDha was first dissolved in 1.5 mL of 0.1 M KOH overnight at 60 °C under stirring. 400 mg of poly(ethylene glycol) glycidyl ether with M_n of 1000, 2000, and 6000 g mol^{-1} were used as crosslinkers for PDha$_{PEGX}$, where X indicates M_n of PEGDGE. The crosslinkers were added to the polymer solution and stirred at 60 °C until gelation was observed. The obtained hydrogels were soaked in 20 mL of deionized water for 48 h with at least two water changes to remove impurities or unreacted polymers and crosslinkers. Hydrogels were freeze-dried before FTIR, solid-state NMR, and elemental analyses.

Calculation of the PDha Ratio in Hydrogel: The elemental contents for different PDha ratios and each crosslinker were calculated by theoretical chemical analysis. Experimentally obtained [C]/[N] ratios were compared with theoretical values to estimate the PDha fraction in the hydrogels.

Rheological Measurements: Hydrogel samples were measured using a modular compact rheometer (Anton Paar mcr 302e) with parallel plate geometry (plate diameter: 15 mm). Disks of swollen hydrogels were prepared with 15 mm and a thickness of 1 mm. Oscillatory measurements were performed at 25 °C. Strain sweep analysis was performed in the range of 0.01–100% of strain at 6.25 rad s^{-1} of the angular frequency to determine the LVR. Time sweep analysis was carried out using 6.25 rad s^{-1} angular frequency for 5 min in LVR.

Swelling Studies: Swelling degrees were calculated by measuring the weights of swollen hydrogels equilibrated in water and the corresponding dried gel on a pre-weighed watch glass. Gels were dried overnight on a hot Teflon plate at 90 °C in air. Surface water or solution on fully swollen gel was excluded by using a soft tissue before weighing. Swelling at pH ranging from 2.2 to 11 was studied using buffer solutions with close ionic strength. Four different buffer systems were used: citrate at pH 2.2-5, phosphate at pH 6–8, borate at pH 9–10, and carbonate at pH 11. For swelling at different salt concentrations, NaCl solutions were prepared. Triplicate measurements were performed to take into account the errors in measurements. The swelling degree of hydrogels was calculated according to Equation (1)

$$\text{Swelling degree} = \frac{m_s}{m_d} \quad (1)$$

where m_s is the mass of the swollen gel, and m_d is the mass of the dry gel.

Reversible Adsorption of [Ru(bpy)$_3$]$^{2+}$: Hydrogels (≈1.7 mg in the dry state) were placed in a 2.5 mL aqueous [Ru(bpy)$_3$]Cl$_2$ solution (0.07 to 0.6 mM) at pH ranging from 7 to 13 adjusted with 0.5 M aqueous KOH solution at 25 °C. The adsorption isotherms and diffusion kinetics at pH 7 were studied. Dye concentration in the supernatant was monitored at regular time intervals by UV–vis spectroscopy, where [Ru(bpy)$_3$]$^{2+}$ has a strong absorbance at 454 nm. For desorption studies, hydrogels that reached equilibrium dye adsorption at pH 7 were quickly washed in 2 mL DI water, and then placed in water at pH 2 (pH adjusted using 1 M aqueous HCl). After 120 min, the hydrogel was removed and placed in fresh water at pH 2 for 120 min. The absorbance spectrum of the solution was taken in regular time intervals. Adsorbed and leached dye amounts were calculated using the extinction coefficient of [Ru(bpy)$_3$]$^{2+}$ at 454 nm, that is, 14 600 M^{-1} cm^{-1}.

Emission Quenching: Quenching of the emission of [Ru(bpy)$_3$]$^{2+}$ in the hydrogels at varying concentrations of the quenchers (Co_4POM and [Mo_3S_{13}]$^{2-}$) was studied through nanosecond time-resolved emission. The sample was excited at 500 nm using an Nd:YAG-pumped optical parametric oscillator (Continuum Surelite). The emission kinetics were recorded in 10 nm increments between 520 and 800 nm.

Light-Driven HER: Swollen hydrogels (10 mg in the dry state) in quasi-cylindrical shape were placed in aqueous [Ru(bpy)$_3$]Cl$_2$ solution at pH 7 overnight in a 5 mL glass vial. After dye adsorption, the supernatant was removed, and H_2O and MeOH were added up to 2 mL total volume. $Na_2[Mo_3S_{13}]\bullet 5H_2O$ dissolved in DMF was added to the reaction vials followed by heating at 50 °C for 15 min to increase diffusion. Finally, AA, TEOA, or TEA as sacrificial e^- donor was added and the solution was purged with argon. Vials were sealed with a septum cap and irradiated with a blue LED light (λ_{max} = 453 nm, with a power of 5 W, 6–8 vials, from 5 cm distance) in a custom-built, air-cooled photoreactor[83] on a platform shaker. Hydrogen production (H_2 accumulated in headspace) was quantified by Agilent A7820A gas chromatograph with molecular sieve A5 column. Detection was afforded by a thermal conductivity detector with nitrogen carrier gas. Catalyst stock solution was freshly prepared each day of analysis. The pH value of the solution was not adjusted when TEA or TEOA were used, however, adjusted to pH 5.5 using aqueous ammonium hydroxide solution for AA solutions.

Light-Driven OER: Quasi-cylindrical swollen hydrogels (10 mg in the dry state) were placed in an aqueous $Na_{10}[Co_4(H_2O)_2(PW_9O_{34})_2]$ solution at a concentration of 40 µM at pH 7 in a custom-built contactless O_2 sensor vial (Pyroscience OXVIAL4) overnight. Then, aqueous [Ru(bpy)$_3$]Cl$_2$ solution was added to the vial, followed by 4 h for dye adsorption. Finally, aqueous $Na_2S_2O_8$ (5 µM) and sodium borate buffer (80 mM, initial pH 8) solutions were added making 2 mL total volume. All vials were prepared in a glovebox under argon, sealed with a septum cap, and directly subjected to O_2 measurements by a fluorescence sensor (Pyroscience FireSting). After 5 min, vials were irradiated with a blue LED light (λ_{max} = 453 nm, to the power of 5 W, single vial, from 1 cm distance) in the photoreactor as described in the HER section above. O_2 amounts were recorded for solution and head-space and the O_2 evolution amounts reported in the paper are the sum of O_2 amounts in the headspace and solution.

Supporting Information

Supporting Information is available from the Wiley Online Library or from the author.

Acknowledgements

T.C. thanks the Deutscher Akademischer Austausch Dienst (DAAD) for the doctoral research fellowship. The German Research Council (DFG) is gratefully acknowledged for financial support (TRR234 "CataLight," project ID: 364549901, projects A04, B03, B11, and Z02). The authors thank Dr. Martin Schulz for assistance, M.Sc. Marcel Langer for the quantification of O_2, and M.Sc. Frieda Nagler for initial experiments regarding PDha-based hydrogels. The authors acknowledge Prof. Dr. Dirk Ziegenbalg and M.Sc. Daniel Kowalczyk for the photoreactor design and establishment. The authors also acknowledge Peggy Laudeley, Katja König, and Dr. Grit Festag for SEC analysis, and the NMR department at Friedrich-Schiller-University Jena for their continuous support. For providing the rheometer facilities, the authors acknowledge the DFG (The Cluster of Excellence "Balance of the Microverse," EXC2051). The authors thank MSc. Kathrin Kowalczuk for assistance during rheological measurements and Yves Carstensen for SEM analysis. The SEM facilities of the Jena Center for Soft Matter (JCSM) were established with a grant from the DFG.

Open access funding enabled and organized by Projekt DEAL.

Conflict of Interest

The authors declare no conflict of interest.

Author Contributions

T.C. and M.L. contributed equally. Conceptualization was done by T.Ç. and F.H.S. Hydrogel synthesis and characterization were done by T.Ç.

 © 2024 The Authors. Macromolecular Rapid Communications published by Wiley-VCH GmbH

15213927, 2024, 5, Downloaded from https://onlinelibrary.wiley.com/doi/10.1002/marc.202300448 by Universitatsbibliothek Mainz, Wiley Online Library on [04/06/2025]. See the Terms and Conditions (https://onlinelibrary.wiley.com/terms-and-conditions) on Wiley Online Library for rules of use; OA articles are governed by the applicable Creative Commons License

ADVANCED SCIENCE NEWS
www.advancedsciencenews.com

Macromolecular Rapid Communications
www.mrc-journal.de

Synthesis of Co_4POM was performed by M.L. Nanosecond time-resolved emission spectra was taken by N.V. FT-IR, UV–vis, and fluorescence spectroscopic analyses, as well as rheological characterization, were performed by T.Ç. The manuscript was drafted by T.Ç., reviewed and edited by T.Ç., M.L., C.S., S.R. and F.H.S. Supervision by F.H.S.

Data Availability Statement

The data that support the findings of this study are available from the corresponding author upon reasonable request.

Keywords

artificial photosynthesis, energy-conversion, hydrogen evolution reaction, oxygen evolution reaction, polyampholyte hydrogel scaffold, visible light-driven catalysis

Received: July 26, 2023
Revised: November 27, 2023
Published online: January 28, 2024

[1] T. A. Faunce, W. Lubitz, A. W. Rutherford, D. MacFarlane, G. F. Moore, P. Yang, D. G. Nocera, T. A. Moore, D. H. Gregory, S. Fukuzumi, K. B. Yoon, F. A. Armstrong, M. R. Wasielewski, S. Styring, *Energy Environ. Sci.* **2013**, *6*, 695.
[2] I. Dincer, C. Acar, *Int. J. Energy Res.* **2015**, *39*, 585.
[3] K. Srirangan, L. Akawi, M. Moo-Young, C. P. Chou, *Appl. Energy* **2012**, *100*, 172.
[4] J. Barber, *Chem. Soc. Rev.* **2009**, *38*, 185.
[5] X. X. Zou, Y. Zhang, *Chem. Soc. Rev.* **2015**, *44*, 5148.
[6] K. Meyer, M. Ranocchiari, J. A. van Bokhoven, *Energy Environ. Sci.* **2015**, *8*, 1923.
[7] R. Hill, F. A. Y. Bendall, *Nature* **1960**, *186*, 136.
[8] K. Kobayashi, *J. Plant Res.* **2016**, *129*, 565.
[9] J. P. Dekker, E. J. Boekema, *Biochim. Biophys. Acta, Bioenerg.* **2005**, *1706*, 12.
[10] M. G. Pfeffer, C. Müller, E. T. E. Kastl, A. K. Mengele, B. Bagemihl, S. S. Fauth, J. Habermehl, L. Petermann, M. Wächtler, M. Schulz, D. Chartrand, F. Laverdière, P. Seeber, S. Kupfer, S. Gräfe, G. S. Hanan, J. G. Vos, B. Dietzek-Ivanšić, S. Rau, *Nat. Chem.* **2022**, *14*, 500.
[11] A. K. Mengele, S. Rau, *JACS Au* **2023**, *3*, 36.
[12] E. M. Aro, I. Virgin, B. Andersson, *Bioch. Biophys. Acta* **1993**, *1143*, 113.
[13] J. Byun, K. Landfester, K. A. I. Zhang, *Chem. Mater.* **2019**, *31*, 3381.
[14] Goudappagouda, V. C. Wakchaure, K. C. Ranjeesh, S. S. Babu, *Aust. J. Chem.* **2016**, *69*, 2.
[15] D. Jeon, J. Park, C. Shin, H. Kim, J. W. Jang, D. W. Lee, J. Ryu, *Sci. Adv.* **2020**, *6*, eaaz3944.
[16] K. Okeyoshi, R. Yoshida, *Angew. Chem., Int. Ed.* **2019**, *58*, 7304.
[17] N. Plumere, O. Rudiger, A. A. Oughli, R. Williams, J. Vivekananthan, S. Poller, W. Schuhmann, W. Lubitz, *Nat. Chem.* **2014**, *6*, 822.
[18] I. Romanenko, A. Rajagopal, C. Neumann, A. Turchanin, C. Streb, F. H. Schacher, *J. Mater. Chem. A* **2020**, *8*, 6238.
[19] H. Sai, A. Erbas, A. Dannenhoffer, D. X. Huang, A. Weingarten, E. Siismets, K. Jang, K. R. Qu, L. C. Palmer, M. O. de la Cruz, S. I. Stupp, *J. Mater. Chem. A* **2020**, *8*, 158.
[20] S. Sebata, S. Y. Takizawa, N. Ikuta, S. Murata, *Dalton Trans.* **2019**, *48*, 14914.
[21] F. Wang, M. Wen, K. Feng, W. J. Liang, X. B. Li, B. Chen, C. H. Tung, L. Z. Wu, *Chem. Commun.* **2016**, *52*, 457.
[22] P. Pachfule, S. Kandambeth, D. Díaz Díaz, R. Banerjee, *Chem. Commun.* **2014**, *50*, 3169.
[23] D. Yang, H. Tenhu, S. Hietala, *Eur. Polym. J.* **2020**, *133*, 109760.
[24] A. S. Weingarten, R. V. Kazantsev, L. C. Palmer, M. McClendon, A. R. Koltonow, A. P. S. Samuel, D. J. Kiebala, M. R. Wasielewski, S. I. Stupp, *Nat. Chem.* **2014**, *6*, 964.
[25] K. Okeyoshi, D. Suzuki, A. Kishimura, R. Yoshida, *Small* **2011**, *7*, 311.
[26] K. Okeyoshi, R. Yoshida, *Chem. Commun.* **2009**, *47*, 1527.
[27] K. Okeyoshi, R. Yoshida, *Soft Matter* **2009**, *5*, 4118.
[28] K. Okeyoshi, R. Yoshida, *Adv. Funct. Mater.* **2010**, *20*, 708.
[29] W. J. Jiang, Y. F. Zhu, G. X. Zhu, Z. J. Zhang, X. J. Chen, W. Q. Yao, *J. Mater. Chem. A* **2017**, *5*, 5661.
[30] S. L. Haag, M. T. Bernards, *Gels* **2017**, *3*, 41.
[31] S. E. Kudaibergenov, *Polym. Adv. Technol.* **2021**, *32*, 906.
[32] T. L. Sun, K. Cui, J. P. Gong, *Polym. Sci., Ser. C* **2017**, *59*, 11.
[33] K. M. Zurick, M. Bernards, *J. Appl. Polym. Sci.* **2014**, *131*, 40069.
[34] S. E. Kudaibergenov, N. Nuraje, V. V. Khutoryanskiy, *Soft Matter* **2012**, *8*, 9302.
[35] G. S. Georgiev, E. B. Kamenska, E. D. Vassileva, I. P. Kamenova, V. T. Georgieva, S. B. Iliev, I. A. Ivanov, *Biomacromolecules* **2006**, *7*, 1329.
[36] K. Ruseva, P. Nedkov, R. Alexandrova, D. Dinev, P. Shestakova, P. Hristov, E. Vassileva, *Polym. Int.* **2019**, *68*, 1626.
[37] D. Zhang, B. P. Ren, Y. X. Zhang, Y. L. Liu, H. Chen, S. W. Xiao, Y. Chang, J. T. Yang, J. Zheng, *J. Colloid Interface Sci.* **2020**, *578*, 242.
[38] J. J. Shen, M. Du, Z. L. Wu, Y. H. Song, Q. Zheng, *RSC Adv.* **2019**, *9*, 2081.
[39] M. Pakizeh, P. May, M. Matthias, M. Ulbricht, *J. Appl. Polym. Sci.* **2020**, *137*, 49595.
[40] H. Idrees, I. M. A. ElSherbiny, M. Hecket, Q. R. Ke, C. Staaks, A. S. G. Khalil, M. Ulbricht, S. Panglisch, *Chem. Ing. Tech.* **2021**, *93*, 1408.
[41] L. W. Li, L. S. Zhang, W. B. Guo, C. Y. Chang, J. Wang, Z. F. Cong, X. Pu, *J. Mater. Chem. A* **2021**, *9*, 24325.
[42] Q. J. Fu, S. W. Hao, L. Meng, F. Xu, J. Yang, *ACS Nano* **2021**, *15*, 18469.
[43] K. T. Leng, G. J. Li, J. J. Guo, X. Y. Zhang, A. X. Wang, X. J. Liu, J. Y. Luo, *Adv. Funct. Mater.* **2020**, *30*, 2001317.
[44] Y. M. Mohan, K. E. Geckeler, *React. Funct. Polym.* **2007**, *67*, 144.
[45] M. Gao, K. Gawel, B. T. Stokke, *Eur. Polym. J.* **2014**, *53*, 65.
[46] S. Kudaibergenov, W. Jaeger, A. Laschewsky, in *Supramolecular Polymers Polymeric Betains Oligormers*, Vol. *201*, Springer, Heidelberg, Berlin.
[47] J. B. Max, D. V. Pergushov, L. V. Sigolaeva, F. H. Schacher, *Polym. Chem.* **2019**, *10*, 3230.
[48] A. Laschewsky, *Polymers* **2014**, *6*, 1544.
[49] A. S. Hoffman, *Adv. Drug Delivery Rev.* **2012**, *64*, 18.
[50] J. Kalia, R. T. Raines, *Curr. Org. Chem.* **2010**, *14*, 138.
[51] B. Choi, X. J. Loh, A. Tan, C. K. Loh, E. Ye, M. K. Joo, B. Jeong, in *In-Situ Gelling Polymers*, Springer Science+Business Media, Springer, New York **2015**, pp. 5–35.
[52] U. Gunther, L. V. Sigolaeva, D. V. Pergushov, F. H. Schacher, *Macromol. Chem. Phys.* **2013**, *214*, 2202.
[53] J.-H. Kruse, P. Biehl, F. H. Schacher, *Macromol. Rapid Commun.* **2019**, *40*, 1800857.
[54] M. Billing, F. H. Schacher, *Macromolecules* **2016**, *49*, 3696.
[55] P. Biehl, M. von der Luhe, F. H. Schacher, *Macromol. Rapid Commun.* **2018**, *39*, 1800017.
[56] M. Billing, G. Festag, P. Bellstedt, F. H. Schacher, *Polym. Chem.* **2017**, *8*, 936.
[57] M. von der Luhe, A. Weidner, S. Dutz, F. H. Schacher, *ACS Appl. Nano Mater.* **2018**, *1*, 232.
[58] A. Nabiyan, J. B. Max, C. Neumann, M. Heiland, A. Turchanin, C. Streb, F. H. Schacher, *Chemistry* **2021**, *27*, 16924.
[59] V. S. Raghuwanshi, G. Garnier, *Adv. Colloid Interface Sci.* **2019**, *274*, 102044.
[60] M. Ghasemlou, F. Daver, E. P. Ivanova, J.-W. Rhim, B. Adhikari, *ACS Appl. Mater. Interfaces* **2019**, *11*, 22897.

 © 2024 The Authors. Macromolecular Rapid Communications published by Wiley-VCH GmbH

15213927, 2024, 5, Downloaded from https://onlinelibrary.wiley.com/doi/10.1002/marc.202300448 by Universitätsbibliothek Mainz, Wiley Online Library on [04/06/2025]. See the Terms and Conditions (https://onlinelibrary.wiley.com/terms-and-conditions) on Wiley Online Library for rules of use; OA articles are governed by the applicable Creative Commons License

[61] A. R. Garcia, R. B. de Barros, J. P. Lourenço, L. M. Ilharco, *J. Phys. Chem. A* **2008**, *112*, 8280.
[62] R. Lunkad, P. Biehl, A. Murmiliuk, P. M. Blanco, P. Mons, M. Štěpánek, F. H. Schacher, P. Košovan, *Macromolecules* **2022**, *55*, 7775.
[63] Y. Zhao, J. Kang, T. Tan, *Polymer* **2006**, *47*, 7702.
[64] Y. X. Zhang, F. P. Wu, M. Z. Li, E. J. Wang, *Polymer* **2005**, *46*, 7695.
[65] K.-T. Huang, K. Ishihara, C.-J. Huang, *Biomacromolecules* **2019**, *20*, 3524.
[66] K. Kalyanasundaram, *Coord. Chem. Rev.* **1982**, *46*, 159.
[67] A. Chettri, J.-H. Kruse, K. Kumar Jha, L. Dröge, I. Romanenko, C. Neumann, S. Kupfer, A. Turchanin, S. Rau, F. H. Schacher, B. Dietzek, *Chemistry* **2021**, *27*, 17049.
[68] P. Chen, T. J. Meyer, *Chem. Rev.* **1998**, *98*, 1439.
[69] Z. Q. Huang, Z. Luo, Y. V. Geletii, J. W. Vickers, Q. S. Yin, D. Wu, Y. Hou, Y. Ding, J. Song, D. G. Musaev, C. L. Hill, T. Q. Lian, *J. Am. Chem. Soc.* **2011**, *133*, 2068.
[70] J. W. Vickers, H. J. Lv, J. M. Sumliner, G. B. Zhu, Z. Luo, D. G. Musaev, Y. V. Geletii, C. L. Hill, *J. Am. Chem. Soc.* **2013**, *135*, 14110.
[71] J. J. Stracke, R. G. Finke, *ACS Catal.* **2014**, *4*, 79.
[72] M. Dave, A. Rajagopal, M. Damm-Ruttensperger, B. Schwarz, F. Nägele, L. Daccache, D. Fantauzzi, T. Jacob, C. Streb, *Sustainable Energy Fuels* **2018**, *2*, 1020.
[73] Y. Lei, M. Yang, J. Hou, F. Wang, E. Cui, C. Kong, S. Min, *Chem. Commun.* **2018**, *54*, 603.
[74] A. Rajagopal, F. Venter, T. Jacob, L. Petermann, S. Rau, S. Tschierlei, C. Streb, *Sustainable Energy Fuels* **2019**, *3*, 92.
[75] U. Alexiev, D. L. Farrens, *Biochim. Biophys. Acta* **2014**, *1837*, 694.
[76] A. Airinei, R. Tigoianu, E. Rusu, D. D. Ortansa, *Dig. J. Nanomater. Biostruct.* **2011**, *6*, 1265.
[77] U. S. Akhtar, E. L. Tae, Y. S. Chun, I. C. Hwang, K. B. Yoon, *ACS Catal.* **2016**, *6*, 8361.
[78] B. Limburg, E. Bouwman, S. Bonnet, *ACS Catal.* **2016**, *6*, 5273.
[79] M. Sender, F. L. Huber, M. C. G. Moersch, D. Kowalczyk, J. Hniopek, S. Klingler, M. Schmitt, S. Kaufhold, K. Siewerth, J. Popp, B. Mizaikoff, D. Ziegenbalg, S. Rau, *ChemSusChem* **2022**, *15*, 202200708.
[80] S. Grimaldi, J.-P. Finet, F. Le Moigne, A. Zeghdaoui, P. Tordo, D. Benoit, M. Fontanille, Y. Gnanou, *Macromolecules* **2000**, *33*, 1141.
[81] S. Harrisson, P. Couvreur, J. Nicolas, *Polym. Chem.* **2011**, *2*, 1859.
[82] R. Gong, D. Mitoraj, D. Gao, M. Mundszinger, D. Sorsche, U. Kaiser, C. Streb, R. Beranek, S. Rau, *Adv. Sustainable Syst.* **2022**, *6*, 2100473.
[83] D. Kowalczyk, P. Li, A. Abbas, J. Eichhorn, P. Buday, M. Heiland, A. Pannwitz, F. H. Schacher, W. Weigand, C. Streb, D. Ziegenbalg, *ChemPhotoChem* **2022**, *6*, 202200044.
[84] Q. Yin, J. M. Tan, C. Besson, Y. V. Geletii, D. G. Musaev, A. E. Kuznetsov, Z. Luo, K. I. Hardcastle, C. L. Hill, *Science* **2010**, *328*, 342.
[85] F. H. M. Freundlich, *Phys. Chem.* **1906**, 385.
[86] I. Langmuir, *J. Am. Chem. Soc.* **1918**, *40*, 1361.
[87] D. N. Sredojević, P. V. Petrović, G. V. Janjić, E. N. Brothers, M. B. Hall, S. D. Zarić, *J. Mol. Model* **2016**, *22*, 30.
[88] M.-Y. Chang, R.-S. Juang, *J. Colloid Interface Sci.* **2004**, *278*, 18.
[89] A. E Pirbazari, E. Saberikhah, M. Badrouh, M. S. Emami, *Water Resour. Ind.* **2014**, *6*, 64.
[90] J. L. Cortina, A. Warshawsky, N. Kahana, V. Kampel, C. H. Sampaio, R. M. Kautzmann, *React. Funct. Polym.* **2003**, *54*, 25.
[91] V. Fierro, V. Torné-Fernández, D. Montané, A. Celzard, *Microporous Mesoporous Mater.* **2008**, *111*, 276.

 © 2024 The Authors. Macromolecular Rapid Communications published by Wiley-VCH GmbH

15213927, 2024, 5, Downloaded from https://onlinelibrary.wiley.com/doi/10.1002/marc.202300448 by Universitatsbibliothek Mainz, Wiley Online Library on [04/06/2025]. See the Terms and Conditions (https://onlinelibrary.wiley.com/terms-and-conditions) on Wiley Online Library for rules of use; OA articles are governed by the applicable Creative Commons License

Macromolecular Rapid Communications

Supporting Information

for *Macromol. Rapid Commun.*, DOI 10.1002/marc.202300448

Poly(dehydroalanine)-Based Hydrogels as Efficient Soft Matter Matrices for Light-Driven Catalysis

*Tolga Çeper, Marcel Langer, Nikita Vashistha, Benjamin Dietzek-Ivanšić, Carsten Streb, Sven Rau and Felix H. Schacher**

WILEY-VCH

Supporting Information

Poly(dehydroalanine)-based hydrogels as efficient soft matter matrices for light-driven catalysis

*Tolga Çeper, Marcel Langer, Nikita Vashistha, Benjamin Dietzek-Ivanšić, Carsten Streb, Sven Rau, and Felix H. Schacher**

Synthesis of PDha

Synthesis of P*t*BAMA

*t*BAMA (either 2.48 mmol, 50 eq. or 19.84 mmol 400 eq.), BlocBuilder (0.05 mmol, 1 eq.), and SG-1 (0.033 mmol, 0.65 eq.) were dissolved in 1 mL 1,4-dioxane, and then freeze-pump-thaw multicycle was performed three times. The reaction was carried out under argon for 10 min at 70 °C. The reaction has been terminated by quenching with liquid N_2, and the polymer precipitated in cold hexane and washed with diethyl ether several times. The product was dried under vacuum resulting in white powder.

Yield = 52%. ^{1}H NMR (300 MHz, $CDCl_3$): δ (ppm) = 3.73 (br s, 3H, OCH_3), 3.15-2.43 (m, 2H, CH_2), 1.34 (s, 9H, $C(CH_3)_3$).

Deprotection of P*t*BAMA to yield PDha

P*t*BAMA was dissolved in TFA (~20 eq.) and heated to 50 °C. The reaction was stopped after 1 hour and the polymer precipitated in cold methanol. After filtering and washing with methanol, deionized water, and diethyl ether, the product was dried under vacuum to give a yellow powder.

Yield = 62%. ^{1}H NMR (300 MHz, D_2O): δ (ppm) = 2.43-2.27 (m, 2H, CH_2).

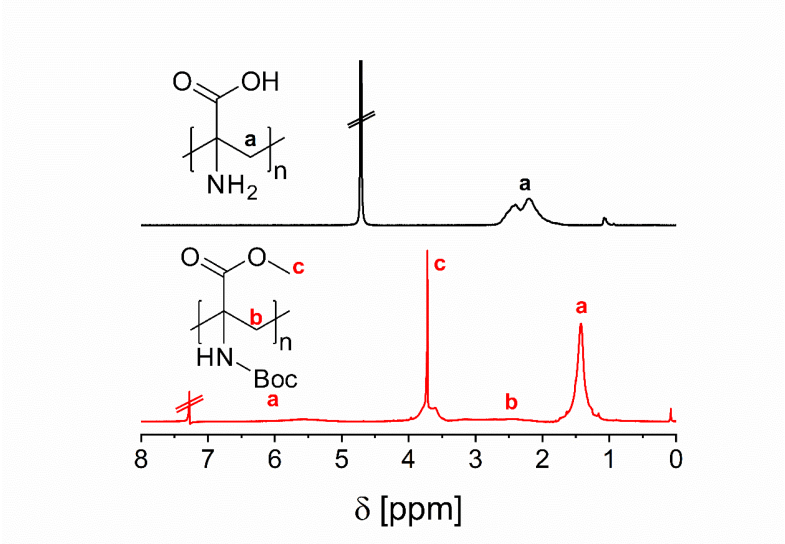


Figure S1. ^{1}H NMR spectrum of P*t*BAMA (bottom, in $CDCl_3$) and PDha (top, in D_2O + NaOD).

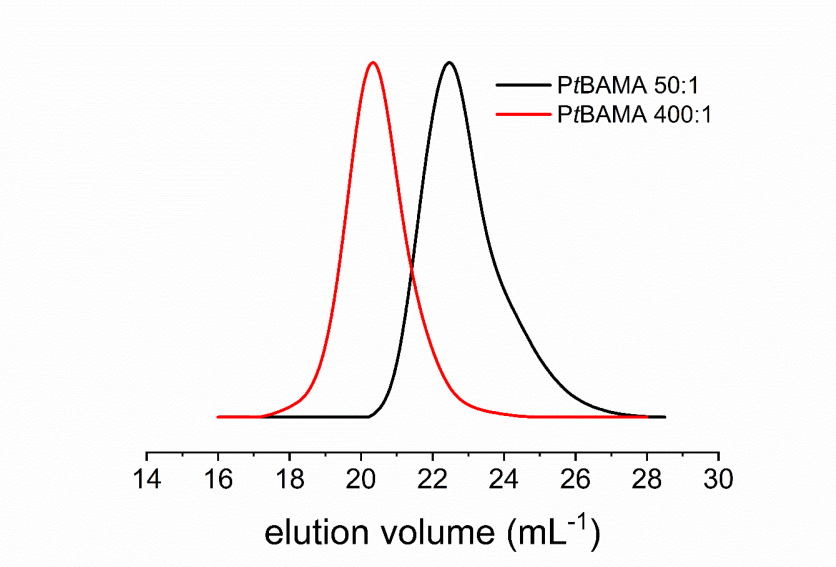


Figure S2. SEC traces of P*t*BAMA synthesized using monomer-to-initiator ratios of 50:1 and 400:1.

Synthesis of catalysts

Synthesis of cobalt polyoxometalate (Co_4POM) as OER catalyst

The polyoxometalate $Na_{10}[Co_4(H_2O)_2(PW_9O_{34})_2]$ x $22H_2O$ was prepared according to the synthesis reported by Hill and colleagues.[84] Na_2WO_4 x $2H_2O$ (35.62 g, 0.11 mol), Na_2HPO_4 x $7H_2O$ (3.23 g, 0.01 mol) and $Co(NO_3)_2$ x $6H_2O$ (6.97 g, 0.02 mol) were suspended in 100 mL water. The pH was adjusted to 7.0 by careful addition of 3 M aqueous HCl solution. The purple suspension was refluxed at 100 °C for 2 h. The hot solution was saturated with NaCl. After cooling to room temperature, purple crystals of $Na_{10}[Co_4(H_2O)_2(PW_9O_{34})_2]$ x $22H_2O$ formed, were removed by filtration and washed with cold water. The product was recrystallized from hot water and air-dried. Yield 13.4% based on Co. The sample identity and purity were assessed by ATR-FTIR.

Yield: 13.4%. ATR-FTIR: $\tilde{\upsilon}$ (cm^{-1}) = 3397 (vb), 1622 (vs), 1025 (vs), 933 (vs), 879 (vs), 704 (vs), 473 (m).

Synthesis of thiomolybdate as HER catalyst

The thiomolybdate $(NH_4)_2[Mo_3S_{13}]$ x $2H_2O$ was prepared by the synthesis reported by Streb et al.[72] An ammonium polysulfide ($(NH_4)_2S_x$) solution (120 mL, 25 wt.-%) was added to the solution of $(NH_4)_6[Mo_7O_{24}]$ x $4H_2O$ (4.0 g, 3.2 mmol) in 20 mL water in a flask. The solution was kept for five days at 96 °C without stirring. Dark-red crystals of $(NH_4)_2[Mo_3S_{13}]$ x $2H_2O$ formed and were removed by filtration, washed with water, ethanol, carbon disulphide and ether. The product (yield 97.9% based on Mo) was obtained by air-drying.

Synthesis parameters and characterization of PDha-based hydrogels

Table S1. Experimental parameters for hydrogel synthesis of PDha using $PEGDGE^2$ as crosslinker.

Entry	PDha	PDha concentration ($mg.mL^{1-}$)	PDha-to-crosslinker ratio (w/w)
1	PDha40	33	1:8
2	PDha40	33	1:4
3	PDha40	33	1:2
4	PDha40	25	1:8
5	PDha40	20	1:8
6	PDha180	20	1:8
7	PDha180	20	1:4
8	PDha180	20	1:2
9	PDha180	20	1:1

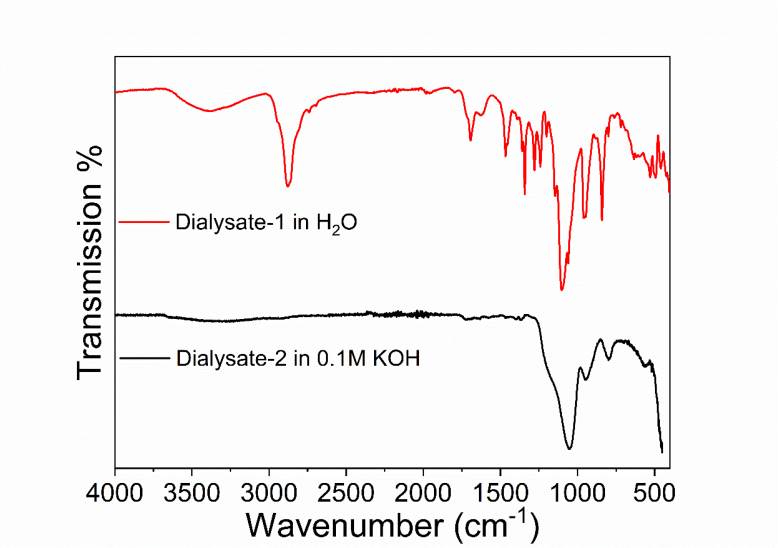


Figure S3. FTIR spectra of freeze-dried polymers from dialysate in water (1) and from subsequent dialysate in 0.1 M KOH (2).

Note: Unreacted polymers obtained in dialysates were examined by FTIR (Figure S3). Contrary to the general procedure carried out in this study, dialysis in water was performed for one day with two water changes in this case. Dialysis continued on the second day in 0.1 M KOH solution to make sure that PDha is completely dissolved, afterwards, only PEG was detected in the dialysate.

Table S2. Experimental ratios of the components of the hydrogels obtained in different reaction times using PEGDGE[2] as crosslinker and their swelling degrees in DI water.

Entry	PDha	PDha concentration ($mg.mL^{1-}$)	PDha-to-crosslinker ratio (w/w)	Time (h)	Exp[a] PDha %	Swelling degree (m_s / m_d)
1	PDha40	33	1:8	18	21	71 ± 8
2	PDha40	33	1:4	18	36	175 ± 46
3	PDha180	20	1:8	3	32	106 ± 6
4	PDha180	20	1:8	6	27	58 ± 4
5	PDha180	20	1:8	24	27	53 ± 7
6	PDha180	20	1:8	6	22	49 ± 3

a Calculated by elemental analysis based on [C]/[N] ratio

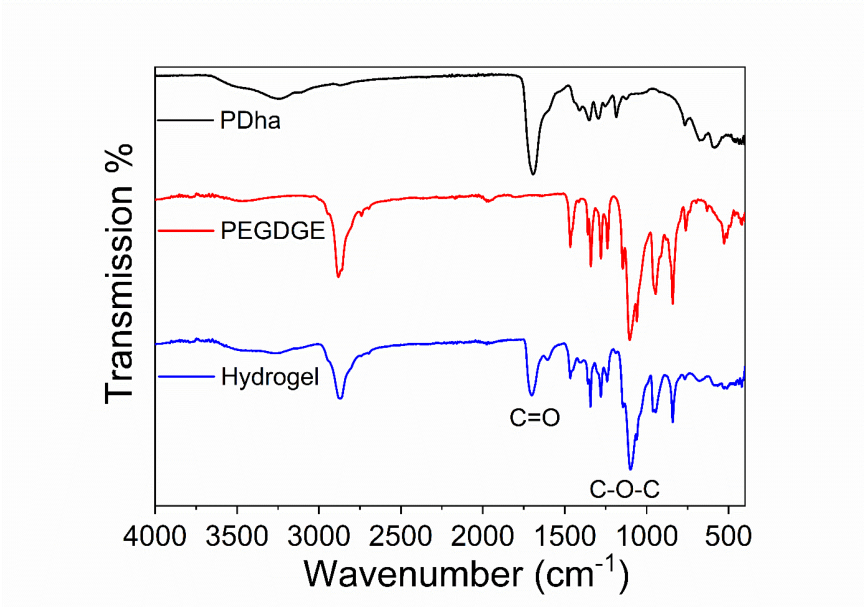


Figure S4. FTIR spectra of PDha, PEGDGE and the corresponding hydrogel.

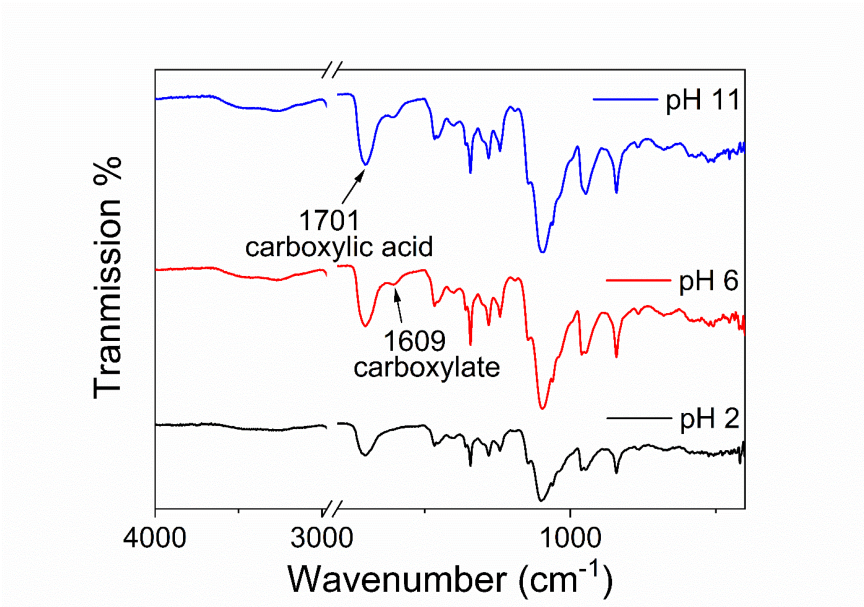


Figure S5. FTIR spectra of $PDha_{PEG2}$ freeze-dried at pH 2, 6 and 11.

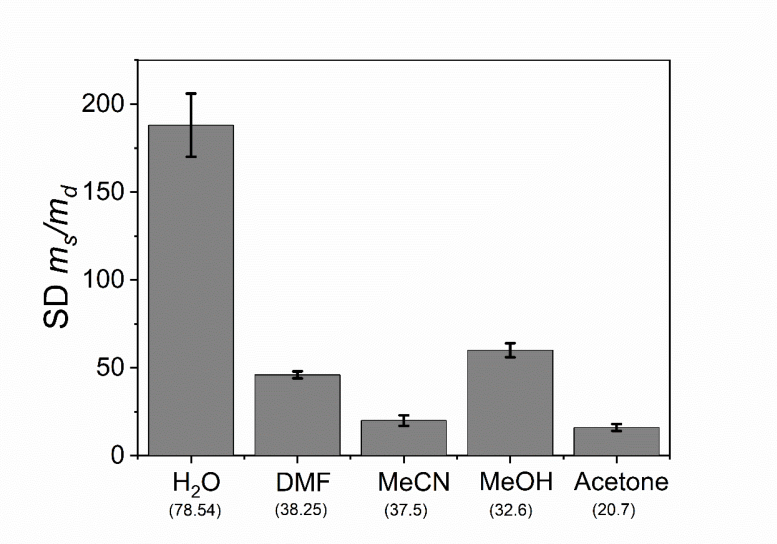


Figure S6. Swelling degrees of $PDha_{PEG2}$ in highly polar solvents with the dielectric constants indicated in parenthesis.

Adsorption of $[Ru(bpy)_3]^{2+}$ by PDha-based hydrogel

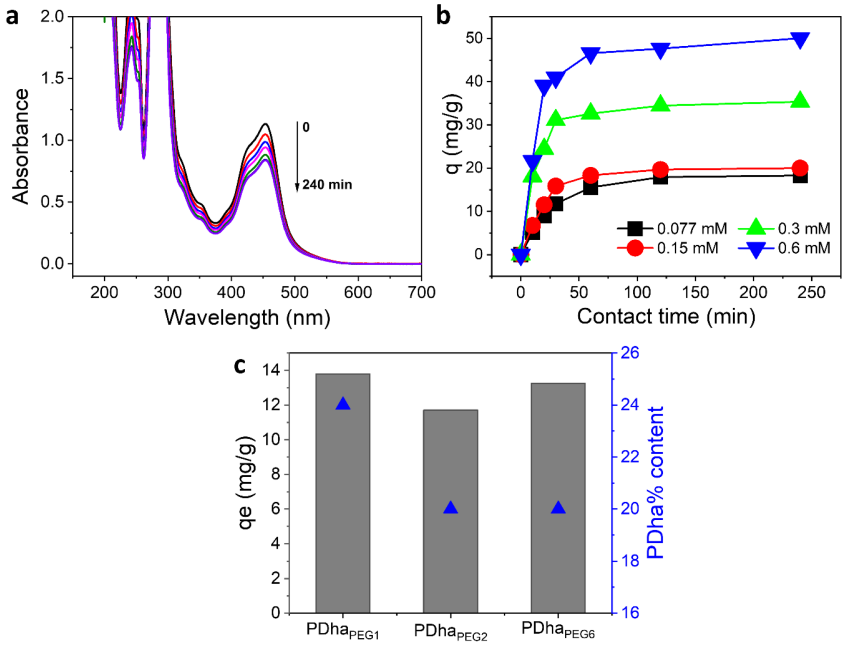


Figure S7. (a) Absorption spectrum of supernatant during adsorption of $[Ru(bpy)_3]^{2+}$ in different time interval, (b) dynamic of $[Ru(bpy)_3]^{2+}$ uptake by $PDha_{PEG6}$ for various initial dye concentration at pH 7, (c) equilibrium adsorption capacity of different $PDha_{PEGX}$ hydrogels for $[Ru(bpy)_3]^{2+}$ with corresponding PDha% content (pH: 7, initial dye concentration: 0.086 mM).

Additional discussion on adsorption isotherm and kinetics

To obtain a better insight on interaction between $PDha_{PEG6}$ hydrogel and $[Ru(bpy)_3]^{2+}$, adsorption isotherm was investigated by two models, Freundlich[85] and Langmuir[86] (Figure S9). Better agreement with Freundlich model indicated multilayer adsorption of $[Ru(bpy)_3]^{2+}$ was possible since the ligands of $[Ru(bpy)_3]^{2+}$ are able to stack each other.[87]

Table S3. Langmuir and Freundlich isotherm constants and correlation coefficients for adsorption of $[Ru(bpy)_3]^{2+}$ on $PDha_{PEG6}$.

Isotherm	Constants		
	Q_L (mg.g^{-1})	K_L (L.mg^{-1})	R^2
Langmuir	74	3.3	0.946
	K_F (mg.g^{-1}(L.mg^{-1})$^{1/n}$)	1/n	R^2
Freundlich	62	0.5	0.964

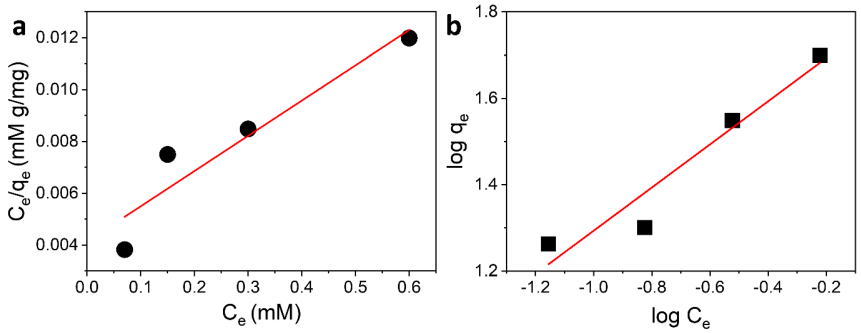


Figure S8. Linear form of isotherms for adsorption $[Ru(bpy)_3]^{2+}$ on $PDha_{PEG6}$ according to (a) Langmuir and (b) Freundlich models.

The dynamic of adsorption was determined by linear regression using two pseudo-models that both basically include all adsorption steps such as external film diffusion, adsorption, and internal particle diffusion[88] (Table S4, Figure S10). Calculated R^2 at 0.077 mM of the initial concentration of adsorbate value was 0.999, therefore the adsorption can be described by the pseudo-first-order model, where the diffusion through the interface is rate-limiting. We noted that at the initial dye concentration higher than 0.077 mM, the adsorption data were deviated from the theory after 60 minutes. When the entire adsorption range is considered up to 4 hours, high R^2 values and similarity between calculated and experimental adsorption capacities

exhibited that kinetics of adsorption followed the pseudo-second-order model at all concentrations, which is expected for the adsorption of cationic and anionic dyes,[89] in which the chemisorption is the rate-controlling step. Calculated by pseudo-second order model, adsorption rates were firstly increasing with the increase of the dye concentration up to 0.3 mM, then adsorption was observed to be slowed down at 0.6 mM despite the adsorption amount increased. This effect was likely due to the most of active sites to be occupied by $[Ru(bpy)_3]^{2+}$ at high concentration.

Diffusion mechanism was further examined using Weber-Morris equation (Intraparticle diffusion model), which has been used for determining the main diffusion resistance for the adsorption that can be external film or intraparticle diffusion resistance.[90] The plot for $[Ru(bpy)_3]^{2+}$ uptake at various initial concentration mainly showed two different regimes which means at least two steps influence the adsorption (Table S4, Figure S9c). In the first stages of adsorption, the external film surrounding hydrogel was significantly resistant to mass transfer, while the intraparticle diffusion was dominant in the gradual adsorption stage.[91]

Table S4. Kinetic parameters for adsorption of $[Ru(bpy)_3]^{2+}$ on $PDha_{PEG6}$ constants and correlation coefficients.

Initial concentration C_0 (mM)	$q_{e,exp}$ (mg.g^{-1})	Pseudo-first-order			Pseudo-first-order for first 60 min		
		$q_{e,cal}$ (mg.g^{-1})	k_1 (min^{-1})	R^2	$q_{e,cal}$ (mg.g^{-1})	k_1 (min^{-1})	R^2
0.077	18.3	778	0.032	0.999	760.3	0.032	0.999
0.15	20	610	0.034	0.971	881	0.042	0.989
0.3	35.4	989	0.028	0.858	1862	0.042	0.943
0.6	50.1	1892	0.023	0.751	4623	0.044	0.965

Initial concentration C_0 (mM)	$q_{e,exp}$ (mg.g^{-1})	Pseudo-second-order			Intraparticle diffusion			
					first region		second region	
		$q_{e,cal}$ (mg.g^{-1})	k_2 (g.mg^{-1}.min^{-1})	R^2	k	R^2	k	R^2
0.077	18.3	20	0.0021	0.998	2.3	0.924	0.34	0.880
0.15	20	22	0.0031	0.996	2.5	0.876	0.21	0.911
0.3	35.4	37	0.0033	0.999	5.6	0.826	0.42	0.966
0.6	50.1	52	0.0021	0.999	8.6	0.824	0.8	0.905

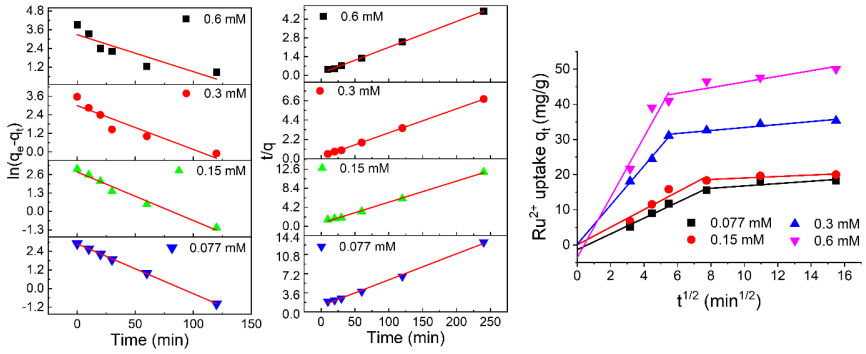


Figure S9. Adsorption kinetics of $[Ru(bpy)_3]^{2+}$ (a) pseudo-first-order, (b) pseudo-second-order and (c) intraparticle diffusion models using $PDha_{PEG6}$ hydrogel.

Emission quenching

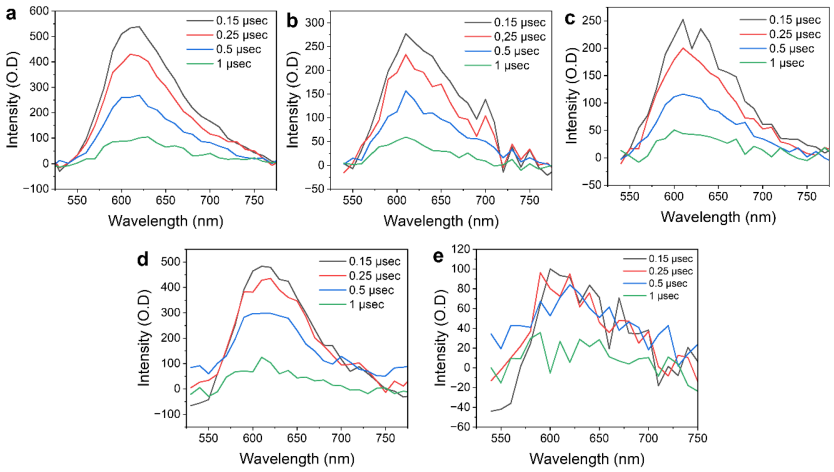


Figure S10. Fluorescence spectra of hydrogel samples at varying time delay containing 95 μM of $[Ru(bpy)_3]^{2+}$ and (a) 0 μM, (b) 17.2 μM (c) 34.5 μM, (d) 69 μM, or (e) 133 μM of Co_4POM.

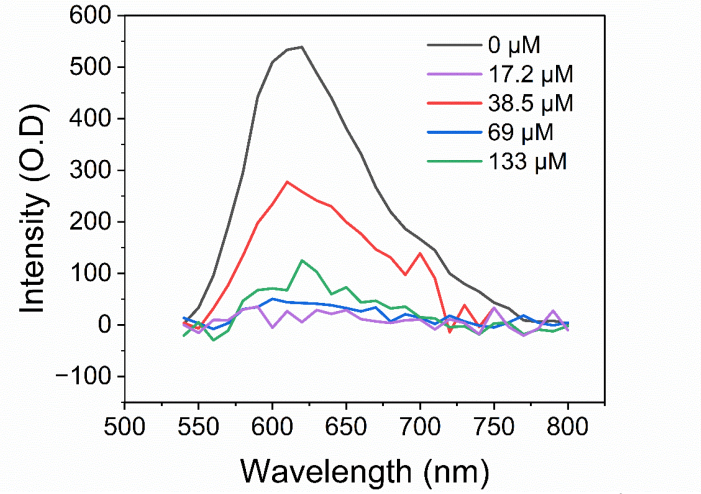


Figure S11. Comparative Fluorescence spectra of PDhaPEG$_2$/[Ru(bpy)$_3$]$^{2+}$ hydrogels with increasing concentration of Co$_4$POM at 1 µs time delay.

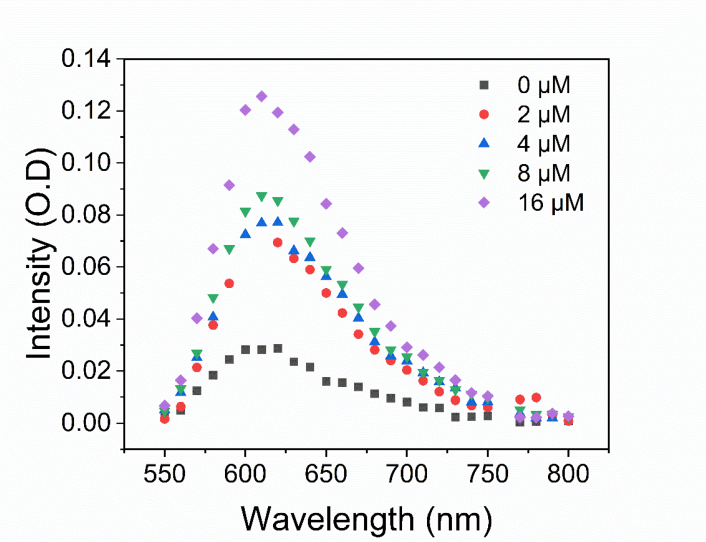


Figure S12. Emission plots of PDhaPEG$_2$/[Ru(bpy)$_3$]$^{2+}$ hydrogel samples with increasing concentrations of [Mo$_3$S$_{13}$]$^{2-}$ at 1 µs time delay.

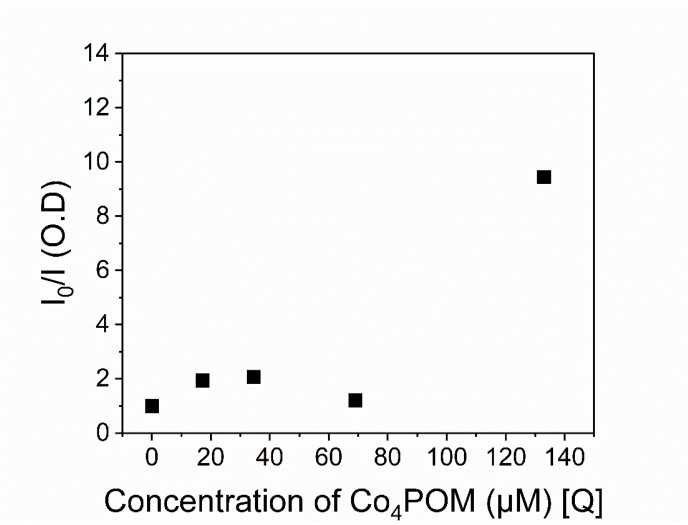


Figure S13. Stern-Volmer plot for PDhaPEG$_2$/$[Ru(bpy)_3]^{2+}$ hydrogels with varying concentration of Co_4POM. The intensity ratio was taken at 0.15 μs.

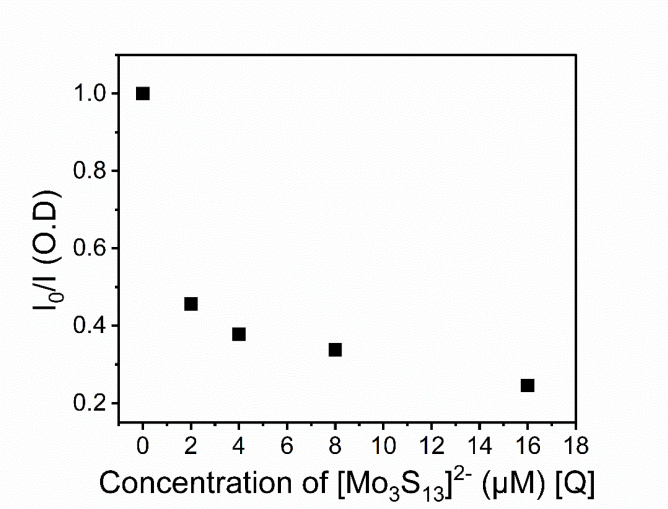


Figure S14. Stern-Volmer plot for PDhaPEG$_2$/$[Ru(bpy)_3]^{2+}$ hydrogels with varying concentration of $[Mo_3S_{13}]^{2-}$ quencher. The intensity ratio was taken at 0.15 μs.

Light-driven HER and OER

Table S5. The effect of catalyst loading conditions and solvent on evolved H_2 amounts (0.267 μM $[Mo_3S_{13}]^{2-}$, 20 μM $[Ru(bpy)_3]^{2+}$ and 0.9 M TEA).

Sample	MeOH %	Cat. loading solvent	Gel for cat. loading	H_2 (μmol)
Benchmark (only in solution)	70	N/A	N/A	0.80
	50	N/A	N/A	0.79
PDha-based gel	70	MeOH/H_2O	Swollen	0.46
	50	MeOH/H_2O	Swollen	0.57
	30	MeOH/H_2O	Swollen	0.17
	70	MeOH/H_2O	Freeze-dried	0.15
	50	MeOH/H_2O	Freeze-dried	0.27
	30	MeOH/H_2O	Freeze-dried	0.12
	50	H_2O	Swollen	0.16
	50	H_2O[a]	Swollen	0.015

[a] sample was hold overnight

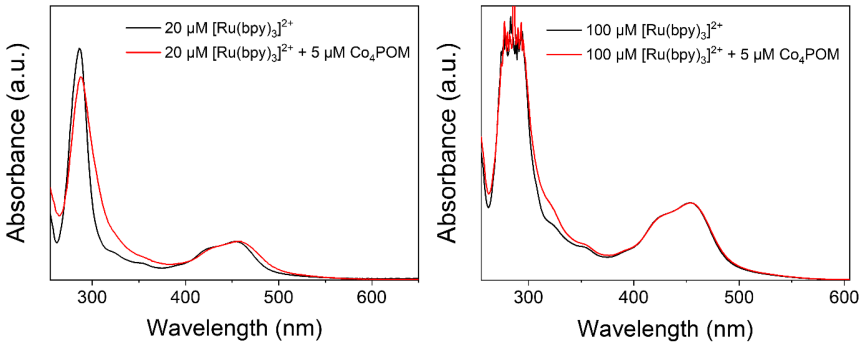


Figure S15. Absorption spectra of $[Ru(bpy)_3]^{2+}$ and Co_4POM in solution at different concentrations.

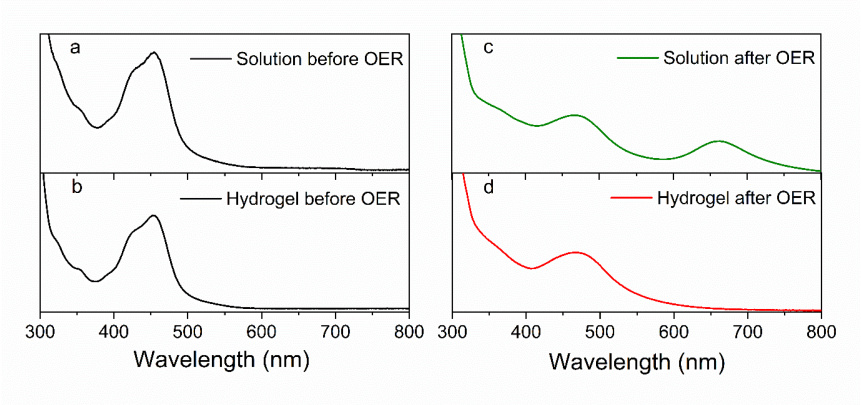


Figure S16. (a-b) UV-Vis absorbance spectra of solution and hydrogel samples before OER and (c-d) after OER.

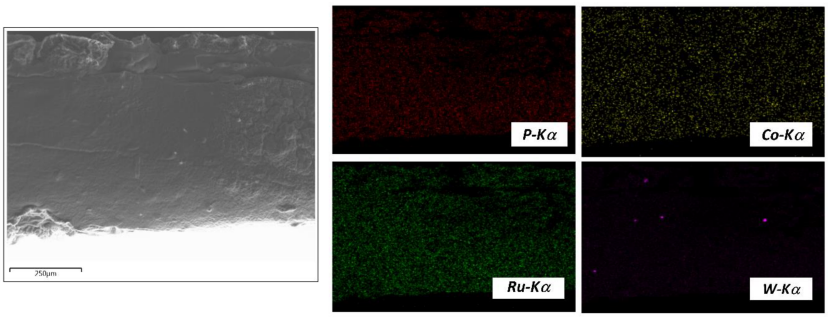


Figure S17. Scanning electron microscopy (SEM) in cross-section of dry gel after loaded by $[Ru(bpy)_3]^{2+}$ and Co_4POM (left), energy dispersive X-ray spectroscopy (EDX) elemental mapping (P, Co, Ru and W) (right).

WILEY-VCH

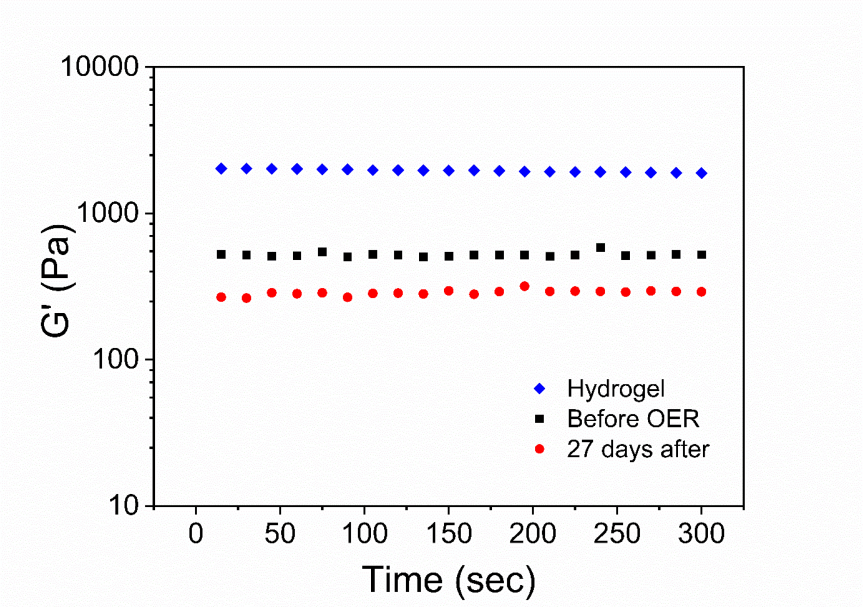


Figure S18. Dynamic oscillatory time sweep measuring storage modulus (G') of the hydrogel before and after OER as well as the neat hydrogel for comparison (measured applying 6.28 rad/s angular frequency in linear viscoelastic region (LVR))

6.5 {MLa-6}: *In situ* Formation of an Active Oxygen Evolution Catalyst *via* Photodegradation of $[Ru(bpy)_3]^{2+}$

Marcel Langer, Alexander K. Mengele, Riccarda Müller, Julius C. Wetzel, Judith Mayer, Sven Rau*, and Carsten Streb*

* *Corresponding authors*

Abstract: *Operando* studies of O_2 quantification and UV-Vis were performed to obtain chemical and mechanistic insights into the role of $[Ru(bpy)_3]^{2+}$ in homogeneous light-driven OER with predominant organic solvent identity and in the presence of $S_2O_8^{2-}$. Under the reported conditions, a rapid oxidative conversion of the PS to OER-active analogs of the blue dimer structure was observed, which are sensitive to changes in solvent type and water content. Moreover, the use of heteroleptic PSs has emerged as an effective strategy to prevent PS photodegradation and thus mitigate intrinsic OER activity in organic media, which is of paramount importance to avoid misinterpretation of new photosystems under study.

Published in: *Dalton Trans.* **2025**, *54*, 4861–4865.

Status: Published

Copyright: Reprinted with permission from "*In situ* formation of an active oxygen evolution catalyst *via* photodegradation of $[Ru(bpy)_3]^{2+}$", M. Langer, A. K. Mengele, R. Müller, J. C. Wetzel, J. Mayer, S. Rau,* and C. Streb,* *Dalton Trans.* **2025**, *54*, 4861-4865.
DOI: 10.1039/d5dt00233h.

© 2025, The Royal Society of Chemistry under the terms of the CC BY 3.0 license.

Author Contributions:

M. Langer	Conceptualization; Fabrication of the O_2 measurement cell; Conducting and supervising all light-driven OER studies; Performing all *operando* UV-Vis studies; Data analysis; Discussion of results; Writing, discussion and revision of the manuscript.
A. K. Mengele	Synthesis and characterization of PS2, PS3 and PS4; Writing of the corresponding part of the manuscript; Discussion and revision of the manuscript.
R. Müller	O_2 quantification measurements to evaluate the light-driven OER reactivity of PS2, PS4, PS5 and $[Ru(bpy)_3]Cl_2$ under purely aqueous conditions, as well as to study the effect of reduced SOA concentrations.
J. C. Wetzel	O_2 quantification measurements and ATR-FTIR to evaluate the effect of additional bpy on the light-driven OER activity of PS1a.
J. Mayer	O_2 quantification measurements to evaluate the light-driven OER reactivity of PS3.
S. Rau	Revision of the manuscript.
C. Streb	Conceptualization; Supervision; Discussion of results; Writing, discussion and revision of the manuscript.

Dalton Transactions

ROYAL SOCIETY OF CHEMISTRY

COMMUNICATION

View Article Online
View Journal | View Issue

Open Access Article. Published on 03 March 2025. Downloaded on 6/4/2025 9:50:52 AM.
This article is licensed under a Creative Commons Attribution 3.0 Unported Licence.

Check for updates

Cite this: *Dalton Trans.*, 2025, **54**, 4861

Received 29th January 2025,
Accepted 28th February 2025

DOI: 10.1039/d5dt00233h

rsc.li/dalton

In situ formation of an active oxygen evolution catalyst *via* photodegradation of $[Ru(bpy)_3]^{2+}$†

Marcel Langer,[a,b] Alexander K. Mengele,[b] Riccarda Müller,[b] Julius C. Wetzel,[a] Judith Mayer,[b] Sven Rau *[b] and Carsten Streb *[a,b]

$[Ru(bpy)_3]^{2+}$ is a widely used molecular photosensitizer (PS) for light-driven reactions in combination with separate catalysts, although the PS alone is known to promote water oxidation under aqueous conditions as well. In contrast, this behavior has not been reported for organic and aqueous solvent mixtures before. Here, we provide mechanistic insights into the role of $[Ru(bpy)_3]^{2+}$ as PS and oxygen evolution catalyst precursor in organic media.

To date, the global energy demand is still largely met by non-sustainable energy sources.[1–3] Green hydrogen, produced by the splitting of water into its elements, is a major alternative to fossil fuels.[4,5] One approach to this end is artificial photosynthesis by using solar energy to drive the water splitting reactions, *i.e.* the oxygen evolution reaction (OER) and the hydrogen evolution reaction (HER).[6–9] Light harvesting in artificial photosynthesis is often performed by molecular photosensitizers (PS).[10–12] The metal complex $[Ru(bpy)_3]^{2+}$ (bpy = 2,2′-bipyridine) is one of the most widely used PS species, as it combines high light absorption in the visible range (λ_{max} = 450 nm), long excited-state lifetimes and photoredox reactivity that enables both oxidative as well as reductive transformations.[13,14] $[Ru(bpy)_3]^{2+}$ can also be deployed in various solvents, as solubility can be controlled by the choice of counter anion (*e.g.* Cl^- for aqueous systems, PF_6^- for polar organic solvents).[15,16] Thus, molecular OER and HER catalyst models can be studied both in aqueous and non-aqueous solvents, which has led to unique insights and significant progress in OER and HER catalysis.[17–22] However, it is worth noting that in aqueous systems $[Ru(bpy)_3]^{2+}$ does not act as an innocent PS. Instead, Yoon and co-workers demonstrated that in aqueous media and in the presence of the sacrificial oxidizing agent (SOA) sodium persulfate ($Na_2S_2O_8$), the complex undergoes fast, light-induced decomposition starting from the oxidized $[Ru^{III}(bpy)_3]^{3+}$. After initial formation of an unknown intermediate, the photosystem then forms either the well-known Ru μ-oxo blue dimer water oxidation catalyst (WOC) $[(bpy)_2(H_2O)RuORu(OH_2)(bpy)_2]^{4+}$ (see Fig. 1, formed at low PS concentrations) or catalytically inactive Ru μ-oxo oligomers (formed at high PS concentrations).[23] In the further course of this light-driven OER, the Ru-dimers can readily be converted by $[Ru(bpy)_3]^{3+}$ into the fully oxidized and water oxidation-active species $[(bpy)_2(O)RuORu(O)(bpy)_2]^{4+}$ (hereafter: $Ru_2(v,v)$).[24,25]

In contrast to this understanding of $[Ru(bpy)_3]^{2+}$ reactivity in water, to the best of our knowledge, no similar mechanistic OER studies have been performed in predominantly organic solvents containing water. However, this is urgently required as mechanistic and catalytic studies on molecular WOCs are often performed in organic media.

Here, we report catalytic and mechanistic studies on the role of $[Ru(bpy)_3]^{2+}$ in light-driven OER experiments in often-used acetonitrile/water mixtures and provide insights into the competing roles of $[Ru(bpy)_3]^{2+}$ as a PS and molecular precursor of an active WOC.

The prototype OER system discussed herein consists of the PS $[Ru(bpy)_3](PF_6)_2$ (1 mM, PS1a) and the SOA $Na_2S_2O_8$ (10 mM) dissolved in a 9 : 1 (v : v) mixture of acetonitrile (MeCN) and water. The reaction conditions were adapted from previous OER studies in mixed aqueous organic solvents, see

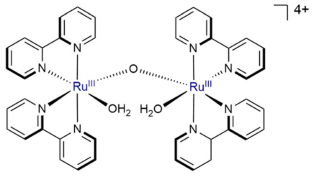


Fig. 1 Structural representation of the WOC "blue dimer" *cis,cis*-$[(bpy)_2(H_2O)Ru^{III}ORu^{III}(OH_2)(bpy)_2]^{4+}$ (=$Ru_2(III,III)$).

[a]*Department of Chemistry, Johannes Gutenberg University Mainz, Duesbergweg 10-14, 55128 Mainz, Germany. E-mail: carsten.streb@uni-mainz.de*
[b]*Institute of Inorganic Chemistry I, Ulm University, Albert-Einstein-Allee 11, 89081 Ulm, Germany*

†Electronic supplementary information (ESI) available. See DOI: https://doi.org/10.1039/d5dt00233h

View Article Online
Communication Dalton Transactions

Open Access Article. Published on 03 March 2025. Downloaded on 6/4/2025 9:50:52 AM.
This article is licensed under a Creative Commons Attribution 3.0 Unported Licence.

ESI† for details.[26] Note that in our study, the reaction solutions do not contain any WOCs. The samples were prepared under inert atmosphere, placed in a custom-built air-cooled photoreactor and irradiated with LED light (λ_{max} = 470 nm, power density: *ca.* 50 mW cm^{-2}; see ESI, Fig. S1†). Oxygen evolution was quantified *in operando*, simultaneously in solution and the gas phase using fiber-optic fluorescent sensors integrated in a sealed glass vial. For reasons of clarity and better comparison, the quantified oxygen is given in µmol. In addition, turnover numbers (TONs) and turnover frequencies (TOFs) are not calculated, as the concentration of the actual catalytically active species remains unknown.

Fig. 2 shows a representative O_2 evolution profile of the prototype OER experiment as described above. Under dark conditions (t = 0–5 min), no oxygen evolution is observed, demonstrating the integrity of the inert-atmosphere setup and the need for light to form O_2 under the given conditions (see ESI, Fig. S2†). Upon irradiation (t > 5 min) and following a short induction phase of less than 1 min, constant oxygen evolution is monitored, which is accompanied by visually detectable gas formation. After approximately 45–60 min, the amount of dissolved oxygen reaches a maximum (*ca.* 2.1 µmol, see blue curve in Fig. 2), indicating that the O_2 saturation level of the solvent mixture is reached. Diffusion into the gas phase continues, as observed by a decrease in the dissolved oxygen, while simultaneously the O_2 values in the gas phase continue to rise. The amounts of O_2 in the gas phase and in the solution, both reach a plateau after *ca.* 3–4 h, indicating the end of the OER process. A total oxygen amount of 24.1 ± 1.9 µmol was obtained, emphasizing the complete consumption of SOA as limiting factor for sustained O_2 evolution. Persulfate is a two-electron acceptor, whereas water oxidation requires the removal of four electrons per O_2 molecule. Thus, the molar amount of $S_2O_8^{2-}$ used (50 µmol, corresponding to 10 mM) can generate 100 µmol of oxidation equivalents, which is equal to a theoretical O_2 yield of 25 µmol. This stoichiometric equivalence was further validated at different SOA concentrations (see ESI, Fig. S3†). Therefore, the O_2 quantities are within the range of measurement accuracy and identical to the number of oxidation equivalents provided by SOA.

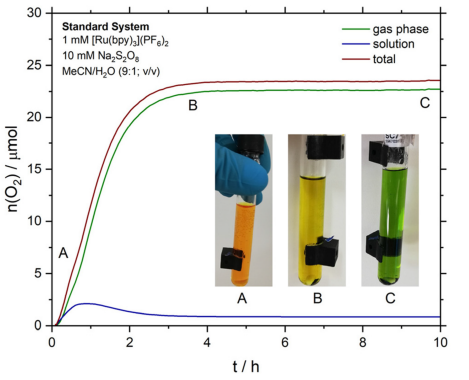


Fig. 2 Light-driven oxygen evolution profile in the gas phase (green curve), in solution (blue curve) and in total (red curve) of the OER system studied. Conditions: $[Ru(bpy)_3](PF_6)_2$ (PS1a; 1 mM), $Na_2S_2O_8$ (10 mM), solvent: MeCN/H_2O (9 : 1; v/v; 5 mL), LED light (λ_{max} = 470 nm; power density: *ca.* 50 mW cm^{-2}). Inset photographs show the pre- and post-catalytic reaction solutions in dependence of the irradiation time: (A): intense orange (t = 0 h), (B): yellow (t ≈ 3–10 h) and (C) green, often accompanied by an oily deposit (t ≥ 10 h).

Notably, during irradiation, the intense orange color of $[Ru(bpy)_3]^{2+}$ fades, indicating (partial) degradation of the PS. Depending on irradiation time and catalytic progress, the post-catalytic solutions were yellow ($t_{irradiation}$ ≈ 3–10 h) or green ($t_{irradiation}$ ≥ 10 h), in the latter case often accompanied by the formation of a green oily deposit (see inset photographs in Fig. 2). Note that reference experiments showed that both PS and SOA were required in the reaction system to drive this degradation and result in species capable of oxygen evolution (see ESI, Fig. S4A and B†). In addition, when $[Ru(bpy)_3](PF_6)_2$ solutions were irradiated in the absence of SOA, no color changes were observed, highlighting that the degradation is linked to a photochemical process in the presence of the SOA. This suggests that in the presence of the SOA, the PS might either undergo a persulfate-dependent oxidation to a Ru^{3+} species (with a characteristic green color), following a mechanism reported earlier by Polyansky and colleagues,[27] or a (oxidative) degradation promoted by persulfate and sulfate radical anions, as demonstrated by Bonnet and co-workers.[28] These findings are also in line with previous reports on $[Ru(bpy)_3]^{2+}$ degradation under aqueous conditions.[23] Note that this PS degradation can be effectively limited using dynamic irradiation conditions and reduced photon flux rates, as shown by Rau, Ziegenbalg and colleagues.[29]

In order to gain in-depth understanding of the fate of $[Ru(bpy)_3]^{2+}$ under irradiation, we performed *operando* UV-Vis spectroscopy under catalytic conditions (see ESI, Fig. S5 and S6†). Upon irradiation, the characteristic ^{1}MLCT (metal-to-ligand charge transfer) band of $[Ru(bpy)_3]^{2+}$ at 452 nm immediately loses intensity, while a new, very broad band with a concentration-dependent maximum emerges at 663 nm under prototype conditions and 672 nm under diluted conditions (by a factor of ten). Another electronic transition at 420 nm also loses intensity but becomes much more pronounced due to the occurrence of a clearly defined maximum. These features are indicative of the oxidation of $[Ru(bpy)_3]^{2+}$ to $[Ru(bpy)_3]^{3+}$, which is expected under the given reaction conditions.[30] The UV-Vis spectrum becomes very similar to the initial spectrum within a timescale of *ca.* 30–45 min, which could indicate the formation of the orange Ru_2(III,IV) dimer (*vide infra*).[23] Interestingly, the formation of a blue-shifted broad signal at 653 nm after 3 h might be assigned to the conversion of $[Ru(bpy)_3]^{2+}$ into "blue dimer" type species with different Ru oxidation states.[23] However, this conversion can only be observed under concentrated PS conditions. Alternatively, the broad band in the *operando* UV-Vis spectrum

 This journal is © The Royal Society of Chemistry 2025

Open Access Article. Published on 03 March 2025. Downloaded on 6/4/2025 9:50:52 AM.
This article is licensed under a Creative Commons Attribution 3.0 Unported Licence.

assigned to $[Ru(bpy)_3]^{3+}$ accumulates very rapidly once light irradiation occurs and is slowly consumed by subsequent catalyst formation. At a certain point in the preceding reaction, enough catalyst has formed and no further $[Ru(bpy)_3]^{3+}$ can accumulate, as it is readily reduced to Ru(II) species by the amount of catalyst present. This interpretation is supported by the correlation of the induction phase for O_2 evolution (see Fig. 2) with the time in which the UV-Vis band at 672 nm (see ESI, Fig. S6C,† orange curve) decreases.

Moreover, the green oily deposit from a typical photocatalytic organic OER experiment was separated by centrifugation and dissolved in water, resulting in the UV-Vis spectrum shown in the ESI Fig. S7.† The observed transitions can be assigned to two different, structurally related Ru-dimer species that form simultaneously. On the one hand, the orange Ru_2(III, IV) dimer can be identified by its characteristic MLCT transition maximum at 464 nm, while another transition maximum at 650 nm is attributed to the blue Ru_2(III,III) dimer.[23] Both dimers combine characteristic ligand-centered (LC) transitions of $\pi\pi^*_{bpy}$ at 208 nm and 288 nm, as well as an additional MLCT band at 242 nm and a very weak shoulder at 383 nm.[31] Another broad absorption in the near-IR with a maximum at 854 nm is assigned to dπdπ interconfigurational transitions of the blue dimer.[32] Thus, these results suggest a similar decomposition pathway of $[Ru(bpy)_3]^{2+}$ during homogeneous light-driven water oxidation using persulfate as SOA under aqueous and non-aqueous conditions, as discussed in the introduction: during the initial catalytic phase, minor concentrations of catalytically active Ru μ-oxo dimers might be formed, followed by formation of catalytically inactive Ru μ-oxo species, such as oligomers, resulting in a complex interplay between different Ru-based active and inactive species.

Further analyses showed that the type of organic solvent plays a crucial role for the observed PS conversion and its respective reactivity for the OER, as replacing MeCN with other polar organic solvents such as *N*,*N*′-dimethyl formamide (DMF) resulted in almost no O_2 evolution (*ca.* 0.04 μmol after 90 min corresponding to >99% less oxygen evolution compared to the prototype system in the presence of MeCN, see ESI, Fig. S8A†). Similarly, experiments in acetone yielded only extremely low O_2 quantities (*ca.* 0.27 μmol after 90 min corresponding to ~98.5% less O_2 evolution compared to the prototype system in the presence of MeCN, see ESI, Fig. S8B†).

Variation of the MeCN : water molar ratio also leads to major reactivity changes: the prototype system (using 9 : 1, v : v MeCN : water) yielded 23.5 μmol O_2 after 6 h irradiation, while identical experiments using 3 : 2, v : v MeCN : water gave only 4.5 μmol (corresponding to an oxygen evolution decrease of ~80%, see ESI, Fig. S8C†), indicating that solvent composition has a significant impact on PS degradation. This is substantiated by earlier reports, which suggest that light- or Ru-oxidation-induced bipyridine-to-MeCN ligand exchange is a typical degradation path for ruthenium bipyridyl photosensitizers.[33–35] Based on these considerations, we can propose a possible reaction scheme as shown in Fig. 3.

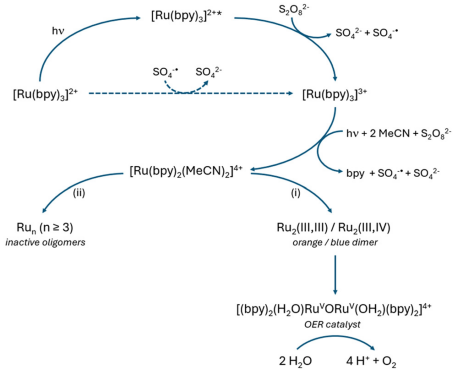


Fig. 3 Postulated reaction scheme for the formation of the active WOC of the blue dimer type using $[Ru(bpy)_3]^{2+}$ in non-aqueous MeCN solution and in the presence of $S_2O_8^{2-}$. (i) Further oxidation to OER-active dimers by $[Ru(bpy)_3]^{3+}$ or $S_2O_8^{2-}$ in the presence of a minor PS^{3+} concentration. (ii) Formation of OER-inactive Ru μ-oxo oligomers when the PS^{3+} concentration is increased. The stoichiometry has been omitted for the sake of clarity, and the water ligand could also be substituted by other ions in the solution, *e.g.* SO_4^{2-}, to form dimer derivatives. Adapted and modified from reference.[23,33]

To demonstrate that loss of bpy is a key factor for the $[Ru(bpy)_3]^{2+}$ degradation under the given conditions, we showed that degradation can be inhibited by the addition of free bpy ligand. *Operando* UV-Vis spectroscopic measurements demonstrate this effect, as no formation of the broad band around 653 nm (indicative of PS degradation) is observed (see ESI, Fig. S9†). To test this hypothesis, we performed OER experiments in the presence of additional bpy ligand using our standard photocatalytic OER setup: when an excess of bpy (100 mM) is present in solution, we observe significantly lower amounts of O_2 (max. 7.3 μmol, ~69% less oxygen compared to the prototype system, see ESI, Fig. S10†). We propose that an excess of bpy prevents the formation of significant quantities of degraded PS, thereby preventing further conversion to the catalytically active OER species.[36,37] Also note that the presence of excess bpy prevented the formation of the characteristic green oily deposit of the Ru dimers. Instead, only precipitation of colorless sodium sulfate was detected by ATR-FTIR spectroscopy (see ESI, Fig. S11†).[38] This indicates that the sulfate sources, that is persulfate, might have several functions in the given system. The primary function of persulfate is to operate as SOA. Then, the compound itself or its reaction products (*e.g.* strongly-oxidizing sulfate radical anions) might act as oxidants to drive the formation of the blue dimer or the oligomeric Ru μ-oxo species.

Finally, we extended our studies to various structurally related ruthenium polypyridyl PS. To this end, we investigated a selection of five additional Ru-based PS (see Fig. 4) to assess how the type of ligand impacts degradation and oxygen evol-

Open Access Article. Published on 03 March 2025. Downloaded on 6/4/2025 9:50:52 AM.
This article is licensed under a Creative Commons Attribution 3.0 Unported Licence.

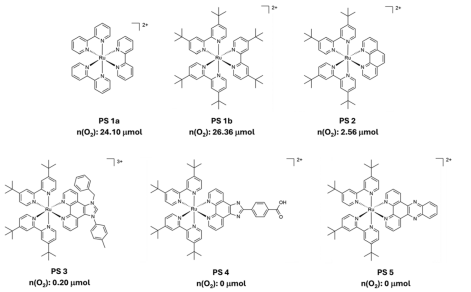


Fig. 4 Various Ru-polypyridyl PS and their maximum light-driven OER reactivity. PS1a: $[Ru(bpy)_3](PF_6)_2$; PS1b: $[Ru(tbbpy)_3](PF_6)_2$; PS2: $[Ru(tbbpy)_2(phen)](PF_6)_2$; PS3: $[Ru(tbbpy)_2(p\text{-tolbip})](PF_6)_3$; PS4: $[Ru(tbbpy)_2(ipphCOOH)](PF_6)_2$ and PS5: $[Ru(tbbpy)_2(dppz)](PF_6)_2$.

ution. All systems were tested as PS under the standard reaction conditions outlined above.

The homoleptic complex $[Ru(tbbpy)_3](PF_6)_2$ (PS1b; tbbpy = 4,4′-di-*tert*-butyl-2,2′-bipyridine) shows comparable OER activity to PS1a (*ca.* 25 µmol after 6 h of irradiation; see ESI, Fig. S12A†), whereas drastically reduced amounts of O_2 were obtained for the heteroleptic $[Ru(tbbpy)_2(phen)](PF_6)_2$ (PS2; phen = 1,10-phenanthroline; *ca.* 2.6 µmol after 3 h of irradiation; see ESI, Fig. S12B†). In contrast, no oxygen evolution was observed for the other PS $[Ru(tbbpy)_2(p\text{-tolbip})](PF_6)_3$ (PS3; *p*-tolbip = 1-(4-methylphenyl)-3-benzyl-1*H*-imidazo[4,5-*f*][1,10] phenanthroline),[39] $[Ru(tbbpy)_2(ipphCOOH)](PF_6)_2$ (PS4; ipphCOOH = 4-(1*H*-imidazol[4,5-*f*][1,10]phenanthroline-2-yl)benzoic acid),[40] and $[Ru(tbbpy)_2(dppz)](PF_6)_2$ (PS5; dppz = dipyrido[3,2-*a*:2′,3′-*c*] phenazine; for details, see ESI, Fig. S12C–E†).[41] These results suggest that the *in situ* formation of an active WOC can be effectively hindered by using heteroleptic PS, which suppress or prevent ligand exchange and Ru-dimer formation.

Conclusions

In summary, we demonstrated that in mixed aqueous/organic solvents, $[Ru(bpy)_3]^{2+}$ can undergo light-induced degradation and formation of catalytically active ruthenium dimer species capable of OER. Compared with a reference experiment performed under purely aqueous conditions, this process is notably faster when performed in organic solvent (see ESI, Fig. S22†). The catalytic system is sensitive to changes in solvent type and water content. Also, we demonstrate that structurally related Ru photosensitizer species show similar reactivity but heteroleptic complexes perform significantly worse. Thus, this report highlights that careful analysis and blank studies are required for each set of reaction conditions when using $[Ru(bpy)_3]^{2+}$ to drive photocatalysis.

Author contributions

M.L.: conceptualization, investigation, writing – original draft, project administration, methodology, data curation, data analysis; A.K.M.: investigation, formal analysis, writing – review and editing; R.M.: investigation, writing – review and editing; J.C.W.: investigation, writing – review and editing; J.M.: investigation, writing – review and editing; S.R.: resources, writing – review and editing; C.S.: conceptualization, funding acquisition, resources, supervision, writing – review and editing.

Data availability

Data for this article, including experimental spectroscopic and analytical data are available at zenodo.org at **https://doi.org/10.5281/zenodo.14760529**.

Conflicts of interest

There are no conflicts to declare.

Acknowledgements

The authors acknowledge Dr Roland Nau and Martin Lämmle, Ulm University, for Ru-PS synthesis. The authors acknowledge funding by the German Science Foundation DFG (TRR 234 “CataLight”, project no: 364549901, projects A1, A4, B3).

References

1 P. J. Megia, A. J. Vizcaino, J. A. Calles and A. Carrero, *Energy Fuels*, 2021, **35**, 16403–16415.
2 S. H. Mohr, J. Wang, G. Ellem, J. Ward and D. Giurco, *Fuel*, 2015, **141**, 120–135.
3 International Energy Agency, *World Energy Outlook*, 2024.
4 S. Batool, M. Langer, S. N. Myakala, M. Heiland, D. Eder, C. Streb and A. Cherevan, *Adv. Mater.*, 2024, **36**, 2305730.
5 F. Qureshi and M. Tahir, *Int. J. Hydrogen Energy*, 2024, **69**, 760–776.
6 B. Zhang and L. Sun, *Chem. Soc. Rev.*, 2019, **48**, 2216–2264.
7 T. J. Meyer, *Acc. Chem. Res.*, 1989, **22**, 163–170.
8 Q. Wang and K. Domen, *Chem. Rev.*, 2020, **120**, 919–985.
9 J. Wang, W. Cui, Q. Liu, Z. Xing, A. M. Asiri and X. Sun, *Adv. Mater.*, 2016, **28**, 215–230.
10 L. Wang, *Catalysts*, 2022, **12**, 919.
11 D. Costabel, A. Nabiyan, A. Chettri, F. Jacobi, M. Heiland, J. Guthmuller, S. Kupfer, M. Wächtler, B. Dietzek-Ivanšić, C. Streb, F. H. Schacher and K. Peneva, *ACS Appl. Mater. Interfaces*, 2023, **15**, 20833–20842.
12 J.-H. Shon and T. S. Teets, *ACS Energy Lett.*, 2019, **4**, 558–566.
13 V. Balzani, G. Bergamini, F. Marchioni and P. Ceroni, *Coord. Chem. Rev.*, 2006, **250**, 1254–1266.

 This journal is © The Royal Society of Chemistry 2025

Open Access Article. Published on 03 March 2025. Downloaded on 6/4/2025 9:50:52 AM.
This article is licensed under a Creative Commons Attribution 3.0 Unported Licence.

14 A. Juris, V. Balzani, F. Barigelletti, S. Campagna, P. Belser and A. von Zelewsky, *Coord. Chem. Rev.*, 1988, **84**, 85–277.
15 A. W. Adamson and J. N. Demas, *J. Am. Chem. Soc.*, 1971, **93**, 1800–1801.
16 M. Biner, H. B. Bürgi, A. Ludi and C. Röhr, *J. Am. Chem. Soc.*, 1992, **114**, 5197–5203.
17 M. P. Santoni, G. La Ganga, V. Mollica Nardo, M. Natali, F. Puntoriero, F. Scandola and S. Campagna, *J. Am. Chem. Soc.*, 2014, **136**, 8189–8192.
18 E. Deponti and M. Natali, *Dalton Trans.*, 2016, **45**, 9136–9147.
19 A. Rajagopal, F. Venter, T. Jacob, L. Petermann, S. Rau, S. Tschierlei and C. Streb, *Sustainable Energy Fuels*, 2019, **3**, 92–95.
20 Z. Huang, Z. Luo, Y. V. Geletii, J. W. Vickers, Q. Yin, D. Wu, Y. Hou, Y. Ding, J. Song, D. G. Musaev, C. L. Hill and T. Lian, *J. Am. Chem. Soc.*, 2011, **133**, 2068–2071.
21 B. Limburg, E. Bouwman and S. Bonnet, *Coord. Chem. Rev.*, 2012, **256**, 1451–1467.
22 B. Schwarz, J. Forster, M. K. Goetz, D. Yücel, C. Berger, T. Jacob and C. Streb, *Angew. Chem., Int. Ed.*, 2016, **55**, 6329–6333.
23 U. S. Akhtar, E. L. Tae, Y. S. Chun, I. C. Hwang and K. B. Yoon, *ACS Catal.*, 2016, **6**, 8361–8369.
24 J. A. Gilbert, D. S. Eggleston, W. R. Murphy, D. A. Geselowitz, S. W. Gersten, D. J. Hodgson and T. J. Meyer, *J. Am. Chem. Soc.*, 1985, **107**, 3855–3864.
25 F. Liu, J. J. Concepcion, J. W. Jurss, T. Cardolaccia, J. L. Templeton and T. J. Meyer, *Inorg. Chem.*, 2008, **47**, 1727–1752.
26 F. L. Huber, S. Amthor, B. Schwarz, B. Mizaikoff, C. Streb and S. Rau, *Sustainable Energy Fuels*, 2018, **2**, 1974–1978.
27 A. Lewandowska-Andralojc and D. E. Polyansky, *J. Phys. Chem. A*, 2013, **117**, 10311–10319.
28 B. Limburg, E. Bouwman and S. Bonnet, *ACS Catal.*, 2016, **6**, 5273–5284.
29 M. Sender, F. L. Huber, M. C. G. Moersch, D. Kowalczyk, J. Hniopek, S. Klingler, M. Schmitt, S. Kaufhold, K. Siewerth, J. Popp, B. Mizaikoff, D. Ziegenbalg and S. Rau, *ChemSusChem*, 2022, **15**, e202200708.
30 J. C. Hidalgo-Acosta, M. A. Méndez, M. D. Scanlon, H. Vrubel, V. Amstutz, W. Adamiak, M. Opallo and H. H. Girault, *Chem. Sci.*, 2015, **6**, 1761–1769.
31 T. R. Weaver, T. J. Meyer, S. A. Adeyemi, G. M. Brown, R. P. Eckberg, W. E. Hatfield, E. C. Johnson, R. W. Murray and D. Untereker, *J. Am. Chem. Soc.*, 1975, **97**, 3039–3048.
32 J. W. Jurss, J. J. Concepcion, J. M. Butler, K. M. Omberg, L. M. Baraldo, D. G. Thompson, E. L. Lebeau, B. Hornstein, J. R. Schoonover, H. Jude, J. D. Thompson, D. M. Dattelbaum, R. C. Rocha, J. L. Templeton and T. J. Meyer, *Inorg. Chem.*, 2012, **51**, 1345–1358.
33 A. Soupart, F. Alary, J. L. Heully, P. I. P. Elliott and I. M. Dixon, *Inorg. Chem.*, 2020, **59**, 14679–14695.
34 B. Durham, J. V. Caspar, J. K. Nagle and T. J. Meyer, *J. Am. Chem. Soc.*, 1982, **104**, 4803–4810.
35 A. Soupart, F. Alary, J.-L. Heully, P. I. P. Elliott and I. M. Dixon, *Coord. Chem. Rev.*, 2020, **408**, 213184.
36 T. M. McCormick, Z. Han, D. J. Weinberg, W. W. Brennessel, P. L. Holland and R. Eisenberg, *Inorg. Chem.*, 2011, **50**, 10660–10666.
37 D. Kim, D. R. Whang and S. Y. Park, *J. Am. Chem. Soc.*, 2016, **138**, 8698–8701.
38 Z. Y. Chen, D. Persson and C. Leygraf, *J. Electrochem. Soc.*, 2005, **152**, B526–B533.
39 M. Lämmle, B. Bagemihl, D. Nauroozi, L. Petermann, A. Pannwitz and S. Rau, *ChemPhotoChem*, 2022, **6**, e202200053.
40 A. Stumper, M. Lämmle, A. K. Mengele, D. Sorsche and S. Rau, *Eur. J. Inorg. Chem.*, 2018, 586–596.
41 A. K. Mengele, D. Weixler, A. Chettri, M. Maurer, F. L. Huber, G. M. Seibold, B. Dietzek, B. J. Eikmanns and S. Rau, *Chem. – Eur. J.*, 2021, **27**, 16840–16845.

Supplementary Information (SI) for Dalton Transactions.
This journal is © The Royal Society of Chemistry 2025

Electronic Supplementary Information

In situ Formation of an Active Oxygen Evolution Catalyst *via* Photodegradation of $[Ru(bpy)_3]^{2+}$

Marcel Langer,[a,b] Alexander K. Mengele,[b] Riccarda Müller,[b] Julius C. Wetzel,[a] Judith Mayer,[b] Sven Rau,*[,b] and Carsten Streb*[,a,b]

Table of Contents

1. Instrumentation 2
2. Experimental procedures 3
3. Influence of irradiation 6
4. Influence of the SOA concentration 6
5. Reference experiments 7
6. *Operando* UV-Vis studies 8
   a) Typical light-induced OER of the prototype system 8
   b) Typical light-induced OER of the prototype system under diluted conditions 9
   c) UV-Vis spectrum of the isolated green oily deposit obtained after a typical light-induced OER experiment 10
7. Influence of the solvent and solvent ratio in photocatalytic OER experiments 11
8. Effect of additional bipyridine (bpy) 12
   a) *Operando* UV-Vis study in the presence of 10 mM bpy 12
   b) O_2 quantification in photocatalytic OER experiments in the presence of additional bpy 13
   c) ATR-FTIR characterization of the colorless precipitate obtained after a photocatalytic OER experiment in the presence of additional bpy 13
9. Different ruthenium polypyridyl-based PS 14
10. Structural characterization data for ipphCOOH and PS4 16
11. Control experiment in purely aqueous media 21
12. Literature 22

1. Instrumentation

Attenuated total reflectance-Fourier-transform infrared spectroscopy (ATR-FTIR) was performed on a Bruker Alpha II equipped with an ATR Platinum Diamond unit. The data were recorded with 24 scans at a resolution of 4 cm^{-1}.

***Operando* UV-Vis absorbance spectroscopy** was performed on an Avantes AvaSpec-ULS2048CL detector unit coupled with an AVA AvaLight-DH-S-BAL light source. The light source, cuvette holder and detector were connected within the system *via* fiber optic cables. Standard quartz glass screw top emission cuvettes (d = 10.0 mm) were used for all inert *operando* UV-Vis measurements. At the beginning, UV-Vis spectra were recorded every second (in the case of the standard experiment 5 s) and after an appropriate time every 3 min (in the case of the standard experiment 5 min). The first 5 min of each measurement were carried out in the dark, followed by irradiation of the homogeneous solutions with blue LED light (λ_{max} = 470 nm, power density: *ca.* 50 mW cm^{-2}).

NMR spectra were recorded either on a Bruker Avance 400 MHz, a Bruker Avance 500 MHz or a Bruker Avance Neo 400 MHz. All spectra were measured at room temperature unless otherwise noted and referenced to the solvent residual peaks (2.50 ppm (quintet, ^{1}H-spectra) or 39.52 ppm (septet, ^{13}C-spectra) for DMSO-d_6; 1.94 ppm (quintet, ^{1}H-spectra) or 1.32 ppm (singlet, ^{13}C-spectra) for MeCN-d_3).

High resolution mass spectrometry (HRMS) was performed using a Fourier Transform Ion Cyclotron Resonance (FT-ICR) mass spectrometer solariX (Bruker Daltonics) equipped with a 7.0 T superconducting magnet and interfaced to an Apollo II Dual ESI/MALDI source. For all MALDI measurements *trans*-2-[3-(4-*tert*-butylphenyl)-2-methyl-2-propenylidene]malononitrile (DCTB) was used as matrix. Spectra were analyzed with the DataAnalysisViewer 4.2 from Bruker and transferred to Origin 2023b. Spectra simulation was performed with mMass Version 5.5.0 and transferred to Origin 2023b as well.

2. Experimental procedures

Chemicals: $[Ru(bpy)_3](PF_6)_2$ (PS1a), $Na_2S_2O_8$, acetonitrile (MeCN for HPLC; gradient grade ≥99.9%), *N,N`*-dimethylformamide (DMF for HPLC; gradient grade ≥99.9%), acetone and bipyridine (bpy) used for oxygen evolution reaction experiments as well as all chemicals used for synthesis in this work were purchased commercially from Sigma Aldrich Chemical Company LTD., Acros Organics B.V.B.A., Carl Roth GmbH & Co. KG and ABCR GmbH & Co. KG and were of reagent grade. The chemicals were used without further purification unless otherwise stated. Purified water in terms of Milli-Q-water (resistivity: 18.2 MΩcm at 298.15 K; Millipore) was used for all studies.

Ligand abbreviations: bpy = 2,2´-bipyridine; tbbpy = 4,4´-di-*tert*-butyl-2,2´-bipyridine; phen = 1,10-phenanthroline; dppz = dipyrido[3,2-*a*:2´,3´-*c*] phenazine; *p*-tolbip = 1-(4-methylphenyl)-3-benzyl-1*H*-imidazo[4,5-*f*][1,10] phenanthroline; ipphCOOH = 4-(1*H*-imidazol[4,5-*f*][1,10]phenanthroline-2-yl)benzoic acid.

Synthesis: 1,10-phenanthroline-5,6-dione,[1] $[RuCl_2(tbbpy)_2]$[2] and $[Ru(tbbpy)_2(p\text{-tolbip})](PF_6)_2$ (PS3)[3] were synthesized according to literature. $[Ru(tbbpy)_3](PF_6)_2$ (PS1b), $[Ru(tbbpy)_2(phen)](PF_6)_2$ (PS2) and $[Ru(tbbpy)_2(dppz)](PF_6)_2$ (PS5) were synthesized according to literature[4] with precipitation of the obtained Cl-containing complex by aqueous NH_4PF_6 solution.

ipphCOOH was synthesized by combining 700.2 mg 1,10-phenathroline-5,6-dione (3.33 mmol, 1.00 eq.), 501.0 mg 4-formyl benzoic acid (3.33 mmol, 1.00 eq.) and 3060 mg (39.7 mmol, 11.9 eq.) ammonium acetate in a 250 mL one-necked round bottom flask. Subsequently, 22 mL acetic acid was added to the flask and the mixture was heated inside a microwave for 30 min with 350 W under vigorous stirring. After cooling to room temperature, the yellow product was collected by filtration and washed several times with water and diethyl ether each. After collection of the yellow solid, it was dried at elevated temperatures (*ca.* 50 °C) under vacuum to yield 1.071 g (3.14 mmol, 94%) of the product, which is well soluble in DMSO.

^{1}H-NMR (400 MHz, r.t., DMSO-d_6): δ 13.86 (broad s, 1H), 9.04 – 9.00 (m, 2H), 8.89 (d, J = 8.1 Hz, 2H), 8.37 (d, J = 8.2 Hz, 2H), 8.16 (d, J = 8.3 Hz, 2H), 7.81 (dd, J = 7.7, 4.2 Hz, 2H).

^{13}C-NMR (101 MHz, r.t., DMSO-d_6): δ 172.13, 167.07, 149.49, 148.08, 143.79, 133.69, 131.53, 130.10, 129.78, 126.20, 123.42.

$[Ru(tbbpy)_2(ipphCOOH)](PF_6)_2$ (**PS4**) was synthesized as follows: In a 250 mL one-necked round bottom flask 200.5 mg $[(tbbpy)_2RuCl_2]$ (0.283 mmol, 1.00 eq.) and 107.2 mg ipphCOOH (0.315 mmol, 1.10 eq.) were dispersed in a mixture of 60 mL EtOH and 20 mL H_2O. The suspension was refluxed for 18 h at 85 °C thereby forming a clear red solution. After removal of EtOH by rotary evaporation, the crude product was precipitated by the addition of a solution of 585 mg NH_4PF_6 dissolved in 10 mL water. Upon filtering off the obtained solid and washing the crude product several times with water and diethyl ether, the red solid was dissolved in DCM, filtered again through celite and then the solvent was removed in vacuo. Finally, 311 mg of the product were obtained (0.246 mmol, 87%).

^{1}H-NMR (500 MHz, 340 K, MeCN-d_3): δ 8.91 (d, J = 8.0 Hz, 2H), 8.53 (d, J = 1.8 Hz, 2H), 8.49 (d, J = 1.7 Hz, 2H), 8.23 (d, J = 6.3 Hz, 2H), 8.11 (d, J = 6.8 Hz, 2H), 7.96 (d, J = 5.1 Hz, 2H), 7.73 – 7.67 (m, 2H), 7.53 (d, J = 5.7 Hz, 2H), 7.49 (dd, J = 6.0, 2.0 Hz, 2H), 7.30 – 7.20 (m, 2H), 1.47 (s, 18H), 1.37 (s, 18H).

^{13}C-NMR (101 MHz, r.t., MeCN-d_3 + TFA): δ 166.71, 164.07, 163.94, 158.05, 157.88, 153.98, 152.36, 152.10, 150.67, 148.45, 135.88, 132.17, 131.81, 129.72, 128.32, 128.17, 127.20, 125.83, 125.57, 122.72, 122.64, 121.88, 36.47, 36.37, 30.56, 30.46.

HRMS (MALDI-FT-ICR; [M] = $C_{56}H_{60}F_{12}N_8O_2P_2Ru$): calcd. for $[M\text{-}2PF_6\text{-}H]^+$ 977.3817, found 977.3821; calcd. for $[M\text{-}PF_6]^+$ 1123.3546, found 1123.3541; calcd. for $[2M\text{-}2PF_6\text{-}H]^+$ 2245.7018, found 2245.7081; calcd. for $[2M\text{-}PF_6]^+$ 2391.6738, found 2391.6710; calcd. for $[3M\text{-}2PF_6\text{-}H]^+$ 3514.0214, found 3514.0305; calcd. for $[3M\text{-}PF_6\text{-}H]^+$ 3658.9856, found 3659.0278.

All high-resolution MS data and NMR data for the structural characterization of ipphCOOH and $[Ru(tbbpy)_2(ipphCOOH)](PF_6)_2$ are provided in chapter 10 of this document.

Oxygen detection: *FireStingO2 optical oxygen meter* (Pyroscience, Germany) and oxygen-sensitive optical sensor spots (*OXSP5*, with optical isolation) were used for the simultaneous quantification of oxygen in the solution and gas phase. The sensor spots were glued to the inner glass wall of a screw-capped, hermetically sealed vial using a transparent silicone glue (*SPGLUE*). Each sensor spot was calibrated separately by a two-point calibration. The O_2 sensor in the gas phase was calibrated against ambient air and argon atmosphere. The sensor in solution was calibrated against the deaerated and untreated, air-equilibrated solvent mixture MeCN/H_2O (9:1, v/v). Prior to light-driven OER studies with different solvents, the sensor spots were recalibrated to the respective solvent mixture. The molar amount of oxygen was calculated based on the molar amounts of oxygen detected in the solution (in µM) and *via* the ideal gas equation ($c = p\ R^{-1}T^{-1}$) for the oxygen partial pressure determined in the gas phase (in mbar). The total amounts of O_2 were calculated using the following equation: $((c_{gas}V_{gas})(c_{solution}V_{solution}))\ V_{total}^{-1}$. For further details on the oxygen sensor equipment and the O_2 quantification set up, the reader is referred to the literature provided by Streb, Rau and co-workers.[5]

Typical light-driven OER experiments: 5 mL deaerated MeCN/H_2O (9:1, v/v) containing 1 mM of the respective PS and 10 mM $Na_2S_2O_8$ were prepared under an inert atmosphere and in the exclusion of light. A hermetically sealed vial (diameter: 12.75 ± 0.25 mm, length: 99.00 ± 0.50 mm) equipped with two fiber-optic fluorescent oxygen sensor spots was used as the reaction vessel. The vial was mounted in a custom-built air-cooled photoreactor (≈ 298 K), and oxygen was detected *in operando* in the solution and in the gas phase (see Figure S1). The first 5 min of each measurement were performed in the dark, followed by irradiation of the homogeneous solutions with blue LED light (λ_{max} = 470 nm, power density: *ca.* 50 mW cm^{-2}). The photocatalytic OER experiments were conducted under moderate magnetic stirring (250 rpm).

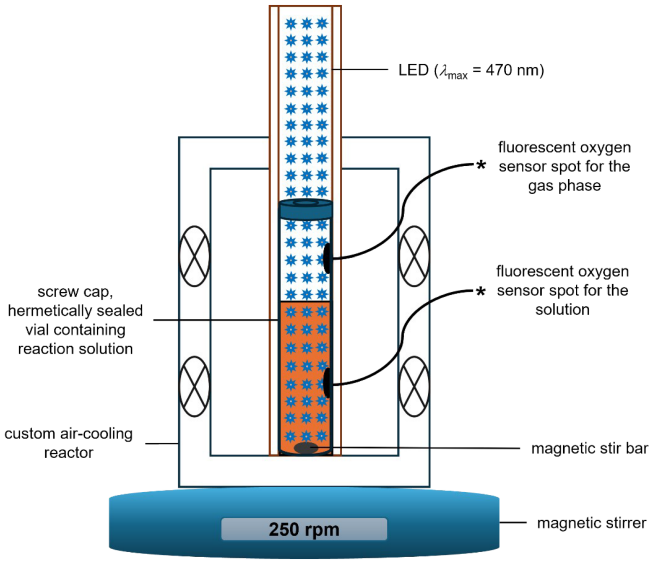


Figure S1: Schematic illustration of the setup used for light-driven OER studies. O_2 evolution was quantified *in operando* in a custom-built air-cooled photoreactor *via* fiber-optic fluorescent oxygen sensor spots in the solution and the gas phase simultaneously.

3. Influence of irradiation

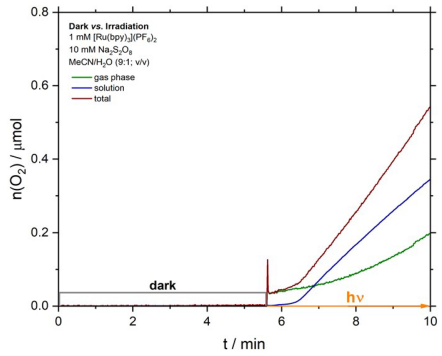


Figure S2: Light-driven OER profile in the gas phase (green), in solution (blue) and in total (red) using LED light (λ_{max} = 470 nm, power density: *ca.* 50 mW cm^{-2}): Negligible amount of O_2 under dark conditions for t = 0-5 min and strong O_2 evolution upon irradiation, providing evidence for the necessity of photons (t > 5 min) to operate light-driven oxygen evolution by the prototype OER system with $[Ru(bpy)_3](PF_6)_2$ (1 mM) and $Na_2S_2O_8$ (10 mM) in MeCN/H_2O (9:1, v/v).

4. Influence of the SOA concentration

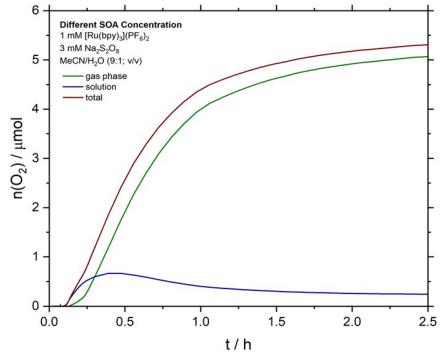


Figure S3: Influence of the SOA concentration on the amount of O_2 evolved during light-driven OER in the gas phase (green), in solution (blue) and in total (red) using $[Ru(bpy)_3](PF_6)_2$ (1 mM) and $Na_2S_2O_8$ (3 mM) in MeCN/H_2O (9:1, v/v); LED light (λ_{max} = 470 nm, power density: *ca.* 50 mW cm^{-2}): Significantly reduced O_2 evolution upon irradiation indicates a stoichiometric equivalence between oxygen evolved and oxidation equivalents from the SOA.

5. Reference experiments

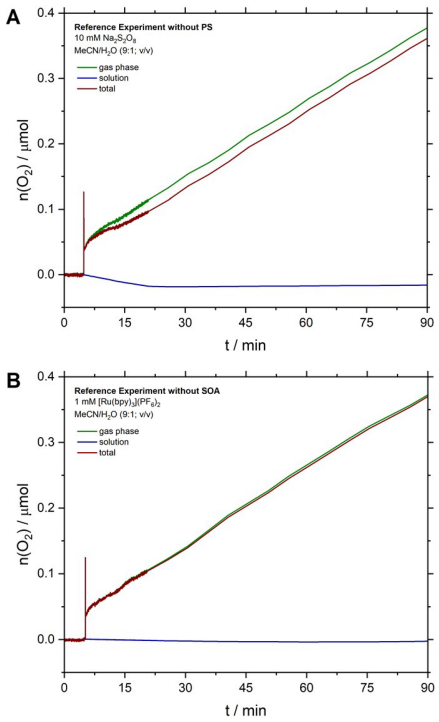


Figure S4: Reference measurements and their light-driven OER profiles in the gas phase (green), in solution (blue) and in total (red) using LED light (λ_{max} = 470 nm, power density: *ca.* 50 mW cm^{-2}): **A)** Negligible O_2 evolution upon irradiation of a PS-free solution containing only $Na_2S_2O_8$ (10 mM) in MeCN/H_2O (9:1, v/v). **B)** Negligible O_2 evolution upon irradiation of an SOA-free solution containing only $[Ru(bpy)_3](PF_6)_2$ (1 mM) in MeCN/H_2O (9:1, v/v). Note that the blue LED might have a significant influence on the detection response of the oxygen sensor spots, resulting in a light-induced signal drift for the gas phase (green curve) and a decreasing signal intensity below zero for the solution (blue curve), as can be observed in both figure panels A and B.

6. *Operando* UV-Vis studies

a) Typical light-induced OER of the prototype system

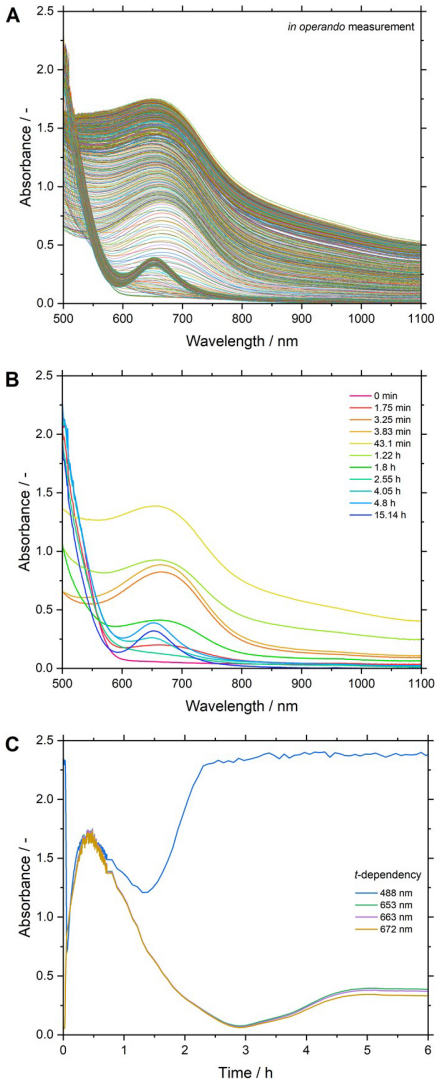


Figure S5: *Operando* UV-Vis spectra of the prototype light-driven OER system with $[Ru(bpy)_3](PF_6)_2$ (1 mM) and $Na_2S_2O_8$ (10 mM) in $MeCN/H_2O$ (9:1, v/v) using LED light (λ_{max} = 470 nm, power density: *ca.* 50 mW cm^{-2}): **A)** Common representation of all UV-Vis spectra recorded in the experiment. **B)** Change of the UV-Vis spectrum on a selected time scale of the entire UV-Vis spectrum above. **C)** Time-dependent change of selected electronic transition bands.

b) Typical light-induced OER of the prototype system under diluted conditions

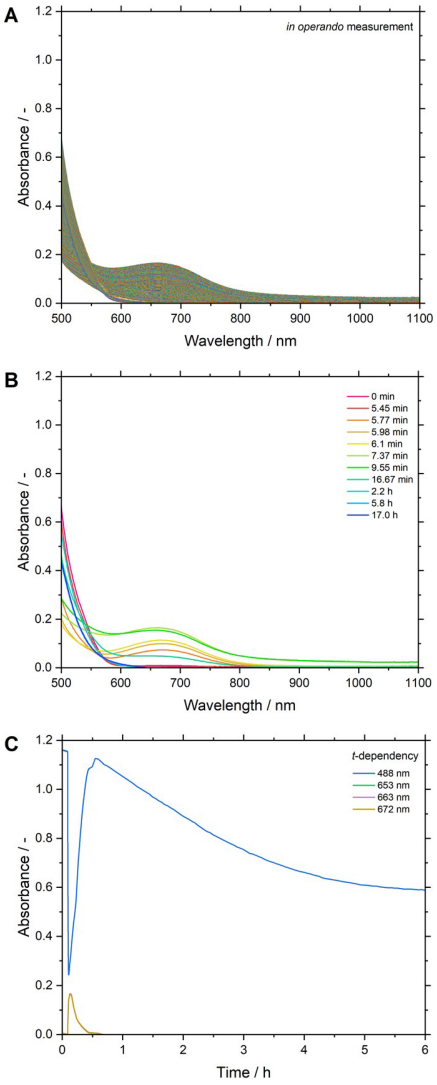


Figure S6: *Operando* UV-Vis spectra of the prototype light-driven OER system under diluted conditions with $[Ru(bpy)_3](PF_6)_2$ (0.1 mM) and $Na_2S_2O_8$ (1 mM) in $MeCN/H_2O$ (9:1, v/v) using LED light (λ_{max} = 470 nm, power density: *ca*. 50 mW cm^{-2}): **A)** Common representation of all UV-Vis spectra recorded in the experiment. **B)** Change of the UV-Vis spectrum on a selected time scale of the entire UV-Vis spectrum above. **C)** Time-dependent change of selected electronic transition bands.

c) UV-Vis spectrum of the isolated green oily deposit obtained after a typical light-induced OER experiment

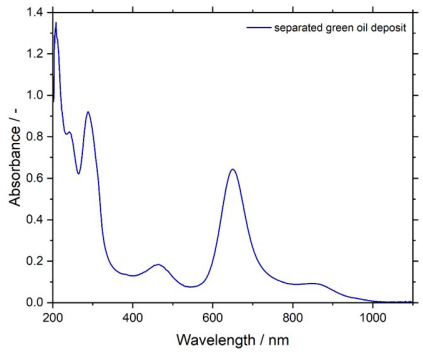


Figure S7: UV-Vis spectrum of the separated green oily deposit obtained after typical light-driven OER of the prototype OER system. Electronic transitions at 464 nm and 650 nm indicate the simultaneous formation of both orange Ru_2(III,IV) and blue Ru_2(III,III) PS dimers.[6] Further electronic transitions can be observed at 208 nm and 288 nm (LC, $\pi\pi^*_{bpy}$), 242 nm (MLCT) and two shoulders at 383 nm and 854 nm ($d\pi d\pi$).

7. Influence of the solvent and solvent ratio in photocatalytic OER experiments

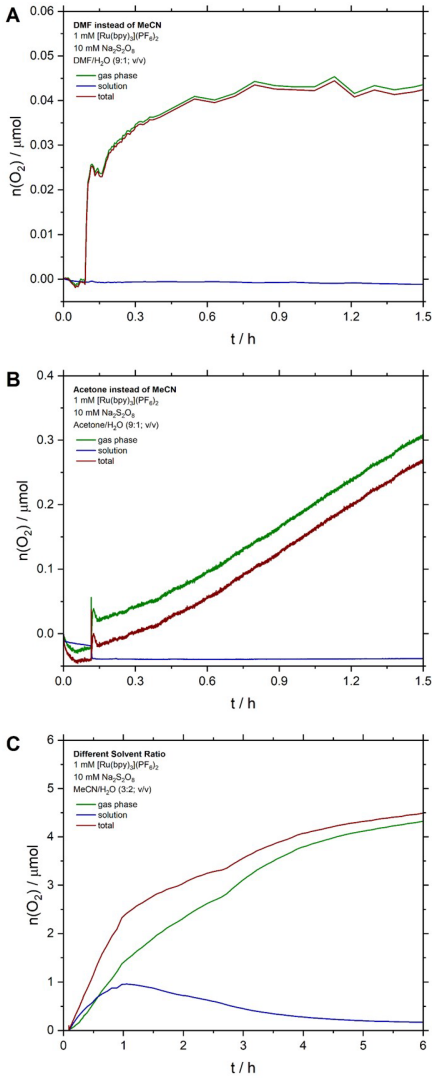


Figure S8: Influence of the solvent and solvent ratio on the amount of O_2 evolved during light-driven OER in the gas phase (green), in solution (blue) and in total (red) under the following conditions: $[Ru(bpy)_3](PF_6)_2$ (1 mM) and $Na_2S_2O_8$ (10 mM) in X/H_2O (9:1, v/v) using LED light (λ_{max} = 470 nm, power density: *ca*. 50 mW cm^{-2}): **A)** Negligible O_2 evolution upon irradiation for X = DMF. **B)** Negligible O_2 evolution upon irradiation for X = acetone. **C)** Significantly reduced O_2 evolution upon irradiation using an increased water content with MeCN/H_2O 3:2 (v/v). Note that the blue LED might have a significant influence on the detection response of the oxygen sensor spots, resulting in a light-induced signal drift for the gas phase (green curve) and a decreasing signal intensity below zero for the solution (blue curve), as can be observed in the figure panels A and B.

8. Effect of additional bipyridine (bpy)

a) *Operando* UV-Vis study in the presence of 10 mM bpy

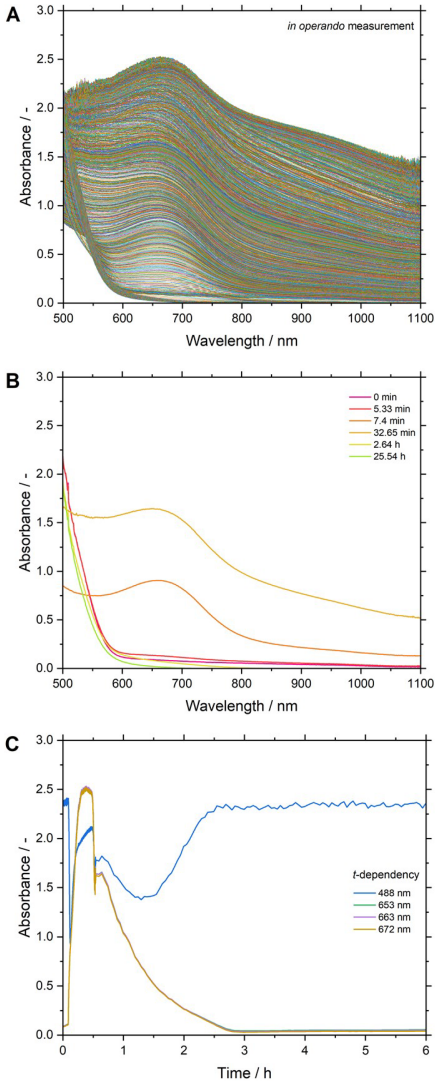


Figure S9: *Operando* UV-Vis spectra showing the effect of additional ligand bpy (10 mM) on the prototype light-driven OER system with $[Ru(bpy)_3](PF_6)_2$ (1 mM) and $Na_2S_2O_8$ (10 mM) in $MeCN/H_2O$ (9:1, v/v) using LED light (λ_{max} = 470 nm, power density: *ca.* 50 mW cm^{-2}): **A)** Common representation of all UV-Vis spectra recorded in the experiment. **B)** Change of the UV-Vis spectrum on a selected time scale of the entire UV-Vis spectrum above. **C)** Time-dependent change of selected electronic transition bands.

b) O_2 quantification in photocatalytic OER experiments in the presence of additional bpy

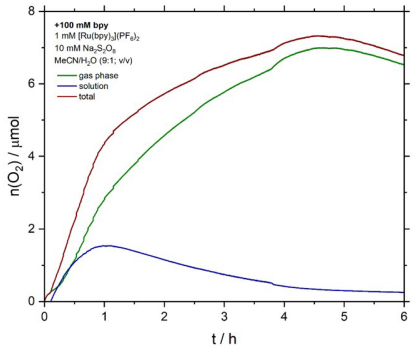


Figure S10: Light-driven OER profile in the gas phase (green), in solution (blue) and in total (red) showing the effect of the additional ligand bpy on the O_2 evolution of the prototype light-driven OER system with $[Ru(bpy)_3](PF_6)_2$ (1 mM) and $Na_2S_2O_8$ (10 mM) in $MeCN/H_2O$ (9:1, v/v) using LED light (λ_{max} = 470 nm, power density: *ca*. 50 mW cm^{-2}). Additional 100 mM bpy results in a significantly reduced amount of O_2 evolved during irradiation.

c) ATR-FTIR characterization of the colorless precipitate obtained after a photocatalytic OER experiment in the presence of additional bpy

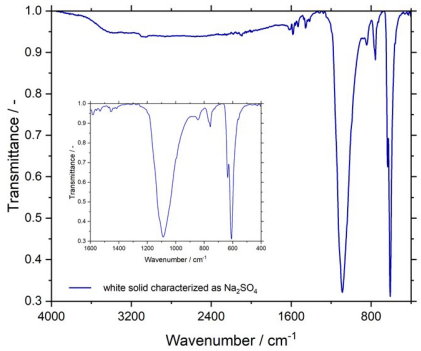
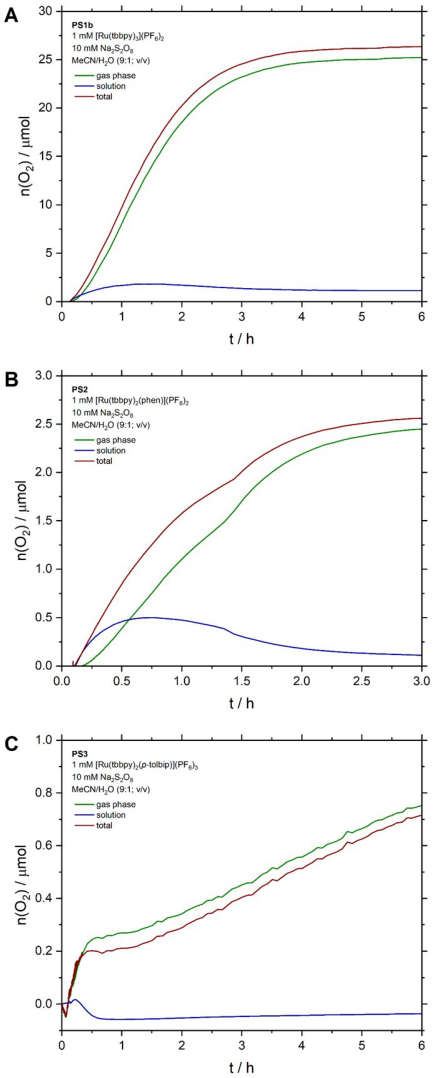


Figure S11: ATR-FTIR spectrum of the separated colorless solid that was obtained after light-driven OER catalysis in the presence of additional 100 mM bpy (conditions: 1 mM $[Ru(bpy)_3](PF_6)_2$, 10 mM $Na_2S_2O_8$, $MeCN/H_2O$ 9:1 (v/v), LED light with λ_{max} = 470 nm and power density *ca*. 50 mW cm^{-2}). Characteristic IR vibrational modes at 1087 cm^{-1}, 635 cm^{-1} and 610 cm^{-1} indicate the formation of sodium sulfate (Na_2SO_4).[7]

9. Different ruthenium polypyridyl-based PS



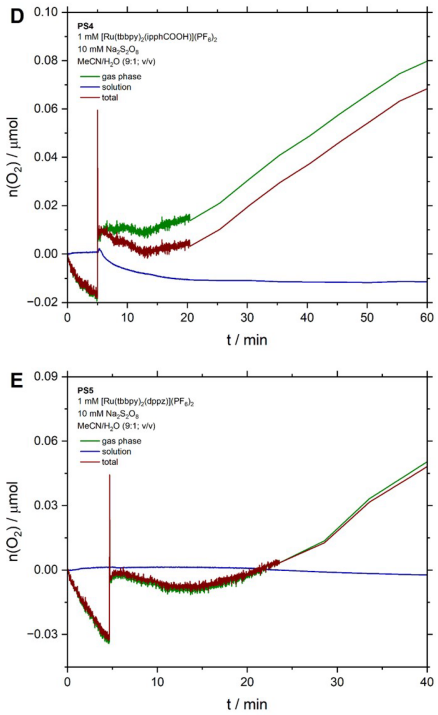


Figure S12: Light-driven OER profile in the gas phase (green), in solution (blue) and in total (red) using various ruthenium polypyridyl-based PS (1 mM) and $Na_2S_2O_8$ (10 mM) in MeCN/H_2O (9:1, v/v), as well as LED light (λ_{max} = 470 nm, power density: *ca.* 50 mW cm^{-2}): **A)** [Ru(tbbpy)$_3$](PF$_6$)$_2$ (PS1b): Slightly increased O_2 evolution upon irradiation compared to the prototype system with [Ru(bpy)$_3$](PF$_6$)$_2$ (PS1a). **B)** [Ru(tbbpy)$_2$(phen)](PF$_6$)$_2$ (PS2): Significantly reduced O_2 evolution upon irradiation. **C)** [Ru(tbbpy)$_2$(*p*-tolbip)](PF$_6$)$_3$ (PS3): Strongly reduced O_2 evolution upon irradiation. **D)** [Ru(tbbpy)$_2$(ipphCOOH)](PF$_6$)$_2$ (PS4): Negligible O_2 evolution upon irradiation. **E)** [Ru(tbbpy)$_2$(dppz)](PF$_6$)$_2$ (PS5): Negligible O_2 evolution upon irradiation.

10.Structural characterization data for ipphCOOH and PS4

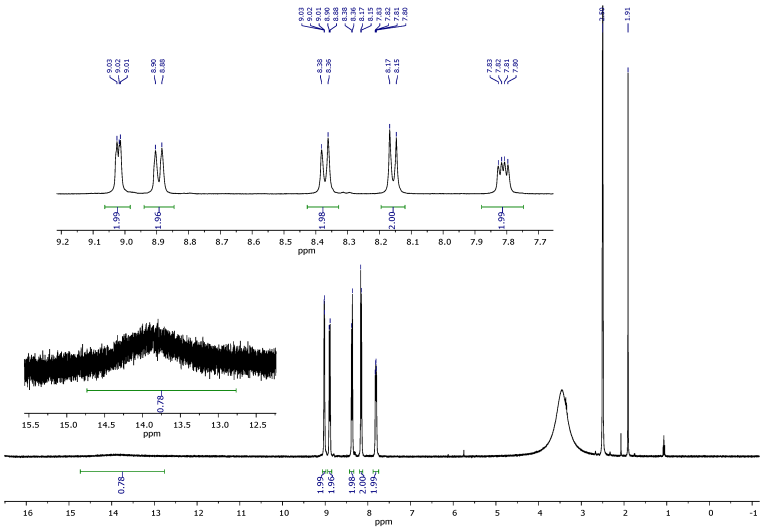


Figure S13: ^{1}H-NMR spectrum of ipphCOOH in DMSO-d_6 at room temperature; the peak at 1.91 ppm can be assigned to residual acetic acid.

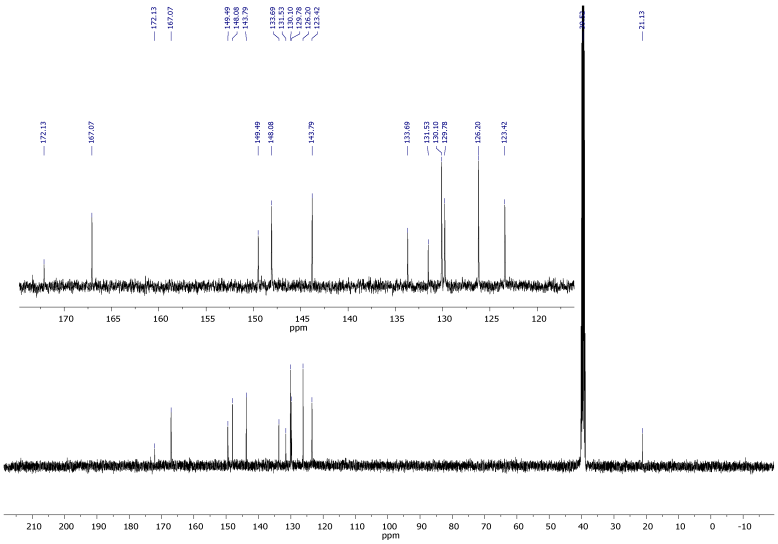


Figure S14: ^{13}C-NMR spectrum of ipphCOOH in DMSO-d_6 at room temperature; the peak at 21.13 ppm can be assigned to residual acetic acid. Only eleven of potential twelve signals between 100 and 200 ppm are observed, indicating peak overlap in one case.

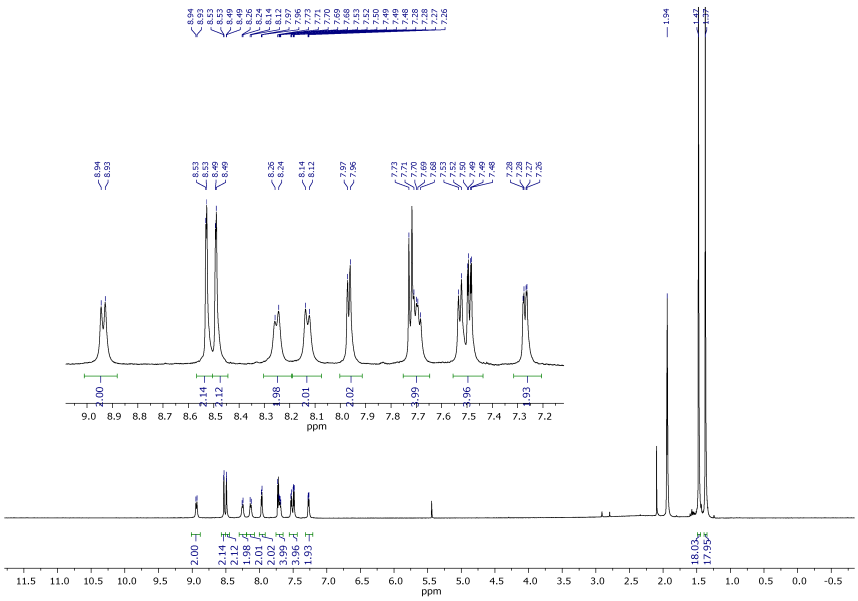


Figure S15: ^{1}H-NMR spectrum of $[Ru(tbbpy)_2(ippCOOH)](PF_6)_2$ in MeCN-d_3 at 340 K.

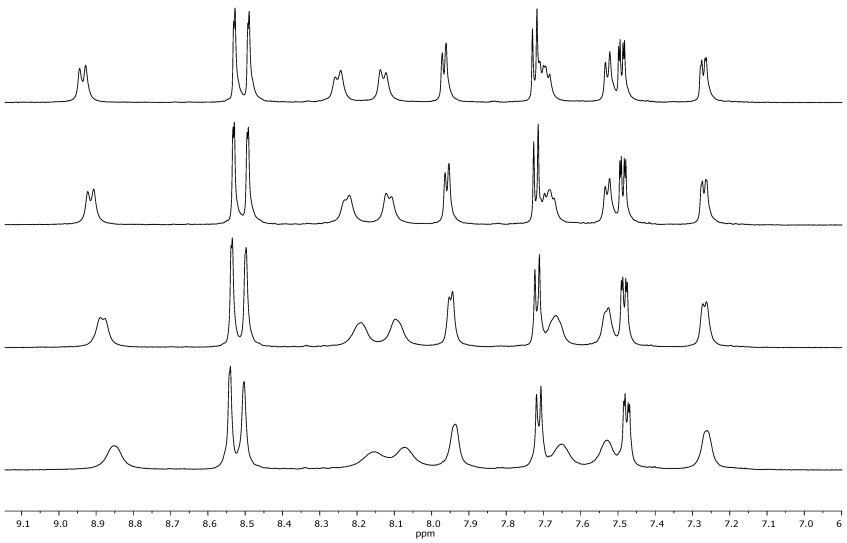


Figure S16: Series of *T*-dependent ^{1}H-NMR spectra of $[Ru(tbbpy)_2(ippCOOH)](PF_6)_2$ in MeCN-d_3. Temperatures from top to bottom: 340 K, 330 K, 315 K, 300 K.

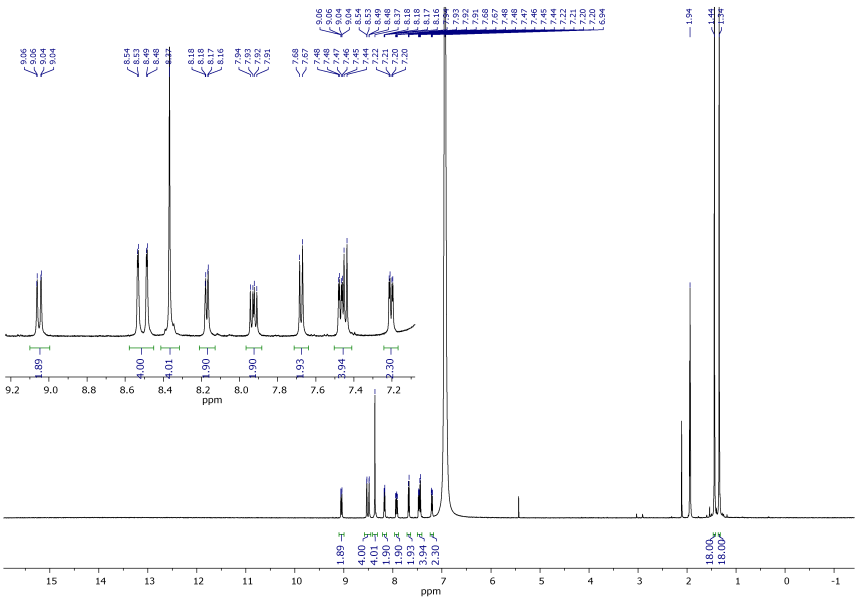


Figure S17: ^{1}H-NMR spectrum of $[Ru(tbbpy)_2(ipphCOOH)](PF_6)_2$ in MeCN-d_3 at room temperature in the presence of a small amount TFA-d.

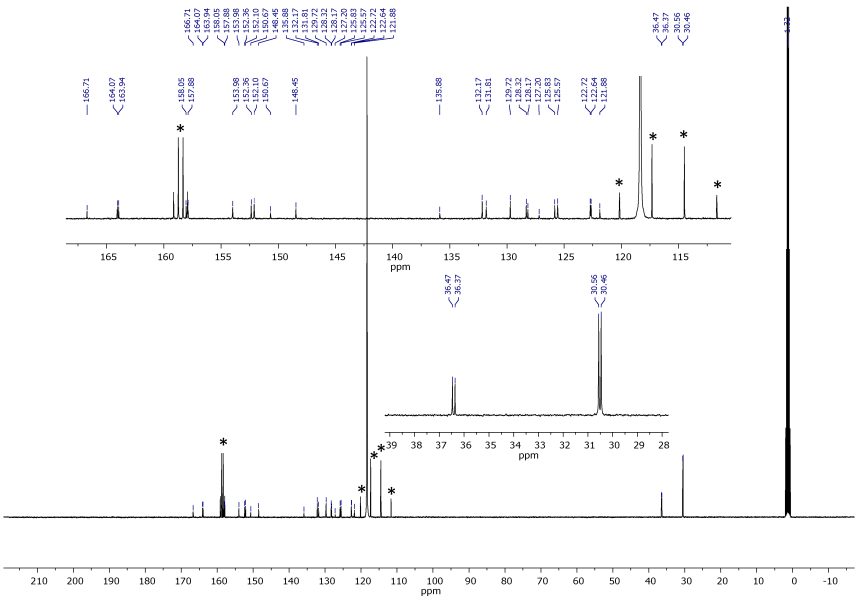


Figure S18: ^{13}C-NMR spectrum of $[Ru(tbbpy)_2(ipphCOOH)](PF_6)_2$ in MeCN-d_3 at room temperature with some TFA added to improve the spectrum. Peaks assigned with an asterisk are due to TFA (see Figure S19).

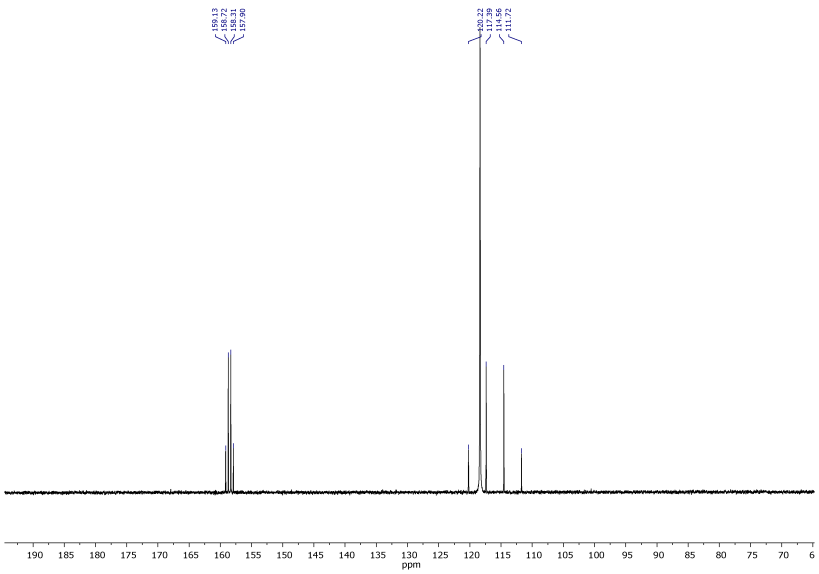


Figure S19: ^{13}C-NMR spectrum of TFA in MeCN-d_3 at room temperature.

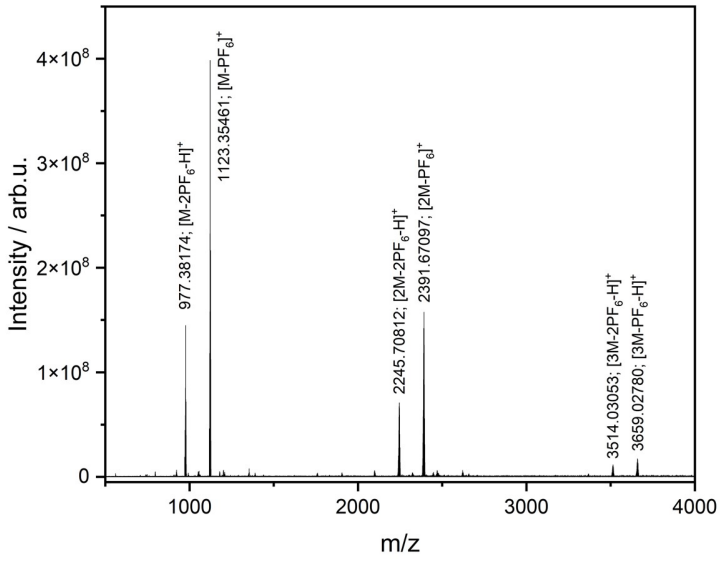


Figure S20: Full high-resolution MALDI-MS spectrum of $[Ru(tbbpy)_2(ipphCOOH)](PF_6)_2$ with peak assignments and detailed m/z values of the respective highest peak.

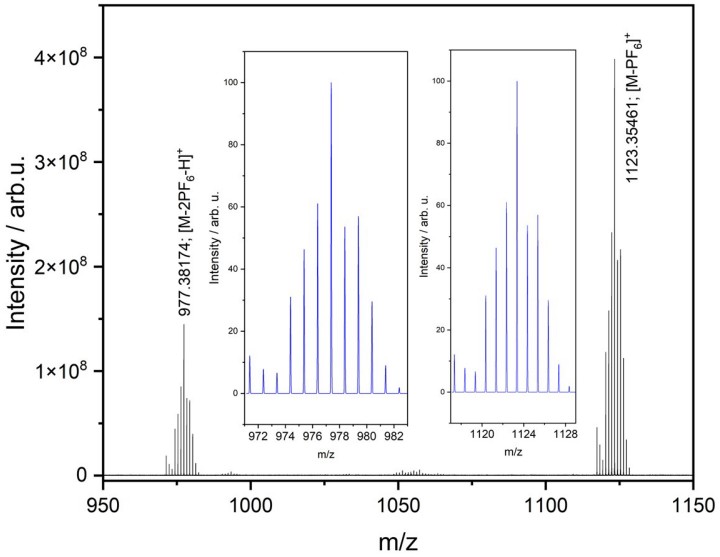


Figure S21: High-resolution MALDI-MS spectrum of $[Ru(tbbpy)_2(ipphCOOH)](PF_6)_2$ in the range of 950-1150 m/z depicting the experimentally obtained MS peaks of highest intensity as well as modelled MS peaks as insets (blue spectra).

11.Control experiment in purely aqueous media

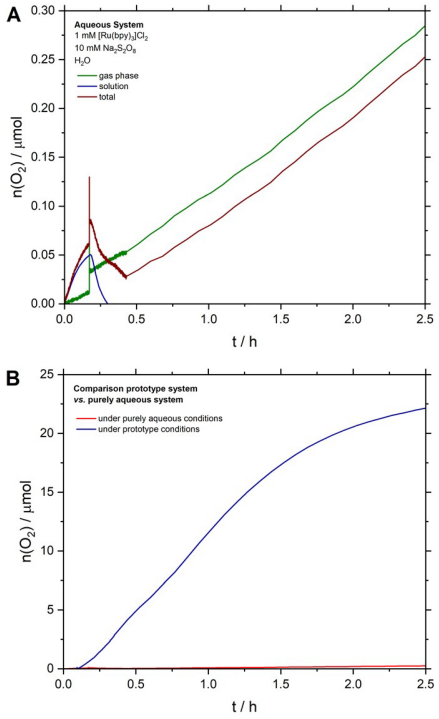


Figure S22: Control experiment: **A)** Light-driven OER profile in the gas phase (green), in solution (blue) and in total (red) for the control experiment in purely aqueous media using the OER system with $[Ru(bpy)_3]Cl_2$ (1 mM) and $Na_2S_2O_8$ (10 mM) in H_2O; LED light (λ_{max} = 470 nm, power density: *ca.* 50 mW cm^{-2}). **B)** Comparison of the total amounts of O_2 evolved in light-driven OER under purely aqueous conditions with $[Ru(bpy)_3]Cl_2$ (1 mM) and $Na_2S_2O_8$ (10 mM) in H_2O (red) and under the prototype conditions reported with $[Ru(bpy)_3](PF_6)_2$ (1 mM) and $Na_2S_2O_8$ (10 mM) in MeCN/H_2O (9:1, v/v) using LED light (λ_{max} = 470 nm, power density: *ca.* 50 mW cm^{-2}) (blue). Reduced O_2 evolution indicates that the underlying processes of light-induced PS degradation and formation of catalytically active ruthenium dimer species are significantly faster under the reported conditions for the OER prototype system.

12.Literature

1 C. Wang, L. Lystrom, H. Yin, M. Hetu, S. Kilina, S. A. McFarland and W. Sun, *Dalton Trans.*, 2016, **45**, 16366–16378.

2 S. Rau, B. Schäfer, A. Grüßing, S. Schebesta, K. Lamm, J. Vieth, H. Görls, D. Walther, M. Rudolph, U. W. Grummt and E. Birkner, *Inorganica Chim. Acta*, 2004, **357**, 4496–4503.

3 M. Lämmle, B. Bagemihl, D. Nauroozi, L. Petermann, A. Pannwitz and S. Rau, *ChemPhotoChem*, 2022, **6**, e202200053.

4 A. K. Mengele, D. Weixler, A. Chettri, M. Maurer, F. L. Huber, G. M. Seibold, B. Dietzek, B. J. Eikmanns and S. Rau, *Chem. Eur. J.*, 2021, **27**, 16840–16845.

5 F. L. Huber, S. Amthor, B. Schwarz, B. Mizaikoff, C. Streb and S. Rau, *Sustain. Energy Fuels*, 2018, **2**, 1974–1978.

6 U. S. Akhtar, E. L. Tae, Y. S. Chun, I. C. Hwang and K. B. Yoon, *ACS Catal.*, 2016, **6**, 8361–8369.

7 Z. Y. Chen, D. Persson and C. Leygraf, *J. Electrochem. Soc.*, 2005, **152**, B526–B533.

Acknowledgement

This page has been removed for reasons of data protection.

This page has been removed for reasons of data protection.

Declaration of Honesty in Academic Work

This scientific work was carried out in the period from January 2021 to March 2022 at the Institute of Inorganic Chemistry I at Ulm University and finalized between April 2022 and June 2025 at the Department of Chemistry at Johannes Gutenberg University Mainz under the chairmanship of [redacted].

I, Marcel Langer, hereby declare on my honor that I have written this dissertation entitled "Embedding Molecular Light-Driven Catalysts in Soft Matter" independently and solely on my own, that I have not used any sources and aids other than those listed in the references and that I have identified and clarified all parts in the dissertation that have been taken literally or analogously from the literature or the Internet. Note that "DeepL Translate" and "DeepL Write" were used throughout this work to help make grammatical corrections and improve readability. The principles of good scientific practice of the Johannes Gutenberg University Mainz in the currently valid version were observed.

I further declare that I have not yet submitted this scientific work in the same or a similar form to any other German university, foreign university or comparable institution for the award of another academic degree or qualification. I have neither successfully or unsuccessfully completed a doctorate or a comparable graduation procedure in this doctoral subject with the doctoral degree "Dr. rer. nat.", nor have I successfully applied for admission to a doctoral examination or a comparable graduation procedure in the subject of this doctorate "Dr. rer. nat." at the Johannes Gutenberg University Mainz or another university with the right to award doctorates. I further affirm that I have not made use of any paid assistance from third parties, in particular no doctoral advice or mediation.

I am aware of the current doctoral degree regulations of Johannes Gutenberg University Mainz dated October 18, 2021 in the version of February 17, 2025 for the acquisition of the degree "Dr. rer. nat.". I hereby apply for the doctoral degree in natural science from Johannes Gutenberg University Mainz for the first time.

Place, Date Marcel Langer

Curriculum Vitae

This page has been removed for reasons of data protection.